Physics of the Solid State, Vol. 43, No. 11, 2001, pp. 1999–2002. Translated from Fizika Tverdogo Tela, Vol. 43, No. 11, 2001, pp. 1921–1924.
Original Russian Text Copyright © 2001 by Pokatilov.

METALS AND SUPERCONDUCTORS

Hyperfine Interaction Parameters of the $ScFe_2$ Laves Alloy with $MgZn_2$ Hexagonal Structure

V. S. Pokatilov

Moscow State Institute of Radio Engineering, Electronics, and Automation, pr. Vernadskogo 78, Moscow, 117454 Russia
e-mail: pokat@cc.nifhi.ac.ru

Received March 30, 2001; in final form, April 24, 2001

Abstract—This paper reports on NMR measurement of hyperfine fields, enhancement factors, and quadrupole splitting for ^{45}Sc nuclei in the $ScFe_2$, $Sc_{0.95}Fe_{2.05}$, and $ScFe_{1.97}Al_{0.03}$ alloys at room temperature and 77 K. The NMR spectra are studied, and the hyperfine-field shifts at ^{45}Sc nucleus sites in the above alloys, caused by Fe substituting for Sc and Al, for Fe in the nearest Sc coordination shells, are determined. © *2001 MAIK "Nauka/Interperiodica".*

1. INTRODUCTION

Intermetallic Laves compounds of RFe_2 stoichiometric composition (where R stands for Sc, Y, Zr, and other 3*d*, 4*d*, and 5*d* elements) have recently been a subject of intense investigation. These alloys are of considerable interest from the standpoint both of the phenomena responsible for their magnetic properties (for instance, the existence of magnetic moments and the magnitude of these moments for the R atoms) and of the application potential involved. These alloys are usually synthesized in one of the following crystalline states: $MgCu_2$-type cubic ($C15$) and $MgNi_2$ ($C36$) and $MgZn_2$ ($C14$) hexagonal [1]. The $ScFe_2$ compounds exhibit polymorphism and can exist in the three above crystalline states [1]. The magnetic properties of the $ScFe_2$ alloys have been very poorly studied in comparison with those of the other RFe_2 alloys (R = Y, Zr, Nb, or a rare-earth element). Some data exist on the hyperfine interaction (HFI) parameters for ^{57}Fe nuclei measured using the Mössbauer technique in the $ScFe_2$ hexagonal alloy ($C14$-type structure) [2, 3] and for ^{57}Fe and ^{45}Sc nuclei determined using the NMR method in the $ScFe_2$ hexagonal alloy ($C36$ structure) [4–6] and cubic ($C15$) alloy [4–6]. The NMR spectra of these Laves alloys exhibit additional unresolved peaks and other features, whose nature remains unclear [4–6]. Because single-phase alloys of this compound are difficult to prepare, the presence of other phases does not permit one to study some fine effects in the spectra, which are due, for instance, to small deviations from stoichiometry and to the specific conditions in which samples of the alloys under study are synthesized, as well as to the influence of impurity *s*, *p*, or *d* atoms on the HFI parameters.

This paper reports on a measurement of the NMR parameters for ^{45}Sc nuclei in single-phase $ScFe_2$, $Sc_{0.95}Fe_{2.05}$, and $ScFe_{1.97}Al_{0.03}$ intermetallic alloys with $C14$ hexagonal structure.

2. SAMPLES AND EXPERIMENTAL TECHNIQUE

Samples of the Laves alloys $ScFe_2$, $Sc_{0.95}Fe_{2.05}$, and $ScFe_{1.97}Al_{0.03}$ were prepared by melting high-purity metals in an arc furnace in a high-purity argon environment. The ingots were crushed and remelted several times. Ingots of the $ScFe_2$ and $ScFe_{1.97}Al_{0.03}$ alloys were additionally remelted at a pressure of ~7 GPa, and an ingot of $Sc_{0.95}Fe_{2.05}$ was annealed at 1273 K for 48 h and quenched in water to preclude polymorphic transformations. X-ray diffraction measurements of powder samples showed them to be single phase and to have a $MgZn_2$ hexagonal structure. The lattice constants of the samples of the alloys studied were a = 4.964 Å and c = 8.106 Å.

The ^{45}Sc NMR spectra were measured using the pulsed technique at 293 and 77 K. The amplitudes of rf pulses (exciting an echo) and of echo signals were calibrated to take into account the influence of their amplification in the transmitting and receiving spectrometer units, as well as the diode regime of measurement at each frequency. During the measurements, the rf pulse amplitude was maintained constant (close to the echo maximum within the frequency range covered). In these conditions, the true NMR spectrum corresponding to the hyperfine-field (resonant-frequency) distribution was obtained by normalizing the measured NMR spectrum through the cubed measurement frequency f^3 [7]. When obtaining NMR spectra of the ^{45}Sc nuclei in $ScFe_2$-based alloy samples, the exciting rf pulse duration was 1 μs and that for the ^{57}Fe nuclei in iron was 10 μs. We also measured the rf magnetic field h_1 in the resonance coil used to obtain the ^{45}Sc NMR spectra, for which purpose proton resonance in an aqueous $CuSO_4$ solution in a corresponding magnetic field and 90° and 180° rf pulses were employed.

3. RESULTS AND DISCUSSION

Figure 1 presents the ^{45}Sc NMR spectra of the samples under study. The NMR spectrum of the $ScFe_2$ alloy (Fig. 1a) measured at room temperature has a maximum at 63.0 MHz corresponding to a hyperfine field B_1 = 6.09 T. At 77 K, the maximum of the spectrum of this alloy lies at 73.68 MHz, so that B_1 = 7.125 T (Fig. 1b). There are unresolved lines on the high-frequency side of the spectrum of this alloy. The intensity of these additional lines in the spectrum of the $Sc_{0.95}Fe_{2.05}$ alloy with an excess of Fe increases (Fig. 1c). The ^{45}Sc NMR spectrum of the $ScFe_2$ alloy shifts toward lower frequencies in an external magnetic field of 5 kOe, and, hence, the hyperfine field at the ^{45}Sc nucleus sites is negative (Fig. 1b).

Sc atoms occupy equivalent positions in the $MgZn_2$ structure and are surrounded by 12 Fe and 4 Sc atoms, which make up a 16-corner Laves polyhedron around the scandium atom [8]. The Fe atoms sit at two inequivalent crystallographic sites, Fe1 and Fe2, the occupancies of these sites being in a 3 : 1 ratio. A Sc atom has 12 Fe atoms (9 Fe2 and 3 Fe1) in its first coordination shell (CS), 4 Sc atoms in the second CS, 15 Fe (12 Fe1 + 3 Fe2) atoms in the third, 13 Sc atoms in the fourth, 9 Fe (6 Fe1 + 3 Fe2) atoms in the fifth, and 9 Sc + 3 Fe2 atoms in the sixth CS. Although a sample of the $ScFe_2$ alloy with $MgZn_2$ structure was prepared as a stoichiometric sample (with due account of component loss during melting), its composition was actually $Sc_{1-x}Fe_{2(1+x)}$, where x is the Fe impurity content. In [9], the resistivity of samples of the $ScFe_2$ ($MgZn_2$-structure) alloy was measured. The results obtained indicated the presence of excess Fe atoms in the samples with stoichiometric composition. ^{45}Sc NMR data obtained on the $ScFe_2$ and $Sc_{0.95}Fe_{2.05}$ alloys suggest that the additional peaks in these spectra may be due to excess Fe atoms occupying the Sc sites in the second, fourth, and sixth scandium CSs. It can be conjectured that the peak at 77.86 MHz (in the $Sc_{0.95}Fe_{2.05}$ sample) is due to one Fe atom being substituted for one Sc atom in the second Sc coordination shell; the 82.57 MHz peak, to two Fe atoms being substituted for two Sc atoms in the same shell; and the peak at 75.27 MHz, to one Fe atom substituting for one Sc atom in the fourth Sc coordination shell. A similar situation is observed in samples of the $ZrFe_2$ alloy [10]. Assuming the excess Fe atoms to be randomly distributed over the second CS around Sc atoms (for 77.62 MHz), one can estimate the number of such atoms in a $ScFe_2$ sample. Using bino-

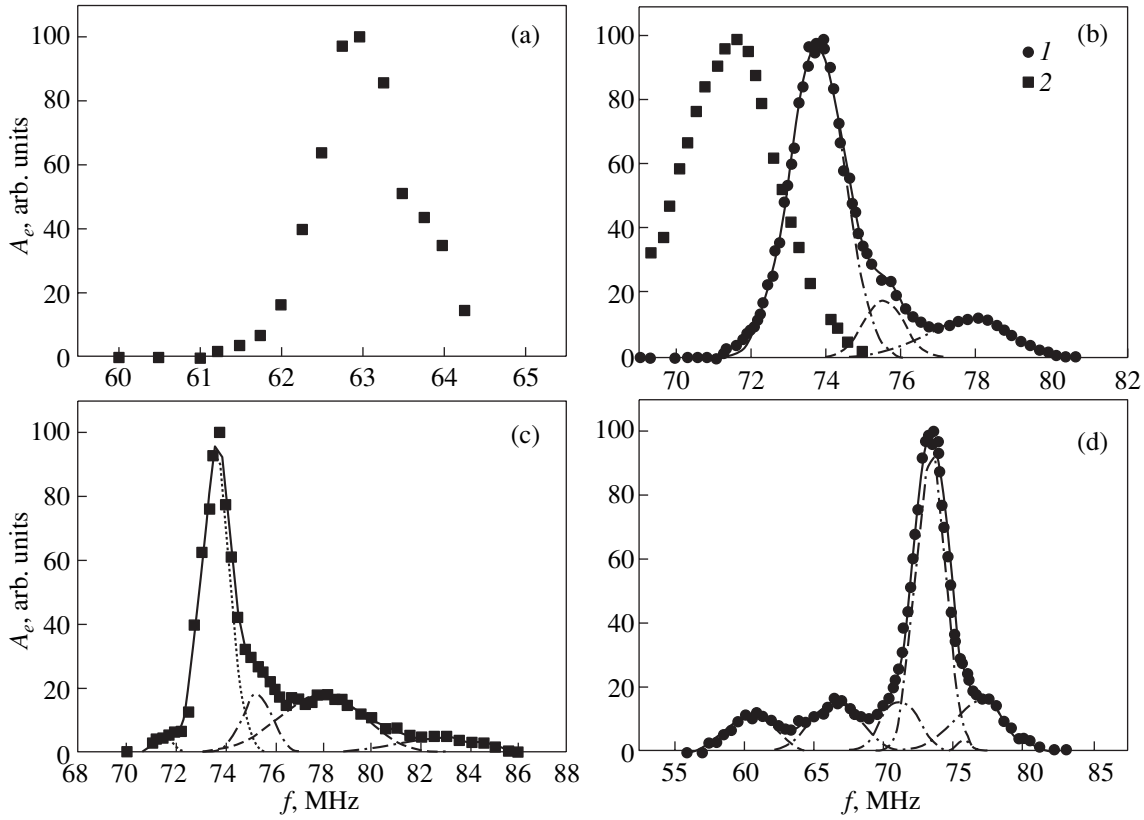

Fig. 1. ^{45}Sc NMR spectra of the samples studied (circles and squares are experimental data; dashed lines are spectra decomposed into constituent Gaussian lines; solid lines are the sum of the Gaussians). (a) $ScFe_2$ at room temperature; (b) $ScFe_2$ at 77 K in an external magnetic field B equal to (*1*) zero and (*2*) 5 kOe; (c) $Sc_{0.95}Fe_{2.05}$ at 77 K; and (d) $ScFe_{1.97}Al_{0.03}$ at 77 K.

mial distribution, we obtain for the ratio of probabilities of a Sc atom having no and one Fe atom in the second CS

$$\frac{P_4^0}{P_4^1} = \frac{1-x}{4x}, \quad (1)$$

where x is the concentration of excess Fe atoms. Figure 1b presents an experimental spectrum of the $ScFe_2$ ($MgZn_2$-structure) alloy decomposed into Gaussian lines using the ORIGIN code. The solid line is the sum of the resolved components. Decomposition of the spectrum yielded constituent peaks at 73.68, 75.45, and 77.62 MHz. Taking the ratio of the peak areas at 73.68 MHz (the nearest Sc atom environment {12 Fe + 4 Sc}) and at 77.62 MHz {12 Fe + (1 Fe + 3 Sc)} and comparing it with Eq. (1) yields $x = 0.046$. Substitution of one Fe atom for one Sc atom in the second CS of an Sc atom shifts the resonant frequency for the ^{45}Sc nuclei by +3.98 MHz or +0.386 T.

Figure 1d presents a ^{45}Sc NMR spectrum for the $ScFe_{1.97}Al_{0.03}$ alloy. In addition to the main peak at ~73.2 MHz and an unresolved peak on the high-frequency side, the spectrum exhibits two additional peaks at low frequencies. These two low-frequency peaks are due to Al atoms appearing in the first CS around the Sc atoms, with the peak at ~66.8 MHz originating from one Al atom and that at ~61.1 MHz, from two Al atoms occupying Fe sites in the first Sc coordination shell. The NMR spectrum was decomposed; the results are shown in Fig. 1d. The solid curve is the sum spectrum. The maxima of these peaks (spectral components) and the possible nearest environment configurations corresponding to these peaks are 73.19 MHz {12 Fe + 4 Sc}, 76.80 MHz {12 Fe + (1 Fe + 3 Sc)}, 66.76 MHz {(11 Fe + 1 Al) + 4 Sc}, 61.10 MHz {(10 Fe + 2 Al) + 4 Sc}, and 70.41 MHz (this is possibly due to Al atoms being present in the third CS around Sc atoms). Substitution of one Al atom for one Fe atom in the first CS of Sc shifts the resonant frequency by –6.4 MHz or –0.619 T. The Al atom has a zero *d*-type magnetic moment, and, therefore, the difference between the resonant frequencies for Sc atoms with 12 and 11 Fe nearest neighbors characterizes the effect of the magnetic moment of one Fe atom on the resonant frequency (hyperfine field) for ^{45}Sc nuclei.

Figure 2 plots the echo amplitude A_e vs. the rf magnetic field h_1 acting on the ^{45}Sc nuclei in our alloys at 77 K. Shown for comparison is an $A_e(h_1)$ dependence measured at 77 K and a frequency of 46.54 MHz on ^{57}Fe in iron powder samples enriched in this isotope. The maxima of the $A_e(h_1)$ curves were found to lie at different rf magnetic field amplitudes h_1^m. In the alloys under study, all values of h_1^m are smaller than those for a pure Fe sample. In magnetically ordered substances, the $A_e(h_1)$ dependence is due to a spread of the enhancement factors η in the domain walls. This effect was considered in detail for a domain wall modeled by a vibrating edge-fixed membrane, and an analytical expression for the dependence of the echo amplitude on h_1 was obtained in [11]. The distribution of enhancement factors in a domain wall can be presented in the form [11]

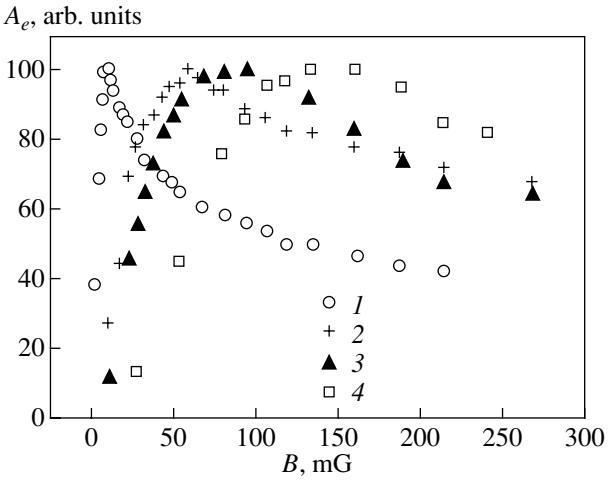

Fig. 2. Echo amplitude A_e vs. rf magnetic field h_1 for ^{45}Sc nuclei in (*1*) $ScFe_2$, (*2*) $Sc_{0.95}Fe_{2.05}$, and (*3*) $ScFe_{1.97}Al_{0.03}$ and (*4*) for ^{57}Fe nuclei in iron powder.

$$\eta(x) = \eta_0 \operatorname{sech}(x)(1-r^2)d_m, \quad (2)$$

where η_0 is the maximum enhancement factor corresponding to nuclei located at the wall center, x is the position of the nucleus in the domain wall on the x axis (measured in units of the wall thickness δ), $r = r_a/r_0$ (r_a is the radial position of the nucleus in the wall and r_0 is the membrane radius), and d_m is the maximum relative displacement of the wall (in units of the maximum wall displacement for the sample under consideration). The decrease in the echo amplitude at high excitation levels, as seen from Eq. (2), is caused by low effective enhancement factors for nuclei at domain wall edges.

Consider one more approach to estimating the enhancement factor in magnetically ordered substances, that described in [12]. Studies of various enhancement factor distributions across the domain wall thickness have established that it is possible to determine the average enhancement factor η_{av} for nuclei in a domain wall. Because real samples feature a variety of types of domain walls and enhancement factor distributions across the wall thickness, the expression given in [12] for the average enhancement factor may provide a good estimate for this parameter in ferro- or ferrimagnetic powders. The relation connecting η_{av}, the rf pulse duration Δt, and the rf magnetic field h_1^m corresponding to the maximum in the $A_e(h_1)$ dependence can be written [12] as

$$\eta_{av}\gamma_n \Delta t h_1^m = 1, \quad (3)$$

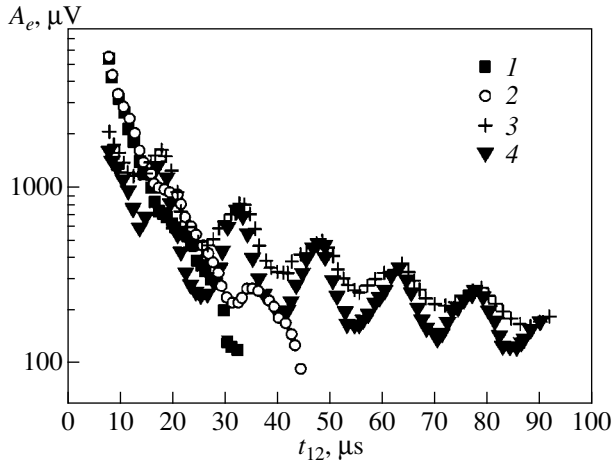

Fig. 3. Echo amplitude A_e plotted as a function of the time interval t_{12} between two echo-exciting rf pulses for different values of the rf magnetic-field amplitude h_1: (*1*) 16, (*2*) 48 mG, (*3*) 1.34, and (*4*) 4.0 G.

where γ_n is the gyromagnetic ratio for the nucleus under study. Let us estimate the average enhancement factors η_{av} for our alloys using the above relation and the experimental data in Fig. 2. The values of η_{av} obtained are as follows: $\eta_{av}(Fe) = 780$, $\eta_{av}(ScFe_2) = 17500$, $\eta_{av}(Sc_{0.95}Fe_{2.05}) = 2600$, and $\eta_{av}(ScFe_{1.97}Al_{0.03}) = 1650$. The average enhancement factors for ^{45}Sc nuclei in domain walls of the corresponding alloys are seen to be considerably larger than that for ^{57}Fe in iron. Note that the value of η_{av} for ^{57}Fe in iron found in this work coincides remarkably well with the value of ≈900 obtained in [13] at 77 K for ^{57}Fe in an isotopic-iron powder. Because the enhancement factor η_{av} is proportional to the displacement susceptibility χ, $ScFe_2$ samples are seen to have larger displacement susceptibilities than iron and an increase in the iron content or addition of Al to $ScFe_2$ sharply reduces χ.

We studied the dependence of the echo amplitude on the time interval t_{12} between two rf pulses exciting an echo at frequencies corresponding to the maxima of the main lines in the alloys under study at 77 K in different rf magnetic fields h_1. These dependences are plotted in Fig. 3 for the $ScFe_2$ sample. At low excitation levels, one observes weak oscillations in the A_e decay curves; however, at high h_1 levels, the echo decay exhibits a clearly pronounced oscillation. According to Fig. 2, at high excitation levels h_1, an echo is observed for nuclei located at the domain wall edge. A similar situation was observed in hexagonal cobalt [14]. As shown in [15], the oscillations in the echo amplitude A_e setting into the $A_e(t_{12})$ dependence are caused by electronic quadrupole interaction. The oscillation period τ is related to the quadrupole splitting $\Delta\nu_q$ through the expression

$$\Delta\nu_q\tau = 1. \quad (4)$$

As follows from Fig. 3, the modulation period τ is 15 ± 1 μs and, hence, $\Delta\nu_q$ = 66.6 kHz. Similar dependences of the echo amplitude decay on t_{12} and h_1 were measured for the $Sc_{0.95}Fe_{2.05}$ and $ScFe_{1.97}Al_{0.03}$ alloys. The modulation period τ of the echo amplitude in these alloys was found to be 15 ± 1 μs at 77 K. Thus, we see that the electron quadrupole splitting in the alloys under study does not depend on the sample preparation technology, slight deviations from the alloy stoichiometry, or small additions of Al atoms.

ACKNOWLEDGMENTS

This study was supported by the Russian Universities Foundation, grant no. 990926.

REFERENCES

1. *Constitution Diagrams of Binary and Multicomponent Systems Based on Iron. Handbook* (Metallurgiya, Moscow, 1986).
2. P. H. Smit and K. H. J. Bushow, Phys. Rev. B **21**, 3839 (1980).
3. J. Shafer and K. H. J. Bushow, J. Magn. Magn. Mater. **6**, 163 (1977).
4. V. Pokatilov, V. Golikova, A. Tvjashchenko, and L. Fomishova, Hyperfine Interact. **59**, 529 (1990).
5. V. S. Pokatilov, I. I. Sadchikov, and O. V. Utenkova, Dokl. Akad. Nauk SSSR **281**, 574 (1985) [Sov. Phys. Dokl. **30**, 250 (1985)].
6. V. S. Pokatilov, I. I. Sadchikov, E. F. Sidokhin, and O. V. Utenkova, Fiz. Met. Metalloved. **62**, 69 (1986).
7. R. H. Dean and R. J. Urwin, J. Phys. C **3**, 1747 (1970).
8. M. Yu. Teslyuk, *Metallic Compounds with Laves Phase Structures* (Nauka, Moscow, 1969).
9. K. Jkeda, T. Nakamichi, and Y. Yamamoto, J. Phys. Soc. Jpn. **36**, 611 (1974).
10. G. Wiesinger, A. Oppelt, and K. H. J. Buschow, J. Magn. Magn. Mater. **22**, 227 (1981).
11. M. B. Stearns, Phys. Rev. **162**, 496 (1980).
12. R. W. N. Kinner, S. J. Campbell, D. H. Chaplin, and G. V. H. Wilson, Phys. Status Solidi A **58**, 507 (1980).
13. D. K. Fowler, D. C. Creach, R. W. N. Kinner, and G. V. H. Wilson, Phys. Status Solidi A **92**, 545 (1985).
14. H. Enokiya, J. Phys. Soc. Jpn. **42**, 796 (1977).
15. H. Abe, H. Yasuoka, and A. Hirai, J. Phys. Soc. Jpn. **21**, 77 (1966).

Translated by G. Skrebtsov

Physics of the Solid State, Vol. 43, No. 11, 2001, pp. 2003–2011. Translated from Fizika Tverdogo Tela, Vol. 43, No. 11, 2001, pp. 1925–1933.
Original Russian Text Copyright © 2001 by Aronin, Abrosimova, Kir'yanov.

METALS AND SUPERCONDUCTORS

Formation and Structure of Nanocrystals in an $Al_{86}Ni_{11}Yb_3$ Alloy

A. S. Aronin, G. E. Abrosimova, and Yu. V. Kir'yanov

Institute of Solid-State Physics, Russian Academy of Sciences, Chernogolovka, Moscow oblast, 142432 Russia

e-mail: aronin@issp.ac.ru

Received May 7, 2001

Abstract—The formation and structure of the nanocrystalline phase in the $Al_{86}Ni_{11}Yb_3$ alloy are investigated using differential scanning calorimetry (DSC), transmission electron and high-resolution electron microscopy, and x-ray diffraction. The nanocrystalline phase is formed upon controlled crystallization of the amorphous alloy prepared by quenching of the melt on a rapidly moving substrate. It is revealed that the nanocrystalline alloy consists of aluminum nanocrystals (5–12 nm in size) randomly distributed in the amorphous matrix. The maximum fraction of the nanocrystalline phase does not exceed 25%. The nanocrystal size substantially increases at the initial stage of isothermal treatment (at 473 K) and then changes insignificantly. It is found that nanocrystals are usually free of defects. However, some nanocrystals have a more complex microstructure with twins and dislocations. The size distributions of nanocrystals are determined at several durations of isothermal treatment. It is demonstrated that the nucleation of nanocrystals predominantly occurs through the heterogeneous mechanism. The experimental distributions are compared with those obtained from a computer simulation. The activation energy of crystallization, the time-lag, and the coefficient of ytterbium diffusion in the alloy are estimated © *2001 MAIK "Nauka/Interperiodica".*

1. INTRODUCTION

Light nanocrystalline alloys (based on Al and Mg) were first produced by partial devitrification of amorphous alloys a few years ago [1, 2]. Among metallic materials, these alloys possess record-high strength characteristics (calculated per gram). Nanocrystalline alloys usually contain 6–15 at. % of a transition metal (Fe or Ni) and several percent of a rare-earth metal (Y, Ce, Nd, or Sm). Although the yield point of these alloys can reach 1.6 GPa [3], the alloy samples remain plastic in a number of cases. The structure of these materials consists of Al nanoparticles and the amorphous matrix. The volume fraction of particles, as a rule, is equal to approximately 0.25. There exist different opinions regarding the mechanism of enhancement of strength properties upon primary crystallization of these materials. According to the first point of view [4], the strength properties are determined by the amorphous matrix. The chemical composition of the amorphous matrix changes upon precipitation of aluminum crystals, which is attended by strengthening of the matrix. The second view accounts for the presence of nanocrystals in the matrix [3]. In this respect, it is important to answer the following questions: Are the Al particles deformable? Do these particles contain dislocations or are they free of dislocations? How can these particles be arranged in the amorphous matrix? One of the purposes of the present work was to obtain answers to these questions.

The second important purpose of this work was to investigate the formation of nanocrystalline particles upon heating of amorphous alloys. The phase transformation under consideration occurs by the mechanism of nucleation and growth. The growth of nanocrystals upon primary crystallization has studied in a number of works. In particular, Nakarato *et al.* [5] showed that the growth of nanocrystals in alloys of the Al–Ni–Ce system is controlled by diffusion. As regards the nanocrystal nucleation, the available data on the mechanisms of this process are rather contradictory. For example, according to Greer [4], the nucleation of Al nanocrystals is considered a homogeneous process, whereas Foley *et al.* [6] treated the nanocrystal nucleation as a heterogeneous process.

It is believed that the homogeneous process due to fluctuation nucleation of particles of critical size can proceed only at temperatures above the glass transition point T_g. At $T < T_g$, the viscosity of the alloy is too high for these fluctuations to occur and the nucleation can proceed only through the heterogeneous mechanism [7]. For light nanocrystalline alloys, it is difficult to determine the temperature range of nucleation with respect to the T_g temperature, because the value of T_g in these alloys is unknown. Consequently, a correct conclusion regarding the nucleation mechanism cannot be made as judged only from the temperature range of the transformation.

In order to draw a reliable inference on the nucleation mechanism responsible for nanocrystallization, it is necessary to determine the size distributions of nanocrystals at different durations of isothermal treat-

1063-7834/01/4311-2003$21.00 © 2001 MAIK "Nauka/Interperiodica"

ment and to carry out the appropriate analysis of these distributions.

In this respect, one more purpose of the present work was to elucidate the mechanism of nanocrystal nucleation in light nanocrystalline alloys.

2. EXPERIMENTAL TECHNIQUE

The $Al_{86}Ni_{11}Yb_3$ amorphous alloy was prepared in the form of ribbons by quenching of the melt. The cooling rate was equal to ~10^6 K/s. The ribbons were 3 mm wide and ~30 μm thick. Measurements of the thermal properties and isothermal treatment of the samples were performed using a Perkin–Elmer DSC-7 differential scanning calorimeter. The x-ray structure investigation was carried out on a Siemens D-500 x-ray diffractometer. The microstructure was examined with a JEM-4000EX high-resolution electron microscope at an accelerating voltage of 400 kV. The direct image of the nanocrystal lattice was obtained using a computer recording of a series of images with different defocusing. The micrographs presented in this work were taken at the optimum defocusing value $\delta = -46$ nm, which corresponds to the Scherzer defocusing ($\delta = 0.286 C_s^{1/2} \lambda^{1/2}$, where $C_s = 1$ mm is the spherical aberration constant and λ is the electron wavelength). Other methodical aspects of this work will be described below.

3. EXPERIMENTAL RESULTS

The as-prepared samples have an amorphous structure. The x-ray diffraction and electron diffraction patterns exhibit only diffuse maxima without crystalline phase peaks. The high-resolution images of the initial alloy structure are characterized by a "mazy" contrast typical of the amorphous structure. Figure 1 displays the thermogram obtained at a heating rate of 40 K/min. Two peaks observed in the thermogram indicate exothermic phase transformations upon heating. The first broad peak with an initial temperature of 463 K is associated with the first crystallization stage (primary crystallization) of the amorphous alloy. At this stage, Al crystals are formed in the amorphous matrix and the reflections from the crystalline phase (Al) together with a diffuse halo appear in the corresponding diffraction patterns. The second (double) peak is attributed to the subsequent crystallization stage (eutectic crystallization), at which the residual amorphous phase undergoes decomposition.

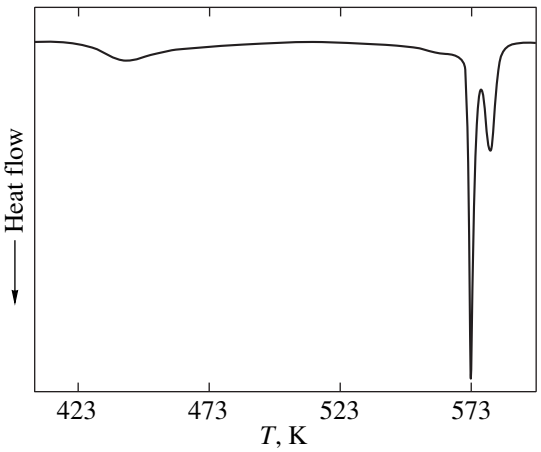

Fig. 1. Thermogram of the alloy upon heating at a rate of 40 K/min.

According to differential scanning calorimetry (DSC), the total thermal effect of crystallization is approximately equal to 116 J/g and the thermal effects of the first and second crystallization stages are 36 and 80 J/g, respectively.

The structural evolution of the $Al_{86}Ni_{11}Yb_3$ amorphous alloy was investigated under the conditions of isothermal treatment at a temperature of 473 K, which was determined from the DSC data. It can be expected that, at this temperature, the formation and growth of crystals at the first crystallization stage will occur at an optimum rate for investigation.

The primary crystallization of the alloy leads to the formation of Al face-centered cubic (fcc) crystals and a change in the amorphous matrix composition. The amorphous matrix becomes enriched in nickel and ytterbium which are virtually insoluble in aluminum. An increase in the treatment duration results in an increase in the fraction of the crystalline phase. The diffraction patterns of the samples after treatment at 473 K for different times are shown in Fig. 2. It can be seen that a peak of the Al fcc phase appears against the background of the diffuse halo, and the intensity of this peak increases with an increase in treatment duration.

The fraction of the crystalline phase can be evaluated from the DSC data with the use of the method described in [8]. The results obtained are depicted in Fig. 3. It is seen that, as the treatment time increases from 5 to 60 min, the fraction of the crystalline phase increases from 0.15 to 0.23. The highest rate of increase in the fraction of the crystalline phase is observed at the early treatment stage. The Al fcc crystals cease to grow when the metastable equilibrium between the crystalline phase and the residual amorphous phase (differing in composition from the initial phase) is attained.

The primary crystallization results in the formation of a structure composed of the amorphous matrix involving randomly distributed Al fcc crystals several nanometers in size. This structure is displayed in Fig. 4. As a rule, the Al nanocrystals are separated from each other by the amorphous matrix. In certain cases, nanocrystals are in direct contact with each other.

Figure 3 shows the dependence of the average nanocrystal size determined from the dark-field electron microscope images. The average grain size varies

from 7 nm (at a treatment time of 5 min) to 13 nm (at a treatment time of 60 min). As can be seen, the average nanocrystal size most strongly changes at the early transformation stages. The experimental size distributions of nanocrystals at treatment durations of 5 and 15 min are plotted in Fig. 5. It should be noted that the fraction of crystals with the smallest sizes could be underestimated due to the difficulty of their observation. This is especially essential for the size distribution obtained at a treatment duration of 5 min, since the distribution is shifted toward the small-size range.

As a rule, nanocrystals are free of defects. However, we observed particles with high-angle boundaries whose misorientation corresponds to twin boundaries. An example of these nanocrystals is depicted in Fig. 6. By using the Fourier transform of the direct image of the lattice of this nanocrystal, we obtained the image of the reciprocal lattice cross section (corresponding to the electron diffraction pattern), which is shown in Fig. 6b. This "diffraction" pattern involves reflections from parts 1 (type *A*) and 2 (type *B*) of the nanocrystal. In this case, the $(\bar{1}11)$ or $(1\bar{1}1)$ plane can be the twin plane and the parts of the twinned crystal have the [110] zone axis (the direction parallel to the incident electron beam). A comparison between the boundary in the image and two possible arrangements of the twin boundary trace in the reciprocal lattice cross section allows us to conclude that the $(\bar{1}11)$ plane is the twin plane in our case. The reflections from twinned part *B* of the crystal can be determined from the reflections from part *A* by using the orientation matrix:

$$\begin{bmatrix} h' \\ k' \\ l' \end{bmatrix} = \frac{1}{3}\begin{bmatrix} \bar{1} & \bar{2} & \bar{2} \\ \bar{2} & 1 & \bar{2} \\ \bar{2} & 2 & 1 \end{bmatrix}\begin{bmatrix} h \\ k \\ l \end{bmatrix}.$$

The schematic representation of this diffraction pattern is depicted in Fig. 6b.

The reciprocal lattice cross section under investigation has a characteristic feature that is typical of other twinned crystals. This feature is a mutual position of reflections from the nanocrystal parts at which the shortest distance between the reflections of different types *A* and *B* in the directions {111} is equal to 1/3 of the shortest distance between the reflections of the same type, *A* (*AA*) or *B* (*BB*), in the same direction.

In light alloys, nanocrystals are free of dislocations. However, the particle shown in Fig. 6a contains two closely spaced dislocations which are not typical of fcc crystals. These dislocations (Fig. 6c) have oppositely directed Burgers vectors $b = 1/2[1\bar{1}0]$ and $1/2[\bar{1}10]$ (the dislocation lines are parallel to [110]) and can move only with the formation of a stacking fault.

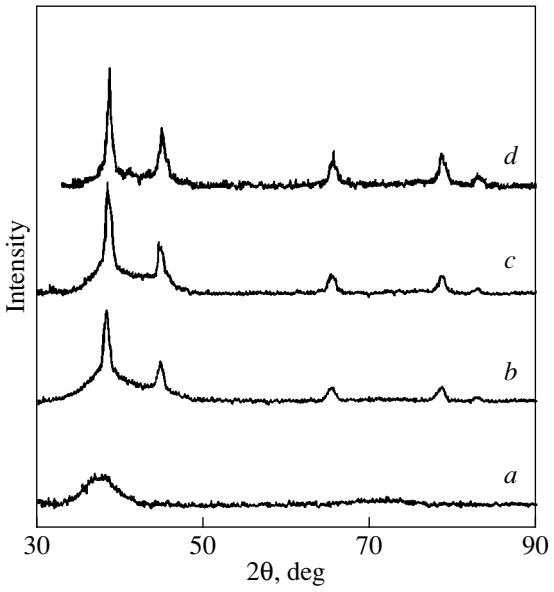

Fig. 2. Diffraction patterns of (*a*) the initial sample and samples annealed at 473 K for (*b*) 5, (*c*) 15, and (*d*) 30 min.

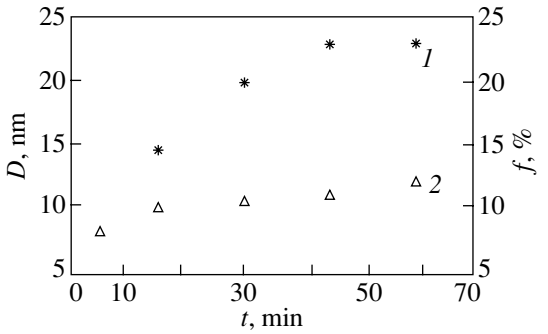

Fig. 3. Dependences of (*1*) the fraction *f* of the crystalline phase and (*2*) the average nanocrystal size *D* on the duration of isothermal treatment.

4. DISCUSSION

Let us discuss the problems associated with the formation of the nanocrystalline structure upon decomposition of the amorphous phase in the $Al_{86}Ni_{11}Yb_3$ alloy. As was noted above, the dependence of the fraction of the crystallized alloy on the treatment duration is plotted in Fig. 3. This fraction was calculated by the formula

$$f = (\Delta h_{1s}/\Delta H_0) - (\Delta h_{1a}/\Delta H_0), \quad (1)$$

where Δh_1 is the enthalpy of the first part of the peak and the shoulder in the thermogram and ΔH_0 is the total enthalpy of crystallization. According to [8], the above dependence can be calculated from the DSC data under the following assumptions: (1) the volume fraction of the crystallized part of the material is proportional to the heat released upon this transformation (this can be

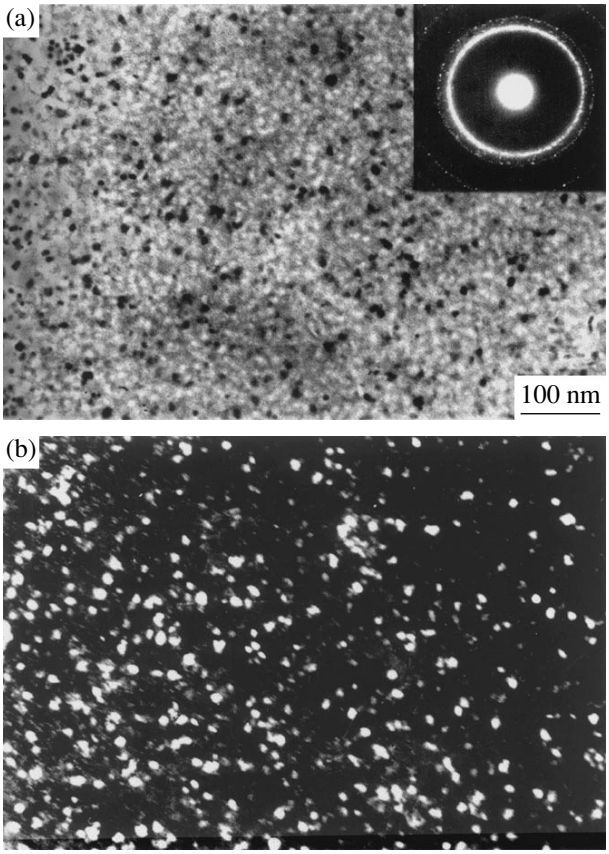

Fig. 4. Microstructure of the alloy annealed for 30 min: (a) bright-field and (b) dark-field images.

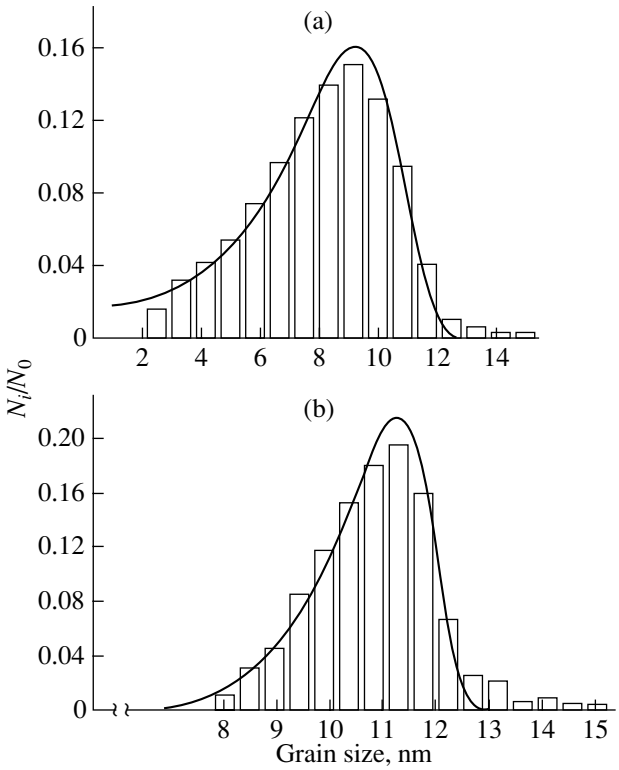

Fig. 5. Size distributions of nanocrystals after isothermal treatment at 473 K for (a) 5 and (b) 15 min. Columns represent the experimental data, and solid lines show the results of calculations.

true when no processes in addition to crystallization occur in the alloy) and (2) the heats of formation of different phases are identical. In order to make sufficiently rough estimates, this approach seems to be justified, because the heats of formation of different phases are actually comparable.

The ratio $(\Delta h_{1s}/\Delta H_0)$ gives the volume fraction of the material crystallized upon primary reaction (the precipitation of α-Al fcc crystals). In the sample subjected to isothermal annealing, the primary reaction took place in part, so that a smaller amount of crystals was formed through the mechanism of the primary crystallization upon repeated heating. Then, the value of $(\Delta h_{1a}/\Delta H_0)$ determines the volume fraction of α-Al fcc crystals precipitated in the course of the repeated heating and the fraction of the alloy crystallized during the initial isothermal treatment can be estimated from formula (1).

As was already noted, the nanocrystalline structure consists of the amorphous matrix with incorporated aluminum particles. By assuming that the maximum fraction of aluminum particles is equal to 23%, that the mean particle size, in this case, is equal to 12 nm, and that the particles are uniformly distributed over the amorphous matrix, the mean thickness of the amorphous layer between particles can be estimated at approximately 8 nm.

The experimental size distributions of nanocrystals exhibit characteristic features. They can be analyzed by comparing the theoretically possible and experimental size distributions of crystals. Figure 7 shows all the possible size distributions of crystals formed according to the nucleation and growth mechanism for homogeneous and heterogeneous nucleation processes.

Let us now compare the theoretical and experimental distributions. The size distributions obtained upon treatment for 5 and 15 min are depicted in Figs. 5a and 5b, respectively. The experimental size distributions are represented by columns. It is apparent that the heterogeneous nucleation with a time-lag proceeds in our case. This is confirmed by the following facts. (1) Small-sized crystals are absent in the distribution obtained upon treatment for 15 min. (2) A sharply descending portion in the small-size range is observed in the distribution at a treatment time of 5 min, which is impossible in the case of homogeneous nucleation. (3) The fraction of large-sized particles (the right-hand branch of the distribution) decreases gradually, which is characteristic of the nonstationary rate of nanocrystal nucleation (with the time-lag).

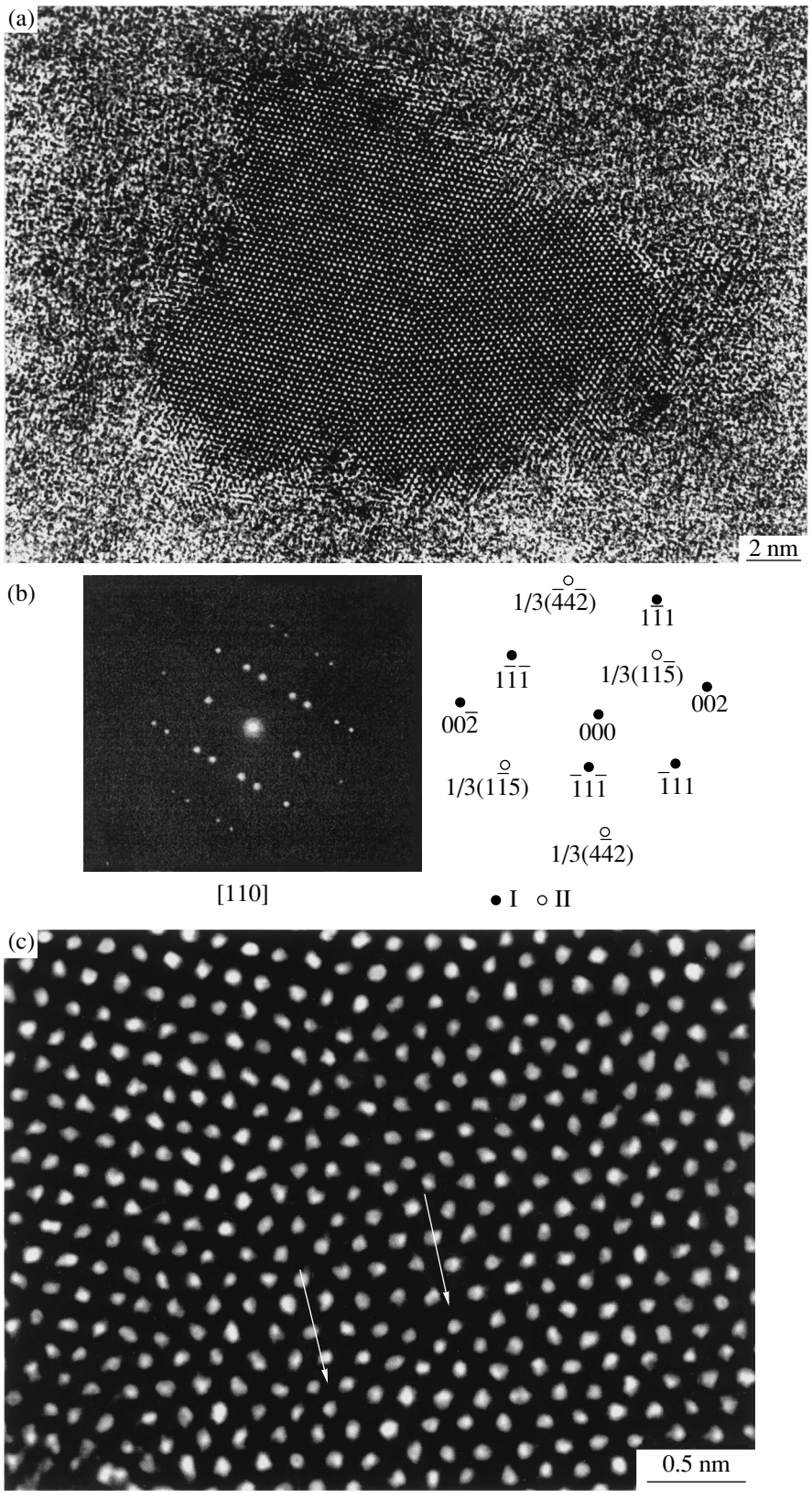

Fig. 6. (a) A nanocrystalline particle in the annealed sample. (b) Fourier transform pattern and its schematic representation for the nanoparticle: reflections I and II correspond to part *A* and twinned part *B* of the nanocrystal, respectively; reflections $(1\bar{1}\bar{1})$ and $(\bar{1}11)$ coincide for both parts. (c) An enlarged image of the nanocrystal region containing dislocations.

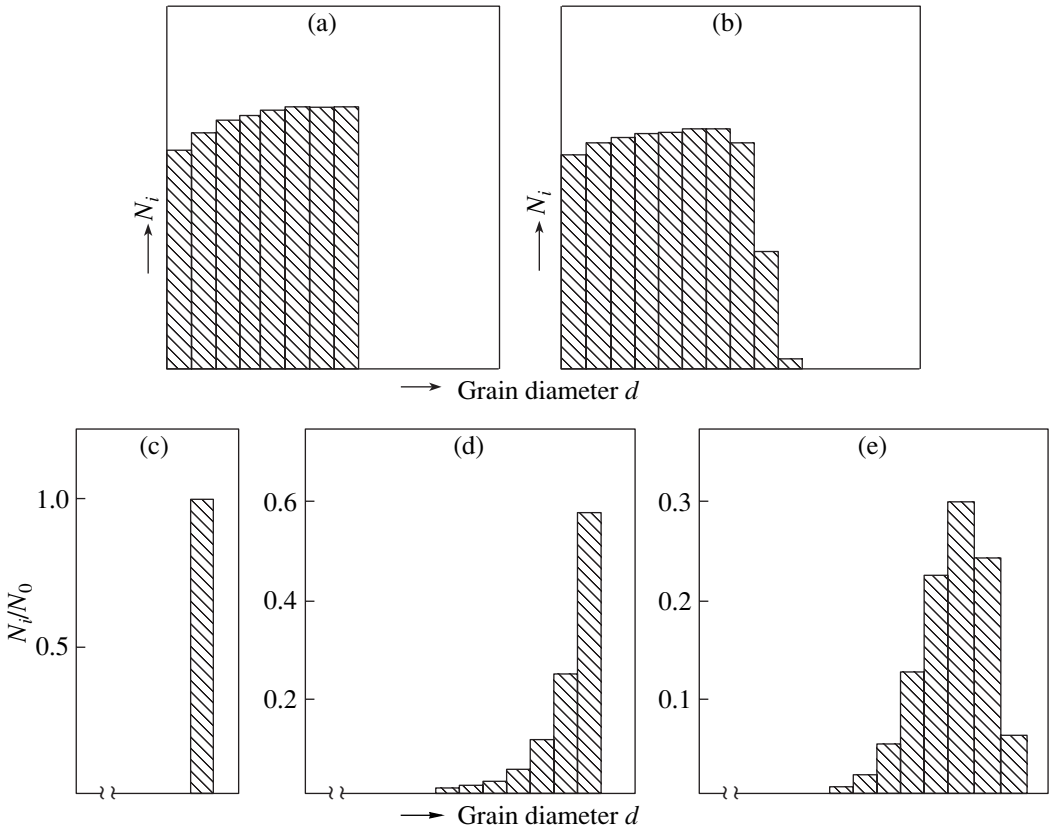

Fig. 7. Histograms of the size distribution of grains for (a, b) homogeneous and (c–e) heterogeneous nucleation processes. (b, e) Histograms for nonstationary nucleation.

Therefore, at the very early stage of annealing of metallic glass, there exists a certain time interval in which the stationary size distribution of subcritical nuclei (corresponding to the classical theory) is reached. In this case, the time-dependent rate $I(t)$ of crystal nucleation is defined by the equation [9]

$$I(t) = I_{st}\{1 + 2\Sigma(-1)^n \exp[-n^2(t/\tau)]\}, \qquad (2)$$

where the summation is performed over n from 1 to ∞, τ is the time-lag (which sharply increases with a decrease in the temperature), and I_{st} is the nucleation rate at stationary conditions. In turn, the I_{st} rate is described by the relationship

$$I_{st} = I_0 \exp(-L\Delta G_c/RT)\exp(-Q_N/RT), \qquad (3)$$

where L is the Loschmidt number, Q_N is the activation energy for the transfer of an atom through the crystallization front surface, and ΔG_c is the free energy necessary for the nucleation.

Under strong supercooling, the value of ΔG_c is very low and

$$I_{st} = I_0 \exp(-Q_N/RT). \qquad (4)$$

We now dwell on the growth of nucleated nanocrystals. Since the concentration gradient of nickel and ytterbium arises in the amorphous matrix near growing aluminum crystals, the matrix is enriched in nickel and ytterbium, whose atoms diffuse over large distances. The growth rate of nucleated crystals decreases with an increase in time. On the other hand, it is known that the primary crystallization or nanocrystallization in amorphous alloys is accompanied by a parabolic variation in the radius of growing crystals with an increase in the isothermal treatment time [7]. In our case, the crystal growth is governed by the bulk diffusion of Ni and Yb in the amorphous matrix that is,

$$r = \alpha\sqrt{Dt}, \qquad (5)$$

where D is the bulk diffusion coefficient, t is the time of isothermal treatment, r is the radius of a growing crystal, and α is the dimensionless parameter of an order of unity. In the present work, we assume that the α parameter does not depend on the fraction of the crystalline phase.

The dependence $r(t)$ implies that the size distribution of nanocrystals in the case of heterogeneous nucleation becomes narrower with time. Indeed, the dispersions of the distributions shown in Figs. 5a and 5b are equal to 15.76 and 4.96 nm^2, respectively. According to the Lifshitz–Slyozov theory [10], the Ostwald ripening

of nanocrystals can also bring about a narrowing and a shift of the histograms of the size distribution of nanocrystals with an increase in time. However, this process does not noticeably contribute to our experimental data and will be discussed below.

After revealing the most probable mechanism of the nucleation and growth of nanocrystals during isothermal treatment of the $Al_{86}Ni_{11}Yb_3$ alloy, the experimental data can be compared with the theoretical results. For this purpose, we performed computer calculations and constructed histograms of the size distribution of nanocrystals for heterogeneous nucleation and diffusion-controlled growth.

In order to carry out these calculations using formulas (2)–(5), it is necessary to determine the following parameters: the number of nuclei N_0 (which is limited in the case of heterogeneous crystallization), the time-lag τ (duration of the nonstationary stage), the nucleation rate I_{st} at stationary conditions, the constant I_0 in the formula determining the stationary rate of crystal nucleation, and the activation energy Q_N for the transfer of an atom through the crystallization front surface.

In calculations, we assumed that $I_0 = 3 \times 10^{30}$ m s^{-1}, which is typical of the nucleation of nanocrystalline aluminum in alloys of aluminum–nickel–rare-earth metal systems [4].

The value of N_0 was determined from the experimental data as follows. Treatment for a time longer than 30 min does not result in a substantial change in the fraction of the crystalline phase (it is equal to approximately 0.23). The average nanocrystal size in this case is approximately 12 nm. Therefore, the number of nanocrystals, i.e., N_0 (by assuming that the heterogeneous nucleation is accomplished and by ignoring the possible Ostwald ripening of nanocrystals), is approximately equal to 2×10^{23} m^{-3}. This estimate is in good agreement with the data available in the literature. For example, according to Greer [4], the value of N_0 upon nanocrystallization can be as large as 10^{25} m^{-3}.

In order to calculate the size distribution of nanocrystals, it is necessary to divide the isothermal treatment time into short time intervals Δt and then to determine the number of nanocrystals formed during each interval Δt [11]. For the heterogeneous crystallization when the number N_0 of active nuclei is limited, we have

$$N_i = I(t)(1 - x_{i-1})(1 - N_0^{-1}\Sigma N_j)\Delta t, \qquad (6)$$

where the summation is performed over j from 1 to i at $\Sigma N_j \le N_0$, $N_i = 0$ for all the other values of i, and x_i is the volume fraction of the material crystallized during the time interval Δt. The fraction x_i is given by

$$x_i = (4\pi/3)D^{3/2}\Sigma N_j\{\Delta t(i + 1 - j)\}^{3/2}, \qquad (7)$$

where the summation is made over j from 1 to i.

The shape and location of the theoretical size distribution depend on the parameters substituted into the formulas. A variation in such parameters as Q_N, τ, and diffusion coefficient D enables us to best fit the theoretical curve to the experimental distribution.

Now, we compare the above-discussed two experimental size distributions of nanocrystals in the $Al_{86}Ni_{11}Yb_3$ alloy subjected to isothermal treatment at 473 K for 5 and 15 min (Fig. 5) with the theoretical distributions.

The histograms for both times should be calculated using the same crystallization parameters. Changes in the shape and location of the distributions should only be associated with different treatment durations (5 and 15 min). This requirement appears to be sufficiently rigid. It was found that both theoretical curves can be reasonably fitted to the experimental distributions at the same parameters Q_N and τ but at different diffusion coefficients D (Fig. 5). In order to achieve good agreement between the distributions, the diffusion coefficient should decrease with an increase in the treatment time (and, correspondingly, in the fraction of crystalline phase formed). Note that a decrease in the diffusion coefficient with an increase in the fraction of the crystallized material is quite typical of the primary crystallization in amorphous alloys [7]. It seems likely that a similar phenomenon would be observed in our case. A comparison of the experimental and calculated data demonstrates that, in the $Al_{86}Ni_{11}Yb_3$ amorphous alloy at 473 K, the effective diffusion coefficient of Ni and Yb is equal to 1.4×10^{-19} m^2 s^{-1} and the time-lag is 150 s. Since the diffusion coefficient of nickel is considerably larger than that of ytterbium, it is assumed that the nanocrystal growth is limited by the diffusion rate of ytterbium. Then, it is this ytterbium diffusion that is determined by the aforementioned diffusion coefficient. It should be noted that Hono *et al.* [12] studied the crystallization of alloys in the Al–Ni–Ce system and observed an increase in the Ce concentration near growing Al nanocrystals and a uniform distribution of Ni in the amorphous matrix. Taking into account that the properties of Ce and Yb atoms are close to each other, the above assumption as to the ratio between the diffusion coefficients of Ni and Yb seems to be quite correct.

As is clearly seen from Fig. 5, one more difference between the calculated and experimental size distributions resides in the presence of a tail of large-sized particles in the experimental histograms. Most likely, the occurrence of large-sized particles can be explained by the presence of a small number of the so-called "frozen-in crystal nuclei" in the initial alloy. The formation of crystals from these nuclei is facilitated. As a result, particles begin to grow earlier (prior to the completion of the time-lag of attaining the stationary size distribution of subcritical nuclei) and reach larger sizes.

We now analyze the possible contribution of the Ostwald ripening to the experimental histograms of the size distributions of nanocrystals. Within the Lifshitz–

Slyozov theory, the evolution of the crystal size is described by the equation

$$\bar{r}^3 - \bar{r}_0^3 = \frac{8}{9}\frac{D\sigma V_m C(\infty)t}{RT}, \quad (8)$$

where $\bar{r}$ is the average particle size, $\bar{r}_0$ is the initial average size, V_m is the molar volume of precipitates, σ is the particle–matrix interface energy, and $C(\infty)$ is the equilibrium solubility of a component far from a particle. The maximum growth rate related to the Ostwald ripening is given by

$$(dr/dt)_{\max} = (8D\sigma V_m C(\infty))/(27RTr^2). \quad (9)$$

The maximum growth rate due to the Ostwald ripening can be estimated from Eq. (9) as approximately 0.2 nm/h (at 473 K, $r \approx 4$ nm after the treatment for 5 min and $D = 1.4 \times 10^{-19}$ m^2 s^{-1}). At $r \approx 5.5$ nm (after treatment for 15 min), the maximum growth rate is less than 0.03 nm/h. It is seen that these rates are immaterial for the considered time interval of the formation and evolution of the nanocrystalline structure (treatment times shorter than 60 min). Ardell [13] introduced the correction for the volume fraction of precipitates into Eq. (8). He derived an equation that differs from the Lifshitz–Slyozov equation in the parameter K, which depends only on the volume fraction of precipitates, that is,

$$\bar{r}^3 - \bar{r}_0^3 = K\frac{8}{9}\frac{D\sigma V_m C(\infty)t}{RT}. \quad (10)$$

Note that $K = 1$ at a zero volume fraction of precipitates, $K \approx 4$ at the fraction of the crystalline phase formed upon treatment of the studied alloy for 5 min, and $K = 7$ at a fraction of 15%, which approximately corresponds to the fraction obtained after treatment for 15 min in our case. Then, the maximum growth rates due to the Ostwald ripening of nanocrystals in the alloy after treatment for 5 and 15 min are less than 1 and 0.2 nm/h, respectively. It is worth noting that these estimates are too large, because the diffusion coefficient decreases with an increase in time [in the present work, the dependence of the parameter α in the equation $dr/dt = (\alpha/2)(D/t)^{1/2}$ on the fraction of the crystalline phase is neglected and this parameter is taken to be constant and equal to unity]. The above rates can be considered upper estimates (upon treatments for 5 and 15 min) of the instantaneous growth rate, which decreases with an increase in time. Therefore, even with due regard for the K parameter related to the volume fraction of precipitates, these rates, in our case, do not affect the evolution of the size distribution of nanocrystals.

Furthermore, in the framework of the Lifshitz–Slyozov theory, it is assumed that the system is in equilibrium and the formation and growth of particles of the second phase at the expense of the matrix do not occur. Consequently, the change in the nanocrystal size due to the Ostwald ripening within the Lifshitz–Slyozov theory can become substantial after completion of the nanocrystal growth from the amorphous phase when the nanocrystal–amorphous matrix system is in a metastable equilibrium. In order for the Ostwald ripening to proceed, this equilibrium should be retained for a sufficiently long time and should not be accompanied by further crystallization of the amorphous matrix. Note that the size distribution of particles in our work was obtained at the stages when the metastable equilibrium between the nanocrystalline and amorphous phases was not attained and the fraction of nanocrystals continued to increase.

Therefore, nanocrystal nucleation during devitrification of the $Al_{86}Ni_{11}Yb_3$ amorphous alloy occurs through the heterogeneous mechanism and from frozen-in crystal nuclei. Since the nucleation occurs through the heterogeneous mechanism, questions arise as to the origin of the centers of the heterogeneous nucleation and to the conditions and time of their formation. In [4, 7], it was assume that a certain set of subcritical nuclei can be formed according to the heterogeneous mechanism (at higher temperatures) during the preparation of an initial amorphous alloy (i.e., during quenching of the melt). These nuclei can serve as centers of heterogeneous nanocrystal nucleation upon subsequent heating. Certainly, the stationary distribution of these nuclei can be attained only for a certain time (time-lag).

5. CONCLUSION

Thus, it was demonstrated that the nanocrystalline structure with nanocrystals 5–12 nm in size is formed in the case of controlled crystallization of the $Al_{86}Ni_{11}Yb_3$ amorphous alloy. The nanocrystals are aluminum particles which, as a rule, are free of defects. However, some nanocrystals consist of twinned regions and contain dislocations. The average nanocrystal size and the fraction of the crystalline phase increase with an increase in the isothermal treatment time. The growth rate of nanocrystals is maximum at the early treatment stage and then decreases. The nanocrystals are formed according to the mechanism of the nonstationary heterogeneous nucleation and from frozen-in crystal nuclei. The time-lag of attaining the stationary size distribution of nuclei and the diffusion coefficient of ytterbium in the amorphous alloy were determined by comparing the experimental and calculated size distributions of nanocrystals.

ACKNOWLEDGMENTS

This work was supported by the Russian Foundation for Basic Research, project nos. 99-02-17477 and 99-02-17459.

We would like to thank J. Walker (University of Cambridge) for performing calorimetric measurements and V.I. Nikitenko and V.B. Timofeev for their participation in discussions of the results.

REFERENCES

1. Y. He, J. F. Poon, and G. Y. Shiflet, Science **241**, 1640 (1988).
2. A. Inoue, T. Ochiai, Y. Horio, and T. Masumoto, Mater. Sci. Eng. A **179/180**, 649 (1994).
3. Y. H. Kim, A. Inoue, and T. Masumoto, Mater. Trans., JIM **32**, 331 (1991).
4. A. L. Greer, in *Nanostructured Materials: Science and Technology*, Ed. by G.-M. Chow and N. I. Noskova (Kluwer, Dordrecht, 1998); NATO ASI Ser., Partnership Sub-Ser. 3, High Technol. **50**, 457 (1998).
5. K. Nakarato, Y. Kawamura, A. P. Tsai, and A. Inoue, Appl. Phys. Lett. **63**, 2644 (1993).
6. J. C. Foley, D. R. Allen, and J. H. Perepezko, Scr. Mater. **35**, 655 (1996).
7. U. Köster and U. Herold, in *Glassy Metals* (Springer-Verlag, Berlin, 1981; Mir, Moscow, 1983), Vol. 1.
8. A. Inoue, H. Tomioke, and T. Masumoto, J. Mater. Sci. **18**, 153 (1983).
9. J. W. Christian, *Theory of Transformations in Metals and Alloys* (Pergamon, Oxford, 1975; Mir, Moscow, 1978), Vol. 1.
10. I. M. Lifshitz and V. V. Slyozov, J. Phys. Chem. Solids **19**, 35 (1961).
11. U. Köster, Z. Metallkd. **75**, 691 (1984).
12. K. Hono, Y. Zhang, A. Inoue, and T. Sakurai, Mater. Trans., JIM **36**, 909 (1995).
13. A. Y. Ardell, Acta Metall. **20**, 61 (1972).

Translated by O. Borovik-Romanova

Physics of the Solid State, Vol. 43, No. 11, 2001, pp. 2012–2017. Translated from Fizika Tverdogo Tela, Vol. 43, No. 11, 2001, pp. 1934–1938.
Original Russian Text Copyright © 2001 by Kuz'michev.

METALS AND SUPERCONDUCTORS

Magnetic Field Penetration into the Weak-Link System of the $YBa_2Cu_3O_{7-x}$ Granular Superconductor

N. D. Kuz'michev

Mordovian State University, ul. Bol'shevitskaya 68, Saransk, 430000 Russia

Received February 13, 2001; in final form, March 30, 2001

Abstract—The differential magnetic susceptibility $\chi_d(H)$ of $YBa_2Cu_3O_{7-x}$ polycrystalline samples is studied experimentally in fields $H < 150$ Oe. The empirical $\chi_d(H)$ dependence is determined. The results are explained on the basis of the critical-state model of a Josephson medium with hypervortices. © *2001 MAIK "Nauka/Interperiodica".*

1. INTRODUCTION

The interest in the magnetic properties of granular high-temperature superconductors (HTSC) has not subsided [1–3]. This is due not only to their practical importance but also to the fact that the microscopic pattern of the magnetic field penetration into a granular HTSC material is not completely clear at present. Polycrystalline granular HTSC materials with Josephson (weak) links between granules display a number of anomalous properties in weak magnetic fields of strength $H < 10$–50 Oe; for example, nonlinearity and the absence of magnetization hysteresis are simultaneously observed in experiments in this region [4–7]. This contradicts both the Meissner effect (linear magnetization) and various modifications of the model of the critical state [8], because this model presumes the existence of hysteresis. Other models of magnetic properties of polycrystalline HTSC materials, such as the model of a superconducting glass [9, 10] and the Josephson loop model [4, 11, 12], also fail to provide an adequate description of experimental results and cannot resolve the above-mentioned contradictions.

The drawbacks to the models are manifested most clearly in the description of the spectrum of magnetization harmonics, which can be obtained experimentally by applying a modulated magnetic field to an HTSC [11, 13, 14], as well as in the description of harmonics in the current–voltage characteristics (IVC) of HTSC materials [15, 16].

2. SAMPLES AND EXPERIMENTAL TECHNIQUE

The polycrystalline $YBa_2Cu_3O_{7-x}$ (YBaCuO) samples were prepared in the form of pellets (nos. 1–3) $d \approx 20$ mm in diameter and $l_1 = 2.4$, $l_2 = 3.4$, and $l_3 = 2.1$ mm in thickness using conventional ceramic technology. Annealing was carried out at a temperature of 950°C in oxygen. The superconducting transition temperature T_c of the prepared samples was 92 K. The samples were of densities $\rho_1 = 4.34$, $\rho_2 = 3.80$, and $\rho_3 = 2.81$ g/cm^3. We used the two-coil compensation method of magnetic susceptibility measurements [5]. A sinusoidal signal from a GZ-118 generator (with the harmonics coefficient 0.005%) was fed into the input induction coil. The output response signal was fed into the input of a selective voltmeter. The response signal can be written in the form [11, 13]

$$\varepsilon(t) = -\mu_0 NS\frac{dM}{dt}. \quad (1)$$

Here, $M = (1/V)\int_V M dV$ is the magnetization averaged over the sample volume V, S is the average cross-sectional area of the sample, N is the number of turns of the compensation coil, and $\mu_0 = 4\pi \times 10^{-7}$ H/m. In the measurements of the first harmonic in the response signals of YBaCuO polycrystals in a constant magnetic field H_0, the amplitude of field modulation was $h = 0.005$ Oe at a frequency of 2 kHz. For such a value of the field modulation depth, the amplitudes of higher harmonics were at the noise level; therefore, they could be disregarded. In this case, the in-phase component of the emf of the first harmonic in the response signal from the sample was proportional to the differential magnetic susceptibility [13]:

$$\varepsilon_1'(t) \approx \mu_0 NS\omega h\chi_d(H_0)\sin(\omega t), \quad (2)$$

where ω is the frequency of the varying magnetic field, h is the amplitude of field modulation, and $\chi_d(H_0)$ is the differential magnetic susceptibility of the sample in the field H_0. The magnitude of the first-harmonic amplitude $\varepsilon_1 = [(\varepsilon_1')^2 + (\varepsilon_1'')^2]^{1/2}$ of the response signal from an HTSC sample was detected with the help of a V6–9 selective voltmeter. The separation of the in-phase (ε_1') and the 90°-out-of-phase (ε_1'') components of the first harmonic was carried out using the synchronous detection method with the help of a UPI-2 lock-in amplifier.

The dependences $\varepsilon_1(H_0)$, $\varepsilon_1'(H_0)$, and $\varepsilon_1''(H_0)$ were investigated at $T \approx 77$ K in liquid nitrogen. The sample was cooled in a zero magnetic field to liquid-nitrogen temperature and exposed to a constant magnetic field varied slowly from zero to $+H_{max}$, then decreased to $-H_{max}$, and then increased again. The $\varepsilon_1(H_0)$, $\varepsilon_1'(H_0)$, and $\varepsilon_1''(H_0)$ dependences were measured with a step of 10 Oe in a constant magnetic field up to $H_{max} = 150$ Oe and with a step of 100 Oe in stronger fields. In all cases, the varying, constant, and slowly varying fields were parallel to the sample axis. The magnetic field of the Earth was compensated for with the help of a system of Hemlholtz coils. The error of the first-harmonic measurements of the response signal was less than 3%.

3. EXPERIMENTAL RESULTS OF THE STUDY OF THE DIFFERENTIAL MAGNETIC SUSCEPTIBILITY OF YBaCuO POLYCRYSTALS

The obtained results are presented in Figs. 1 and 2. An analysis of ε_1' and ε_1'' as functions of the constant field proved that the values of these quantities decrease rapidly upon an increase in the magnetic field from 0 to 30 Oe. Upon further increase in the field, ε_1 and ε_1' smoothly attain saturation. The value of ε_1'' is equal, on average, to less than one tenth of the corresponding in-phase component ε_1'. The irreversible behavior of the dependences $\varepsilon_1(H_0)$, $\varepsilon_1'(H_0)$, and $\varepsilon_1''(H_0)$ is observed only when the maximum field exceeds a certain value H_{irr}, which depends on the technological conditions of sample preparation.

Taking into account the results obtained on the differential magnetic susceptibility of YBaCuO polycrystals for $h = 0.005$ Oe and the theoretical concepts developed in [4–6, 9–18], it was found that for the description of the magnetic properties of the investigated samples, the most suitable expression for the amplitude of the harmonic $\varepsilon_1'(t) = \varepsilon_1'(H_0, h)\sin(\omega t)$ is

$$\varepsilon_1'(H_0, h) = \mu_0 NS\omega h\left(A + \frac{B}{\cosh^{\alpha}\left(\frac{H_0}{H^*}\right)}\right), \qquad (3)$$

where A, B, α, and H^* are the parameters characterizing the polycrystal. The quantity A is apparently responsible for the Meissner screening by granules of the polycrystal. Using the least square technique, we determined the values of these parameters for each sample. The results are presented in the table.

The error in determining the parameters A, B, H^*, and α amounts to less than 5% (A and B are dimensionless quantities). The average value $\langle\alpha\rangle \approx 2.0$. It follows

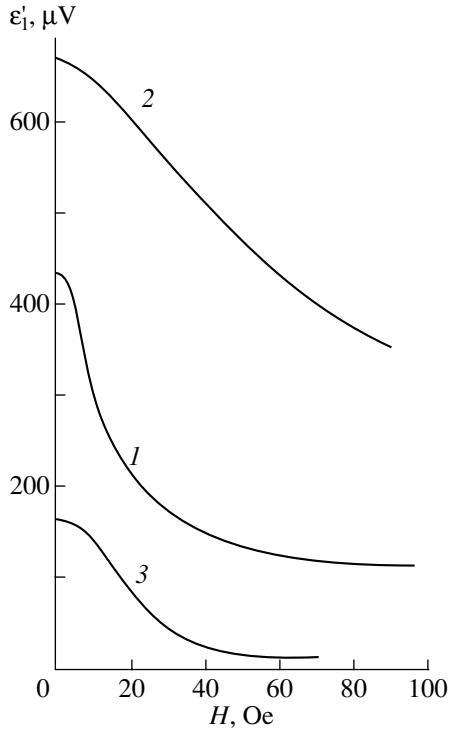

Fig. 1. Dependence of the in-phase component $\varepsilon_1' \sim \chi_d$ of the first harmonic in the response signal from $YBa_2Cu_3O_{7-x}$ ceramic samples on a constant magnetic field. The numbers on the curves are the sample numbers.

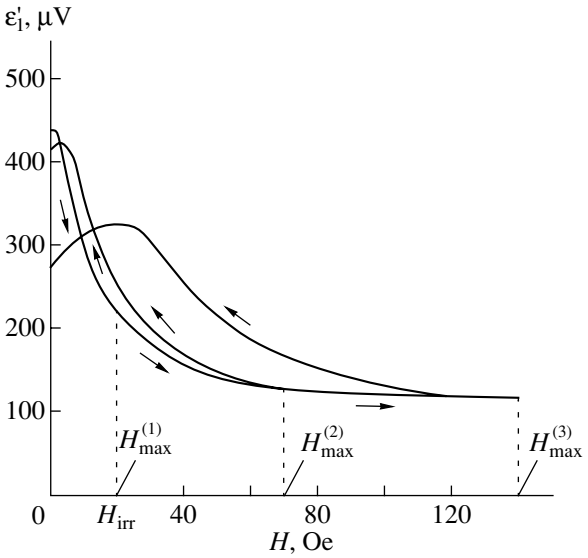

Fig. 2. Dependence of ε_1' of $YBa_2Cu_3O_{7-x}$ ceramic sample no. 1 on a constant magnetic field for three values of H_{max} (H_{max} is the maximum field of a magnetization cycle). The arrows indicate the direction of magnetic field variation. The field $H_{max}^{(1)}$ coincides with the field H_{irr}.

from Eq. (3) that the initial magnetization curve can be described by the expression

$$M = AH + BH^* \tanh\left(\frac{H}{H^*}\right). \quad (4)$$

4. THEORETICAL MODEL

The model describing the penetration of a time-dependent magnetic field into a weak-link system of a granular HTSC material is based on the concept of the critical state of a Josephson medium. It is assumed that the carriers of supercurrent in the subsystem of weak intergranular links of the polycrystal are in a coherent state (Josephson medium; see, for example, [9–11, 17, 19]). This coherent state corresponds to the order parameter (wave function) $\Psi = \sqrt{n}\, e^{i\Theta}$, where n is the effective concentration of supercurrent carriers and Θ is their phase. Let us consider an HTSC sample placed in an external magnetic field of strength H. If $H < H_{c1J}$ (H_{c1J} is the lower critical field of weak links), then the static magnetic field penetrates into the array of weak links to the Josephson depth $\lambda_J \sim 0.01$–10 mm for an HTSC [9, 10, 17, 20–23] and no Josephson vortices are formed. An exact estimate of the value of H_{c1J} has not yet been obtained. The reported values range from 0.001 to 100 Oe (see, for example, [10, 17, 19]). The magnetic flux trapping by the sample is possible in the case of the pinning of formed vortices. If we take for H_{c1J} the irreversible-magnetization field $H_{\rm irr}$ of the HTSC material (table), we obtain the following results. The values of λ_J, H_{c1J}, and j_{c1J} are connected through the relation [20–23]

$$H_{c1J} = \frac{4}{\pi}\lambda_J j_{cJ} \sim \lambda_J j_{cJ}. \quad (5)$$

Assuming that $j_{cJ} \sim 0.1$–10 A/cm^2 [10], we obtain an estimate of $\lambda_J \sim 1$–10^3 cm, which contradicts the available data ($\lambda_J \sim 0.01$–10 mm). We must assume that either $j_{cJ} \sim 10^3$–10^5 A/cm^2 or $H_{c1J} \sim 10^{-2}$–10^{-4} Oe. The latter corresponds to the model of hypervortices [17, 19]. For $H_{c1J} \sim 10^{-4}$ Oe, the hypervortex diameter ~0.5 mm corresponds to macroscopic sizes. The following analysis will be based on the model of hypervortices.

In order to describe the penetration of a time-dependent magnetic field into a subsystem of weak intergranular links, we will use the concept of the critical state. The varying magnetic field penetrates into the sample in the form of hypervortices and, in accordance with Maxwell's equations, induces an electric field of strength **E** in the system of weak links. This field produces a superconduction current of density **j**, which screens the external magnetic field.

This effect can be described by Maxwell's equation, which is used in describing the critical state of type II superconductors with a large number of centers that pin Abrikosov vortices (see, for example, [8, 18, 20, 21]):

$$\mathrm{curl}\mathbf{H} = j\frac{\mathbf{E}}{E}. \quad (6)$$

According to models of the Josephson medium, the screening supercurrent density j [see Eq. (6)] must be proportional to the Josephson critical current I_{cJ}, which is defined by the Ambegaokar–Baratoff formula [20–23]

$$I_{cJ} = \frac{\pi\Delta(T)}{2eR_n}\tanh\left[\frac{\Delta(T)}{2kT}\right]. \quad (7)$$

Here, $\Delta(T)$ is the superconducting energy gap at temperature T, e is the electron charge, k is Boltzmann's constant, and R_n is the normal resistance of the junction ($R_n = \rho_n(l/S)$, with ρ_n being the resistivity and l and S being the length and the cross-sectional area of the junction, respectively).

The current j screening the magnetic field in a cylindrical sample is defined as

$$j = \left\langle j_{cJ}\left|\frac{\sin(\pi\Phi/\Phi_0)}{\pi\Phi/\Phi_0}\right|\right\rangle\frac{\partial\Theta}{\partial\varphi}. \quad (8)$$

Here, the angle brackets denote averaging over all Josephson junctions in the sample, $\Phi = \oint\mathbf{A}d\mathbf{l}$ is the magnetic flux penetrating into the sample in the form of vortices (Josephson vortices or hypervortices), **A** is the vector potential of the magnetic field (the magnetic field is concentrated in a vortex), $\Phi_0 = \pi\hbar/e = 2.07 \times 10^{-7}$ G cm^2 is the flux quantum, Θ is the phase of the screening current, and φ is the polar angle of the cylindrical system of coordinates. In accordance with Eq. (7), the Josephson critical current density is

$$j_{cJ} = \frac{\Delta(T)}{4e\rho_n r}\tanh\left[\frac{\Delta(T)}{2kT}\right], \quad (9)$$

where ρ_n is the resistivity of the Josephson medium in the normal state and r is the radial coordinate in the cylindrical sample. Indeed, an annular layer of radius r, width a, and height b has a resistance $R = \rho(2\pi r/ab)$. The current in the ring is $I \sim 1/R$, and, accordingly, the current density $j = I/ab \sim 1/(2\pi\rho r)$. This gives the following expression for the screening supercurrent density:

$$j = \frac{\Delta}{4e\rho_n r}\tanh\left(\frac{\Delta}{2kT}\right)\frac{\partial\Theta}{\partial\varphi}\left\langle\left|\frac{\sin\left(\pi\dfrac{\Phi}{\Phi_0}\right)}{\pi\dfrac{\Phi}{\Phi_0}}\right|\right\rangle \quad (10)$$

$$\approx \frac{\Delta}{4\pi e\rho_n r}\tanh\left(\frac{\Delta}{2kT}\right).$$

Here, we assume that $\langle|\sin(\pi\Phi/\Phi_0)|\rangle \sim 1$ and $\partial\Phi/\partial\varphi = \Phi/\Phi_0 = \pm N$ (N is the number of vortices formed in the

sample). The sign of $\partial\Theta/\partial\varphi$ depends on the direction of variation of the external magnetic field, i.e., on $\partial H/\partial t$.

In the vicinity of T_c ($T < T_c$), in accordance with Eq. (10), we have $j \propto \frac{1}{r}\frac{n\Delta^2}{kT_c}$. Moreover, the Ambegaokar–Baratoff formula (7) for $I_c(T)$is identical to the Abrikosov–Gor'kov formula for the temperature dependence of concentration $n(T)$ of supercurrent carriers [21, 23, 24]. Consequently, $|\Psi|^2 \propto \frac{n\Delta^2}{(kT_c)^2}$ and the screening current in Eq. (10) is given by

$$\mathbf{j} = \frac{e\hbar}{mi}(\Psi^*\nabla\Psi - \Psi\nabla\Psi^*). \quad (11)$$

Here, $\Psi = \sqrt{n}e^{i\Theta}$ and $i^2 = -1$. In the cylindrical system of coordinates, the φ component j_φ of the current in Eq. (11) is given by

$$j_\varphi = \frac{e\hbar n}{mr}\frac{\partial\Theta}{\partial\varphi}.$$

Equation (6) for the critical state in the case of a long cylinder has the form

$$\frac{\partial H_z}{\partial r} = \frac{e\hbar n}{mr}\frac{\partial\Theta}{\partial\varphi}. \quad (12)$$

This equation is another form of Eq. (10). In contrast to formula (10), we must put $\partial\Theta/\partial\varphi = \pm 1$ into Eq. (12). This is due to the fact that $\partial\Theta/\partial\varphi = \pm N(\sim H)$ and $n \sim 1/N(\sim 1/H)$, because the formed vortices involve a part of the supercurrent carriers that participate in the formation of the macroscopic screening current. As a result, the right-hand side of Eq. (12) is independent of H. Taking into account Eq. (10), we introduce the notation

$$H^s = \frac{e\hbar n}{m} = \frac{\Delta}{4\pi e^2\rho_n}\tanh\left(\frac{\Delta}{2kT}\right).$$

In this model, the equation describing the penetration of the magnetic field into the array of weak links in a long cylinder ($L \gg R$, where L is the length of the cylinder and R is its radius; the external magnetic field has the axial direction), which uniformly fill the cylinder volume, and an analogous equation for a large plate (the magnetic field is directed along the z axis parallel to the plane of the plate) have the form

$$\frac{\partial H_z}{\partial r} = \frac{H^s}{r}\frac{\partial\Theta}{\partial\varphi}, \quad (13)$$

$$\frac{\partial H_z}{\partial x} = H^s\frac{\partial\Theta}{\partial y}, \quad (14)$$

respectively, where $\partial\Theta/\partial\varphi = \pm 1$ and $\partial\Theta/\partial y \cong \pm\pi/l$ ($l \gg b$, l is the length and width of the square plate and b is its thickness).

The solution to Eq. (13) with the boundary condition $H_z(R) = H$ (the axial external magnetic field strength H increases; i.e., $\partial\Theta/\partial\varphi = +1$) has the form

$$H_z(r) = \begin{cases} H, & r > R \\ H - H^s\ln\dfrac{R}{r}, & r \le R \\ 0, & r < \rho. \end{cases} \quad (15)$$

The magnetic field does not penetrate into the region of the cylinder where $r < \rho = R\exp(-|H|/H^s)$. Using solution (15), we can write the magnetization of the cylinder in the form

$$M = -H^s e^{-|H/H^s|}\sinh\left(\frac{H}{H^s}\right). \quad (16)$$

The solution to Eq. (14) with the boundary condition $H_z(\pm b/2) = H$ (the field also increases) has the form

$$H_z(x) = \begin{cases} H, & |x| \ge \dfrac{b}{2} \\ H - j^*\left(\pm\dfrac{b}{2} - x\right), & \rho \le |x| \le \dfrac{b}{2} \\ 0, & |x| \le \rho. \end{cases} \quad (17)$$

Here, $\rho = H/j^* - b/2$ and $j^* = H^s(\partial\Theta/\partial y) = \frac{\pi}{l}H^s$ is the screening current density. It follows from solution (17) that the magnetization of the plate is

$$M = -M_0\left[2\left(\frac{H}{H_p}\right) - \mathrm{sgn}(H)\left(\frac{H}{H_p}\right)^2\right]. \quad (18)$$

Here, $H_p = \frac{1}{2}j^*b$ and $M_0 = \frac{1}{2}H_p$. Expression (18) is valid for $H < H_p$. For $H > H_p$, the magnetization is $M(H) = -M_0$.

5. DISCUSSION OF RESULTS

Let us estimate the field H^s and the current density j^*. We assume that the effective concentration of supercurrent carriers in weak links (the concentration of tunneling pairs)[1] is $n \sim 10^{19}$–10^{20} cm^{-3}, the length is $l \sim 1$–10 cm, and the mass of a supercurrent carrier is $2m$ (m is the mass of a free electron). The results of calculations are $H^s \sim 1$–20 Oe and $j^* \sim 1$–10 A/cm^2. These estimates are in accordance with our experimental results (see Section 3) if we assume that $H^* = H^s$, as well as with the results obtained in [4, 10, 12]. Indeed,

[1] The concentration of supercurrent carriers in $YBa_2Cu_3O_{7-x}$ granules is approximately equal to 10^{21}–10^{22} cm^{-3} [10].

Parameters of the investigated YBaCuO samples

Sample number	Model parameters in Eq. (3)				H_{irr}, Oe
	A	B	H^*, Oe	α	
1	0.10	0.305	9.7	1.9	19
2	0.32	0.35	24.5	1.9	82
3	0.018	0.15	17	2.3	23

the nonlinear component of dependence in Eq. (4) is very close to the dependence in Eq. (16), except for the region near $H = 0$. It was mentioned above that the right-hand side of Eqs. (13) and (14) is independent of the external field strength H. This effect is similar to the one described by the well-known Bean model of the critical state [8], in which the critical current density is independent of H. Our results, as well as the results of many other experimental investigations [10, 12, 25–27], confirm this conclusion. Bean's model of the critical state [8] is successfully employed for describing the magnetic properties of hard type II superconductors. This model predicts the existence of a magnetization hysteresis for these materials. Our experimental results (Fig. 2 and table), as well as the results obtained by other authors (see, for example, [4, 5, 12, 25]), point towards the absence of magnetization hysteresis in $YBa_2Cu_3O_{7-x}$ polycrystalline samples for $H < H_{irr} \sim$ 20–80 Oe. In the model considered in Section 4 and in the model of hypervortices [17, 19], this effect can be explained as follows. It was mentioned by us earlier that the theoretical model presented in Section 4 is based on the concept of a Josephson medium in which hypervortices are formed. According to the estimates obtained at the beginning of Section 4, the hypervortex diameter is of the order of ~10–500 μm and embraces a large number of granules of the polycrystal, whose size is ~0.1–10 μm. This means that continuous or netlike hypervortices are formed. As the magnetic field increases and attains a value H_{irr}, these vortices are gradually transformed into conventional Josephson vortices between granules; after the attainment of the value H_{c1g} by the field, Abrikosov vortices are formed in the granules. Hypervortices are low-mobility formations [17, 19]. With increasing magnetic field, the diameter of hypervortices decreases and their number increases so that they gradually fill the entire volume of the sample. This process is accompanied by the emergence of and increase in a macroscopic peripheral screening supercurrent. In a decreasing field, the process is reversed; therefore, there is no magnetic hysteresis in the sample.

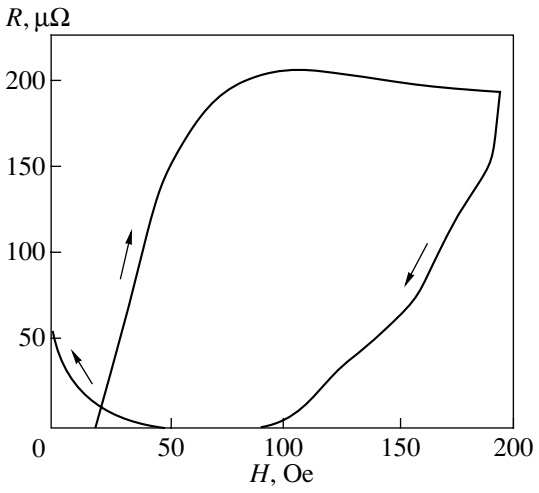

Fig. 3. Magnetic-field dependence of the resistance R of a $YBa_2Cu_3O_{7-x}$ ceramic sample carrying a dc current I = 100 mA at $T \approx 77$ K. The arrows show the direction of magnetic field variation.

The pinning and motion of Josephson vortices for $H > H_{irr}$ are described by the well-known models of the critical state, magnetic flux creep, and the viscous flow of vortices. The magnetic hysteresis and, accordingly, the flux trapping for $H > H_{irr}$ take place in the case of pinning of Josephson vortices by nonsuperconducting inclusions and by pores in $YBa_2Cu_3O_{7-x}$ polycrystalline samples. This can be explained using the well-known Kim model of the critical state ($j_c \sim 1/(H_0 + |H|)$). The motion of Josephson vortices leads to the emergence of a resistance, while their pinning leads to magnetic-flux trapping and to hysteresis of magnetization and magnetoresistance. This fact has been confirmed by experimental investigations of the magnetoresistance of HTSC ceramics [28] (Fig. 3). It can be seen from Fig. 3 that a dc resistance appearing for $H \approx$ 20 Oe increases with the field and hysteresis is observed when the field varies in the opposite direction in the region of $H \sim$ 30–70 Oe. As the field decreases to zero, a residual resistance is preserved, which gradually decreases to zero.

Let us estimate the size of a nonuniformity, assuming that a vortex carries a magnetic flux quantum $\Phi_0 \approx 2 \times 10^{-7}$ Mx. For $H_{irr} \sim$ 20 Oe, we obtain $a \sim 1$ μm.

The model considered by us here is basically close to the models considered in [4–6, 12], in which a ceramic material is regarded as an aggregate of microscopic current loops containing Josephson junctions. The only difference is that, in our model, a screening current loop occupies the entire sample and is inter-

sected by a large number of Josephson junctions (weak links). A magnetic field penetrates into the sample in the form of hypervortices (in comparison to microscopic current loops carrying a magnetic-flux quantum). The magnetic response of the sample is formed by this macroscopic screening current alone, as in the models of the critical state. We assume here that the reason for the emergence of this macroscopic current is associated with the penetration of hypervortices into the bulk of the sample and their transformation into Josephson vortices.

As a result, analyzing the available data, preference was given precisely to this reason, although other reasons can also be applicable when describing the magnetic properties of granular HTSC materials on the basis of Eqs. (6) and (10)–(12).

In the model presented by us here, the emergence of magnetization harmonics (a consequence of the nonlinearity of the magnetization $M(H)$ given by Eq. (16) or Eq. (18)), as well as their temperature dependence [see Eq. (10)], receives a natural explanation. The out-of-phase component M_n'' of the magnetization harmonics appears as a result of the magnetic moment relaxation in the sample, $M = M(H, t)$. This topic will be covered in our next publication.

ACKNOWLEDGMENTS

The author is grateful to A.I. Golovashkin and G.F. Zharkov for fruitful discussions of the results of this publication.

REFERENCES

1. A. A. Kozlovskiĭ and V. F. Khirnyĭ, Fiz. Tverd. Tela (St. Petersburg) **42** (10), 1780 (2000) [Phys. Solid State **42**, 1825 (2000)].
2. S. L. Ginzburg and N. E. Savitskaya, Zh. Éksp. Teor. Fiz. **117**, 227 (2000) [JETP **90**, 202 (2000)].
3. M. A. Zelikman, Fiz. Tverd. Tela (St. Petersburg) **42** (10), 1768 (2000) [Phys. Solid State **42**, 1813 (2000)].
4. C. Jeffries, Q. Lam, Y. Kim, *et al.*, Phys. Rev. B **37**, 9840 (1988).
5. A. I. Golovashkin, N. D. Kuz'michev, I. S. Levchenko, *et al.*, Fiz. Tverd. Tela (Leningrad) **31** (4), 233 (1989) [Sov. Phys. Solid State **31**, 1409 (1989)].
6. A. I. Golovashkin, N. D. Kuz'michev, I. S. Levchenko, *et al.*, Fiz. Tverd. Tela (Leningrad) **32**, 1374 (1990) [Sov. Phys. Solid State **32**, 802 (1990)].
7. Kh. R. Rostami, A. A. Sukhanov, and V. V. Mantorov, Fiz. Nizk. Temp. **22**, 58 (1996) [Low Temp. Phys. **22**, 42 (1996)].
8. C. Bean, Phys. Rev. Lett. **8**, 250 (1962).
9. C. Ebner and D. Stroud, Phys. Rev. B **31**, 165 (1985).
10. J. R. Clem, Physica C (Amsterdam) **153–155**, 50 (1988).
11. N. D. Kuz'michev, Pis'ma Zh. Tekh. Fiz. **17** (7), 56 (1991) [Sov. Tech. Phys. Lett. **17**, 259 (1991)].
12. C. Jeffries, Q. Lam, Y. Kim, *et al.*, Phys. Rev. B **39**, 11526 (1989).
13. N. D. Kuz'michev, Zh. Tekh. Fiz. **64** (12), 63 (1994) [Tech. Phys. **39**, 1236 (1994)].
14. N. D. Kuz'michev, Pis'ma Zh. Tekh. Fiz. **20** (22), 39 (1994) [Tech. Phys. Lett. **20**, 906 (1994)].
15. N. D. Kuz'michev, M. A. Vasyutin, A. I. Golovashkin, and I. S. Levchenko, Fiz. Tverd. Tela (St. Petersburg) **37** (7), 2207 (1995) [Phys. Solid State **37**, 1203 (1995)].
16. N. D. Kuz'michev and M. A. Vasyutin, Fiz. Tverd. Tela (St. Petersburg) **40** (2), 202 (1998) [Phys. Solid State **40**, 180 (1998)].
17. É. B. Sonin, Pis'ma Zh. Éksp. Teor. Fiz. **47**, 415 (1988) [JETP Lett. **47**, 496 (1988)].
18. R. G. Mints and A. L. Rakhmanov, *Instabilities in Superconductors* (Nauka, Moscow, 1984).
19. É. B. Sonin and A. K. Tagantsev, Zh. Éksp. Teor. Fiz. **95**, 994 (1989) [Sov. Phys. JETP **68**, 572 (1989)].
20. V. V. Shmidt, *The Physics of Superconductors: An Introduction* (Nauka, Moscow, 1982).
21. A. A. Abrikosov, *Fundamentals of the Theory of Metals* (Nauka, Moscow, 1987; North-Holland, Amsterdam, 1988).
22. L. Solymar, *Superconductive Tunnelling and Applications* (Chapman and Hall, London, 1972; Mir, Moscow, 1974).
23. I. O. Kulik and I. K. Yanson, in *Josephson Effect in Superconducting Tunnel Structures* (Nauka, Moscow, 1970).
24. J. R. Schrieffer, *Theory of Superconductivity* (Benjamin, New York, 1964; Nauka, Moscow, 1970).
25. S. L. Ginzburg, I. D. Luzyanin, I. R. Metskhvarishvili, *et al.*, Pis'ma Zh. Éksp. Teor. Fiz. **69**, 184 (1999) [JETP Lett. **69**, 196 (1999)].
26. J. Sun, M. Scharen, L. Bourne, and J. Schrieffer, Phys. Rev. B **44**, 5275 (1991).
27. W. Xing, B. Heinrich, J. Chrzanowski, *et al.*, Physica C (Amsterdam) **205**, 311 (1993).
28. M. A. Vasyutin, A. I. Golovashkin, N. D. Kuz'michev, and I. S. Levchenko, Preprint No. 85, FIAN (Lebedev Inst. of Physics, USSR Academy of Sciences, Moscow, 1990).

Translated by N. Wadhwa

Physics of the Solid State, Vol. 43, No. 11, 2001, pp. 2018–2024. Translated from Fizika Tverdogo Tela, Vol. 43, No. 11, 2001, pp. 1939–1944.
Original Russian Text Copyright © 2001 by Zhelezina, Maksimova.

METALS AND SUPERCONDUCTORS

Surface Impedance of a Superconducting Slab in the Mixed State: Effect of the Surface Barrier

N. V. Zhelezina and G. M. Maksimova

Lobachevskiĭ State University, pr. Gagarina 23, Nizhni Novgorod, 603600 Russia

e-mail: maksimova@phys.unn.runnet.ru

Received January 25, 2001; in final form, April 5, 2001

Abstract—The effect of the surface barrier on the surface impedance Z of a type-II superconductor slab with a finite thickness is investigated in dc magnetic fields H_0, which are aligned parallel or perpendicular to the slab plane. It is demonstrated that, in a perpendicular geometry, the surface resistivity $\rho_s = \mathrm{Re}Z$ has a maximum when the depth of penetration of the ac magnetic field is of the order of the slab thickness (size effect). For a parallel orientation of the magnetic field H_0, the effect of the Bean–Livingston surface barrier manifests itself as a decrease in the dissipative loss and a change in the field dependence of the surface resistivity characterized by a magnetic hysteresis. It is shown for the first time that, under the conditions of persistent trapped magnetic flux, the dependence $\rho_s(H_0)$ is a decreasing function, which is associated, in particular, with a nontrivial suppression of the size effect. © *2001 MAIK "Nauka/Interperiodica".*

1. INTRODUCTION

Investigation into the high-frequency properties of type-II superconductors and, especially, the properties of high-temperature superconductors has attracted the particular attention of many researchers (see, for example, [1–4]). The response of a superconductor sample to an ac magnetic field in the presence of a dc magnetic field is characterized by the surface impedance, which depends on the temperature, the strength of the dc magnetic field, and the amplitude and frequency of the ac magnetic field. Examination of these functional dependences can provide important information on the properties of quasiparticle excitations, density of states, and vortex-lattice dynamics. The problem of the linear response of type-II superconductors has already been considered in a number of works (see, for example, [5–12]). In particular, it was established that, at ac field frequencies ω higher than the depinning frequency ω_d, vortices move freely and the penetration of the ac magnetic field into the sample is governed by the skin depth δ [5, 6]. Coffey and Clem [7–9] calculated the surface impedance of a superconductor in the mixed state with due regard for the vortex–vortex interaction, magnetic-flux pinning, and the flux creep. Sonin *et al.* [10] demonstrated that, in the case when allowance for the nonlocal interaction between vortices is included in the analysis, the penetration of the ac magnetic field into a superconductor is determined not only by the skin-layer width but also by another considerably smaller scale on which the vortex lattice is strongly deformed. The calculation of the impedance in a dc magnetic field normal to the sample surface provided conclusive evidence that the extra short-wavelength mode makes the dominant contribution to the impedance of samples with a strong surface pinning. It turned out that the energy of an incident wave corresponds to the short-wavelength mode when the motion of the vortex ends is suppressed by strong surface pinning. Consequently, the decrease in the contribution of the long-wavelength mode responsible for the energy dissipation results in a substantial suppression of the ac losses in the range of sufficiently low frequencies. The inferences drawn in [10] were experimentally confirmed by Berezin *et al.* [12], who examined the field and frequency dependences of the real part of the surface impedance for a bulk sample.

In the case when the dc magnetic field is aligned with the sample surface, it is necessary to take into account the Bean–Livingston surface barrier, which, as is known, considerably affects the magnetic characteristics of type-II superconductors (see, for example, [13–15]). Recent studies [16–18] have revealed that the behavior of the third harmonic of magnetic susceptibility is governed primarily by the mechanism of irreversibility, viz., bulk pinning or the surface barrier. The formation of a vortex-free region near the superconductor surface due to the Bean–Livingston barrier leads to a partial screening of the vortex system and a drastic decrease in the absorption in the ac magnetic field [11].

For the most part, the surface impedance in the cited works has been calculated for semi-infinite samples, which, in actual fact, correspond to bulk samples whose sizes considerably exceed the depth of penetration of the ac magnetic field. However, the investigation into the nonlinear response of a hard superconductor slab showed that the real part of the impedance has a characteristic maximum when the wave penetration depth is comparable to the sample thickness (see, for example,

[19, 20]); i.e., there exists a size effect similar to the Fischer–Kao effect for normal metals [21].

In the present work, we derived an expression for the surface impedance of a superconducting slab of arbitrary thickness without bulk inhomogeneities. In the transverse geometry when the dc magnetic field is perpendicular to the slab surface, the linear response was determined using the equations of two-mode electrodynamics. It was demonstrated that the dependence of the real part of the surface impedance on the external dc magnetic field exhibits a maximum due to the manifestation of the size effect. The behavior of this maximum was examined at different slab thicknesses and ac field frequencies. A similar calculation in the parallel geometry showed that, in the case when the Bean–Livingston barrier prevents the penetration of vortices through the sample surface and the number of these vortices remains constant, the surface resistivity decreases significantly and its dependence on the dc magnetic field is changed.

2. SURFACE IMPEDANCE OF A SUPERCONDUCTING SLAB IN A PERPENDICULAR DC MAGNETIC FIELD

Let us consider a superconducting slab of thickness d ($0 \le x \le d$) in a transverse dc magnetic field $\mathbf{H}_0 = (H_0, 0, 0)$ ($H_{c1} \ll H_0 \ll H_{c2}$), which produces a vortex lattice with the density $n_0 = H_0/\Phi_0$ (where Φ_0 is the magnetic flux quantum). The ac magnetic field aligned parallel to the surface of the superconducting slab brings about the displacement $\mathbf{u}(x, t)$ of the vortices from their equilibrium positions and, consequently, distortion (tilting) of the vortex lines. The magnetic induction $\mathbf{B}_1$ due to this distortion is defined by the expression [7, 11]

$$\mathbf{B}_1 = (\mathbf{H}_0 \cdot \nabla)\mathbf{u} - \mathbf{H}_0(\nabla \cdot \mathbf{u}) = -[\nabla \cdot [\mathbf{H}_0 \cdot \mathbf{u}]]. \quad (1)$$

It is assumed that the intervortex spacing a satisfies the condition $a \ll \lambda$, where λ is the London penetration length. With this assumption and taking into account expression (1), the set of equations for the determination of the mean magnetic field $\mathbf{h}(x, t) = \mathbf{h}(x)\exp(-i\omega t)$ inside the slab [$h(x = 0) = h(x = d) = H_1$, $H_1 \ll H_0$] can be written in the following form:

$$\mathbf{h} - \lambda^2 \frac{\partial^2 \mathbf{h}}{\partial x^2} = H_0 \frac{\partial \mathbf{u}}{\partial x}, \quad (2)$$

$$\eta \frac{\partial \mathbf{u}}{\partial t} = \frac{1}{c}[\mathbf{j}\Phi_0] + \frac{\Phi_0}{H_0} C_{44}^* \frac{\partial^2 \mathbf{u}}{\partial x^2}, \quad (3)$$

$$\mathbf{j} = \frac{c}{4\pi}\mathrm{rot}\mathbf{h}. \quad (4)$$

Here, c is the velocity of light, $\eta = \Phi_0 H_{c2}/c^2\rho_n$ is the coefficient of viscosity, ρ_n is the resistivity in the normal phase, and C_{44}^* is the renormalized tilt modulus given by [10]

$$C_{44}^* = \frac{\Phi_0 H_0}{16\pi^2\lambda^2}\ln\frac{a}{\xi}, \quad (5)$$

where ξ is the radius of the vortex core. It should be noted that the tilt modulus thus determined is of the local nature, whereas the long-range intervortex interaction responsible for the nonlocality is accounted for in the Lorentz force acting on the vortex [the first term on the right-hand side of Eqs. (3)] [22]. Under the assumption that solutions to the set of equations (2)–(4) are described by the exponential dependence $u(x, t) \propto h(x, t) \propto \exp(kx - i\omega t)$, we obtain the dispersion equation for determining the frequency dependence of the wave vector k. The solutions to this equation for the long-wavelength (k_1) and short-wavelength (k_2) modes in the frequency range $\omega \ll \omega_c$ are represented by the relationships[1]

$$k_1^2 = -\frac{i\omega}{\lambda^2(\omega_c + \omega_b)}, \quad (6)$$

$$k_2^2 = \frac{1}{\lambda^2}\left(1 + \frac{\omega_b}{\omega_c}\right), \quad (7)$$

$$\omega_c = \frac{\Phi_0 C_{44}^*}{H_0\lambda^2\eta}, \quad \omega_b = \frac{\Phi_0 H_0}{4\pi\lambda^2\eta}. \quad (8)$$

By adopting the Maxwell equations for deducing the ac electric field $\mathbf{E}(x, t)$ and solving the set of equations (2)–(4), we determine the surface impedance of the slab in the transverse magnetic field, that is,

$$Z = \frac{4\pi}{c}\frac{E(0)}{h(0)}. \quad (9)$$

Further analysis will be performed with due regard for the boundary conditions for the vortex displacement $u(x)$, which characterize the surface quality.

(a) In the absence of surface defects, the vortex ends can freely move along the slab surfaces. The appropriate boundary condition has the form $(\partial\mathbf{u}/\partial x)|_{x = 0, d} = 0$, which leads to the following formula for the surface impedance:

$$Z = \frac{4\pi i\omega}{\lambda^2 c^2}\left(\frac{(1 - \lambda^2 k_2^2)}{k_1}\tanh\frac{k_1 d}{2} - \frac{(1 - \lambda^2 k_1^2)}{k_2}\tanh\frac{k_2 d}{2}\right)(k_2^2 - k_1^2)^{-1}. \quad (10)$$

[1] Formulas (6) and (7) differ from the corresponding expressions obtained in [10] in the sign ahead of the k^2 quantity, because, in [10], k is the wave vector.

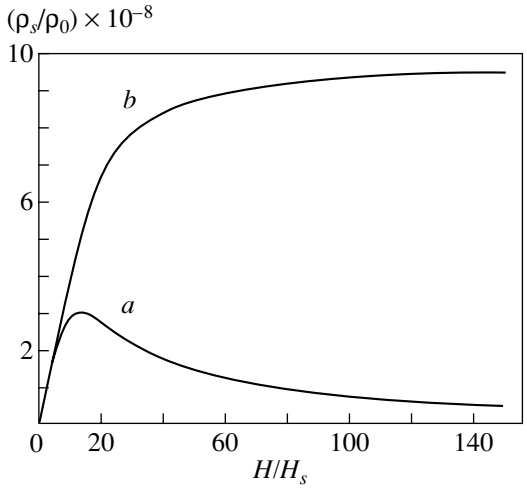

Fig. 1. Surface impedance of the superconducting slab of thickness d in a perpendicular magnetic field: (a) real and (b) imaginary parts. Conditions: $d = 200\lambda$, $\rho_0 = 4\pi\omega_0\lambda/c^2$, $\omega_0 = 1$ Hz, and H_s is determined according to formula (21).

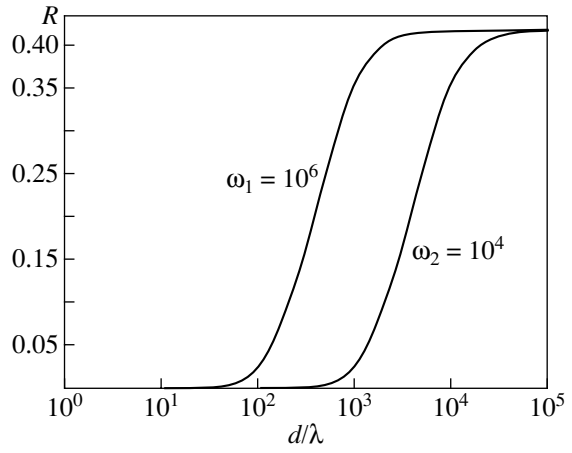

Fig. 2. Dependences of the maximum surface resistance $R = \rho_{s_{max}}/\chi_n$ (where $\chi_n = 2\pi\omega d/c^2$) on the slab thickness.

Specifically, the surface resistivity $\rho_s = \mathrm{Re}\,Z$ for a semi-infinite sample ($d \longrightarrow \infty$) is determined by the flux-flow resistivity $\rho_f = \Phi_0 H_0/c^2\eta$ [6]:

$$\rho_s = \frac{(2\pi\rho_f\mu\omega)^{1/2}}{c}. \tag{11}$$

Here, $\mu = \omega_b/(\omega_c + \omega_b)$. For a sufficiently dense vortex lattice [$H_0 \gg \Phi_0\ln(a/r_c)/4\pi\lambda^2$], we obtain $\mu \approx 1$. This implies that the last term in relationship (3) can be ignored. In this case, the bulk losses are determined only by the long-wavelength mode. As follows from formula (10) for the surface impedance Z, the surface resistivity of a superconducting slab of finite thickness is a nonmonotonic function of the dc magnetic field H_0, which reaches a maximum in the dc field $H_0 = H^*$ at a thickness $d \propto k_1^{-1}(H^*)$; i.e., the size effect takes place. The size effect revealed in this case is similar to the Fischer–Kao effect for normal metals [21]. Its analog was also observed in hard superconductors (see, for example, [19]).

Figure 1 displays the calculated field dependences of the real and imaginary parts of the surface impedance for a superconducting slab of thickness $d = 200\lambda$ ($\lambda = 1300$ Å) without surface pinning. The ac field frequency ω is equal to 10^7 Hz. These conditions can be realized, for example, in YBaCuO crystals at temperatures close to the melting temperature of the vortex lattice. Lütke-Entrup *et al.* [4] proved that, under these conditions, the depinning frequency related to both bulk and surface pinning of vortices does not exceed 10^7 Hz. The maximum surface resistance $R = \rho_{s_{max}}/\chi_n$ (where $\chi_n = 2\pi\omega d/c^2$ is the surface reactance in the normal state) depends on the slab thickness d/λ and the ac field frequency. As the ratio d/λ increases, the maximum surface resistance R tends to a constant value that is independent of the superconductor parameters and the ω frequency (Fig. 2). Fisher *et al.* [19] obtained a similar dependence of the surface resistance R for hard superconductors in the framework of the nonlocal model of the critical state; however, the maximum value of R was approximately halved.

(b) We now dwell on a strong surface pinning of vortex line ends. From the set of equations (2)–(4) with the boundary condition $\mathbf{u}|_{x=0,\,d} = 0$, we deduce the relationship

$$Z = \frac{4\pi i\omega\lambda^2}{c^2}(k_1^2 - k_2^2)\Big((1-\lambda^2k_1^2)k_2\coth\frac{k_2d}{2} - (1-\lambda^2k_2^2)k_1\coth\frac{k_1d}{2}\Big)^{-1}. \tag{12}$$

At $d \longrightarrow \infty$, the surface resistivity of a semi-infinite sample [10] can be found from the real part of the impedance Z in relationship (12) according to the formula

$$\rho_s = \frac{(2\pi\rho_f\mu\omega)^{1/2}}{c}\frac{\omega}{\omega_c}. \tag{13}$$

As can be seen from this formula, the absorption in the case of strong surface pinning decreases considerably (owing to the smallness of the parameter $\omega/\omega_c \ll 1$). This effect is explained by the fact that the amplitude ratio of the long-wavelength and short-wavelength modes is small: $h_1/h_2 \propto \sqrt{\omega/\omega_c} \ll 1$ [10]. Consequently, the contribution of the long-wavelength mode responsible for the energy dissipation in the superconductor bulk becomes small compared to that in the case of weak surface pinning. The numerical calculations

demonstrated that the $\rho_s(H_0)$function for superconducting slabs of finite thickness also has a maximum. However, the width of this maximum (with respect to the dc magnetic field H_0) is rather large. As a result, the size effect for superconducting slabs with strong surface pinning is weakly pronounced.

3. STRUCTURE OF THE MIXED STATE OF A SUPERCONDUCTING SLAB IN A PARALLEL DC MAGNETIC FIELD

Now, we consider the case when the dc magnetic field $\mathbf{H}_0 = (0, 0, H_0)$ is directed parallel to the slab surface. In the continuous approximation, the mean magnetic field inside the slab is determined by the equation [9]

$$H - \lambda^2 \frac{d^2 H}{dx^2} = \Phi_0 n_0(x). \tag{14}$$

Here, $n_0(x)$ is the averaged vortex density, which is nonzero in the region with a zero current density ($j(x) = 0$). The solution of Eq. (14) yields

$$H(x) = \frac{H_0}{\cosh[(d/2 - a)/\lambda]} \times \begin{cases} \cosh[(x - d/2 + a)/\lambda], & 0 \le x \le d/2 - a \\ 1, & d/2 - a \le x \le d/2 + a \\ \cosh[(x - d/2 - a)/\lambda], & d/2 + a \le x \le d. \end{cases} \tag{15}$$

In this case, the vortices are located in the central region of the film:

$$n_0(x) = \frac{H_0/\Phi_0}{\cosh[(d/2 - a)/\lambda]}, \quad \frac{d}{2} - a \le x \le \frac{d}{2} + a. \tag{16}$$

The parameter a, which corresponds to the half-width of the region occupied by the vortices, is related to the trapped magnetic flux $\Phi = N\Phi_0$ (where N is the number of vortices already entered the slab) by the expression

$$\Phi = \frac{2aH_0}{\cosh[(d/2 - a)/\lambda]}. \tag{17}$$

The distribution described by relationships (15)–(17) at a specified Φ determines the set of metastable states in the field range $H_{ex}(\Phi) \le H_0 \le H_{en}(\Phi)$. The field $H_{en}(\Phi)$, in which the barrier to the vortex penetration (entry) becomes zero, can be found from the condition of the equality between the current density at the slab surface and the depairing current density: $j_s = c\Phi_0/(12\sqrt{3}\,\pi^2\xi\lambda^2)$. In the implicit form, this field can be determined using the equation

$$\Phi = 2H_{en}\sqrt{1 - \frac{H_s^2}{H_{en}^2}\tanh\frac{d}{2\lambda}} \times \left[\frac{d}{2} - \lambda\arctan\left(\frac{H_s}{H_{en}}\tanh\frac{d}{2\lambda}\right)\right]. \tag{18}$$

Here, H_s is the field attributed to the entry of the first vortex, that is,

$$H_s = \frac{4\pi\lambda j_s}{c\tanh(d/2\lambda)}. \tag{19}$$

We assume that the vortices begin to leave the slab when the distance between the boundary of the region occupied by the vortices and the slab surface (a) is of the order of the vortex core size ξ. In this case, the magnetic field which suppresses the barrier to the vortex exit can be represented in the form

$$H_{ex}(\Phi) = \frac{\Phi\cosh\xi/\lambda}{d - 2\xi}. \tag{20}$$

The intersection point of $H_{en}(\Phi)$ and $H_{ex}(\Phi)$ specifies (in our model) the field $H_{c2} \propto \Phi_0/\xi^2$. For a semi-infinite sample ($d \longrightarrow \infty$), formulas (18)–(20) take the form [23]

$$H_{en} = \sqrt{B^2 + H_s^2}, \quad H_{ex} = B\cosh\frac{\xi}{\lambda}, \quad H_s = \frac{4\pi\lambda j_s}{c}, \tag{21}$$

where $B = \Phi/d$ is the induction.

4. A SUPERCONDUCTING SLAB IN AC MAGNETIC FIELDS (A PARALLEL GEOMETRY)

Let us now consider a superconducting slab with a fixed trapped magnetic flux Φ in a magnetic field H_0, which is aligned with the slab surface and satisfies the condition

$$H_{ex}(\Phi) \le H_0 \le H_{en}(\Phi). \tag{22}$$

In the absence of bulk pinning, the vortices are distributed with the density $n_0(x)$, which is defined by formulas (16) and (17). In the case when a weak ac magnetic field $H_1\exp(-i\omega t)$ is applied parallel to the dc field H_0 and the total field satisfies condition (22), the number of vortices in the slab (and, correspondingly, the flux Φ) remains unchanged. Under the action of an alternating current, the vortices inside the slab begin to move, which, in turn, brings about a change in their density and, consequently, displacement of the vortex region boundary. In the geometry under consideration, the

equation for the coordination part of the ac magnetic field $h(x)\exp(-i\omega t)$ inside the slab has the form

$$h(x) - \lambda^2 \frac{d^2 h(x)}{dx^2} - \Phi_0 n_1(x) = 0. \quad (23)$$

The change in the vortex density $n_1(x, t) = n_1(x)\exp(-i\omega t)$ due to the response of the sample to the ac magnetic field can be obtained from the continuity equation and the equation determining the vortex displacement u_x along the x axis:

$$\frac{\partial n_1}{\partial t} + \frac{\partial}{\partial x}\left(n_0 \frac{\partial u_x}{\partial t}\right) = 0, \quad (24)$$

$$\eta \frac{\partial u_x}{\partial t} = \frac{\Phi_0}{c} j(x, t). \quad (25)$$

It should be noted that the vortex motion equations (3) and (25) involve the superconduction current density $j(x, t)$. This implies that the normal current component j_n is ignored, which is valid in the range of sufficiently low frequencies. Coffey and Clem [7, 9] considered the contribution from the normal component of the current density in the framework of the two-fluid model. Within this model, the Lorentz force acting on the vortex is given by

$$F = \frac{\Phi_0}{c} j = \frac{\Phi_0}{c}(j_s + j_n). \quad (26)$$

However, as was shown by Placais *et al.* [22], expression (26) is incompatible with the Onsager equations and the inclusion of j_n in the interaction with vortices would be more correctly performed in terms of the microscopic theory.

The set of equations (23)–(25) can be easily reduced to a sole equation for the field $h(x)$ that is,

$$h(x) - \lambda^2 \frac{d^2 h(x)}{dx^2} + \frac{d}{dx}\left(\frac{\Phi_0^2 n_0}{4\pi i \eta \omega} \frac{dh}{dx}\right) = 0. \quad (27)$$

Note that the field distribution is symmetric with respect to the midplane of the film. Therefore, Eq. (27) should be solved in the vortex-free region $0 \le x \le d/2 - a$ (I) and the vortex region $d/2 - a \le x \le d/2 + a$ (II) with the boundary condition $h_I(0) = H_1$ and the matching conditions at the boundaries of these regions:[2]

$$h_I = h_{II}\Big|_{\frac{d}{2}-a}, \quad \frac{dh_I}{dx} = \left(1 + \frac{i\Phi_0^2 n_0}{4\pi\eta\omega\lambda^2}\right)\frac{dh_{II}}{dx}\Big|_{\frac{d}{2}-a}. \quad (28)$$

[2] The second condition (28) is the condition for continuity of the tangential components of the electric field, because the superconductor in an alternating field is characterized by the conductivity $\sigma_I = c^2 i/4\pi\omega\lambda^2$ in the Meissner state and $\sigma_{II} = \sigma_I/(1 + i\Phi_0^2 n_0/4\pi\omega\eta\lambda^2)$ in the mixed state.

The solution of Eq. (27) has the form

$$h_I(x) = H_1\left(\cosh\frac{x - d/2 + a}{\lambda} + \gamma \sinh\frac{x - d/2 + a}{\lambda}\right) \times (\cosh b - \gamma \sinh b)^{-1}, \quad (29)$$

$$h_{II}(x) = \frac{H_1}{\cosh(a/\alpha)} \frac{\cosh[(x - d/2)/\alpha]}{\cosh b - \gamma \sinh b}, \quad (30)$$

$$b = \frac{d/2 - a}{\lambda}, \quad \alpha = \lambda\left(1 + \frac{il}{\lambda \cosh b}\right)^{1/2},$$
$$l = \left(\frac{\Phi_0 H_0}{4\pi\eta\omega}\right)^{1/2}, \quad \gamma = -\tanh\frac{a}{\alpha}\left(1 + \frac{il}{\lambda\cosh b}\right)^{1/2}. \quad (31)$$

As was noted above, when the number of vortices is constant, the boundary of the region occupied by the vortices harmonically varies with time:

$$a(t) = a + a_1 \exp(-i\omega t),$$

where a_1 is determined from the condition $\Phi = \text{const}$ according to the formula

$$a_1 = -\frac{i\Phi_0 H_1 \tanh(a/\alpha)}{4\pi\eta\omega\alpha(\cosh b - \gamma \sinh b)}.$$

From the above solution, we obtain the surface impedance of the superconducting slab of thickness d in the parallel geometry:

$$Z = \frac{4\pi i\omega\lambda}{c^2} \frac{\gamma - \tanh b}{1 - \gamma \tanh b}. \quad (32)$$

5. RESULTS AND DISCUSSION

Now, we analyze the behavior of the surface impedance Z in different limiting cases.

(1) According to formula (32), the surface impedance Z in the Meissner state (i.e., in the case when $a = 0$) has the form

$$Z = -\frac{4\pi i\omega\lambda}{c^2} \tanh\frac{d}{2\lambda}. \quad (33)$$

At frequencies $\omega \le 10^{12}$ Hz under the condition $\lambda/\delta_n \ll 1$ (where δ_n is the skin depth in the normal state), the normal component j_n of the current density can be ignored. In this case, as follows from relationship (33), the response of the slab to the ac magnetic field has a nearly inductive nature [7].

(2) Let us now compare the expressions for the surface impedance of the superconducting slab in the mixed state for parallel [formula (32)] and perpendicular [formulas (10)–(12)] orientations of the dc magnetic field. If the vortex-free region is absent ($b = 0$), the sur-

face impedance defined by formula (32) coincides with the corresponding expression for the perpendicular geometry. Analysis of formula (32) at $b \neq 0$ demonstrates that the occurrence of the vortex-free regions associated with the Bean–Livingston surface barrier results in the following: (i) substantial suppression of the dissipative loss [11] and (ii) changes in the frequency and field dependences of the surface resistivity. In particular, for thick slabs ($d \longrightarrow \infty$) and a small width $b(H_0, B)$ of the vortex-free region when

$$\frac{\lambda}{l} \ll b(H_0, B) \ll 1, \quad \frac{\lambda}{l} = \sqrt{\frac{\omega}{\omega_b}}, \tag{34}$$

the real part of the impedance ReZ is determined by the expression

$$\rho_s = \mathrm{Re}Z = \frac{(2\pi\rho_f\omega)^{1/2}}{c}\left(\frac{\lambda^2}{l^2b^2}\right). \tag{35}$$

In this expression, the surface resistivity is less than that determined by relationship (11) for the perpendicular geometry by a factor of $\lambda^2/l^2b^2 \ll 1$. For example, the parameter $\lambda^2/l^2b^2 \approx 1$ is of the order of 10^{-3} for the superconducting slab of thickness $d = 10^4\lambda \approx 1$ mm at a frequency $\omega = 10^7$ Hz and $H_0 = H_s \approx 0.4$ T. As was noted by Sonin and Traito [11], the frequency dependence of the ρ_s function for a semi-infinite sample is transformed from $\rho_s \propto \omega^{1/2}$ in the perpendicular geometry to $\rho_s \propto \omega^{3/2}$ in the parallel geometry.

(3) Another important feature of the surface barrier manifests itself in the fact that the surface resistivity depends not only on the ac field frequency ω and the dc magnetic field H_0 but also on the trapped magnetic flux Φ. The last circumstance leads to magnetic hysteresis of the resistivity $\rho_s(H_0)$. The characteristic hysteresis loop $\rho_s(H_0)$ of the superconducting slab in a magnetic field H_0 varying in the range $H_{ex2} \le H_0 \le H_{en1}$ ($\Phi_1 > \Phi_2$) is displayed in Fig. 3. In the field ranges $H_{ex1} \le H_0 \le H_{en1}$ and $H_{ex2} \le H_0 \le H_{en2}$, the number of vortices in the slab remains constant and the surface resistivity $\rho_s(H_0, \Phi_1)$ reversibly varies according to formula (32). When the magnetic field decreases from H_{ex1} to H_{ex2}, the vortices leave the slab. In this case, the vortex-free regions are virtually absent and the dependence $\rho_s(H_0)$ is described by formula (32) at $b = 0$ (the dashed line in Fig. 3). As the magnetic field increases from H_{en2} to H_{en1}, the vortices enter the sample and the curve of the surface resistivity in this range coincides with the envelope of the family $\rho_s(H_0, \Phi)$ at the points $H_0 = H_{en}(\Phi)$ (Fig. 4). It should also be noted that, at a fixed trapped magnetic flux Φ, the surface resistivity $\rho_s(H_0)$ is a decreasing function in the field range $H_{ex}(\Phi) \le H_0 \le H_{en}(\Phi)$ (Fig. 4). In this range, the function $\rho_s(H_0)$ for the perpendicular orientation of the magnetic field has a maximum, whereas the interaction of vortices with the surface (i.e., the Bean–Livingston surface barrier) in the parallel geometry suppresses this effect.

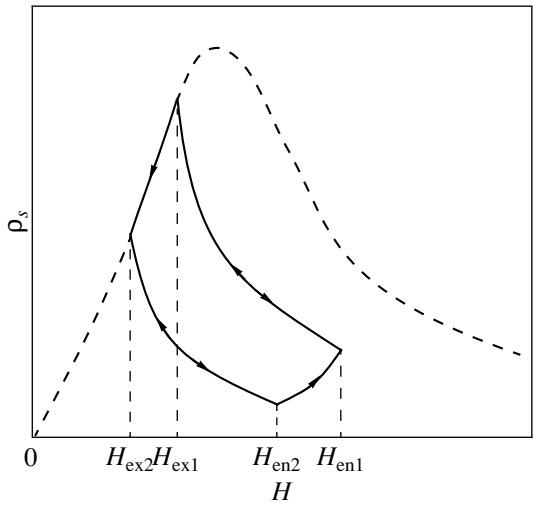

Fig. 3. Hysteresis of the surface resistivity of the superconducting slab in a parallel magnetic field with due regard for the Bean–Livingston barrier.

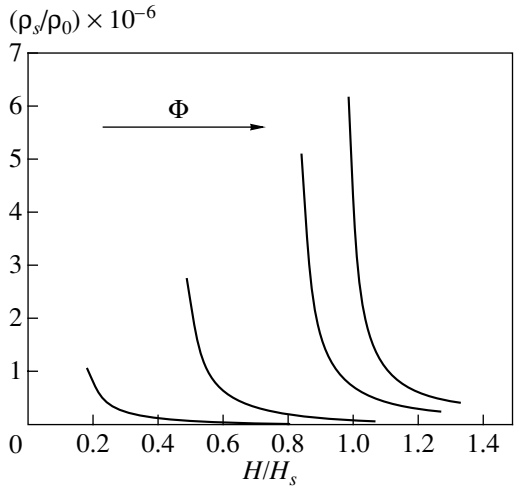

Fig. 4. Plots of the $\rho_s(H_0)$ function for the superconducting slab in a parallel magnetic field (with due regard for the Bean–Livingston barrier) at different trapped magnetic fluxes Φ ($d = 200\lambda$, $\rho_0 = 4\pi\omega_0\lambda/c^2$, and $\omega_0 = 1$ Hz). The arrow shows the direction of increase in the magnetic flux.

ACKNOWLEDGMENTS

We are grateful to I.L. Maksimov, D.Yu. Vodolazov, L.M. Fisher, and V.A. Yampol'skiĭ for valuable discussions of the results.

This work was supported by the Russian Foundation for Basic Research (project no. 01-02-16593), the Min-

istry of Science and Technology of the Russian Federation (project no. 107-1(00)), the Ministry of Education of the Russian Federation (project no. É 00-3.4-331), and the International Center of Advanced Research (Nizhni Novgorod, project no. 99-02-3).

REFERENCES

1. M. R. Trunin, J. Supercond. **11** (3), 381 (1998).
2. C. K. Ong, X. S. Rao, and B. B. Jin, Supercond. Sci. Technol. **12**, 827 (1999).
3. B. B. Jin, X. S. Rao, C. J. Tan, and C. K. Ong, Physica C (Amsterdam) **316**, 224 (1999).
4. N. Lütke-Entrup, B. Placais, P. Mathieu, *et al.*, Physica B (Amsterdam) **284–288**, 719 (2000).
5. I. Gittleman and B. Rosenblum, Phys. Rev. Lett. **16** (17), 734 (1966).
6. L. P. Gor'kov and N. B. Kopnin, Usp. Fiz. Nauk **116**, 413 (1975) [Sov. Phys. Usp. **18**, 496 (1975)].
7. M. W. Coffey and J. R. Clem, Phys. Rev. Lett. **67** (3), 386 (1991).
8. J. R. Clem and M. W. Coffey, Phys. Rev. B **46** (22), 14662 (1992).
9. M. W. Coffey and J. R. Clem, Phys. Rev. B **46** (18), 11757 (1992).
10. E. B. Sonin, A. K. Tagantsev, and K. B. Traito, Phys. Rev. B **46** (9), 5830 (1992).
11. E. B. Sonin and K. B. Traito, Phys. Rev. B **50** (18), 13547 (1994).
12. V. A. Berezin, E. V. Il'ichev, and V. A. Tulin, Zh. Éksp. Teor. Fiz. **105** (1), 207 (1994) [JETP **78**, 110 (1994)].
13. L. Burlachkov, Phys. Rev. B **47** (13), 8056 (1993).
14. I. L. Maksimov and A. E. Elistratov, Appl. Phys. Lett. **72** (13), 1650 (1998).
15. I. L. Maksimov and G. M. Maksimova, Pis'ma Zh. Éksp. Teor. Fiz. **65** (5), 405 (1997) [JETP Lett. **65**, 423 (1997)].
16. C. J. van der Beek, M. V. Indenbom, G. D'Anna, and W. Benoit, Physica C (Amsterdam) **258**, 105 (1996).
17. G. M. Maksimova, D. Yu. Vodolazov, M. V. Balakina, and I. L. Maksimov, Solid State Commun. **111**, 367 (1999).
18. G. M. Maksimova, D. Yu. Vodolazov, and I. L. Maksimov, cond-mat/9911287; Physica C **356** (1–2), 67 (2001).
19. L. M. Fisher, I. F. Voloshin, V. S. Gorbachev, *et al.*, Physica C (Amsterdam) **245**, 231 (1995).
20. F. Pérez Rodríguez, N. M. Makarov, V. A. Yampol'skii, *et al.*, Appl. Phys. Lett. **67** (3), 419 (1995).
21. H. Fischer and Y.-H. Kao, Solid State Commun. **7**, 275 (1969).
22. B. Placais, P. Mathieu, Y. Simon, *et al.*, Phys. Rev. B **54** (18), 13083 (1996).
23. J. R. Clem, in *Low Temperature Physics: LT-13*, Ed. by K. D. Timmerhaus, W. J. O'Sullivan, and E. F. Hammel (Plenum, New York, 1974), Vol. 3, p. 102.

Translated by O. Borovik-Romanova

Physics of the Solid State, Vol. 43, No. 11, 2001, pp. 2025–2031. Translated from Fizika Tverdogo Tela, Vol. 43, No. 11, 2001, pp. 1945–1951.
Original Russian Text Copyright © 2001 by Lomtev.

METALS AND SUPERCONDUCTORS

Inverted Satellites of a Solitary Oscillating Pearl Vortex in a Thin Magnetic Superconductor Film

A. I. Lomtev

Donetsk Physicotechnical Institute, National Academy of Sciences of Ukraine, Donetsk, 83114 Ukraine
e-mail: lomtev@kinetic.ac.donetsk.ua

Received April 9, 2001

Abstract—An electrodynamic equation is derived for the magnetic field of an isolated Pearl vortex moving along an arbitrary trajectory in an ultrathin film of a magnetic superconductor. This equation is valid for any type of magnetic order in the magnetic subsystem. The magnetic structure of an isolated oscillating Pearl vortex is investigated in a thin magnetic superconductor film. Oscillations of the vortex and the presence of the magnetic subsystem are shown to lead to a significant renormalization of the vortex field in comparison with the Pearl solution. New phenomena of inverted satellites are predicted in which an inverted precursor appears in front of the vortex and an inverted wake is formed behind the latter at a distance of the order of $10\lambda_{\text{eff}}$ from the vortex center. These phenomena can be observed in magnetooptical experiments. © *2001 MAIK "Nauka/Interperiodica".*

1. There are many magnetic superconductors that show surprising and nontrivial properties [1–3]. Superconductivity and magnetism have been found to exist in ternary compounds [4] and high-temperature superconductors such as *RE*BaCuO and *RE*CuO (*RE* is a rare-earth ion). One of the most important properties of HTSC materials is the fairly strong antiferromagnetic correlation of copper-ion spins exhibited by them in CuO_2 planes in the superconducting state [5].

An external magnetic field penetrates into a bulk type II superconductor in the form of Abrikosov vortices [6] and magnetizes the magnetic subsystem at distances of the order of the London penetration depth λ around the normal core of a flux vortex. A fairly heavy dc or ac electric transport current flowing through a superconductor in a rarefied mixed state suppresses flux vortex pinning, with the result that the vortex array or nearly isolated Abrikosov vortices are forced to move uniformly or to oscillate [7]. High-power microwave radiation can also give rise to harmonic oscillations of the Abrikosov vortex array or isolated flux vortices.

Krivoruchko [8] investigated the magnetic structure of an isolated Abrikosov vortex moving uniformly and slowly through a bulk magnetic superconductor with a thickness along the magnetic field of $d \gg \lambda$; he was the first to predict the formation of an inverted wake at large distances (of the order of 10λ) behind the vortex. In [9], it was first predicted that if an isolated Abrikosov vortex oscillates in a bulk magnetic superconductor, an inverted precursor arises before this vortex, an inverted wake is formed behind it, and they are located at a distance of the order of 10λ from the vortex center.

As was first pointed in [10], vortices move under the action of the Lorentz force, which results from the superconduction current. In a highly rarefied mixed state, the vortex density is low and the distance between them is $d_0 \gg \lambda$. In this case, there is no electric transport current in the bulk of the superconductor (because of the Meissner effect) and the current flows only through the skin depth near the interfaces. It is in the skin depth that the Lorentz force acts on a flux vortex. Since a vortex line is continuous along the z axis in the bulk of a superconductor far from its surface, the vortex will move uniformly or oscillate; therefore, its motion can be considered two-dimensional.

The solutions to the relevant two-dimensional problems found in [8, 9] are valid only in the bulk of a superconductor or, more specifically, in the regions at distances $L_0 \gg \lambda$ from the interfaces, where the system can be assumed to be approximately two-dimensional. In the vicinity of the air/superconductor surface, these solutions should be modified and it is not clear whether the inverted satellites will persist in rigorous solutions to three-dimensional problems; this issue needs further consideration. At the same time, it is very difficult, if at all feasible, to observe inverted satellites formed near an Abrikosov vortex in the bulk of a superconductor. As we will see further on, this problem does not arise in the case of a thin superconductor film.

It should be noted that the time dependence of the magnetic field of an Abrikosov vortex is essentially different in the cases of its uniform motion [8] and harmonic oscillation [9]. In the former case, the configuration of a magnetic field with an inverted wake does not vary in time, whereas in the latter, the structure of both the inverted precursor and the inverted wake is radically altered over an oscillation period.

1063-7834/01/4311-2025$21.00 © 2001 MAIK "Nauka/Interperiodica"

An external magnetic field penetrates in the form of two-dimensional Pearl vortices [11–13] into a thin magnetic superconductor film (with a thickness of $d \ll \lambda$) and magnetizes the magnetic subsystem at distances of the order of the effective Pearl penetration depth $\lambda_{eff} = \lambda^2/d \gg \lambda$ around the normal core of a vortex in the film. When a fairly heavy dc or ac transport current flows through a superconductor film in the rarefied mixed state, virtually isolated Pearl vortices are forced to move at a constant velocity v or to oscillate with a time-varying velocity $v(t)$. The velocity of a vortex is proportional to the transport current that produces the magnetic field. It should be noted that since Maxwell's equations are linear (in the case where the superposition principle holds), the corrections to the entire magnetic field of a Pearl vortex that are due to the transport current and that are proportional to the vortex velocity v or $v(t)$ do not affect the solutions obtained; these corrections are negligibly small even in comparison with the magnetic field of the inverted satellites of the Pearl vortex (because $v/c \ll 1$ and $v(t)/c \ll 1$) and can be ignored.

In [14], the magnetic structure of an isolated two-dimensional Pearl vortex moving uniformly in a thin magnetic superconductor film was investigated using an equation derived for the vector potential $\mathbf{A}(\mathbf{r}, t)$ and it was shown that the vortex motion and the presence of the magnetic subsystem give rise to a significant renormalization of the vortex field in comparison with the Pearl solution. It was predicted that an inverted wake is formed behind a moving vortex at a distance of the order of $10\lambda_{eff}$ from its center and that this phenomenon can be observed in magnetooptical experiments.

It is also of interest to investigate the magnetic field of the Pearl vortex in a more intricate case where the vortex motion is different from being slow and uniform. The magnetic structure of an isolated Pearl vortex oscillating harmonically in a thin film of a magnetic superconductor has not yet been analyzed. In this paper, we perform this analysis in the case of an ultrathin film whose thickness along the external magnetic field is $d \ll \lambda$. In the geometry in question, the problem is reduced to the case of a Pearl vortex in an infinitely thin two-dimensional film, where the physical vortex characteristics, such as the field and the current, can be assumed to be independent of the coordinate z along the normal to the plane of the film.

We assume that the system under study is two-dimensional with respect to both the superconducting and magnetic properties; therefore, the magnetic permeability of the film can be written as $\mu(\mathbf{r} - \mathbf{r}', t - t') = \mu(\boldsymbol{\rho} - \boldsymbol{\rho}', t - t')\delta(z - z')$, where $\mathbf{r} = (x, y, z)$, $\boldsymbol{\rho} = (x, y)$, and $\delta(z)$ is the Dirac δ function. In the coordinate system chosen, the xy plane coincides with the film plane and the magnetic field of the vortex is parallel to the z axis.

The conduction electrons are assumed to interact with the spin subsystem via the electromagnetic (dipole) field, while the spin–spin exchange interaction is ignored. We use the London approximation, in which the structure of the vortex core is of no importance, because $\lambda \gg \xi$ and even $\lambda_{eff} \gg \xi$ (ξ is the correlation length). When considering isolated vortices in a thin film in a highly rarefied mixed state in the range of magnetic fields $H_{c1} < B < H_{c2}$ (H_{c1} and H_{c2} are the lower and upper critical fields of the superconductor, respectively), we actually suggest that the separation between vortices is $d_0 \gg \lambda_{eff}$. However, since $d \ll \lambda$, the transport current flows through the entire thickness of the film.

We use a kinematic approach, in which it is assumed that the dynamic equations for the Pearl vortex have already been solved with allowance for pinning and various processes of dissipation [7, 15] and only those solutions are chosen that correspond to harmonic oscillations of an isolated vortex line.

It should be noted that, in the general case, the deformation of vortices in a superconductor in the mixed state is of importance [16]. However, in the case of a highly rarefied mixed state considered here, this deformation is small because of the low vortex concentration and does not affect the formation of inverted satellites (precursor and wake) of an oscillating Pearl vortex.

2. As in [17–19], we start from Maxwell equations in which the magnetic induction $\mathbf{B}(\mathbf{r}, t) = \mathrm{curl}\mathbf{A}(\mathbf{r}, t)$ is determined by the persistent superconduction current $\mathbf{j}(\mathbf{r}, t)$, the magnetization $\mathbf{M}(\mathbf{r}, t)$, and the displacement current:

$$\begin{aligned} \mathrm{curl}\mathbf{B}(\mathbf{r}, t) &= 4\pi c^{-1}\mathbf{j}(\mathbf{r}, t) \\ &+ 4\pi\mathrm{curl}\mathbf{M}(\mathbf{r}, t) + c^{-1}\partial\mathbf{D}(\mathbf{r}, t)/\partial t, \\ \mathrm{curl}\mathbf{E}(\mathbf{r}, t) &= -c^{-1}\partial\mathbf{B}(\mathbf{r}, t)/\partial t. \end{aligned} \quad (1)$$

For simplicity, the electric displacement $\mathbf{D}(\mathbf{r}, t)$ is assumed to be related to the electric field $\mathbf{E}(\mathbf{r}, t)$ through the local constitutive equation $\mathbf{D}(\mathbf{r}, t) = \varepsilon_0\mathbf{E}(\mathbf{r}, t)$, where the permittivity ε_0 is considered to be constant.

The displacement current is usually neglected in the first equation of set (1). However, as we will see later, the displacement current affects the dependence of the renormalized magnetic field of the Pearl vortex on the functional form of the permeability of the system.

From the London equation [in the London potential gauge $\mathrm{div}\mathbf{A}(\mathbf{r}, t) = 0$], one can derive the relation between the current, the vector potential, and the phase of the order parameter $\Theta(\mathbf{r}, t)$:

$$\mathbf{j}(\mathbf{r}, t) = \frac{c}{4\pi\lambda^2}[\mathbf{S}(\boldsymbol{\rho}, t) - \mathbf{A}(\mathbf{r}, t)], \quad (2)$$

where the vector function $\mathbf{S}(\boldsymbol{\rho}, t)$ is determined by the order parameter phase gradient:

$$\mathbf{S}(\boldsymbol{\rho}, t) = \frac{\Phi_0}{2\pi}\nabla\Theta(\boldsymbol{\rho}, t), \quad (3)$$

with Φ_0 being the flux quantum.

The function $\mathbf{S}(\boldsymbol{\rho}, t)$ satisfies the equation

$$\mathrm{curl}\mathbf{S}(\boldsymbol{\rho}, t) = \hat{\mathbf{z}}\Phi_0\delta(\boldsymbol{\rho} - \boldsymbol{\rho}_0(t)), \tag{4}$$

where $\hat{\mathbf{z}}$ is the unit vector (parallel to the z axis) along the magnetic field of the vortex situated at the point $\boldsymbol{\rho}_0(t)$.

In the case of a thin film of a magnetic superconductor, Eq. (2) for the current density can be represented in the form

$$\begin{aligned}\mathbf{j}(\mathbf{r}, t) &= \mathbf{I}(\boldsymbol{\rho}, t)\delta(z) = \mathbf{j}(\boldsymbol{\rho}, t)d\delta(z)\\ &= \frac{c}{4\pi\lambda_{\mathrm{eff}}}[\mathbf{S}(\boldsymbol{\rho}, t) - \mathbf{A}(\mathbf{r}, t)]\delta(z).\end{aligned} \tag{5}$$

From Eqs. (1)–(5), it follows that

$$\begin{aligned}\mathrm{curl}\,\mathrm{curl}\mathbf{H}(\mathbf{r}, t) &= \lambda_{\mathrm{eff}}^{-1}\mathrm{curl}\{[\mathbf{S}(\boldsymbol{\rho}, t) - \mathbf{A}(\mathbf{r}, t)]\delta(z)\}\\ &\quad - \varepsilon_0 c^{-2}\partial^2\mathbf{B}(\mathbf{r}, t)/\partial t^2.\end{aligned} \tag{6}$$

Using the formula $\mathrm{curl}(\varphi\mathbf{A}) = \varphi\mathrm{curl}\,\mathbf{A} + \nabla\varphi\times\mathbf{A}$ and the obvious equation $\{\nabla\delta(z)\times[\mathbf{S}(\boldsymbol{\rho}, t) - \mathbf{A}(\mathbf{r}, t)]\}_z = 0$, Eq. (6) can be reduced to a closed equation for the magnetic field of a Pearl vortex oscillating about its equilibrium position in a thin magnetic superconductor film:

$$\begin{aligned}\mathrm{curl}\,\mathrm{curl}\mathbf{H}(\mathbf{r}, t) &= \lambda_{\mathrm{eff}}^{-1}[\hat{\mathbf{z}}\Phi_0\delta(\boldsymbol{\rho} - \mathbf{a}_0\sin\omega_0 t)\\ &\quad - \mathbf{B}(\mathbf{r}, t)]\delta(z) - \varepsilon_0 c^{-2}\partial^2\mathbf{B}(\mathbf{r}, t)/\partial t^2.\end{aligned} \tag{7}$$

Here, the time dependence of the position vector of the oscillating vortex is taken to be $\boldsymbol{\rho}_0(t) = \mathbf{a}_0\sin\omega_0 t$, where $\mathbf{a}_0$ and ω_0 are the amplitude and frequency of harmonic oscillations, respectively. The magnetic induction is related to the magnetic field through an integral constitutive equation,

$$\mathbf{B}(\boldsymbol{\rho}, z, t) = \int_{-\infty}^{t} dt' \int_{-\infty}^{\infty} d\boldsymbol{\rho}'\mu(\boldsymbol{\rho} - \boldsymbol{\rho}', t - t')\mathbf{H}(\boldsymbol{\rho}', z, t'). \tag{8}$$

We note that for fields $\mathbf{H}(\mathbf{r}, t) = \hat{\mathbf{z}}H(\mathbf{r}, t)$ and $\mathbf{B}(\mathbf{r}, t) = \hat{\mathbf{z}}B(\mathbf{r}, t)$, we have $\mathrm{div}\mathbf{B}(\mathbf{r}, t) = 0$ and $\mathrm{div}\mathbf{H}(\mathbf{r}, t) = 0$.

Taking the spatial Fourier transform of Eq. (7), we obtain an equation for the time-dependent Fourier component of the magnetic field of the oscillating Pearl vortex:

$$\begin{aligned}&(q^2 + p^2)\mathbf{H}(\mathbf{q}, p, t) + \varepsilon_0 c^{-2}\partial^2\mathbf{B}(\mathbf{q}, p, t)/\partial t^2\\ &+ \lambda_{\mathrm{eff}}^{-1}\mathbf{B}(\mathbf{q}, t) = \hat{\mathbf{z}}\Phi_0\lambda_{\mathrm{eff}}^{-1}\exp(-i\mathbf{q}\mathbf{a}_0\sin\omega_0 t),\end{aligned} \tag{9}$$

where $\mathbf{q} = (q_x, q_y)$ is a two-dimensional vector, $q = (q_x^2 + q_y^2)^{1/2}$ is its magnitude, and

$$\mathbf{B}(\mathbf{q}, t) = \int_{-\infty}^{\infty}\frac{dp}{2\pi}\mathbf{B}(\mathbf{q}, p, t). \tag{10}$$

By using the expansion of the exponential in terms of Bessel functions of integral order $J_n(x)$ [20],

$$\begin{aligned}\exp(-i\mathbf{q}\mathbf{a}_0\sin\omega_0 t) &= \cos(\mathbf{q}\mathbf{a}_0\sin\omega_0 t) - i\sin(\mathbf{q}\mathbf{a}_0\sin\omega_0 t)\\ &= J_0(\mathbf{q}\mathbf{a}_0) + 2\sum_{m=1}^{\infty}J_{2m}(\mathbf{q}\mathbf{a}_0)\cos(2m\omega_0 t)\\ &\quad - i2\sum_{m=0}^{\infty}J_{2m+1}(\mathbf{q}\mathbf{a}_0)\sin[(2m+1)\omega_0 t],\end{aligned} \tag{11}$$

and taking the temporal Fourier transform of Eq. (9) after substitution of Eq. (8), one can obtain an algebraic equation

$$\begin{aligned}&[q^2 + p^2 - \varepsilon_0\omega^2 c^{-2}\mu(\mathbf{q}, \omega)]\mathbf{H}(\mathbf{q}, p, \omega)\\ &+ \lambda_{\mathrm{eff}}^{-1}\mu(\mathbf{q}, \omega)\mathbf{H}(\mathbf{q}, \omega) = \hat{\mathbf{z}}\Phi_0\lambda_{\mathrm{eff}}^{-1}I(\mathbf{q}, \omega)\end{aligned} \tag{12}$$

whose solution is

$$\mathbf{H}(\mathbf{q}, \omega) = \hat{\mathbf{z}}\Phi_0\frac{I(\mathbf{q}, \omega)}{\mu(\mathbf{q}, \omega) + R(\mathbf{q}, \omega)}. \tag{13}$$

Here, $I(\mathbf{q}, \omega)$ is a spectral function given by

$$\begin{aligned}I(\mathbf{q}, \omega) &= 2\pi\Bigg\{J_0(\mathbf{q}\mathbf{a}_0)\delta(\omega)\\ &+ \sum_{m=1}^{\infty}J_{2m}(\mathbf{q}\mathbf{a}_0)[\delta(\omega + 2m\omega_0) + \delta(\omega - 2m\omega_0)]\\ &- \sum_{m=0}^{\infty}J_{2m+1}(\mathbf{q}\mathbf{a}_0)[\delta(\omega + (2m+1)\omega_0)\\ &- \delta(\omega - (2m+1)\omega_0)]\Bigg\};\end{aligned} \tag{14}$$

$R(\mathbf{q}, \omega)$ is an additional renormalization function due to the displacement current,

$$\begin{aligned}R(\mathbf{q}, \omega) &= R_1(\mathbf{q}, \omega) - iR_2(\mathbf{q}, \omega)\\ &= \lambda_{\mathrm{eff}}\left\{\int_{-\infty}^{\infty}\frac{dp}{2\pi}[p^2 + q^2 - \varepsilon_0\omega^2 c^{-2}\mu(\mathbf{q}, \omega)]^{-1}\right\}^{-1};\end{aligned} \tag{15}$$

and we also define

$$\mathbf{H}(\mathbf{q}, \omega) = \int_{-\infty}^{\infty}\frac{dp}{2\pi}\mathbf{H}(\mathbf{q}, p, \omega). \tag{16}$$

The real and imaginary parts of the additional renormalization function (15) are

$$R_1(\mathbf{q}, \omega) = 2\lambda_{\mathrm{eff}}\{a(\mathbf{q}, \omega)/2$$

$$+ [a^2(\mathbf{q}, \omega) + b^2(\mathbf{q}, \omega)]^{1/2}/2\}^{1/2},$$
$$R_2(\mathbf{q}, \omega) = 2\,\mathrm{sgn}(\omega)\lambda_{\mathrm{eff}}\{-a(\mathbf{q}/\omega)/2 \quad (17)$$
$$+ [a^2(\mathbf{q}, \omega) + b^2(\mathbf{q}, \omega)]^{1/2}/2\}^{1/2}.$$

Here, the functions $a(\mathbf{q}, \omega)$ and $b(\mathbf{q}, \omega)$are expressed through the real and imaginary parts of the permeability of the system as

$$a(\mathbf{q}, \omega) = q^2 - \varepsilon_0\frac{\omega^2}{c^2}\mu_1(\mathbf{q}, \omega),$$
$$b(\mathbf{q}, \omega) = \varepsilon_0\frac{\omega^2}{c^2}\mu_2(\mathbf{q}, \omega). \quad (18)$$

3. Since $\lambda \gg a$ (a is the crystal lattice parameter), one can use a hydrodynamic approximation for the magnetic subsystem. In the paramagnetic temperature range, the permeability of the two-dimensional film can be written as [21]

$$\mu(\mathbf{q}, \omega) = \mu_1(\mathbf{q}, \omega) + i\mu_2(\mathbf{q}, \omega) = 1 + \frac{i4\pi\chi_0 Dq^2}{\omega + iDq^2}, \quad (19)$$

where χ_0 is the static magnetic susceptibility and the spin diffusion coefficient for a two-dimensional Heisenberg magnet is given by [22] $D = (1/3)(2\pi)^{1/2}Ja^2[s(s+1)]^{1/2}$ (J is the intralayer exchange constant and s is the spin).

Strictly speaking, superconduction currents screen the long-wavelength part of the exchange and electromagnetic interactions, thereby renormalizing the parameters of the magnetic subsystem [23]. However, when considering the paramagnetic temperature range and making only order-of-magnitude estimates, we can ignore this circumstance.

Let us introduce dimensionless variables $\boldsymbol{\kappa} = \mathbf{q}\lambda_{\mathrm{eff}}$, $\Omega = \omega\lambda_{\mathrm{eff}}/v_0$, $\Omega_0 = \omega_0\lambda_{\mathrm{eff}}/v_0$, $\tau = tv_0/\lambda_{\mathrm{eff}}$, and $\eta = v_0/c$, where $v_0 = D/\lambda_{\mathrm{eff}}$ is the characteristic velocity.

Taking the inverse (frequency) Fourier transform, we find from Eqs. (13)–(16) the time dependence of the spatial Fourier component of the magnetic field of the oscillating Pearl vortex:

$$\mathbf{H}(\boldsymbol{\kappa}, \tau) = \mathbf{H}_0(\boldsymbol{\kappa}, \tau) + \mathbf{H}_1(\boldsymbol{\kappa}, \tau), \quad (20)$$

where

$$\mathbf{H}_0(\boldsymbol{\kappa}, \tau) = \hat{\mathbf{z}}\Phi_0\frac{\exp(-i\kappa_x A_0\sin\Omega_0\tau)}{1 + 4\pi\chi_0 + 2\kappa}, \quad (21)$$

$$\mathbf{H}_1(\boldsymbol{\kappa}, \tau) = \mathbf{H}_{1\mathrm{Re}}(\boldsymbol{\kappa}, \tau) - i\mathbf{H}_{1\mathrm{Im}}(\boldsymbol{\kappa}, \tau), \quad (22)$$

$$\mathbf{H}_{1\mathrm{Re}}(\boldsymbol{\kappa}, \tau) = 2\hat{\mathbf{z}}\Phi_0\sum_{m=1}^{\infty} J_{2m}(\kappa_x A_0) \times\left[\frac{F_1(\boldsymbol{\kappa}, \tau, m)}{F_2(\boldsymbol{\kappa}, m)} - \frac{\cos(2m\Omega_0\tau)}{1 + 4\pi\chi_0 + 2\kappa}\right], \quad (23)$$

$$\mathbf{H}_{1\mathrm{Im}}(\boldsymbol{\kappa}, \tau) = 2\hat{\mathbf{z}}\Phi_0\sum_{m=0}^{\infty} J_{2m+1}(\kappa_x A_0) \times\left[\frac{F_3(\boldsymbol{\kappa}, \tau, m)}{F_4(\boldsymbol{\kappa}, m)} - \frac{\sin((2m+1)\Omega_0\tau)}{1 + 4\pi\chi_0 + 2\kappa}\right]. \quad (24)$$

Here, the vortex is assumed to oscillate along the x axis, $A_0 = a_0/\lambda_{\mathrm{eff}}$ is the dimensionless amplitude, and the functions F_1, F_2, F_3, and F_4 are given by

$$F_1(\boldsymbol{\kappa}, \tau, m) = [\mu_1(\boldsymbol{\kappa}, 2m\Omega_0) + R_1(\boldsymbol{\kappa}, 2m\Omega_0)]\cos(2m\Omega_0\tau) - [\mu_2(\boldsymbol{\kappa}, 2m\Omega_0) - R_2(\boldsymbol{\kappa}, 2m\Omega_2)]\sin(2m\Omega_0\tau),$$
$$F_2(\boldsymbol{\kappa}, m) = [\mu_1(\boldsymbol{\kappa}, 2m\Omega_0) + R_1(\boldsymbol{\kappa}, 2m\Omega_0)]^2 + [\mu_2(\boldsymbol{\kappa}, 2m\Omega_0) - R_2(\boldsymbol{\kappa}, 2m\Omega_0)]^2,$$
$$F_3(\boldsymbol{\kappa}, \tau, m) = [\mu_2(\boldsymbol{\kappa}, (2m+1)\Omega_0) - R_2(\boldsymbol{\kappa}, (2m+1)\Omega_0)] \times\cos[(2m+1)\Omega_0\tau] + [\mu_1(\boldsymbol{\kappa}, (2m+1)\Omega_0) + R_1(\boldsymbol{\kappa}, (2m+1)\Omega_0)]\sin[(2m+1)\Omega_0\tau], \quad (25)$$
$$F_4(\boldsymbol{\kappa}, m) = [\mu_1(\boldsymbol{\kappa}, (2m+1)\Omega_0) + R_1(\boldsymbol{\kappa}, (2m+1)\Omega_0)]^2 + [\mu_2(\boldsymbol{\kappa}, (2m+1)\Omega_0) - R_2(\boldsymbol{\kappa}, (2m+1)\Omega_0)]^2.$$

According to Eqs. (15), (17), and (18), the renormalization function is

$$R_1(\boldsymbol{\kappa}, \Omega) = 2\{\alpha(\boldsymbol{\kappa}, \Omega)/2 + [\alpha^2(\boldsymbol{\kappa}, \Omega) + \beta^2(\boldsymbol{\kappa}, \Omega)]^{1/2}/2\}^{1/2}, \quad (26)$$
$$R_2(\boldsymbol{\kappa}, \Omega) = 2\,\mathrm{sgn}(\Omega)\{-\alpha(\boldsymbol{\kappa}, \Omega)/2 + [\alpha^2(\boldsymbol{\kappa}, \Omega) + \beta^2(\boldsymbol{\kappa}, \Omega)]^{1/2}/2\}^{1/2}, \quad (27)$$

where

$$\alpha(\boldsymbol{\kappa}, \Omega) = \kappa^2 - \varepsilon_0\eta^2\Omega^2\mu_1(\boldsymbol{\kappa}, \Omega),$$
$$\beta(\boldsymbol{\kappa}, \Omega) = \varepsilon_0\eta^2\Omega^2\mu_2(\boldsymbol{\kappa}, \Omega), \quad (28)$$

and the real and imaginary parts of the permeability take the form

$$\mu_1(\boldsymbol{\kappa}, \Omega) = 1 + 4\pi\chi_0\kappa^4/(\Omega^2 + \kappa^4),$$
$$\mu_2(\boldsymbol{\kappa}, \Omega) = 4\pi\chi_0\Omega\kappa^4/(\Omega^2 + \kappa^4). \quad (29)$$

Equations (20)–(28) are valid for any type of magnetic ordering in the magnetic subsystem, i.e., for any character of dispersion of the permeability $\mu(\mathbf{q}, \omega)$.

We note that there are essential differences between these expressions for the Fourier component of the magnetic field of the oscillating Pearl vortex in a two-dimensional superconductor and the corresponding

expression [9, Eq. (7)] for the same component of the oscillating Abrikosov vortex in a three-dimensional superconductor. First, the dependence on the two-dimensional wave vector **q** is different, and, second, the characteristic spatial scales of field variation are different: in the three-dimensional case, this scale is λ, whereas in a two-dimensional superconductor, it is $\lambda_{\text{eff}} \gg \lambda$.

Taking the inverse Fourier transform with respect to the two-dimensional wave vector **q**, we obtain from Eqs. (20)–(29) an integral representation for the magnetic field of the isolated oscillating two-dimensional Pearl vortex in a thin magnetic superconductor film:

$$\mathbf{H}(x, y, t) = \mathbf{H}_0(x, y, t) + \mathbf{H}_1(x, y, t), \tag{30}$$

$$\mathbf{H}_0(x, y, t) = \frac{\hat{\mathbf{z}}\Phi_0}{(\pi\lambda_{\text{eff}})^2} \times \int_0^\infty d\kappa_x \int_0^\infty d\kappa_y \frac{\cos[\kappa_x(X - A_0\sin(\Omega_0\tau))]\cos(\kappa_y Y)}{1 + 4\pi\chi_0 + 2\kappa}, \tag{31}$$

$$\mathbf{H}_1(x, y, t) = \mathbf{H}_{1S}(x, y, t) + \mathbf{H}_{1A}(x, y, t), \tag{32}$$

$$\mathbf{H}_{1S}(x, y, t) = \frac{1}{(\pi\lambda_{\text{eff}})^2} \times \int_0^\infty d\kappa_x \int_0^\infty d\kappa_y \mathbf{H}_{1\text{Re}}(\boldsymbol{\kappa}, \tau)\cos(\kappa_x X)\cos(\kappa_y Y), \tag{33}$$

$$\mathbf{H}_{1A}(x, y, t) = \frac{1}{(\pi\lambda_{\text{eff}})^2} \times \int_0^\infty d\kappa_x \int_0^\infty d\kappa_y \mathbf{H}_{1\text{Im}}(\boldsymbol{\kappa}, \tau)\sin(\kappa_x X)\cos(\kappa_y Y), \tag{34}$$

where we have introduced the dimensionless coordinates $X = x/\lambda_{\text{eff}}$ and $Y = y/\lambda_{\text{eff}}$.

According to Eqs. (30)–(34), the dominant positive contribution to the magnetic field of the oscillating Pearl vortex comes from the function $\mathbf{H}_0(x, y, t)$ centered at the point $x_C(t) = a_0\sin\omega_0 t$. Information on the inverted satellites is contained in the integrals in Eqs. (33) and (34), which are centered at the origin. $\mathbf{H}_{1S}(x, y, t)$ is a symmetric function of x and y, while $\mathbf{H}_{1A}(x, y, t)$ is symmetric in y and antisymmetric in x. Let us discuss how the regions of the inverted magnetic field arise along the direction of oscillations (the x axis). This effect is most pronounced at the instants $t_n \approx \pm n\pi\omega_0^{-1}$ (n = 0, 1, 2, …), where the point $x_C(t_n)$, at which the function $\mathbf{H}_0(x, y, t)$ is centered, is close to the origin. In this case, the strongly localized positive function $\mathbf{H}_0(x, y, t)$ falls off steeply to zero. The functions $\mathbf{H}_{1S}(x, y, t)$ and $\mathbf{H}_{1A}(x, y, t)$ are more weakly localized in comparison with $\mathbf{H}_0(x, y, t)$ and can take both positive and negative values. The inverted precursor is the result of superposition of a negative minimum of $\mathbf{H}_{1S}(x, y, t)$ and a positive maximum of $\mathbf{H}_{1A}(x, y, t)$, whereas the inverted wake is the sum of two negative minima of these functions.

The typical values of χ_0 for antiferromagnets are 10^{-3}–10^{-5}. The characteristic velocity $v_0 \propto Jsa(a/\lambda_{\text{eff}})$ is $(\lambda_{\text{eff}}/a) \propto 10^3$–$10^4$ times lower than the spin-wave velocity $v_s \propto Jsa$. In the CuO_2 planes, because of strong intralayer exchange, the spin-wave velocity is fairly high: $v_s \propto (0.5\text{–}1.3)\times 10^7$ cm/s [3]; therefore, $v_0 \propto 10^3$–10^4 cm/s. We note that the experimentally observed maximum velocities of Abrikosov vortices in bulk superconductors are of the same order of magnitude, $v_A \approx 6.6\times 10^3$ cm/s [24].

The maximum velocity of the oscillating vortex $V_0 = a_0\omega_0$ is much lower than the relaxation velocity of the magnetic subsystem, which is of the order of v_s. Therefore, in our case, the magnetic subsystem closely follows the changes in the magnetic field of the oscillating Pearl vortex, renormalizing this field because of spatial and time dispersion of the permeability and causing the formation of an inverted precursor in front of the vortex and of an inverted wake behind it at large distances from its center.

The stationary vortex field distribution, averaged over an oscillation period, differs essentially from the standard one and has the form

$$\mathbf{H}_{\text{av}}(x, y) = \frac{\hat{\mathbf{z}}\Phi_0}{2\pi^3\lambda_{\text{eff}}^2} \times \int_{-\pi}^{\pi} d\varphi \int_0^\infty d\kappa_x \int_0^\infty d\kappa_y \frac{\cos[\kappa_x(X - A_0\sin\varphi)]\cos(\kappa_y Y)}{1 + 4\pi\chi_0 + 2\kappa}. \tag{35}$$

Numerical analysis shows that if we put $\chi_0 \propto 10^{-3}$–10^{-4} (which is comparable with the magnetic susceptibility of the copper subsystem of HTSC materials), the frequency $\Omega_0 \propto 10^3$, the amplitude $a_0 = 5\lambda_{\text{eff}}$, $\varepsilon_0 = 30$, and the parameter $\eta \propto 10^{-5}$–10^{-6}, then at the instant $\tau_0 = \pi$, the minima of the inverted-precursor and inverted-wake fields will be situated symmetrically about the vortex center at distances $r_{01} = r_{02} \approx 5\lambda_{\text{eff}}$ from it and will be equal to $H_{\min 1,2} = H(r_{01,2}, \tau_0)(\pi\lambda_{\text{eff}})^2/\Phi_0 \propto 10^{-3}$–$10^{-4}$. For $\chi_0 \propto 10^{-2}$ (such values of the magnetic susceptibility are typical of ternary and HTSC compounds with rare-earth ions near the magnetic-ordering temperature $T_N \propto 1$ K), $\Omega_0 = 1$, $a_0 = 5\lambda_{\text{eff}}$, $\tau = \pi$, $\eta = 10^{-5}$, and $\varepsilon_0 = 30$, the distribution of the reduced magnetic field of the vortex $H = (\pi\lambda_{\text{eff}})^2 H(X, 0, \tau = \pi)/\Phi_0$ along the x axis (as a function of X at $Y = 0$) has two minima: $H_{\min 1} \propto -10^{-2}$ at $r_{01} \propto 5\lambda_{\text{eff}}$ (inverted precursor) and $H_{\min 2} \propto -7\times 10^{-2}$ at $r_{02} \propto 3\lambda_{\text{eff}}$ (inverted wake, see figure). We note that when the oscillation phase is $\omega_0 t = \Omega_0\tau = \pi$, the vortex moves to the left and the maximum of its magnetic field

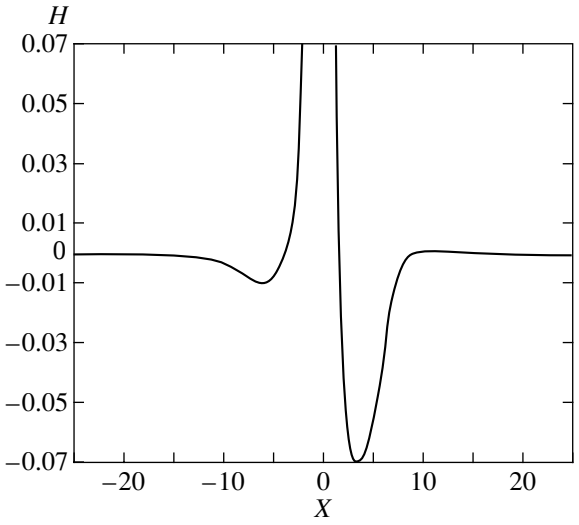

Distribution of the instantaneous reduced magnetic field of an oscillating Pearl vortex $H = (\pi\lambda_{eff})^2 H(X, 0, \tau = \pi)/\Phi_0$ along the x axis (as a function of X at $Y = 0$), in which the minima correspond to an inverted precursor in front of the vortex and to an inverted wake behind it.

goes through the point $x = 0$ at this instant (the maximum of the dimensionless magnetic field is roughly 8 at this point).

According to Eq. (35), the vortex field distribution averaged over an oscillation period essentially depends on the amplitude A_0, is positive everywhere, and differs significantly from the standard magnetic field distribution of a fixed Pearl vortex. The stationary distributions of the reduced average magnetic field of a Pearl vortex $2\pi^3\lambda_{eff}^2 H_{av}(X, 0)/\Phi_0$ along the x axis (as a function of X at $Y = 0$) and of $2\pi^3\lambda_{eff}^2 H_{av}(0, Y)/\Phi_0$ along the y axis (as a function of Y at $X = 0$) are similar to those of the Abrikosov vortex presented in [9, Figs. 2, 3] for five different values of the amplitude a_0. These distributions differ only in that the spatial scale of the Abrikosov vortex λ should be replaced by the characteristic spatial scale λ_{eff} of the Pearl vortex and, in addition, the exponential falloff of the field to zero in the case of the Abrikosov vortex should be replaced by a power-law falloff of the Pearl vortex.

4. We note that there is an essential difference in the time dependence of the magnetic field distribution of the Pearl vortex between the cases of uniform motion [14] and harmonic oscillations. In the former case, the configuration of the field distribution with an inverted wake is time-independent, whereas in the latter, the structure of both the inverted precursor and the inverted wake essentially varies in time over an oscillation period.

When the longitudinal component of the magnetic field of a vortex is inverted, vortices are attracted to one another [25, 26]. Therefore, moving vortices will be aligned in chains in a thin film of a magnetic superconductor. This effect can be essential in switching and memory devices based on Pearl vortices.

Stationary and nonstationary domain structures, labyrinth patterns of bubble domains and Bloch lines, moving vortex lattices, and isolated moving vortices can be easily visualized and observed on the surface of a sample in magnetooptical experiments. Therefore, in contrast to the inverted wake of a uniformly moving Abrikosov vortex [8] and the inverted precursor and wake of an oscillating Abrikosov vortex [9] in a bulk magnetic superconductor, the inverted precursor and wake of an oscillating two-dimensional surface Pearl vortex in a two-dimensional magnetic superconductor can be observed in magnetooptical experiments on thin magnetic superconductor films.

From the results of [14] and this paper, one can conclude that the more intricate the vortex motion and the character of magnetic ordering dictated by the features of the permeability $\mu(\mathbf{k}, \omega)$, the richer and more diversified the pattern of inverted satellites that accompany a moving Pearl vortex in a thin film of a magnetic superconductor.

ACKNOWLEDGMENTS

The author is grateful to Yu.E. Kuzovlev for permission to employ his computer-simulation code KGCP and to Yu.V. Medvedev for his interest in this study and encouragement.

REFERENCES

1. A. I. Buzdin, L. N. Bulaevskiĭ, M. L. Kulich, and S. V. Panyukov, Usp. Fiz. Nauk **144** (4), 597 (1984) [Sov. Phys. Usp. **27**, 927 (1984)].
2. A. I. Buzdin and L. N. Bulaevskiĭ, Usp. Fiz. Nauk **149** (1), 45 (1986) [Sov. Phys. Usp. **29**, 412 (1986)].
3. Yu. A. Izyumov, N. M. Plakida, and Yu. N. Skryabin, Usp. Fiz. Nauk **159** (4), 621 (1989) [Sov. Phys. Usp. **32**, 1060 (1989)].
4. *Superconductivity in Ternary Compounds*, Vol. 2: *Superconductivity and Magnetism*, Ed. by E. Fisher and M. Maple (Springer, Heidelberg, 1982; Mir, Moscow, 1985).
5. *Physical Properties of High Temperature Superconductors*, Ed. by D. M. Ginsberg (World Scientific, Singapore, 1989; Mir, Moscow, 1990), Chaps. 4, 6.
6. A. A. Abrikosov, Zh. Éksp. Teor. Fiz. **32** (6), 1442 (1957) [Sov. Phys. JETP **5**, 1174 (1957)].
7. L. P. Gor'kov and N. B. Kopnin, Usp. Fiz. Nauk **116** (3), 413 (1975) [Sov. Phys. Usp. **18**, 496 (1975)].
8. V. N. Krivoruchko, Pis'ma Zh. Éksp. Teor. Fiz. **55** (5), 285 (1992) [JETP Lett. **55**, 284 (1992)].
9. A. I. Lomtev, Fiz. Tverd. Tela (St. Petersburg) **42** (9), 1542 (2000) [Phys. Solid State **42**, 1584 (2000)].
10. P. G. de Gennes and J. Matrikon, Rev. Mod. Phys. **36** (1), 45 (1964).
11. J. Pearl, Appl. Phys. Lett. **5** (4), 65 (1964).

12. P. G. de Gennes, *Superconductivity of Metals and Alloys* (Benjamin, New York, 1966; Mir, Moscow, 1968), Chap. 3.
13. A. A. Abrikosov, *Fundamentals of the Theory of Metals* (Nauka, Moscow, 1987; North-Holland, Amsterdam, 1988), Chap. 18.
14. A. I. Lomtev, Pis'ma Zh. Éksp. Teor. Fiz. **71** (10), 618 (2000) [JETP Lett. **71**, 426 (2000)].
15. V. N. Krivoruchko and Yu. A. Dimashko, Sverkhprovodimost: Fiz., Khim., Tekh. **5** (6), 967 (1992).
16. E. B. Sonin, A. K. Tagantsev, and K. B. Traito, Phys. Rev. B **46** (9), 5830 (1992).
17. E. M. Lifshitz and L. P. Pitaevskiĭ, *Course of Theoretical Physics*, Vol. 5: *Statistical Physics* (Nauka, Moscow, 1978; Pergamon, New York, 1980), Part 2, Chap. 5.
18. H. Umezawa, H. Matsumoto, and M. Tachiki, *Thermo-Field Dynamics and Condensed States* (North-Holland, Amsterdam, 1982; Mir, Moscow, 1985), Chap. 11.
19. M. Tinkham, *Introduction to Superconductivity* (McGraw-Hill, New York, 1975; Atomizdat, Moscow, 1980), Chap. 5.
20. *Handbook of Mathematical Functions*, Ed. by M. Abramowitz and I. A. Stegun (Dover, New York, 1964; Nauka, Moscow, 1979), Chap. 9.
21. B. I. Halperin and P. C. Hohenberg, Phys. Rev. **188** (2), 898 (1969).
22. P. M. Richards and M. B. Salamon, Phys. Rev. B **9** (1), 32 (1974).
23. A. I. Buzdin, Pis'ma Zh. Éksp. Teor. Fiz. **40** (5), 193 (1984) [JETP Lett. **40**, 956 (1984)].
24. A. N. Samus', A. F. Popkov, V. I. Makhov, *et al.*, Sverkhprovodimost: Fiz., Khim., Tekh. **4** (7), 1324 (1991).
25. A. M. Grishin, A. Yu. Martynovich, and S. V. Yampol'skiĭ, Zh. Éksp. Teor. Fiz. **97** (6), 1930 (1990) [Sov. Phys. JETP **70**, 1089 (1990)].
26. A. I. Buzdin and A. Yu. Simonov, Zh. Éksp. Teor. Fiz. **98** (6), 2074 (1990) [Sov. Phys. JETP **71**, 1165 (1990)].

Translated by Yu. Epifanov

Physics of the Solid State, Vol. 43, No. 11, 2001, pp. 2032–2036. Translated from Fizika Tverdogo Tela, Vol. 43, No. 11, 2001, pp. 1952–1956.
Original Russian Text Copyright © 2001 by Aliev, Alieva, Seleznev.

SEMICONDUCTORS AND DIELECTRICS

Features of Hole Scattering in Electroplastically Deformed Germanium Crystals

M. A. Aliev, Kh. O. Alieva, and V. V. Seleznev

Institute of Physics, Dagestan Scientific Center, Russian Academy of Sciences, Makhachkala, 367003 Russia

Received January 30, 2001

Abstract—The effect of specific features of scattering center formation during electroplastic deformation on the electric properties of germanium is investigated. © *2001 MAIK "Nauka/Interperiodica".*

An analysis of the influence of defect formation in the course of electroplastic deformation of silicon crystals on their electric properties revealed a number of peculiarities in the behavior of the Hall mobility of holes [1]. A comparative analysis of the observed features and the results of earlier investigations [2–5] devoted to the influence of deformation-produced defects on the mobility of charge carriers and their comparison with the modern concepts of the evolution of defect structures [6, 7] led to certain assumptions concerning the features of scattering mechanisms in real crystals of elemental semiconductors. In this connection, it is interesting to continue investigations of related objects in order to better understand the nature of carrier scattering and the mechanisms responsible for it.

The experiments were made on plastically deformed germanium samples with different structural parameters, such as the density of defects, impurity composition, type of dislocation dynamics, and relative orientation of the directions of the current and dislocations.

Here, we present an investigation of the electric properties of monocrystalline germanium samples cut from crystals subjected to electroplastic (EPD) and thermoplastic deformation (TPD). The deformation was accompanied by diffusion of indium impurity atoms along the preferred direction of dislocation emergence.

We investigated *p*-germanium single crystals with resistivity $\rho = 43\ \Omega$ cm at room temperature, which were initially doped with gallium to an uncompensated-acceptor concentration $N_A - N_D = 9 \times 10^{13}$ cm^{-3}. The growth dislocation density did not exceed 10^2 cm^{-2}. Crystals in the form of prisms $12 \times 10 \times 5$ mm in size with edges coinciding with the [110], [111], and [112] directions, respectively, were deformed along the [110] axis in the stationary creep mode at a temperature T = 700°C for 30 minutes. The reference samples were subjected to thermal treatment under deformation. Before the deposition of the diffusing impurity, the sample surface was cleaned using the ion-plasma technique. The electric properties were measured on three samples cut from a deformed crystal in three different ways: from the face subjected to impurity diffusion and along and across the slip planes. After grinding and chemical polishing, indium contacts were fused in a high-vacuum setup for 20 min at T = 350°C. The quality of the contacts was verified on a curve tracer, and then samples with ohmic contacts were selected. Measurements of the dc electrical conductivity and the Hall effect were made in the temperature range 4.2–400 K in a magnetic field of 8 kOe with the help of the compensation technique in a metallic cryostat, which made it possible to control and maintain the temperature to within ±0.1 K in helium vapor and to within ±1 K in nitrogen vapor.

The nontraditional methodical and technological approaches used by us for forming the structures enriches the physical properties of a crystal but considerably complicates its quantitative description. This is due to the fact that as a result of deformation, the crystal becomes similar to an open system which is far from thermodynamic equilibrium and whose properties change under shear stress. At the shear instability points, self-organization of dissipative dislocation structures takes place [8]. It can be expected that new materials with controllable properties can be obtained by using this method [9].

Figures 1 and 2 show the temperature dependences of the Hall mobility of holes in the samples under investigation on the log–log scale. It follows from the curves that a considerable difference in the scattering of charge carriers in the reference and thermoplastically deformed samples is observed in the temperature range $T < 100$ K, while for electroplastically deformed samples, the difference begins to manifest itself at lower temperatures $T < 80$ K.

It can be seen from curves *5–7* in Fig. 1 that the most typical and distinguishing feature of samples corresponding to the TPD mode and cut across the slip plane is the presence of minima in the mobility $\mu(T)$ in the vicinity of $T \approx 25$ K, whose depth increases with the

1063-7834/01/4311-2032$21.00 © 2001 MAIK "Nauka/Interperiodica"

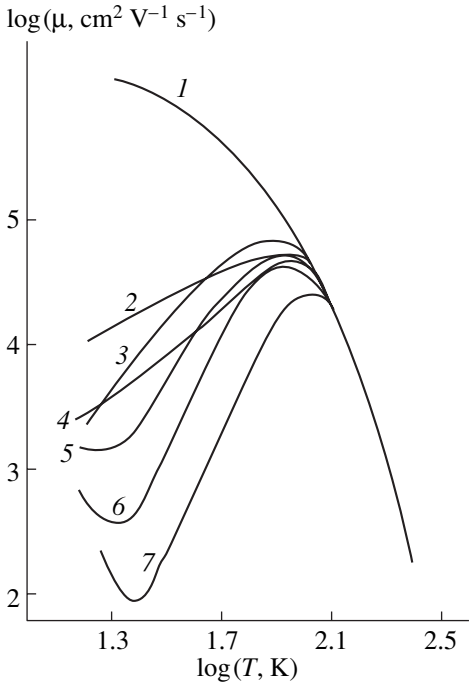

Fig. 1. Temperature dependence of the Hall mobility of holes in *p*-germanium samples subjected to thermoplastic deformation at $T = 700°C$: (*1*) initial sample; (*2*) $\varepsilon = 1\%$ with indium diffusion; (*3*) $\varepsilon = 1\%$, $\mathbf{I} \parallel \mathbf{D}$; (*4*) $\varepsilon = 1.5\%$ with indium diffusion; (*5*) $\varepsilon = 1.5\%$, $\mathbf{I} \parallel \mathbf{D}$; (*6*) $\varepsilon = 1\%$, $\mathbf{I} \perp \mathbf{D}$, and (*7*) $\varepsilon = 1.5\%$, $\mathbf{I} \perp \mathbf{D}$.

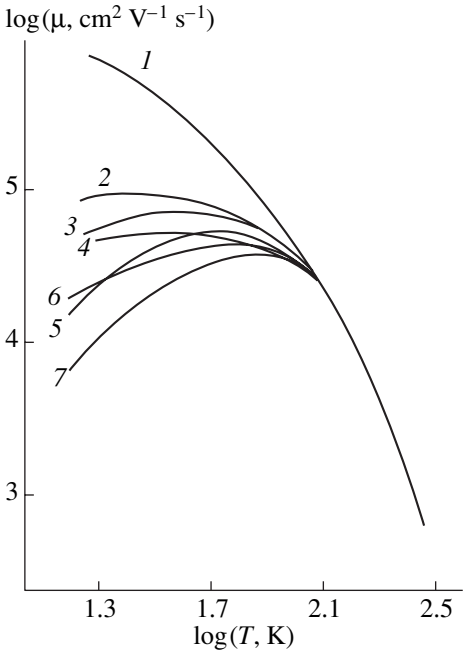

Fig. 2. Temperature dependence of the Hall mobility of holes in *p*-germanium samples subjected to electroplastic deformation at $T = 700°C$: (*1*) initial sample; (*2*) $\varepsilon = 1\%$ with indium diffusion; (*3*) $\varepsilon = 1\%$, $\mathbf{I} \parallel \mathbf{D}$; (*4*) $\varepsilon = 1.5\%$ with indium diffusion; (*5*) $\varepsilon = 1.5\%$, $\mathbf{I} \parallel \mathbf{D}$; (*6*) $\varepsilon = 1\%$, $\mathbf{I} \perp \mathbf{D}$, and (*7*) $\varepsilon = 1.5\%$, $\mathbf{I} \perp \mathbf{D}$.

strain ε. The change in the mobility amounts to more than four orders of magnitude for samples subjected to TPD and to less than two orders of magnitude for samples subjected to EPD. It should be observed that, according to electron-microscopic data, the density of dislocations in samples subjected to TPD is two orders of magnitude higher than in samples subjected to EPD for the same strain. In the case of samples deformed in the EPD mode, there are no distinct minima on the $\mu(T)$ dependence but the steepness of the temperature dependence of the mobility increases with the strain (curves *5–7* in Fig. 2). The common features typical to both deformation modes are the existence of anisotropy in the mobility of the majority charge carriers (this is manifested much more weakly for samples with EPD) and the identical effect of indium impurity atoms, diffusing to the bulk of the crystal simultaneously with the generation of dislocations, on the carrier scattering. For example, the impurity–dislocation interaction for small strains considerably suppresses the scattering (curves *2*, *4* in Figs. 1, 2), while an increase in the strain considerably enhances the scattering of charge carriers (curves *5–7* in Figs. 1, 2); the latter is responsible for anomalously low values of the mobility (especially for the TPD mode).

The above comparative analysis suggests that, in both modes of deformation of germanium crystals, identical sources of scattering of charge carriers are generated. It should be noted, however, that the structural formation of new scattering centers generated in the course of deformation, as well as their quantitative characteristics, differs considerably for the two deformation modes. We note, for example, that in contrast to the TPD mode, all the structural particles participating in the process in the case of the electroplastic mode of deformation, namely, the impurity and intrinsic atoms, as well as the charged carriers of the subsystem (holes) and simultaneously generated dislocations, interact in the dynamic flow and in a certain direction of motion. Thus, the conditions for crystal deformation in the EPD mode are facilitated by the presence of an additional perturbation of the dislocation system in the form of a directional current pulse [10, 11]. We can also assume that the scattering centers formed as a result of the structure evolution in the two deformation modes also differ in such properties as thermal stability and electrical and chemical activity. For this reason, a more ordered structure of deformation-produced defects is formed, in our opinion, in the EPD mode. It is well known that dislocations can lead to a considerable anisotropy of carrier scattering in the case of their nonuniform orientation distribution [12].

Let us analyze the above-mentioned anisotropy in the electric properties of samples subjected to both regimes of deformation. It should be recalled that the mobility $\mu_\perp$ was obtained while measuring the current perpendicular to the slip planes {111}. Obviously, the scattering properties of dislocations for such an orien-

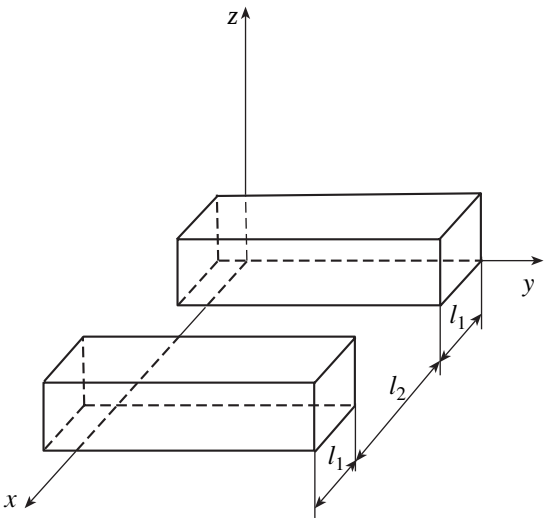

Fig. 3. Schematic diagram illustrating the model of a crystal with dislocation tubes.

tation are manifested most significantly. The mobility $\mu_\parallel$ corresponds to resistance measurements for a current parallel to the slip planes. In the case of a small strain and of the concentration of dislocation clusters in individual planes being separated by large dislocation-free regions, we can naturally expect that $\mu_\parallel > \mu_\perp$; the resistance in the parallel direction is shunted by dislocation-free regions between preferred slip planes.

In order to substantiate the above qualitative explanation, we consider the following model of a deformed crystal, which takes into account the nonuniformity in the distribution of dislocation clusters in the crystal (Fig. 3). We present the crystal in the form of alternating layers with different conductivities and different carrier concentrations, which are perpendicular to the x axis. Layers of thickness l_1 have a conductivity σ_1 and a carrier concentration n_1, while layers of thickness l_2 distributed between them have parameters σ_2 and n_2. We direct the magnetic field along the z axis and the electric contacts along the x and y directions, alternately.

The current is directed along the x axis, the magnetic field along the z axis, and the value of V_H is measured along the y axis. The expressions for the current density have the form

$$j_x = \frac{\sigma_i}{1 + \Omega^2\tau_i^2}(E_x + \Omega\tau_i E_y), \tag{1}$$

$$j_y = \frac{\sigma_i}{1 + \Omega^2\tau_i^2}(-\Omega\tau_i E_x + E_y), \tag{2}$$

where $i = 1, 2, \ldots$; τ_i is the relaxation time in the layers; $\sigma_i = \dfrac{e^2 n_i \tau}{m} = en_i\mu_i$ is the conductivity in the layers; $\Omega = \dfrac{eH}{mc}$ is the cyclotron frequency; and E is the electric field.

From the condition $j_y = 0$, it follows that

$$E_y = \Omega\tau E_x. \tag{3}$$

Then, expression (1) implies that

$$j_x = \sigma_2 E_x. \tag{4}$$

The voltage V_x applied along the x axis is distributed among the layers. The voltage applied to a pair of layers l_1 and l_2 is

$$\Delta V_x = \frac{V}{N}, \quad N = \frac{L_x}{l_1 + l_2}; \tag{5}$$

L_x, L_y, and L_z are the crystal dimensions.

The distribution of ΔV_x is proportional to the resistances of the layers:

$$\frac{\Delta V_{1x}}{\Delta V_{2x}} = \frac{l_1\sigma_2}{l_2\sigma_1}. \tag{6}$$

This relation and the equality $\Delta V_{1x} + \Delta V_{2x} = \Delta V_x$ give

$$\Delta V_{1x} = \Delta V_x \frac{l_1\sigma_2}{l_2\sigma_1 + l_1\sigma_2}, \quad \Delta V_{2x} = \Delta V_x \frac{l_2\sigma_1}{l_2\sigma_1 + l_1\sigma_2}. \tag{7}$$

For the electric fields acting in layers l_1 and l_2, we obtain from relations (7)

$$E_{1x} = \Delta V_x \frac{\sigma_2}{l_1\sigma_2 + l_2\sigma_1}, \quad E_{2x} = \Delta V_x \frac{\sigma_1}{l_1\sigma_2 + l_2\sigma_1}. \tag{8}$$

Using relations (3) and (4), we obtain the relation

$$E_y = \frac{H}{ecn} j_x \tag{9}$$

for the Hall electric field, which leads to the following relation for the Hall voltage:

$$\Delta E_y = \frac{H}{ecn_j}\frac{J_x}{H_z}. \tag{10}$$

In the measurements of the Hall potential difference, averaging is carried out over the length of a Hall contact and along the x axis.

Equation (10) gives

$$\Delta V_y = \frac{HI_x}{ecL_x}\frac{1}{l_1 + l_2}\left(\frac{l_1}{n_1} + \frac{l_2}{n_2}\right). \tag{11}$$

Using the definition of the Hall coefficient, we can write

$$R_1 = \frac{1}{ec}\frac{1}{l_1 + l_2}\left(\frac{l_1}{n_1} + \frac{l_2}{n_2}\right). \tag{12}$$

Using relation (4) with the field values (8) in the layers and taking into account relations (5), we obtain

$$j_x = \frac{\sigma_1\sigma_2(l_1 + l_2)}{l_2\sigma_1 + l_1\sigma_2}\frac{V}{L_x}, \tag{13}$$

which leads to the following expression for the effective conductivity $\sigma_\perp^{\text{eff}}$:

$$\sigma_\perp^{\text{eff}} = \frac{\sigma_1\sigma_2(l_1 + l_2)}{\sigma_1 l_2 + \sigma_2 l_1}. \tag{14}$$

In accordance with relations (14) and (12), the effective mobility is given by

$$\begin{aligned}\mu_\perp^{\text{eff}} &= \sigma_\perp^{\text{eff}} R_\perp = \frac{1}{e}\frac{(l_1/n_1 + l_2/n_2)}{\sigma_1 l_1 + \sigma_2 l_2}\sigma_1\sigma_2 \\ &= \frac{e}{m}\frac{l_1/n_1 + l_2/n_2}{l_1/n_1\tau_1 + l_2/n_2\tau_2}.\end{aligned} \tag{15}$$

Now, we consider the case where the current is passed along the y axis. From the condition $j_x = 0$, the Hall electric field is found to be

$$E_x = -\Omega\tau_i E_y. \tag{16}$$

The current density along the y axis is different in layers l_1 and l_2:

$$j_y(1) = \sigma_1 E_y, \quad j_y(2) = \sigma_2 E_y. \tag{17}$$

The preset total current is

$$I = \int dx dz\, j_y = L_z N(l_1\sigma_1 + l_2\sigma_2)E_y. \tag{18}$$

This leads to the following expression for the effective conductivity $\sigma_\parallel^{\text{eff}}$:

$$\sigma_\parallel^{\text{eff}} = \frac{l_1\sigma_1 + l_2\sigma_2}{l_1 + l_2}. \tag{19}$$

Using relations (16) and (17), we derive an expression for the Hall voltage:

$$\begin{aligned}\Delta V_x &= -\int dx E_x \\ &= \int dx\frac{\lambda\tau j_y}{\sigma_1} = \frac{H}{ec}NE_y\left(\frac{\sigma_1 l_1}{n_1} + \frac{\sigma_2 l_2}{n_2}\right).\end{aligned} \tag{20}$$

In accordance with relations (20) and (18), the Hall coefficient is given by

$$R_\parallel = \frac{1}{ec}\frac{\tau_1 l_1 + \tau_2 l_2}{n_1\tau_1 l_1 + n_2\tau_2 l_2}. \tag{21}$$

Ultimately, we obtain from relations (19) and (21) the following expression for the effective mobility:

$$\mu_\parallel^{\text{eff}} = \frac{e}{m}\frac{\tau_1 l_1 + \tau_2 l_2}{l_1 + l_2}. \tag{22}$$

Comparing Eq. (12) for $R_\perp$ and Eq. (21) for $R_\parallel$, we note that the Hall coefficient becomes isotropic ($R_\perp = R_\parallel$) when the concentrations n_1 and n_2 are equal. Thus, in order to relate our model to the results obtained on the mobility anisotropy, we must put $n_1 \neq n_2$.

A comparison of Eqs. (15) and (22) for the mobility shows that

$$\mu_\parallel^{\text{eff}} \neq \mu_\perp^{\text{eff}} \quad \text{for} \quad \tau_1 \neq \tau_2.$$

Thus, in order to fit the model to the experimental data, we must put $n_1 \neq n_2$ and $\tau_1 \neq \tau_2$. We will assume that the carrier scattering in the layer l_1 is more effective and that $\tau_1 < \tau_2$. The layer simulates the slip plane with a dislocation pile-up if the value of l_1 is comparable to the radius of the Read cylinders or to the effective distance over which the dislocation-induced deformation is acting. The carrier concentration in this layer is lower than the concentration in the bulk because of electrostatic expulsion from the region occupied by charged dislocations; consequently, it is natural to assume that $n_1 < n_2$. For a small deformation, when the slip planes filled with dislocation clusters are scarce, we can assume that $l_1 < l_2$. Let us consider the limiting case when the inequalities between these parameters are strong. In this case, the characteristics for the direction parallel to the slip planes become

$$\mu_\parallel^{\text{eff}} = \frac{e\tau_2}{m}, \quad R_\parallel^{\text{eff}} = \frac{1}{ecn_2}, \quad \sigma^{\text{eff}} = \sigma_2; \tag{23}$$

they involve the parameters of an intermediate layer, which is natural under the assumption concerning the shunting of the current by high-conductivity regions. The characteristics for the direction perpendicular to the slip planes are determined by the relationship between the quantities l_1/n_1 and l_2/n_2.

Assuming that

$$l_1/n_1 > l_2/n_2, \tag{24}$$

we obtain

$$\mu_\perp^{\text{eff}} = e\tau_1/m, \quad R_\perp^{\text{eff}} = 1/ec\frac{l_1}{l_2 n_2}, \quad \sigma_\perp^{\text{eff}} = \frac{l_2}{l_1}\sigma_1. \tag{25}$$

This case (24) corresponds to the experimental situation, i.e., to inequalities $\mu_\perp^{\text{eff}} < \mu_\parallel^{\text{eff}}$, $R_\perp > R_\parallel$, and $\sigma_\perp^{\text{eff}} < \sigma_\parallel^{\text{eff}}$.

In the case of the opposite inequality

$$l_1/n_1 < l_2/n_2, \tag{26}$$

we arrive at the relations

$$\begin{aligned}R_\perp^{\text{eff}} &= \frac{1}{ecn_2}, \quad \sigma_\perp^{\text{eff}} = \frac{l_2}{l_2/n_2\tau_2 + l_1/n_1\tau_1}\frac{e^2}{m}, \\ \mu_\perp^{\text{eff}} &= \frac{e}{m}\frac{l_1/n_1}{l_2/n_2\tau_2 + l_1/n_1\tau_1}.\end{aligned} \tag{27}$$

In accordance with relations (27) and (23), the difference between $\mu_\perp$ and $\mu_\parallel$ disappears in this case.This can easily be verified by selecting the limiting numerical values of the parameters l, n, and τ and substituting them into the corresponding formulas.

Let us now consider the physical pattern of manifestation of the scattering properties of defects upon the introduction of impurity atoms into a plastically deformed crystal. For small deformations, when a strong anisotropy of mobility exists in the absence of impurity diffusion, the value of μ increases both in the TPD and in the EPD mode in the presence of diffused indium acceptor impurities. This fact can be interpreted as follows. Doping with indium noticeably increases the concentration of ionized impurities. Since the mobility increases instead of decreases, this can be due to the mutual suppression of two scattering mechanisms associated with dislocations and impurities. Such a situation can be realized if the electric interaction between dislocations and carriers, associated with the charge of dislocation lines, is significant in the dislocation scattering.

It should be noted that, for small deformations, when the number of dislocations is small and they are arranged in the form of planar clusters, their limiting charging can be attained because the electrostatic barrier prevents the further trapping of holes. It is well known that, in *p*-Ge, dislocations behave as donors which acquire a positive charge after capturing holes. The introduced negatively charged indium acceptor atoms must pile up on dislocation lines in noticeable numbers. In this case, the combined (dislocation and impurity) electrostatic interaction with carriers can be compensated to a considerable extent. Only in this case can an increase in the mobility μ be expected in crystals with either deformation mode. Thus, we assume that, for the most part, the indium ions do not become effective scatterers but they noticeably reduce the scattering ability of dislocations.

Such an interpretation is also supported by the fact that the ionic radius of indium differs significantly from the radius of the host atoms. Consequently, it can be expected that indium ions are "replaced" by dislocations more easily than gallium atoms, which are the initial dopant in germanium crystals. As a result, a significant component of the electrostatic scattering potential is suppressed, thereby causing an increase in the effective mobility.

The considerably smaller anisotropy of the mobility for samples with EPD with transverse and longitudinal orientations of the current lines relative to the slip planes is probably associated with the involvement of a larger number of slip planes even at early stages of deformation in view of the localization of the thermal effect of the current, which was presumed in [13]. This assumption correlates with the well-known fact of the absence of mobility anisotropy in samples subjected to thermoplastic deformation at high temperatures [14].

As regards the minimum of thermal mobility in the TPD mode, its dislocation origin is indisputable; this minimum can be associated with a manifestation of resonance scattering at a shallow dislocation level. A minimum for the transverse orientation can also be observed in formula (15) if we assume that, as the temperature decreases, a transition from inequality (25) to inequality (27) and further to inequality (24) takes place. In this case, $\mu_\perp$ attains the value $e\tau_2/m$, which coincides with $\mu_\parallel$. Thus, a tendency to nonmonotonic behavior of $\mu_\perp$ is present in the model considered by us here, but the magnitude of the effect cannot be matched easily with experimental data. Detailed experiments are required in order to draw more exact conclusions.

REFERENCES

1. M. A. Aliev, Kh. O. Alieva, and V. V. Seleznev, Fiz. Tverd. Tela (St. Petersburg) **40** (10), 1816 (1998) [Phys. Solid State **40**, 1646 (1998)].
2. V. G. Eremenko, V. I. Nikitenko, and E. B. Yakimov, Pis'ma Zh. Éksp. Teor. Fiz. **26** (2), 72 (1977) [JETP Lett. **26**, 65 (1977)].
3. Yu. A. Osipyan and S. A. Shevchenko, Pis'ma Zh. Éksp. Teor. Fiz. **18** (4), 256 (1973) [JETP Lett. **18**, 153 (1973)].
4. I. V. Klyatsina, M. A. Kozhukh, S. M. Ryvkin, *et al.*, Fiz. Tekh. Poluprovodn. (Leningrad) **13** (6), 1089 (1979) [Sov. Phys. Semicond. **13**, 638 (1979)].
5. I. V. Klyatsina, M. A. Kozhukh, S. M. Ryvkin, *et al.*, Pis'ma Zh. Éksp. Teor. Fiz. **29** (5), 268 (1979) [JETP Lett. **29**, 239 (1979)].
6. V. E. Panin, Izv. Vyssh. Uchebn. Zaved., Fiz. **41** (1), 7 (1998).
7. T. Suzuki, H. Yoshinaga, and S. Takeuchi, *Dislocation Dynamics and Plasticity* (Syokabo, Tokyo, 1986; Mir, Moscow, 1989).
8. I. Prigogine, *From Being to Becoming: Time and Complexity in the Physical Sciences* (Freeman, San Francisco, 1980; Nauka, Moscow, 1985).
9. V. S. Ivanova, A. S. Balankin, I. Zh. Bunin, and A. A. Oksogoev, *Synergetics and Fractals in Materials Science* (Nauka, Moscow, 1994).
10. M. A. Aliev, Kh. O. Alieva, and V. V. Seleznev, Fiz. Tverd. Tela (St. Petersburg) **37** (12), 3732 (1995) [Phys. Solid State **37**, 2057 (1995)].
11. T. A. Kontorova, Fiz. Tverd. Tela (Leningrad) **9**, 1235 (1967) [Sov. Phys. Solid State **9**, 961 (1967)].
12. O. V. Kononchuk, V. I. Orlov, O. V. Feklisova, *et al.*, Fiz. Tekh. Poluprovodn. (St. Petersburg) **30** (2), 256 (1996) [Semiconductors **30**, 143 (1996)].
13. M. A. Aliev, Kh. O. Alieva, and V. V. Seleznev, Fiz. Tverd. Tela (St. Petersburg) **38** (11), 3372 (1996) [Phys. Solid State **38**, 1839 (1996)].
14. V. F. Gantmakher and Y. B. Levinson, *Carrier Scattering in Metals and Semiconductors* (Nauka, Moscow, 1984; North-Hooland, New York, 1987).

Translated by N. Wadhwa

Physics of the Solid State, Vol. 43, No. 11, 2001, pp. 2037–2043. Translated from Fizika Tverdogo Tela, Vol. 43, No. 11, 2001, pp. 1957–1962.
Original Russian Text Copyright © 2001 by Dymnikov.

SEMICONDUCTORS AND DIELECTRICS

Selection Rules for Matrix Elements of the Generalized Momentum Operator π at the Γ Point in III–V Semiconductors

V. D. Dymnikov

Ioffe Physicotechnical Institute, Russian Academy of Sciences, Politekhnicheskaya ul. 26, St. Petersburg, 194021 Russia

Received March 5, 2001

Abstract—Exact selection rules for matrix elements of the generalized momentum operator $\boldsymbol{\pi}$ at the Γ point in semiconductors of the GaAs-type without an inversion center are deduced for the first time with thorough account of spin–orbit interaction, which manifests itself in both splitting and mixing of orbital states. In particular, selection rules are obtained for forbidden optical transitions $\Gamma_7 \longrightarrow \Gamma_8$ in the valence band. The selection rules are formulated in terms of Clebsch–Gordan coefficients and reduced matrix elements. The relation between the reduced matrix elements and the mixing parameters of the wave functions is derived. © *2001 MAIK "Nauka/Interperiodica".*

1. INTRODUCTION

Matrix elements of the momentum operator at the Γ point play an extremely important role in the III–V semiconductors. These matrix elements characterize optical transitions in direct bandgap materials and determine the mass spectrum and *g*-factors of charge carriers. Various multiband versions of the **kp** method of the perturbation theory constructed on the basis of these matrix elements are constantly being improved upon and are widely used in investigations of electronic and optical properties of three-dimensional and low-dimensional semiconductor structures (see, for example, [1–3]). Usually, the matrix elements involved in Kane's model [4], which takes into account tetrahedral symmetry and spin–orbit splitting of bands, are used in calculations. According to Kane's model, the spectrum of charge carriers at the Γ point has a simple structure: the electrons are described by *s*-type wave functions in the Γ_6 conduction band and by *p*-type wave functions in the Γ_7 and Γ_8 valence bands. However, while Kane's model is satisfactory in many cases, it is not a general model, because it does not take into account the spin–orbit interaction in full measure. According to [4], the spin–orbit interaction gives rise only to splitting of orbital states at the center of the Brillouin zone, while the theory of symmetry [5] leaves room not only for splitting but also for spin–orbit mixing of space functions of various symmetries at the Γ point. This circumstance is usually disregarded, because it is seemingly believed to be of little importance. However, there are situations in which the mixing of wave functions plays a decisive role. The splitting of the Γ_8 valence band in the linear approximation in **k** (**k** is the quasi-momentum) and the optical transitions $\Gamma_7 \longrightarrow \Gamma_8$ inside the valence band are examples of such situations. It is customary to consider these intraband transitions to be forbidden [6], but the theory of symmetry allows them. The possible important role of the forbidden transitions $\Gamma_7 \longrightarrow \Gamma_8$ was suggested by the experiments performed in [7] on the absorption of radiation by free holes in *p*-GaSb. Preliminary calculations carried out in the three-band model [8] count in favor of this conclusion.

The mixing of wave functions at the Γ point means that the spectrum of charge carriers has a complicated structure because of the correlation between their orbital motion and spin; this structure is more complicated than that assumed in Kane's model. The fine details of the electronic states may prove to be essential in studying the polarization properties of charge carriers in both three-dimensional and low-dimensional materials. Recent research on the transverse *g*-factor ($g_\perp$) of heavy holes in a GaAs/AlGaAs (001) quantum well [9] has shown that the measured quantity $g_\perp$ is directly connected to the Luttinger parameter *q* [10], which characterizes the three-dimensional properties of GaAs and has a relativistic nature [11]. When calculating the parameter *q*, satisfactory agreement with experimental data was achieved in [9] only by going beyond Kane's model and allowing for spin–orbit mixing. Comprehensive study of the polarization properties of charge carriers is also of interest because of the practical use of III–V semiconductors and structures made on their basis as sources of polarized electrons [12].

The above-mentioned examples indicate that Kane's model is of limited usefulness for a number of problems and that it needs to be generalized taking the spin–orbit interaction into complete account. In the present work, the general expressions for spin–orbit harmonics are derived for all bands at the Γ point with due regard for the spin–orbit mixing and selection rules for the matrix

elements of the generalized momentum operator $\boldsymbol{\pi}$ between all states at the center of the Brillouin zone are established. The results are represented in terms of Clebsch–Gordan coefficients and reduced matrix elements. The reduced matrix elements are written using the mixing parameters of the wave functions; therefore, they are convenient for use in practical calculations of concrete models of mixing.

The results obtained in this paper allow one to study, in particular, the forbidden optical transitions $\Gamma_7 \longrightarrow \Gamma_8$ and to obtain information on the space symmetry of excited states at the Γ point using optical methods. The energies and symmetry of excited states are also extremely important in researching the Γ_8 valence band splitting that is linear in $\mathbf{k}$, which has been poorly investigated to date. In addition, the selection rules established allow one to develop a new version of the $\mathbf{k}\boldsymbol{\pi}$ method in which the spin–orbit interaction is accurately taken into account and, within this approach, to obtain the most general expressions for the effective masses and *g*-factors of charge carriers allowed by tetrahedral symmetry at the Γ point for all bands in the III–V semiconductors.

2. WAVE FUNCTIONS

The states of electrons in crystals of tetrahedral symmetry at the Γ point are described by wave functions $\Psi_n(\mathbf{r})$ that satisfy the Schrödinger equation:

$$H\Psi_n = (H_0 + H_{\text{rel}})\Psi_n = E_n\Psi_n, \tag{1}$$

$$H_0 = \frac{\mathbf{p}^2}{2m} + V(\mathbf{r}), \tag{2}$$

$$H_{\text{rel}} = -\frac{\mathbf{p}^4}{8m^3c^2} + \frac{\hbar^2}{8m^2c^2}\Delta V + \frac{\hbar}{4m^2c^2}\boldsymbol{\sigma}(\nabla V \times \mathbf{p}). \tag{3}$$

Here, m is the electron mass, $V(\mathbf{r})$ is the periodic potential, $\boldsymbol{\sigma}$ are the Pauli matrices, $\mathbf{p} = -i\hbar\nabla$, the index n enumerates the energy bands, and E_n is the energy of an electron in the nth band. The Hamiltonian H in Eq. (1) is written in the relativistic approximation, which is correct to the first order in the parameter c^{-2} [13]. The relativistic term H_{rel} in Eq. (3) is the sum of three terms. The first two terms produce a shift in the levels of the Hamiltonian H_0 given by Eq. (2) and intermixing of wave functions related to the same type of coordinate representation. The third term in Eq. (3) is spin-dependent and is responsible for spin–orbit splitting and mixing of the wave functions at the Γ point that belong to different types of representations according to which the eigenfunctions of the operator H_0 are transformed. Hereafter, the Dirac notation is used for the wave functions at the Γ point:

$$\Psi_n(\mathbf{r}) \equiv |\Gamma_n\rangle. \tag{4}$$

Disregarding the spin, the energy levels of the Hamiltonian H_0 in III–V semiconductors are related to five types of states, the wave functions of which are transformed according to the irreducible representations Γ_1, Γ_2, Γ_3, Γ_4, and Γ_5 [5]. The Γ_1 and Γ_2 states are nondegenerate, the Γ_3 state is doubly degenerate, and the Γ_4 and Γ_5 states are triply degenerate. The basis functions $|\Gamma_\alpha\rangle$ ($\alpha = 1, 2, 3, 4, 5$) for the irreducible representations at the Γ point are written as [5]

$$|\Gamma_1\rangle = s, \tag{5}$$

$$|\Gamma_2\rangle = s_1 = x^4(y^2 - z^2) + y^4(z^2 - x^2) + z^4(x^2 - y^2), \tag{6}$$

$$|\Gamma_3\rangle = \frac{1}{\sqrt{2}}(2z^2 - x^2 - y^2), \quad \sqrt{\frac{3}{2}}(x^2 - y^2), \tag{7}$$

$$|\Gamma_4\rangle = x, y, z, \tag{8}$$

$$|\Gamma_5\rangle = \epsilon_1, \epsilon_2, \epsilon_3, \tag{9}$$

where

$$\epsilon_1 = x(y^2 - z^2), \quad \epsilon_2 = y(z^2 - x^2), \quad \epsilon_3 = z(x^2 - y^2). \tag{10}$$

In formulas (5)–(10), s is the tetrahedral-group invariant and x, y, and z are coordinate functions which are transformed under tetrahedral symmetry operations as coordinates of the position vector x, y, and z. All basis functions in Eqs. (5)–(10) are assumed to be real and normalized to unity. Here and henceforth, the coordinate axes are taken to be along the directions [100], [010], and [001]. The z axis is along [001] and taken to be the axis of quantization.

The eigenfunctions of the Hamiltonian (1) belong to the spinor representations Γ_n ($n = 6, 7, 8$) [5, 14]. They are formed from orbital functions similar to those in Eqs. (5)–(9) and from the spin functions $\alpha = \begin{pmatrix}1\\0\end{pmatrix}$ and $\beta = \begin{pmatrix}0\\1\end{pmatrix}$ by using multiplication rules for representations $\Gamma_\alpha \times \mathcal{D}_{\frac{1}{2}}$ ($\alpha = 1, 2, 3, 4, 5$), where $\mathcal{D}_{\frac{1}{2}}$ is the representation according to which the spin functions are transformed. The multiplication table for representations is given in [5]. The final results for all spinor states at the Γ point in a III–V semiconductor are presented below. The Γ_6 states are doubly degenerate, and their basis functions $|\Gamma_6; M\rangle$ ($M = \pm 1/2$) can be written as

$$|\Gamma_6; M\rangle = \sum_{\Gamma_1} C_{\Gamma_6\Gamma_1}|\Gamma_6(\Gamma_1); M\rangle + \sum_{\Gamma_5} C_{\Gamma_6\Gamma_5}|\Gamma_6(\Gamma_5); M\rangle, \tag{11}$$

where

$$\left|\Gamma_6(\Gamma_1);\frac{1}{2}\right\rangle = is\alpha, \quad \left|\Gamma_6(\Gamma_1);-\frac{1}{2}\right\rangle = is\beta, \tag{12}$$

$$\begin{cases} \left|\Gamma_6(\Gamma_5);\frac{1}{2}\right\rangle = -\frac{1}{\sqrt{3}}[(\epsilon_1 + i\epsilon_2)\beta + \epsilon_3\alpha] \\ \left|\Gamma_6(\Gamma_5);-\frac{1}{2}\right\rangle = \frac{1}{\sqrt{3}}[\epsilon_3\beta - (\epsilon_1 - i\epsilon_2)\alpha]. \end{cases} \tag{13}$$

The states in the Γ_7 band are also doubly degenerate, and the basis functions $|\Gamma_7; M\rangle$ ($M = \pm 1/2$) can be written as

$$|\Gamma_7; M\rangle = \sum_{\Gamma_2} C_{\Gamma_7\Gamma_2}|\Gamma_7(\Gamma_2); M\rangle + \sum_{\Gamma_4} C_{\Gamma_7\Gamma_4}|\Gamma_7(\Gamma_4); M\rangle, \tag{14}$$

where

$$\left|\Gamma_7(\Gamma_2);\frac{1}{2}\right\rangle = is_1\alpha, \quad \left|\Gamma_7(\Gamma_2);-\frac{1}{2}\right\rangle = is_1\beta, \tag{15}$$

$$\begin{cases} \left|\Gamma_7(\Gamma_4);\frac{1}{2}\right\rangle = -\frac{1}{\sqrt{3}}[(x + iy)\beta + z\alpha] \\ \left|\Gamma_7(\Gamma_4);-\frac{1}{2}\right\rangle = -\frac{1}{\sqrt{3}}[z\beta - (x - iy)\alpha]. \end{cases} \tag{16}$$

The Γ_8 states in a III–V semiconductor are fourfold degenerate. Their wave functions $|\Gamma_8; M\rangle$ ($M = 3/2, 1/2$) can be represented as

$$|\Gamma_8; M\rangle = \sum_{\Gamma_3} C_{\Gamma_8\Gamma_3}|\Gamma_8(\Gamma_3); M\rangle + \sum_{\Gamma_4} C_{\Gamma_8\Gamma_4}|\Gamma_8(\Gamma_4); M\rangle + \sum_{\Gamma_5} C_{\Gamma_8\Gamma_5}|\Gamma_8(\Gamma_5); M\rangle, \tag{17}$$

where

$$\begin{cases} \left|\Gamma_8(\Gamma_3);\frac{3}{2}\right\rangle = \frac{i}{\sqrt{2}}(2z^2 - x^2 - y^2)\beta \\ \left|\Gamma_8(\Gamma_3);\frac{1}{2}\right\rangle = i\sqrt{\frac{3}{2}}(x^2 - y^2)\alpha \\ \left|\Gamma_8(\Gamma_3);-\frac{1}{2}\right\rangle = -i\sqrt{\frac{3}{2}}(x^2 - y^2)\beta \\ \left|\Gamma_8(\Gamma_3);-\frac{3}{2}\right\rangle = -\frac{i}{\sqrt{2}}(2z^2 - x^2 - y^2)\alpha, \end{cases} \tag{18}$$

$$\begin{cases} \left|\Gamma_8(\Gamma_4);\frac{3}{2}\right\rangle = -(x + iy)\frac{\alpha}{\sqrt{2}} \\ \left|\Gamma_8(\Gamma_4);\frac{1}{2}\right\rangle = \frac{1}{\sqrt{3}}\left[-(x + iy)\frac{\beta}{\sqrt{2}} + \sqrt{2}z\alpha\right] \\ \left|\Gamma_8(\Gamma_4);-\frac{1}{2}\right\rangle = \frac{1}{\sqrt{3}}\left[(x - iy)\frac{\alpha}{\sqrt{2}} + \sqrt{2}z\beta\right] \\ \left|\Gamma_8(\Gamma_4);-\frac{3}{2}\right\rangle = (x - iy)\frac{\beta}{\sqrt{2}}, \end{cases} \tag{19}$$

$$\begin{cases} \left|\Gamma_8(\Gamma_5);\frac{3}{2}\right\rangle = \frac{1}{\sqrt{3}}\left[(\epsilon_1 - i\epsilon_2)\frac{\alpha}{\sqrt{2}} + \sqrt{2}\epsilon_3\beta\right] \\ \left|\Gamma_8(\Gamma_5);\frac{1}{2}\right\rangle = -(\epsilon_1 - i\epsilon_2)\frac{\beta}{\sqrt{2}} \\ \left|\Gamma_8(\Gamma_5);-\frac{1}{2}\right\rangle = (\epsilon_1 + i\epsilon_2)\frac{\alpha}{\sqrt{2}} \\ \left|\Gamma_8(\Gamma_5);-\frac{3}{2}\right\rangle = \frac{1}{\sqrt{3}}\left[-(\epsilon_1 + i\epsilon_2)\frac{\beta}{\sqrt{2}} + \sqrt{2}\epsilon_3\alpha\right]. \end{cases} \tag{20}$$

The summations in formulas (11), (14), and (17) are carried out over all indicated representations of the operator H_0. The phase factors of the spin–orbit harmonics in Eqs. (12), (13), (15), (16), and (18)–(20) are chosen such that the coefficients $C_{\Gamma_n\Gamma_\alpha}$ in Eqs. (11), (14), and (17) are real.

The general character of mixing described by Eqs. (11), (14), and (17) indicates that charge carriers in the III–V semiconductors are in relatively complicated states which cannot be described by Kane's model. For example, the admixture of the Γ_5 to Γ_1 state in the Γ_6 conduction band means that the electron cannot be generally described by a wave function of the *s* type; therefore, it possesses not only a spin but also, because of the Γ_5 admixture, a nonzero orbital angular momentum per unit cell, which can basically influence the polarization properties of the electron. This fact was not noted earlier.

3. SELECTION RULES

In this section, we present selection rules for the operator $\mathbf{k}\boldsymbol{\pi}$, where $\mathbf{k}$ is the quasi-momentum and $\boldsymbol{\pi}$ is the generalized momentum operator:

$$\boldsymbol{\pi} = \mathbf{p} + \mu(\boldsymbol{\sigma} \times \nabla V), \quad \mu = \frac{\hbar}{4mc^2}. \tag{21}$$

The matrix elements are calculated between all wave functions at the Γ point. The selection rules are formulated in terms of Clebsch–Gordan coefficients and reduced matrix elements. The reduced matrix elements are expressed through the mixing coefficients of the

wave functions. This approach seems to be the most convenient for use in practice.[1]

Calculations carried out with the help of the wave functions (11) and (17) give the following selection rules for the $\Gamma_6 \rightleftharpoons \Gamma_8$ transitions:

$$\langle \Gamma_6;\, M|\mathbf{k}\boldsymbol{\pi}|\Gamma_8;\, M'\rangle = k_{M'-M} C^{\frac{3}{2}M'}_{1M'-M\frac{1}{2}M} A^{\Gamma_6\Gamma_8}, \qquad M = \pm\frac{1}{2}, \quad M' = \pm\frac{3}{2}, \pm\frac{1}{2}, \tag{22}$$

$$A^{\Gamma_6\Gamma_8} = \sum_{\Gamma_1\Gamma_4} C_{\Gamma_6\Gamma_1} C_{\Gamma_8\Gamma_4} \left[-i\langle s|p_x|x\rangle - \mu\left\langle s\left|\frac{\partial V}{\partial x}\right|x\right\rangle\right]$$

$$+ \sqrt{3}\sum_{\Gamma_3\Gamma_5} C_{\Gamma_6\Gamma_5} C_{\Gamma_8\Gamma_3} \left[i\left\langle \epsilon_1|p_x|x^2-y^2\right\rangle - \mu\left\langle \epsilon_1\left|\frac{\partial V}{\partial x}\right|x^2-y^2\right\rangle\right]$$

$$+ \frac{1}{\sqrt{3}}\sum_{\Gamma_5\Gamma_4} C_{\Gamma_6\Gamma_5} C_{\Gamma_8\Gamma_4} \left[i\langle \epsilon_3|p_y|x\rangle + 3\mu\left\langle \epsilon_3\left|\frac{\partial V}{\partial x}\right|x\right\rangle\right] \tag{23}$$

$$+ \sum_{\Gamma_5\Gamma_{5'}} C_{\Gamma_6\Gamma_5} C_{\Gamma_8\Gamma_{5'}} \left[-i\langle \epsilon_3|p_y|\epsilon_1'\rangle + \mu\left\langle \epsilon_3\left|\frac{\partial V}{\partial y}\right|\epsilon_1'\right\rangle\right].$$

In formula (22), k_α ($\alpha = 1, 0, -1$) are cyclic components of the vector $\mathbf{k}$ [16] and $C^{JM}_{j_1 m_1 j_2 m_2}$ are the Clebsch–Gordan coefficients.

The selection rules for the $\Gamma_6 \rightleftharpoons \Gamma_7$ transitions follow from relations (11) and (14):

$$\langle \Gamma_6;\, M|\mathbf{k}\boldsymbol{\pi}|\Gamma_7;\, M'\rangle = k_{M'-M} C^{\frac{1}{2}M'}_{1M'-M\frac{1}{2}M} B^{\Gamma_6\Gamma_7}, \qquad M = \pm\frac{1}{2}, \quad M' = \pm\frac{1}{2}, \tag{24}$$

$$B^{\Gamma_6\Gamma_7} = \sum_{\Gamma_1\Gamma_4} C_{\Gamma_6\Gamma_1} C_{\Gamma_7\Gamma_4} \left[-i\langle s|p_x|x\rangle + 2\mu\left\langle s\left|\frac{\partial V}{\partial x}\right|x\right\rangle\right]$$

$$+ \sum_{\Gamma_5\Gamma_2} C_{\Gamma_6\Gamma_5} C_{\Gamma_7\Gamma_2} \left[i\langle \epsilon_1|p_x|s_1\rangle + 2\mu\left\langle \epsilon_1\left|\frac{\partial V}{\partial x}\right|s_1\right\rangle\right] \tag{25}$$

$$+ \sum_{\Gamma_5\Gamma_4} C_{\Gamma_6\Gamma_5} C_{\Gamma_7\Gamma_4} \left[-\frac{2}{\sqrt{3}} i\langle \epsilon_3|p_y|x\rangle\right].$$

[1] The formal selection rules formulated in a number of monographs (see, for example, [14, 15]) do not allow one to trace the relation of the matrix elements to the character of the spin–orbit mixing.

The selection rules for the $\Gamma_7 \rightleftharpoons \Gamma_8$ transitions are formulated with the help of relations (14) and (17):

$$\langle \Gamma_7;\, M_1|\mathbf{k}\boldsymbol{\pi}|\Gamma_8;\, M_2\rangle = \left[-\sqrt{\frac{10}{3}} k_{+1} C^{\frac{1}{2}M_1}_{\frac{3}{2}M_2 21} + \sqrt{\frac{5}{3}} k_0 \left(C^{\frac{1}{2}M_1}_{\frac{3}{2}M_2 2-2} - C^{\frac{1}{2}M_1}_{\frac{3}{2}M_2 22}\right) + \sqrt{\frac{10}{3}} k_{-1} C^{\frac{1}{2}M_1}_{\frac{3}{2}M_2 2-1}\right] C^{\Gamma_7\Gamma_8}, \tag{26}$$

$$M_1 = \pm\frac{1}{2}, \quad M_2 = \pm\frac{3}{2}, \pm\frac{1}{2},$$

$$C^{\Gamma_7\Gamma_8} = \sum_{\Gamma_2\Gamma_5} C_{\Gamma_7\Gamma_2} C_{\Gamma_8\Gamma_5} \left[-i\langle s_1|p_x|\epsilon_1\rangle - \mu\left\langle s_1\left|\frac{\partial V}{\partial x}\right|\epsilon_1\right\rangle\right]$$

$$+ \sum_{\Gamma_4\Gamma_3} C_{\Gamma_7\Gamma_4} C_{\Gamma_8\Gamma_3} \left[i\langle x|p_x|x^2-y^2\rangle - \mu\left\langle x\left|\frac{\partial V}{\partial x}\right|x^2-y^2\right\rangle\right] \tag{27}$$

$$+ \sum_{\Gamma_4\Gamma_{4'}} C_{\Gamma_7\Gamma_4} C_{\Gamma_8\Gamma_{4'}} \left[i\langle x|p_y|z'\rangle - \mu\left\langle x\left|\frac{\partial V}{\partial y}\right|z'\right\rangle\right]$$

$$+ \sum_{\Gamma_4\Gamma_5} C_{\Gamma_7\Gamma_4} C_{\Gamma_8\Gamma_5} \left[\frac{i}{\sqrt{3}}\langle x|p_y|\epsilon_3\rangle - \sqrt{3}\mu\left\langle x\left|\frac{\partial V}{\partial y}\right|\epsilon_3\right\rangle\right].$$

Each of the selection rules in Eqs. (22), (24), and (26) is characterized by one parameter, namely, by the reduced matrix element. This follows from the formulas for multiplication of the representations [5]:

$$\Gamma_6 \times \Gamma_4 = \Gamma_8 + \Gamma_7, \quad \Gamma_7 \times \Gamma_4 = \Gamma_6 + \Gamma_8. \tag{28}$$

The reduced matrix elements (23), (25), and (27) are real, because the mixing coefficients $C_{\Gamma_n\Gamma_\alpha}$ are real. The derivation of the selection rules in Eqs. (22), (24), and (26) is given in the Appendix.

The $\Gamma_8 \rightleftharpoons \Gamma_{8'}$ transitions, in contrast to the transitions considered above, are characterized by two parameters. This follows from the relation

$$\Gamma_8 \times \Gamma_4 = 2\Gamma_8 + \Gamma_6 + \Gamma_7. \tag{29}$$

Using wave functions (17), one can derive the following selection rules for the $\Gamma_8 \rightleftharpoons \Gamma_{8'}$ transitions:

$$\langle \Gamma_8;\, M|\mathbf{k}\boldsymbol{\pi}|\Gamma_8;\, M'\rangle = \frac{1}{3}\mathcal{D}_s^{\Gamma_8\Gamma_{8'}} (I^s)_{MM'} + \frac{1}{3}\mathcal{D}_A^{\Gamma_8\Gamma_{8'}} (I^A)_{MM'}. \tag{30}$$

Here, I^s is a Hermitian 4×4 matrix and I^A is an anti-Hermitian 4×4 matrix. These matrices can be expressed in terms of the matrices J_x, J_y, and J_z of the angular momentum $J = 3/2$ as

$$I^s = k_x\{J_x, J_y^2 - J_z^2\} + k_y\{J_y, J_z^2 - J_x^2\} + k_z\{J_z, J_x^2 - J_y^2\}, \tag{31}$$

$$I^A = i(k_x\{J_y, J_z\} + k_y\{J_z, J_x\} + k_z\{J_x, J_y\}), \quad (32)$$

where

$$J_x = \begin{pmatrix} 0 & \frac{\sqrt{3}}{2} & 0 & 0 \\ \frac{\sqrt{3}}{2} & 0 & 1 & 0 \\ 0 & 1 & 0 & \frac{\sqrt{3}}{2} \\ 0 & 0 & \frac{\sqrt{3}}{2} & 0 \end{pmatrix},$$

$$J_y = \begin{pmatrix} 0 & -i\frac{\sqrt{3}}{2} & 0 & 0 \\ i\frac{\sqrt{3}}{2} & 0 & -i & 0 \\ 0 & i & 0 & -i\frac{\sqrt{3}}{2} \\ 0 & 0 & i\frac{\sqrt{3}}{2} & 0 \end{pmatrix}, \quad (33)$$

$$J_z = \begin{pmatrix} \frac{3}{2} & 0 & 0 & 0 \\ 0 & \frac{1}{2} & 0 & 0 \\ 0 & 0 & -\frac{1}{2} & 0 \\ 0 & 0 & 0 & \frac{3}{2} \end{pmatrix}.$$

The symbol $\{\ldots\}$ in formulas (31) and (32) denotes the anticommutator, $\{A, B\} = AB + BA$.

The reduced matrix elements $\mathscr{D}_s^{\Gamma_8\Gamma_{8'}}$ and $\mathscr{D}_A^{\Gamma_8\Gamma_{8'}}$ in Eq. (30) are written as

$$\mathscr{D}_s^{\Gamma_8\Gamma_{8'}} = -\sum_{\Gamma_3\Gamma_4}(C_{\Gamma_8\Gamma_3}C_{\Gamma_{8'}\Gamma_4} + C_{\Gamma_{8'}\Gamma_3}C_{\Gamma_8\Gamma_4})$$
$$\times\left[i\langle x^2 - y^2|p_x|x\rangle + \mu\left\langle x^2 - y^2\left|\frac{\partial V}{\partial x}\right|x\right\rangle\right]$$
$$-\sum_{\Gamma_4\Gamma_{4'}}(C_{\Gamma_8\Gamma_4}C_{\Gamma_{8'}\Gamma_{4'}} + C_{\Gamma_{8'}\Gamma_4}C_{\Gamma_8\Gamma_{4'}})\mu\left\langle x\left|\frac{\partial V}{\partial y}\right|z'\right\rangle$$
$$+\sum_{\Gamma_5\Gamma_{5'}}(C_{\Gamma_8\Gamma_5}C_{\Gamma_{8'}\Gamma_{5'}} + C_{\Gamma_{8'}\Gamma_5}C_{\Gamma_8\Gamma_{5'}})\mu\left\langle \epsilon_3\left|\frac{\partial V}{\partial y}\right|\epsilon_1'\right\rangle \quad (34)$$
$$-\sqrt{3}\sum_{\Gamma_3\Gamma_5}(C_{\Gamma_8\Gamma_3}C_{\Gamma_{8'}\Gamma_5} + C_{\Gamma_{8'}\Gamma_3}C_{\Gamma_8\Gamma_5})$$
$$\times\left[i\langle x^2 - y^2|p_x|\epsilon_1\rangle + \mu\left\langle x^2 - y^2\left|\frac{\partial V}{\partial x}\right|\epsilon_1\right\rangle\right]$$
$$+\frac{2}{\sqrt{3}}\sum_{\Gamma_4\Gamma_5}(C_{\Gamma_8\Gamma_4}C_{\Gamma_{8'}\Gamma_5} + C_{\Gamma_{8'}\Gamma_4}C_{\Gamma_8\Gamma_5})i\langle x|p_y|\epsilon_3\rangle.$$

$$\mathscr{D}_A^{\Gamma_8\Gamma_{8'}} = -\sum_{\Gamma_3\Gamma_4}(C_{\Gamma_8\Gamma_3}C_{\Gamma_{8'}\Gamma_4} - C_{\Gamma_{8'}\Gamma_3}C_{\Gamma_8\Gamma_4})$$
$$\times\left[i\langle x^2 - y^2|p_x|x\rangle - 2\mu\left\langle x^2 - y^2\left|\frac{\partial V}{\partial x}\right|x\right\rangle\right]$$
$$+\frac{1}{2}\sum_{\Gamma_4\Gamma_{4'}}(C_{\Gamma_8\Gamma_4}C_{\Gamma_{8'}\Gamma_{4'}} - C_{\Gamma_{8'}\Gamma_4}C_{\Gamma_8\Gamma_{4'}})i\langle x|p_y|z'\rangle$$
$$+\frac{1}{2}\sum_{\Gamma_5\Gamma_{5'}}(C_{\Gamma_8\Gamma_5}C_{\Gamma_{8'}\Gamma_{5'}} - C_{\Gamma_{8'}\Gamma_5}C_{\Gamma_8\Gamma_{5'}})i\langle \epsilon_1|p_y|\epsilon_3'\rangle \quad (35)$$
$$+\sqrt{3}\sum_{\Gamma_3\Gamma_5}(C_{\Gamma_8\Gamma_3}C_{\Gamma_{8'}\Gamma_5} - C_{\Gamma_{8'}\Gamma_3}C_{\Gamma_8\Gamma_5})$$
$$\times\left[i\langle x^2 - y^2|p_x|\epsilon_1\rangle - 2\mu\left\langle x^2 - y^2\left|\frac{\partial V}{\partial x}\right|\epsilon_1\right\rangle\right]$$
$$+\frac{1}{\sqrt{3}}\sum_{\Gamma_4\Gamma_5}(C_{\Gamma_8\Gamma_4}C_{\Gamma_{8'}\Gamma_5} - C_{\Gamma_{8'}\Gamma_4}C_{\Gamma_8\Gamma_5})i\langle x|p_y|\epsilon_3\rangle.$$

The real quantities $\mathscr{D}_s^{\Gamma_8\Gamma_{8'}}$ and $\mathscr{D}_A^{\Gamma_8\Gamma_{8'}}$ are symmetric and antisymmetric, respectively, with respect to the permutation of symbols Γ_8 and Γ_8':

$$\mathscr{D}_s^{\Gamma_8\Gamma_{8'}} = \mathscr{D}_s^{\Gamma_{8'}\Gamma_8}, \quad \mathscr{D}_A^{\Gamma_8\Gamma_{8'}} = -\mathscr{D}_A^{\Gamma_{8'}\Gamma_8}. \quad (36)$$

From relations (36), it follows that the intraband transitions are characterized by one parameter, $\mathscr{D}_s^{\Gamma_8\Gamma_8}$, because $\mathscr{D}_A^{\Gamma_8\Gamma_8} = 0$.

With reference to the conduction band Γ_6 and the valence bands Γ_8 and Γ_7, the following reduced matrix elements connecting these bands are of interest: $A^{\Gamma_6\Gamma_8}$, $B^{\Gamma_6\Gamma_7}$, $C^{\Gamma_7\Gamma_8}$, and $\mathscr{D}_s^{\Gamma_8\Gamma_8}$. From formulas (23), (25), (27), and (34), it follows that if we suppose the wave functions in the band Γ_6 to be *s*-type functions and

those in the bands Γ_8 and Γ_7 to be p-type functions, then in the absence of mixing, we have

$$A^{\Gamma_6\Gamma_8} = B^{\Gamma_6\Gamma_7} = -i\langle s|p_x|x\rangle,$$
$$C^{\Gamma_7\Gamma_8} = 0, \quad \mathscr{D}_s^{\Gamma_8\Gamma_8} = 0; \tag{37}$$

i.e., the situation postulated in Kane's model takes place [5]. The spin–orbit mixing results in the inequality of quantities $A^{\Gamma_6\Gamma_8}$ and $B^{\Gamma_6\Gamma_7}$ and in nonzero matrix elements $C^{\Gamma_7\Gamma_8}$ and $\mathscr{D}_s^{\Gamma_8\Gamma_8}$.

ACKNOWLEDGMENTS

The author is grateful to E.L. Ivchenko for stimulating discussions, V.I. Perel' and his coworkers for useful discussions, and O.V. Konstantinov for valuable remarks.

APPENDIX

Let us derive expressions (22), (24), and (26). Since the dependence of matrix elements upon the projections M and M' of the angular momentum is invariant with respect to the specific form of the reduced matrix elements, it is convenient to use wave functions in the simplest form when deriving the selection rules. We assume that the wave functions in bands Γ_6, Γ_7, and Γ_8 have a concrete space symmetry and are given by Eqs. (12), (16), and (18).

We introduce the notation for the spin functions

$$\alpha = \chi_{\frac{1}{2}\frac{1}{2}}, \quad \beta = \chi_{\frac{1}{2}\frac{1}{2}} \tag{A1}$$

and for the functions of the Γ_4 representation

$$\psi_{11} = -\frac{1}{\sqrt{2}}(x+iy),$$
$$\psi_{10} = z, \quad \psi_{1-1} = \frac{1}{\sqrt{2}}(x-iy). \tag{A2}$$

Then, wave functions (16) and (18) in bands Γ_7 and Γ_8 can be written as

$$|\Gamma_7(\Gamma_4); M\rangle = \sum_{M_1M_2} C^{\frac{1}{2}M}_{1M_1\frac{1}{2}M_2}\psi_{1M_1}\chi_{\frac{1}{2}M_2}, \tag{A3}$$

$$|\Gamma_8(\Gamma_4); M\rangle = \sum_{M_1M_2} C^{\frac{3}{2}M}_{1M_1\frac{1}{2}M_2}\psi_{1M_1}\chi_{\frac{1}{2}M_2}. \tag{A4}$$

Here, the quantities $C^{JM}_{j_1M_1j_2M_2}$ are the Clebsch–Gordan coefficients.

By expressing the operator $\mathbf{k\pi}$ in terms of the covariant and contravariant components of vectors in the cyclic basis [16], we obtain

$$\langle\Gamma_6(\Gamma_1); m|\mathbf{k}\cdot\boldsymbol{\pi}|\Gamma_8(\Gamma_4); M\rangle = \sum_{M_1M_2a} C^{\frac{3}{2}M}_{1M_1\frac{1}{2}M_2}$$
$$\times\left\langle is\chi_{\frac{1}{2}m}\left|p^\alpha k_\alpha + \mu(\nabla V\times k)^\alpha\sigma_\alpha\right|\psi_{1M_1}\chi_{\frac{1}{2}M_2}\right\rangle \tag{A5}$$
$$= k_{M-m}C^{\frac{3}{2}M}_{1-M-m\frac{1}{2}m}A^{\Gamma_6\Gamma_8},$$

$$A^{\Gamma_6\Gamma_8} = -i\langle s|p_x|x\rangle - \mu\left\langle s\left|\frac{\partial V}{\partial x}\right|x\right\rangle \tag{A6}$$

and, similarly,

$$\langle\Gamma_6(\Gamma_1); m|\mathbf{k}\cdot\boldsymbol{\pi}|\Gamma_7(\Gamma_4); M\rangle$$
$$= k_{M-m}C^{\frac{1}{2}M}_{1M-m\frac{1}{2}m}B^{\Gamma_6\Gamma_7}, \tag{A7}$$

$$B^{\Gamma_6\Gamma_7} = -i\langle s|p_x|x\rangle + 2\mu\left\langle s\left|\frac{\partial V}{\partial x}\right|x\right\rangle. \tag{A8}$$

When deriving expressions (A5) and (A7), the following relations were used [16]:

$$p^\alpha = (-1)^\alpha p_{-\alpha}, \quad \langle s|p^\alpha|\psi_{1M_1}\rangle = \langle s|p_x|x\rangle\delta_{\alpha M_1},$$

$$(\nabla V\times k)^\alpha = i\sqrt{2}\sum_{\nu\lambda}C^{1\alpha}_{1\nu1\lambda}(\nabla V)^\nu k^\lambda, \quad \alpha,\nu,\lambda = \pm1.0,$$

$$(\sigma_\alpha)_{mM_2} = \sqrt{3}C^{\frac{1}{2}m}_{\frac{1}{2}M_21\alpha},$$

$$\left\langle s|\nabla V)^\nu|\psi_{1M_1}\right\rangle = \left\langle s\left|\frac{\partial V}{\partial x}\right|x\right\rangle\delta_{\nu M_1},$$

$$\sum_{M_1M_2\alpha}C^{JM}_{1M_1\frac{1}{2}M_2}C^{\frac{1}{2}m}_{\frac{1}{2}M_21\alpha}C^{1\alpha}_{1M_11\lambda}$$
$$= (-1)^{J+\frac{1}{2}+\lambda}\sqrt{6}C^{JM}_{1-\lambda\frac{1}{2}m}\begin{Bmatrix}1 & \frac{1}{2} & J\\ \frac{1}{2} & 1 & 1\end{Bmatrix}.$$

Here, $\delta_{\alpha\beta}$ is the Kronecker delta and $\begin{Bmatrix}a & b & c\\ d & e & f\end{Bmatrix}$ is a 6j symbol. The reduced matrix elements $A^{\Gamma_6\Gamma_8}$ in Eq. (A6) and $B^{\Gamma_6\Gamma_7}$ in Eq. (A8) correspond to a concrete space symmetry of wave functions (12), (16), and (18). Generally, when the functions $|\Gamma_6; M\rangle$, $|\Gamma_7; M\rangle$, and $|\Gamma_8; M\rangle$ have the form of Eqs. (11), (14), and (17), the quantities $A^{\Gamma_6\Gamma_8}$ and $B^{\Gamma_6\Gamma_7}$ should be replaced by expressions (23)

and (25). This can be verified directly by calculating any one matrix element in Eqs. (22) and (24).

Let us now verify formulas (26). For this purpose, we first calculate the matrix elements $\langle\Gamma_7(\Gamma_4);M|\mathbf{k}\boldsymbol{\pi}|\Gamma_8(\Gamma_{4'});M'\rangle \equiv (\mathbf{k}\boldsymbol{\pi})_{MM'}$. The result is

$$\begin{aligned}
\sqrt{3}(\mathbf{k}\boldsymbol{\pi})_{\frac{1}{2}\frac{3}{2}\frac{1}{2}} &= -(\mathbf{k}\boldsymbol{\pi})_{-\frac{1}{2}\frac{1}{2}\frac{1}{2}} = k_{-1}C^{\Gamma_7\Gamma_8},\\
(\mathbf{k}\boldsymbol{\pi})_{\frac{1}{2}-\frac{3}{2}} &= (\mathbf{k}\boldsymbol{\pi})_{-\frac{1}{2}\frac{3}{2}\frac{1}{2}} = \sqrt{\frac{2}{3}}k_0C^{\Gamma_7\Gamma_8},\\
\sqrt{3}(\mathbf{k}\boldsymbol{\pi})_{-\frac{1}{2}-\frac{3}{2}} &= -(\mathbf{k}\boldsymbol{\pi})_{\frac{1}{2}-\frac{1}{2}} = k_{+1}C^{\Gamma_7\Gamma_8},\\
(\mathbf{k}\boldsymbol{\pi})_{\frac{1}{2}\frac{1}{2}\frac{1}{2}} &= (\mathbf{k}\boldsymbol{\pi})_{-\frac{1}{2}-\frac{1}{2}} = 0,
\end{aligned} \tag{A9}$$

$$C^{\Gamma_7\Gamma_8} = -i\langle x|p_y|z'\rangle - \mu\left\langle x\left|\frac{\partial V}{\partial y}\right|z'\right\rangle. \tag{A10}$$

In order to write relations (A9) in terms of Clebsch–Gordan coefficients, it is sufficient to express the matrix elements $\langle\Gamma_7(\Gamma_4);M|\mathbf{kp}|\Gamma_8(\Gamma_{4'});M'\rangle \equiv (\mathbf{kp})_{MM'}$ through these coefficients, because the quantities $(\mathbf{k}\boldsymbol{\pi})_{MM'}$ and $(\mathbf{kp})_{MM'}$ differ only in their reduced matrix elements. From Eqs. (A3) and (A4), it follows that

$$(\mathbf{kp})_{MM'} = \sum_{M_1M_2m} C^{\frac{1}{2}M}_{1M_1\frac{1}{2}m}C^{\frac{3}{2}M'}_{1M_2\frac{1}{2}m}\langle\psi_{1M_1}|\mathbf{kp}|\psi'_{1M_2}\rangle. \tag{A11}$$

The matrix elements in Eq. (A11) can be related to the 3×3 matrix I:

$$\begin{aligned}
\langle\psi_{1M_1}|\mathbf{kp}|\psi'_{1M_2}\rangle &= i\langle x|p_y|z'\rangle(I)_{M_1M_2},\\
M_1, M_2 &= 1, 0, -1,
\end{aligned} \tag{A12}$$

where

$$I = \begin{pmatrix} 0 & -k_{+1} & k_0\\ -k_{-1} & 0 & k_{+1}\\ -k_0 & k_{-1} & 0\end{pmatrix}. \tag{A13}$$

The matrix I in Eq. (A13) can be expressed through the polarization operators T_{2s} ($s = 0, 1, 2$) [16]:

$$I = \sqrt{2}k_{+1}T_{21} + k_0(T_{22} - T_{2-2}) - \sqrt{2}k_{-1}T_{2-1}. \tag{A14}$$

Taking into account that, in the cyclic basis, the matrix elements of the operators T_{2s} are given by the formulas [16]

$$(T_{2s})_{M_1M_2} = \sqrt{\frac{5}{3}}C^{1M_1}_{1M_22s} \tag{A15}$$

and using the relation [16]

$$\sum_{M_1M_2m} C^{\frac{3}{2}M'}_{1M_2\frac{1}{2}m}C^{\frac{1}{2}M}_{1M_1\frac{1}{2}m}C^{1M_1}_{1M_22s} = -C^{\frac{1}{2}M}_{\frac{3}{2}M'2s}, \tag{A16}$$

one can obtain an expression for the matrix element $(\mathbf{kp})_{MM'}$ from Eqs. (A14), (A12), and (A11). If we replace the matrix element $i\langle x|p_y|z'\rangle$ in that expression by $C^{\Gamma_7\Gamma_8}$ given by Eq. (A10), then, in accordance with Eq. (A9), we obtain

$$\begin{aligned}
\langle\Gamma_7(\Gamma_4);\,M|\mathbf{k}\cdot\boldsymbol{\pi}|\Gamma_8(\Gamma_{4'});\,M'\rangle = \Bigg[&-\sqrt{\frac{10}{3}}k_{+1}C^{\frac{1}{2}M_1}_{\frac{3}{2}M_221}\\
&+\sqrt{\frac{5}{3}}k_0\left(C^{\frac{1}{2}M_1}_{\frac{3}{2}M_22-2} - C^{\frac{1}{2}M_1}_{\frac{3}{2}M_222}\right) + \sqrt{\frac{10}{3}}k_{-1}C^{\frac{1}{2}M_1}_{\frac{3}{2}M_22-1}\Bigg]C^{\Gamma_7\Gamma_8}.
\end{aligned} \tag{A17}$$

In the general case of spin–orbit mixing, where the wave functions have the form of Eqs. (14) and (17), expression (A17) is transformed into Eq. (26) with the reduced matrix element given by Eq. (27). This can be verified by calculating any one matrix element in the left-hand side of Eq. (26).

REFERENCES

1. M. Cardona, N. E. Christensen, and G. Fasol, Phys. Rev. B **38** (3), 1806 (1988).
2. C. Pryor, Phys. Rev. B **57** (11), 7190 (1998).
3. O. Stier, M. Grundman, and D. Bimberg, Phys. Rev. B **59** (8), 5688 (1999).
4. E. O. Kane, J. Phys. Chem. Solids **1**, 249 (1957).
5. G. Dresselhaus, Phys. Rev. **100** (2), 580 (1955).
6. *Semiconductors and Semimetals*, Vol. 3: *Optical Properties of III–V Compounds*, Ed. by R. K. Willardson and A. C. Beer (Academic, New York, 1967; Mir, Moscow, 1970).
7. G. N. Iluridze, A. N. Titkov, and E. M. Chaĭkina, Fiz. Tekh. Poluprovodn. (Leningrad) **21** (1), 80 (1987) [Sov. Phys. Semicond. **21**, 48 (1987)].
8. V. D. Dymnikov, in *Proceedings of the III All-Russia Conference on Physics of Semiconductors, Moscow, 1997*, p. 211.
9. X. Marie, T. Amand, P. Le Jeune, *et al.*, Phys. Rev. B **60** (8), 5811 (1999).
10. J. M. Luttinger, Phys. Rev. **102** (4), 1030 (1956).
11. J. C. Hensel and K. Suzuki, Phys. Rev. Lett. **22**, 838 (1969).
12. A. V. Subashiev, Yu. A. Mamaev, Yu. P. Yashin, and J. E. Clendenin, Phys. Low-Dimens. Struct., No. 1/2, 1 (1999).
13. V. B. Berestetskii, E. M. Lifshitz, and L. P. Pitaevskii, in *Course of Theoretical Physics*, Vol. 4: *Quantum Electrodynamics* (Nauka, Moscow, 1989; Pergamon, New York, 1982).
14. G. L. Bir and G. E. Pikus, *Symmetry and Strain-Induced Effects in Semiconductors* (Nauka, Moscow, 1972; Wiley, New York, 1975).
15. G. F. Koster, J. O. Dimmock, R. G. Wheeler, and H. Statz, *Properties of the Thirty-Two Point Groups* (MII Press, Cambridge, 1963).
16. D. A. Varshalovich, A. N. Moskalev, and V. K. Khersonskii, *Quantum Theory of Angular Momentum* (Nauka, Leningrad, 1975; World Scientific, Singapore, 1988).

Translated by O. Ivanov

Physics of the Solid State, Vol. 43, No. 11, 2001, pp. 2044–2047. Translated from Fizika Tverdogo Tela, Vol. 43, No. 11, 2001, pp. 1963–1965.
Original Russian Text Copyright © 2001 by Gorban', Okhrimenko.

SEMICONDUCTORS AND DIELECTRICS

Exciton Absorption Parameters in $TlGaS_2$ Crystals

I. S. Gorban'†* and O. B. Okhrimenko**

**Shevchenko National University, Vladimirskaya ul. 64, Kiev, 03127 Ukraine*

***Institute of Semiconductor Physics, National Academy of Sciences of Ukraine, Kiev, 03028 Ukraine*

Received October 17, 2000; in final form, April 2, 2001

Abstract—It is shown that, because the shape of the exciton absorption curve in crystalline $TlGaS_2$ is described by the Fano antiresonance profile, the experimentally observed exciton peak corresponds to a modified state which is the result of the configuration interaction of a discrete state (exciton) with the quasi-continuum of conduction-band states. The oscillator strength for the transition to the discrete ("pure") exciton state is calculated as $F_0 = 1.22 \times 10^{-2}$. The exciton transition selection rules are calculated for two assumed symmetry groups, D_{2h} and D_{4h}. An analysis of the selection rules for the dipole-allowed exciton transition permits one to conclude that the symmetry group for the $TlGaS_2$ crystal is D_{2h}. © *2001 MAIK "Nauka/Interperiodica".*

1. INTRODUCTION

The $TlGaS_2$ crystal is classified with the ternary layered semiconductors. Literature data suggest that the narrow peak observed at the fundamental absorption edge is due to direct-exciton formation at the Brillouin zone center [1].

The symmetry group of the $TlGaS_2$ crystal remains to be completely ascertained. The symmetry factor group which is most frequently used for describing the properties of this crystal is C_{2h}; however, the number of Raman- and IR-active modes calculated using this group of symmetry far exceeds that of Raman scattering (RS) and IR lines observed in experimental spectra [2, 3].

In [2], the structure of the $TlGaS_2$ layer is symmetrized by slightly displacing the intralayer atoms until they form a tetragonal structure with space group D_{2d}^5. By introducing an interlayer inversion operation and retaining the layer symmetry elements, the authors of [2] obtained a hypothetical structure with space group D_{4h}^{15} and a double-layer unit cell. With this approximation, the mode number allowed by the theory agrees better with the one obtained experimentally [2]. In this case, one can assume D_{2d}, D_{2h}, and D_{4h} as possible layer symmetry groups. Analysis of the polarization dependences and study of the structure of the RS and IR spectra suggested two possible symmetry groups for the $TlGaS_2$ crystal, namely, D_{2h} [2] and D_{4h} [3].

Comparison of the selection rules for exciton transitions with experimental data may permit one to pinpoint the preferable group from the above two. To do this, one has to establish whether the observed excitons are allowed in the dipole approximation. This question can be answered by calculating the oscillator strength for the transition to the exciton state.

The present communication reports on the determination of the exciton-band symmetry and on a calculation of the oscillator strength for the exciton transition from optical absorption spectra obtained at 1.8 K. At this temperature, the exciton–phonon coupling is weaker than the exciton–photon coupling and, therefore, the exciton absorption line profile is only weakly distorted.

2. EXPERIMENT

The samples for the measurements were prepared by cleaving. The samples used in the measurements were thin platelets with a thickness d = 0.0020–0.0070 cm. The crystal purity was verified according to the absence of impurity- or defect-induced luminescence; the surface parallelism, according to the perfection of the interference pattern in the transmission region. We studied absorption spectra in both the $\mathbf{E} \parallel \mathbf{z}$ and $\mathbf{E} \perp \mathbf{z}$ polarizations ($\mathbf{z}$ is the optical crystal axis perpendicular to the layer plane).

The figure presents an absorption spectrum of the $TlGaS_2$ crystal (d = 21 μm) obtained at 1.8 K.

3. CALCULATION OF THE OSCILLATOR STRENGTH

In calculating the oscillator strength, one usually makes use of the integrated absorption coefficient derived from the area bounded by the transmission curve. However, at low temperatures (about 1.8 K), this calculation yields incorrect values [4]. Therefore, calculation of the oscillator strength for transitions to the exciton state at low temperatures must take polariton effects into account. We calculated [5] the oscillator strength for the transition to the exciton state in $TlGaS_2$

† Deceased.

with due account of the polariton effects, $F = 1.33 \times 10^{-2}$; this corresponds to a dipole-allowed transition.

4. EXCITON ABSORPTION LINE SHAPE

A line shape analysis for exciton absorption in $TlGaS_2$ [6] showed the exciton absorption peak in crystalline $TlGaS_2$ to be best fitted by the Fano antiresonance profile [7]:

$$f(\varepsilon, q) = \frac{(q+\varepsilon)^2}{1+\varepsilon^2}, \quad (1)$$

where

$$\varepsilon = \frac{E - E_{ex} - E'}{\frac{1}{2}\Gamma_a}, \quad (2)$$

E_{ex} is the energy corresponding to the discrete state (exciton), E'' is the correction to the discrete state energy due to the configuration interaction, $E_{ex} + E''$ determines the experimentally measured position of the resonance line, and Γ_a is the half-width of the antiresonance profile.

The best fit parameters were found to be $E_{ex} = 2.605$ eV, $\Gamma_a = 0.011$ eV, and the Fano antiresonance parameter $q = 3.5$. In accordance with [7], the quantity q^2 is determined by the intensity ratio (i.e., in effect, the ratio of the corresponding oscillator strengths) for the optical transition to the modified discrete state Φ and to an unperturbed continuum state ψ_E:

$$\frac{1}{2}\pi q^2 = \frac{|(\Phi|\mathbf{p}|i)|^2}{|(\psi_E|\mathbf{p}|i)|^2\Gamma_a}, \quad (3)$$

where $\mathbf{p}$ is the dipole moment operator and Γ_a is the half-width of the antiresonance profile. Because the experimentally measured absorption line position corresponds to a modified state arising as a result of configuration interaction between a discrete state (in our case, of the exciton) and the continuum (electronic states in the conduction band), the oscillator strength of the transition to the exciton state in $TlGaS_2$ determined in [5] actually corresponds to a transition to the modified state. The oscillator strength for a transition to the pure exciton state can be determined from the expression [7]

$$|(\varphi|\mathbf{p}|i)|^2 = \frac{1}{2}\pi(q^2-1)\Gamma_a|(\psi_E|\mathbf{p}|i)|^2$$
$$= |(\Phi|\mathbf{p}|i)|^2 - \frac{1}{2}\pi\Gamma_a|(\psi_E|\mathbf{p}|i)|^2 = \frac{q^2-1}{q^2}|(\Phi|\mathbf{p}|i)|^2, \quad (4)$$

where φ is the discrete-state wave function.

Because the oscillator strength for the modified state calculated earlier is $F = 1.33 \times 10^{-2}$, that for the transition to the pure exciton state, according to Eq. (4), is $F_0 = 1.22 \times 10^{-2}$. Thus, the transition to a pure exciton state is dipole-allowed.

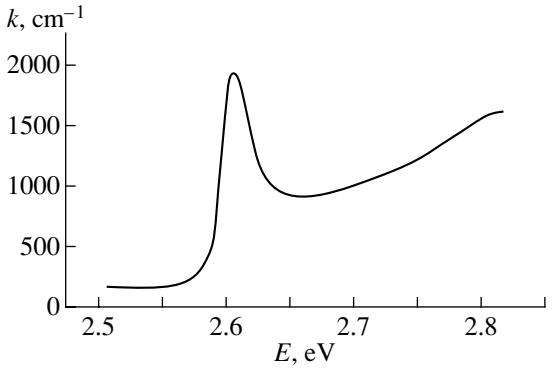

Absorption spectrum of $TlGaS_2$ obtained at 1.8 K.

5. EXCITON BAND SYMMETRY

Analysis of the selection rules for an exciton transition using group theory should also yield a dipole-allowed transition.

The valence band in $TlGaS_2$ is believed to be derived from single-electron states of the sulfur ions; the conduction band, from those of the gallium ions [8].

According to the LCAO method, the electron wave functions in the valence band are represented as a linear combination of wave functions of the outer filled electronic shells of the ions that make up the crystal. Because only the highest valence-band and the lowest conduction-band levels are considered, the bands should be derived only from those shells which are the first to undergo changes in the cases where an ion loses or acquires an electron.

According to [9, 10], the formula of the $TlGaS_2$ compound can be presented as $Tl^+(Ga^{3+}S_2^{2-})^{1-}$. Taking into account the configurational changes that the S^{2-} and Ga^{3+} ions undergo in losing or acquiring an electron, we come to the conclusion that the valence-band top is derived from the p states of the $3p^5$ sulfur ion (the $^2P_{1/2}$ term) and that the conduction band originates from the s states of the $3d^{10}4s$ gallium ion (the $^2S_{1/2}$ term).

Consider the classification of the valence- and conduction-band levels according to the irreducible representations of the two possible symmetry groups, D_{2h} [2] and D_{4h} [3].

According to [11], the site symmetry of the S and Ga atoms in a layer with symmetry D_{4h} is described by the following groups: C_{2v} for S and D_{2d} for Ga. To find the symmetry of the valence and conduction bands, we use the correlation diagram method. According to this method, the states of these bands should be induced by irreducible representations of the corresponding site-symmetry groups.

Because the valence band of $TlGaS_2$ is derived from the p states of sulfur ($^2P_{1/2}$ term), the states of the valence band are induced by local functions, whose symmetry is described by the E' representation of the double group C'_{2v}, and the states of the conduction band, which are derived from the Ga s states, are induced by local functions, with their symmetry being described by irreducible representations E'_2 of the double group D'_{2d}. We shall use the correlation diagrams for the two possible factor groups of the crystal, D_{2h} and D_{4h}, to analyze the selection rules for the excitonic transitions. This shall be done assuming D_{4h} to be the layer symmetry group in both cases, so that the site symmetry of the gallium and sulfur atoms will be retained in both cases.

(1) We assume D_{4h} to be the factor group of the crystal. According to the correlation diagram, the E' representation of group C'_{2v} is formally compatible with four representations of the D'_{4h} group, more specifically, E'_{1g}, E'_{1u}, E'_{2g}, and E'_{2u}. The representation corresponding to the $^2p_{1/2}$ state should formally be a twofold representation of the D'_{4h} group. Because the electronic configuration under study contains 5 p electrons, the $^2P_{1/2}$ state has odd parity and the E'_{1g} and E'_{2g} representations should be excluded from the consideration. Of the two remaining representations, E'_{1u} and E'_{2u}, preference should be given to E'_{1u}, because it can be derived directly from the expressions used in determining the representation corresponding to the original level $^2P_{1/2}$ in symmetry group D'_{4h}.

Consider, in the same manner, the $^2S_{1/2}$ state for the s electron bound to a Ga^{3+} ion. The electronic configuration forming in this case corresponds to an even-parity state; therefore, of the two representations of the D'_{2h} group, E'_{2g} and E'_{2u}, specified in the correlation diagram, one should choose E'_{2g}. We thus obtain

$$\Gamma_v = E'_{1u}, \quad \Gamma_c = E'_{2g}. \tag{5}$$

For the S state of the exciton, we come to

$$\Gamma_{ex} = B_{1u} + B_{2u} + E_u, \tag{6}$$

and for the exciton P state,

$$\Gamma_{ex}(p_{x,y}) = A_{1g} + A_{2g} + B_{1g} + B_{2g} + 2E_g, \tag{7}$$

$$\Gamma_{ex}(p_z) = B_{1g} + B_{2g} + E_g. \tag{8}$$

Because the ground state of the crystal is totally symmetric, the dipole-allowed components of the S exciton are E_u in the $\mathbf{E} \parallel \mathbf{y}$ and $\mathbf{E} \parallel \mathbf{x}$ polarizations, while for the P exciton, all components are dipole-forbidden.

(2) We assume D_{2h} to be the factor group of the crystal. In this case, the correlation diagram is constructed following the scenario typical of layered crystals. Namely, one considers, sequentially, the change in the local state symmetry in the transition from the atom site symmetry group in a layer (C_{2v} for sulfur and D_{2d} for gallium) through the layer symmetry group (D_{4h}) to the crystal symmetry group (D_{2h}). On making assumptions similar to those introduced when considering the D_{4h} symmetry group, we obtain

$$\Gamma_c = E^+, \quad \Gamma_v = E^-. \tag{9}$$

For the exciton states, this yields

$$\begin{aligned}
\Gamma_{ex}(s) &= E^+ \times E^- = A_u + B_{1u} + B_{2u} + B_{3u}, \\
\Gamma_{ex}(p_z) &= E^+ \times E^- \times B_{1u} = A_g + B_{1g} + B_{2g} + B_{3g}, \\
\Gamma_{ex}(p_x) &= E^+ \times E^- \times B_{2u} = A_g + B_{1g} + B_{2g} + B_{3g}, \\
\Gamma_{ex}(p_y) &= E^+ \times E^- \times B_{3u} = A_g + B_{1g} + B_{2g} + B_{3g}.
\end{aligned} \tag{10}$$

In this case, the selection rules yield the following dipole-allowed transitions for the S-exciton components: B_{1u} in the $\mathbf{E} \parallel \mathbf{z}$ polarization, B_{2u} for $\mathbf{E} \parallel \mathbf{y}$, and B_{3u} for the $\mathbf{E} \parallel \mathbf{x}$ polarization. The P exciton is forbidden by the selection rules in the dipole approximation.

The above selection rules for the exciton transitions permit determination of the crystal symmetry group. Because the experiment shows the exciton transition to be allowed in the dipole approximation and the absorption peak is seen in both the $\mathbf{E} \parallel \mathbf{z}$ and $\mathbf{E} \perp \mathbf{z}$ polarizations, one should consider D_{2h} to be the crystal symmetry group.

6. CONCLUSION

Thus, the results obtained in this work permit one to conclude that the symmetry of the valence and conduction bands is described by the E^- and E^+ irreducible representations of the D'_{2h} group, respectively; the S-exciton symmetry, by the $B_{1u} + B_{2u} + B_{3u}$ representations of the D_{2h} group. The oscillator strength of the pure exciton state calculated under the assumption that the exciton absorption curve is best fitted by the Fano antiresonance profile is $F_0 = 1.22 \times 10^{-2}$.

REFERENCES

1. S. G. Guseinov, G. D. Guseinov, N. Z. Gasanov, and S. B. Kyazimov, Phys. Status Solidi B **133** (1), K25 (1986).

2. N. N. Syrbu, V. É. L'vin, I. B. Zadnipru, *et al.*, Fiz. Tekh. Poluprovodn. (St. Petersburg) **26** (2), 232 (1992) [Sov. Phys. Semicond. **26**, 130 (1992)].
3. Yu. I. Durnev, B. S. Kul'budzhev, V. I. Torgashev, and Yu. I. Yuzin, Izv. Akad. Nauk SSSR, Ser. Fiz. **53** (7), 1300 (1989).
4. A. S. Davydov, *Theory of Solid State* (Nauka, Moscow, 1976).
5. I. S. Gorban' and O. B. Okhrimenko, Ukr. Fiz. Zh. **44** (9), 1115 (1999).
6. I. S. Gorban' and O. B. Okhrimenko, Dokl. Akad. Nauk Ukr., No. 4, 106 (1998).
7. U. Fano, Phys. Rev. **124** (6), 1866 (1961).
8. S. F. Terekhova, N. A. Onishchenko, and G. D. Guseĭnov, Ukr. Fiz. Zh. **28** (10), 1557 (1983).
9. N. M. Gasanly, N. N. Mel'nik, A. S. Ragimov, and V. I. Tagirov, Fiz. Tverd. Tela (Leningrad) **26** (2), 558 (1984) [Sov. Phys. Solid State **26**, 336 (1984)].
10. S. G. Abdullaeva, S. S. Abdinbekov, and G. G. Guseĭnov, Dokl. Akad. Nauk Az. SSR **36** (8), 34 (1980).
11. N. M. Gasanly, B. N. Mavrin, Kh. E. Sterin, *et al.*, Phys. Status Solidi B **86** (1), K49 (1978).

Translated by G. Skrebtsov

Physics of the Solid State, Vol. 43, No. 11, 2001, pp. 2048–2050. Translated from Fizika Tverdogo Tela, Vol. 43, No. 11, 2001, pp. 1966–1968.
Original Russian Text Copyright © 2001 by Solodukha, Liberman.

SEMICONDUCTORS AND DIELECTRICS

Specific Features of Hopping Conduction in Bismuth-Containing Oxide Layered Ceramics

A. M. Solodukha and Z. A. Liberman

Voronezh State University, Universitetskaya pl. 1, Voronezh, 394693 Russia

Received December 5, 2000; in final form, March 5, 2001

Abstract—The dynamic conduction of bismuth-containing oxide layered ceramics of the composition $Sr_2Bi_2TiNb_2O_{12}$ is investigated in a weak alternating field at frequencies of 0.5–500 kHz in the temperature range 300–700 K. It is demonstrated that the high-temperature conduction can be adequately described in terms of theoretical concepts using the effective medium method and corresponds to two-dimensional hopping transfer. The concentration of nodes in the system through which charge-carrier hopping occurs is estimated. © *2001 MAIK "Nauka/Interperiodica".*

1. INTRODUCTION

Although ceramic materials are widely used in various electrical devices owing to their unique properties, the exact mechanisms of their conduction are not yet completely understood. This is explained by the fact that ceramics are a rather complex object of investigation primarily due to their inhomogeneous polycrystalline structure, which possesses a high concentration of pores. In this structure, charge transfer can occur through several different mechanisms simultaneously, so that the overall picture of electrical conduction is rather intricate. In this case, it is important to answer the question as to whether the charge transport due to carrier transitions through potential barriers at grain boundaries prevails or if the conduction along the intercrystallite boundaries plays a dominant role and the properties of the crystallites by themselves are of no significance.

The purpose of this work was to investigate ac the conduction in $Sr_2Bi_2TiNb_2O_{12}$ ceramics. This compound belongs to the family of layered bismuth-containing perovskite-like oxides with the general formula $A_{m-1}Bi_2B_mO_{3m+3}$ [1]. In our case, $m = 3$, A = Sr, and the element B_3 is replaced by the isovalent combination B_2B' where $B_2 = Ti_2$ and B' = Nb.

2. SAMPLE PREPARATION AND EXPERIMENTAL TECHNIQUE

The samples were prepared in the form of pellets approximately 2 mm thick according to the standard ceramic technology. The sample density was 6.9 g/cm^3. The electrodes were fabricated by firing in a silver paste. Measurements were performed on a BM-507 impedometer in the temperature range 300–700 K at frequencies of 0.5–500 kHz according to the procedure described in [2]. The maximum error in determining the impedance modulus and the phase shift did not exceed ±6%. The measuring field strength was less than 10 V/cm. The experimental data were processed on a computer using a smoothing procedure.

3. RESULTS AND DISCUSSION

3.1. The temperature dependences of the conduction G for the sample at different frequencies of the measuring field are depicted in Fig. 1a. It is seen that the G conduction decreases only slightly with an increase in the temperature, which is especially pronounced at low frequencies. At $T > 450$ K, the temperature dependence of G has a shape characteristic of semiconductor materials. For this reason, we focused our attention on the temperature range above 450 K. It was found that the electrical conductivity at these temperatures is governed by a relationship typical of hopping charge transfer: $\mathrm{Re}\,\sigma(\omega) \sim \omega^s$, where σ is the effective conductivity, ω is the cyclic frequency of an alternating electric field ($\omega = 2\pi f$, where f is the frequency expressed in Hz), and s is a parameter ($s = 0.65$ at 700 K). However, judging only from this dependence, it is impossible to determine the particular mechanism of electrical conduction. Moreover, in the case of systems such as the ceramics under investigation, the dispersion can be associated with mobile carriers and dipoles. As is seen from Figs. 1b and 1c, the conduction dispersion is substantially more pronounced compared to the capacitance dispersion. Therefore, it would be more correct to represent the results in terms of the complex impedance Z^* and the complex dielectric modulus M^*, as was done by Macdonald [3]. In order to analyze the mechanisms of hopping conduction, we used the theoretical approach developed in the framework of the effective medium method, which was described by Bryksin *et al.* [4, 5]. Within this approach, the theoretical treatment is

1063-7834/01/4311-2048$21.00 © 2001 MAIK "Nauka/Interperiodica"

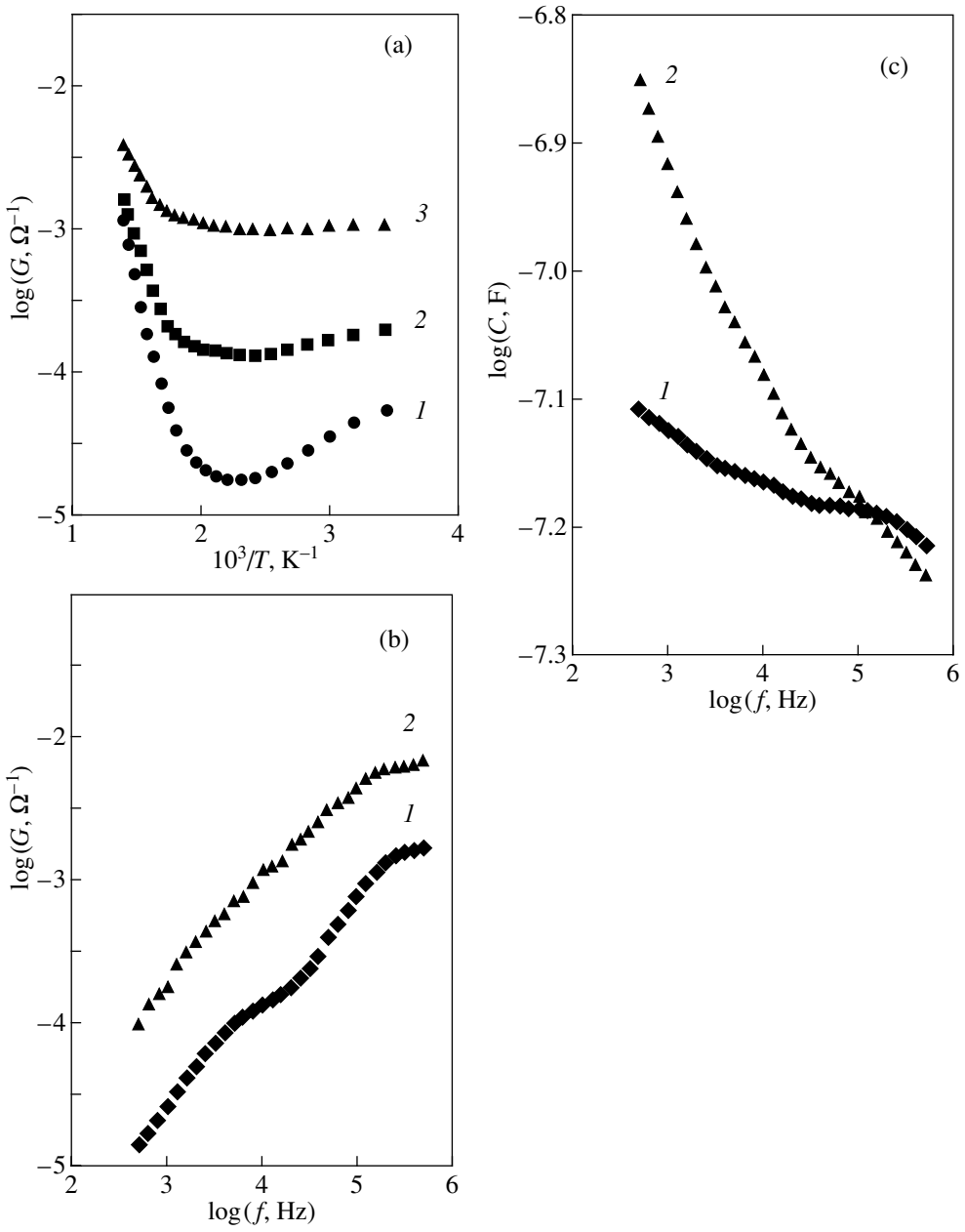

Fig. 1. (a) Dependences of the electrical conduction of the sample on the reciprocal of temperature at frequencies of (*1*) 1, (*2*) 10, and (*3*) 100 kHz. Dependences of (b) the electrical conduction and (c) the capacitance on the frequency of the measuring field at temperatures of (*1*) 500 and (*2*) 700 K.

carried out in terms of the dimensionless function, which is the reciprocal of the dielectric loss tangent:

$$\cot\delta = (\varepsilon' - \varepsilon_\infty)/\varepsilon'', \quad (1)$$

$$\varepsilon'' = [G(\omega) - G(0)]/\omega C_0. \quad (2)$$

Here, ε' and ε'' are the real and imaginary parts of the complex permittivity, respectively; $G(\omega)$ and $G(0)$ are the real parts of the ac and dc admittances, respectively; C_0 is the capacitance of the measuring cell; and ε_∞ is the real part of the permittivity at $\omega \longrightarrow \infty$.

In order to analyze the experimental results in accordance with expressions (1) and (2), it is necessary to determine the dc resistance $R_0 = 1/G(0)$ and ε_∞. The latter quantity can be determined from the formula $C_\infty = \varepsilon_\infty C_0$, where C_∞ is the electrical capacitance of the sample at $\omega \longrightarrow \infty$.

For the samples under investigation, the shape of the hodograph curves for Z^* and M^* permitted us to perform extrapolation only at temperatures of approximately 700 K for $\omega \longrightarrow 0$ and $\omega \longrightarrow \infty$ and to determine the values of $R_0 = 10^6\ \Omega$ and $\varepsilon_\infty = 235$ (Fig. 2). The

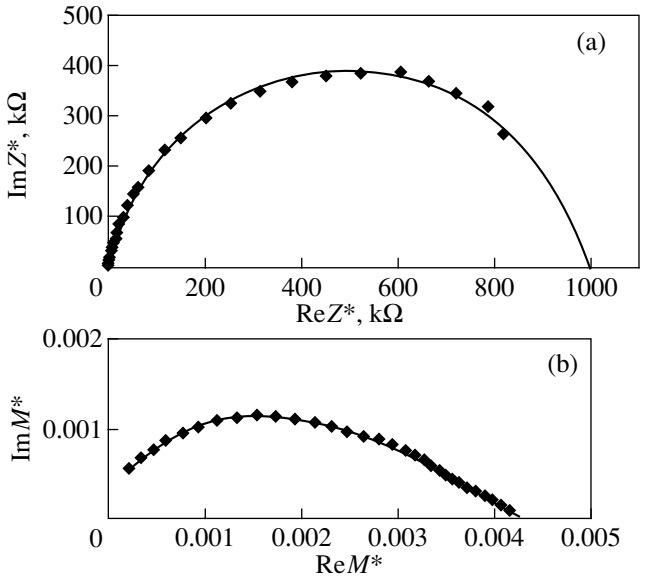

Fig. 2. Hodographs of (a) the impedance and (b) the dielectric modulus at 700 K.

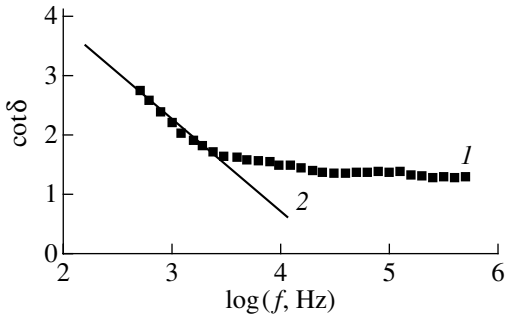

Fig. 3. (*1*) Dependence of the dielectric loss cotangent on the measuring field frequency at a temperature of 700 K and (*2*) a straight line with slope $2/\pi \log e$.

dielectric loss cotangent as a function of the logarithm of the measuring field frequency at 700 K is shown in Fig. 3. It can be seen from Fig. 3 that the experimental curve has a linear portion in the low-frequency range. Brykcin and Kleinert [5] proved that this behavior is a characteristic feature of hopping transfer in two-dimensional systems. Therefore, according to the data obtained in [5], we can write the following relationships:

$$\cot\delta = (2/\pi)\ln(32W_c/\omega), \qquad (3)$$

$$W_c = \nu_{ph}\exp[(-4\sqrt{\ln 2}\alpha N^{-1/2})/\sqrt{\pi}], \qquad (4)$$

where W_c is the critical hopping probability, which corresponds to the probability of forming an infinite cluster in the percolation theory; α is the reciprocal of the localization length; N is the node concentration in the system; and ν_{ph} is the phonon frequency.

It is also seen from Fig. 3 that the slope of the low-frequency portion is equal to $2/\pi$ (or $2/\pi \log e$ when changing over to the decimal logarithm); i.e., this value is in agreement with the coefficient theoretically predicted in [5]. It was demonstrated [5] that this coefficient is independent of the disorder parameter $\alpha N^{-1/2}$ and is characteristic of the frequency dependence of the conduction in two-dimensional systems for the hopping mechanism of charge transfer. From the aforesaid it follows that, in our case, this mechanism corresponds to charge transfer over the intercrystallite boundaries and pore surfaces in the studied samples.

3.2. Using expressions (3) and (4), we can estimate the node concentration N. To accomplish this, we extrapolate the low-frequency portion of the frequency dependence of $\cot\delta$ (see Fig. 3) until it intersects the vertical axis at the point corresponding to $\log f = 0$. As a result, we obtain $\cot\delta = 6.6$. Setting $\nu_{ph} = 10^{12}$ Hz and $\alpha = 0.8$ nm, as was done in [6], we determine the value of $N \approx 10^{17}$ m^{-2}, which falls within the permissible limits.

It is of interest to evaluate one more parameter of the theory, namely, the ratio of the mean distance between the nodes to the localization length: $\kappa = 4\alpha N^{-1/2}/\sqrt{\pi}$. In our case, this quantity is equal to 9 and falls in the range of possible values considered in [5].

REFERENCES

1. E. G. Fesenko, A. T. Shuvaev, V. G. Smotrakov, *et al.*, Neorg. Mater. **30** (8), 1057 (1994).
2. A. M. Solodukha and O. K. Zhukov, Izmer. Tekh., No. 6, 68 (1983).
3. J. R. Macdonald, Phys. Rev. B **49** (14), 9428 (1994).
4. V. V. Bryksin, M. N. D'yakonov, V. M. Muzhdaba, and S. D. Khanin, Fiz. Tverd. Tela (Leningrad) **23** (5), 1516 (1981) [Sov. Phys. Solid State **23**, 886 (1981)].
5. V. V. Brykcin and P. Kleinert, Fiz. Tverd. Tela (St. Petersburg) **37** (6), 1637 (1995) [Phys. Solid State **37**, 889 (1995)].
6. N. F. Mott and E. A. Davis, *Electronic Processes in Non-Crystalline Materials* (Clarendon, Oxford, 1979; Mir, Moscow, 1982), Vol. 1.

Translated by N. Korovin

Physics of the Solid State, Vol. 43, No. 11, 2001, pp. 2051–2059. Translated from Fizika Tverdogo Tela, Vol. 43, No. 11, 2001, pp. 1969–1976.
Original Russian Text Copyright © 2001 by Voronkov, Sazonov.

SEMICONDUCTORS AND DIELECTRICS

Quasi-solitonic Propagation Modes of Two-Component Acoustic Video Pulses in a Paramagnetic Crystal

S. V. Voronkov and S. V. Sazonov

Kaliningrad State Technical University, Kaliningrad, 236000 Russia

e-mail: nst@alg.kaliningrad.ru

Received March 26, 2001

Abstract—Nonlinear propagation of longitudinal–transverse acoustic pulses down to a length of one cycle (video pulses) in a low-temperature paramagnetic crystal in the direction parallel to an external magnetic field is investigated theoretically. The case of a crystal with paramagnetic impurity ions with effective $S = 1/2$ spin is considered. It is shown that, due to spin–phonon interaction, two-component acoustic pulses can propagate in the form of high-power quasi-solitons. Conditions are determined for the formation of exponentially localized subsonic rational solitons which propagate with a velocity higher than the velocity of transverse sound and which have a transverse component with a rotating plane of polarization. *© 2001 MAIK "Nauka/Interperiodica".*

1. INTRODUCTION

Over the last decade and a half, several reports on the generation of laser pulses roughly one cycle long (electromagnetic video pulses) have been published [1–3]; this initiated theoretical studies into the interaction of such pulses and matter (see, e.g., review [4]). Nonstationary coherent effects (such as photon echo and self-induced transparency) produced by video pulses have specific features [5, 6] in comparison with the corresponding effects caused by resonant quasi-monochromatic pulses with a well-defined carrier frequency. Since such a frequency is absent in electromagnetic video pulses, one cannot use the slowly varying amplitude (and phase) approximation in studying the interaction of these pulses and matter.

Acoustic picosecond video pulses have also been generated in many laboratories [7–9], and their propagation in various media has been studied theoretically. Different solitonic modes were considered [10–13] separately for longitudinal and transverse acoustic pulses. It was shown in [14] that when paramagnetic impurity ions in a crystal are excited by a series of transverse acoustic video pulses, acoustic echoes with both transverse and longitudinal structure can arise. In a solid, an acoustic pulse can have two components, longitudinal and transverse, which may lead to specific features unique to two-component acoustic solitons.

In this paper, we investigate quasi-solitonic propagation modes of longitudinal–transverse (two-component) acoustic video pulses in crystals with paramagnetic impurities. Solitons in the form of localized traveling video pulses will be referred to upon occasion as solitons, but they will not be assumed to have to interact elastically with one another.

Paramagnetic impurity ions are assumed to have an effective spin $S = 1/2$ (Kramers doublets) and to be placed in an external magnetic field **B**. As an example, we refer to paramagnetic Co^{2+} ions being in a cubic MgO crystal [15].

Following [6, 14, 16], we assume that

$$\omega_0 \tau_p \ll 1, \tag{1}$$

where ω_0 is the frequency characterizing the Kramers doublet splitting and τ_p is the video-pulse duration.

We note that in [17] the interaction of paramagnetic ions and nonresonant longitudinal–transverse soliton-like acoustic pulses was considered under the assumption that the pulse duration τ_p was such that $\omega_0 \tau_p \gg 1$, which is opposite to inequality (1).

Inequality (1) can be called the condition for spectral overlap, because, according to Eq. (1), the bandwidth of a video pulse is $\delta\omega \sim \tau_p^{-1} \gg \omega_0$. Therefore, the spectrum of a pulse contains Fourier components that can induce resonant quantum transitions between the Zeeman sublevels of paramagnetic ions; these transitions can be fairly strong if condition (1) is fulfilled.

2. SELF-CONSISTENT SET OF CONSTITUTIVE AND WAVE EQUATIONS

Condition (1) will be fulfilled if, for example, the Zeeman splitting is $\omega_0 \sim 10^{10}$ s^{-1} and the duration of an acoustic video pulse is $\tau_p \sim 10^{-11}$ s. The characteristic spatial length of such pulses is $l \simeq a\tau_p$, where a is the sound velocity in a solid. For $a \sim 5 \times 10^5$ cm/s [18], we have $l \sim 5 \times 10^{-6}$ cm, which is two orders of magnitude larger than the lattice parameter $h \sim 5 \times 10^{-8}$ cm. There-

1063-7834/01/4311-2051$21.00 © 2001 MAIK "Nauka/Interperiodica"

fore, we can ignore acoustic spatial dispersion (which is significant for shorter pulses [9, 10, 12, 13, 17]). For the interaction between acoustic pulses and the spin subsystem (Kramers doublets) to be significant, the initial difference in population of the levels must be noticeable. This imposes a restriction on the temperature of the paramagnetic crystal [13] $T < \hbar\omega_0/k_B$, where $\hbar$ is Planck's constant and k_B is the Boltzmann constant. At $\omega_0 \sim 10^{10}$ s^{-1}, we have $T < 0.1$ K, which corresponds to ultralow temperatures.

Let an acoustic pulse travel in a cubic crystal along an external magnetic field **B** applied parallel to one of the fourfold axes (z axis). The Hamiltonian of the spin subsystem interacting with lattice deformations can be written as [12, 18]

$$\hat{H} = \hat{H}_s + \hat{H}_{\text{int}}, \tag{2}$$

where

$$\hat{H}_s = \sum_j \hbar\omega_0 \hat{S}_z^j,$$

$$\hat{H}_{\text{int}} = \sum_j \frac{\hbar\omega_0}{g}\{F_{11}\mathscr{E}_{zz}\hat{S}_z^j + F_{44}(\mathscr{E}_{xz}\hat{S}_x^j + \mathscr{E}_{yz}\hat{S}_y^j)\}. \tag{3}$$

Here, $\hat{S}_\alpha^j \equiv \hat{S}_\alpha(\mathbf{r}_j)$ are spin operators of the jth paramagnetic ion, which are proportional to the Pauli matrices $\hat{\sigma}_\alpha$; $\hat{S}_\alpha^j = \hat{\sigma}_\alpha/2$ ($\alpha = x, y, z$); $\mathbf{r}_j$ is the position vector of the jth paramagnetic ion; $\mathscr{E}_{ij} = (\partial U_i/\partial x_j + \partial U_j/\partial x_i)/2$ are the components of the strain tensor (in our case, $\mathscr{E}_{zz} = \partial U_z/\partial z$, $\mathscr{E}_{xz} = 0.5\partial U_x/\partial z$, $\mathscr{E}_{yz} = 0.5\partial U_y/\partial z$); U_i ($i = x, y, z$) are the components of the displacement vector **U** of lattice sites; and F_{11} and F_{44} are the longitudinal and transverse spin–phonon coupling coefficients, respectively (in the Voigt notation [18]: $xx \longrightarrow 1$, $yy \longrightarrow 2$, $zz \longrightarrow 3$, $yz \longrightarrow 4$, $xz \longrightarrow 5$, $xy \longrightarrow 6$). The Zeeman splitting frequency ω_0 is expressed through the Landé g factor, the Bohr magneton μ_B, and the external magnetic field as $\omega_0 = g\mu_B B/\hbar$; the summation in Eq. (3) is carried out over all paramagnetic impurity ions in the crystal.

In the case of the spin $S = 1/2$ under study, spin–phonon interaction is due to modulation of the Landé g factors effected by the strain field of an acoustic pulse [10, 12, 18]. At $t \longrightarrow -t$, we have $S_\alpha^j \longrightarrow -S_\alpha^j$ ($\alpha = x, y, z$) and $\mathbf{B} \longrightarrow -\mathbf{B}$ ($\omega_0 \longrightarrow -\omega_0$); therefore, Hamiltonian (3) is invariant under time reversal. In Eq. (3), this invariance is due to the fact that the spin–phonon coupling coefficients are multiplied by $\sim\omega_0$.

In what follows, we employ a semiclassical approach in which the dynamics of the spin subsystem is described quantum-mechanically, while the strain is considered to be a classical field. Therefore, in addition to Eqs. (2) and (3), we should write the classical Hamiltonian of the acoustic field:

$$H_a = \frac{1}{2}\int\left\{\frac{p_x^2 + p_y^2 + p_z^2}{\rho} + \lambda_{11}\left(\frac{\partial U_z}{\partial z}\right)^2 + \lambda_{44}\left[\left(\frac{\partial U_x}{\partial z}\right)^2 + \left(\frac{\partial U_y}{\partial z}\right)^2\right]\right\}d^3\mathbf{r}, \tag{4}$$

where p_j ($j = x, y, z$) are the components of the momentum density of the lattice, ρ is the mean density of the crystal, and λ_{11} and λ_{44} are the elastic moduli of the second order; integration in Eq. (4) is performed over the entire volume of the crystal.

In the semiclassical approach [12, 17], the dynamic variables of the elastic field obey Hamilton's equations,

$$\frac{\partial \mathbf{U}}{\partial t} = \frac{\delta\tilde{H}}{\delta\mathbf{p}}, \quad \frac{\partial \mathbf{p}}{\partial t} = -\frac{\delta\tilde{H}}{\delta\mathbf{U}}, \tag{5}$$

where $\tilde{H} = H_a + \langle\hat{H}_{\text{int}}\rangle$ and $\langle\ldots\rangle$ denotes the quantum-mechanical average.

It is convenient to represent $\langle\hat{H}_{\text{int}}\rangle$ in Eq. (5) in the form

$$\langle\hat{H}_{\text{int}}\rangle = \int\frac{n\hbar\omega_0}{g}\{F_{11}\mathscr{E}_{zz}\langle\hat{S}_z(\mathbf{r})\rangle + F_{44}(\mathscr{E}_{xz}\langle\hat{S}_x(\mathbf{r})\rangle + \mathscr{E}_{yz}\langle\hat{S}_y(\mathbf{r})\rangle)\}d^3\mathbf{r}. \tag{6}$$

Here, $n = \sum_j \delta(\mathbf{r} - \mathbf{r}_j)$ is the concentration of paramagnetic impurity ions, $\delta(\mathbf{r} - \mathbf{r}_j)$ is the Dirac δ function, $\langle\hat{S}_\alpha(\mathbf{r})\rangle = \mathrm{Tr}(\hat{\rho}\hat{S}_\alpha)$, and $\hat{\rho}$ is the density operator of the spin subsystem, which obeys the quantum Liouville equation

$$i\hbar\frac{\partial\hat{\rho}}{\partial t} = [\hat{H}, \hat{\rho}]. \tag{7}$$

Using Eqs. (2)–(7), we find

$$\frac{\partial^2\Omega_\perp}{\partial t^2} - a_\perp^2\frac{\partial^2\Omega_\perp}{\partial z^2} = \frac{n\hbar\omega_0^2}{\rho g^2}F_{44}^2\frac{\partial^2 S_\perp}{\partial z^2}, \tag{8}$$

$$\frac{\partial^2\Omega_\parallel}{\partial t^2} - a_\parallel^2\frac{\partial^2\Omega_\parallel}{\partial z^2} = \frac{n\hbar\omega_0^2}{\rho g^2}F_{11}^2\frac{\partial^2 W}{\partial z^2}, \tag{9}$$

$$\frac{\partial S_\perp}{\partial t} = i(\omega_0 + \Omega_\parallel)S_\perp - i\Omega_\perp W, \tag{10a}$$

$$\frac{\partial W}{\partial t} = \mathrm{Im}(\Omega_\perp^* S_\perp), \tag{10b}$$

where $\Omega_\perp = (\omega_0 F_{44}/g)(\mathscr{E}_{xz} + i\mathscr{E}_{yz})$; $\Omega_\parallel = (\omega_0 F_{11}/g)\mathscr{E}_{zz}$; $a_\perp = \sqrt{\lambda_{44}/\rho}$ and $a_\parallel = \sqrt{\lambda_{11}/\rho}$ are the velocities of transverse and longitudinal sound, respectively; and the

dynamic variables $S_\perp$ and W are the transverse magnetic moment and the negative of the longitudinal magnetic moment (or the inverse population), respectively, which are expressed in terms of the density matrix elements as $S_\perp = \rho_{12}$ and $W = (\rho_{22} - \rho_{11})/2$ ($-1/2 \le W \le 1/2$).

As is obvious from Eq. (10), in the case of an acoustic pulse traveling along the direction of the external magnetic field, the transverse strain induces quantum transitions between the Kramers doublet components, while the longitudinal strain modulates the frequency of these transitions.

In what follows, we analyze the self-consistent set of wave and constitutive equations (7)–(10).

3. REDUCED WAVE EQUATIONS

It follows from Eq. (10a) that $S_\perp \sim \Omega_\perp \tau_p$. Therefore, the ratio of the right-hand side of Eq. (8) to one of the two terms on the left-hand side is $\varepsilon \sim (n\hbar\omega_0 F_{44}^2/g^2\rho a^2)(\omega_0\tau_p)$. Putting $n \sim 10^{19}$ cm^{-3}, $\omega_0 \sim 10^{10}$ s^{-1}, $F_{44}/g \sim 10^2$ [18], $\rho \sim 5$ g/cm^3, and $a \sim 3 \times 10^5$ cm/s, we obtain $\varepsilon \sim 10^{-7}\omega_0\tau_p \ll 1$ [see also Eq. (1)]. A similar conclusion can also be arrived at for Eq. (9). Therefore, one can employ the single-propagation-direction approximation to Eqs. (8) and (9); that is, the pulse shape can be assumed to vary slowly in the comoving frame of reference [19]. This will be taken into account in what follows.

To solve Eqs. (10), we rewrite them in the matrix form:

$$\frac{\partial \mathbf{R}}{\partial t} = i\hat{A}\mathbf{R},$$

$$\mathbf{R} = \begin{pmatrix} S_\perp/\sqrt{2} \\ S_\perp^*/\sqrt{2} \\ W \end{pmatrix}, \tag{11}$$

$$\hat{A} = \begin{pmatrix} \omega_0 + \Omega_\parallel & 0 & -\Omega_\perp/\sqrt{2} \\ 0 & -(\omega_0 + \Omega_\parallel) & \Omega_\perp^*/\sqrt{2} \\ -\Omega_\perp^*/\sqrt{2} & \Omega_\perp/\sqrt{2} & 0 \end{pmatrix}. \tag{12}$$

It follows from Eqs. (10)–(12) that the square of the Bloch vector $\mathbf{R}^2 = |S_\perp|^2 + W^2$ is an integral of motion.

It can be seen from Eq. (10a) that, when Eq. (1) is true, one of the two following inequalities or both of them hold (since $|S_\perp|$ and W are finite):

$$|\Omega_\perp|/\omega_0 \gg 1, \quad \Omega_\parallel/\omega_0 \gg 1. \tag{13}$$

(We will consider all possible cases in the next section.) Therefore, one can solve Eqs. (10) using the method of successive approximations, with ω_0 being a small parameter. Furthermore, it follows from Eqs. (12) and (13) that Eq. (11) is a linear equation with large variable coefficients; hence, it can be approximately solved using the WKB method [20, 21]. In this paper, however, we will apply another method, which leads to the same final results but is more efficient than the WKB method [22].

It is easy to verify that the condition [23]

$$\int_{t_0}^{t} [\hat{A}(t), \hat{A}(t')]dt' = 0 \tag{14}$$

is not fulfilled and, therefore, a solution to Eq. (11) cannot be represented in the form of a matrix exponential acting on the initial vector $\mathbf{R}(t_0)$ [23]. However, inequality (1) allows one to consider the limiting case $t \longrightarrow t_0$. During the time $\Delta t = t - t_0 \longrightarrow 0$, the matrix $\hat{A}$ is changed only slightly, $\hat{A}(t) \approx \hat{A}(t')$ for $(t_0 \le t' \le t)$. Therefore, Eq. (14) is approximately valid and we can write

$$\mathbf{R}(t) = \hat{U}(t, t_0)\mathbf{R}(t_0), \tag{15}$$

where the evolution operator has the form [22]

$$\hat{U}(t, t_0) = \lim_{\substack{t \to t_0 \\ \|\hat{A}\| \to \infty}} \exp\left(i\int_{t_0}^{t} \hat{A}(t')dt'\right), \tag{16}$$

with $\|\hat{A}\|$ being the norm of the matrix $\hat{A}$.

If the eigenvalues of the matrix $\hat{\theta} \equiv \int_{t_0}^{t} \hat{A}(t')dt'$ are all different, the exponential in Eq. (16) can be calculated using the Sylvester identity [24]:

$$\exp(i\hat{\theta}) = \sum_j \prod_{k \ne j} \frac{\hat{\theta} - \lambda_k \hat{I}}{\lambda_j - \lambda_k} \exp(i\lambda_j), \tag{17}$$

where $\hat{I}$ is the unit matrix and $\{\lambda_k\}$ is the set of eigenvalues of the matrix $\hat{\theta}$, which are determined from the equation $\det(\hat{\theta} - \lambda\hat{I}) = 0$. In the limit as $\Delta t \longrightarrow 0$, we have $\hat{\theta} = \int_{t_0}^{t} \hat{A}dt' \approx \hat{A}\Delta t$, $\lambda \approx p\Delta t \approx \int_{t_0}^{t} p dt'$, and $\det(\hat{\theta} - \lambda\hat{I}) = (\Delta t)^3 \det(\hat{A} - p\hat{I}) = 0$. Therefore, if $\{p_j\}$ is the set of eigenvalues of the matrix $\hat{A}$, then in the limit as $\Delta t \longrightarrow 0$ and $\|\hat{A}\| \longrightarrow \infty$, the set $\{\lambda_j\} = \left\{\int_{t_0}^{t} p_j dt'\right\}$ forms the eigenvalue spectrum of the matrix $\hat{\theta} = \int_{t_0}^{t} \hat{A}dt'$.

It follows from the above discussion that, using Eq. (17), we can represent the evolution operator (16) in the form

$$\hat{U}(t, t_0) = \sum_j \exp\left(i\int_{t_0}^{t} p_j dt'\right)\prod_{k\neq j}\frac{\hat{A} - p_k\hat{I}}{p_j - p_k}, \qquad (18)$$

where summation is carried out over all eigenvalues of the matrix $\hat{A}$.

In our case, the matrix $\hat{A}$ is Hermitian, because its eigenvalues are real: $p_1 = 0$ and $p_2 = -p_3 = \sqrt{\Omega_\parallel^2 + |\Omega_\perp|^2}$ (we have neglected ω_0 in the zeroth approximation). Therefore, Eq. (18) takes the form

$$\hat{U}(t, t_0) = \hat{I} - 2\frac{\hat{A}^2}{\Omega^2}\sin^2\frac{\theta}{2} + i\frac{\hat{A}}{\Omega}\sin\theta, \qquad (19)$$

where

$$\Omega = \sqrt{\Omega_\parallel^2 + |\Omega_\perp|^2}, \quad \theta = \int_{-\infty}^{t}\Omega dt'. \qquad (20)$$

Here, we have formally put $t_0 = -\infty$, assuming that the fundamental change in R (due to $\Omega_\perp$ and $\Omega_\parallel$) occurs during a short time $\Delta t \sim \tau_p$ and, hence, $\Omega_\parallel$ and $\Omega_\perp$ vanish as $t_0 \longrightarrow -\infty$.

Taking into account that, at $t = -\infty$ (before the acoustical action), $W = W_\infty$ and $S_\perp = S_\perp^* = 0$ and using Eqs. (15) and (19), we obtain

$$S_\perp = -iW_\infty\frac{\Omega_\perp}{\Omega}\sin\theta + 2W_\infty\frac{\Omega_\parallel\Omega_\perp}{\Omega^2}\sin^2\frac{\theta}{2}, \qquad (21)$$

$$W = W_\infty\left(1 - 2\frac{|\Omega_\perp|^2}{\Omega^2}\sin^2\frac{\theta}{2}\right). \qquad (22)$$

Putting $\Omega_\parallel = 0$ in Eqs. (21) and (22), we arrive at the results obtained in [25] for the case of transverse electromagnetic pulses.

We represent $\Omega_\perp$ in the form

$$\Omega_\perp = F\exp(i\phi), \qquad (23)$$

where F is the real amplitude and ϕ is the phase which defines the rotation of polarization plane of the transverse pulse component. Then, we substitute Eq. (21) into Eq. (10a) and insert the result, as well as Eq. (22), into the right-hand sides of Eqs. (8) and (9). Then, inserting Eq. (23) and using the single-propagation-direction approximation, we arrive at a set of reduced equations for the dynamical parameters of the acoustic pulse:

$$\frac{\partial F}{\partial z} = \mu_\perp W_\infty(\omega_0 + \Omega_\parallel)\frac{F}{\Omega}\sin\theta, \qquad (24)$$

$$\frac{\partial\phi}{\partial z} = -\mu_\perp W_\infty\cos\theta, \qquad (25)$$

$$\frac{\partial\Omega_\parallel}{\partial z} - \alpha\frac{\partial\Omega_\parallel}{\partial\tau} = -2\mu_\parallel W_\infty\frac{\partial}{\partial\tau}\left(\frac{|\Omega_\perp|^2}{\Omega^2}\sin^2\frac{\theta}{2}\right), \qquad (26)$$

where $\tau = t - z/a_\perp$, $\mu_\perp = n\hbar\omega_0^2F_{44}^2/(2g^2\rho a_\perp^3)$, $\mu_\parallel = n\hbar\omega_0^2F_{11}^2/(2g^2\rho a_\parallel^2 a_\perp)$, and $\alpha = (a_\perp/2)(1/a_\perp^2 - 1/a_\parallel^2)$. When deriving Eq. (23), it was taken into account that $\omega_0\Omega_\parallel/\Omega^2 \ll 1$ because of Eq. (13). In the absence of the longitudinal component ($\Omega_\parallel = \mu_\parallel = 0$), we have $\Omega = F = \partial\theta/\partial\tau$ [see Eq. (20)]; substituting this into Eq. (24), we obtain the sine–Gordon equation for the transverse component of the pulse:

$$\frac{\partial^2\theta}{\partial z\partial\tau} = \mu_\perp\omega_0 W_\infty\sin\theta.$$

The corresponding solitons with a rotating polarization plane were considered in [25, 26]. Here, we investigate a more general set of equations, (23) and (24) [or Eqs. (24)–(26)], which also take into account the dynamics of the longitudinal component of the acoustic video pulse.

4. TRANSVERSE–LONGITUDINAL SOLITONS

We seek solutions $\Omega_\parallel$ and F in the form of stationary traveling pulses $\Omega_\parallel(\xi)$ and $F(\xi)$, where $\xi = t - z/v = \tau - (1/v - 1/a_\perp)z$ and v has the meaning of the velocity of the pulse. Assuming that $\Omega_\parallel$, F, and all their derivatives vanish at $\xi \longrightarrow \pm\infty$, we obtain from Eqs. (24) and (26)

$$\dot{F} = \beta_\perp(\omega_0 + \Omega_\parallel)(F/\Omega)\sin\theta, \qquad (27a)$$

$$\Omega_\parallel = -\beta_\parallel(F/\Omega)^2\sin^2(\theta/2), \qquad (27b)$$

where $\beta_\perp = -\mu_\perp W_\infty(1/v - 1/a_\perp)^{-1}$, $\beta_\parallel = -2\mu_\parallel W_\infty(1/v - 1/a_\perp + \alpha)^{-1}$, and the superscript dot on F indicates the derivative with respect to ξ.

Let us first consider the case where only the first condition in Eqs. (13) is met, i.e., $\omega_0^2, \Omega_\parallel^2 \ll |\Omega_\perp|^2 = F^2$. This is not to say that $\Omega_\parallel$ can be neglected altogether, because $\Omega_\parallel$ and ω_0 can be comparable in magnitude and $\Omega_\parallel$ can markedly affect the dynamics of propagation of the acoustic video pulse [see Eqs. (24), (27a)]. In view of the inequality $|\Omega_\perp| \gg \Omega_\parallel$, the solitons considered in this section can be called transverse–longitudinal video pulses. Under the assumptions made, we have $\Omega = \dot{\theta} \approx F$ and $\Omega_\parallel \approx -\beta_\parallel\sin^2(\theta/2)$ and Eq. (27a) takes the form

$$\ddot{\theta} = \sigma\sin\theta + \nu\sin 2\theta. \qquad (28)$$

Here, $\sigma = \beta_\perp(\omega_0 - \beta_\parallel/2)$ and $\nu = \beta_\perp\beta_\parallel/4$.

We assume that the spin subsystem was at thermodynamic equilibrium before the acoustical action; i.e.,

$W_\infty = -|W_\infty| = -0.5\tanh(\hbar\omega_0/2k_BT)$. In this case, Eq. (28) [see Eqs. (25), (27b)] has two possible solutions in the form of solitary traveling pulses. We consider these solutions separately.

(1) $\sigma > 0$ and $\beta_\perp > 0$. In this case,

$$F = \dot{\theta} = \frac{\Omega_{\perp m}\cosh\xi}{1+\lambda^2\sinh^2\xi}, \tag{29a}$$

$$\Omega_\parallel = -\frac{\Omega_{\parallel m}}{1+\lambda^2\sinh^2\xi}, \tag{29b}$$

$$\phi = \kappa z + \frac{2\kappa v\tau_p}{\sqrt{1-\lambda^2}}\operatorname{arctanh}\left(\frac{\tanh\xi}{\sqrt{1-\lambda^2}}\right). \tag{30}$$

Here, $\xi = (t - z/v)\tau_p$, $\lambda = \Omega_{\perp m}\tau_p/2 < 1$ [see Eq. (29b)], and $\kappa = -\mu_\perp W_\infty = \mu_\perp|W_\infty|$; the velocity v and the characteristic amplitudes of the transverse ($\Omega_{\perp m}$) and longitudinal ($\Omega_{\parallel m}$) components are expressed in terms of the pulse duration τ_p as

$$\frac{1}{v} = \frac{1}{a_\perp} + \omega_0\mu_\perp|W_\infty|\tau_p^2, \tag{31}$$

$$\Omega_{\perp m} = 2\sqrt{\sigma} = \frac{2}{\tau_p}\sqrt{1-\frac{2\mu_\parallel|W_\infty|/\omega_0}{\alpha+\omega_0\mu_\perp|W_\infty|\tau_p^2}},$$
$$\Omega_{\parallel m} = \beta_\parallel = \frac{2\mu_\parallel|W_\infty|}{\alpha+\omega_0\mu_\perp|W_\infty|\tau_p^2}. \tag{32}$$

It can be seen from Eqs. (23) and (30) that the parameter κ characterizes the rotation angle (per unit length) of the polarization plane of the transverse pulse component. Under the condition defined by Eq. (1), this parameter does not depend on the pulse length (as is the case with an electromagnetic video pulse [22, 26]) but it is sensitive to changes in the initial inverse population $|W_\infty|$ and in the external magnetic field (see expressions for $\mu_\perp$ and W_∞). If we look along the direction of propagation of the video pulse (along **B** or the opposite direction), the polarization plane of the transverse component rotates counterclockwise because $\kappa > 0$ (Fig. 1). This component has a double-humped profile with a local minimum at the center, and it propagates in combination with a negative longitudinal component whose intensity has a minimum at the center. As can be seen from Eq. (29a), the entire area of the video pulse is $\theta_\infty \equiv \int_{-\infty}^{+\infty}\Omega dt' \approx \int_{-\infty}^{+\infty}F dt' = 2\pi$.

(2) $\sigma < 0$ and $\beta_\perp > 0$. Under these conditions, we have

$$F = \dot{\theta} = -\frac{\tilde{\Omega}_{\perp m}\sinh\xi}{1+\tilde{\lambda}^2\cosh^2\xi},\ \Omega_\parallel = -\frac{\tilde{\Omega}_{\parallel m}(1+\tilde{\lambda}^2)}{1+\tilde{\lambda}^2\cosh^2\xi}, \tag{33}$$

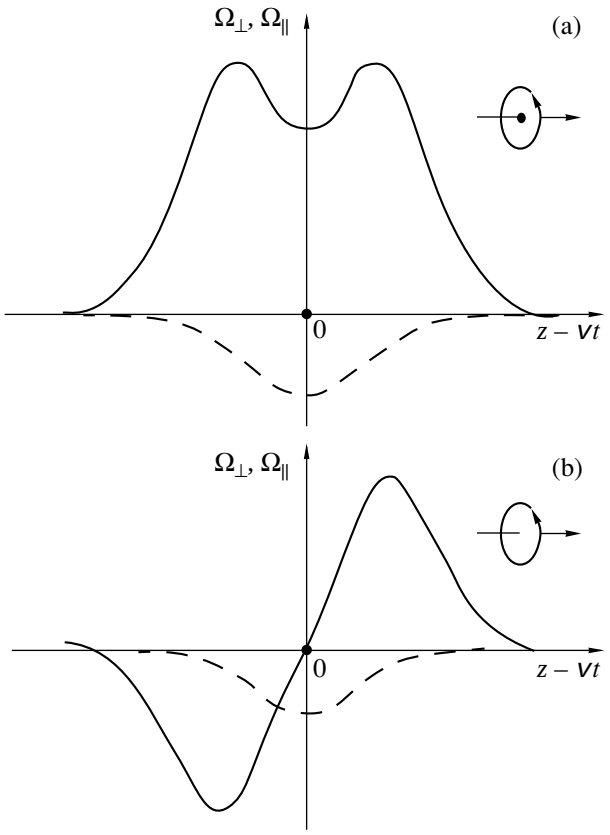

Fig. 1. Profiles of two-component subsonic ($v < a_\perp, a_\parallel$) acoustic solitons propagating in a thermodynamically equilibrium medium described (a) by Eqs. (23), (30), and (31) and (b) by Eqs. (23), (38), and (39). The solid and dashed curves correspond to the profiles of the transverse and longitudinal components, respectively. The directions of the propagation of the pulse and of the polarization plane rotation of the transverse component are shown on the right.

$$\phi = \kappa z + \frac{2\kappa v\tau_p}{\sqrt{1+\tilde{\lambda}^2}}\operatorname{arctanh}\left(\frac{\tanh\xi}{\sqrt{1+\tilde{\lambda}^2}}\right), \tag{34}$$

where $\tilde{\lambda} = \tilde{\Omega}_{\perp m}\tau_p/2$, $\tilde{\Omega}_{\parallel m} = \Omega_{\parallel m}/(1+\tilde{\lambda}^2)$, and

$$\tilde{\Omega}_{\perp m} = 2\sqrt{|\sigma|} = \frac{2}{\tau_p}\sqrt{\frac{2\mu_\parallel|W_\infty|/\omega_0}{\alpha+\omega_0\mu_\perp|W_\infty|\tau_p^2}-1}, \tag{35}$$

while the dependence of the velocity of the pulse on its length is given by Eq. (31).

The rotation angle (per unit length) of the polarization plane of the transverse component κ given by Eq. (33) is similar to that for the soliton described by Eq. (29a). They differ only in the shape of the profile of the corresponding transverse components. In the case of the soliton described by Eq. (29a), the transverse component has a double-humped profile (as indicated above), while in the case of Eq. (33), this component has the shape of a bipolar pulse (Fig. 1b). In the latter

case, the area of the transverse component is equal to zero.

From Eqs. (32) and (35), it follows that there are limitations on the length of the solitons described by Eqs. (29) and (33), respectively:

$$(\omega_0\tau_p)^2 \gg 2\left(\frac{F_{11}a_\perp}{F_{44}a_\parallel}\right)^2(1-q), \tag{36}$$

where $q = g^2\rho(a_\parallel^2 - a_\perp^2)/(2n|W_\infty|\hbar\omega_0 F_{11}^2)$. It should be remembered that the condition in Eq. (1) is also assumed to be fulfilled. Putting $g = 2$, $\rho = 2$ g/cm^3, $a_\parallel^2 - a_\perp^2 \sim 10^{11}$ cm^2/s^2, $n \sim 10^{19}$ cm^{-3}, $\omega_0 \sim 10^{10}$ s^{-1}, $F_{11} \sim 10^2$, and $|W_\infty| = 1/2$ (for $k_BT \ll \hbar\omega_0$), we obtain $q \sim 10^6$. Therefore, if the velocities of longitudinal and transverse sound are different, only solitons described by Eqs. (29) can arise in actual crystals. A MgO host crystal with Co^{2+} impurity ions is an example of this. In the case where the velocities of longitudinal and transverse sound are exactly equal ($a_\parallel = a_\perp$), we have $q = 0$. At the same time, typically, $F_{11} > F_{44}$ [18, 27]; therefore, the inequalities in Eqs. (1) and (36) can be simultaneously true only for solitons described by Eq. (33). The condition $a_\parallel = a_\perp$ is more closely fulfilled in ionic crystals of alkali halides with central interatomic forces [28]. For example, solitons with a rotating polarization plane of the transverse component described by Eq. (33) can be observed in NaBr crystals with Co^{2+} impurity ions. As seen from the estimates made above, the condition $a_\parallel = a_\perp$ must be fulfilled with a relative accuracy of $\sim 10^{-6}$, which is a challenging task. If the difference between the velocities $a_\parallel$ and $a_\perp$ is larger, the formation of solitons of the Eq. (33) type is open to question but solitons described by Eqs. (29) can be observed.

For the material parameters indicated above, it follows from Eq. (32) that $(\Omega_{\parallel m}/\Omega_{\perp m})^2 \ll 1$ if $\omega_0\tau_p \ll q \sim 10^6$. This limitation is much less severe than Eq. (1) and can be easily met. At the same time, for solitons described by Eq. (33) at $\alpha = 0$, we have $\tilde{\Omega}_{\parallel m}/\tilde{\Omega}_{\perp m} \sim (\omega_0\tau_p)^2\sqrt{\mu_\perp/\mu_\parallel}$. Therefore, the condition $\tilde{\Omega}_{\parallel m}/\tilde{\Omega}_{\perp m} \ll 1$ is fulfilled if $(\omega_0\tau_p)^2 \ll \sqrt{\mu_\parallel/\mu_\perp} = F_{11}/F_{44}$. This condition is not inconsistent with Eq. (1), because usually $F_{11} > F_{44}$, as indicated above.

From Eqs. (22), (23), (29), and (33), it follows that, in the case of solitons of both types, the population inversion is not full due to the presence of the longitudinal component.

Let us estimate the dynamical parameters of the solitonlike pulses considered above. According to Eq. (13), $|\Omega_\perp|/\omega_0 \sim F_{44}|\mathscr{E}_\perp| \gg 1$. Putting $F_{44} \sim 10^2$, we obtain $|\mathscr{E}_\perp| \sim 0.1$. For $\omega_0 \sim 10^{10}$ s^{-1}, the pulse duration is $\tau_p \sim |\Omega_\perp|^{-1} \sim (\omega_0 F_{44}|\mathscr{E}_\perp|)^{-1} \sim 10$ ps. At $\rho \simeq 2$ g/cm^3 and $a_\perp \sim 3 \times 10^5$ cm/s, we find that the intensity of the acoustic soliton is $I \sim \rho a_\perp^3|\mathscr{E}_\perp|^2 \sim 10^7$ W/cm^2 and the pressure within the soliton is $P \sim \rho a_\perp^2|\mathscr{E}_\perp| \sim 10$ kbar. Acoustic pulses with such parameters can be realized experimentally [9].

5. RATIONAL SOLITONS

Now, we consider the case where both inequalities in Eq. (13) are true; therefore, the components $\Omega_\parallel$ and $|\Omega_\perp|$ (or F) of the acoustic pulse are comparable in value. In accordance with Eq. (13), we neglect ω_0 in comparison with $\Omega_\parallel$ in Eq. (27a). Putting $F = A\Omega_\parallel$, where A is a constant to be determined, we have $\dot{\theta} = \Omega = \sqrt{1+A^2}\Omega_\parallel \operatorname{sgn}\Omega_\parallel = -\sqrt{1+A^2}\Omega_\parallel \operatorname{sgn}\beta_\parallel$ [see Eq. (27b)]. Substituting these expressions into Eqs. (27) and differentiating Eq. (27b), one can find that the compatibility condition is $A^2 = (\mu_\perp/\mu_\parallel)(a_\parallel - v)/(v - a_\perp)$. Here, it has been assumed that the difference between $a_\perp$ and $a_\parallel$ is small, i.e., $(a_\parallel - a_\perp)/a_\parallel \ll 1$, and, as is usually the case in a solid, $a_\parallel \geq a_\perp$ ($\alpha \geq 0$) [28]. Further, we integrate Eq. (27b) and obtain

$$\Omega_\parallel = -\frac{\Omega_{\parallel m}\operatorname{sgn}\beta_\parallel}{1+\xi^2}, \quad F = \frac{\Omega_{\perp m}}{1+\xi^2}, \tag{37}$$

$$\phi = \kappa z + 2\kappa v\tau_p \arctan\xi, \tag{38}$$

where $\Omega_{\parallel m} = 2/(\tau_p\sqrt{1+A^2})$ and $\Omega_{\perp m} = 2A/(\tau_p\sqrt{1+A^2})$.

The relation between the pulse duration τ_p and the velocity of the soliton described by Eq. (37) is given by

$$(v - a_\perp)^2 + (\mu_\perp/\mu_\parallel)(a_\parallel - v)(v - a_\perp) = (\mu_\perp W_\infty a_\perp a_\parallel \tau_p)^2. \tag{39}$$

From Eqs. (38) and (23), it follows that the polarization plane of the transverse component of the soliton described by Eq. (37) rotates counterclockwise (if we look along the propagation direction of the pulse) in a thermodynamically equilibrium medium ($W_\infty < 0$) and rotates clockwise in a nonequilibrium medium ($W_\infty > 0$) (Fig. 2).

A two-component video pulse from Eq. (37) falls off according to a power law rather than exponentially, in contrast to solitons of Eqs. (29) and (33). Therefore, it can be referred to as a rational soliton [29]. From the expression for A^2, it is seen that the velocity of the rational soliton lies within the range between $a_\perp$ and $a_\parallel$ (regardless of the sign of W_∞), while for the velocity of solitons considered in the preceding section, we have $v < a_\perp$ for $W_\infty < 0$.

The approximation $|\Omega_\parallel| \gg \omega_0$ corresponds to the case where the dynamic transition frequency $\omega_d \equiv \omega_0 + \Omega_\parallel$ [see Eq. (10a)] in the region of the video pulse differs significantly from ω_0. In a thermodynamically

equilibrium medium ($W_\infty < 0$, $\beta_\parallel > 0$), we have $\Omega_\parallel < 0$, as seen from Eq. (37). Therefore, $\omega_d < 0$, which corresponds to dynamic population inversion of the quantum levels: the ground level becomes an excited one, and vice versa. A similar effect takes place in the case of electromagnetic video pulses propagating in isotropic para- and ferromagnets [30]: the population is inverted in the medium which was initially at equilibrium. It is well known that in a nonequilibrium medium with an inverse population, the velocity of solitons is higher than that of the corresponding linear waves that induce quantum transitions in this medium [31]. In our case, the transitions are caused by the transverse component of the pulse; hence, $v > a_\perp$.

If a medium initially possesses an inverse population ($W_\infty > 0$, $\beta_\parallel < 0$), then $\Omega_\parallel > 0$ [see Eq. (37)]. In this case, $\omega_d > 0$ and the dynamic population inversion of the quantum levels does not occur. Therefore, in the presence of the longitudinal component of an acoustic video pulse, the population remains inverted and $v > a_\perp$ as before.

In the approximation $|\Omega_\parallel| \gg \omega_0$ discussed here, we have $\omega_d \approx \Omega_\parallel$; that is, the dynamic transition frequency virtually does not depend on the frequency ω_0 for the initial Zeeman splitting but is instead determined fundamentally by the longitudinal component of the acoustic video pulse ($\omega_d \approx -|\Omega_\parallel|$ in the medium that was initially at equilibrium and $\omega_d \approx |\Omega_\parallel|$ in the medium that initially possessed an inverse population). For this reason, the velocity v is independent of the sign of W_∞ [see Eq. (39)]. On the other hand, the presence of a magnetic field is a necessary condition. First, there is no spin–phonon interaction in the absence of **B** in the case of $S = 1/2$ (see Section 3), and, second, the initial inverse population W_∞ becomes zero at $\mathbf{B} = 0$ ($\omega_0 = 0$) with the consequence that the spin–phonon coupling responsible for the soliton formation also vanishes [see Eqs. (8), (9), (23), (24)].

It follows from Eqs. (20) and (37) that the entire area of the longitudinal–transverse rational soliton is $\theta_\infty = \int_{-\infty}^{+\infty} \Omega dt' = 2\pi$. Figure 3 shows the dependence of the duration of the rational soliton on its velocity as calculated from Eq. (39). It can be seen that the pulse duration τ_p increases monotonically with velocity v in the case of $\eta \equiv \mu_\perp/\mu_\parallel = (F_{44}a_\parallel/F_{11}a_\perp)^2 < 2$. If $\eta > 2$, τ_p has a maximum in the range between $a_\perp$ and $a_\parallel$. In both cases, $\tau_p \longrightarrow 0$ as $v \longrightarrow a_\perp$ and τ_p tends to a finite value as $v \longrightarrow a_\parallel \tau_p$.

The amplitude of the longitudinal component $\Omega_{\parallel m}$ decreases with increasing velocity for $\eta < 1$ and increases for $\eta > 1$ (Fig. 4).

The $\Omega_{\perp m}(v)$ dependence is more intricate. At $\eta < 9$, $\Omega_{\perp m}$ decreases monotonically with increasing velocity; at $\eta > 9$, the $\Omega_{\perp m}(v)$ dependence has two extrema at v_1 and v_2 between which $\Omega_{\perp m}$ increases; however, it decreases outside of this velocity interval with increasing velocity (Fig. 4). In addition, $\Omega_{\perp m} \longrightarrow \infty$ as $v \longrightarrow a_\perp$ and $\Omega_{\perp m} \longrightarrow 0$ as $v \longrightarrow a_\parallel$.

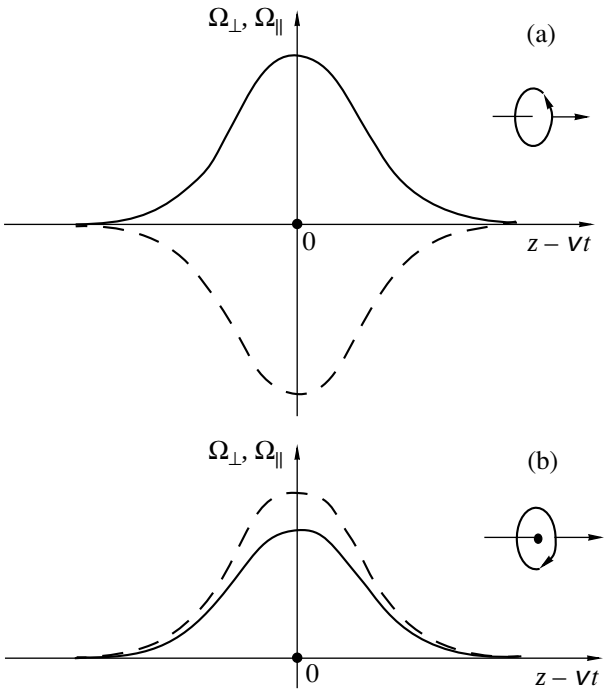

Fig. 2. Profiles of rational solitons ($a_\perp < v < a_\parallel$) propagating in (a) an equilibrium medium and (b) a medium with an inverse population. The notation is the same as in Fig. 1.

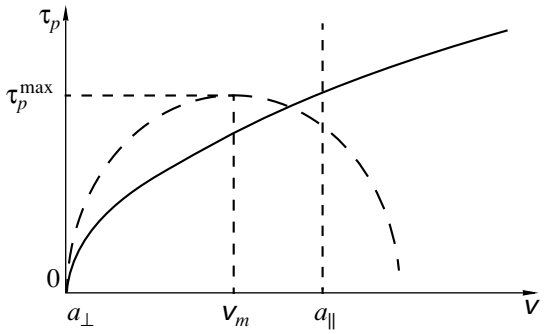

Fig. 3. Dependence of the rational-soliton length τ_p on its velocity v. The solid curve corresponds to the case of $\eta < 2$, where τ_p increases monotonically with v. The dashed curve describes the velocity dependence in the case of $\eta > 2$; here, τ_p has a maximum in the range between $a_\perp$ and $a_\parallel$ at $v_m = [\eta(a_\parallel + a_\perp) - 2a_\perp]/2(\eta - 1)$; $\tau_p^{\max} = (a_\parallel - a_\perp)/(2|W_\infty|\mu_\parallel a_\perp a_\parallel \sqrt{\eta - 1})$.

For a rational soliton to be formed, the amplitudes of both the transverse and longitudinal components of an

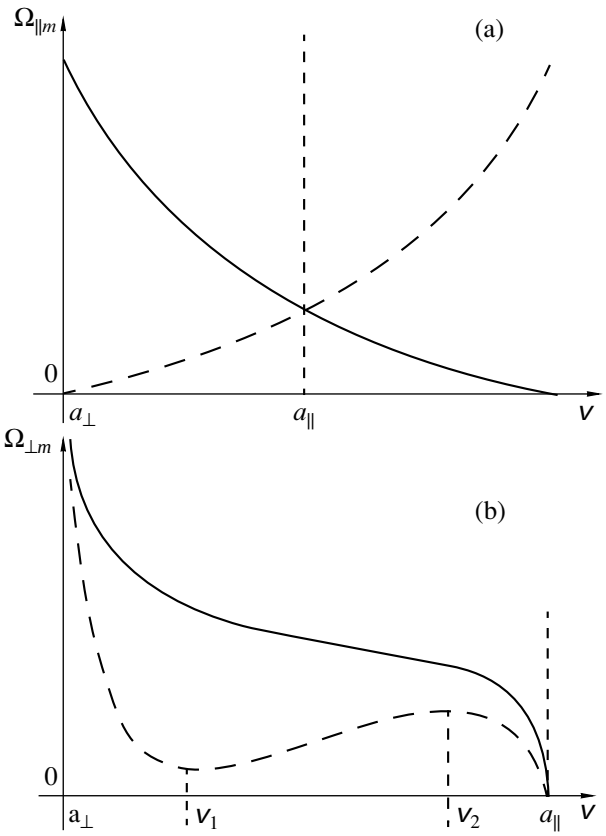

Fig. 4. (a) Dependence of the amplitude of the longitudinal component of the rational soliton $\Omega_{\|m}$ on the velocity v; the solid and dashed curves correspond to the cases of $\eta < 1$ and $\eta > 1$, respectively. (b) Dependence of the amplitude of the transverse component of the rational soliton $\Omega_{\perp m}$ on the velocity v; the solid and dashed curves correspond to the cases of $\eta < 9$ and $\eta > 9$, respectively; in the latter case, there are two extrema at v_1 and v_2 ($\Omega_{\perp m}$ increases with v in the range between them), $v_{1,2} = (a_\| + a_\perp)/2 + [(a_\| - a_\perp)/4][1 \pm \sqrt{(\eta - 9)/(\eta - 1)}]$.

acoustic pulse generated at the entrance of a medium must satisfy inequalities (13). Therefore, the intensity of rational solitons is several times larger than that of exponentially localized acoustic video pulses (for which only one of inequalities (13), namely, that for the transverse component, is satisfied) and is of the order of 10^8 W/cm^2.

6. CONCLUSIONS

Thus, we investigated [in the spectral-overlap approximation defined by Eq. (1)] quasi-solitonic propagation modes of two-component acoustic video pulses traveling along an external magnetic field in paramagnetic crystals. It was found that in order to avoid the effects of acoustic spatial dispersion and of nonlocality of spin–phonon interaction on the formation of soliton-like pulses, one should use ultralow temperatures ($T \simeq 0.1$ K) and magnetic fields in which the Zeeman splitting is $\omega_0 \sim 10^{10}$ s^{-1}. An increase in temperature as large as a few kelvins should be accompanied by an increase in magnetic-field strength by an order of magnitude, because the initial inverse population of the spin subsystem decreases markedly, which leads to a decrease in the strength of spin–phonon interaction. On the other hand, if B (or ω_0) is increased, the video-pulse length should be taken to be shorter (down to 1 ps) in order to satisfy inequality (1). For such pulse lengths, one should take spatial dispersion into account.

It is well known that dynamic coupling with crystal lattice vibrations is strongest when the effective spin of paramagnetic ions is equal to $S = 1$ [18]. Mathematically, study of the propagation of acoustic video pulses in a system of $S = 1$ spins is more intricate than that performed in this paper for the case of $S = 1/2$ spins; nevertheless, this study is of great practical importance.

ACKNOWLEDGMENTS

This study was supported by the Russian Foundation for Basic Research, project no. 00-02-17436a.

REFERENCES

1. D. H. Auston, K. P. Cheung, I. A. Valdmanis, and D. A. Kleinmann, Phys. Rev. Lett. **53**, 1555 (1984).
2. P. C. Becker, H. L. Fragnito, J. Y. Bigot, *et al.*, Phys. Rev. Lett. **63**, 505 (1989).
3. J. T. Darrow, B. B. Hu, X. C. Chang, and D. H. Auston, Opt. Lett. **15**, 323 (1990).
4. A. I. Maĭmistov, Kvantovaya Élektron. (Moscow) **30**, 287 (2000).
5. A. Yu. Parkhomenko and S. V. Sazonov, Pis'ma Zh. Éksp. Teor. Fiz. **67**, 887 (1998) [JETP Lett. **67**, 934 (1998)].
6. A. Yu. Parkhomenko and S. V. Sazonov, Zh. Éksp. Teor. Fiz. **114**, 1595 (1998) [JETP **87**, 864 (1998)].
7. A. C. Tam, Appl. Phys. Lett. **45**, 510 (1984).
8. V. É. Gusev and A. A. Karabutov, *Laser Optical Aacoustics* (Nauka, Moscow, 1991).
9. S. A. Akhmanov and V. É. Gusev, Usp. Fiz. Nauk **162** (3), 3 (1992) [Sov. Phys. Usp. **35**, 153 (1992)].
10. S. V. Sazonov, J. Phys.: Condens. Matter **4**, 6485 (1992).
11. S. V. Sazonov and L. S. Yakupova, J. Phys.: Condens. Matter **4**, 6479 (1992).
12. S. V. Sazonov, J. Phys.: Condens. Matter **6**, 6295 (1994).
13. S. V. Sazonov, Izv. Vyssh. Uchebn. Zaved., Fiz. **36** (7), 94 (1993).
14. V. Yu. Man'kov and S. V. Sazonov, Fiz. Tverd. Tela (St. Petersburg) **41**, 623 (1999) [Phys. Solid State **41**, 560 (1999)].
15. E. B. Tucker, Phys. Rev. **143**, 264 (1966).
16. É. M. Belenov and A. V. Nazarkin, Pis'ma Zh. Éksp. Teor. Fiz. **51**, 252 (1990) [JETP Lett. **51**, 288 (1990)].
17. S. V. Sazonov, Zh. Éksp. Teor. Fiz. **118**, 20 (2000) [JETP **91**, 16 (2000)].

18. J. W. Tucker and V. W. Rampton, *Microwave Ultrasonics in Solid State Physics* (North-Holland, Amsterdam, 1972; Mir, Moscow, 1975).
19. B. M. Vinogradova, O. V. Rudenko, and A. P. Sukhorukov, *Theory of Waves* (Nauka, Moscow, 1990).
20. N. N. Moiseev, *Asymptotic Methods of Nonlinear Mechanics* (Nauka, Moscow, 1981).
21. A. H. Nayfeh, *Introduction to Perturbation Techniques* (Wiley, New York, 1981; Mir, Moscow, 1984).
22. A. Yu. Parkhomenko and S. V. Sazonov, Kvantovaya Élektron. (Moscow) **27**, 139 (1999).
23. I. A. Lappo-Danilevskiĭ, *Application of Matrix Functions to the Theory of Linear Systems of Ordinary Differential Equations* (Gostekhizdat, Moscow, 1957).
24. F. R. Gantmacher, *The Theory of Matrices* (Nauka, Moscow, 1966, 2nd ed.; Chelsea, New York, 1959).
25. S. V. Sazonov and E. V. Trifonov, J. Phys. B **27**, L7 (1994).
26. S. V. Sazonov, Zh. Éksp. Teor. Fiz. **107**, 20 (1995) [JETP **80**, 10 (1995)].
27. V. A. Golenishchev-Kutuzov, V. V. Samartsev, N. K. Solovarov, and B. M. Khabibulin, *Magnetic Quantum Acoustics* (Nauka, Moscow, 1997).
28. C. Kittel, *Introduction to Solid State Physics* (Wiley, New York, 1956; Fizmatlit, Moscow, 1963).
29. M. J. Ablowitz and H. Segur, *Solitons and the Inverse Scattering Transform* (SIAM, Philadelphia, 1981; Mir, Moscow, 1987).
30. S. V. Sazonov and E. V. Trifonov, Zh. Éksp. Teor. Fiz. **103**, 1527 (1993) [JETP **76**, 744 (1993)].
31. A. N. Oraevskiĭ, Usp. Fiz. Nauk **168**, 1311 (1998) [Phys. Usp. **41**, 1199 (1998)].

Translated by Yu. Epifanov

Physics of the Solid State, Vol. 43, No. 11, 2001, pp. 2060–2062. Translated from Fizika Tverdogo Tela, Vol. 43, No. 11, 2001, pp. 1977–1979.
Original Russian Text Copyright © 2001 by Krieger, Semenov, Chekhova.

SEMICONDUCTORS AND DIELECTRICS

Investigation of the Mobility of Paraffin Molecules in Channel Urea Clathrates by Nuclear Magnetic Resonance Relaxation Spectroscopy

Ju. H. Krieger, A. R. Semenov, and G. N. Chekhova

Institute of Inorganic Chemistry, Siberian Division, Russian Academy of Sciences, pr. Akademika Lavrent'eva 3, Novosibirsk, 630090 Russia

e-mail: krieger@che.nsk.su

Received March 26, 2001

Abstract—The temperature dependence of the proton spin-lattice relaxation time (T_1) is investigated for channel urea clathrates with paraffin molecules. The results obtained are interpreted within the reorientational model of paraffin molecules and their fragments in clathrate channels. The specific features of the dynamics of normal paraffins in urea clathrates are associated with incommensurate regions in the structure of these compounds. *© 2001 MAIK "Nauka/Interperiodica".*

1. INTRODUCTION

Intercalation compounds belong to an interesting class of solids with a high mobility of guest molecules and ions. The crystal structure of these compounds involves cavities, channels, and layers occupied by molecules or ions. As a rule, the guest molecules and ions possess a rather high mobility. Another important property inherent in intercalation compounds is the occurrence of incommensurate regions in their structure over a wide range of temperatures. This feature is associated with the differences in the host lattice spacing along the channel axis and the mean distance between intercalated guest molecules or ions [1–3] and clearly manifests itself in channel-type intercalation compounds [4]. In our recent works, we demonstrated that the incommensurate structure in intercalation compounds can be formed either through variations in the ion concentration [5, 6], or by properly choosing guest molecules whose length is not a multiple of the host lattice spacing. The latter variant can be easily accomplished in urea clathrates with normal paraffins of different lengths.

Urea clathrates with different organic molecules are representative of a wide class of intercalation compounds [7]. Parsonage and Pemberton [8] proved that urea clathrates crystallize in a hexagonal lattice with the space group $P6_12$. In these structures, the urea molecules are linked to one another through hydrogen bonds and form one-dimensional channels filled with guest molecules (Fig. 1). Figure 2 shows variations in the difference between the length of a guest molecule in a clathrate channel [9] and the nearest multiple of the host (urea) lattice spacing along the channel for different guest *n*-paraffins. The multiple ratios between the lattice parameters of the guest and host subsystems are observed in the urea clathrates with $N = 7$ and 16. For the other clathrates, the guest-to-host spacing ratio has a nonintegral value. Unfortunately, this essential feature was disregarded in earlier studies concerned with the mobility of paraffin molecules in urea clathrates [10, 11].

2. SAMPLE PREPARATION AND EXPERIMENTAL TECHNIQUE

In this work, we thoroughly investigated the mobility of different *n*-paraffin molecules in urea clathrates,

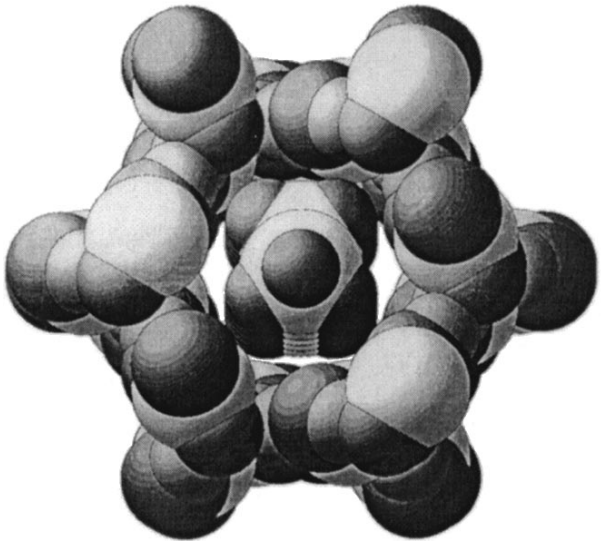

Fig. 1. A structure of channel urea clathrates with paraffin molecules.

1063-7834/01/4311-2060$21.00 © 2001 MAIK "Nauka/Interperiodica"

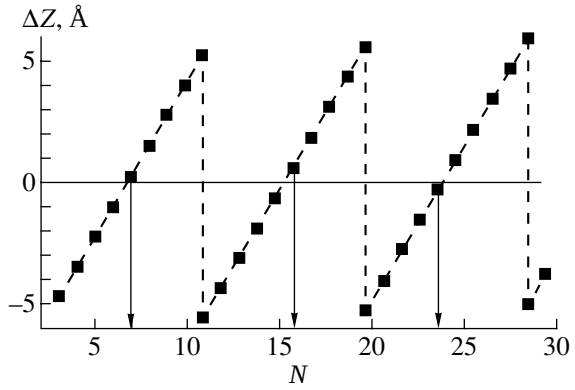

Fig. 2. Variations in the mismatch between the host lattice spacing and the length of the guest paraffin molecule C_NH_{2N+2} in urea clathrates.

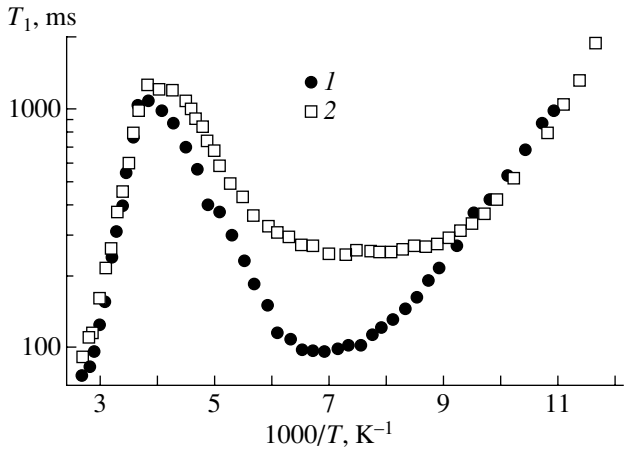

Fig. 3. Temperature dependences of the time of proton spin-lattice relaxation in urea clathrates with paraffin molecules: (*1*) $N = 16$ and (*2*) $N = 20$.

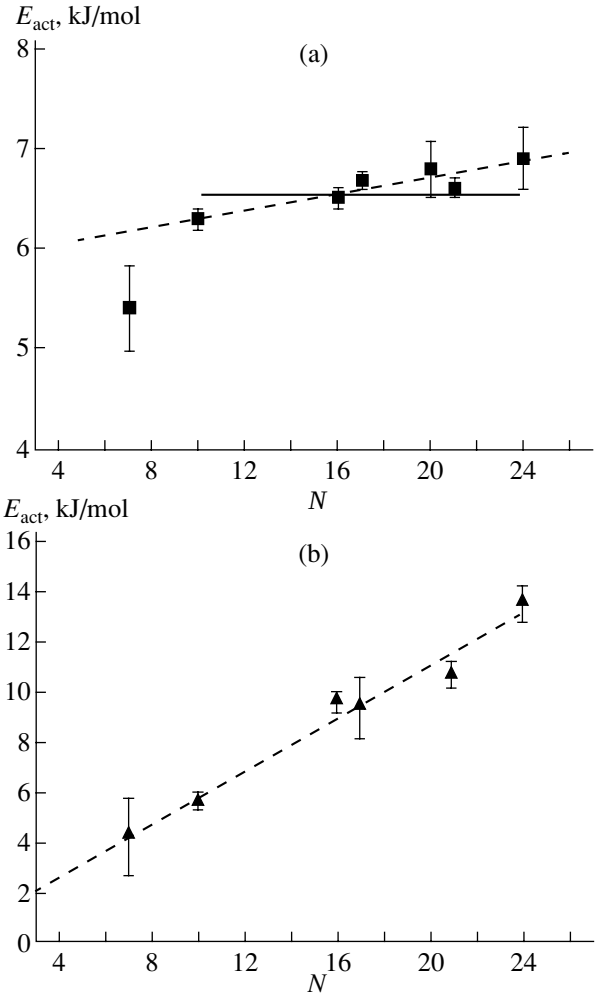

Fig. 4. Activation energies of the motion of normal paraffins in urea clathrates at (a) low and (b) high temperatures.

namely, the normal C_NH_{2N+2} paraffin molecules of different lengths (N = 7, 10, 16, 17, 20, 21, and 24) and *n*-paraffins with $N = 16$ and 20 in channels of urea-d_4. The samples with a nondeuterated host matrix were synthesized according to the procedure described in [12]. The urea used in the deuterated samples was prepared by fourfold or fivefold recrystallization from a D_2O solution. All the operations were performed in a dry chamber. The main properties of the samples were in good agreement with the data available in the literature [13].

The nuclear spin-lattice relaxation times T_1 were measured at a resonance frequency of 26 MHz. The use of a pulse sequence with highly efficient rectangular pulses [14] and signal integration make it possible to measure the nuclear spin-lattice relaxation time T_1 with an accuracy better than 5%. The heating and cooling of the samples were carried out in a gaseous nitrogen stream whose temperature was specified accurate to within 1–3 K. The temperature variations were performed as follows: the sample temperature was first decreased monotonically from room temperature, then increased monotonically to room temperature, maintained constant (at room temperature) within at least half a day, and again increased.

3. RESULTS AND DISCUSSION

Figure 3 displays typical temperature dependences of the proton spin-lattice relaxation time for urea clathrates with paraffin molecules at integral ($N = 16$) and obviously nonintegral ($N = 20$) ratios between the lattice parameters of the guest and host subsystems. According to Cope and Parsonage [15], all the studied compounds undergo phase transitions, which this is also confirmed by our results.

The dependence of the activation energies observed at temperatures above minima of the relaxation curves

on the number of carbon chain links N in the intercalated paraffin molecules is shown in Fig. 4a. A similar dependence of the activation energies at lower temperatures is depicted in Fig. 4b. Analysis of these dependences allowed us to conclude that the spin-lattice relaxation at temperatures above the minima of the relaxation curves can be associated with the rotation of paraffin molecules about their own axes of symmetry, which structurally coincide with the axis of a hexagonal channel of the urea clathrate. An increase in the length of the guest molecule should be accompanied by a proportional increase in the rotation barrier; this was observed in the experiment.

At the same time, the activation energy of the motion of normal paraffin molecules in urea clathrates at temperatures below the minima of the relaxation curves is virtually independent of the length of the intercalated guest molecule for all the studied paraffins (except, possibly, for the shortest paraffin molecule). This suggests that the low-temperature relaxation of all protons in urea clathrates is determined only by the rotation of terminal methyl groups of the guest molecules. This inference is in qualitative agreement with the behavior of the spin-lattice relaxation time $T_{1\min}$ at the minima of the temperature dependences: the $T_{1\min}$ time increases monotonically with an increase in the length of the paraffin molecule for all the studied systems almost without exception. However, the numerical values of T_1 at these minima are inconsistent with the experimental data, as was the case in our recent work [3]. In [3], we proposed different models of motion for guest molecules or ions in order to explain the above discrepancy. In our opinion, the spread in the activation energies of reorientation of the methyl groups due to the difference in their mutual arrangement with respect to the host matrix is the decisive factor that affects the behavior of the spin-lattice relaxation time T_1. We believe that this difference is quite evident in the case of a lattice mismatch between the guest and host subsystems. This assumption is confirmed by the data on T_1 at integral ($N = 16$) and obviously nonintegral ($N = 20$) ratios between the lattice spacings of the guest and host compounds (Fig. 3). The difference in the mutual arrangement of the methyl groups and, consequently, the spread in their activation energies lead not only to a change in the T_1 time at the minimum of the temperature dependence but also to a change in the shape of the temperature dependence of the spin-lattice relaxation time, which already defies description by the appropriate formulas with a unique correlation time. The data on T_1 for the deuterated samples also indicate an inhomogeneity of the system and a spread in the correlation times of reorientation of the methyl groups. The drastic decrease in relaxation time at high temperatures is associated with the well-understood 180° reorientation of the NH_2 groups involved in urea molecules. The activation parameters of this motion are identical for all the studied clathrates and agree well with the available data [3].

4. CONCLUSION

Thus, the above investigation has demonstrated that the nuclear spin-lattice relaxation in the studied compounds of urea clathrates with *n*-paraffins is caused by two main types of motion of intercalated guest molecules: (1) at high temperatures, it is the rotation of the guest molecule as a whole; and (2) at temperatures corresponding to the minimum relaxation time T_1 and below, it is the rotation of the methyl groups, which cannot be described by the formulas with the same correlation time. Unfortunately, more detailed information on the correlation time distribution and mutual arrangement of the methyl groups cannot be obtained from the currently available methods of nuclear magnetic resonance relaxation spectroscopy.

REFERENCES

1. Ju. H. Krieger, S. G. Kozlova, S. P. Gabuda, *et al.*, Fiz. Tverd. Tela (Leningrad) **27**, 3121 (1985) [Sov. Phys. Solid State **27**, 1875 (1985)].
2. M. D. Hollingsworth and K. D. M. Harris, in *Comprehensive Supramolecular Chemistry*, Ed. by J. L. Atwood, J. E. D. Davies, and D. D. MacNicol (Pergamon, New York, 1996), Vol. 6, p. 177.
3. A. M. Panich, Ju. H. Krieger, A. R. Semenov, *et al.*, J. Phys.: Condens. Matter **12**, 5765 (2000).
4. A. R. Semenov, G. N. Chekhova, Ju. H. Krieger, and Yu. A. Dyadin, Zh. Struct. Khim. **38** (5), 857 (1997).
5. Ju. H. Krieger, G. V. Sikorskaya, and V. E. Fedorov, Zh. Struct. Khim. **34** (6), 135 (1993).
6. Ju. H. Krieger, A. V. Mishchenko, A. R. Semenov, *et al.*, Fiz. Tverd. Tela (St. Petersburg) **42** (2), 251 (2000) [Phys. Solid State **42**, 257 (2000)].
7. L. C. Fetterly and Emirvil, in *Non-Stoichiometric Compounds*, Ed. by L. Mandelcorn (Academic, New York, 1964; Khimiya, Moscow, 1971).
8. N. Q. Parsonage and R. C. Pemberton, Trans. Faraday Soc. **63**, 311 (1967).
9. H.-U. Lenne, H.-C. Mez, and W. Schlenk, Ann. Chem. **732**, 70 (1970).
10. D. F. R. Gilson and C. A. McDowell, Mol. Phys. **4**, 125 (1961).
11. J. D. Bell and R. E. Richards, Trans. Faraday Soc. **65**, 2529 (1969).
12. G. N. Chekhova, Yu. A. Dyadin, and T. V. Rodionova, Izv. Sib. Otd. Akad. Nauk SSSR, Ser. Khim., No. 12, 78 (1979).
13. G. N. Chekhova and Yu. A. Dyadin, Izv. Sib. Otd. Akad. Nauk SSSR, Ser. Khim., No. 2, 66 (1986).
14. A. R. Semenov and Ju. H. Krieger, Inventor's Certificate No. 1 226 215.
15. A. F. G. Cope and N. G. Parsonage, J. Chem. Thermodyn. **1**, 99 (1969).

Translated by O. Borovik-Romanova

Physics of the Solid State, Vol. 43, No. 11, 2001, pp. 2063–2066. Translated from Fizika Tverdogo Tela, Vol. 43, No. 11, 2001, pp. 1980–1983.
Original Russian Text Copyright © 2001 by V. V. Sobolev, Smirnov, V. Val. Sobolev.

SEMICONDUCTORS AND DIELECTRICS

The Probabilities of Optical Transitions in an Al_2O_3 Crystal in the 9–30 eV Range

V. V. Sobolev, S. V. Smirnov, and V. Val. Sobolev

Udmurt State University, Krasnoarmeĭskaya ul. 71, Izhevsk, 426034 Russia

e-mail: sobolev@uni.udm.ru

Received November 15, 2000; in a final form, March 29, 2001

Abstract—The spectra of elementary oscillators of optical transitions in corundum in the region of 8–30 eV are determined for the first time. The parameters of the oscillators are calculated using experimental reflection spectra taken from four different papers. The main features of the spectra are established. © *2001 MAIK "Nauka/Interperiodica".*

1. INTRODUCTION

Aluminum oxide (corundum, α-Al_2O_3) is a radiation-resistant and chemically inert insulator with high optical transparency in a wide range of wavelengths [1]. Due to the complex nature of interatomic interactions, its structure is usually considered rhombohedral or trigonal for the sake of simplicity. Various experimental studies indicate that corundum has a very complicated electronic structure [1–8]. According to theoretical considerations, the valence and conduction bands consist of a very large number of closely situated bands [9–13]. Therefore, one should expect measured optical spectra of corundum to be composed of many transition bands, among them strongly overlapping ones which can even be hidden in an integral curve. At present, the available experimental and theoretical information on the electronic structure of corundum is rather ambiguous and incomplete.

The aim of the present work is to obtain new information regarding the structure of elementary transitions in corundum in the most important range of fundamental absorption (8–30 eV). Of special interest are the probabilities of transitions, which cannot be easily determined experimentally and are very tedious to calculate theoretically.

2. CALCULATION METHODS

To accomplish these tasks, first, we calculated sets of optical fundamental functions of corundum (ε_2, ε_1, etc.) using the integral Kramers–Kronig relations and analytical formulas. Next, the calculated spectra of the dielectric functions were decomposed into elementary constituent bands and their main parameters—the energy positions of peaks E_i, half-widths H_i, and their areas S_i proportional to the transition probabilities—were determined. The calculation methods used to determine the set of optical functions and to decompose the dielectric function spectrum into components have been described in detail and repeatedly applied [14–17].

3. RESULTS OF CALCULATIONS AND DISCUSSION

The reflection spectra $R(E)$ measured with polarization $\mathbf{E} \perp \mathbf{C}$ and $\mathbf{E} \parallel \mathbf{C}$ for α-Al_2O_3 were obtained in some works in the regions (2–110 eV) [7] and (5–30 eV) [6] and also in the regions (5–43 eV) [8] and (7–20 eV) [5] most likely for $\mathbf{E} \perp \mathbf{C}$. Using the $R(E)$ spectra from these four papers, we calculated four sets of fundamental optical functions of corundum, including $\varepsilon_2(E)$ and $\varepsilon_1(E)$. Next, the $\varepsilon_2(E)$ spectra were decomposed into components and the parameters E_i, H_i, and S_i and the band heights $\varepsilon_{2\max}$ were determined, which are represented in Fig. 1 by vertical lengths of four types, I [7], II [6], III [8], and IV [5], plotted from zero up (down) for the polarization of light $\mathbf{E} \perp \mathbf{C}$ ($\mathbf{E} \parallel \mathbf{C}$). These four sets of optical functions were then analyzed in detail taking into account the particular method of recording the reflection spectra used in [5–8]. As a result, some distinctive features of the spectra of the four groups were established.

The experimental reflection spectrum measured in [7], as well as other functions calculated on its basis, seems to be the most reliable. The $\varepsilon_2(E)$ spectrum calculated on the basis of $R(E)$ [7] in the region 8–30 eV was decomposed by us into 15 components for $\mathbf{E} \perp \mathbf{C}$ and $\mathbf{E} \parallel \mathbf{C}$, indicated by the first and second numbers in parentheses, respectively: *1* (9.22, 9.22), *2* (10.8, 10.9), *3* (12.0, 12.2), *4* (13.1, 12.8), *5* (14.0, 13.7), *6* (15.0, 14.8), *7* (16.0, 16.2), *8* (17.4, 17.7), *9* (18.7, 19.0), *10* (20.7, 20.8), *11* (22.9, –), *12* (–, 23.65), *13* (24.6, –), *14* (26.6, 26.65), and *15* (29.15, 29.25) eV; the component numbers are shown in Fig. 1. From the 15 components, only three (*11–13*) are fully polarized. The areas of the component bands determine their intensities and transition probabilities up to a constant factor. An anal-

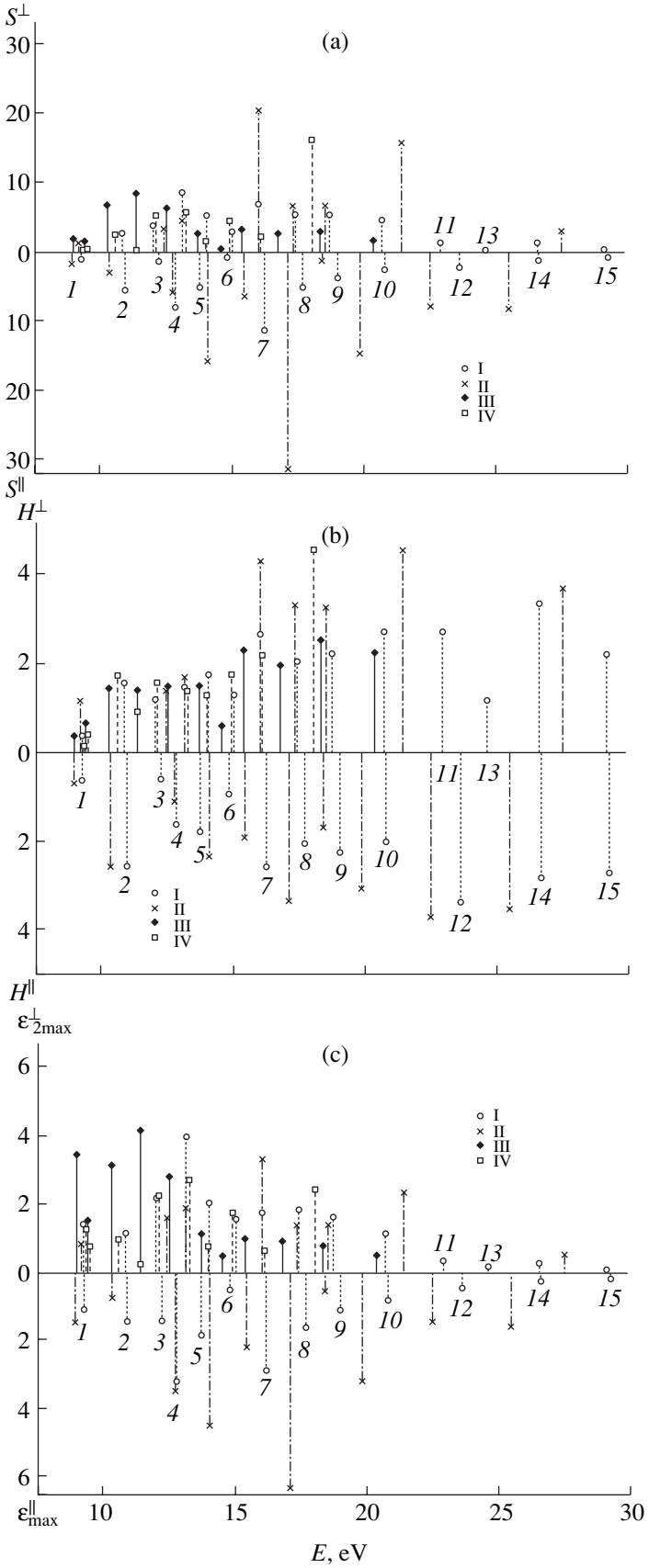

Fig. 1. Spectra of transition parameters of corundum (a) S, (b) H, and (c) ε_{2max} resulting from four types of calculations (I–IV).

ysis of the areas of the components showed that the transition probabilities for the polarization $\mathbf{E} \perp \mathbf{C}$ are higher by factors of approximately 2 (2), 1.6 (*7, 14*), and 1.3 (*15*), than those for $\mathbf{E} \parallel \mathbf{C}$. At the same time, for components *6*, *3*, *10*, and *9*, the transition probabilities for the polarization $\mathbf{E} \perp \mathbf{C}$ are ~4, 3, 2, and 1.5 times lower, respectively, than those for $\mathbf{E} \parallel \mathbf{C}$. For components *1*, *4*, *5*, and *8*, the transition probabilities depend on the polarization only slightly. The splitting energies of the components ΔE_P for $\mathbf{E} \perp \mathbf{C}$ and $\mathbf{E} \parallel \mathbf{C}$ related to the half-widths at half maximum H_i are equal to 0.6 (*3*), 0.4 (*4–6*), 0.3 (*8, 9*), 0.16 (*7*), 0.10 (*2*, *10*, *15*), 0.04 (*14*), and 0.00 (*1*). According to theoretical considerations, the valence and conduction bands of corundum are closely situated in a wide energy range with only small gaps between them. Therefore, it is natural to suggest that the comparatively large differences noticed between the energies E_i and the areas S_i for the bands making up the fine doublet structure of the components with $\mathbf{E} \perp \mathbf{C}$ and $\mathbf{E} \parallel \mathbf{C}$ could be due to an accidental coincidence in energies of two transitions differently polarized and occurring between different pairs of bands at different points of the Brillouin zone. The parameters H_i and $\varepsilon_{2\max}$ were also found to be appreciably dependent on light polarization.

We now discuss, in short, the results of calculations of the $\varepsilon_2(E)$ components performed by us on the basis of the $R(E)$ spectra from papers [5, 6, 8]. The large differences between the $R(E)$ spectra from these papers and the $R(E)$ spectrum from [7] and the discrepancies between the results of [5, 6, 8] are naturally manifested in the parameters of the bands of $\varepsilon_2(E)$ spectra calculated by us. In our calculations of group II performed on the basis of the $R(E)$ data from [6] (5–30 eV), we determined the components *1*, *2*, *4*, *5*, *7–10*, *12*, and *14* ($\mathbf{E} \perp \mathbf{C}$); that is, the components *3*, *6*, *13*, and *14* (*2*, *5*, *6*, *11*, *12*, and *15*) did not appear for the polarization $\mathbf{E} \parallel \mathbf{C}$ ($\mathbf{E} \perp \mathbf{C}$). The reflection spectra in [5] were studied only for $\mathbf{E} \perp \mathbf{C}$ and in a smaller energy range, 7–20 eV. Due to a large decrease in $R(E)$ [8] in the energy range $E > 20$ eV, the calculated values of $\varepsilon_2(E)$ proved too small to fulfill decomposition into components. Therefore, we determined a smaller number of components for them and only for $\mathbf{E} \perp \mathbf{C}$, namely, *1–10* and *1–7*, *9* for the calculations of groups III and IV, respectively.

For the polarization $\mathbf{E} \parallel \mathbf{C}$, the spectrum bands of group II, when compared with the data of group I, are strongly shifted in energy, as a rule, and the $\varepsilon_{2\max}$ are several times overestimated but have the same half-width H_i. Bands *3*, *6*, *13*, and *15* were not observed at all, and the intensities of the other bands—*5*, *8*, *10*, *12*, and *14* (*2*, *4*, *7*, and *9*)—proved strongly overestimated (underestimated). With the other polarization ($\mathbf{E} \perp \mathbf{C}$), the data for the parameters S_i, H_i, and $\varepsilon_{2\max}$ in calculations of groups II, III, and IV, as a rule, are noticeably different from each other and from the data for group I. For this polarization in calculations of groups II, III, and IV, we identified 8, 10, and 8 bands, respectively. In this case, we did not detect components *3*, *5*, *6*, *11–13*, *15* (group II), *11–15* (group III), and *8*, *10–15* (group IV).

We now discuss, in short, possible reasons for the occurrence of noticeable discrepancies between the experimental spectra from [5–8]. We suggest that the Al_2O_3 samples studied in [7] are of the best quality, because (1) intensive impurity bands near the long-wavelength absorption edge are observed only in [5, 6, 8] and (2) special attention was given to the preparation of the perfect surface used in [7], whereas the employed surface treatment was not described in [5, 6, 8]. It is generally recognized that the use of synchrotron radiation allows one to measure reflection spectra with higher precision in comparison to techniques that use a glow discharge of gases. Synchrotron radiation was used in [6, 7], and glow discharge of gases was used in [5, 8]. Taking into account the above-mentioned, we suggest that the most correct measurements of the reflection spectra were performed in [7]; therefore, the most correct parameters of the $\varepsilon_2(E)$ components were determined using these spectra.

The reflection spectra obtained in different works, as well as the spectra of dielectric functions, are noticeably distinguishable one from another in a wide energy range. Therefore, how changes in $R(E)$ will affect changes in $\varepsilon_2(E)$ is unclear. It was interesting to investigate this issue using, as an example, four reflection spectra of sapphire crystals measured on various samples using different methods.

4. CONCLUSION

Thus, the parameters of the most intensive optical transitions of corundum have been established for the first time in the region of 8–30 eV, including their energies, intensities, and polarization dependences. We have demonstrated a strong dependence of these results on the experimental technique of reflectance spectra measurement employed. Analyzing the features of the sets of fundamental optical functions of corundum, we have selected the most reliable from the four known, and using it, we have determined the most correct parameters of the transitions.

Detection of a large number of components hidden in the integral curves of the spectra of the optical functions and determination of the probabilities and energies of the transition components allow one to explain many of the properties of corundum in a new way and provide a closer approach to constructing theoretical models of the electronic structure and optical spectra of corundum and oxides of the M_2O_3 group.

ACKNOWLEDGMENTS

This work was supported by the Competition Center of the Fundamental Natural Sciences (St. Petersburg State University).

REFERENCES

1. V. B. Lazarev, V. V. Sobolev, and I. S. Shaplygin, *Chemical and Physical Properties of Simple Metal Oxides* (Nauka, Moscow, 1983).
2. V. A. Fomichev, Fiz. Tverd. Tela (Leningrad) **8**, 2892 (1966) [Sov. Phys. Solid State **8**, 2312 (1966)].
3. I. A. Brytov and Yu. N. Romashchenko, Fiz. Tverd. Tela (Leningrad) **20**, 664 (1978) [Sov. Phys. Solid State **20**, 384 (1978)].
4. A. Balzarotti, A. Bianconi, and E. Burrattini, Phys. Status Solidi B **63**, 77 (1974).
5. V. N. Abramov, M. G. Karin, A. I. Kuznetsov, and K. K. Sidorin, Fiz. Tverd. Tela (Leningrad) **21**, 80 (1979) [Sov. Phys. Solid State **21**, 47 (1979)].
6. V. V. Arutyunyan, A. K. Babayan, and V. A. Gevorkyan, Fiz. Tverd. Tela (St. Petersburg) **37**, 443 (1995) [Phys. Solid State **37**, 240 (1995)].
7. T. Tomiki, Y. Ganaha, T. Shficenbaru, *et al.*, J. Phys. Soc. Jpn. **62**, 573 (1993).
8. R. H. French, D. J. Jones, and S. J. Loughin, J. Am. Ceram. Soc. **77**, 412 (1994).
9. J. P. Batra, J. Phys. C **15**, 5399 (1982).
10. S. Ciraci and J. P. Batra, Phys. Rev. B **28**, 982 (1983).
11. L. Salasco, R. Dovesi, and R. Orlando, Mol. Phys. **72**, 267 (1991).
12. W. J. Ching and J.-N. Xu, J. Am. Ceram. Soc. **77**, 404 (1994).
13. V. Holm, R. Ahuja, Y. Yourdshahyan, *et al.*, Phys. Rev. B **59**, 12777 (1999).
14. V. V. Sobolev and V. V. Nemoshkalenko, *The Methods of Computational Physics in the Theory of Solid State. Electronic Structure of Semiconductors* (Naukova Dumka, Kiev, 1988).
15. V. V. Sobolev, Zh. Prikl. Spektrosk. **63**, 143 (1996).
16. V. V. Sobolev and A. I. Kalugin, Fiz. Tverd. Tela (St. Petersburg) **41**, 1614 (1999) [Phys. Solid State **41**, 1480 (1999)].
17. A. N. Timoshkin, V. Val. Sobolev, and V. V. Sobolev, Fiz. Tverd. Tela (St. Petersburg) **42**, 37 (2000) [Phys. Solid State **42**, 37 (2000)].

Translated by N. Kovaleva

Physics of the Solid State, Vol. 43, No. 11, 2001, pp. 2067–2070. Translated from Fizika Tverdogo Tela, Vol. 43, No. 11, 2001, pp. 1984–1987.
Original Russian Text Copyright © 2001 by Zhuravlev, Poplavnoĭ.

SEMICONDUCTORS AND DIELECTRICS

Electron Density Calculations for $MgCO_3$ Using the Sublattice Technique

Yu. N. Zhuravlev and A. S. Poplavnoĭ

Kemerovo State University, ul. Krasnaya 6, Kemerovo, 650043 Russia

e-mail: zhur@phys.kemsu.ru

Received January 8, 2001; in final form, April 12, 2001

Abstract—Self-consistent valence electron densities of a $MgCO_3$ crystal and of its constituent sublattices are calculated on the basis of the local-density functional theory. The coupling between the sublattices is characterized by the density difference, introduced as the difference between the total electron density and the densities of individual sublattices. Intra- and interlattice hybridization effects are considered. It is shown that the density difference is in qualitative agreement with the experimental deformational density. © *2001 MAIK "Nauka/Interperiodica".*

1. INTRODUCTION

The experimental potentialities that permit determination of the electron density distribution function and potential in crystals at varying but comparatively high accuracy have been extended considerably. The change in the total electron density upon the introduction of an atom into a crystal (the so-called deformation density), rather than the total electron density itself, is important for practical applications. Theoretical calculations of the deformation density on the basis of various methods of the band theory have also been perfected to a certain degree mainly due to the development of self-consistent Hartree–Fock methods and the theory of the local density functional (TLDF).

The deformation density characterizes the resultant effect of the redistribution of electrons among various atoms and of the electron transitions from atomic sites to interstices. The redistribution effect is traditionally explained in terms of a local approach in the language of hybridization of orbitals of neighboring atoms, as is usually done in molecular quantum chemistry. The role of the long-range order in the formation of chemical bonds in crystalline solids remains unclear in this case. In order to investigate this role, we propose an approach based on introducing the concepts of sublattices and density difference for describing the change in the electron density of atoms undergone during combination into a crystal lattice. The application of this approach to MgO crystals [1] made it possible to establish the fact that the main peculiarities in the valence density distribution in rare-earth oxides are determined by the oxygen sublattice, while the electron density of the magnesium sublattice is smeared quite uniformly over the unit cell. In this work, we apply the sublattice technique to a $MgCO_3$ crystal, in which the covalent component of the chemical bond exists along with the ionic component in the CO_3 molecular complex, for determining the role played by sublattices in the formation of the valence electron density.

2. METHOD AND OBJECT OF INVESTIGATION

We consider a crystal consisting of s sublattices formed by identical atoms. In order to single out a sublattice, it is expedient to assume an electron distribution which ensures its electrical neutrality. Then, we will carry out self-consistent calculations of the electron structure of the crystal and of all the sublattices using a unified model. In all cases, the structural parameters are defined in accordance with the actual geometrical structure of the lattice. The results of self-consistent calculations include the hybridization effects between all atoms for the crystal and only between atoms of the same species for the sublattices. In order to calculate the hybridization effects between the sublattices, we introduce the density difference $\Delta\rho(\mathbf{r})$:

$$\Delta\rho(\mathbf{r}) = \rho^{\text{crys}}(\mathbf{r}) - \sum_s \rho_s^{\text{sub}}(\mathbf{r}). \quad (1)$$

If the electron densities are normalized to the number of electrons, then the integral of the density difference over a unit cell is equal to zero and, hence, the maps of $\Delta\rho(\mathbf{r})$ contain regions of both positive and negative values, which gives a visual impression of the charge transfer between the sublattices. In this approach, the effects of hybridization between identical atoms constituting sublattices and between sublattices constituting a crystal are separated.

The method described above was applied by us for calculating the electron density of magnesium carbonate $MgCO_3$ (space group D_{3d}^6; $Z = 2$ [2]). Magnesite is an abundant technological material used, for example,

for obtaining refractory materials and magnesium oxide, which is used widely in optics. The electron structure of this compound is not only interesting in itself but also from the point of view of model concepts on the nature of cation–oxygen interactions and of the order–disorder phase transition associated with the rotation of the carbonate group and its possible pyramidal deformation, which is in contrast to the planar structure required by the symmetry [3, 4].

We calculated the electron density in the framework of the TLDF using pseudopotentials [5] on the basis of numerical atomic $s^1p^3d^5$ pseudoorbitals determined from atomic calculations with the same pseudopotentials fit to the known energy-level diagrams [6] by varying the occupation numbers. In order to calculate the overlap integrals and the pseudo-Hamiltonian matrix, the basis functions were expanded into a series in 2500 plane waves. The details of the numerical realization of the method are described in [7].

3. RESULTS OF CALCULATIONS

The distributions of the total valence density of $MgCO_3$ and the densities of the sublattices in an anion plane are presented in Fig. 1. The numerical values of the electron density are given in units of $e \cdot Å^{-3}$ (e is the electron charge), and the distances are given in angströms.

The maximum electron density $\rho_{MgCO_3}(\mathbf{r})$ is concentrated in the vicinity of the positions of oxygen atoms and embraces them from the outer side relative to the carbon atoms. The density has a minimum at the position of the carbon atom; then, the value of $\rho_{MgCO_3}(\mathbf{r})$ increases towards oxygen atoms with small peaks at 0.45 and 1.02 Å and finally attains its principal peak at 1.46 Å (the length of the C–O bond is equal to 1.2857 Å). The low peak existing at the middle of the O–O bonds amounts to 20% of the value of $\rho_{MgCO_3}(\mathbf{r})$ on the oxygen atom. The last closed loop of $\rho_{MgCO_3}(\mathbf{r})$, which embraces a complex anion, has a shape close to a sphere of radius ~2 Å. It should be noted that the thickness of the anion layer in the direction of the C_3 axis, which was also estimated from the last closed density loop, was also found to be ~2 Å.

Let us now consider the electron density $\rho_O(\mathbf{r})$ of the oxygen sublattice. It can be seen from Fig. 1 that the loops of $\rho_{MgCO_3}(\mathbf{r})$ and $\rho_O(\mathbf{r})$ beyond the anion virtually coincide and differ only in numerical value. Thus, the electron density of the crystal in this region is formed

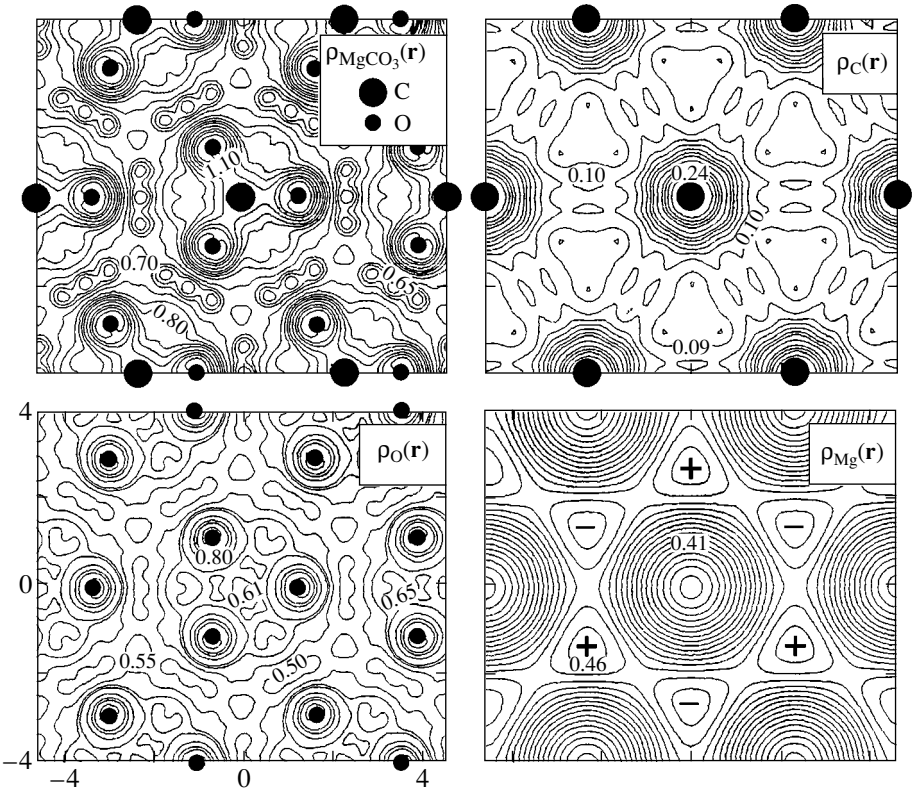

Fig. 1. Total valence density $\rho_{MgCO_3}(\mathbf{r})$ and the densities $\rho_O(\mathbf{r})$, $\rho_C(\mathbf{r})$, and $\rho_{Mg}(\mathbf{r})$ of the oxygen, carbon, and magnesium sublattices, respectively, in the anion plane.

mainly due to oxygen states. Within the anion, charges between the oxygen atoms are formed and a density peak of height ~1 $e \cdot Å^{-3}$ appears on the C–O bond behind the position of the oxygen nucleus. The minimum value ~0.5 $e \cdot Å^{-3}$ of the density corresponds to the middle of the bond between neighboring anions. The oxygen atoms of neighboring anions have no common loops on the plane. The common loop with $\rho_O(\mathbf{r}) = 0.5\ e \cdot Å^{-3}$ encloses each individual anion. A low density peak of 0.55 $e \cdot Å^{-3}$ lies in a position between the three anions under and above which magnesium atoms are located.

The electron density $\rho_C(\mathbf{r})$ of the carbon sublattice has a sixfold symmetry axis, and the density associated with carbon atoms is almost spherically symmetric relative to their positions in the lattice. In this distribution, there exists a peak ~0.26 $e \cdot Å^{-3}$ corresponding approximately to the middle of the C–O bond. The density $\rho_C(\mathbf{r})$ has a minimum (~0.09 $e \cdot Å^{-3}$) at points above and below which magnesium atoms are located. There exist low paired peaks of height ~0.1 $e \cdot Å^{-3}$ at the anion–anion bond, which serve as bridges between carbon positions.

The electron density $\rho_{Mg}(\mathbf{r})$ of the magnesium sublattice is also symmetric relative to the sixfold axis. Magnesium atoms transfer a considerable part of their valence charge to the anionic plane, which is facilitated by the hybridization of their *s* orbitals with virtual *p* and *d* orbitals. A density $\rho_{Mg}(\mathbf{r})$ has a minimum at the center of an anion, and its value increases towards the anion periphery. The peaks of the density of the metal lie at six positions between the exact same anions at which low density peaks of the oxygen sublattice are located. Thus, the two sublattices synchronously form the features of the total density.

The absence of a rigid covalent bond between molecular groups and the fact that the symmetry of the carbon and magnesium sublattices is higher than the crystal symmetry are factors that facilitate the orientational disorder of the CO_3 carbonate group; this has been observed experimentally [3, 4].

Figure 2 shows the density difference $\Delta\rho(\mathbf{r})$ calculated by using formula (1) in the anionic plane and in the plane containing nearest C, O, and Mg atoms. The density difference has negative values (in *e* units) only in a very small region in the vicinity of an oxygen atom in the direction towards the carbon atom. Two peaks of $\Delta\rho(\mathbf{r})$ with a height of 0.05 $e \cdot Å^{-3}$ lie in the anionic plane symmetrical relative to the C–O bond at a distance 0.45 Å from an oxygen atom. The principal peak of $\Delta\rho(\mathbf{r})$ lies on the C–O bond at a distance of ~0.5 Å from a carbon atom. At this atom, the value of the density is positive and increases from the center to the periphery. Thus, the interaction of sublattices, which is strongest between the oxygen and carbon sublattices, leads to a complex redistribution of the electron charge, which can be characterized as a covalent type of chemical bond. The density difference in the vicinity of a Mg atom has negative values over a fairly wide region. Thus, an ionic bond is formed between the cation and anion planes due to the charge transfer from the cation to the anion plane.

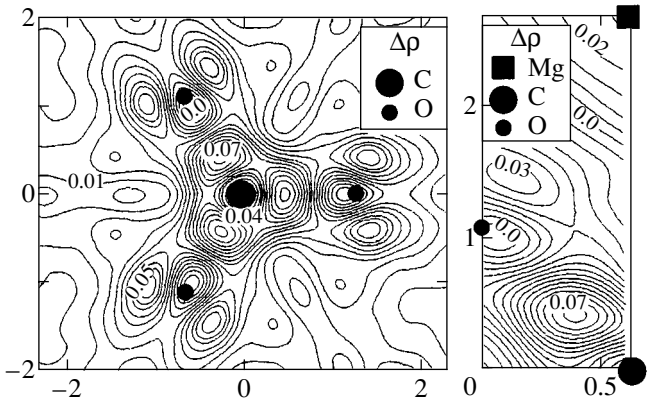

Fig. 2. Density difference $\Delta\rho$ in the anion plane and in a plane containing nearest neighbor Mg, C, and O atoms.

4. COMPARISON WITH EXPERIMENT AND DISCUSSION

The deformation density of $CaCO_3$, $MgCO_3$, and $MnCO_3$ was investigated in [3] using the method of synchrotron x-ray diffraction. The experimental data obtained in [3] for $MgCO_3$ were meticulously processed in [4], and the deformation density of this compound was calculated theoretically using the Hartree–Fock method. It was proved that the results of theoretical calculations are in good agreement with the experimental data. A slight discrepancy was observed for positions near oxygen atoms, for which the theory predicts nearly spherically symmetric density peaks on lines perpendicular to the C–O bonds, while in experiments, these peaks have elliptic cross sections. Moreover, in the experimental density maps, the centers of these peaks are displaced insignificantly relative to the oxygen position as compared to the theoretical peaks.

Let us now compare the results of our calculations of the density difference in the anion plane (see Fig. 2) with the theoretical and experimental deformation density maps presented in Figs. 2a and 2b in [4]. The arrangements and the profiles of the peaks and minima for the density difference calculated by us were found to be closer to those for the experimental deformation density. The most significant distinction is that both theoretical and experimental deformation densities are negative in the vicinity of oxygen and carbon atoms, while the density difference has funnel-shaped minima in this region and only a small part of the minimum in the vicinity of an oxygen atom corresponds to negative values. This distinction is due to the fact that, while calculating the deformation density, we subtract from the

total density the densities of free atoms and not the densities of sublattices in which intralattice hybridization has already taken place.

The pronounced similarity observed by us for $MgCO_3$ between the density difference defined by Eq. (1) and the deformation density is due to the fact that the strongest hybridization effects in this compound take place between the atoms of the CO_3 carbonate group, while the hybridization between other sublattices is much weaker. It should be borne in mind, however, that the density difference and the deformation density are essentially different quantities. The difference between them is especially large in the case when hybridization effects in the sublattices are stronger than those between them. Such cases are presently being investigated by us.

REFERENCES

1. Yu. N. Zhuravlev, Yu. M. Basalaev, and A. S. Poplavnoĭ, Zh. Strukt. Khim. **42** (2), 211 (2001).
2. E. N. Haslen, V. A. Streltsov, and N. R. Streltsova, Acta Crystallogr. B **49**, 980 (1993).
3. E. N. Haslen, V. A. Streltsov, N. R. Streltsova, and N. Ishizawa, Acta Crystallogr. B **51**, 925 (1995).
4. M. Catti and A. Pavese, Acta Crystallogr. A **52**, 413 (1996).
5. G. B. Bachelet, D. R. Hamann, and M. Schluter, Phys. Rev. B **26** (8), 4199 (1982).
6. A. A. Radtsig and B. M. Smirnov, *Reference Data on Atoms, Molecules, and Ions* (Springer, Berlin, 1985; Énergoatomizdat, Moscow, 1986).
7. Yu. N. Zhuravlev, Yu. M. Basalaev, and A. S. Poplavnoĭ, Izv. Vyssh. Uchebn. Zaved., Fiz., No. 3, 96 (2000).

Translated by N. Wadhwa

Physics of the Solid State, Vol. 43, No. 11, 2001, pp. 2071–2073. Translated from Fizika Tverdogo Tela, Vol. 43, No. 11, 2001, pp. 1988–1990.
Original Russian Text Copyright © 2001 by Aduev, Aluker, Shvayko.

SEMICONDUCTORS AND DIELECTRICS

Radiation-Stimulated Pulse Conductivity of CsBr Crystals

B. P. Aduev, É. D. Aluker, and V. N. Shvayko

Kemerovo State University, ul. Krasnaya 6, Kemerovo, 650043 Russia

e-mail: lira@kemsu.ru

Received April 12, 2001

Abstract—The radiation-stimulated pulse conductivity of CsBr crystals is investigated upon picosecond excitation with electron beams (0.2 MeV, 50 ps, 0.1–10 kA/cm^2). The time resolution of the measuring technique is ~150 ps. It is shown that the lifetime of conduction band electrons is limited by their bimolecular recombination with autolocalized holes (V_k centers). A delay in the conduction current pulse build-up is revealed. This effect is explained within the proposed model, according to which the Auger recombination of valence band electrons and holes of the upper core band substantially contributes to the generation of conduction band electrons. © *2001 MAIK "Nauka/Interperiodica".*

1. INTRODUCTION

Investigation of dielectric crystals under excitation with electron beams of picosecond duration and measurements of the relaxation kinetics of the conduction current induced by an exciting pulse can provide the most direct information on the possible mechanism of generation, transfer, recombination, and trapping of band charge carriers in these materials.

In our previous works [1–8], we investigated the radiation-stimulated conductivity of NaCl, KCl, KBr, and CsI crystals upon excitation with an electron beam (0.2 MeV, 50 ps, 0.1–10 kA/cm^2). The present work is a continuation of these investigations.

2. SAMPLE PREPARATION AND EXPERIMENTAL TECHNIQUE

The CsBr crystals were grown from the high-purity salt by the Stockbarger technique. The samples were 10×10 mm in size and 2 mm thick. A cylindrical hole 2 mm in diameter was drilled at the center of the sample so that the bottom thickness was equal to 50 μm. This value is considerably less than the mean path of 0.2-MeV electrons in CsBr. The latter circumstance provided uniformity of the excitation produced. Platinum electrodes ≤1 μm thick were deposited into the hole and onto the opposite face of the sample through cathodic sputtering deposition. In order to prevent edge effects, the sample was irradiated through a collimator 1 mm in diameter. The time resolution of the measuring channel was 150 ps. The measuring technique was described in detail in [9].

3. RESULTS AND DISCUSSION

The normalized oscillograms of conduction current pulses for a CsBr crystal at a temperature of 300 K and different excitation current densities are displayed in Fig. 1. For comparison, Fig. 1 shows the oscillogram of a conduction current pulse for a KCl crystal, which coincides with the pulse characteristic of the measuring channel.

It can be seen from Fig. 1 that the kinetics of conduction in CsBr exhibits a number of specific features as compared to NaCl and CsI crystals. Unlike the case of crystals with a NaCl-type lattice, the inertialess component that repeats the pulse characteristics of the measuring channel is absent. The data processing of oscillogram *1* (Fig. 1), which was measured at the lowest excitation current density, showed that the decay of the conduction current pulse is described by the second-

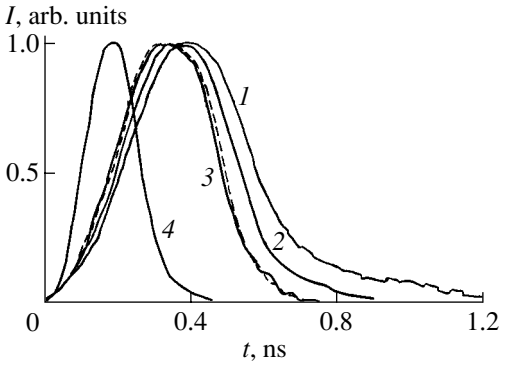

Fig. 1. Normalized oscillograms of the conduction current pulses for (*1–3*) CsBr and (*4*) KCl. The dashed line shows the results of calculations according to formula (10). Excitation current density j, A/cm^2: (*1*) 190, (*2*) 1100, and (*3*) higher than 4500.

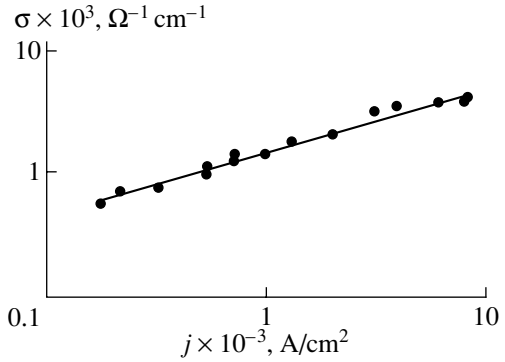

Fig. 2. Dependence of the conductivity for the CsBr crystal on the excitation current density at $T = 300$ K.

order kinetics, as is the case in CsI crystals [1–3]. This suggests that, under the experimental conditions, the lifetime of conduction band electrons in CsBr is limited by their recombination with autolocalized holes (V_k centers), as was proved earlier for CsI [1–3].

As the excitation density increases, the duration of the conduction current pulse decreases and reaches a certain limit: the half-amplitude duration for CsBr is twice that for KCl (Fig. 1, oscillograms *3*, *4*). The experimental conditions were identical for both samples, and their capacitances were comparable.

The current–voltage characteristics in the studied range of excitation current densities are linear in fields up to 5×10^4 V/cm. From the current–voltage characteristics, we calculated the electrical resistance R and the conductivity of the sample:

$$\sigma = \frac{1}{R}\frac{l}{S}, \tag{1}$$

where l is the sample thickness and S is the diameter of the collimator.

Figure 2 shows the conductivity σ as a function of the excitation current density j at 300 K on the logarithmic scale. This dependence is well approximated by the power law

$$\sigma \sim j^{\delta} \tag{2}$$

with the exponent $\delta = 0.5 \pm 0.02$. This result allows us to conclude that, as in crystals with a NaCl-type lattice [5], the quasi-stationary mode of excitation is realized at relatively high current densities of the electron beam, whereas the exponent $\delta = 0.5$ in relationship (2) and the results of kinetic measurements at relatively low excitation densities indicate a dominant bimolecular e–V_k recombination [2, 5].

In these experiments, the constant duration of the conduction current pulse over a wide range of excitation densities is of particular interest, because the electron lifetime in terms of the bimolecular recombination model is represented as

$$\tau = \frac{1}{\nu S n} \sim \sigma^{-1} \sim j^{-0.5}, \tag{3}$$

where ν is the thermal velocity, n is the band electron concentration, and S is the effective cross section of the e–V_k recombination. It should be expected that an increase in the excitation current density be accompanied by a decrease in the duration of the conduction current pulse up to the width of the pulse characteristic of the measuring channel.

Note that the instability of the exciting pulse shape and the error in measurement of the pulse duration do not exceed 10% and cannot affect the above result. Therefore, we can assume that the mechanism of generation of band electrons in CsBr is characterized by a certain delay with respect to the exciting pulse duration.

Let us consider a possible model of this process. As a rule, conduction band electrons and valence band holes are involved in processes associated with band charge carriers. However, ionization of the crystal matrix by high-energy particles occurs with the formation of holes attributed to the lower-lying core band rather than to the valence band. In this case, a hole from the lower-lying band recombines with a valence band electron. This process is accompanied by the emission of an x-ray photon. However, it was found that a number of wide-gap ionic crystals exhibit emission in the visible and ultraviolet spectral ranges [10]. This emission was identified as transitions between the valence band and the upper core band of the crystal. The attendant luminescence was referred to as the core–valence band luminescence or the cross luminescence. The condition for the occurrence of cross luminescence is specified by the relationship [10]

$$E_{q1} > E_{q2} + E_v. \tag{4}$$

Here, E_{q1} and E_{q2} are the first and second band gaps, respectively, and E_v is the width of the valence band of the crystal. Note that the bandwidth of the cross luminescence corresponds to the valence band width.

In the case when $E_{q1} > E_{q2}$ and $(E_{q1} + E_v) > E_{q1}$, condition (4) is satisfied only partly and the bandwidth of the cross luminescence is substantially less than E_v. This situation is actually observed in the CsBr crystal [10]. It seems likely that, in this case, both radiative valence-band-to-core transitions and Auger transitions with the generation of an electron–hole pair become possible. The aforesaid is illustrated in Fig. 3. Transitions of type *1* from the valence band bottom to the top of the upper core band correspond to radiative transitions. Transitions of type *2* from the valence band top that do not obey condition (4) are the Auger transitions with the generation of a conduction band electron and a valence band hole. It is reasonable to assume that the rate constant of the Auger transitions $\alpha = \tau^{-1}$ is comparable to the rate constant α for the radiative transitions,

which were observed during the cross luminescence. For the CsBr crystal, the duration τ of the radiation transition at 300 K is equal to 70 ps [10].

Now, we make quantitative estimations in terms of the proposed model. The balance equation for the hole concentration n_v in the valence band can be written in the following form:

$$\frac{dn_v}{dt} = G(t) - \frac{n_v}{\tau}, \tag{5}$$

where $G(t)$ is the rate of hole generation in the first core band. It is assumed that $G(t)$ coincides with the excitation function and can be described by the formula [4]

$$G(t) = \exp\left(-\frac{2t^2}{\omega^2}\right), \tag{6}$$

where ω = 150 ps is the Gaussian parameter, which characterizes the excitation pulse duration, and τ is the characteristic time of the Auger transition, which coincides with the lifetime of cross luminescence.

The balance equation for the electron concentration in the conduction band is represented as

$$\frac{dn}{dt} = \frac{n_v}{\tau} - \alpha n^2. \tag{7}$$

Here, the first term describes the generation of electrons due to Auger transitions between the core band and the valence band and the second term accounts for the bimolecular recombination of electrons and holes.

Let us now consider the case of high excitation current densities when the quasi-stationary approximation is applied to conduction band electrons. From Eq. (7), we obtain the expression

$$n = \left(\frac{n_v}{\alpha\tau}\right)^{1/2}. \tag{8}$$

The solution of Eq. (7) has the form

$$n_v = \int_{-\infty}^{t} G(t')e^{-\frac{(t-t')}{\tau}}dt'. \tag{9}$$

By substituting solution (9) into expression (8), we derive the following formula for processing of the experimental oscillograms:

$$n(t) \sim j(t) \sim \left[\frac{1}{\tau}\int_{-\infty}^{t} G(t')e^{-\frac{(t-t')}{\tau}}dt'\right]^{1/2}. \tag{10}$$

Here, $j(t)$ is the experimentally measured shape of the conduction current pulse.

The dashed line in Fig. 1 represents the results of calculations according to formula (10) at τ = 50 ps. Both curves obtained at the τ value, which is close to that measured from the cross luminescence [10], virtually coincide with each other. This indicates that the above model is quite reasonable.

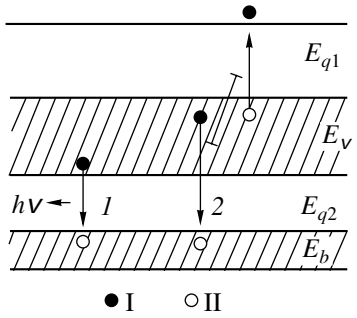

Fig. 3. A schematic representation of valence-band-to-core transitions: (*1*) radiative transitions and (*2*) nonradiative Auger transitions. Designation: E_{q1} and E_{q2} are the first and second band gaps, respectively; E_v and E_b are the widths of the valence band and the upper core band, respectively; and I and II are an electron and a hole, respectively.

Thus, the proposed model explains the delay of increase in the concentration of band electrons contributing to conduction.

ACKNOWLEDGMENTS

This work was supported by the "Russian Universities—Basic Research" Program.

REFERENCES

1. B. P. Aduev, G. M. Belokurov, and V. N. Shvayko, Fiz. Tverd. Tela (St. Petersburg) **37** (2), 2537 (1995) [Phys. Solid State **37**, 1392 (1995)].
2. B. P. Aduev, A. V. Igolinskiĭ, and V. N. Shvayko, Fiz. Tverd. Tela (St. Petersburg) **38** (3), 948 (1996) [Phys. Solid State **38**, 525 (1996)].
3. B. P. Aduev, E. D. Aluker, G. M. Belokurov, and V. N. Shvayko, Phys. Status Solidi B **208**, 137 (1998).
4. B. P. Aduev and V. N. Shvayko, Fiz. Tverd. Tela (St. Petersburg) **40** (1), 66 (1998) [Phys. Solid State **40**, 57 (1998)].
5. B. P. Aduev, V. M. Fomchenko, and V. N. Shvayko, Fiz. Tverd. Tela (St. Petersburg) **41** (3), 429 (1999) [Phys. Solid State **41**, 384 (1999)].
6. B. P. Aduev and V. N. Shvayko, Fiz. Tverd. Tela (St. Petersburg) **41** (7), 1200 (1999) [Phys. Solid State **41**, 1093 (1999)].
7. B. P. Aduev, É. D. Aluker, V. M. Fomchenko, and V. N. Shvayko, Fiz. Tverd. Tela (St. Petersburg) **43** (2), 246 (2001) [Phys. Solid State **43**, 255 (2001)].
8. B. P. Aduev, É. D. Aluker, V. M. Fomchenko, and V. N. Shvayko, Fiz. Tverd. Tela (St. Petersburg) **43** (7), 1185 (2001) [Phys. Solid State **43**, 1229 (2001)].
9. B. P. Aduev, É. D. Aluker, G. M. Belokurov, *et al.*, in *Proceedings of the I All-Russia Symposium "Solid-State Ionizing-Radiation Detectors," Yekaterinburg, 1997*, p. 126.
10. P. A. Rodnyĭ, Fiz. Tverd. Tela (St. Petersburg) **34** (7), 1975 (1992) [Sov. Phys. Solid State **34**, 1053 (1992)].

Translated by N. Korovin

Physics of the Solid State, Vol. 43, No. 11, 2001, pp. 2074–2082. Translated from Fizika Tverdogo Tela, Vol. 43, No. 11, 2001, pp. 1991–1998.
Original Russian Text Copyright © 2001 by Yudin, Shchegoleva, Pisarenko.

DEFECTS, DISLOCATIONS, AND PHYSICS OF STRENGTH

Kinetics of Thermal Relaxation of Mesodefect Networks in Amorphous Co–Ni–P Films in a Stochastic-Flow Model

V. V. Yudin, S. A. Shchegoleva, and T. A. Pisarenko

Institute of Physics and Information Technologies, Far-East State University, Vladivostok, 690600 Russia

e-mail: yudin@ifit.phys.dvgu.ru

Received March 6, 2001

Abstract—Structural relaxation of mesodefect networks in amorphous Co–Ni–P films during low-temperature isothermal annealing (T = 175°C) is studied. A mathematical model in which network structures are presented in the form of stochastic flows of intersections of network boundaries is used. The two-stage nature of the annealing process, which is also reflected in the correlation radius, is established in terms of the first two moments of the empirical distributions. It is found that the flow statistics is of the Weibull class. In the identified Weibull statistics, two scale components are distinguished at a 98% confidence level. The short-wavelength (SW) component is characterized by an extremal form of behavior of the α dimension, while the corresponding dependence of the long-wavelength component of the network hierarchy is linear and the values of the dimension do not exceed unity. The entropy of the zero spectrum of correlation functions of intersection flows of network boundaries for an annealing time ~1 h indicates considerable ordering of the SW component of the network mesostructure. Different spatial scales of the network hierarchy of mesodefects of the amorphous state evolve along different channels, which could ensure high structural stability under the appropriate influences.
© 2001 MAIK "Nauka/Interperiodica".

1. INTRODUCTION

The network concept of the amorphous state received wide recognition in the 1980s [1–13]. In this approach, amorphous planar media, including metallic glasses of the transition-metal–metalloid (TM–MD) and the rare-earth metal–transition metal (REM–TM) type, can be treated as structurally continuous hierarchic systems consisting of network-type mesodefects. In general, the topology of such mesostructures can be interpreted as fluctuating fields of the material density. The electron-microscopic images of mesodefect networks were transformed into the sign-representation by using standard sign-procedures, which made it possible to obtain patterns of the network boundaries proper. The topology of such network structures can be diverse. Some of them [10–12] possess a clearly manifested mesh-type morphology, while others [7, 9, 10] (including the amorphous Co–Ni–P films (AFs) under investigation) possess a complex tree-fragmentary topology. The latter mesostructures cannot be described using standard statistical methods of representation in terms of the mesh-size distribution function. For this reason, a more general method of presentation and processing of such network structures with a "torn" topology was employed. This method is based on the model of stochastic flows of network boundaries intersected (NBIF) by a scanning line [11, 12, 14]. The stochastic flow model [14–16] will make it possible to analyze various kinetic aspects of the amorphous state [10, 12], e.g., for comparatively soft thermal effects for long holding times. The main problem in which we are interested is associated with the search for mechanisms that ensure the stability of the amorphous state during structural relaxation processes. It has been emphasized by us more than once [10, 16] that metallic glasses of the TM–MD and the REM–TM type, as well as ultradisperse films, possess an elevated stability in conservative ageing if the network hierarchy of mesodefects possesses a potential of sufficiently high order. A certain "prolongation" (slowness) of the disintegration of the amorphous state was observed. The latter peculiarity should be reflected in the corresponding class of the NBIF distribution functions. Consequently, one of the main goals of the present work is the identification of the statistics of the distances between neighboring intersections of network boundaries with a scanning line. We expect that the processes of thermal structural relaxation of amorphous films will be manifested selectively on different spatial scales of the network hierarchy [1–13]. We consider the processes of thermal structural relaxation under the assumption that the amorphous ordering on the atomic level persists [13], which is usually manifested in typical halo diffraction patterns. In this case, the delayed decay of the amorphous state can probably be explained in terms of the combined effect of the mesoscopic hierarchy of the subnetworks [10, 16]. During structural relaxation, a number of perturbing factors that are usually present because of the nonequilibrium conditions of obtaining metallic glasses are removed. Such a relaxed amorphous state should be attributed to the ideal amorphous state. The approach to the relaxation kinetics of the amorphous

state at a mesoscopic level, which is proposed by us here, will make it possible to work out the appropriate developments in technology.

2. EXPERIMENTAL TECHNIQUE AND THE PROCESSING ALGORITHMS

The AFs of Co–Ni–P (9–13 at. % P, $h \sim 300$ nm) were obtained through electrochemical deposition (at the Kirenskiĭ Institute of Physics, Krasnoyarsk). Annealing was carried out *in situ* on a JEM-1000 electron microscope (at the Baĭkov Institute of Metallurgy, Russian Academy of Sciences) at a temperature of 175°C. The isothermal annealing time was 1.5 h. The electron microscope photography of the AFs was carried out at 5-min intervals. It was found in [1–13] that AFs exhibited a multiscale network structure of mesodefects, which was handled using special computational processors [16, 17] for obtaining sign networks.

Figure 1 shows the light-field electron-microscopic image of one of the amorphous Co–Ni–P films under investigation with the corresponding microscopic diffraction pattern. Thin AFs are characterized by a phase contrast under a transmission electron microscope, whose origin is associated with the electron density fluctuations of the material [4, 7, 8, 18, 19].

In the general case, multicomponent films in the fluctuating field representation can be considered at three levels. The first (and most universal) level comprises material density fluctuation fields, which exist in single-phase media. The next level is formed by concentration fields whose part in the spinodal decay is significant [20]. Although the spinodal decay has something in common with the processes of structural relaxation in AFs, this concerns, in all probability, the last stages of the space–time evolution of fluctuation fields [21–24]. It was stated in [23] that structural relaxation in rapidly quenched multicomponent alloys is accompanied by spinodal decay with respect to the free volume (density) and by concentration stratification. The most complete correlation theory of decay phenomena and ordering in solids far from equilibrium was developed by Stefanovich [24], who studied the diffusion stage of relaxation of a large-scale glass structure followed by binodal heterophase evolution. It was emphasized in [24, Chapter 1] that a spatially inhomogeneous stochastic distribution of concentration and density sets in at nonequilibrium stages of glass formation. The spatial scale of the corresponding inhomogeneities is larger than the characteristic atomic scales. In our opinion, this is merely a manifestation of an implicit form of the network mesostructural hierarchy of blurred spatial inhomogeneities of amorphous media, including metallic and quartz glasses [1–13, 16, 21].

Finally, the third level corresponds to the chemical-composition fluctuation fields. It follows from [22, Subsections 3.3, 3.4] that the late stage of the space–time evolution of amorphous alloys is characterized by

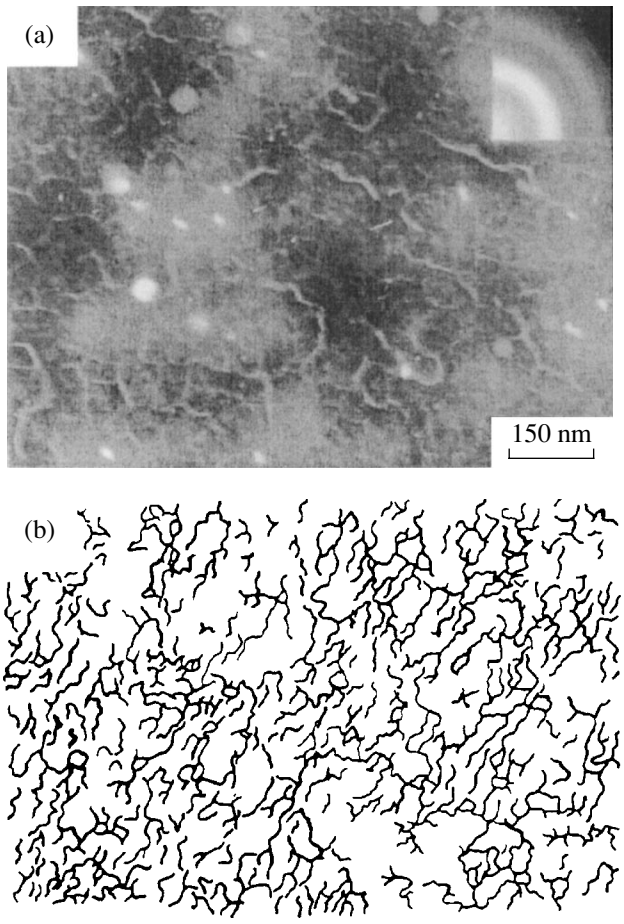

Fig. 1. (a) Light-field electron-microscopic image and electron diffraction pattern of a Co–Ni–P amorphous film after 55-min of low-temperature isothermal annealing at T = 175°C and (b) its sign network representation.

the formation of a foam polydomain structure whose size is inversely proportional to the degree of nonstationarity (the cooling rate). Increases in the macroscopic order parameter in amorphous alloys are due to the synchronization of atomic-density distribution waves in the chemical-potential field averaged over the component contents. Variations in the concentration and in the chemical composition of amorphous media also contribute to other types of electron-microscopic contrast [18, 19, 25]; this was not observed in our dark-field electron-microscopic images [10].

As a result of high-temperature annealing, the meshes form an ensemble of grains or crystallites of the corresponding scale, while the regions of changes in density are transformed into large-angle boundaries in polycrystalline films and small-angle boundaries in ultradispersed films [16]. The electron-microscopic contrast at such deep stages of structural relaxation becomes an ordinary diffraction contrast [18, 25, 26].

Mesodefect networks in the AFs were investigated using the concept of stochastic flows [11, 12, 14]. These

flows are constructed in an oblique-angled line raster with the help of an automated microphotometer. The ensemble of realizations of quasi-stochastic flows is formed by 4×4 cross sections separated from one another by 40 nm; this enabled us to assume that this raster is formed by independent cross sections. The total sampling size for reference annealing times of 35, 55, and 70 min was 207, 186, and 217 readings, respectively. We fixed the points of intersection of the scanning lines and the sign network and then measured the distance between neighboring intersections.

(1) Let us consider the probabilistic formalism of the description of stochastic flows. The statistical analysis of NBIF will be based on the theory of stochastic flows [14, 15]. As is usually the case in probability theory [27], it is natural to introduce the integral [$F(x)$] and differential [$f(x)$] probability distribution functions, in terms of which the so-called reliability function is defined as [14]

$$R(x) = P\{X > x\} = 1 - F(x) = \int_x^\infty f(u)du, \quad (1)$$

where $R(0) = 1$ and $R(\infty) = 0$. Obviously, $f(x) = -R'(x)$. In our problem, the reliability is the probability of occurrence of an additional event consisting in movement along the scanning line over the mesh without encountering the next network boundary. Another useful characteristic is the entropy functional, which is defined as

$$H_{\alpha\beta}(x') = \int_0^{x'} f^\alpha(x)(1 - f(x))^\beta dx, \quad (2)$$

where it is assumed that $\alpha > 0$ and $\beta > 0$ ($\alpha = \beta = 1$ in our case). Obviously, $H_{11}[f(x)]$ has the properties of entropy [28]; namely, it is a nondecreasing, monotonic, and convex function approaching its asymptotic form. For small values of the argument (zero-asymptotic form), it is convenient to introduce the derivative of the entropy with respect to the spatial size, $\left.\frac{dH_{11}[f(x)]}{dx}\right|_{x \approx 0} = r_H(x)$, which determines the stochasticity radius.

In an elementary statistical analysis, at the initial stage, the moments of empirical distributions (μ and σ^2 are the first and second moments) are normally used. The kinetic dependences of these moments are the main characteristics of structural relaxation. We can also construct an analog of the phase space or correlation field [29, 30]. Another useful characteristic is the ratio $\mu/\sigma(t_T)$, which is especially convenient for studying modulated processes and structures. This quantity characterizes the width of the size distribution of inhomogeneities.

(2) The next level of a statistical analysis of stochastic flows involves identification of the one-dimensional flow statistics. In the $\{\log H[R^{-1}(x)];\ \log x\}$ coordinates, the plots become linear for empirical statistics, which indicates that the distributions under investigation belong to the Weibull class:

$$f(x) = \alpha\lambda x^{\alpha-1}\exp\{-\lambda x^\alpha\}, \quad (3)$$

where λ is the scale parameter. The main parameter of the Weibull statistics (W statistics) is the exponent $\alpha = \frac{d\log H[R(x)]}{d\log x}$, which characterizes the dimensionality of the inhomogeneity (or mesh-size) space [31, 32].

Modern mathematical statistics [33] makes it possible to solve the identification problem for the distribution function in the *m*-alternative version. For this purpose, we must consider the space of empirical statistics and introduce a certain probabilistic or information distance and (if possible) a metric into this space [28, 33]. Then, the corresponding criteria for the verification of hypotheses which solve the problem of statistics classification are formulated [11]. The adequacy criterion is based on the closeness of the linear approximation in the above-indicated coordinates. If we manage to identify the class of statistics at the corresponding confidence level, we can further use the standard moments method of parametrization of the W statistics [11, 27].

(3) A higher level of statistical treatment of NBIF corresponds to correlation analysis of the stochastic flows [14, 16, 29, 30]. Stochastic flows are treated in terms of amplitudes, and the sign interpolation is constructed. The obtained NBIF realizations are subjected to correlation analysis. Subsequently, the autocorrelograms themselves are subjected to consecutive adaptive Hilbert filtration (CAHF) [7, 10, 16]. The obtained spectrum of the NBIF correlation function zeros is the final result of the processing.

3. RESULTS AND DISCUSSION

(1) In the statistical kinetics of processes of structural relaxation of AFs, the establishment of dependences at the level of first and second moments of the NBIF empirical distribution is a simple procedure (Fig. 2a). In order to identify the mesostructural relaxation of the network structure of an AF, it is convenient to go over to the reduced $\mu/\sigma(t_T)$ representation (Fig. 2b) of the (μ, σ) phase plane (Fig. 2d). The stochasticity radius $r_H(t_T)$ is shown in Fig. 2c. The results of statistical analysis (Figs. 2a, 2b) will be considered simultaneously. At $t_T < t_T^* \sim 1$ h ($T = 175$°C), the one-dimensional distribution is slightly displaced into the long-wavelength (LW) region; the variance of the NBIF distribution does not change in this case. This is the effect produced by the low-temperature isothermal annealing on the network mesostructures of Co–Ni–P AFs at the first stage, which preserves the electron halo diffraction pattern typical of the amorphous state [4, 5, 10]. From the point of view of a mesostructural network

level, the meshes slightly grow (by 13% on the average) at the first stage of low-temperature annealing but the degree of stochasticity remains unchanged. The displacement of the global mode towards the LW region is comparatively small, because the network, which is an integral object of the system, suppresses the processes of mesh-size differentiation. Figure 2c confirms our interpretation, because $r_H(t_T) \cong 8$ nm remains completely unchanged. The first stage of low-temperature annealing does not change the degree of ordering, i.e., the stochasticity of the network hierarchy [34]. The meshes have grown only slightly on the average, and the network mesostructure has not been destroyed.

Let us now consider the second stage of low-temperature annealing at the same level of description. Apparently, the mechanisms of network kinetics change for $t_T \geq t_T^* \sim 1$ h at $T = 175$°C. The results (Figs. 2a, 2b, 2d) indicate that the one-dimensional NBIF distribution function is now displaced towards the short-wavelength (SW) region and $|\Delta\sigma| \sim 20\%$. The NBIF distribution is displaced to the SW region and becomes narrower: its variance decreases considerably. An important feature of this annealing stage is that the translation of the NBIF distribution to the SW region is isomorphous. The integrity of the network system and the amorphous nature of the halo diffraction pattern are preserved in this case [5, 10].

The correlation field (Fig. 2d) is characterized on the average by a linear regression, but its fine structure also displays the two-stage mode of annealing of Co–Ni–P AFs. The first stage indicates that the NBIF distribution is displaced to the LW region and the correlation field is slightly blurred. The second stage is characterized by a hard linear regression with a synchronous decrease in moments μ and σ^2. This stage of thermal kinetics obeys the similarity principle [22, 24].

The network structure of a Co–Ni–P AF subjected to low-temperature annealing behaves concertedly (cooperatively), its organization being not only preserved but even improved (Figs. 2c, 2d). This is a purely synergetic effect [31, 32, 35].

(2) The central aspect in problems of statistical kinetics of mesostructural relaxation in AFs is the identification of the analytical form of the one-dimensional distribution function over empirical data. We solved the multialternative problem of identification of the NBIF distribution function by proposing four feasible statistics classes (Norm, χ, Γ, and Weibull). For this purpose, a space of statistics was formed into which information or divergence measures of closeness (similarity) were introduced [10, 11, 16, 33]. In these terms, the criteria for verifying statistical hypotheses in the *m*-alternative situation were formulated [33]. As in [11], we had to disregard the Norm, χ, and Γ hypotheses. It was found that the *W* distribution in Eq. (3) is the closest to the empirical statistics [11, 32]. Figure 3 presents the linearized dependence of the NBIF statistics in the

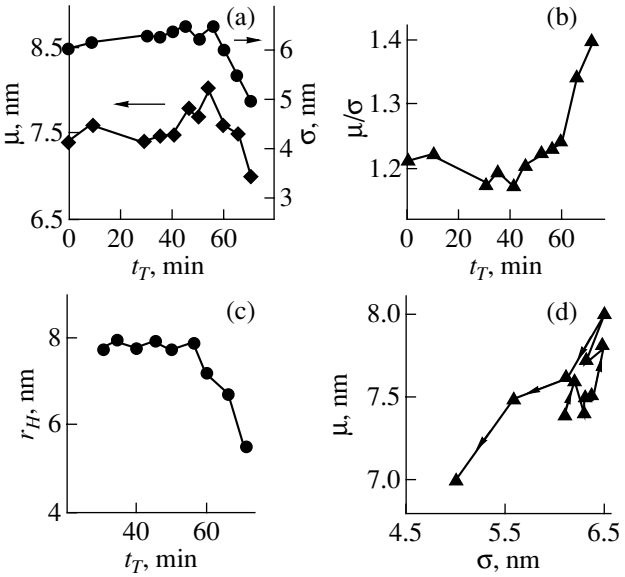

Fig. 2. (a) First two moments of the empirical NBIF statistics [the mathematical expectation $\mu(t_T)$ and the standard deviation $\sigma(t_T)$ of a Co–Ni–P amorphous film subjected to isothermal annealing ($T = 175$°C)]; (b) kinetic dependence of the normalized first moment; (c) kinetic dependence of the stochasticity radius of the NBIF statistics entropy as a function of the upper limit, and (d) the correlation field of the NBIF statistics at the level of the first two moments.

$\{\log(x), \log H[R^{-1}(x)]\}$ coordinates, where $H[R^{-1}(x)] = -\log R(x)$ and $R(x)$ is the reliability defined by Eq. (1). The two-component nature of the *W* statistics can be seen clearly in Fig. 3: two different (SW and LW) spatial scales are well pronounced. The kink between the two *W*-components corresponds to the region of the global mode in the empirical distributions (Fig. 3) that forms a 63% quantile ($\lambda^* \leq 5$ nm). The SW range corresponds to a stochastic wave structure (SWS) with a modulation labyrinth topology [10, 16]. According to our estimates [10], SWS corresponds to the region $2 \text{ nm} \leq \lambda \leq 5.5$ nm. The LW scale belongs to conventional network structures ($5 \text{ nm} \leq \lambda \leq 30$–$40$ nm) for the wavelength range covered in our experiments [7, 9].

In the problems of statistical kinetics (especially in the flow representation [11, 12, 14, 32]), the space of sizes (mesh cross sections of the general form) plays the major role. Histograms as sampling estimates of the *W* statistics are strongly asymmetric (Fig. 3); they are extended on the right-hand side of the global mode and fall off according to a power (hyperbolic) law with fractional exponents. This is indicative of the long range of network mesostructures in Co–Ni–P AFs [4, 7, 8, 22, 36].

The parametrization of the *W* representation in Eq. (3) was carried out using the moments method [27], which makes it possible to estimate two parameters (α and λ). The dimensionality α is defined as the deriva-

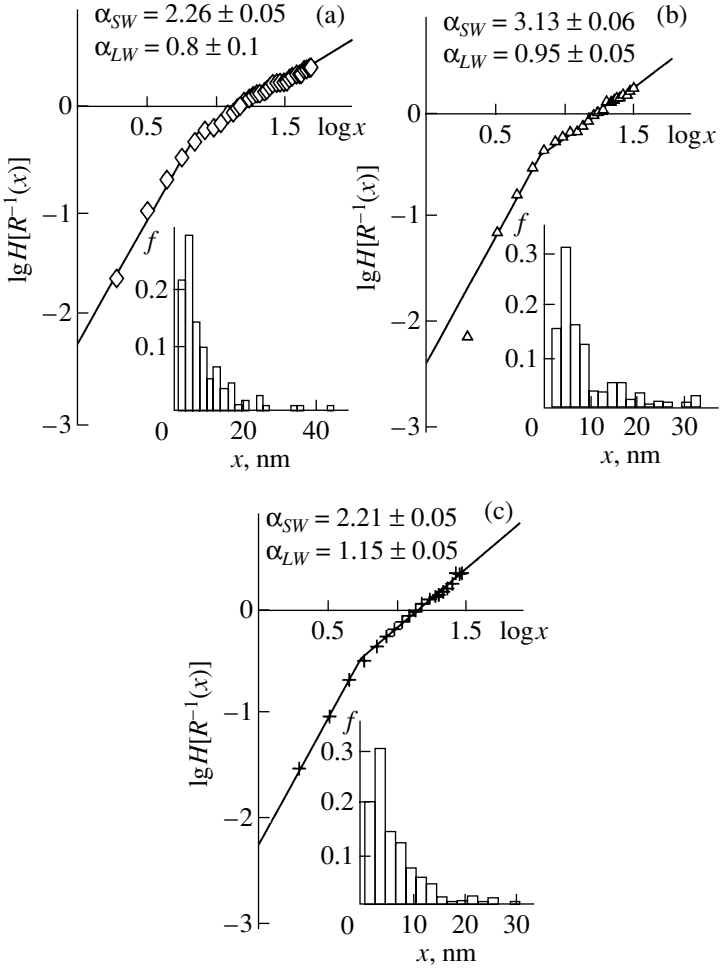

Fig. 3. Linearized Weibull statistics in the log–log coordinates for the one-dimensional NBIF statistics of Co–Ni–P amorphous films: (a–c) Weibull statistics for three different values of the annealing time t_T = 35, 55, and 70 min, respectively. Histograms of the distributions of network boundary intersections are given for the same values of the annealing parameters.

tive of the logarithm of the NBIF reliability entropy in the $R(q)$ space of inhomogeneities (the sizes of mesh cross sections). The ratio of the entropy action to the geometrical entropy for the size space is the fractal dimension in itself [35–38]. This is precisely the theoretical informative meaning of the parameter α for the W statistics in Eq. (3) [11, 31].

Figure 4 illustrates the thermal kinetics of the dimension α for each component of the network structure. The LW component is a weak linear function of t_T and $\alpha_{LW}(t_T) \sim 1$ on the average, while the SW component is characterized by a much higher dimension: $2.3 \le \alpha_{SW}(t_T) \le 3.1$, the peak being attained for $t_T^* \sim 1$ h as in the (μ, σ) approximation.

(3) A deeper level of statistical kinetic investigation corresponds to a spectral or correlation representation [16, 29, 30, 32]. One of the selected NBIF correlation functions is presented in Fig. 5a. As usual, the stochastic component prevails in the zero-asymptotic form (Fig. 5b), while the oscillatory component is manifested for large spatial displacements [29, 30]. The operation that separates these components is known as filtration [10, 16, 29, 30, 39] and will be used by us here not for flow realizations but for the correlation functions. The stochastic NBIF component in the correlation function (Fig. 5b) is nearly linear: it exhibits a weak quadratic dependence. Usually, the correlation radius of spatial stochasticity is introduced; its kinetic dependence $r_{cor}(t_T)$ is shown in Fig. 5c. It can be seen from this figure that in the case of 30-min isothermal annealing (T = 175°C), $r_{cor}(t_T \cong 30 \text{ min}) = 20$ nm; this is followed by a clearly manifested minimum for $r_{cor}(t_T \sim 1 \text{ h}) = 13$ nm and then by an insignificant increase in the value of r_{cor}. It can be concluded that $t_T^* \sim 1$ h is the characteristic time over which the extent of ordering [34] of the network mesostructure of Co–Ni–P AFs increases. Figures 6a–6c display the spectra of the correlation function zeros for the annealing times indicated above after the CAHF procedure [10, 13, 16, 39].

It is convenient to carry out the subsequent analysis using the entropy functionals [28] of the zero spectrum. Figure 6 shows the estimates of the entropy functionals [28] for the three annealing times indicated above in the case when the components are not separated, as well as for the high-frequency and low-frequency components. It can be seen that the behavior of the entropy in the case with unseparated components has a minimum at $t_T \sim 1$ h. The structural relaxation over the zero spectrum apparently improves the organization of the network hierarchy on the whole over such periods of time at $T = 175$°C [32]. The application of CAHF considerably enhances the difference between the components. The entropy has a clearly manifested minimum on the SW scale in the range of $t_T \leq 1$ h, while on the LW scale of network kinetics, the entropy increases monotonically, remaining, on the average, close to the value corresponding to a uniform distribution [29, 30]. This means that the first stage of low-temperature isothermal annealing facilitates the formation of a higher degree of ordering only on the SW scale. The LW components possess a stable white-spectral disorder at both annealing stages [29, 30, 34]. It can be stated that the conditions of isothermal annealing chosen by us for Co–Ni–P AFs lead to uniform (on the average) size spectra, which emphasize the conservative nature of the LW range of the network hierarchy in structural relaxation processes. The estimates indicative of the white spectrum [34] for LW-scale networks rule out the subsequent evolution of such networks. In fact, strongly frustrated network structures were obtained even during the preparation of Co–Ni–P AFs.

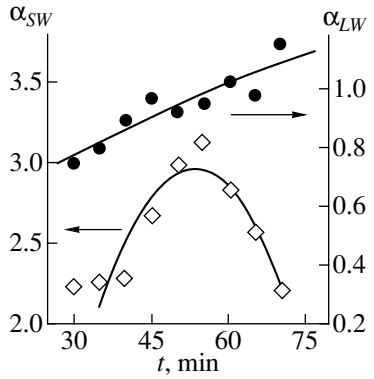

Fig. 4. Kinetic dependences of the dimensionalities $\alpha_{SW, LW}$ for Weibull statistics on two spatial scales (2–5 nm for the SW scale and 5–40 nm for LW) of the network structures of Co–Ni–P amorphous films.

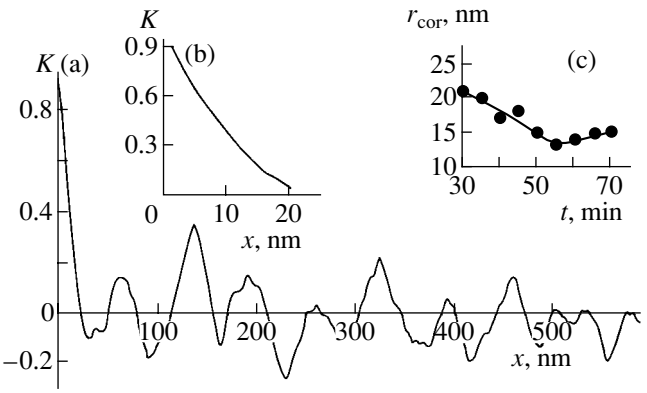

Fig. 5. (a) Sample estimate of the NBIF autocorrelation function for Co–Ni–P amorphous films; (b) correlation function of the stochastic component of network mesodefects; and (c) kinetic dependence of the correlation radius in the course of isothermal annealing at low temperatures.

In our research, we can single out three main results which significantly change the classical concepts of structural relaxation processes in amorphous media [20]. Usually, the concept of the relaxation time spectrum is employed, which naturally presumes exponential dependences, for example, for the diffusion coefficient in amorphous media. In [20, Chapter 24], the role of diffusion in amorphous media is considered and the generally accepted idea of the "corresponding forms of cooperative motion of a group of neighboring atoms" is formulated. On the basis of the data presented in [20, Table 24.1], Savchuk [12] constructed a correlation dependence between the preexponential factor $D_0 = \exp(S_0/k)$ and the activation energy Q. It turns out that linear regression holds at a sufficiently high confidence level. This means that diffusion-controlled structural relaxation processes have the invariant $S_0/kQ = \text{inv}$, indicating a certain thermodynamic similarity [22, 24]. The residual configurational entropy of glasses is considered in [40]. The problem of the preexponential factor, which varies, according to Cantor and Cahn [20], over 20 orders of magnitude, is also worth mentioning. The amorphous state which is obtained using various nonstationary techniques (e.g., fast cooling) is strongly degenerate in the configuration space of atomic clusters of various dimensionalities [22, 31, 40]. The entropy invariant indicates that the structure of the configurational space possesses a fractal property [31, 35, 38]. In one of our results on the classification of NBIF statistics, precisely the Weibull statistics was identified. This statistics is a more general version of the exponential distribution and is known as the Kohlrausch–Williams–Watts distribution [36]. Even this result shows that the early stages of structural relaxation processes in AFs are characterized by a certain long-range interaction [4, 10]. In all probability, the concept of the relaxation time spectrum in this case has to be extended to cover time scales that correspond to various spatial scales [4, 6]. According to [35, 36, 38], fractality is estimated from different types of dimensionality, among which correlation information dimensionalities play a certain role. In our case [11, 31], such characteristics are α dimensionalities for separated scales of LW and SW mesostructures (Fig. 4). Thus, the structural relaxation in AFs in the initial mild form should be attributed to fractal

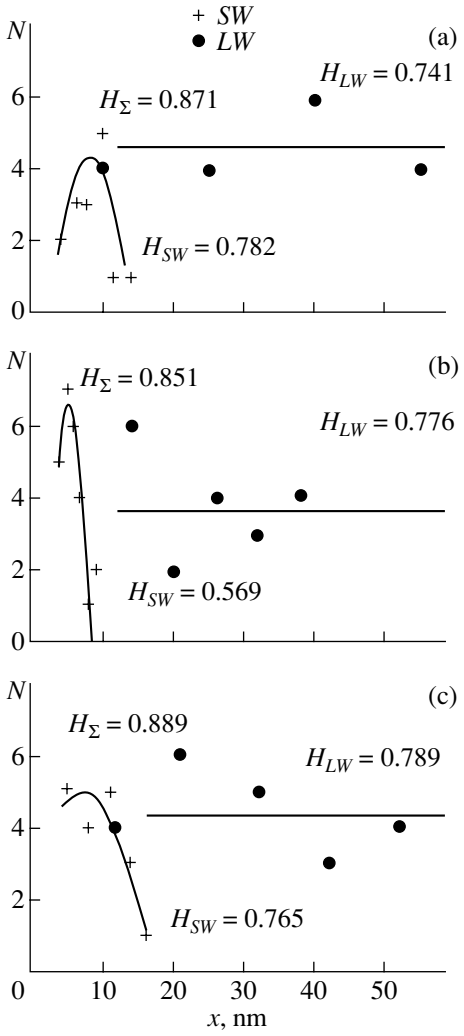

Fig. 6. Zero spectra of the NBIF autocorrelation functions of Co–Ni–P amorphous films subjected to low-temperature annealing after CAHF for SW and LW scales for three different annealing times: t_T = (a) 35, (b) 55, and (c) 70 min. H_Σ, H_{SW}, and H_{LW} are the total entropy without separation of components and the entropies of the correlation function zeros for the SW and LW scales, respectively.

kinetic processes. Structural relaxation occurs simultaneously on the SW and LW scales in spaces with different dimensionalities. From this point of view, destruction and amorphization should be regarded as processes occurring in spaces with continuously varying dimensionality [22, 35]. Another specific feature of thermal structural relaxation in Co–Ni–P AFs on the mesoscopic scale is the emergence of ordering in the SWS at least at the early stages of structural evolution in AFs (Figs. 2, 5c, 6). This is a typically synergetic feature [35, 38], indicating that structural relaxation is not merely the process of transition to the equilibrium state [22]. In this respect, the concept of space–time evolution [22] is more appropriate to the kinetic description. This evolution is not confined to the degradation branch in the structural morphology. Finally, it should be emphasized that the synergetic nature of structural evolution is manifested only on the mesoscopic level, while physical kinetics on the atomic level remains traditional (Brownian movement, diffusion, etc.).

Thus, the network relaxation of Co–Ni–P AFs under thermal actions used by us is structurally selective on various scales of spatial inhomogeneities [10, 13, 16, 32]. An amorphous film is, on the whole, a system that is stable to thermal effects up until the entropy of zeros of the correlation function attains the value $H_{\max} \sim 0.9$. It should also be noted that mesostructures on SW scales are more dynamic, which ensures a comparatively high thermal stability. The network structures of the Co–Ni–P AFs under investigation form a hierarchic system in which interaction between its different levels may be a source of AF stability [6, 10, 12, 13, 16, 32]. This result leads to the hypothesis that the evolution of a Co–Ni–P amorphous film without disruption of its amorphous structure and macroscopic continuity occurs as long as the film can compensate for the changes on the SWS level. When the zero spectrum attains the entropy maximum on the SW scale and, accordingly, the entropy of the LW component attains its maximum value, the degradation processes associated with the disruption of the amorphous structure and macroscopic continuity of the AF start to dominate in the medium on the whole [6–10, 16, 32]. If low-entropy network structures could be obtained using the corresponding technology of obtaining AFs with a mature hierarchy of networks, the stability of such AFs would be quite high on the macroscopic level. Such AFs with low-entropy networks would also be stabler against the effects of nonthermal origin.

4. CONCLUSIONS

We can now formulate the following conclusions.

(1) The kinetics of the network structure of a Co–Ni–P AF subjected to low-temperature isothermal annealing at T = 175°C at the level of the first and second moments of the NBIF distribution function indicates that the network is adaptable and that its organization does not deteriorate but actually improves. The process of structural relaxation can be divided into two stages even from an analysis of the behavior of μ and σ. For $t_T \sim t_T^* \sim 1$ h, the network meshes slightly grow; their size distribution is slightly displaced towards larger sizes, but the variance remains virtually unchanged. The second stage is characterized by a concerted decrease in μ and σ, which ensures isomorphic translation of the NBIF distribution to the SW region.

(2) It was found that the network structure of a Co–Ni–P AF has SW and LW components belonging to the reciprocal $R(q)$ space with completely different dimensionalities. The DW component of the network structure is a weak function of t_T, while the exponent $\alpha_{LW}(t_T) \sim 1$ on the average. On the other hand, the SW

component is characterized by a much higher dimensionality, $2.3 \le \alpha_{SW}(t_T) \le 3.1$, the exponent α being maximum for an annealing time of ~1 h.

(3) The stochastic components of the NBIF correlation functions of network mesodefects in a Co–Ni–P AF have a weak nonlinearity in the region of 3–20 nm. The kinetic dependence of the correlation radius of the stochastic component in the vicinity of $t_T \sim 1$ h also has a minimum (~13 nm). This indicates a reduction of the stochasticity region in the relaxed amorphous state.

(4) An AF should be regarded at the mesoscopic level as a hierarchic system whose spatial levels (LW and SW components) exhibit completely different behavior in structural relaxation processes. It was noted, for example, that Co–Ni–P AFs have stable amorphous ordering on the atomic scale (halo diffraction patterns) for the annealing parameters at hand. Such an amorphous stability can be ensured only by the ordering of the network hierarchy on the mesoscopic level.

(5) The results of physical and numerical experiments proved that the network component of the system of mesodefects in an AF exhibit a white spectrum of the correlation function zeros. Obviously, structural inhomogeneities cannot evolve in the structural relaxation processes in any other statistics of stationary states in view of the equal probabilities of zero spectra. The equally probable distribution in the zero spectrum of the correlation function only becomes more dominant during annealing. Thus, the structure at the network level (10–60 nm) cannot compensate for the changes that occur during dissipative processes, because it has exhausted its potentialities at the stage of preparation of the Co–Ni–P AF.

(6) The SWS component (2–5 nm) manifests itself in a completely different way in the process of structural relaxation of the amorphous state. It is characterized by a narrow distribution with a low entropy of the zero spectrum. However, the main point here is that the SW component even experiences ordering for $t_T \le 1$ h, which gradually dissipates at later stages. In our opinion, it is the SWS level that preserves, to a certain extent, the amorphous disorder on the atomic scale. Until the zero spectrum of the correlation function of subnetworks becomes white on the whole, the entire film will preserve its amorphous state.

REFERENCES

1. H. J. Leamy, G. H. Gilmer, and A. G. Dirks, in *Current Topics in Materials Science*, Ed. by E. Kaldis (North-Holland, Amsterdam, 1979, 1980; Mir, Moscow, 1983), Vols. 5, 6.
2. J. C. Phillips, Phys. Today, No. 2, 27 (1982).
3. K. Handrich and S. Kobe, *Amorphe Ferro- und Ferrimagnetika* (Akademie, Berlin, 1980; Mir, Moscow, 1982).
4. V. V. Yudin, E. I. Rudik, A. V. Matokhin, *et al.*, Fiz. Tverd. Tela (Leningrad) **24** (2), 443 (1982) [Sov. Phys. Solid State **24**, 250 (1982)].
5. V. V. Yudin, G. P. Timakova, A. V. Matokhin, *et al.*, Fiz. Tverd. Tela (Leningrad) **25** (7), 1953 (1983) [Sov. Phys. Solid State **25**, 1127 (1983)].
6. V. V. Yudin, A. G. Alekseev, T. A. Verkhovskaya, *et al.*, Poverkhnost, No. 8, 97 (1984).
7. V. V. Yudin, V. S. Plotnikov, A. V. Matokhin, and L. A. Yudina, in *Proceedings of the 8th European Congress on Electron Microscopy, Budapest, 1984*, Vol. 2, p. 905.
8. V. V. Yudin, in *Digest of the International Symposium on Magnetics of Amorphous Materials, Balatonszeplak, Hungary, 1985*, p. 174.
9. V. V. Yudin, A. V. Matokhin, V. S. Plotnikov, *et al.*, Poverkhnost, No. 12, 54 (1985).
10. V. V. Yudin, Author's Abstract of Doctoral Dissertation (Inst. Fiz. Sib. Otd. Akad. Nauk SSSR, Krasnoyarsk, 1987).
11. V. V. Yudin, T. A. Pisarenko, E. A. Lyubchenko, and E. G. Savchuk, Kristallografiya **44** (3), 413 (1999) [Crystallogr. Rep. **44**, 373 (1999)].
12. E. G. Savchuk, Author's Abstract of Candidate's Dissertation (IAPU Dal'nevost. Otd. Ross. Akad. Nauk, Vladivostok, 1991).
13. N. I. Chukhriĭ, V. V. Yudin, A. M. Frolov, and L. A. Yudina, Poverkhnost, No. 4, 56 (1999).
14. D. Cox and P. Lewis, *The Statistical Analysis of Series of Events* (London, 1966; Mir, Moscow, 1969).
15. E. L. Kuleshov and V. V. Yudin, Izv. Akad. Nauk SSSR, Tekh. Kibern., No. 3, 148 (1979).
16. V. V. Yudin, *Stochastic Magnetic Structure of Films with Microporous System* (Nauka, Moscow, 1987).
17. V. K. Fishchenko, Author's Abstract of Candidate's Dissertation (IAPU Dal'nevost. Otd. Ross. Akad. Nauk, Vladivostok, 1995).
18. J. M. Cowley, *Diffraction Physics* (Elsevier, New York, 1975; Mir, Moscow, 1979).
19. *Modern Electron Microscopy in Matter Research*, Ed. by B. B. Zvyagin (Nauka, Moscow, 1982).
20. *Amorphous Metallic Alloys*, Ed. by F. E. Luborsky (Butterworth, London, 1983; Metallurgiya, Moscow, 1987).
21. A. V. Matokhin, Author's Abstract of Candidate's Dissertation (Inst. Fiz. Sib. Otd. Akad. Nauk SSSR, Krasnoyarsk, 1984).
22. A. N. Olemskoĭ and I. V. Koplyk, Usp. Fiz. Nauk **165** (10), 1105 (1995) [Phys. Usp. **38**, 1061 (1995)].
23. É. P. Fel'dman, V. M. Yurchenko, and T. N. Mel'nik, in *Proceedings of the 7th All-Russia Conference "Amorphous Precision Alloys: Technology–Properties–Application," Moscow, 2000*, p. 42.
24. L. I. Stefanovich, Author's Abstract of Doctoral Dissertation (Fiz.-Tekh. Inst. Nats. Akad. Nauk Ukrainy, Donetsk, 1999).
25. P. B. Hirsch, A. Howie, R. B. Nicholson, D. W. Pashley, and M. J. Whelan, *Electron Microscopy of Thin Crystals* (Plenum, New York, 1965; Mir, Moscow, 1968).
26. G. Schimmel, Elektronenmikroskopische Methodik (Springer, Heidelberg, 1969; Mir, Moscow, 1972).

27. *Handbook of Theory of Probability and Mathematical Statistics*, Ed. by V. S. Korolyuk, N. I. Portenko, A. V. Skorokhod, and A. F. Turbin (Nauka, Moscow, 1985).
28. R. L. Stratonovich, *Information Theory* (Sov. Radio, Moscow, 1975).
29. G. Jenkins and D. Watts, *Spectral Analysis and Its Applications* (Holden-Day, San Francisco, 1966; Mir, Moscow, 1971), Vol. 1.
30. M. G. Kendall and A. Stuart, *The Advanced Theory of Statistics*, Vol. 3, *Design and Analysis, and Time Series* (Griffin, London, 1966; Nauka, Moscow, 1976).
31. T. A. Pisarenko, Author's Abstract of Candidate's Dissertation (Dal'nevost. Gos. Univ., Vladivostok, 2000).
32. S. A. Shchegoleva, Author's Abstract of Candidate's Dissertation (Dal'nevost. Gos. Univ., Vladivostok, 2000).
33. V. M. Zolotorev, *Modern Theory of Summation of Independent Random Quantities* (Nauka, Moscow, 1986).
34. J. M. Ziman, *Models of Disorder: The Theoretical Physics of Homogeneously Disordered Systems* (Cambridge Univ. Press, Cambridge, 1979; Mir, Moscow, 1982).
35. T. S. Akhromeeva, S. P. Kurdyumov, G. G. Malinetskiĭ, and A. A. Samarskiĭ, *Nonstationary Structures and Diffusion Chaos* (Nauka, Moscow, 1992).
36. *Fractals in Physics*, Ed. by L. Pietronero and E. Tosatti (North Holland, Amsterdam, 1986; Mir, Moscow, 1988).
37. V. V. Yudin and T. A. Pisarenko, in *Proceedings of the 1st International Workshop "Fractals and Applied Synergetics," Moscow, 1999*, p. 154.
38. *Chaotic Systems*, Special Issue of Proc. IEEE **75** (8) (1987).
39. V. V. Yudin, E. I. Makogina, S. V. Dolzhikov, and N. I. Chuckry, in *Proceedings of the 8th European Congress on Electron Microscopy, Budapest, 1984*, Vol. 1, p. 277.
40. S. I. Stishov, Usp. Fiz. Nauk **154** (1), 93 (1988) [Sov. Phys. Usp. **31**, 52 (1988)].

Translated by N. Wadhwa

Physics of the Solid State, Vol. 43, No. 11, 2001, pp. 2083–2086. Translated from Fizika Tverdogo Tela, Vol. 43, No. 11, 2001, pp. 1999–2002.
Original Russian Text Copyright © 2001 by Vlasov.

DEFECTS, DISLOCATIONS, AND PHYSICS OF STRENGTH

Interaction of Point Defects with an Edge Dislocation in the Gradient Theory of Elasticity

N. M. Vlasov

State Research Institute, Luch Scientific–Industrial Joint Company, Podol'sk, Moscow oblast, 142100 Russia

e-mail: iifedik@podolsk.ru

Received February 27, 2001

Abstract—Interaction between a point defect and an edge dislocation is studied in the framework of the gradient theory of elasticity. The change in the energy of the system caused by a displacement of the point defect relative to the dislocation line is calculated. The results of the theoretical analysis are used to describe edge dislocation pinning by impurity atoms. © *2001 MAIK "Nauka/Interperiodica".*

According to the classical theory of elasticity, the interaction potential of an impurity atom with an edge dislocation has the form [1, 2]

$$V = -\beta\frac{\sin\theta}{r}, \quad \beta = \frac{\mu b(1+\nu)\delta v}{3\pi(1-\nu)}, \tag{1}$$

where r and θ are the polar coordinates ($0 \le \theta \le 2\pi$), μ is the shear modulus, ν is Poisson's ratio, b is the magnitude of the Burgers vector of the dislocation, and δv is the crystal volume change introduced by the impurity atom. If $\delta v > 0$ (the impurity atom increases the crystal volume), then the potential V is positive for $\pi \le \theta \le 2\pi$. In this case, the impurity atom is attracted to the dislocation region in which the dilatation is positive. In order to get rid of the divergence of the potential V at $r \longrightarrow 0$, it is usually assumed that the dislocation has a core a few interatomic distances in diameter. The contribution from the cores to the elastic energy in the vicinity of dislocations (for reasonable values of their density) is no more than 10%. Such models are adequate for use in solving various problems in solid state physics. It is inviting to apply the gradient theory of elasticity (GTE) to calculating the stress fields of structural imperfections. In the framework of this theory, simple expressions having clear physical interpretations have been derived for the stress fields of some structural defects [3–5]. The virtue of these expressions is that they have no singularities at the dislocation lines. The interaction potential between an impurity atom and a crystal imperfection also changes. Therefore, it is interesting to investigate how the modified interaction potential will affect the pinning of an edge dislocation by impurity atoms.

Using the stress tensor of an edge dislocation derived in the GTE [3–5], we can easily find the interaction potential:

$$V = \beta\left[-\frac{1}{r} + \frac{K_1\left(\frac{r}{\sqrt{c}}\right)}{\sqrt{c}}\right]\sin\theta, \tag{2}$$

where $K_1(x)$ is the modified first-order Bessel function of the second kind and $\sqrt{c}$ is the gradient coefficient. The value of this coefficient is chosen using physical arguments; for example, for an edge dislocation, $\sqrt{c} \approx \frac{a}{4}$, where a is the lattice parameter. At $r \longrightarrow 0$, $K_1\left(\frac{r}{\sqrt{c}}\right) \longrightarrow \frac{\sqrt{c}}{r}$ and, therefore, the potential V has no singularity at the origin. Mathematically, one should find a function which tends to $1/r$ as $r \longrightarrow 0$ and vanishes at infinity; in this case, the potential V will not be singular as $r \longrightarrow 0$. The virtue of the modified interaction potential is that the function mentioned above is derived in the GTE (which takes into account the second derivatives of the strain tensor in Hooke's law). It is necessary to stress that the model in which the interaction between an impurity atom and an edge dislocation is described in terms of the GTE does not involve the atomic crystal structure; the crystal is considered to be a continuum, a dislocation is represented as a dislocation line, and point defects (substitutional or interstitial impurity atoms) are treated as dilatation centers. This model consistently describes the interaction of impurity atoms with an edge dislocation in the region $0 \le r \le \frac{a}{4}$. Microscopic models based on the crystal lattice theory have nothing to do with this approach and will not be discussed here.

1063-7834/01/4311-2083$21.00 © 2001 MAIK "Nauka/Interperiodica"

Let a point defect be situated below the extra plane of an edge dislocation $\left(\theta = \frac{3\pi}{2}\right)$. In this case, the dimensionless interaction potential is given by (for an arbitrary value of the gradient coefficient)

$$\frac{V\sqrt{c}}{\beta} = \frac{1}{x} - K_1(x), \quad x = \frac{r}{\sqrt{c}}. \tag{3}$$

The point at which the potential $\frac{V\sqrt{c}}{\beta}$ has a maximum is given by a root to the transcendental equation:

$$K_0(x) + \frac{K_1(x)}{x} - \frac{1}{x^2} = 0, \tag{4}$$

where $K_0(x)$ and $K_1(x)$ are modified zero- and first-order Bessel functions of the second kind, respectively; these functions are tabulated in [6]. The root x_0 of Eq. (4) is roughly equal to 1.115. If $\sqrt{c} = \frac{a}{4}$, the V has a maximum at $\frac{r_0}{a} \approx 0.278$ and, therefore, the energy of the dislocation–point defect system is minimum. As the point defect is displaced toward or away from the dislocation, the energy of the system increases. Its increase (per unit length) due to a displacement of the point defect from its equilibrium position is given by

$$\frac{\Delta W\sqrt{c}}{L\beta} = \frac{1}{x_0} - K_1(x_0) - \frac{1}{x} + K_1(x). \tag{5}$$

Here, L indicates that the energy increase relates to a unit length along the dislocation line. If $x > x_0$, the energy of the system is increased and the point defect experiences a force directed toward its equilibrium position. In the case of $x < x_0$, the increase in energy and the restoring force are greater (for the same displacement of the defect). Mathematically, this occurs because the behavior of the Bessel function is different at large and small values of the argument. For $x > x_0$, the function $K_1(x)$ falls off exponentially and tends to zero at infinity, whereas for $x < x_0$, $K_1(x) \longrightarrow \frac{1}{x}$. In both cases ($x \longrightarrow 0$ and $x \longrightarrow \infty$), the overall increase in the energy of the system is the same and equals $\frac{1}{x_0} - K_1(x_0)$. However, the rate of increase in energy is different in these two limiting cases. Therefore, the restoring-force field is also asymmetric relative to the equilibrium position of the point defect near a dislocation line; more specifically, the point defect situated in the equilibrium position is much easier to move away from the dislocation than toward it. The restoring force acting on the point defect can be found as the derivative of the energy of the system (per unit length) with respect to the defect displacement:

$$\frac{F\sqrt{c}}{L\beta} = \frac{1}{x^2} - K_0(x) - \frac{K_1(x)}{x}. \tag{6}$$

At $x = x_0$, this expression vanishes, because x_0 is a solution to the transcendental equation (4). It can be shown that $\frac{F\sqrt{c}}{L\beta}$ passes through a maximum as x increases from x_0 to ∞ but $\frac{F\sqrt{c}}{L\beta}$ increases indefinitely as x decreases from x_0 to zero, because $K_0(x)$ has a logarithmic singularity at $x \longrightarrow 0$. Therefore, the point defect can be moved away from the dislocation line (if one applies a force strong enough to overcome the maximum restoring force), but it cannot be moved up to the dislocation line because the restoring force increases indefinitely (by a logarithmic law) as $x \longrightarrow 0$. These results were obtained using the GTE to calculate the stress field of the edge dislocation. The distance x_0 corresponds to the energy parameter of the dislocation core in the classical elasticity theory, which lies in the range between $b/3$ and $b/4$ (b is the magnitude of the dislocation Burgers vector) [7]. In the core, the binding energy between the point defect and the dislocation is significantly smaller than its maximum value. Therefore, point defects will move to the region of maximum interaction potential.

The expressions derived are illustrated in Fig. 1. The mutual arrangement of the point defect and the edge dislocation is shown in Fig. 1a. This configuration corresponds to the maximum value of the interaction potential (Fig. 1b). The dashed curve in Fig. 1b is the interaction potential in the classical elasticity theory (which corresponds to Eq. (3) with the function $K_1(x)$ discarded). It is seen that both dependences in Fig. 1b coincide for $x > 4$; this is because the Bessel functions exponentially decrease as their argument becomes large. A different situation takes place for small values of the dimensionless distance. As $r \longrightarrow 0$, the interaction potential tends to zero in the GTE but increases indefinitely in the classical theory. The energy of the system as a function of the position of the point defect is shown in Fig. 1c. This energy tends to the same value as $x \longrightarrow 0$ and $x \longrightarrow \infty$, so that the curve is asymmetric relative to the equilibrium position of the point defect. The variation of the restoring force acting on the defect is shown in Fig. 1d. The curve in Fig. 1d is highly asymmetric relative to the point $x = x_0$, and its behavior is qualitatively different in the regions $x > x_0$ and $x < x_0$. In the region $x > x_0$, the restoring force passes through a maximum, which corresponds to the inflection point on the curve of the energy of the system. In the range $x < x_0$, there is no maximum and the restoring force increases indefinitely as $x \longrightarrow 0$. The restoring force in

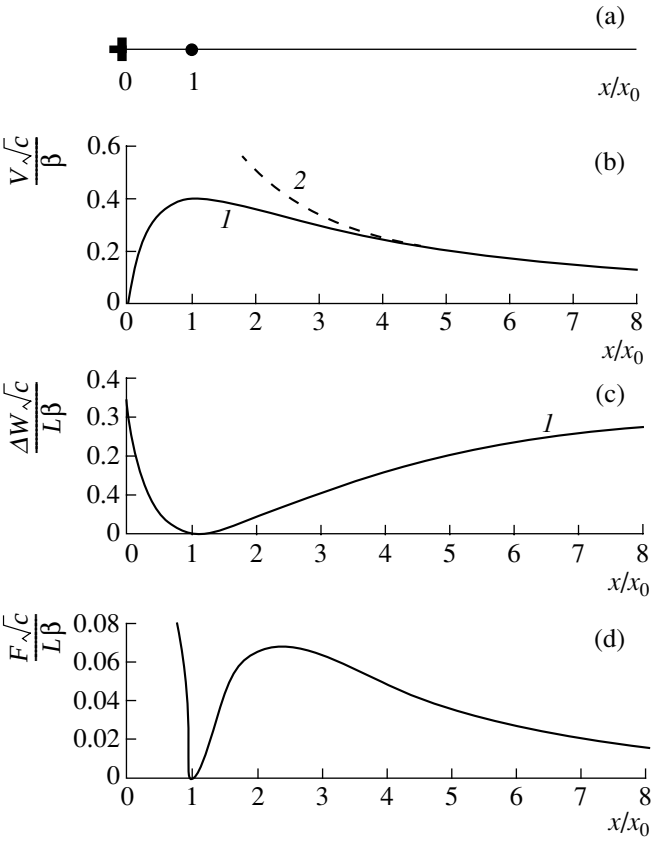

Fig. 1. Interaction between an edge dislocation and a point defect in the gradient theory of elasticity: (a) the mutual arrangement of the point defect and the edge dislocation, (b) the interaction potential between the point defect and the edge dislocation, (c) the dependence of the energy of the system on the point defect position, and (d) the restoring force acting on the point defect.

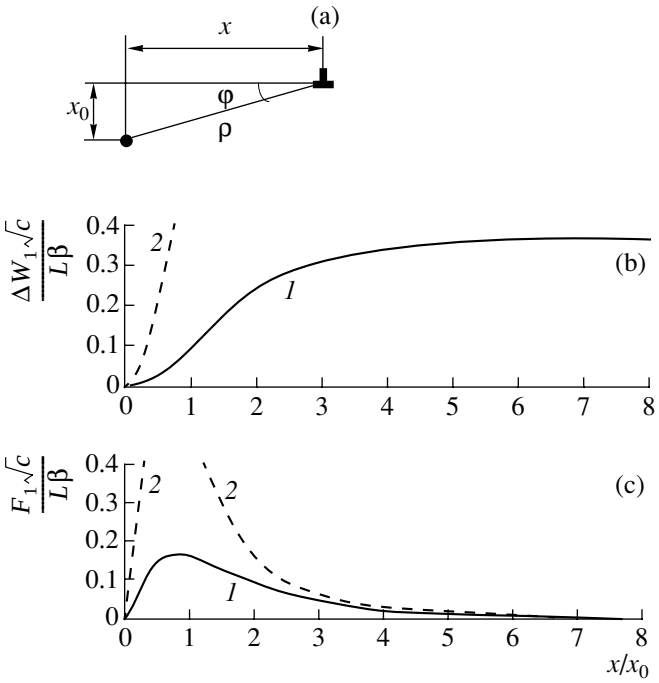

Fig. 2. Edge dislocation pinning by a point defect: (a) mutual arrangement of the point defect and the dislocation displaced from its equilibrium position, (b) energy of the system as a function of the dislocation displacement, and (c) pinning force exerted on the edge dislocation by the point defect; (*1*) is the gradient theory of elasticity and (*2*) is the classical elasticity theory.

the region $x > x_0$reaches its maximum value at $\frac{x}{x_0} \approx 2.4$, whereas in the region $x < x_0$, it reaches the same value at $\frac{x}{x_0} \approx 0.85$. Therefore, a small displacement of the point defect from its equilibrium position toward the dislocation line is sufficient for the restoring force to become as large as its maximum value in the range $x > x_0$. This means that point defects cannot reach a dislocation line, because interaction with it will drive them back to their equilibrium positions. It is reasonable to suggest that clusters of impurity atoms will be arranged in the region $x \geq x_0$ near an edge dislocation. Thus, the GTE supports the validity of the physical model of an edge dislocation with a core a few interatomic distances in diameter, which allows one to get rid of the singularity in the interaction potential. This model has been used to investigate edge dislocation pinning by an impurity atmosphere [8, 9].

Now, we consider pinning of an edge dislocation by impurity atoms in the framework of the GTE. An impurity atom (point defect) is assumed to be in its equilibrium position below the extra plane of an edge dislocation (Fig. 2a). If the dislocation moves, but the point defect is at rest, the energy of the system will increase. Its increase (per unit length) as a function of the dimensionless dislocation displacement is given by

$$\frac{\Delta W_1\sqrt{c}}{L\beta} = \left[\frac{1}{x_0} - K_1(x_0)\right]\sin\theta - \left[\frac{1}{\rho} - K_1(\rho)\right]\sin\varphi, \quad (7)$$

where $\rho = \sqrt{x^2 + x_0^2}$, $|\sin\theta| = 1$, $|\sin\varphi| = \frac{x_0}{\rho}$, and $x_0 = \frac{r_0}{\sqrt{c}}$. Using simple algebra, we obtain

$$\frac{\Delta W\sqrt{c}}{L\beta} = \frac{x^2}{x^2 + x_0^2} - K_1(x_0) + \frac{x_0 K_1(\sqrt{x^2 + x_0^2})}{\sqrt{x^2 + x_0^2}}. \quad (8)$$

The dependence of the dimensionless energy of the system on the displacement of the edge dislocation is shown in Fig. 2b. At the initial point, the defect was in equilibrium at the distance x_0 from the dislocation. As the dislocation moves, with the point defect being at rest, a restoring force will act on it. Therefore, the point

defect pins the edge dislocation. The pinning force equals the derivative of the energy of the system (per unit length) with respect to the dislocation displacement:

$$\frac{F_1\sqrt{c}}{L\beta} = \frac{2xx_0^2}{(x^2+x_0^2)^2} - \frac{xx_0}{x^2+x_0^2} \times \left[K_0(\sqrt{x^2+x_0^2}) + \frac{2K_1(\sqrt{x^2+x_0^2})}{\sqrt{x^2+x_0^2}}\right]. \quad (9)$$

This dependence is shown in Fig. 2c. For comparison, Figs. 2b and 2c (dashed lines) show the corresponding dependences given in accordance with the classical elasticity theory [Eqs. (8), (9) without the terms involving the Bessel functions]. It is seen that the curves differ quantitatively rather than qualitatively. This is also obvious from Eqs. (8) and (9). In the GTE, the increase in energy with dislocation displacement and the strength of dislocation pinning by an impurity atom are smaller than those in the classical elasticity theory. Therefore, the analysis of edge dislocation pinning by an impurity atom in terms of the GTE does not yield fundamentally new results. In essence, application of the GTE to the description of an edge dislocation is equivalent to the assumption that the dislocation has a core whose characteristic diameter depends on the gradient coefficient. This conclusion can be drawn immediately from the main result of the analysis performed in this paper: a point defect cannot make a close approach to a dislocation line, because the repulsive force increases indefinitely. For this reason, point defects are situated, as a rule, at a distance from a dislocation line (in their equilibrium positions). This distance corresponds to the energy parameter of the edge dislocation core in the classical elasticity theory.

REFERENCES

1. J. P. Hirth and J. Lothe, *Theory of Dislocations* (McGraw-Hill, New York, 1967; Atomizdat, Moscow, 1972).
2. K C. Teodosiu, *Elastic Models of Crystal Defects* (Springer, Berlin, 1982; Mir, Moscow, 1985).
3. M. E. Gutkin and E. S. Aĭfantis, Fiz. Tverd. Tela (St. Petersburg) **41** (12), 2158 (1999) [Phys. Solid State **41**, 1980 (1999)].
4. M. E. Gutkin, K. N. Mikaelyan, and E. S. Aĭfantis, Fiz. Tverd. Tela (St. Petersburg) **42** (9), 1606 (2000) [Phys. Solid State **42**, 1652 (2000)].
5. K. N. Mikaelyan, M. E. Gutkin, and E. S. Aĭfantis, Fiz. Tverd. Tela (St. Petersburg) **42** (9), 1613 (2000) [Phys. Solid State **42**, 1659 (2000)].
6. L. N. Karmazina and É. A. Chislova, *Tables of Bessel Functions of Imaginary Argument and Their Integrals* (Akad. Nauk SSSR, Moscow, 1958).
7. T. Suzuki, H. Yosinaga, and S. Takeucti, *Dislocation Dynamics and Plasticity* (Syokabo, Tokyo, 1986; Mir, Moscow, 1989).
8. N. M. Vlasov, Fiz. Met. Metalloved. **56** (3), 583 (1983).
9. N. M. Vlasov and V. A. Zaznoba, Fiz. Tverd. Tela (St. Petersburg) **41** (3), 451 (1999) [Phys. Solid State **41**, 404 (1999)].

Translated by Yu. Epifanov

Physics of the Solid State, Vol. 43, No. 11, 2001, pp. 2087–2093. Translated from Fizika Tverdogo Tela, Vol. 43, No. 11, 2001, pp. 2003–2009.
Original Russian Text Copyright © 2001 by Kardashev, Demenkov, Plaksin, V. Stepanov, P. Stepanov, Chernov.

DEFECTS, DISLOCATIONS, AND PHYSICS OF STRENGTH

Effect of Acoustic Strain on the Radiation-Induced Luminescence of Pyrolithic Boron Nitride

B. K. Kardashev*, P. V. Demenkov, O. A. Plaksin**, V. A. Stepanov**, P. A. Stepanov**, and V. M. Chernov****

**Ioffe Physicotechnical Institute, Russian Academy of Sciences, ul. Politekhnicheskaya 26, St. Petersburg, 194021 Russia*
e-mail: b.kardashev@pop.ioffe.rssi.ru

***Leĭpunskiĭ Institute of Physics and Power Engineering, pl. Bondarenko 1, Obninsk, Kaluga oblast, 249020 Russia*

Received April 11, 2001

Abstract—A study is reported on the effect of ultrasound vibrations of an approximate frequency of 100 kHz on the radiation-induced luminescence generated in pyrolytic boron nitride by proton irradiation (8 MeV energy, 1.6×10^{12} p/cm^2 s flux). The influence of ultrasound vibrations manifests itself at large strain amplitudes ($\sim 10^{-4}$), where nonlinear, amplitude-dependent absorption of ultrasound is observed to occur. The data obtained are assigned to a radiation-induced change in the recrystallization kinetics, where low-angle boundaries disappear (radiation annealing). © *2001 MAIK "Nauka/Interperiodica".*

1. INTRODUCTION

Radiation-induced luminescence (RIL) of ceramic dielectric materials is generated as a result of the relaxation of carriers formed by radiation in the conduction band. This results, as shown in [1, 2], in selective stimulation of diffusion at grain boundaries. The free electrons and holes produced under irradiation relax at structural defects (grain boundaries), thus increasing the diffusion hopping frequency of a lattice atom and an impurity atom by

$$\Delta\nu = \nu_0 n\tau, \quad (1)$$

where ν_0 is the natural atomic vibration frequency ($\sim 10^{13}$ s); n is the number of atom excitation events at a boundary per unit time or, in other words, the relaxation frequency of the radiation-produced carriers (this quantity is directly proportional to the irradiation dose rate $\dot{D}$); and τ is the characteristic atomic-vibration thermalization time (10^{-11}–10^{-12} s). This was verified for the case of partial recrystallization of pyrolytic boron nitride observed to occur under proton irradiation [2].

Pyrolytic boron nitride (BN) prepared through chemical vapor deposition is characterized by a well-developed system of grain boundaries [3, 4]. Aggregates up to 2000 nm in size are present and made up of grains with dimensions $R \sim 120$–180 nm and with wide boundaries. Inside the grains, there is a network of small cells with narrow boundaries (weakly misoriented crystallites) $r \sim 20$–40 nm in size. Irradiation with protons at a dose rate of $\sim 10^4$ Gy/s (8 MeV energy, 3×10^{12} p/cm^2 s flux level) gives rise to partial recrystallization, which involves the disappearance of the network of small cells representing low-angle boundaries. The frequency of diffusion hopping given by Eq. (1) was shown [2] to correspond to effective temperatures of 1450–1540 K. It is in this temperature interval that boron nitride-based materials recrystallize.

As pointed out in [2], the kinetics of radiation-induced BN recrystallization can be studied directly in the course of irradiation using the RIL method. This is made possible by the fact that the luminescence centers in materials based on graphitelike boron nitride form a quasi-continuous band in the band gap and are localized at low-angle boundaries [5]. As the irradiation dose increases, the RIL intensity undergoes an irreversible decrease caused by the decreasing density of the low-angle boundaries.

It is known, however, that radiation-induced changes in the microstructure can also affect other properties of materials, including acoustic properties. Such parameters as the elastic-vibration decrement and the elastic modulus measured in an acoustic experiment may increase noticeably or decrease with changing microstructure of the sample. The present study made use of an experimental technique based on simultaneous measurement of the RIL intensity and of the acoustomechanical properties (Young's modulus and the acoustic vibration decrement) of pyrolytic BN in the course of proton irradiation at different strain amplitudes. The experiment was motivated by the fact that large-amplitude ultrasound vibrations can noticeably affect recrystallization kinetics under conditions where the external vibrational load is comparable to the internal stress, whose level is known to depend on the presence of various defects, including grain boundaries, in the material.

The study was aimed primarily at revealing specific features in the recrystallization kinetics of boron nitride

acted upon simultaneously by proton irradiation and an oscillating mechanical load.

2. EXPERIMENTAL

This study was made on samples of pyrolytic boron nitride measuring $15 \times 3 \times 0.5$ mm with a total impurity content of no more than 5×10^{-3} wt %. The irradiation was accomplished using protons (8 MeV energy, flux level up to 1.6×10^{12} p/cm^2 s, dose rate up to 3×10^4 Gy/s) on an ÉGP-10M accelerator (RF SRC, PPI, Obninsk). The experiments were carried out in air under atmospheric pressure.

A resonant composite piezoelectric-oscillator technique was employed to measure the acoustomechanical properties (Young's modulus and the acoustical vibration decrement) and to produce an ultrasound strain in the sample. A quartz transducer was used to excite and gauge ultrasound vibrations in the sample under study. Boron nitride samples shaped as rectangular plates were pasted onto a transducer connected to a measuring circuit. The sample and the transducer make up a composite oscillator in which a standing acoustic wave is excited. The principle of operation of the composite oscillator and the block diagram of the setup are described in detail in [6]. The automated setup allows prompt and high-precision measurement of the resonant frequency and decrement of the composite oscillator. Knowing these parameters, the resonant frequency and the decrement of the quartz transducer, one can readily calculate Young's modulus E and the decrement δ of acoustic vibrations of the sample under study. The relevant relations can be found in [6].

The RIL kinetics was measured at a wavelength of 400 nm, which corresponds to the maximum of the RIL intensity in boron nitride [2]. A proton beam 1 cm in diameter hit the sample center at the standing-wave antinode (the amplitude maximum). The luminescence was focused by a condenser lens onto the entrance slit of a monochromator and was detected by a PM tube. The RIL and acoustic characteristics were measured at 1 s intervals during the whole experiment. A new sample was used in each measurement at a given amplitude, because irradiation changed the sample structure irreversibly. The measurements were performed at fixed (to within 2%) relative strain amplitudes ranging from 10^{-6} to 2.5×10^{-4}.

3. RESULTS OF THE MEASUREMENTS AND DISCUSSION

Figure 1 presents, as an illustrated example, the variation of the RIL intensity, vibration decrement δ, and Young's modulus E with time obtained for one of the BN samples in the course of irradiation. During the first ~100 s of irradiation, the Young's modulus and the acoustic vibration decrement are seen to change substantially. This is due primarily to the increase in sample temperature. Estimates of the temperature under proton irradiation based on the energy dissipation of ~1 W/cm^2, as well as temperature measurements made with attached thermocouples, showed that the sample temperature can increase up to 200°C. However, even after the temperature has stabilized, one observes, as a rule, a further smooth increase in the Young's modulus and a noticeable decrease in the acoustic vibration decrement. As the irradiation dose is increased, the RIL intensity also decreases irreversibly; this was mentioned previously.

Similar measurements were performed at various strain amplitudes ε: 10^{-6}, 2×10^{-6}, 5×10^{-5}, and 2.5×10^{-4}. An increase in ε entails, as a rule, an increase in the modulus and in the decrement variation rate. This is illustrated in Fig. 2, which presents, graphically, the relative variation of E and δ with increasing irradiation dose. The reference points E_0 and δ_0 are the values of the sample modulus and decrement at the start of the irradiation. As ε exceeds 5×10^{-5}, the slope of the curves measured at doses above 2×10^{15} p/cm^2 is seen to increase noticeably. At large ε, the rate of RIL intensity variation is also seen to increase. The properly treated RIL data are presented in Fig. 3.

The growth of the variation rate of the modulus and acoustic vibration decrement and the corresponding growth of the luminescence decay rate with increasing strain amplitude can apparently be related to the effect of acoustic vibrations on the rate of radiation-induced recrystallization. This effect can be caused by two factors. First, absorption of the acoustic vibration energy by structural defects (for instance, by grain boundaries) can increase atomic mobility and boundary migration velocity (similar to the selective increase in atomic diffusion initiated by the electron–hole relaxation of radiation-induced carriers at the boundaries). Second, strain is known to substantially affect the thermodynamic potential of grain boundaries, so that the recrystallization rate may grow under the application of an external load, i.e., as a result of an increasing driving force of recrystallization.

As for the first effect, a noticeable increase in the boundary mobility (compared to the radiation-induced process) can occur only in the case where the acoustic vibration energy dissipated in the volume of a boron nitride sample is comparable to the ionizing contribution of the proton irradiation. The specific absorbed energy of mechanical vibrations (per unit mass and unit time) is given by the expression

$$W^* = \nu^2 l^2 \delta \varepsilon^2, \qquad (2)$$

where ν is the vibration frequency (10^5 Hz), l is the sample length (~10^{-2} m), δ is the acoustic vibration decrement (~10^{-3}), and ε is the strain amplitude (~10^{-4}). The value $W^* \sim 1$ Gy/s estimated from Eq. (2) turns out to be much less than the dose rate ~3×10^3 Gy/s of the absorbed proton irradiation. A comparison shows that

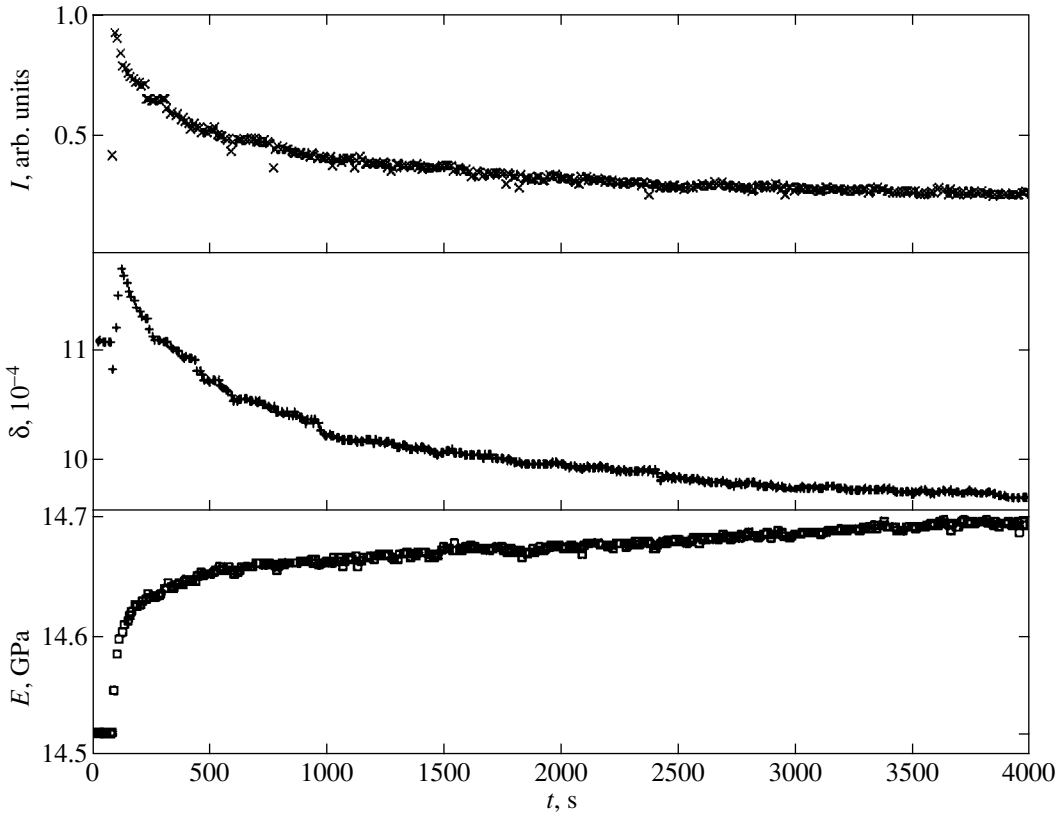

Fig. 1. Evolution of the RIL intensity I, acoustic vibration decrement δ, and Young's modulus E of boron nitride with time under proton irradiation (8 MeV energy, dose rate 1.6×10^{12} p/cm^2 s) at a relative strain amplitude $\varepsilon = 2.5 \times 10^{-4}$.

absorption of the acoustic vibration energy cannot bring about a noticeable rise in the recrystallization rate.

The force that drives the recrystallization is apparently the free energy excess associated with the existence of grain boundaries. The rate of recrystallization, i.e., the rate of increase in the area S of individual crystallites, is proportional to the surface density of the boundary energy [7]:

$$\dot{S} \sim \Delta Z, \tag{3}$$

where $\Delta Z = Gb$, G is the shear modulus, and **b** is the Burgers vector.

Equation (3) yields the well-known square root dependence of grain size variation with time. In the case of deformation, the external force (load per unit area) exerted on the boundary is $\sigma = E\varepsilon$; for the corresponding term added to the surface energy density, we obtain

$$\Delta Z_\varepsilon = E\varepsilon R. \tag{4}$$

ΔZ_ε is the work expended in displacing the boundary through a distance R. Thus, in the presence of an external load, the recrystallization kinetics is described by the relation

$$\dot{S} \sim (Gb + E\varepsilon R). \tag{5}$$

If one considers the process of partial recrystallization as a decrease in the density of low-angle boundaries absorbed by high-angle boundaries of larger grains, then R in Eq. (5) is the size of the largest grains inside which the area of small crystallites can be varied as $S \sim r^2$. Equation (5) can be used to derive a relation for the RIL intensity I, which is proportional to the density of grain boundaries (l/r). Because the recrystallization rate is proportional to the diffusion hopping frequency of atoms ($\dot{S} \sim \Delta\nu$) and, in accordance with Eq. (1), to the irradiation dose rate $\dot{D}$, integration of Eq. (5) yields the variation of RIL intensity with irradiation dose:

$$\frac{\dot{D}^2}{I^2} \sim (Gb + E\varepsilon R)\int \dot{D}dt. \tag{6}$$

Equation (6) was derived with due account of the fact that the RIL intensity is also proportional to the irradiation dose rate. Figure 3 presents the results of the RIL measurements at different strain amplitudes plotted as

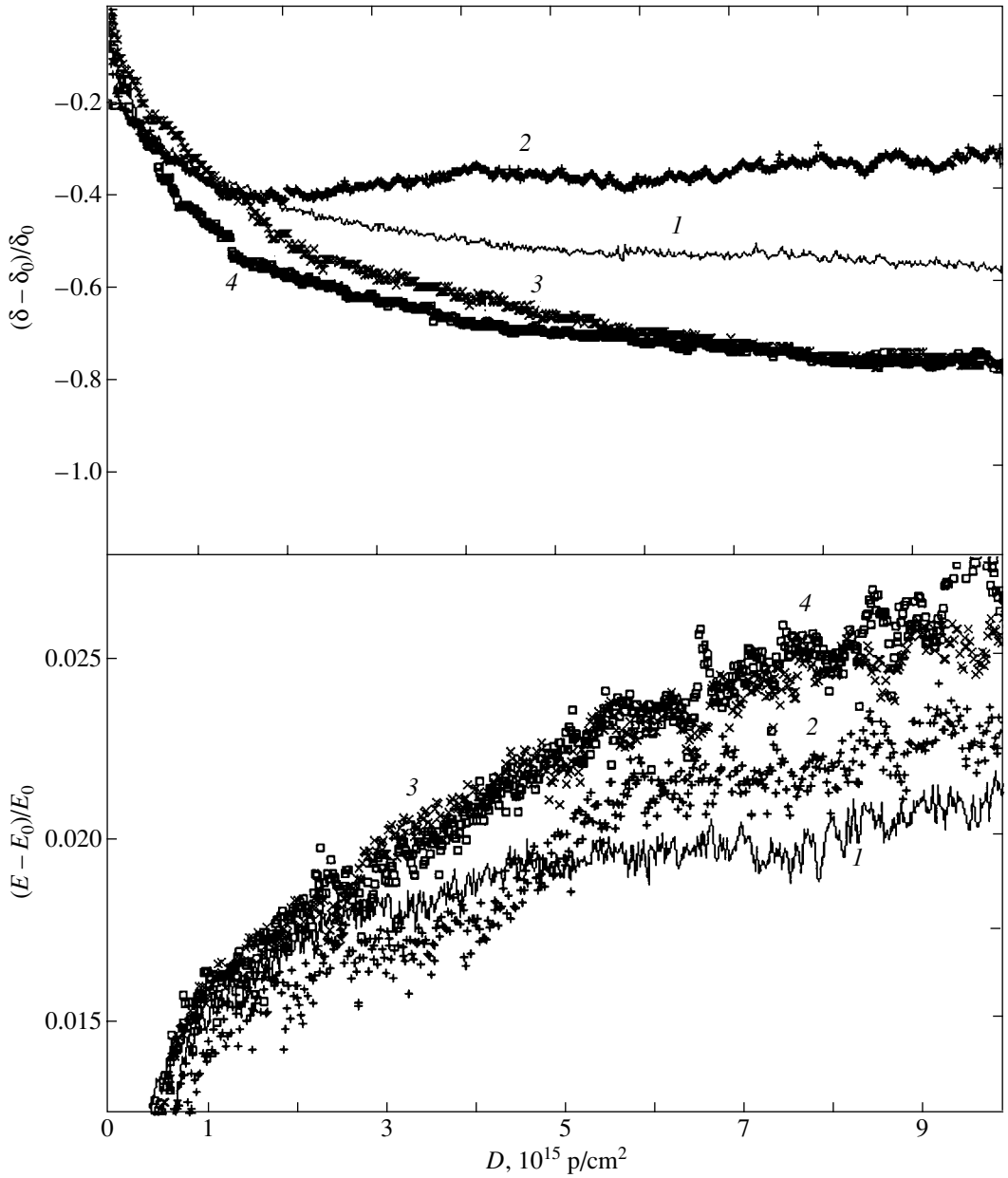

Fig. 2. Relative variations of the acoustic vibration decrement δ and Young's modulus E under proton irradiation measured at different values of the strain amplitude ε: (*1*) 1.0×10^{-6}, (*2*) 2.0×10^{-6}, (*3*) 5.0×10^{-5}, and (*4*) 2.5×10^{-4}.

$(\dot{D}/I)^2 - D$. The experimental relations are seen to be linear; this is in agreement with Eq. (6) (except for the data obtained at $\varepsilon = 5 \times 10^{-5}$). At a strain amplitude $\varepsilon = 2.5 \times 10^{-4}$, the slope is twice that seen in the absence of vibrations or at small strain amplitudes. According to Eq. (6), this increase occurs for $\varepsilon \sim b/R$, which is in agreement with the parameters of the real BN microstructure, for which $R \sim 10^2$–10^3 nm ($b \sim 10^{-1}$ nm). Our analysis shows that the effect of acoustic vibrations (the strain ε or stress $\sigma = E\varepsilon$) on the kinetics of radiation-induced recrystallization is indeed related to an increase in the thermodynamic potential of low-angle boundaries (provided their mobility is high).

However, the thermodynamic approach cannot take into account all the conditions under which an external oscillating mechanical load can affect the radiation-stimulated recrystallization kinetics. A careful analysis of the plots in Fig. 3 shows that, contrary to Eq. (6), there is no proportionality to ε; indeed, the relations measured at $\varepsilon = 0$, 1.0×10^{-6}, and 2.0×10^{-6} are practically indistinguishable from one another. Moreover, at $\varepsilon = 5.0 \times 10^{-5}$, the relation plotted in the coordinates of Fig. 3 is nonlinear: the luminescence intensity variation

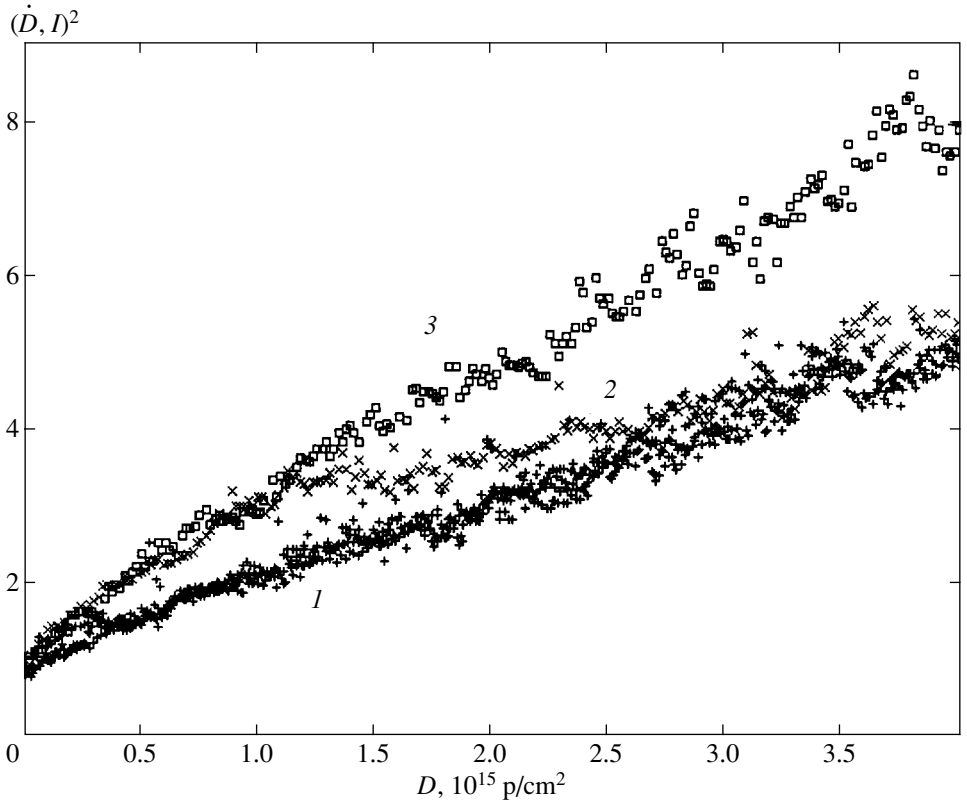

Fig. 3. Dependence of the boron nitride RIL intensity I on proton irradiation dose constructed as $(\dot{D}/I)^2$ vs. D for different values of the strain amplitude ε: (*1*) 0, 1.0×10^{-6}, and 2.0×10^{-6}; (*2*) 5.0×10^{-5}; and (*3*) 2.5×10^{-4}.

rate is high only at the very beginning of irradiation (almost as for $\varepsilon = 2.5 \times 10^{-4}$); as the dose continues to increase, it drops to the level corresponding to zero mechanical load or small strain amplitudes. Only for $\varepsilon = 2.5 \times 10^{-4}$ does the slope of the straight line in Fig. 3 increase by a factor of two, to remain constant thereafter up to high irradiation doses.

It is significant that the amplitude $\varepsilon = 2.5 \times 10^{-4}$ is in the region of nonlinear amplitude-dependent internal friction (ADIF), which is clearly seen from Fig. 4. According to Fig. 4, $\varepsilon = 5 \times 10^{-5}$ in the very beginning of the nonlinear region of ADIF. A large amplitude of mechanical stress (strain) in the ADIF region, at which linear defects (dislocations) making up low-angle boundaries are capable of moving considerable distances away from their equilibrium positions, is apparently an additional condition for mechanical vibrations to act efficiently on boron nitride recrystallization. Only under these conditions can mechanical vibrations favor annihilation of the low-angle boundaries formed from dislocations opposite in sign or assist their fast migration (during the vibration half-period ~10^{-5} s) toward the wide boundaries of larger grains.

Variations in the vibration decrement and in the Young's modulus do not lend themselves to description in terms of simple relations of the type of Eq. (6). Unlike the RIL, acoustomechanical properties may depend not only on the presence of low-angle boundaries in a material but also on other microstructural elements (slip planes [8] along (001), grain boundaries, growth cones, etc. [3, 4]), whose state and density may vary in the course of irradiation. This accounts for the more complex behavior of δ and E with irradiation dose. Figure 2 reveals the tendency of the δ and E variation rate to increase with increasing strain amplitude ε. However, this pattern also exhibits exclusions. For instance, after the decrement in a sample subjected to a strain of $\varepsilon = 2 \times 10^{-6}$ is decreased at the start of irradiation, it undergoes an increase at large doses. The pattern of the curves may obviously depend on specific features of the microstructure of each sample.

As with the decrease in the RIL intensity, the irreversible decrease in the amplitude-independent acoustic-vibration decrement (for small amplitudes) and the noticeable growth in the Young's modulus (Fig. 4) can be related to the irradiation-induced decrease in the concentration of low-angle boundaries, although one cannot exclude the possibility that other components of the microstructure on which the energy of the acoustic wave can be dissipated also play a certain role. The effect of low-angle boundaries on the absorption of acoustic vibration energy at a frequency of about

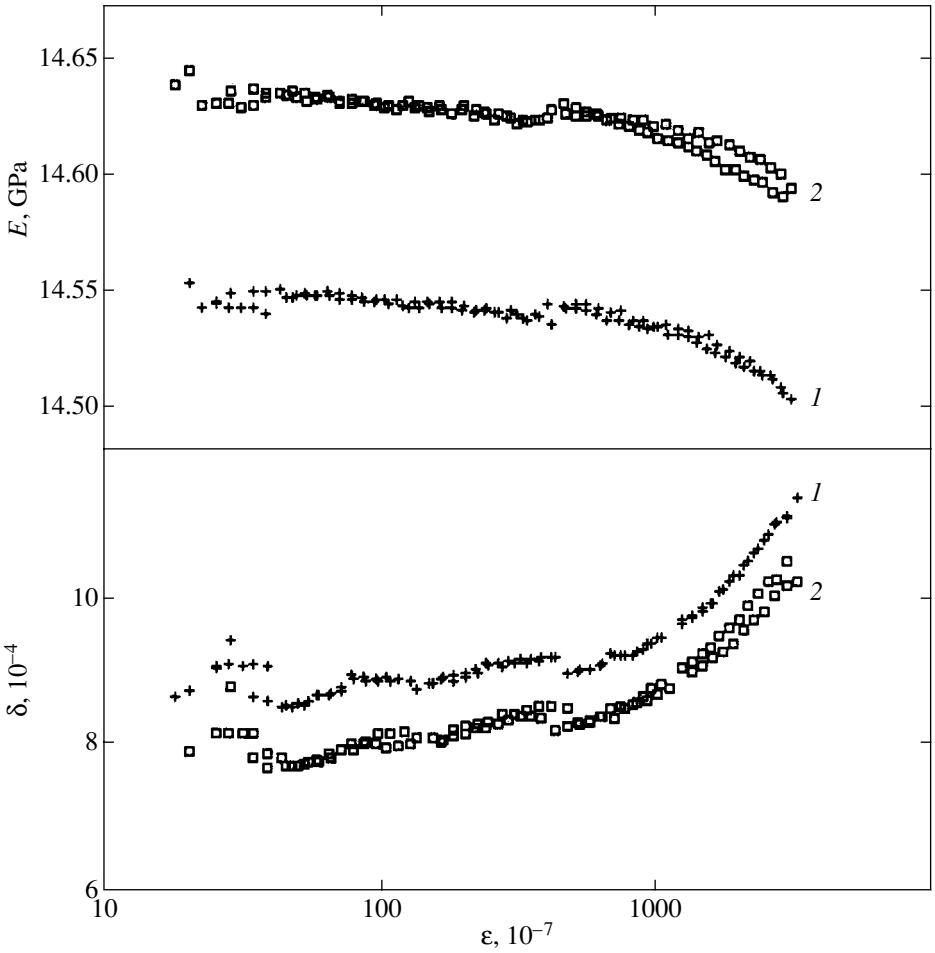

Fig. 4. Amplitude dependences of Young's modulus E and decrement δ (*1*) before and (*2*) after proton irradiation (to a dose of 1.2×10^{16} p/cm^2). The measurements were made at room temperature successively under increasing and decreasing vibration strain amplitude ε.

10^5 Hz was first observed in [9], where internal friction in elastically bent aluminum single crystals subjected to quasi-static deformation was studied. It was shown that internal friction in a sample containing low-angle boundaries passes through a peak under some external load. We observed a clear correlation between the behavior of the acoustic characteristics of boron nitride and RIL, which suggests a possible contribution of low-angle boundaries to the vibration energy absorption. This contribution can originate from a change in internal stresses in the sample. As for the Young's modulus, its variation can also be connected with a change in the internal stresses because of the anharmonicity of lattice vibrations (through higher order elastic constants). Indeed, internal stresses can vary when low-angle boundaries disappear as a result of radiation-stimulated recrystallization of the material.

Interestingly, after the irradiation, the nonlinear ADIF and Young's modulus defect change only insignificantly. This is well illustrated in Fig. 4. Obviously enough, the amplitude-dependent damping of mechanical vibrations in pyrolytic BN is not associated with the presence of low-angle boundaries and other structural defects, whose concentration variations would entail, in this case, a change in the pattern of the amplitude dependences. The ADIF also, apparently, does not depend on the level of internal stresses in a sample. If we assume that the origin of the ADIF is connected, for instance, with individual dislocations (which are not contained in low-angle boundaries), then it may be concluded that irradiation does not affect the quantity of these dislocations. The barriers which have to be overcome by dislocations in their motion also do not change.

4. CONCLUSIONS

Thus, our study showed that the rate of radiation-induced recrystallization of pyrolytic boron nitride undergoing mechanical vibrations can increase as a result of the external mechanical stresses increasing the thermodynamic potential of low-angle boundaries. An essential condition for this effect to be observable is a

sufficiently high amplitude of these vibrations; more specifically, it should lie within the region of nonlinear amplitude-dependent ultrasound damping.

ACKNOWLEDGMENTS

One of the authors (B.K.K.) is grateful to the Russian Foundation for Basic Research for their support, project no. 00-01-00482.

REFERENCES

1. V. A. Stepanov, Zh. Tekh. Fiz. **68** (8), 67 (1998) [Tech. Phys. **43**, 938 (1998)].
2. V. A. Stepanov and P. A. Stepanov, Opt. Spektrosk. **85** (6), 974 (1998) [Opt. Spectrosc. **85**, 893 (1998)].
3. O. I. Buzhinskij, I. V. Opimach, and A. V. Kabyshev, J. Nucl. Mater. **173**, 179 (1990).
4. O. I. Buzhinskij, V. V. Lopatin, and B. N. Sharupin, J. Nucl. Mater. **196–198**, 1118 (1992).
5. O. A. Plaksin, V. A. Stepanov, P. A. Stepanov, *et al.*, J. Nucl. Mater. **233–237**, 1355 (1996).
6. S. P. Nikanorov and B. K. Kardashev, *Elasticity and Dislocation Inelasticity of Crystals* (Nauka, Moscow, 1985).
7. M. A. Shtremel', *Alloy Strength*, Part II: *Deformation* (Mosk. Inst. Stali Splavov, Moscow, 1997).
8. V. A. Stepanov and P. A. Stepanov, Opt. Spektrosk. **78** (3), 431 (1995) [Opt. Spectrosc. **78**, 387 (1995)].
9. V. I. Ivanov, M. A. Vorob'ev, B. K. Kardashev, *et al.*, Izv. Akad. Nauk SSSR, Ser. Fiz. **44** (2), 337 (1980).

Translated by G. Skrebtsov

Physics of the Solid State, Vol. 43, No. 11, 2001, pp. 2094–2098. Translated from Fizika Tverdogo Tela, Vol. 43, No. 11, 2001, pp. 2010–2014.
Original Russian Text Copyright © 2001 by Smirnov, Burenkov, Kardashev, Singh, Goretta, de Arellano-López.

DEFECTS, DISLOCATIONS, AND PHYSICS OF STRENGTH

Elasticity and Inelasticity of Silicon Nitride/Boron Nitride Fibrous Monoliths

B. I. Smirnov*, Yu. A. Burenkov*, B. K. Kardashev*, D. Singh, K. C. Goretta**, and A. R. de Arellano-López*****

**Ioffe Physicotechnical Institute, Russian Academy of Sciences, ul. Politekhnicheskaya 26, St. Petersburg, 194021 Russia*
e-mail: smir.bi@pop.ioffe.rssi.ru
***Argonne National Laboratory, Argonne, Illinois, 60439 USA*
****Universidad de Sevilla, Sevilla, 41080 Spain*

Received April 4, 2001

Abstract—A study is reported on the effect of temperature and elastic vibration amplitude on Young's modulus E and internal friction in Si_3N_4 and BN ceramic samples and Si_3N_4/BN monoliths obtained by hot pressing of BN-coated Si_3N_4 fibers. The fibers were arranged along, across, or both along and across the specimen axis. The E measurements were carried out under thermal cycling within the 20–600°C range. It was found that high-modulus silicon-nitride specimens possess a high thermal stability; the $E(T)$ dependences obtained under heating and cooling coincide well with one another. The low-modulus BN ceramic exhibits a considerable hysteresis, thus indicating evolution of the defect structure under the action of thermoelastic (internal) stresses. Monoliths demonstrate a qualitatively similar behavior (with hysteresis). This behavior of the elastic modulus is possible under microplastic deformation initiated by internal stresses. The presence of microplastic shear in all the materials studied is supported by the character of the amplitude dependences of internal friction and the Young's modulus. The experimental data obtained are discussed in terms of a model in which the temperature dependences of the elastic modulus and their features are accounted for by both microplastic deformation and nonlinear lattice-atom vibrations, which depend on internal stresses. © *2001 MAIK "Nauka/Interperiodica".*

1. INTRODUCTION

Investigation of the physical-mechanical properties of ceramic-based composites is of considerable scientific and applied interest. This is due primarily to their exhibiting, in addition to large high-temperature creep resistance, high strength [1, 2]. On the other hand, they are characterized by catastrophic brittle fracture associated with fast propagation of nuclear cracks. This has stimulated repeated attempts at fabricating ceramic materials with a structure that would preclude catastrophic crack development, for instance, through partial exfoliation of the material itself, which gives rise to crack deflection [3]. The most successful approach seems to be the development of fibrous monoliths (FM) obtained through compression of ceramic fibers coated by a special binder [4]. The most promising among the various FMs was found to be the Si_3N_4/BN fibrous monolith [4–8].

This paper reports on the first integrated investigation of the Young's modulus and internal friction of both the constituents of this monolith (Si_3N_4 and BN) and the monolith itself, Si_3N_4/BN, with differently oriented filaments. The results obtained are compared with the FM structural information.

2. SPECIMENS AND EXPERIMENTAL TECHNIQUE

The fibrous monoliths were fabricated in the USA (Advanced Research, Tucson, AZ) from Si_3N_4/BN filaments ≈325 μm in diameter containing a polymer binder and representing Si_3N_4 cores (85 vol %) coated by a layer of BN (15 vol %). In addition to commercial Si_3N_4 (92 wt %), the cores contained oxides, namely, Y_2O_3 (6 wt %) and Al_2O_3 (2 wt %), added for material densification.

In the first stage of fabrication, monolayer sheets of parallel-oriented filaments were obtained. To produce plates, these sheets were stacked sequentially one upon another and maintained under pressure at 160°C. The adjacent sheets could be aligned either uniaxially or at right angles to one another ([0°/90°] architecture).

In the next stage, the rectangular plates thus prepared were subjected to pyrolysis under slow heating up to 600°C for 42 h in a nitrogen flow. After this, the plates were maintained under a uniaxial pressure of ≈28 MPa at 1740°C for 1 h, in the course of which part of the oxides diffused from the Si_3N_4 into the BN [9, 10]. This procedure produced fibrous monoliths with a density of more than 98% of the theoretical value. The final structure of the uniaxial fibrous monoliths is shown in Fig. 1; its SEM micrograph, in Fig. 2. After

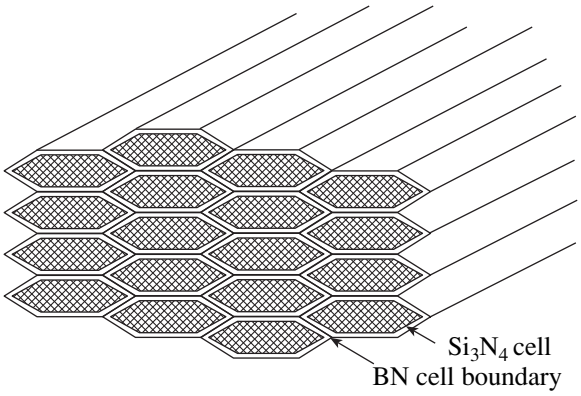

Fig. 1. Schematic of the fibrous monolith structure.

pressing, the filaments are seen to be ≈100 μm thick and ≈220 μm wide.

For subsequent comparison, Si_3N_4 and BN monolithic ceramics were prepared using the same technology; they contained Y_2O_3 and Al_2O_3 oxides in about the same concentrations as the corresponding phases of the Si_3N_4/BN fibrous monoliths [9].

The specimens prepared for acoustic measurements were rods of a rectangular 10–20 mm^2 cross section $l \approx$ 25 mm long. This length provided a resonant vibration frequency f of about 100 kHz. Young's modulus E was determined using a resonance method under electrostatic excitation of longitudinal vibrations of the specimen [11] from the relation $E = 4\rho l^2 f^2 n^{-2}$, where n is the number of the excited harmonic (in our case, $n = 1$) and ρ is the specimen density. The electrodes necessary for the acoustic measurements were prepared by pasting 10-μm-thick aluminum foil to the specimen side and end faces. The density ρ was determined by hydrostatic weighing at room temperature. The experiments were carried out within the temperature range T = 20–600°C in a helium-filled chamber. The average heating rate was ≈2°C per minute. The composite oscillator method [12] was also used, which, in addition to data on the Young's modulus, permits investigation of ultrasound absorption (internal friction) and of the inelastic (microplastic) properties of a specimen. Data on the microplasticity are derived from measurements of the E modulus and the elastic vibration decrement δ within a broad range of vibrational strain amplitudes ε, where nonlinear, amplitude-dependent absorption δ_h forms in the specimen material at sufficiently large ε. Similar integrated studies of E and δ were carried out earlier on boron nitride ceramics fabricated using various technologies [13].

Acoustic measurements on fibrous monoliths were made using specimens with different architectures, namely, Si_3N_4/BN[0] (with filaments aligned with the specimen axis), Si_3N_4/BN[90] (with filaments perpendicular to the specimen axis), and Si_3N_4/BN[0/90] (alternating filament alignment).

3. RESULTS OF THE STUDIES AND DISCUSSION

Data on the density ρ of the various materials and the values of Young's modulus E and of the amplitude-independent decrement δ_i measured at room temperature are presented in the table. The values of E were obtained by averaging over the two measurement methods (electrostatic and composite oscillator). The magnitude of E is seen to decrease and that of δ_i to increase in the order Si_3N_4, Si_3N_4/BN[0], Si_3N_4/BN[0/90], Si_3N_4/BN[90], and BN.

Figure 3 displays the temperature dependences $E(T)$ obtained for Si_3N_4 and BN specimens under heating and cooling within the 20–600°C range. In Si_3N_4, the elasticity modulus is seen to decrease gradually with increasing temperature, with the $E(T)$ curves obtained in the heating and cooling runs coinciding. Such a behavior of E is characteristic of many materials, both

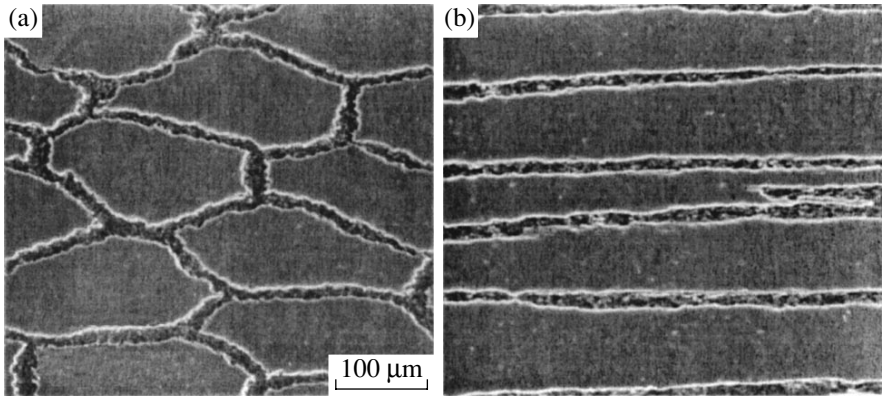

Fig. 2. SEM images of the Si_3N_4/BN[0] structure (a) across and (b) along the filament axis.

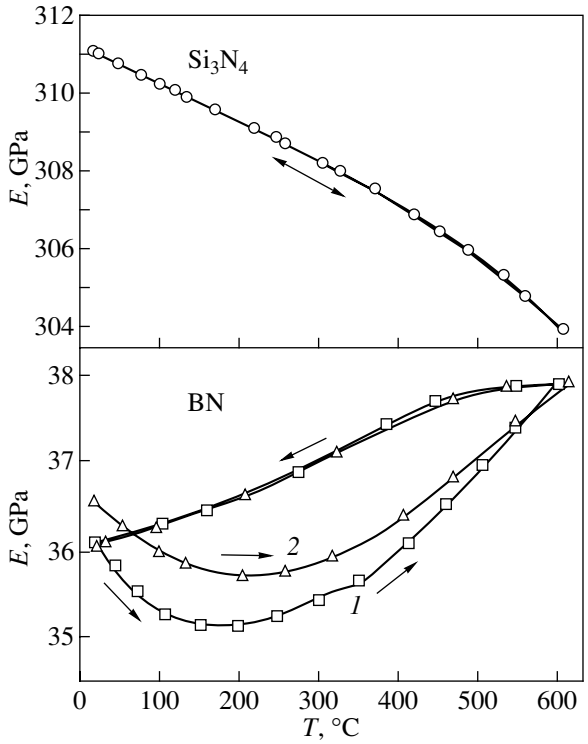

Fig. 3. Temperature dependences of the Young's modulus of Si_3N_4 and BN specimens measured under heating and subsequent cooling; the arrows identify the direction of temperature variation; the numbers on the curves refer to the order in which the experiments with a given specimen were performed; the repeated experiment for BN was carried out 36 days later.

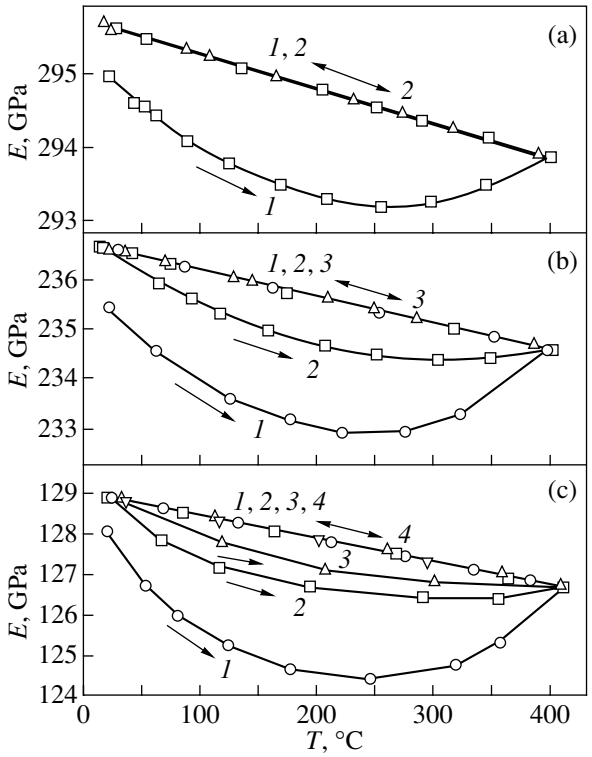

Fig. 4. Temperature dependences of the Young's modulus obtained for Si_3N_4/BN specimens with the filament alignment (a) [0], (b) [0/90], and (c) [90] under heating and subsequent cooling; the arrows identify the direction of temperature variation and the numbers on the curves refer to the order in which experiments with a given specimen were performed.

single- and polycrystals. At the same time, in BN, as already pointed out in [13], the Young's modulus varies with temperature in an unusual manner; more specifically, under heating, it first (up to ≈200°C) decreases and then starts to increase, until it exceeds its original room-temperature value for $T > 400$°C. When cooled, the material exhibits hysteresis and E falls off continuously. A repeated experiment carried out 36 days later revealed a similar hysteresis, although prolonged room-temperature storage after the first experiment brought about a slight increase in E.

Figure 4 plots the temperature dependences of the Young's modulus for fibrous monoliths of different architecture. We readily see that Si_3N_4/BN[0] (Fig. 4a) and BN (Fig. 3) subjected to heating exhibit a decrease followed by an increase in E. At the same time, in the cooling run, the magnitude of E, while revealing a hysteresis, increases rather than decreases, as is the case with Si_3N_4. Also, the room-temperature value of E somewhat increases after the heating–cooling cycle. In a repeated experiment, the $E(T)$ dependence becomes fully reversible.

Density ρ, Young's modulus E, amplitude-independent vibration decrement δ_i (room-temperature data) and temperature coefficients $\Delta E/\Delta T$ of the materials studied

Material	ρ, g/cm^3	E, GPa	$\Delta E/\Delta T$, MPa/K	δ_i, 10^{-5}
Si_3N_4	3.30	314	–10.31	9.5
BN	2.25	36	3.66	902
Si_3N_4/BN[0]	3.09	290 (272)	–4.70 (–8.21)	93 (143)
Si_3N_4/BN[0/90]	3.10	228	–5.39	204 (143)
Si_3N_4/BN[90]	3.08	131 (181*)	–5.96	680 (143)

Note: Given in parentheses are the values calculated using the mechanical rule of mixtures or (*) the brick model [4].

Similar scenarios are observed for Si_3N_4/BN with the [0/90] and [90] architectures, the only exclusion being that, in the former case, the hysteresis in the $E(T)$ dependence decreases gradually to disappear only in the third thermocycle (Fig. 4b), whereas in the latter, it vanishes in the fourth cycle (Fig. 4c). At the same time, the room-temperature value of E for these specimens increases slightly only after the first cycle.

Interestingly, the values of the modulus E measured in a cooling run vary practically linearly for all materials, at least at temperatures below 400°C. The temperature coefficients $\Delta E/\Delta T$ for this case are given in the table.

The table also presents the values of the modulus E, temperature coefficient $\Delta E/\Delta T$, and decrement δ_i calculated in accordance with the mechanical rule of mixtures by using the experimental data for Si_3N_4 and BN. The values of E were obtained using the relations presented in [4]. The Young's modulus for the Si_3N_4/BN[0] monolith was calculated from

$$E_{[0]} = E_{BN}V_{BN} + E_{SN}(1 - V_{BN}).$$

Here, the indices BN and SN refer to BN and Si_3N_4, respectively, and V_{BN} is the volume fraction of the boron nitride (15%). The expressions for $\Delta E/\Delta T$ ([0] architecture) and δ_i (for all materials) are similar:

$$(\Delta E/\Delta T)_{[0]} = (\Delta E/\Delta T)_{BN}V_{BN} + (\Delta E/\Delta T)_{SN}(1 - V_{BN}),$$
$$\delta_i = (\delta_i)_{BN}V_{BN} + (\delta_i)_{SN}(1 - V_{BN}).$$

The Young's modulus for the Si_3N_4/BN[90] monolith was calculated in accordance with the brick model [4].

A comparison of calculated and experimental values reveals disagreement and a large influence of the low-modulus component (BN) on most of the parameters (particularly on the decrement δ_i and the temperature coefficient $\Delta E/\Delta T$). This is seen particularly clearly in the case of Si_3N_4/BN[90]. A similar conclusion that BN plays an important role can be drawn from a comparison of the plots in Figs. 3 and 4. The contribution of the softer, low-modulus component BN is here fairly large even for the Si_3N_4/BN[0] monolith, whose E is only slightly inferior in absolute value to that of the pure Si_3N_4 ceramic. Obviously enough, the initial variation of the E modulus occurring under heating is dominated for all specimens by the behavior of the modulus of boron nitride.

The E modulus can behave in this way in the presence of internal stresses and microplastic deformation of the soft monolith component. Internal stresses can be created in a monolith under elastic loading, as well as because of different thermal expansion coefficients of the constituent materials or of the anisotropy of these coefficients in one of the materials. In particular, the expansion coefficients in hexagonal boron nitride along the a and c axes are even opposite in sign (see review [14]). These internal stresses can affect the Young's modulus through higher order elastic constants. Microplastic deformation can affect the Young's modulus either directly (additional vibrational inelastic strain reduces the modulus) or through the local internal stresses forming in these conditions. At the same time, microdeformation (both irreversible and, possibly, reversible) may bring about relaxation of the internal stresses, which may grow or decrease in a specimen depending on the temperature and specimen prehistory (both thermal and mechanical). A combination of these factors produces the observed effects in the measured elasticity modulus.

The ability of the boron nitride prepared using the technology described above to undergo inelastic (microplastic) deformation revealed itself clearly in a study of the amplitude dependences of the Young's modulus and decrement [13]. The relations obtained for this material had practically the same pattern as those characteristic of plastic metals and alloys. The amplitude-dependent Young's modulus defect, $(\Delta E/E)_h$ and the vibrational decrement $\delta_h = \delta - \delta_i$ obtained in this work as functions of the vibrational strain amplitude ε for various specimens at room temperature are displayed in Fig. 5. We readily see that as the amplitude ε increases, all materials exhibit a certain manifestation of the inelastic components δ_h and $(\Delta E/E)_h$. The

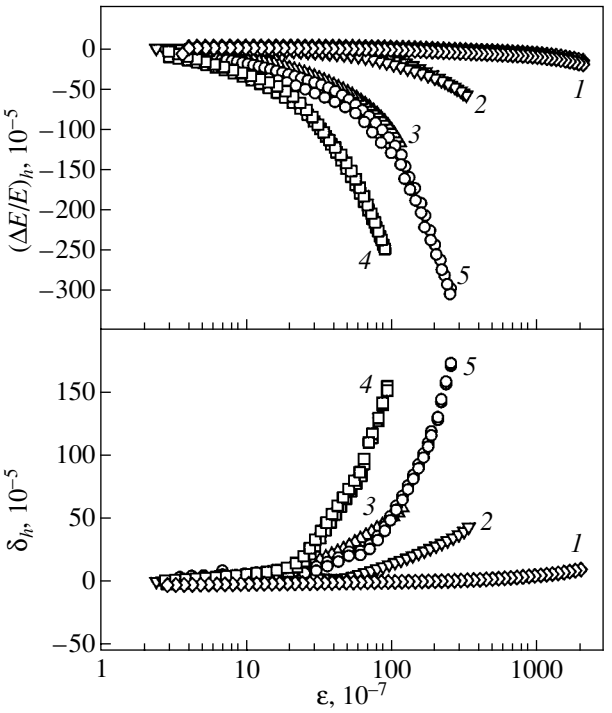

Fig. 5. Amplitude-dependent Young's modulus defect $(\Delta E/E)_h$ and elastic vibrational decrement $\delta_h = (\delta - \delta_i)$ plotted vs. vibrational strain amplitude ε for (*1*) Si_3N_4, (*2*) Si_3N_4/BN[0], (*3*) Si_3N_4/BN[0/90], (*4*) Si_3N_4/BN[90], and (*5*) BN. The measurements were carried out at room temperature.

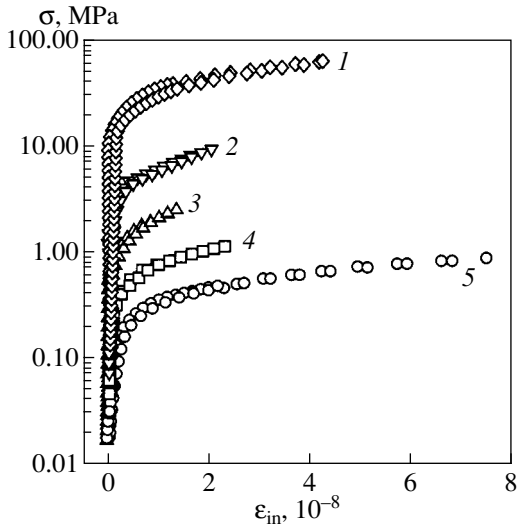

Fig. 6. Stress–inelastic strain diagrams derived from room-temperature acoustic data for (*1*) Si_3N_4, (*2*) Si_3N_4/BN[0], (*3*) Si_3N_4/BN[0/90], (*4*) Si_3N_4/BN[90], and (*5*) BN.

increase in δ_h and $(\Delta E/E)_h$ with amplitude grows in the order Si_3N_4, Si_3N_4/BN[0], BN, and Si_3N_4/BN[0/90], Si_3N_4/BN[90], which differs from the order in which E and δ_i vary. This is seen particularly clearly when one compares curves *4* and *5* for the Si_3N_4/BN[90] monolith and the BN ceramic, respectively; namely, the decrement δ_h and the modulus defect in the monolith are in considerable excess of those in BN, although the BN content in the monolith is only 15%. This situation is easy to understand if one takes into account the architecture of the fibrous monolith under consideration and the above-mentioned ability of boron nitride to undergo microplasticity. This most likely originates from the fact that the real strain amplitude in the component BN of Si_3N_4/BN[90] at the given average amplitude ε is $\varepsilon_{BN} \gg \varepsilon$.

The level of inelastic strain in the materials studied in this work can be deduced from Fig. 6. Acoustic measurements carried out within a broad range of vibrational strain amplitudes permit one to estimate the mechanical properties of the materials also in the stress–strain coordinates, which are more appropriate for use in mechanical testing. Figure 6 presents such deformation diagrams for the materials studied in this work. Plotted along the vertical axis is the amplitude of the vibrational stress $\sigma = E\varepsilon$, and along the horizontal axis, the inelastic strain $\varepsilon_{in} \approx \varepsilon(\Delta E/E)_h$ is plotted (the graphs were plotted using the data in Fig. 5). One readily sees that the level of stresses required for the same microplastic strain to become revealed decreases in the order Si_3N_4, Si_3N_4/BN[0], Si_3N_4/BN[0/90], Si_3N_4/BN[90], and BN. The same order, as already mentioned, is characteristic of the Young's modulus and of the amplitude-independent decrement (table).

4. CONCLUSION

Thus, we have shown that the acoustic method permits one to monitor not only the elastic properties of such macroscopically brittle objects as the Si_3N_4/BN fibrous monoliths but also their microplastic characteristics. The hypothesis on the presence of microplastic shear in the above monoliths of different architecture is supported by the character of the amplitude dependences of internal friction and of the Young's modulus and by the temperature dependence of the latter.

ACKNOWLEDGMENTS

This study was supported by the Russian Foundation for Basic Research (project no. 00-01-00482), NATO (grant no. PST.CLG.977016), and DOE USA (contract no. W-31-109-Eng-38).

REFERENCES

1. J. L. Routbort, K. C. Goretta, A. Domínguez-Rodríguez, and A. R. de Arellano-López, J. Hard Mater. **1**, 221 (1990).
2. H. T. Lin and P. F. Becher, J. Am. Ceram. Soc. **73**, 1378 (1990).
3. W. J. Clegg, K. Kendall, N. McN. Alfoed, *et al.*, Nature (London) **347**, 455 (1990).
4. D. Kovar, B. H. King, R. W. Trice, and J. W. Halloran, J. Am. Ceram. Soc. **80**, 2471 (1997).
5. G. A. Danko, G. E. Hilmas, J. W. Halloran, and B. King, Ceram. Eng. Sci. Proc. **18** (3), 607 (1997).
6. J. L. Routbort, K. C. Goretta, E. T. Park, *et al.*, Ceram. Eng. Sci. Proc. **20** (3), 427 (1999).
7. M. Tlustochowicz, D. Singh, W. A. Ellingson, *et al.*, Ceram. Trans. **103**, 245 (2000).
8. D. Singh, T. A. Cruse, D. J. Hermanson, *et al.*, Ceram. Eng. Sci. Proc. **21** (3), 597 (2000).
9. R. W. Trice and J. W. Halloran, J. Am. Ceram. Soc. **82**, 2502 (1999).
10. R. W. Trice and J. W. Halloran, J. Am. Ceram. Soc. **83**, 311 (2000).
11. Yu. A. Burenkov, S. P. Nikanorov, and A. V. Stepanov, Izv. Akad. Nauk SSSR, Ser. Fiz. **35**, 525 (1971).
12. S. P. Nikanorov and B. K. Kardashev, *Elasticity and Dislocation Inelasticity of Crystals* (Nauka, Moscow, 1985).
13. B. K. Kardashev, Yu. A. Burenkov, B. I. Smirnov, *et al.*, Fiz. Tverd. Tela (St. Petersburg) **43** (6), 1048 (2001) [Phys. Solid State **43**, 1084 (2001)].
14. V. S. Lysanov, V. S. Neshpor, and L. I. Fel'dgun, Zh. Vses. Khim. O-va. im. D. I. Mendeleeva **30**, 536 (1985).

Translated by G. Skrebtsov

Physics of the Solid State, Vol. 43, No. 11, 2001, pp. 2099–2104. Translated from Fizika Tverdogo Tela, Vol. 43, No. 11, 2001, pp. 2015–2020.
Original Russian Text Copyright © 2001 by Myshlyaev, Shpeĭzman, Kamalov.

DEFECTS, DISLOCATIONS, AND PHYSICS OF STRENGTH

On the Multistage Nature of Deformation of the Microcrystalline Aluminum–Lithium Alloy 1420 under Superplasticity Conditions

M. M. Myshlyaev*, V. V. Shpeĭzman, and M. M. Kamalov***

** Baĭkov Institute of Metallurgy and Materials Science, Russian Academy of Sciences, Leninskiĭ pr. 49, Moscow, 117334 Russia*

e-mail: myshlyae@issp.ac.ru

*** Ioffe Physicotechnical Institute, Russian Academy of Sciences, Politekhnicheskaya ul. 26, St. Petersburg, 194021 Russia*

e-mail: shpeizm.v@pop.ioffe.rssi.ru

Received April 4, 2001

Abstract—The constant-rate tensile deformation and creep of aluminum–lithium alloy 1420 with a grain size of 3 μm (obtained by equal-channel angular extrusion) exhibiting superplasticity at temperatures of 600–670 K and relative-deformation rates of 10^{-2}–10^{-3} s^{-1} are considered. It is shown that, upon tension at a constant rate V_m, a steady-state segment appears in the true stress σ_t–true strain ε_t dependence, which is described by the expression $\dot{\varepsilon}_t \sim \sigma_t^n \exp(-U/kT)$ with constant coefficients, and that the rate of deformation $\dot{\varepsilon}_t$ is close to the creep rate at comparable stresses and strains. The conclusion is made that, upon deformation under superplasticity conditions, an equilibrium structure is formed, which remains unaltered in the process of further deformation until the sample goes over (because of geometrical conditions) to a prefracture state. © *2001 MAIK "Nauka/Interperiodica".*

INTRODUCTION

At present, there exist numerous examples of deformation-related self-organization on both microscopic and macroscopic levels. For dislocation structures, this is the appearance, from a chaos of dislocations, of structures with modulated dislocation densities [1, 2], fragmented and block structures with dislocations mainly located in the block boundaries [3–7], and the occurrence of various collective effects in dislocation ensembles, especially upon large deformations [8–11]. In an analysis of the macroscopic characteristics of deformation, the self-organization and the multistage nature manifest themselves most clearly in creep phenomena, i.e., in the deformation processes that develop under equilibrium external conditions at constant stresses σ and temperatures T. In many materials, in very wide ranges of σ and T, there is observed, after a nonsteady and, as a rule, short first stage, an extended stage of steady-state creep occurring at a constant rate $\dot{\varepsilon}$, which passes then into a stage of accelerated creep and terminates in fracture. It is the steady-state stage that is considered as the stage with an unaltered structure, which appears as a result of the action of constant σ and T. Contrary to creep, the deformation at constant T and $\dot{\varepsilon}$ (active uniaxial deformation) is always considered to be a non-steady-state occurring under changing stress and structure. The stages of such deformation are usually considered in terms of the strain-hardening coefficient $d\sigma/d\varepsilon$.

In this paper, we show that such a contraposition of creep and active loading is by no means always justified. There exist conditions under which the development of deformation at $\dot{\varepsilon}$ = const leads to a dependence of the true-deformation rate $\dot{\varepsilon}_t$ on the true stress σ_t that is identical to the well-known power dependence of the steady-state creep rate on stress with temperature-independent parameters. This effect can be treated as a consequence of the establishment of a certain characteristic structure that does not change with the degree of deformation at a definite stage of deformation despite the fact that its rate and the magnitude of the operative stresses change continuously. Another problem that is discussed in this paper is a multistage nature of active deformation under superplasticity conditions. The large extension of the deformation permits one to clearly elucidate the specific features of this stage and their changes upon transitions from one stage to another.

1. EXPERIMENTAL

The experiments were carried out on a polycrystalline alloy of Al with 5.5% Mg, 2.1% Li, and 0.1% Zr developed recently in Russia and known as aluminum–lithium alloy 1420 [12–14]. The superplastic behavior of this alloy in the temperature range of 600–800 K was

reported in [15–17]; that of the alloy with an ultrafine-grained structure, in [18–22]. The ultrafine-grained structure was obtained through repeated equichannel angular (ECA) extrusion with a 90° rotation of the rod after each passage [23, 24]. The initial rods for ECA extrusion were cut from a hot-rolled plate with a recrystallized structure with grains of about 20 μm. The rods were quenched in water from 743 K and then subjected to tenfold ECA extrusion in air at 643 K. The resultant rods were 20 mm in diameter and 70–80 mm long. The quenching and ECA extrusion were performed in the Ufa State Technical University of Aviation (UGATU). The structural state of the rods was qualitatively similar to that observed in [21, 22]. The structure was characterized by an average grain size of about 3 μm (sometimes, grains 10–15 μm in size were encountered) and a developed substructure consisting of subgrains, dislocation cells, and dislocation tangles, containing precipitates of Al_2LiMg and particles of the δ (Al_3Zr) and δ' (Al_3Li) phases.

The ECA-extruded rods were used to prepare flat dumbbell-shaped samples for mechanical tests. The gage portion of samples had a cross section of 2×0.85 mm and a length of 5 mm. The front and lateral sides of the samples were carefully polished. The surface layers were removed to eliminate damage due to mechanical treatment. The differences in both the thickness and the width of the gage portion of the samples did not exceed 0.01 mm. The samples were prepared in such a way that the symmetry axis of a sample was parallel to the rod axis. X-ray diffraction showed that the broadening was caused by both the small size of coherent domains (210 nm) and lattice distortions (the relative change in the lattice parameter $\Delta a/a$ due to internal stresses was 1.3×10^{-3}).

The samples were deformed in an Instron testing machine under conditions of uniaxial tension at a constant rate of 0.5–50 mm/min at a specified temperature within the range 593–668 K. The errors of measuring the applied load and sample elongation were no more than 0.25 and 1%, respectively. In the course of testing, the temperature was maintained constant to within ±3 K. To determine deformation and creep rate, the setup described in [25] was used. A distinctive feature of this setup is the use of a shaped lever to maintain a constant stress upon continuous elongation of the sample. The method of the calculation of the lever shape is described in [25, 26] and is based on two assumptions: the uniformity of deformation along the sample and the constancy of volume upon plastic deformation. Note that this method has not been used previously for testing samples under superplasticity conditions. The large elongations (up to 1800–1900%, which corresponds to an almost 20-fold decrease in the load at the sample in the course of a test) required high accuracy in designing the lever and allowance for all factors that could affect the deformation of the sample (e.g., its shape, temperature gradient, etc.). The errors of determining the rate of deformation at large deformations in the case of creep appear to be greater than those in experiments at a constant rate of tension because of the inaccuracy of maintaining a required stress with the help of a shaped lever. This hinders the traditional analysis of creep using the known dependences of the creep rate on stress and temperature.

Below, we consider the process of structural self-organization due to deformation and compare two most common regimes of loading (tension at a constant rate and creep); the very phenomenon of superplasticity of microcrystalline aluminum alloy 1420, as well as its characteristics and the possible mechanisms of deformation, are described in [22].

2. RESULTS AND DISCUSSION

Figure 1a displays a typical tensile test diagram in the load P–elongation Δl coordinates obtained at a temperature of 643 K and a rate of motion of the mobile grip of the testing machine of $V_m = 5$ mm/min, which corresponds to a rate of relative deformation of the sample of 1.7×10^{-2} s^{-1}; Fig. 1b shows a creep curve taken at a deformation rate close to this value. The creep stress was in this case $\sigma = 19$ MPa. The initial portion of the diagram (the first 80% of the total deformation) is shown separately in the inset in Fig. 1a. It is seen that after ~20% deformation, the load begins to fall. In the case of creep, the initial portion of the transient creep at a rate decreasing in time usually occupies (in the elongation Δl–time t coordinates) no more than 10% of the total time of creep (Fig. 1b). As follows from Fig. 1a, the long descending branch of the tensile curve continues up to the moment of the division of the sample into two halves, i.e., almost to 2000%. It is clearly seen that, at such large deformations, the method of tests at a constant rate V_m and the constructing of $P(\Delta l)$ dependences or $\sigma(\varepsilon)$ dependence, which differs from the former dependences only in scale (here, $\sigma = P/s_0$ and $\varepsilon = \Delta l/l_0$ are the conventional stress and strain and s_0 and l_0 are the initial cross-sectional area and length of the gage portion of the sample, respectively) are inconvenient and possess low informative capability. In Fig. 2, the dependences shown in Fig. 1 are reconstructed in the true stress σ_t–true strain ε_t coordinates ($\sigma_t = P/s = Pl/s_0l_0$ and $\varepsilon_t = \ln l/l_0$, where l and s are the current length and cross-sectional area of the gage portion of the sample, respectively) and in the true strain ε_t–time t coordinates. The main difference of these curves from those plotted in conventional coordinates is a significant (by more than an order of magnitude) extension of the segments corresponding to hardening (to $\varepsilon_t \approx 150$–200%, Fig. 2a) and transient creep (to $\varepsilon_t \approx 200$–250%, Fig. 2b).

The data shown in Figs. 1a and 2a permit us to suggest some considerations on the relation between the particular sections of the tensile curve and the shape of a sample deformed under superplasticity conditions. In

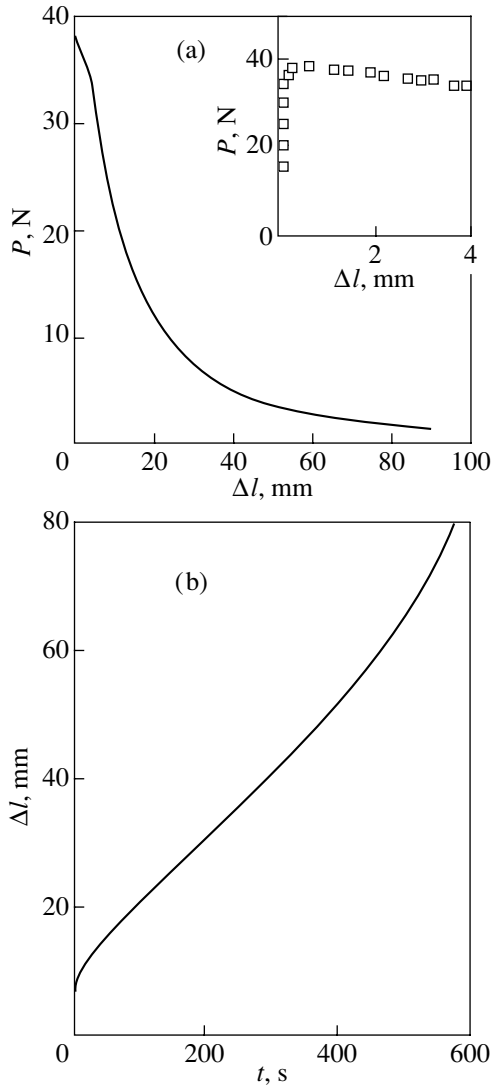

Fig. 1. (a) Load–elongation curve upon tension at a constant rate of 1.7×10^{-2} mm/s and (b) creep curve at $\sigma = 19$ MPa for aluminum–lithium alloy 1420. $T = 643$ K.

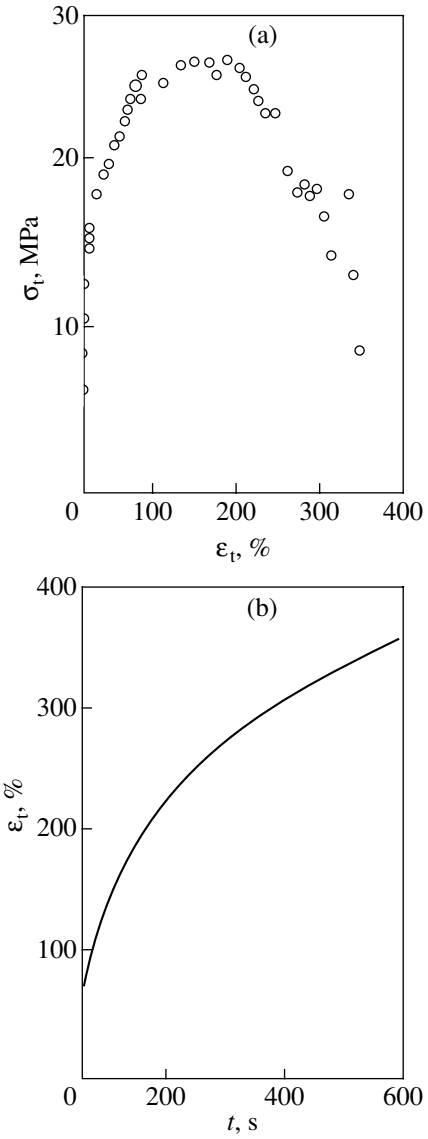

Fig. 2. The same dependences as displayed in Fig. 1 but replotted in true stress–true strain coordinates.

contrast to conventional (not superplastic) deformation, for which it is assumed that the maximum of the diagram in conventional coordinates corresponds to the moment of loss of stability by the sample, i.e., to the onset of necking, in our case, the sample is deformed more or less uniformly to $\varepsilon_t \sim 200\%$, which exceeds the abscissa of the maximum not only in conventional but even in true coordinates (Fig. 3). Therefore, we may suppose that the loss of stability of the sample shape leading, in the final end, to fracture under superplasticity conditions is not related to any special point in the tensile curve.

Figure 4 (curves *1*, *2*) displays the dependences of the true strain rate $\dot{\varepsilon}_t = d\varepsilon_t/dt = d(\ln(l/l_0))/dt$ on the magnitude of true strain for conventional tensile tests at a constant rate and for creep. It is seen that the $\dot{\varepsilon}_t(\varepsilon_t)$ dependences are similar for different regimes of loading.[1] Note that in spite of the constant rate of tension in the course of the test (constant velocity of motion of the mobile grip of the testing machine), the rate of true deformation changes by a factor of 20. However, this is one more advantage of the diagrams of this type: the results of a single test permit one to construct the dependence of the rate of deformation on stress (Fig. 5).

As follows from the data shown in Fig. 5, we can separate two regions in the tensile diagram. The first region corresponds to the initial stage of deformation, in which the rate of deformation is approximately con-

[1] The spike at the end of curve *2* in Fig. 4 is likely due to a short stage of accelerated creep having been fixed in this case.

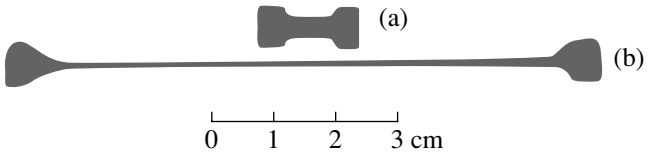

Fig. 3. The appearance of (a) the initial test sample and (b) deformed sample at the stationary stage of deformation.

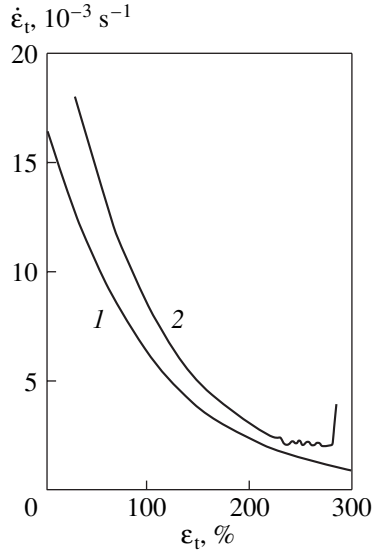

Fig. 4. True strain rate–true strain dependences $\dot{\varepsilon}_t(\varepsilon_t)$ for (*1*) tension at a constant velocity $V_m = 1.7 \times 10^{-2}$ mm/s and (*2*) creep at $\sigma = 19$ MPa. $T = 643$ K.

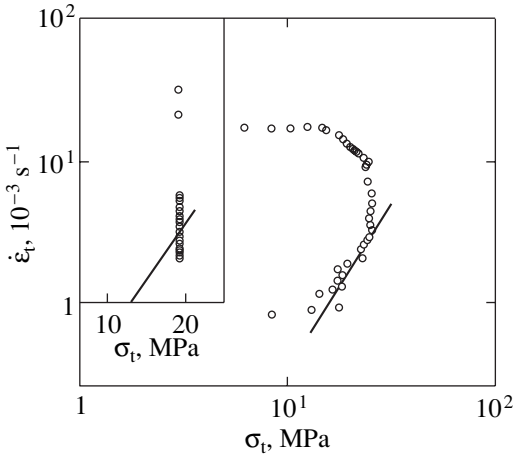

Fig. 5. True strain rate–true stress dependence $\dot{\varepsilon}_t(\sigma_t)$ for tension at a constant rate of 1.7×10^{-2} mm/s. In the inset, the same dependence for creep is given.

stant (at small deformations) or decreases with increasing stress but remains sufficiently high. In Fig. 2a, the ascending branch (material hardening) corresponds to this region. The apparent anomalous dependence of the deformation rate on the stress can be explained by precisely these changes in the material structure. To the second region, in which the rate of deformation decreases with decreasing stress, there corresponds a power dependence of the type $\dot{\varepsilon}_t \sim \sigma_t^n$, where $n = 2.3$. This value of n coincides with that obtained in various works concerning the investigation of superplasticity [16, 27–29]; therefore, we can suppose that this is the region of an equilibrium structure, where deformation is developed without hardening. The falloff of the flow stresses ("apparent softening") observed in Fig. 2a is a consequence of the chosen method of deformation, in which the parameter is the constant velocity of motion of the mobile grip of the testing machine. In order to maintain this velocity constant when the structure remains unaltered, the sample "is forced" to simultaneously change both the rate of true deformation and stress. This region begins almost directly after the maximum of the σ_t–ε_t diagram and occupies (under some test conditions) up to 200% of the region of true deformation. A comparison of the rate of deformation in this region with that in the region close to the steady-state stage shows that these rates are virtually coincident (inset in Fig. 5). Except for the points corresponding to the creep rate in the clearly non-steady-state region, the other points are located near the point of the tensile curve that corresponds to the chosen magnitude of the creep stress $\sigma = 19$ MPa. This confirms the concept of the second stage of the tensile curve as a certain sufficiently extended special stage caused by the preliminarily developed deformation and in which no substantial structural rearrangements occurs.

The last point in Fig. 5 is an outlier; it corresponds to a sharp softening, which terminates in the sample fracture. Sometimes, this region was longer; in other cases, especially at low temperatures and low loading rates, it was entirely absent. At large loading rates, the diagram was similar to that shown in Fig. 2a; however, the stresses and strains corresponding to the maximum and the deformation at fracture could strongly differ even for the same test conditions. At medium rates of deformation, the scatter of the maximum stresses and strains was small but the diagram could terminate at quite various deformations. Figure 6 displays the tensile diagrams for three samples that were tested under the same conditions. The slopes of the regions of hardening and the magnitudes of the fracture stresses is seen to differ only slightly. These features appear to be due to the fact that, for such an extended (in terms of deformation) region of hardening, the deformation paths can differ somewhat (especially, at large rates of loading and high stresses), which can lead to the formation of similar but slightly quantitatively different structure characteristics. Nevertheless, the deformation in the

second region for all samples tested develops in a similar manner. This was shown in [22], where data were given for six samples tested at three different temperatures and three velocities of motion of the mobile grip of the testing machine, which were satisfactorily described in double logarithmic coordinates $\ln\dot{\varepsilon}_t - \ln\sigma_t$ by three parallel straight lines in terms of T. Thus, the experimental data can be described using the well-known formula

$$\dot{\varepsilon}_t = \frac{A}{T}\left(\frac{\sigma_t}{\sigma_0}\right)^n \exp\left(-\frac{U}{kT}\right), \quad (1)$$

where U is the activation energy of the deformation process, k is the Boltzmann constant, $\sigma_0 = 1$ MPa, and A is a constant determined by the characteristics of the process on a microscopic level.

In analyzing the steady-state portion of the deformation curve, we obtained $U = 0.98$ eV and $n = 2.23 \pm 0.10$ from the slopes of the $T\ln\dot{\varepsilon}_t(1/T)$ and $\ln\dot{\varepsilon}_t(\ln\sigma_t)$ dependences, respectively, and $n = 2.05 \pm 0.05$ by using the differential method of sudden change in the rate of deformation.

In this paper, we also used the differential technique for estimating the activation energy of creep and the exponential n. The temperature jumps were $\Delta T = \pm 25$ K and the load jumps were $\Delta P = \pm 1$ N, which corresponded to the change in the true stress $\Delta\sigma_t = \pm 3$ MPa. At the moment of the beginning of a jump, the conditions were as follows: $T = 643$ K, $\sigma_t = 19$ MPa, and $\dot{\varepsilon} = 5 \times 10^{-3}$ s^{-1}. The estimations of n and U were performed using the formulas

$$n = \frac{\ln\dot{\varepsilon}_1 - \ln\dot{\varepsilon}_2}{\ln\sigma_1 - \ln\sigma_2}, \quad (2)$$

$$U = \frac{k(\ln T_1\dot{\varepsilon}_1 - \ln T_2\dot{\varepsilon}_2)}{1/T_2 - 1/T_1}. \quad (3)$$

Here, indices 1 and 2 refer to the magnitudes of the corresponding parameters before and after a jump in stress or temperature. The measurements showed that $n = 2.24$ and $U = 0.95$ eV for the selected point of the creep curve; these values are close to the magnitudes calculated from the measurements of deformation at a constant tensile rate. Thus, we may assume that for both regimes of loading there exists a stage of deformation that is close to the steady-state one, is described by Eq. (1) with the same parameters, and, consequently, is controlled, as was shown in [22], by self-diffusion along grain boundaries, which is typical of superplastic deformation of fine-grained materials caused by grain-boundary sliding.

As to the portion of the curve of deformation at a constant tensile rate preceding fracture, it is obvious that it correlates with the analogous section of the creep curve. As in the latter, this portion is very short, so that special experimental techniques should be used to analyze it. Its origin is likely to be purely geometric: the cross section of the sample becomes so small that its further decrease leads to a fast division of the sample into parts with a 100% reduction of area at the interface. An attempt to relate it to deformation-induced softening and to describe it using Eq. (1) resulted in very small values of n and U and in a dependence of the coefficient A on the initial rate of deformation. It turned out that the main contribution to the change in the strain rate came from the change in the preexponential. This means that either Eq. (1) cannot be applied to describe the final portion of the deformation curve or the gradient of deformation along the sample length distorts the dependence of the average rate of deformation on the average stress and the need arises to pass to local stress and strain.

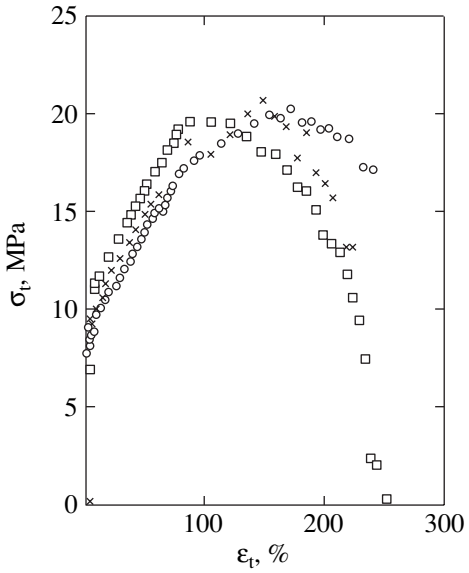

Fig. 6. Tensile deformation curves for three samples stretched at a rate of 1.7×10^{-1} mm/s. $T = 668$ K.

ACKNOWLEDGMENTS

This work was supported in part by the Russian Foundation for Basic Research (project nos. 00-01-00482 and 01-02-16505) and by the Scientific Council of MNTP, "Physics of Solid-State Nanostructures" (project no. 97-3006). We are also grateful to R.K. Islamgaliev, Ufa State Technical University of Aviation (UGATU), who kindly supplied us with the ECA extruded rods used in the investigation.

REFERENCES

1. M. M. Myshlyaev, Fiz. Tverd. Tela (Leningrad) **7** (2), 591 (1965) [Sov. Phys. Solid State **7**, 468 (1965)].
2. D. L. Holt, J. Appl. Phys. **8**, 3197 (1970).
3. M. M. Myshlyaev, Kryst. Res. Technol. **14** (10), 1185 (1979).

4. B. I. Smirnov, R. S. Chudnova, and V. V. Shpeĭzman, Fiz. Tverd. Tela (Leningrad) **23** (10), 2964 (1981) [Sov. Phys. Solid State **23**, 1729 (1981)].
5. M. M. Myshlyaev, Author's Abstract of Doctoral Dissertation (Inst. Fiz. Tverd. Tela, Chernogolovka, 1981).
6. V. V. Rybin, *Large Plastic Deformations and Fracture of Metals* (Metallurgiya, Moscow, 1986).
7. M. M. Myshlyaev, Annu. Rev. Mater. Sci. **11**, 31 (1981).
8. V. E. Panin, V. A. Likhachev, and Yu. V. Grinyaev, *Structural Levels of Solid Deformation* (Nauka, Novosibirsk, 1985).
9. V. I. Vladimirov, in *Problems of Theory of Crystal Defects* (Nauka, Leningrad, 1987), p. 43.
10. M. M. Myshlyaev, I. I. Khodos, Sh. Kh. Khannanov, and Z. M. Usmanova, Fiz. Khim. Obrab. Mater., No. 4, 91 (1977).
11. V. A. Likhachev, M. M. Myshlyaev, and O. N. Sen'kov, *Superplastic Behavior of Aluminum during Torsion* (Inst. Fiz. Tverd. Tela, Chernogolovka, 1981), p. 36.
12. I. N. Fridlyander, *Aluminum Wrought Structural Alloys* (Metallurgiya, Moscow, 1979).
13. I. N. Fridlyander, V. S. Sandler, and Z. N. Archakova, in *Aluminum Alloys. Commercial Aluminum Alloys* (Metallurgiya, Moscow, 1984), p. 207.
14. I. N. Fridlyander, Aluminium–Lithium Alloys **3**, 1359 (1989).
15. I. N. Fridlyander, N. L. Kolobnev, L. V. Khokhlatova, and E. Yu. Semyonova, Aluminium **5** (11), 21 (1990).
16. I. Ya. Novikov, V. K. Portnoĭ, I. L. Konstantinov, and N. I. Kolobnev, in *Material Science of Aluminum Alloys* (Nauka, Moscow, 1985), p. 84.
17. M. Kh. Rabinovich, O. A. Kaĭbyshev, and V. G. Trifonov, Metalloved. Term. Obrab. Met., No. 9, 59 (1981).
18. M. V. Markushev, C. C. Bampton, M. Yu. Murashkin, and D. A. Hardwick, Mater. Sci. Eng., A **234–236**, 927 (1997).
19. P. B. Berbon, N. K. Tsenev, R. Z. Valiev, *et al.*, in *Proc. of the TMS Annual Meeting on Superplasticity and Superplastic Forming, San Antonio, 1998*, Ed. by A. K. Ghosh and Th. R. Bieler (The Minerals, Metals and Materials Society, Warrendale, Pa, 1998), p. 127.
20. P. B. Berbon, M. Furukawa, Z. Horita, *et al.*, in *Hot Deformation of Aluminum Alloys II: Proc. of the 2nd Symposium, Rosemont, 1998*, Ed. by T. R. Bieler, L. A. Lalli, and S. R. MacEwen (The Minerals, Metals and Materials Society, Warrendale, Pa, 1998), p. 111.
21. M. M. Myshlyaev, L. D. Grigor'eva, and M. A. Prokunin, in *Proc. of the XVIII Russia Conference on Electron Microscopy, Chernogolovka, 2000*, p. 178.
22. M. M. Myshlyaev, M. A. Prokunin, and V. V. Shpeĭzman, Fiz. Tverd. Tela (St. Petersburg) **43** (5), 833 (2001) [Phys. Solid State **43**, 865 (2001)].
23. V. M. Segal, V. L. Reznikov, A. E. Drobyshevskiy, and V. I. Kopylov, Russ. Metall. **1**, 99 (1981).
24. V. M. Segal, Mater. Sci. Eng., A **197**, 157 (1995).
25. S. N. Zhurkov and É. E. Tomashevskiĭ, Zh. Tekh. Fiz. **25**, 66 (1955).
26. V. V. Shpeĭzman, in *Machines and Devices for Material Tests* (Metallurgiya, Moscow, 1968), p. 7.
27. V. A. Likhachev, M. M. Myshlyaev, and O. N. Sen'kov, in *Problems of Mechanics of Deformed Solid*, No. 14 (Leningr. Gos. Univ., Leningrad, 1982), p. 179.
28. M. V. Grabski, *Structural Superplasticity of Metals* (Slask, Katowice, 1973; Metallurgiya, Moscow, 1975), translated from Polish.
29. O. A. Kaĭbyshev, *Plasticity and Superplasticity of Metals* (Metallurgiya, Moscow, 1975).

Translated by S. Gorin

Physics of the Solid State, Vol. 43, No. 11, 2001, pp. 2105–2109. Translated from Fizika Tverdogo Tela, Vol. 43, No. 11, 2001, pp. 2021–2024.
Original Russian Text Copyright © 2001 by Golovin, Ivolgin, Korenkov, Farber.

DEFECTS, DISLOCATIONS, AND PHYSICS OF STRENGTH

Size Effect and Time-Dependent Nanohardness of ZrO_2-based Ceramics

Yu. I. Golovin*, V. I. Ivolgin*, V. V. Korenkov*, and B. Ya. Farber**

**Tambov State University, Tambov, 392622 Russia*

e-mail: golovin@tsu.tmb.ru

***Zircoa Corporation, Cleveland, OH, USA*

Received March 15, 2001; in final form, April 16, 2001

Abstract—A modified setup and a method of dynamic indentation with a triangular symmetric force pulse of controllable amplitude and duration are employed for analyzing the time-dependent elastic properties of ZrO_2-based ceramics in a contact time range of 20 ms–4 s. It is shown that the duration of the loading–unloading cycle considerably affects the dynamic hardness: the variation of the contact time from 20 ms to 4 s leads to a 20% change in the dynamic hardness for P_{max} = 25 mN. The variation of the hardness sensitivity m to the strain rate upon a transition from the initial stage of indenter intrusion to the next stages from m_1 = 1.56 to m_2 = 0.49 may point to the difference in the mechanisms of mass transfer of a material under an indenter at these stages.
© 2001 MAIK "Nauka/Interperiodica".

Until the mid-1970s, ZrO_2-based ceramics did not arouse any special interest as structural or technological materials and the only property which found practical application was their high melting point. The potentialities of practical applications of these ceramics were considerable extended after the discovery of a controllable transition of the tetragonal structure of ZrO_2 into a monoclinic structure with the help of stabilizing impurities (Y_2O_3, CeO_2, MgO, CaO). Zirconia-based ceramics are unique materials in that they are characterized by a very high value of fracture toughness K_{1C} comparable to that of steel. The combination of high fracture toughness and hardness H with chemical inertness and the low friction factor make it possible to use these ceramics as a promising wear-resistant material, although the reasons for their high wear resistance have not yet been unambiguously determined. It is widely believed that it is sufficient to ensure high values of K_{1C} for this purpose [1]. However, a material with a high fracture toughness but with an insufficiently high hardness (and vice versa) can exhibit a tendency to rapid wear [2]; consequently, a certain optimal combination of the values of K_{1C} and H is required. In this case, we obviously speak of dynamic and not static hardness. The operational conditions for materials of friction pairs, ball mills, etc. can be simulated to a fairly high degree of accuracy using rapid local deformation under an indenter at a strain rate $\dot{\varepsilon} = \frac{1}{h}\frac{dh}{dt}$ of the order of 10^3–10^5 s^{-1}, i.e., high-rate dynamic micro- and nanoindentation. For small values of the indenter penetration depth h, such high values of $\dot{\varepsilon}$ can be easily attained for moderate linear rates of indentation. For example, for $h \approx$ 0.1–1 μm, the required rates are $\frac{dh}{dt} \approx$ 0.1–1 cm/s.

Pressing an indenter continuously into a material to a depth h of the order of tens or hundreds of manometers has been widely used in investigations over the last two decades, including in the study of ceramic materials [3–6]. This method is suitable for studying both static and time-dependent properties of materials, but most attention has been paid to the slow stage of indenting, viz., creep at $\dot{\varepsilon} \sim 10^{-2}$–$10^{-5}$ s^{-1} [7–11]. For contact times of the indenter with the sample of the order of 10^{-3}–10^{-2} s, which are close to real contact times in abrasive wear, a large spread of experimental data was observed in all experiments [12–16]. As a result, the millisecond contact time range remains virtually unexplored. The possibility of studying the time-dependent properties of materials using the method of dynamic indentation over micro- and nanovolumes under loading by a rectangular pulse of force was reported by us earlier [17–23]. In the present work, a modified setup and the method of dynamic indentation by a triangular pulse of force with a controllable amplitude and duration are used for studying the time-dependent elastoplastic properties of polycrystalline (tetragonal zirconia polycrystals, TZPs) ZrO_2-based ceramics with various thermal histories and grain sizes (table) in the contact time range 20 ms–4 s.

The experimental setup, whose prototype was described in detail earlier in [20–23], was modified in order to increase space and time resolution. In the new system of the electrodynamic activator, the interaction of the current passing through a coil, mounted at the

Characteristics of various samples of ZrO_2-based ceramics

Sample no.	Static (Vickers) hardness H_V, GPa	Fracture toughness K_{1C}, MPa $m^{-1/2}$	Relative mass loss in wear tests I, %	Grain size d, μm
1	11.2	7	0.4	0.3
2	10.5	7.5	0.11	0.5–0.7
3	10.6	8.5	0.6	0.5–0.7
4	9.5	>10	11	3

end of a rod, with the field of a permanent magnet fixed at a bulk frame of the setup was used. The loading parameters (amplitude, shape, temporal characteristics, the number of loading cycles, etc.) were programmed on a PC and covered the loading time range from 10^{-2} to 50 s for a maximum load of 250 mN on the indenter. The signals from the loading device, force sensors and displacement pickups, as well as other auxiliary measuring devices (in all, eight information channels), were transformed from an analog to digital form with the help of a decimal A/D converter and were fed through an interface to the computer used for controlling the experiment and for processing the results. The speed of the A/D converter permitted a time resolution of 50 μs in the single-channel version of data recording; the introduction of each subsequent data recording channel automatically increased the discretization time by 50 μs. For four-channel version of the A/D converter connection, which was mainly used in the present work, the time resolution within a channel was 0.2 ms. The capacitive displacement pickup ensured operation in three intervals of measurements: 10, 1, and 0.1 μm with resolutions 10, 1, and 0.1 nm, respectively; the piezoelectric force sensor ensured a resolution of 10 μN. The experimentally determined compliance of the suspension system of the indenter was 10^{-1} m/N, while the compliance of the setup as a whole, which was taken into account for the correction of the indenter penetration depth, was 1.567×10^{-7} m/N.

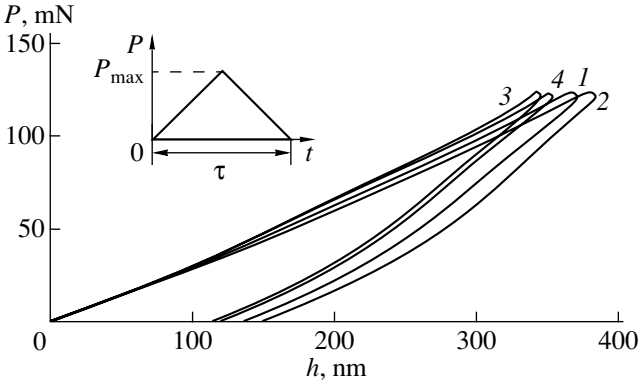

Fig. 1. Typical curves describing the dependence of load P on the indenter penetration depth h for all ZrO_2-based samples in a loading–unloading cycle for the loading rate 6.25×10^3 mN/s (P_{max} = 125 mN, τ = 20 ms). The numbers on the curves are the sample numbers in the table.

All samples were in the form of balls ~1.5 mm in diameter. The wear test was carried out for one hour on a laboratory ball mill under hard conditions: the angular velocity of the propeller in the mill was 360 s^{-1}. A continuous water flow was pumped through the mill under a high pressure for cooling. The values of the relative mass loss $I = \Delta m/m$ in such tests for various samples are given in the table. For measurements in a nanoindentometer, the balls were sealed in a polymer matrix and then ground to half their diameter and polished with a diamond paste. It is known that ZrO_2-based ceramics virtually do not experience surface strain-hardening or loss of strength in the course of meticulous grinding and polishing. All measurements were made at a temperature of T = 293 K. The indenter was in the form of a Berkovich diamond pyramid. The results were averaged over ten measurements for each loading time and loading force used. The measurements were made for loading rates ranging from 62.5 to 12.5×10^3 mN/s.

The hardness H was measured by applying a symmetric triangular pulse of force to the indenter for five fixed values of the maximum load P_{max}: 25, 50, 75, 100, and 125 mN (see inset to Fig. 1). In turn, the duration τ of the loading–unloading cycle was varied from 20 ms to 4 s for each fixed value of P_{max}. The current values of load P, indenter penetration depth h, and time t were recorded continuously in the course of indentation (Fig. 1). The value of H was calculated using the following two methods: (1) as the ratio of the load P at a given instant to the area of the indentation projection at the same instant and (2) as the ratio of the maximum load P_{max} applied to the indenter to the maximum area of the indentation projection calculated from the maximum value of h. The results of such calculations for sample no. 3 are presented in Fig. 2. Both methods of determining H give close results and indicate the presence of the size effect [24–27]. The latter is usually explained in terms of the application of an unjustified method of calculating the area of the indentation projection under the assumption of its ideal geometrical similarity to the shape and size of the pressed-in indenter [28, 29], disregarding its finite sharpness, peculiarities of sharpening, and the formation of heaps and dips along the indentation perimeter. According to McElhaney *et al.* [28], corrections that take this fact into account do not exceed 20% for $h \geq$ 200–300 nm, while the effect observed in Fig. 2 for the dynamic hardness is approximately equal to 300%. Such a magnitude of the effect is preserved for all loading rates, including those for which the hardness attains its quasistatic value.

The anomalously high values of hardness for all loading rates were typically observed within time inter-

vals 2–50 ms after the beginning of indentation. In the case of a jumplike loading, 50 to 90% of the entire imprint is formed during this time [30] and the mechanism of mass transfer from the region under the indenter can change. Precisely this time range is beyond the detection ability of commercial nanotesters with a low indentation rate (~1 nm/s) and a small time resolution (~0.1 s). On the other hand, the processes occurring in the material under the indenter at the initial stage of its incursion are complex and have been insufficiently studied; it can be stated with a high degree of confidence that the indentation process is not self-similar precisely at this stage of its development. For this reason, the description of the P vs. h loading curve using the simple expression $P = Ch^n$ of the classical Meyer law [31], where C = const and the exponent n is usually assumed to be constant and close to two, cannot be regarded as adequate for the indentation process. The experimentally observed value of n varies from 1.5 to 2.0 for ceramics [24]. For TZP, the value of n obtained in [32] was 1.912, but at the initial stage of indenter incursion (up to times of the order of 50 ms), the value of n may differ even from this mean value [33, 34]; i.e., it may change in the course of measurements. In our experiments, the value of n jumpwise changed the slope at a depth from 50 to 200 nm (depending on the loading rate) from lower to higher values upon an increase in h, which can apparently be due to a change in the dominating mechanism of deformation.

Figure 2 also shows that the value of dynamic hardness in ZrO_2 (sample no. 3) is affected to a considerable extent by the duration of the loading–unloading cycle. The rate dependence of hardness in various materials has been being investigated since the early 1980s [12–16], when it was found that, in the first approximation, the value of H decreases linearly upon an increase in the time of active contact interaction of the indenter with the material under investigation. However, this dependence was in fact extrapolated from a range of much longer times to a range of contact times shorter than 100 ms [12] or the results were approximated in view of a large spread in experimental data [15]. Figure 3 shows the time dependence of hardness determined using the second method for P_{max} = 125 mN for three ZrO_2 ceramic samples. In semilogarithmic coordinates, the experimental results for all the samples can be approximated by a linear dependence to within 10%. The time-dependent properties of hardness are usually estimated quantitatively using the coefficient m characterizing the strain-rate sensitivity of hardness: $m = d(\ln H)/d(\ln \dot{\varepsilon})$; it equals the slope of the $H = f(\dot{\varepsilon})$ curve in the log–log coordinates [13, 34]. Figure 4 shows the dependence of dynamic hardness on the strain rate for all the investigated samples for two values of the depth of penetration of the indenter. The upper group of the curves corresponds to h_1 = 200 nm; the lower group, to h_2 = 650 nm. The slopes of these curves are quite close within each group: $m_1 = 1.56 \pm 0.03$ for the upper group

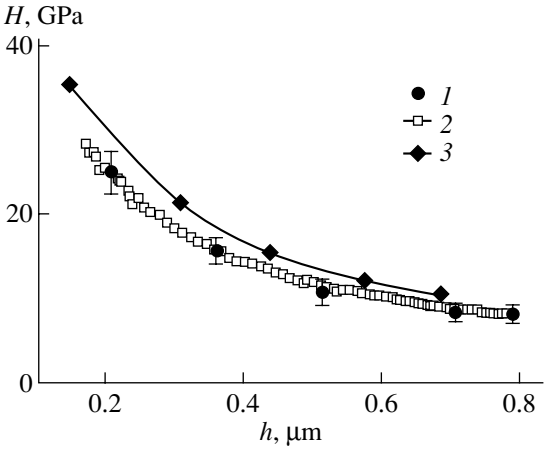

Fig. 2. Dynamic hardness as a function of the indenter penetration depth in ZrO_2 (sample no. 3): (*1*, *3*) hardness determined from P_{max} for τ = 2 s and 20 ms, respectively, and (*2*) current values of dynamic hardness for τ = 2 s.

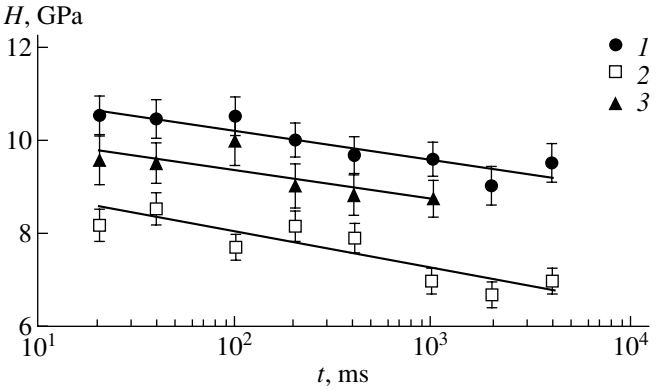

Fig. 3. Time dependence of hardness determined for P_{max} = 125 mN for ZrO_2 ceramic sample nos. 1–3.

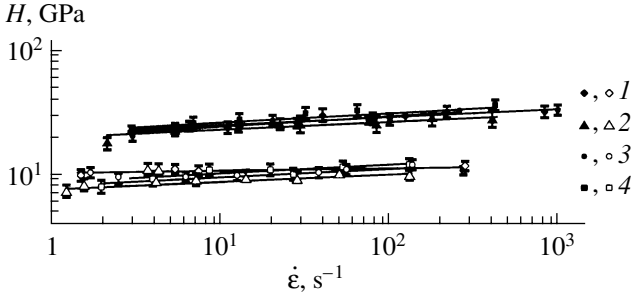

Fig. 4. Dynamic hardness as a function of strain rate (in the log–log coordinates) for ZrO_2 ceramics at the initial (h_1 = 200 nm, the upper group of curves) and final (h_2 = 650 nm, the lower group of curves) stages of active loading. Figures *1–4* are the sample numbers. Dark symbols correspond to h_1; light symbols, to h_2.

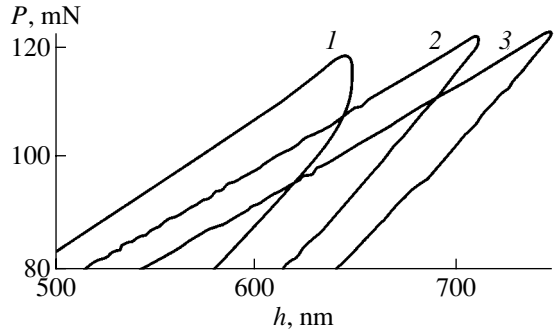

Fig. 5. *P–h* diagrams (sample no. 2) for the same maximum load P_{max} = 125 mN and various durations of loading: (*1*) 20 ms, (*2*) 200 ms, and (*3*) 2 s.

of curves and $m_2 = 0.49 \pm 0.03$ for the lower group. Such a noticeable difference in coefficients *m* for different values of *h* (such that $\frac{m_1}{m_2} \approx \frac{h_1}{h_2}$) can also be due to the change in the dominating mechanisms of plastic deformation of the material upon a transition from the initial stage of penetration of the indenter to the next stages.

The $H = f(\dot{\varepsilon})$curves in the log–log coordinates do not pass through the origin but intercept the segments $H_0' = 20.2 \pm 0.25$ GPa and $H_0'' = 8.0 \pm 0.3$ GPa on the ordinate axis, respectively, which makes it possible to separate the time-dependent and time-independent components of hardness. An extrapolation of these dependences to the range of values $\dot{\varepsilon} \sim 10^6$ s^{-1}, typical of the operation conditions in ball mills, gives, approximately, a fivefold increase in the value of *H* as compared to its static value for *h* = 200 nm and a twofold increase for *h* = 650 nm. In addition, the rate dependence of hardness can also be determined directly from the *P–h* diagram. For this purpose, it is sufficient to compare the sharpness of the peak of the *P–h* diagram in the vicinity of P_{max} for various loading rates (Fig. 5) but for the same maximum loads. The shorter the duration of a loading–unloading cycle, the larger the equivalent radius of curvature of the top of the *P–h* diagram and the larger the mismatching between the position of h_{max} and the maximum load applied to the indenter.

Thus, our investigations of ZrO_2-based ceramics enabled us to separate two (time-dependent and time-independent) components of hardness. The hardness sensitivity to the strain rate has been determined in the range $\dot{\varepsilon} = 1–10^3$ s^{-1}. It has also been proved that the complex-stressed state of the material under the indenter at the initial stage of its penetration (whose duration is 5–50 ms) cannot be described by using simple models in which a strictly quadratic dependence between the load and the penetration depth of the indenter is assumed.

ACKNOWLEDGMENTS

This research was supported by the Russian Foundation for Basic Research, project no. 01–02–16573, and the Ministry of Education of the Russian Federation, grant no. E00-34-123.

REFERENCES

1. R. H. Hannink, P. M. Kelly, and B. C. Muddle, J. Am. Ceram. Soc. **83** (3), 461 (2000).
2. P. Kallas, Wear **198** (1), 77 (1996).
3. T. F. Page, W. C. Oliver, and C. J. McHargue, J. Mater. Res. **7** (2), 450 (1992).
4. C. Friedrich, G. Berg, E. Broszeit, and C. Berger, Thin Solid Films **290–291**, 216 (1996).
5. M. Sakai, Acta Metall. Mater. **41** (6), 1751 (1993).
6. S. I. Bulychev and V. P. Alekhin, *Material Tests by Continuous Indentation of Indenter* (Mashinostroenie, Moscow, 1990).
7. B. N. Lucas and W. C. Oliver, Mater. Res. Soc. Symp. Proc. **239**, 337 (1992).
8. B. N. Lucas, W. C. Oliver, G. M. Pharr, and J. L. Loubet, Mater. Res. Soc. Symp. Proc. **436**, 233 (1997).
9. B. N. Lucas, W. C. Oliver, and J. E. Swindeman, Mater. Res. Soc. Symp. Proc. **522**, 3 (1998).
10. A. L. Yurkov, J. Mater. Sci. Lett. **12** (10), 767 (1993).
11. V. Raman and R. Berriche, J. Mater. Res. **7** (3), 627 (1992).
12. C. J. Fairbanks, R. S. Polvani, S. M. Wiedhorn, *et al.*, J. Mater. Sci. Lett. **1** (4), 391 (1982).
13. B. N. Lucas and W. C. Oliver, Mater. Res. Soc. Symp. Proc. **356**, 645 (1995).
14. D. S. Stone and K. B. Yoder, J. Mater. Res. **9** (10), 2524 (1994).
15. P. Grau, G. Berg, H. Meinhard, and S. Mosch, J. Am. Ceram. Soc. **81** (6), 1557 (1998).
16. B. N. Lucas and W. C. Oliver, Metall. Mater. Trans. A **30**, 601 (1999).
17. Yu. I. Golovin and A. I. Tyurin, Pis'ma Zh. Éksp. Teor. Fiz. **60** (10), 722 (1994) [JETP Lett. **60**, 742 (1994)].
18. Yu. I. Golovin and A. I. Tyurin, Fiz. Tverd. Tela (St. Petersburg) **38** (6), 1812 (1996) [Phys. Solid State **38**, 1000 (1996)].
19. Yu. I. Golovin and A. I. Tyurin, Kristallografiya **40** (5), 884 (1995) [Crystallogr. Rep. **40**, 818 (1995)].
20. Yu. I. Golovin and A. I. Tyurin, Materialovedenie, No. 1, 14 (2001); No. 2, 10 (2001).
21. I. Yu. Golovin, V. I. Ivolgin, V. V. Korenkov, and A. I. Tyurin, Pis'ma Zh. Tekh. Fiz. **23** (16), 15 (1997) [Tech. Phys. Lett. **23**, 621 (1997)].
22. I. Yu. Golovin, V. I. Ivolgin, V. V. Korenkov, and A. I. Tyurin, Zh. Tekh. Fiz. **70** (5), 82 (2000) [Tech. Phys. **45**, 605 (2000)].
23. I. Yu. Golovin, V. I. Ivolgin, V. V. Korenkov, and A. I. Tyurin, Izv. Vyssh. Uchebn. Zaved., Mater. Élektron. Tekh., No. 2, 29 (2000).
24. J. Gong, J. Wu, and Z. Guan, Mater. Lett. **38** (2), 197 (1999).

25. A. Iost and R. Bigot, J. Mater. Sci. **31**, 3573 (1996).
26. H. Li and R. C. Bradt, J. Mater. Sci. **28** (4), 917 (1993).
27. G. Farges and D. Degout, Thin Solid Films **181** (12), 365 (1989).
28. K. W. McElhaney, J. J. Vlassak, and W. D. Nix, J. Mater. Res. **13** (5), 1300 (1998).
29. C.-J. Lu and D. B. Bogy, Int. J. Solids Struct. **32** (12), 1759 (1995).
30. Yu. I. Golovin and A. I. Tyurin, Fiz. Tverd. Tela (St. Petersburg) **42** (10), 1818 (2000) [Phys. Solid State **42**, 1865 (2000)].
31. A. E. Giannakopoulos and S. Suresh, Scr. Mater. **40** (10), 1191 (1999).
32. J. Gong, J. Wu, and Z. Guan, J. Eur. Ceram. Soc. **19**, 2625 (1999).
33. G. M. Pharr and W. C. Oliver, J. Mater. Res. **4** (1), 94 (1989).
34. M. J. Mayo, R. W. Siegel, A. Narayanasamy, and W. D. Nix, J. Mater. Res. **5** (5), 1073 (1990).

Translated by N. Wadhwa

Physics of the Solid State, Vol. 43, No. 11, 2001, pp. 2110–2114. Translated from Fizika Tverdogo Tela, Vol. 43, No. 11, 2001, pp. 2025–2029.
Original Russian Text Copyright © 2001 by Zhuravlev, Oshlakov.

MAGNETISM AND FERROELECTRICITY

Effect of the Domain Structure on Ferromagnetic Resonance in Easy-Axis Ferromagnets

V. A. Zhuravlev and A. A. Oshlakov

Tomsk State University, Tomsk, 634050 Russia

e-mail: ptica.rff@elefot.tsu.ru

Received January 19, 2001

Abstract—The results of experimental and theoretical investigations of ferromagnetic resonance (FMR) in ferrite single crystals having hexagonal structure and magnetocrystalline anisotropy of the easy-axis type are reported. Experiments are carried out on disk-shaped samples of materials differing in anisotropy strength. The values of the effective anisotropy fields and the gyromagnetic ratios (*g*-factors) of the materials are determined from measured frequency dependences of the FMR field along the easy and hard magnetization directions for homogeneously magnetized samples. It is shown that if the FMR spectra are also measured for the same samples in the presence of a domain structure, then one can experimentally determine not only the above-mentioned parameters but also the saturation magnetization of uniaxial magnetic materials. It is shown that the theory of the FMR frequency spectrum of a partially magnetized sample with a simple domain structure in the form of a system of plane-parallel layers is in good agreement with the experiment. © *2001 MAIK "Nauka/Interperiodica".*

1. The ferromagnetic resonance (FMR) theory in the presence of a domain structure (DS) in materials with uniaxial magnetocrystalline anisotropy (MCA) was developed by Smit and Beljers in [1]. They considered the case where a monocrystalline sample has the form of an ellipsoid of revolution and possesses a stripe DS and the magnetic field ($\mathbf{H}_0$) is applied in the plane perpendicular to the easy magnetization axis (EMA). The axis of the ellipsoid of revolution was along the EMA. For this orientation of $\mathbf{H}_0$, the DS period is not changed when the sample is magnetized; therefore, the contribution from each magnetic subsystem to the resonance frequencies and absorption is the same. The results of [1] were generalized in [2] to the case where the sample has bubble domains in addition to the stripe DS. The case of a sample magnetized by a field applied parallel to the EMA was also considered in [2]. The displacement of the domain walls and the rotation of the magnetization vectors in domains were taken into account. The former process leads to a change in the relative volume of neighboring domains and in the DS demagnetization factors. The FMR theory for materials with a stripe DS and an arbitrary orientation of $\mathbf{H}_0$ relative to the anisotropy axis of an ellipsoidal sample was developed in [3, 4].

In this paper, we report on experimental investigations of the FMR frequency spectrum for uniaxial materials which either have a DS or are magnetized to saturation. Investigations are carried out on $BaFe_{12}O_{19}$ (Ba*M*) and $BaSc_{1.1}Fe_{10.9}O_{19}$ (BaSc*M*) hexaferrite monocrystals (which differ in MCA strength) in the case where the samples are magnetized in the plane perpendicular to the EMA. The experimental results are compared with theoretical findings.

2. Our theoretical calculations are similar to those performed in [1–6]; we will not discuss them in detail. We point out only the main distinctions in our model and present the relations that are necessary for analysis of the experimental data. A sample having the form of an ellipsoid of revolution and characterized by the demagnetization factors $N_{\perp 0}$ and N_{z0} ($2N_{\perp 0} + N_{z0} = 1$) is considered. The ellipsoid axis coincides with the *z* axis of the (*x*, *y*, *z*) coordinate system and with the EMA, which is the *c* axis of the hexagonal crystal. The MCA energy is written in terms of the anisotropy constants k_i of the first, second, and third orders. It is necessary to take into account the higher order anisotropy constants, because, under certain conditions (see, e.g., [7–9]), they can contribute considerably to the MCA of uniaxial ferromagnets in the plane perpendicular to the EMA. The magnetizing field $\mathbf{H}_0$ is applied along the *y* axis. The sample is assumed to be divided into alternate plane-parallel domains with opposite magnetization directions. The domains have the same volume, and their walls are perpendicular to the *xy* plane. The DS orientation relative to the field $\mathbf{H}_0$ is determined by the N_x, N_y, and N_z demagnetization factors, as in [2]. If the domain walls are parallel to $\mathbf{H}_0$, then $N_x + N_z = 1$ and $N_y = 0$, while for the perpendicular orientation, we have $N_x = 0$ and $N_y + N_z = 1$. The characterization of the DS in terms of demagnetization factors makes it possible to consider bubble domains [2] together with stripe domains. Theoretical analysis of FMR in the presence of a DS in the field $\mathbf{H}_0$ directed along the EMA is not

1063-7834/01/4311-2110$21.00 © 2001 MAIK "Nauka/Interperiodica"

carried out by us, because the first anisotropy constant plays a crucial role in this case and the results are identical to those reported in [2–6].

The total energy of the system is written as

$$U = -\frac{1}{2}H_0(M_{1y} + M_{2y}) + \frac{\pi}{2}\{N_{\perp 0}[(M_{1x} + M_{2x})^2 + (M_{1y} + M_{2y})^2] + N_{z0}(M_{1z} + M_{2z})^2\} + \frac{\pi}{2}[N_x(M_{1x} - M_{2x})^2 + N_y(M_{1y} - M_{2y})^2 + N_z(M_{1z} - M_{2z})^2] + \frac{1}{2}\sum_{i=1}^{3}\frac{k_i}{M_0^{2i}}[(M_{1x}^2 + M_{1y}^2)^i + (M_{2x}^2 + M_{2y}^2)^i]. \quad (1)$$

Here, M_0 is the saturation magnetization and M_{nx}, M_{ny}, and M_{nz} are the projections of the domain magnetization vectors $\mathbf{M}_n$ ($n = 1, 2$). In Eq. (1), the first term is the Zeeman energy, the second is the demagnetization energy due to the sample surface, the third is the DS demagnetization energy, and the last term is the MCA energy. The term describing the domain wall energy is omitted in Eq. (1). In hexaferrites of the *M* type, the domain wall thickness is approximately 0.01 μm; therefore, the volume of a domain wall is considerably smaller than that of a domain, whose thickness is ~10 μm [2].

When solving the static problem, we assumed that, in the absence of the magnetizing field, the vector $\mathbf{M}_1$ is parallel and the vector $\mathbf{M}_2$ is antiparallel to the *z* axis. The application of a magnetic field $\mathbf{H}_0$ leads to deviation of the vectors $\mathbf{M}_n$ from the *z* axis through the angles ϑ_1 and ϑ_2, respectively. Due to the symmetry of the problem in the *xy* plane, the vectors $\mathbf{M}_n$ and $\mathbf{H}_0$ are in the same plane and $\vartheta_2 = \pi - \vartheta_1$. In contrast to [1–6], we calculated the equilibrium values of ϑ_1 and ϑ_2 for fields lower than the saturation field, which is equal to

$$H_S = H_\Theta + 4\pi N_{\perp 0} M_0, \quad (2)$$

using a numerical method under the condition for the total energy of the system given by Eq. (1) to be a minimum. In Eq. (2), $H_\Theta = 2(k_1 + 2k_2 + 3k_3)/M_0$ is the anisotropy field in the plane perpendicular to the hexagonal axis *c*.

The dynamical problem of determination of the frequencies of natural oscillations of the sample magnetization in the presence of the DS was solved using a method proposed in [2, 10]. We considered a set of coupled equations of motion for the magnetization vectors of neighboring domains. The effective static and dynamical magnetic fields involved in these equations were determined from Eq. (1) for the energy. The linearized set of homogeneous equations for the variable components of the sample magnetization ($\mathbf{m}_{nx}$, $\mathbf{m}_{ny}$, $\mathbf{m}_{nz}$) in a matrix representation has the form

$$[D] \times [m] = 0, \quad (3)$$

where $[m] = (m_{1x}, m_{1y}, m_{1z}, m_{2x}, m_{2y}, m_{2z})^T$ is the variable magnetization vector and $[D]$ is the 6×6 matrix of coefficients. The natural frequencies were found from the equation

$$\det[D] = 0. \quad (4)$$

This equation has two positive roots for the resonance frequencies (ω_{res}). These roots correspond to two spectrum branches which are excited by a microwave magnetic field $\mathbf{h}$ parallel or perpendicular to $\mathbf{H}_0$. Depending on the DS orientation, the calculated frequencies correspond to the situations shown in Fig. 1 and are labeled *1–4*. The same notation is used in Fig. 2 and when we compare the calculated resonance fields and frequencies of the corresponding oscillation modes with experimental results. For $H_0 = 0$ and $N_z = 0$, two

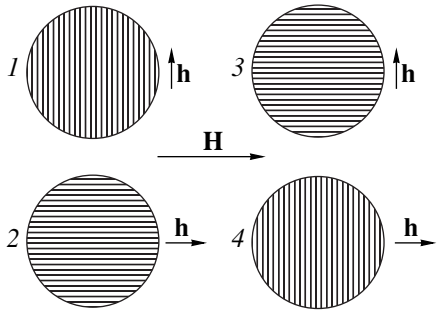

Fig. 1. Relative positions of the DS and the static and microwave magnetic fields for which the resonance frequencies were calculated. Labels *1* and *4* correspond to the oscillation modes with $N_x = 0$; labels *2* and *3*, to modes with $N_y = 0$.

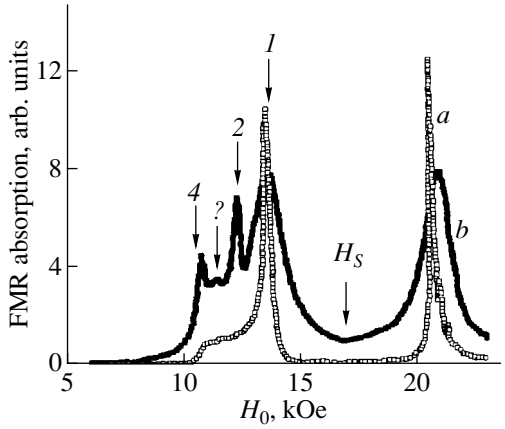

Fig. 2. FMR curves for Ba*M* hexaferrite samples. Curves *a* and *b* correspond to the samples whose sizes are given in the caption to Fig. 3.

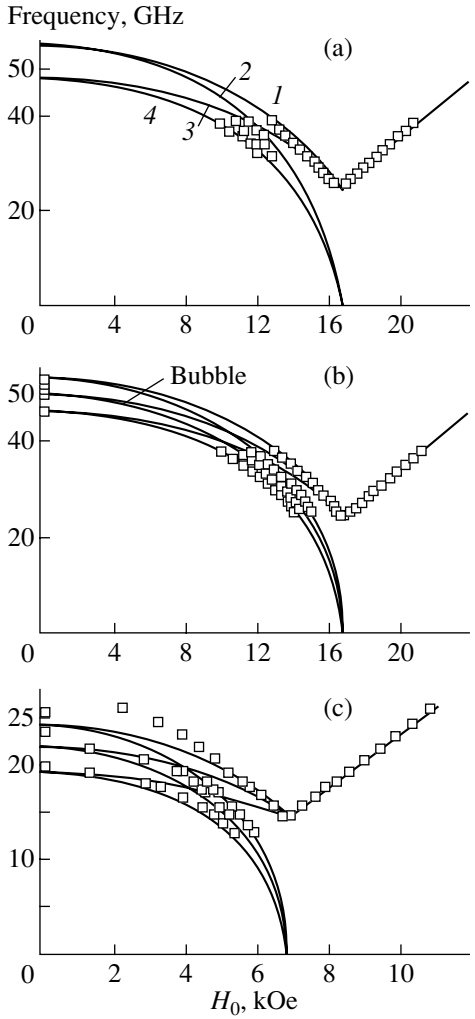

Fig. 3. Field dependences of the resonance frequencies: (a) Ba*M*, diameter ∅ = 1.4 mm, thickness h = 0.06 mm; (b) Ba*M*, ∅ = 2.6 mm, h = 0.11 mm, and (c) BaSc*M*, ∅ = 2.6 mm, h = 0.095 mm. The notation for the calculated oscillation modes in Figs. 3b and 3c is the same as that in Fig. 3a.

modes of natural ferromagnetic resonance are observed. These modes have frequencies

$$\begin{aligned}(\omega_1/\gamma)^2 &= H_{a1}(H_{a1} + 4\pi N_{\perp 0}M_0),\\ (\omega_2/\gamma)^2 &= (H_{a1} + 4\pi M_0)(H_{a1} + 4\pi N_{\perp 0}M_0).\end{aligned} \quad (5)$$

An increase in $\mathbf{H}_0$ leads to a decrease in frequency for all oscillation modes. In this case, the frequencies of modes *2* and *4* (Fig. 1), which are excited by microwave fields parallel to $\mathbf{H}_0$, are decreased to zero at a field $H_0 = H_S$ (Fig. 3), while the frequencies of the other modes (*1*, *3*), which are excited by a transverse microwave field, become equal to the frequency $\omega_{r\perp}$ for the sample magnetized to saturation:

$$(\omega_{r\perp}/\gamma)^2 = H_0[H_0 - H_\Theta - 4\pi(N_{\perp 0} - N_{z0})M_0]. \quad (6)$$

If the DS is oriented at an arbitrary angle with respect to $\mathbf{H}_0$, then the resonance frequencies will be located in the sectors restricted by curves *1*, *3* and *2*, *4*, respectively [4]. At the field $H_0 = H_S$, Eq. (6) is reduced to the following formula, which can be used to determine the value of $4\pi M_0$ from the experiment:

$$(\omega_{r\perp}/\gamma)^2 = 4\pi N_{z0}M_0H_S. \quad (7)$$

When the sample is magnetized along the EMA, the FMR frequencies in the presence of the DS are independent of the magnetizing field and remain equal to ω_1 and ω_2 until the sample becomes uniformly magnetized, which is realized for fields $H_0 \geq 4\pi M_0 N_{z0}$ [4]. The FMR frequency for the uniformly magnetized sample is equal to

$$\omega_{r\parallel}/\gamma = H_0 + H_{a1} + 4\pi M_0(N_{\perp 0} - N_{z0}). \quad (8)$$

Comparing formulas (6) and (8), one can see that in this case (where the axis of the ellipsoid of revolution coincides with the EMA), the anisotropy field $H_{a1} = 2k_1/M_0$ is replaced by $H'_{a1} = H_{a1} + 4\pi M_0(N_{\perp 0} - N_{z0})$.

3. The experimental investigations were carried out by means of an FMR spectrometer within the 15–55 GHz frequency range for magnetizing fields up to 21 kOe. For frequencies up to 38 GHz, the measurements were carried out by means of a resonator technique using rectangular multimode resonators which support the TE_{10p} oscillation modes. These resonators were inserted in a waveguide circuit and operated in a transmission mode. At higher frequencies, a waveguide measuring technique was utilized. All experiments were carried out at room temperature. Disk-shaped samples less than 3 mm in diameter were used. The disk axis coincided with the hexagonal axis of the crystal. A sample was placed into an antinode of the microwave magnetic field in such a way that, when the sample was rotated, the orientation of the magnetizing field H_0 was changed from the direction along the disk axis to the direction in the disk plane and the microwave magnetic field always remained in the direction of the disk plane. The FMR measurements were performed at certain fixed frequencies in the form of dependences of the microwave power transmission coefficient through the resonator (waveguide) upon H_0. In order to ensure identical experimental conditions, the measurements of the resonance curves were carried out for a magnetization field that was always decreased from its maximal value. The natural FMR spectra (at $H_0 = 0$) were recorded in the frequency scanning regime.

The experiment was carried out as follows. The frequency dependences of the resonance fields (H_{res}) were measured on uniformly magnetized samples in magnetizing fields directed along the disk axis and lying in its plane. The obtained data were processed by the least squares method using Eqs. (6) and (8), and the gyromagnetic ratio (γ) and the anisotropy fields H_Θ and H'_{a1}

Measured parameters of the materials

Material	γ, GHz/kOe	$4\pi M_0$, kG	H_{a1}, kOe	H_Θ, kOe
Ba*M*	2.8 ± 0.02	4.8 ± 0.1	16.7 ± 0.1	16.7 ± 0.1
BaSc*M*	2.78 ± 0.02	4.0 ± 0.1	7.0 ± 0.1	6.8 ± 0.1

were found. The sample demagnetization factors were calculated using the Osborne formulas (see, for example, [11]). The saturation magnetization ($4\pi M_0$) was determined from the experimental values of $\omega_{r\perp}$ and H_S using formula (7). Then, the contributions from shape anisotropy and MCA to H'_{a1} were separated.

The parameters of the studied materials thus obtained are presented in the table. These parameters were used to plot the theoretical field dependences of the resonance frequencies for samples with the DS. Note that for the Ba*M* sample, the parameters measured by us correlate well with the literature data [12].

4. Let us discuss the results obtained in the present work. Figure 2 shows the resonance curves measured at a frequency of 36.76 GHz. Figures 3a and 3b present the field dependences of the resonance frequencies for two samples of Ba*M* hexaferrite differing in size. The disk dimensions are indicated in the caption to Fig. 3. In the region of fields higher than H_S, the uniform FMR resonance curve is observed. Several magnetostatic peaks are located on its high-field slope. For a thin sample (Fig. 2, curve *a*), the intensity of these peaks is low, while the resonance curve for a larger sample (Fig. 2, curve *b*) represents a superposition of two oscillation modes with approximately equal intensities. For fields lower than the saturation field, the FMR peak is observed. This peak, as well as the uniform FMR peak, is excited by a transverse ($\mathbf{h} \perp \mathbf{H}_0$) microwave magnetic field (mode *1* in Fig. 1). The line width (ΔH) for this peak is close to that for uniform FMR. A broad diffuse absorption region on the low-field slope is observed for a thin sample. It is well-known (see, for instance, [2, 12]) that the plane-parallel DS in uniaxial hexaferrites normally has a meander form at low magnetizing fields. Its orientation with respect to the magnetizing field in different regions of the sample can be different. The angle between the DS and the field **H** can vary from 0 to $\pi/2$. Such a distribution should lead to a wide absorption band. However, this region can be divided into several resonance ranges; their fields are presented in Fig. 3a. According to Fig. 2, this diffusion region is transformed into a group of well-pronounced maxima with increasing sample size. The resonance fields of these maxima are close to the calculated ones for the oscillation modes excited by the field $\mathbf{h} \parallel \mathbf{H}_0$, in spite of the fact that the sample is located at an antinode of the microwave field that is perpendicular to the magnetizing field. A similar effect was also observed in [2]. One can suppose that the above-mentioned oscillation modes are due to the nonuniformity of the microwave field in the vicinity of the sample. This nonuniformity arises because the sample sizes are comparable to the wavelength of the field. Moreover, the induced secondary microwave field has a component along the field $\mathbf{H}_0$. In addition, a complimentary peak (marked by the symbol "?") is observed between the peaks of oscillation modes *2* and *4*. The value of its resonance field is close to the calculated one for the oscillations with $N_x = N_y = 1/2$ (bubbles) for $\mathbf{h} \parallel \mathbf{H}_0$. However, the bubbles should not appear for $\mathbf{H}_0$ applied in the difficult magnetization direction. Figure 3c presents the field dependences of the resonance frequencies for a BaSc*M* hexaferrite disk with a lower anisotropy field. The results of measurements for this material are similar to those presented above for the Ba*M* hexaferrite. However, it can be seen that, for BaSc*M*, a noticeable difference in the experimental and calculated resonance frequencies is observed. This is especially evident for the high-frequency oscillation mode (mode *1* in Fig. 1), the frequency of which is strongly influenced by the DS [for $H_0 = 0$, its frequency is equal to ω_2 given by Eq. (5)]. For the low-frequency mode (mode *4* in Fig. 1), whose frequency is determined fundamentally by MCA and is equal to ω_1 for $H_0 = 0$, good agreement between the calculation and experiment is observed for low fields H_0. Such a behavior is due to the fact that the DS of this material probably differs from the plane-parallel stripe DS for which the calculation was done. Moreover, the anisotropy field of this material is comparable in value to the demagnetizing field. This leads to an increased influence in the closure domains at the surface of the sample. These domains have not been taken into account in our calculations.

5. Thus, combined studies of the field dependences of the FMR resonance frequencies on samples which either have a DS or are magnetized to saturation provide the opportunity to experimentally determine, on a single sample, not only the anisotropy fields H_{a1} and H_Θ and the gyromagnetic ratio γ but also the saturation magnetization of a material. Although the sample was placed at an antinode of the microwave magnetic field oriented perpendicular to the magnetizing field, the modes that can be excited only by a longitudinal microwave field are present in the spectrum of the excited oscillation modes. The presence of these modes is probably due to the nonuniformity of **h** in the vicinity of the sample. The resonance frequencies measured for the Ba*M* hexaferrite are close to the calculated values, because the DS model used by us adequately describes the experimentally observed DS. For the BaSc*M* hexaferrite with a lower anisotropy field, one observes a

noticeable deviation of the measured frequencies from the calculated values for those oscillation modes that strongly depend upon the DS. We note that, according to Fig. 2, the line width for the domain oscillation mode *1* is close to that for a uniform FMR. This provides an opportunity to utilize this oscillation mode (for practical purposes) instead of a uniform FMR, which occurs at a considerably higher magnetization field.

ACKNOWLEDGMENTS

The authors are grateful to L.N. Bezmaternykh for kindly providing the hexaferrite monocrystals used in this study and to E.P. Naĭden for useful discussions and his interest in this work.

REFERENCES

1. J. Smit and H. G. Beljers, Philips Res. Rep. **10**, 113 (1955).
2. F. J. Rachford, P. Lubits, and C. Vittoria, J. Appl. Phys. **53**, 8940 (1982).
3. L. G. Onoprienko, Fiz. Met. Metalloved. **13** (1), 151 (1962).
4. K. B. Vlasov and L. G. Onoprienko, Fiz. Met. Metalloved. **15** (1), 45 (1963).
5. L. Neel, R. Pauthenet, G. Rimet, and V. S. Giron, J. Appl. Phys. **31**, 27 (1960).
6. L. G. Onoprienko, Fiz. Met. Metalloved. **13** (1), 149 (1962).
7. M. Acquarone, J. Phys. C **12**, 1373 (1979).
8. E. P. Naĭden, V. I. Mal'tsev, G. I. Ryabtsev, *et al.*, Izv. Vyssh. Uchebn. Zaved., Fiz. **34** (1), 14 (1991).
9. V. A. Zhuravlev, Fiz. Tverd. Tela (St. Petersburg) **41** (6), 1050 (1999) [Phys. Solid State **41**, 956 (1999)].
10. C. Vittoria, Phys. Rev. B **10**, 3945 (1974).
11. A. G. Gurevich, *Magnetic Resonance in Ferrites and Antiferromagnets* (Nauka, Moscow, 1973).
12. J. Smit and H. P. J. Wijn, *Ferrites* (Wiley, New York, 1959; Inostrannaya Literatura, Moscow, 1962).

Translated by A. Sonin

Physics of the Solid State, Vol. 43, No. 11, 2001, pp. 2115–2120. Translated from Fizika Tverdogo Tela, Vol. 43, No. 11, 2001, pp. 2030–2034.
Original Russian Text Copyright © 2001 by Karetnikova, Nefedov, Sapozhnikov, Fraerman, Shereshevskiĭ.

MAGNETISM AND FERROELECTRICITY

Inhomogeneous States and the Mechanism of Magnetization Reversal of a Chain of Classical Dipoles

I. R. Karetnikova, I. M. Nefedov, M. V. Sapozhnikov, A. A. Fraerman, and I. A. Shereshevskiĭ

Institute of the Physics of Microstructures, Russian Academy of Sciences, Nizhni Novgorod, 603600 Russia

e-mail: andr@ipm.sci-nnov.ru

Received January 30, 2001

Abstract—The inhomogeneous states (solitons) in a single chain of classical dipoles are studied numerically and analytically. An analytical solution to the problem is based on the long-wave approximation for dipole sums which holds for high magnetic fields perpendicular to the dipole chain. The analytical and numerical solutions are in reasonable agreement. The magnetization reversal is investigated by numerical simulation based on the Landau–Lifshitz stochastic equations. It is demonstrated that the magnetization reversal of a dipole chain at a finite temperature has a thermal activation nature and occurs through the formation of a stable phase nucleus (a soliton at the edge of the chain) and its growth (the motion of the soliton along the chain). © *2001 MAIK "Nauka/Interperiodica".*

1. INTRODUCTION

The considerable interest expressed in ordered systems of ferromagnetic nanoparticles is associated primarily with prospects for the creation of superdense information (>10^{10} bit/cm^2) recording and storage devices based on these systems. On the other hand, the investigation of an ensemble of single-domain magnetic particles offers a unique opportunity to study in detail collective effects brought about by well-defined interparticle interactions. Since the size of a particle is rather large (compared to the interatomic distance), the magnetic moment of particles can be treated as a classical quantity. The static magnetic fields generated by single-domain particles are the fundamental cause of interparticle interaction. As a rule, this interaction is theoretically investigated in the dipole approximation. A particle is considered to be a point dipole with a magnetic moment proportional to its volume. This approximation is satisfied in two cases: (a) the distance between the particles is substantially larger than their sizes and (b) the particles have a nearly spherical form. In this work, the inhomogeneous states (solitons) in a chain of classical dipoles and their role in magnetization reversal at a finite temperature were studied analytically and numerically. The ordered chains of ferromagnetic nanoparticles can be synthesized either through the process of self-organization [1] or by nanolithography [2, 3]. As far as we know, experimental investigations have been performed with systems of chains rather than with individual chains. However, in view of the smallness of the interchain interaction as compared to the intrachain interaction [4], the theoretical investigation of a single chain of classical dipoles is of great importance in the understanding of the experimentally observed phenomena.

2. A SOLITON IN A ONE-DIMENSIONAL CHAIN OF THREE-DIMENSIONAL DIPOLES

First, we calculate the spectrum of small (linear) excitations in an infinite chain. The nonexcited state corresponds to the parallel orientation of dipoles $\mathbf{M} = (M_0, 0, 0)$. By linearizing the Landau–Lifshitz equation, we obtain the following relationships for the Fourier transforms of the small corrections $\mathbf{m}$ in dimensionless variables:

$$\frac{\partial m_x}{\partial \tau} = 0, \quad \frac{\partial m_y}{\partial \tau} = -2m_z(\mathbf{D}(k) + 2D(0)),$$
$$\frac{\partial m_z}{\partial \tau} = 2m_y(D(k) + 2D(0)), \quad D(k) = \sum_{n=1}^{\infty} \frac{\cos kn}{n^3}, \tag{1}$$

where $\tau = t\gamma M_0$, t is the time, γ is the gyromagnetic ratio, and M_0 is the magnetization of the dipole chain. The distance between the nearest-neighbor dipoles is taken equal to unity. When deducing relationships (1), we took into account the condition $D_{zz} = D_{yy} = -D_{xx}/2 = 1/n^3$ and the fact that all the off-diagonal components of the dipole tensor are equal to zero: $D(0) \equiv D(k = 0)$. It is a simple matter to determine the dependence of the frequency of natural oscillations on the wave number, that is,

$$\omega(k) = 2(D(k) + 2D(0)). \tag{2}$$

1063-7834/01/4311-2115$21.00 © 2001 MAIK "Nauka/Interperiodica"

The frequencies of small-amplitude oscillations are nonzero due to the anisotropy of the dipole–dipole interaction. Thus, the calculation of the mean-square deviation angle of dipoles with respect to the X axis in the Gaussian approximation results in a finite value. However, this does not mean that a long-range order exists in a one-dimensional chain of dipoles at a finite temperature [5]. The long-range order is disturbed in this system under nonlinear excitations, as is the case in the one-dimensional Ising model. The problem of determining the correlation radius (or the equilibrium concentration of excitations) is much more complex than that in the Ising model. This is due to the fact that the Ising excitations form an ideal gas and their equilibrium concentration is $\sim\exp(-2J/T)$, where J is the energy of the spin–spin interaction. In a dipole system, the solitons interact with each other. Since the problem of calculating the thermodynamic characteristics of a chain of three-dimensional classical dipoles has not yet been solved, the determination of the energy and the structure of nonlinear excitations (solitons) in this system is of particular interest. Note that the solitons also play a significant role in the processes of magnetization reversal of a dipole chain at a finite temperature.

The energy of a single chain of dipoles in an external magnetic field can be written as follows:

$$E = \frac{1}{2}\sum_{n\neq m}^{\infty}\frac{1}{|n-m|^3}[M_y(n)M_y(m) + M_z(n)M_z(m) - M_x(n)M_x(m)] - \mathbf{H}\sum_n \mathbf{M}(n). \quad (3)$$

Since analytical determination of the extremals of this functional is very complex, we consider a special case when the external magnetic field is sufficiently high and is directed across the dipole chain, $\mathbf{H} = (0, H, 0)$. As will be shown below, this allows us to use the long-wave approximation. Now, we rewrite the energy defined by Eq. (3) in the Fourier representation:

$$E = \frac{1}{2\pi}\int_{-\infty}^{\infty}(D(k)[M_y(k)M_y(-k) + M_z(k)M_z(-k) - 2M_x(k)M_x(-k)] - HM_y(k))dk. \quad (4)$$

By using the integral representation of $D(k)$ [6],

$$D(k) = \sum_{n=1}^{\infty}\frac{\cos kn}{n^3} = \int_0^{\infty}\frac{t^2(e^t\cos k - 1)}{1 - 2e^t\cos k + e^{2t}}dt, \quad (5)$$

we obtain the following relationship in the long-wave approximation ($k \longrightarrow 0$):

$$D(k) \simeq \zeta(3) + \frac{1}{2}\left(k^2\ln k - \frac{3}{2}k^2\right), \quad (6)$$

where $\zeta(3) \simeq 1.2$ is the Riemann function. In relationship (6), the first term describes the chain anisotropy, the second term corresponds to the magnetodipole interaction in the continuous medium approximation, and the third term (the "pseudoexchange" term) is introduced due to the discreteness of the system under consideration. The energy functional in the long-wave approximation takes the following form:

$$E = \int_{-\infty}^{\infty}\left(\frac{3}{2}\left[\left(\frac{\partial M_x}{\partial n}\right)^2 - \frac{1}{2}\left(\frac{\partial M_y}{\partial n}\right)^2\right] - 3\zeta(3)M_x^2 - HM_y\right)dn - \pi\int_{-\infty}^{\infty}\int_{-\infty}^{\infty}\left(\frac{\partial M_x}{\partial n}\frac{\partial M_x}{\partial m} - \frac{1}{2}\frac{\partial M_y}{\partial n}\frac{\partial M_y}{\partial m}\right)\frac{1}{|n-m|}dndm. \quad (7)$$

Expression (4) implies that, in high fields H, the z component of the magnetic moment becomes zero. The absolute minimum of this functional corresponds to the homogeneous distribution of the magnetic moment: $\cos\varphi_0 = H/6\zeta(3)$, where φ is the angle between the direction of the magnetic field and the magnetic moment. In the case when the external field H is close to the anisotropy field $6\zeta(3)$, the deviation of the **M** vector from the Y axis is insignificant. We restrict our treatment to the case of the terms proportional to $\sim\varphi^4$ and obtain the equation for the extremals of functional (7), that is,

$$\frac{\partial^2\psi}{\partial x^2} + 2(\psi - \psi^3) + 2\pi\frac{\partial}{\partial x}\int_{-\infty}^{\infty}\frac{\partial\psi}{\partial y}\frac{dy}{|x-y|} = 0, \quad (8)$$

where $\varphi = \varphi_0\psi$, $x = ln$, $\varphi^2 = 2(1 - h)$ is the equilibrium value of the angle, $l^2 = 2/(\zeta(3)\varphi^2)$ is the characteristic dimension of the problem, and $h = H/6\zeta(3)$. For $h \longrightarrow 1$, we have $l \gg 1$ and the long-wave approximation is justified. Our main concern here is the solutions to Eq. (8) that satisfy the boundary conditions $\psi(x \longrightarrow \pm\infty) = \pm 1$. We seek a solution to Eq. (8) in the form

$$\psi = \tanh x + f(x). \quad (9)$$

The first term describes both the nucleus of a soliton whose size increases with an increase in the field according to the root law $\sim(1 - h)^{0.5}$ and the attainment of an asymptotic value ± 1. From the symmetry of the problem and the boundary conditions, we obtain $f(-x) = -f(x)$. Let us determine the law of variation in the $f(|x| \longrightarrow \infty) \longrightarrow 0$ function at large x values, which, in turn, specifies the law of the interaction between the

solitons at large distances. Under the assumption that $f(x) \ll \tanh x$, we obtain

$$\frac{\partial^2 f}{\partial x^2} - 4f + \frac{6}{\cosh^2 x} f = -2\pi \frac{\partial}{\partial x} \int_{-\infty}^{\infty} \frac{1}{\cosh^2 y} \frac{dy}{|x-y|} - 2\pi \frac{\partial}{\partial x} \int_{-\infty}^{\infty} \frac{\partial f}{\partial y} \frac{dy}{|x-y|}. \quad (10)$$

At large x, the first two terms on the left-hand side of Eq. (10) can be ignored. By virtue of the properties of the $f(x)$ function, the appropriate distribution of magnetic charges has a zero net charge. In fact, the relationship $\partial\varphi/\partial x \sim \partial M_x/\partial x = \mathrm{div}\mathbf{M}$ determines the charge density in magnetostatics. Hence, the second term on the left-hand side of this equation can also be disregarded. Consequently, we have

$$f(x) \sim \mp \frac{1}{x^2}, \quad x \longrightarrow \pm\infty. \quad (11)$$

This result is easily understood if it is remembered that the soliton (domain wall) under consideration is charged in the magnetostatic sense. To every soliton there corresponds a negative magnetic charge distributed inside the nucleus. At large distances (compared to the nucleus size), this charge can be treated as a point change inducing a field which is directed toward the center of the soliton and decreases as $1/x^2$.

In order to verify the above assumptions concerning the structure of the soliton in a one-dimensional chain of dipoles and to elucidate its structure in low fields, we carried out numerical calculations. The numerical simulation was based on a system of Landau–Lifshitz equations (see below). The soliton solutions were chosen by specifying of the initial conditions. Figure 1 depicts the calculated dependence of the self-energy of a soliton on the external magnetic field. In high fields, the soliton energy is well approximated by the expression $E = 3/4(6\zeta(3) - H)^{1.5}$. This dependence of the soliton energy on the external field follows from expression (7). In fact, the soliton energy is proportional to the ratio of the equilibrium angle squared ($\varphi^2 \sim (1-h)$) to the soliton "thickness" ($l \sim (1-h)^{-0.5}$). As a result, we have the relationship $E \sim (1-h)^{1.5}$.

The results of calculations of the magnetization distribution in a soliton are displayed in Fig. 2. The numerical simulation lends support to the validity of our concept of soliton structure in high fields ($H \sim 6\zeta(3)$). Figure 3 shows the field dependence of the integral y component of the soliton magnetization,

$$\langle M_y \rangle = \int_{-\infty}^{\infty} (\cos\varphi - \cos\varphi_0) dx.$$

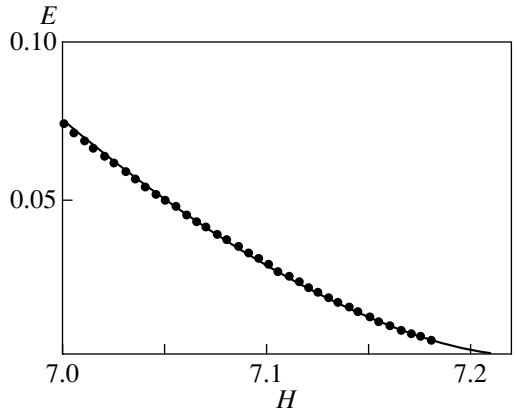

Fig. 1. The field dependence of the self-energy of a soliton in the field range close to the saturation field (in dimensionless units). The solid line shows the approximation according to the formula $E = 0.76(6\zeta(3) - H)^{1.5}$. Points correspond to the results of the numerical solution.

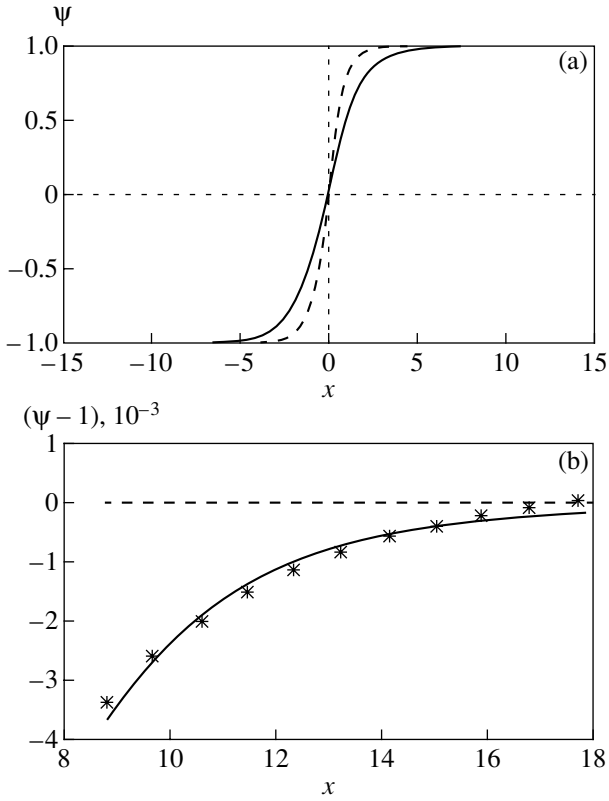

Fig. 2. (a) Distribution of the magnetization in a soliton in the external field $h = 0.9844$ (in dimensionless units). The dashed line corresponds to $\psi = \tanh x$, and the solid line shows the results of the numerical simulation. (b) Distribution of the magnetization for large distances. Points represent the results of the numerical solution, and the solid line corresponds to $\psi = 1 - 1/x^2$.

As the external magnetic field decreases, the structure of the soliton becomes different from that determined analytically. Specifically, when the field H is equal to

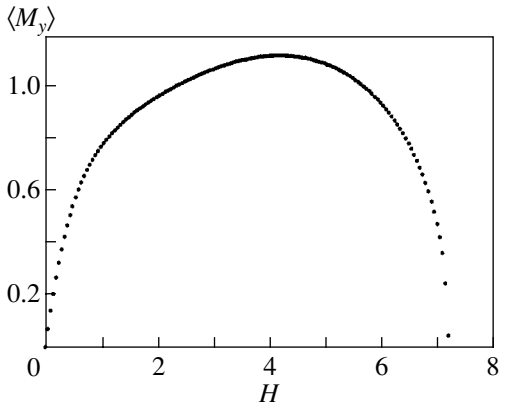

Fig. 3. Dependence of the y component $\langle M_y \rangle$ of the integral magnetic moment of a soliton on the external field (the results of the numerical solution are given in dimensionless units).

Fig. 4. Distribution of magnetic dipole moments in the absence of an external field.

zero, the y component of the soliton magnetic moment vanishes and the soliton nucleus has an "antiferromagnetic" structure (Fig. 4).

3. THE THERMAL ACTIVATION MECHANISM OF MAGNETIZATION REVERSAL OF A SINGLE CHAIN OF DIPOLES

As was noted above, the solitons play a significant role in the magnetization reversal of a single chain of dipoles. Now, we consider a chain of particles whose dipole moment is directed along the X axis. If the system is placed in an external field aligned opposite to the magnetic moment, the initial state remains metastable up to a certain field H_c. At $H > H_c$, the dipoles are oriented along the field and the dipole chain undergoes a magnetization reversal; in this case, H_c is the coercive field of the chain. A standard analysis of the system for stability leads to the relationship

$$H_c = 2\min[D(k) + 2\zeta(3)],$$

where $D(k)$ is determined by expression (5). Note that the minimum value of $D(k)$ corresponds to the Brillouin zone boundary. For this reason, the above mechanism of magnetization reversal was referred to as the fanning mechanism [7]. At a finite temperature, the processes of magnetization reversal can proceed in a different manner. It is known that the metastable state breaks down through the formation of a critical nucleus of the stable phase and its growth. This mechanism, as applied to the magnetization reversal of a thin ferromagnetic cylinder, was considered in [8, 9]. The key to understanding how the magnetization reversal occurs in this case lies in solving the problem of the structure and the energy of the critical nucleus, because the probability of the magnetization reversal is proportional to $\exp(-E_c/kT)$, where E_c is the energy of the critical nucleus, T is the temperature, and k is the Boltzmann constant.

It is assumed that, in a single chain of dipoles oriented in the positive direction of the X axis, there arises a nucleus containing l particles whose magnetic moments are aligned with the applied field. The change in the energy of the system due to the formation of the nucleus can be written as

$$\Delta E(l) = \varepsilon(l) - 2hl. \tag{12}$$

Here, the first term corresponds to the increase in the energy due to the formation of two solitons at the boundary of the nucleus and the second term accounts for the decrease in the energy of the system due to interaction with an external field. The surface contribution to the energy $\varepsilon(l)$ contains the self-energy of two solitons and the energy of their interaction. It is clear that, at sufficiently large L, the interaction of solitons is caused by their magnetostatic charge proportional to $-\mathrm{div}\mathbf{M}$. The energy of their interaction is proportional to $4/l$. The attraction of solitons brings into existence a critical nucleus with size $l_c \sim 1/\sqrt{h}$ and energy $E_c \simeq 2\varepsilon_0 - 4\sqrt{h}$ (where ε_0 is the self-energy of a single soliton). Therefore, a critical nucleus of the new phase can occur in the system under consideration with a probability proportional to $\sim\exp(-E_c(h)/T)$.

The validity of this hypothesis was tested by numerical simulation of magnetization reversal in a chain of dipoles. The numerical calculation consists in solving the system of Landau–Lifshitz stochastic equations, which has the following form in dimensionless variables:

$$\frac{\partial \mathbf{m}}{\partial \tau} = -[\mathbf{mh}] - \lambda[\mathbf{m}[\mathbf{mh}]], \tag{13}$$

where $h_i(x) = h_{0i} - \sum_y D_{ik}(\mathbf{x} - \mathbf{y})m_k(\mathbf{y}) + \xi_i(\mathbf{x}, \tau)$ is the total magnetic field acting on a particle with coordinate $\mathbf{x}$. The dimensionless variables are chosen as follows: $\mathbf{m} = \mathbf{M}/M_s$, $\mathbf{h} = \mathbf{H}/M_s$, $\tau = t\gamma M_s/(1 + \lambda^2)$, and $\mathbf{x} = \mathbf{r}/v^{1/3}$. Here, M_s is the magnetic moment of the particle (in our calculations, we used the value of $M_s = 800$ G, which corresponds to permalloy), v is the volume of the particle ($v = 8 \times 10^{-18}$ cm^3), $\gamma = 1.76 \times 10^7$ Oe^{-1} s^{-1}, and λ is the dimensionless damping constant ($\lambda = 0.1$). The distance between the particles was taken equal to 50 nm. The effective field $\mathbf{h}(x)$ acting on a particle at the point $\mathbf{x}$ involves the homogeneous external field $\mathbf{h}_0$, the field induced by all other particles at this point, and a random field $\xi(\mathbf{x}, \tau)$, which simulates the action of the thermo-

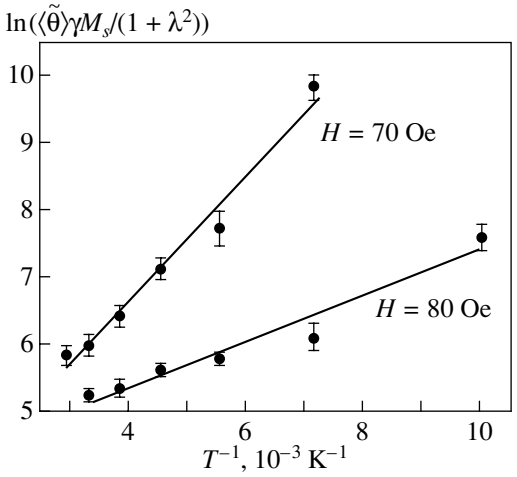

Fig. 5. Dependences of the logarithm of the latent time of magnetization reversal for a chain of 50 particles on the reciprocal of temperature T^{-1} in external fields H = 70 and 80 Oe.

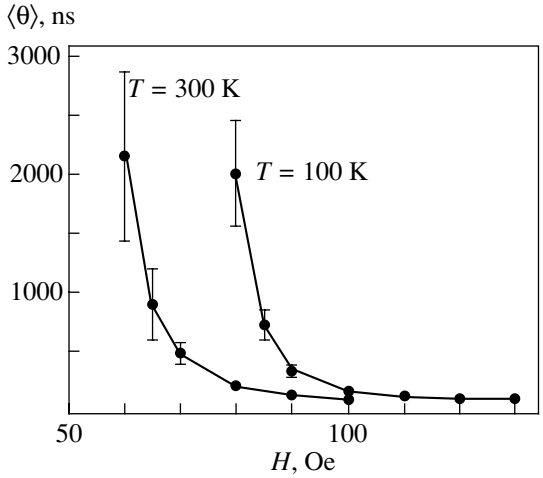

Fig. 6. Dependences of the latent time of magnetization reversal θ for a chain of 50 particles on the external field at two temperatures. Averaging is performed over 20 and 30 realizations for T = 300 and 100 K, respectively.

stat on the particle. The field ξ is assumed to be a delta-correlated random Gaussian quantity, that is,

$$\begin{aligned} \langle \xi_i \rangle &= 0, \\ \langle \xi_i(\mathbf{x}, \tau_p)\xi_j(\mathbf{y}, \tau_q)\rangle &= \Gamma^2 \delta_{ij}\delta(\mathbf{x}-\mathbf{y})\delta_{pq}. \end{aligned} \tag{14}$$

According to the fluctuation–dissipative theorem, the intensity of fluctuations is proportional to temperature, $\Gamma^2 = 2kT\lambda/M_s^2 \nu\Delta\tau$, where $\Delta\tau$ is the time integration step.

Let us assume that $\alpha(T, h_0)$ is the probability of formation of a critical nucleus in a unit time. In order to calculate the probability α, we consider a random quantity θ, the instant of formation of a nucleus. The probability density of this quantity has the form $p(\theta) = \alpha\exp(-\alpha\theta)$. Therefore, the mean time interval preceding the formation of a nucleus (the latent period of the nucleus) is defined as $\langle\theta\rangle = 1/\alpha$. The computational algorithm of this quantity is as follows. First, we choose the initial conditions in the form

$$\mathbf{m}(t = 0) = (1, 0, 0).$$

In this case, it is assumed that the external magnetic field is aligned opposite to the X axis, i.e., $\mathbf{h} = (-h_0, 0, 0)$. We solve system (13) up to the instant of time θ, when one-half the total number of dipoles in the chain has turned over: $\sum m_x(n, \theta) = 0$. The time θ is slightly longer than the time of the formation of an irreversibly growing nucleus of the new phase $\tilde{\theta}$. Since $\tilde{\theta} - \theta \ll \theta$, we disregard this difference (the chain consists of 50 particles). By repeating this procedure K times (in our simulation, we chose K = 30), we obtain sample values for the random quantity $\tilde{\theta}_i$ at specified external field and temperature. As a result, we have $\langle\tilde{\theta}\rangle \simeq \left(\sum_{i=1}^{K}\tilde{\theta}_i\right)/K = 1/\alpha$.

In our simulation, we more often observed the formation of the nucleus at the end of the chain, which was likely due to a decrease in the energy of the critical nucleus at the end of the chain as compared to its energy in the bulk.

The dependence of $\log\langle\tilde{\theta}\rangle$ on T^{-1} is well approximated by a straight line, which proves the activation nature of the magnetization reversal (Fig. 5). Figure 6 shows the dependence of the latent period of the nucleus on the external magnetic field. Despite the probabilistic character of the magnetization reversal, this dependence can be characterized by a critical value. For example, at T = 300 K, when the field is higher than 60 Oe, the time of the magnetization reversal shortens. It can be assumed that the coercive field is equal to 60 Oe. It is quite reasonable that this "critical" field decreases with an increase in the latent time, which is specified by the conditions of performing the experiment.

ACKNOWLEDGMENTS

We would like to thank D.I. Kryzhkov for his assistance in the execution of the calculations.

This work was supported by the Russian Foundation for Basic Research, project no. 00-02-16485.

REFERENCES

1. A. Sugavara and M. R. Sheinfein, Phys. Rev. B **56** (14), R8499 (1997).
2. S. A. Gusev, L. A. Mazo, I. M. Nefedov, *et al.*, Pis'ma Zh. Éksp. Teor. Fiz. **68** (6), 475 (1998) [JETP Lett. **68**, 509 (1998)].
3. P. R. Cowburn, D. K. Koltsov, A. O. Adeyeye, *et al.*, Phys. Rev. Lett. **83** (5), 1042 (1999).
4. V. M. Rozenbaum, V. M. Ogenko, and A. A. Chuĭko, Usp. Fiz. Nauk **161** (10), 79 (1991) [Sov. Phys. Usp. **34**, 883 (1991)].
5. S. A. Cannas, Phys. Rev. B **52** (5), 3034 (1995).
6. A. P. Prudnikov, Yu. A. Brychkov, and O. I. Marichev, *Integrals and Series*, Vol. 1: *Elementary Functions* (Nauka, Moscow, 1981; Gordon and Breach, New York, 1986).
7. J. S. Jacobs and C. P. Bean, Phys. Rev. **100** (4), 1060 (1955).
8. H.-B. Braun, Phys. Rev. Lett. **71** (21), 3557 (1993).
9. A. Z. Patashinskiĭ and V. L. Pokrovskiĭ, *Fluctuation Theory of Phase Transitions* (Nauka, Moscow, 1982, 2nd ed.; Pergamon, Oxford, 1979).

Translated by O. Moskalev

Physics of the Solid State, Vol. 43, No. 11, 2001, pp. 2121–2125. Translated from Fizika Tverdogo Tela, Vol. 43, No. 11, 2001, pp. 2035–2039.
Original Russian Text Copyright © 2001 by Arzhavitin, Efimova, Ustimenkova, Finkel'.

MAGNETISM AND FERROELECTRICITY

Anomalies of Internal Friction of Ferrimagnetic Spinel $Li_{0.5}Fe_{2.5}O_4$ in Various Structural States

V. M. Arzhavitin*, N. N. Efimova, M. B. Ustimenkova**, and V. A. Finkel'***

** National Science Center, Kharkov Institute of Physics and Technology, Kharkov, 61108 Ukraine*
e-mail: finkel@kipt.kharkov.ua
*** Kharkov National University, Kharkov, 61077 Ukraine*

Received March 27, 2001

Abstract—The results of high-temperature ($20 \le T \le 800$°C) relaxation and magnetic investigations of ferrite $Li_{0.5}Fe_{2.5}O_4$ in various structural states are given. Anomalies of internal friction caused by the occurrence of ferrimagnetic and structural (ordering type) second-order phase transitions and by vibrations of domain walls of ferrimagnetic and antiphase domains were revealed. It is shown that the 1 : 3 ordering of Fe^{3+} and Li^+ ions in the octahedral sublattice of the spinel leads to a decrease in the Curie temperature, a change in the character of the temperature dependence of the low-field magnetization, and a narrowing of the temperature range of the structural phase transition, as well to a substantial weakening of dissipation processes connected with vibrations of ferrimagnetic domain walls in the field of elastic stresses. © *2001 MAIK "Nauka/Interperiodica".*

INTRODUCTION

Lithium ferrite $Li_{0.5}Fe_{2.5}O_4$ appears to be the simplest representative of the class of inverse spinels; its crystal lattice contains only one type of magnetically active ion (Fe^{3+}), and the distribution of the cations Fe^{3+} and Li^+ between the tetrahedral (*A*) and octahedral (*B*) sublattices is as follows: $Fe^{3+}[Li^+_{0.5}Fe^{3+}_{1.5}]O^{2-}_4$. This ferrite has the greatest Curie temperature among all known spinels ($T_C \ge 600°C$). The magnetic properties of $Li_{0.5}Fe_{2.5}O_4$ have been studied in much detail, although the data on the magnitude of T_C and the character of the temperature dependence of the low-field magnetization are controversial (see, e.g., [1–5]). It is also known that the process of 1 : 3 atomic ordering occurs in the *B* sublattice of $Li_{0.5}Fe_{2.5}O_4$ at temperatures $T_{1:3} \le 750$°C, which leads to a regular arrangement of three Fe^{3+} ions and one Li^+ ion along crystallographic directions <110>; as a result of this ordering-type phase transition, the space group O^7_h–$Fd3m$ is reduced to O^7–$P4_13$ [4].[1]

As we know, the relaxation properties of $Li_{0.5}Fe_{2.5}O_4$ have not been studied earlier. Meanwhile, for many reasons, the investigation of the lithium ferrite with various degrees of ordering by using the internal-friction (IF) method is of a fundamental interest.

First, on the one hand, the results of numerous relaxation experiments on metallic and insulating ferro-, antiferro-, and ferrimagnets show that the IF method is sensitive to magnetic transformations in a very wide frequency range; on the other hand, the classical Landau–Khalatnikov theory [8] predicts the appearance of anomalies of absorption for only high-frequency (in a megahertz range) acoustic vibrations upon the relaxation of the order parameter in the vicinity of a second-order phase transition, so that no anomalies in the sound absorption seemed should be observed at low frequencies (1–10^2 Hz).

Second, as was already mentioned above, this ferrite exhibits a rather specific type of ionic ordering (1 : 3 ordering in the *B* sublattice) and it is absolutely unclear if the method of low-frequency internal friction is sensitive to structural phase transitions of this type.

Third, the method of IF is sensitive to the processes of domain-structure evolution [9], and we know that two types of domains should coexist in this multiaxial ferrimagnet, i.e., magnetic and structural (antiphase domains [7]). The character of dissipative processes in such situations has not been studied earlier, as far as we know.

In this connection, the aim of this paper is to study, in a wide temperature range, the low-frequency IF of samples of lithium ferrite $Li_{0.5}Fe_{2.5}O_4$ in ordered and disordered states. It is obvious that the investigation of the behavior of the IF of $Li_{0.5}Fe_{2.5}O_4$ alone is hardly sufficiently informative for analysis of the effects related to the simultaneous occurrence of two types (magnetic and structural) of phase transitions and to the evolution and (possibly) interaction of two types of domain structures. For this reason, the program of the investigations that was realized in this work also envisaged, along with measurements of low-frequency IF at 20–800°C, precise magnetic measurements in the same temperature range.

[1] Such a transformation apparently should be accompanied by a doubling of the lattice parameter [6, 7].

1. EXPERIMENTAL

As the objects for the investigation of relaxation and magnetic properties, we used polycrystalline samples obtained by the standard powder-metallurgy method (see, e.g., [2]). A mixture of initial components (pure powders of Li_2CO_3 and Fe_2O_3) corresponding to the stoichiometric composition of the lithium ferrite $Li_{0.5}Fe_{2.5}O_4$ was subjected to wet milling and subsequent preliminary annealing at ~1000°C for 5 h. The thus-obtained ferrite charge ground in the process of a secondary wet milling was used to press samples for relaxation and magnetic measurements (rectangular parallelepipeds with characteristic dimensions of $2 \times 2 \times 8$ mm for IF measurements and $2 \times 2 \times 25$ mm for magnetic measurements), which were then sintered at ~1250°C for 5 h in air. X-ray diffraction showed that they were almost completely single-phase.

To obtain $Li_{0.5}Fe_{2.5}O_4$ samples in the ordered state (i.e., with a 1 : 3 superstructure in the octahedral sublattice) and in the disordered state, we used various regimes of cooling to room temperature, namely, a slow cooling with a furnace or quenching in air from the sintering temperature. The choice of the regime of heat treatment was based on the results of x-ray diffraction analysis. In the diffraction patterns of slowly cooled samples, superlattice reflections (110), (210), (211), etc. were present, whereas the diffraction patterns of quenched samples contained only reflections characteristic of the space group O_h^7–$Fd3m$, which indicates the absence of 1 : 3 ordering of Fe^{3+} and Li^+ ions in the *B* sublattice. A cyclic variation of the heat treatment regimes permitted us to obtain both ordered and dislocation states on the same sample.

Measurements of the IF parameters, i.e., of the logarithmic decrement Q^{-1} and the resonance frequency of vibrations ν (the vibration frequency is related to the effective elastic modulus E as $\nu^2 \sim E$), at temperatures of 20–800°C were conducted by the pendulum method using bending vibrations in a frequency range of 57–68 Hz with a relative deformation amplitude $\varepsilon \sim 10^{-6}$ on a specially constructed setup [10]. As a rule, the measurements were carried out in the course of heating of the samples.

The polytherms $\sigma_H(T)$ and isotherms $\sigma_T(H)$ of the magnetization were measured by the induction method using a microfluxmeter F-190 as the indicator of the signal; the signal from the magnetic field was compensated for by an additional (compensation) coil. The sensitivity of the setup was $\sim 10^{-3}$ G cm^3 g^{-1}. The relative error of measuring magnetization ($\Delta\sigma$) was no more than ~2%.

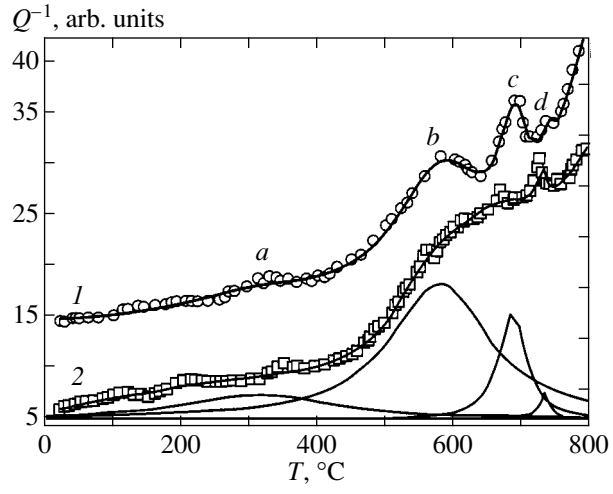

Fig. 1. Temperature dependence of the logarithmic decrement Q^{-1} of (*1*) disordered and (*2*) ordered samples of $Li_{0.5}Fe_{2.5}O_4$ at 20–800°C.

2. RESULTS AND DISCUSSION

The IF spectra $Q^{-1}(T)$ obtained upon heating of $Li_{0.5}Fe_{2.5}O_4$ samples in various structural states are displayed in Fig. 1. A number of anomalies (peaks) are seen in the $Q^{-1}(T)$ curves. Computer processing of the IF spectra permits their being interpreted as a set of four Lorentzians (*a*, *b*, *c*, and *d*) against the background of exponential $Q^{-1}(T)$ dependences. As an illustration, this figure also shows (in the bottom) the resolution of the $Q^{-1}(T)$ spectrum into components for a disordered sample.

As can be seen from Fig. 1, there are several differences between the IF spectra of disordered (quenched) and ordered (slowly cooled) samples. The main features of the evolution of the $Q^{-1}(T)$ curves that are observed upon the passage from a disordered spinel to a spinel with a 1 : 3 ordering of Fe^{3+} and Li^+ ions are as follows: (1) the most high-temperature peak *d* is markedly increased and insignificantly shifted to lower temperatures; (2) peak *c* becomes weaker, somewhat shifting into the region of lower temperatures; (3) peak *b* is narrowed and is also shifted toward lower temperatures; and (4) peak *a* becomes diffuse and virtually indiscernible against the IF background.

In the $\nu(T)$ curves, only two weak peaks could be separated; they correspond to peaks *b* and *d* in the $Q^{-1}(T)$ curves.

The results of measurements of temperature dependences of magnetization (the $\sigma_H(T)$ polytherms in a magnetic field H = 18 Oe at 20–650°C) of the $Li_{0.5}Fe_{2.5}O_4$ samples studied are displayed in Fig. 2. The $\sigma_H(T)$ curves obtained in fields H = 3–48 Oe are similar. Note that the $\sigma_H(T)$ dependences for $Li_{0.5}Fe_{2.5}O_4$ samples are in essence analogous to the temperature dependences of the initial susceptibility $\chi_0(T)$, since the magnetization isotherms $\sigma_T(H)$ (Fig. 3) are almost linear and completely reversible (exhibit no hysteresis) in a rather wide range of magnetic fields. This permits us to consider the temperature at which $\sigma_H(T)$ becomes zero as the Curie temperature of the sample. An estimation

of T_C values based on measurements of $\sigma_H(T)$ yields $T_C \sim 610$°C for the disordered samples and ~595°C for the samples with the 1 : 3 ordering in the *B* sublattice. These values of T_C are close to the position of peaks *b* in the $Q^{-1}(T)$ (Fig. 1) and $\nu(T)$ curves.

The values of T_C for the samples studied were refined based on the measurements of the magnetization isotherms $\sigma_T(H)$ in the vicinity of these temperatures (Fig. 3).

According to the Landau theory of second-order phase transitions, the equation of state of ferro- and ferrimagnets near the Curie point is as follows [8]:

$$\alpha\sigma + \beta\sigma^3 = H, \quad (1)$$

where $\alpha(T)$ and $\beta(T)$ are thermodynamic coefficients.

Equation (1) is linearized in the Belov–Arrott coordinates $\left(\frac{H}{\sigma} - \sigma^2\right)$. The inset in Fig. 3 displays the data obtained in these coordinates for a disordered sample. As is seen, the $\frac{H}{\sigma}(\sigma^2)$ curve passes through zero at $T_C = 608 \pm 2$°C. The Curie temperature for a sample with 1 : 3 ordering determined by the Belov–Arrott method is 595 ± 2°C.

Thus, the combined results of relaxation and magnetic measurements permit one to unambiguously solve the problem of the nature of the observed *b*-type anomalies in the temperature dependences of the IF parameters of the lithium ferrite $Li_{0.5}Fe_{2.5}O_4$.

At the same time, as was already noted, the appearance of features in the temperature dependences of the low-frequency IF upon second-order magnetic phase transitions seems to contradict the Landau–Khalatnikov theory [8]. We think that the observed anomalies in the $Q^{-1}(T)$ dependences near T_C are caused not by the direct relaxation of the order parameter in the vicinity of the phase transition but by the accompanying effect of significant magnetostrictive deformations of the crystal lattice near T_C; i.e., they are related to the second derivatives of the thermodynamic potential. Thus, the anomalies of IF near T_C in the case of the ferromagnetic rare-earth metal gadolinium [11], in which such deformations reach 10^{-3} [12, 13], were revealed even at a frequency of 1 Hz.

The nature of the highest-temperature relaxation effect (peak *d* in the $Q^{-1}(T)$ and $\nu(T)$ curves) related to the phase transition due to the atomic ordering of Fe^{3+} and Li^+ ions in the octahedral sublattice of $Li_{0.5}Fe_{2.5}O_4$ is also undisputed. In this paper, we obtained strong evidence that the transformation at the $T_{1:3}$ temperature is a second-order phase transition: near $T_{1:3}$, characteristic features of the type of Landau's λ anomalies appear in the Q^{-1} and ν behavior (see Fig. 1), and in the $Q^{-1}(T)$ curves, no hysteresis is observed upon heating and cooling of the samples through the temperature of the phase transition (Fig. 4).

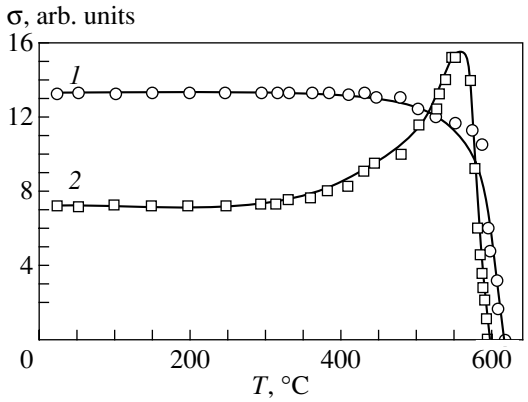

Fig. 2. Temperature dependence of the relative magnetization of (*1*) disordered and (*2*) ordered samples of $Li_{0.5}Fe_{2.5}O_4$ in a field $H = 18$ Oe at $T = 20$–650°C.

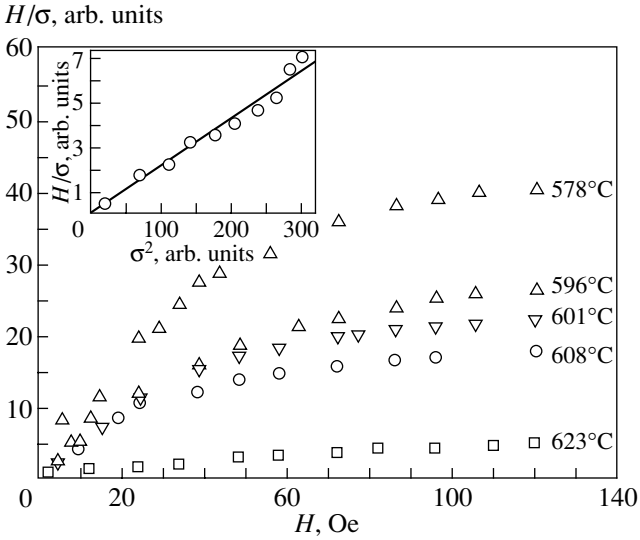

Fig. 3. Magnetization isotherms of a quenched sample of $Li_{0.5}Fe_{2.5}O_4$ near T_C. The inset shows the $\frac{H}{\sigma}(\sigma^2)$ dependence of a quenched sample of $Li_{0.5}Fe_{2.5}O_4$ at $T = 608$°C.

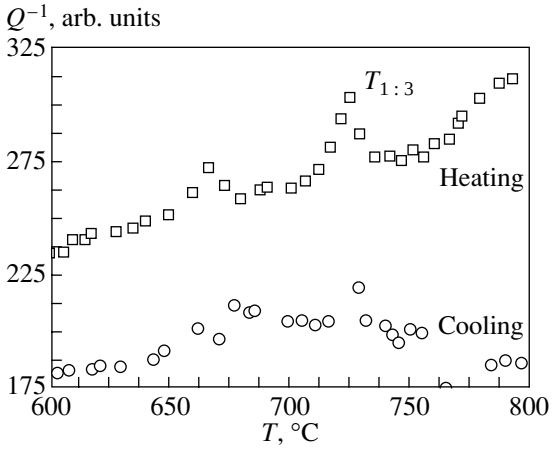

Fig. 4. Temperature dependence of the logarithmic decrement Q^{-1} of a sample of $Li_{0.5}Fe_{2.5}O_4$ upon cooling and heating in a temperature range of 600–800°C.

The IF features caused by the occurrence of magnetic and structural transitions at temperatures T_C and $T_{1:3}$ are preceded on the low-temperature side by the appearance of anomalies in the $Q^{-1}(T)$ curves (peaks *a* and *c* in Fig. 1). The relaxation effects can be supposed to be explained by the absorption of low-frequency sound caused by resonance vibrations of the walls of magnetic and structural domains in the field of elastic stresses. The appearance of an IF peak *c* at $T < T_{1:3}$ can be due to dissipative processes at the boundaries of antiphase domains that arise in a diffusive way in the process of the structural phase transition of the ordering type [6, 14]. This assumption is supported by the fact that the $Q^{-1}(T)$ peak *c* in the ordered samples is sharper but substantially lower in its intensity then that for the disordered samples, in which the 1 : 3 superstructure is formed during heating (Figs. 1, 4).

Note that the IF anomalies in the acoustic frequency range caused by the vibrations of walls of ferrimagnetic domains were observed previously also for other ferrite spinels (see, e.g., [8, 15]). In addition, the mechanism related to magnetoelastic hysteresis, which is traditionally discussed in studying IF in magnets (see, e.g., [16]), does not work in this case; indeed, it follows from the magnetization measurements in $Li_{0.5}Fe_{2.5}O_4$ at $T \le T_C$ that the $\sigma_T(H)$ curves for both ordered and disordered samples are reversible (Fig. 3). This is not surprising, since the energy of magnetocrystalline anisotropy of lithium ferrite is relatively small; this is caused by spin–orbit interaction of Fe^{3+} ions in the *S* state, which appears only in higher-order perturbation theory [17]. Note also that the presence or absence of 1 : 3 ordering should affect the energy of single-ion anisotropy. This is well confirmed by the results of this paper and follows from the difference in the shapes of the curves $\sigma_H(T) \sim \chi_0(T)$: in the ordered state, as $T \longrightarrow T_C$, a Hopkinson effect is observed; i.e., the appearance of an asymmetric maximum in the $\sigma_H(T)$ curve is observed (curve *2* in Fig. 2). As is well known [17], the appearance of a maximum in the curves of the temperature dependence of magnetic susceptibility,

$$\chi(T) = \frac{\sigma_s^2(T)}{K(T)}, \qquad (2)$$

is due to the fact that the spontaneous magnetization σ_s falls off at $T \longrightarrow T_C$ more slowly than the anisotropy constant *K*. The $\sigma_H(T)$ curve shown in Fig. 2 (curve *1*) is typical of magnetically soft materials with a predominant shape anisotropy [18].

Thus, it is evident that the observed anomaly is due to purely relaxation-related losses caused by irreversible vibrations of domain walls.

As is seen from Fig. 1, the IF peak *a* at ~310°C caused by damping of low-frequency sound at ferrimagnetic domain walls in $Li_{0.5}Fe_{2.5}O_4$ is clearly pronounced in the disordered sample but is virtually absent in the sample with 1 : 3 ordering of the Fe^{3+} and Li^+ ions. The appearance of this effect, in our opinion, can be explained by the substantial differences in the microstructure of the ordered and disordered samples of the ferrite studied. Indeed, in the ordered sample (at $T \le T_{1:3}$), the grains of the polycrystalline aggregate are divided into numerous antiphase domains whose boundaries are formed as a result of shifts of neighboring domains by a lattice half-period. These walls serve as efficient stoppers for the motion of ferrimagnetic domains. In the disordered sample, in which the formation of the 1 : 3 superstructure is suppressed by rapid quenching, such a mechanism of domain-wall pinning is absent and only grain boundaries can serve as obstacles for domain motion. Naturally, in the last case, the dissipative processes related to domain-wall vibrations are stronger.

The shift of T_C toward higher temperatures in the presence of disordering in the *B* sublattice of the $Li_{0.5}Fe_{2.5}O_4$ ferrite, found in magnetic and relaxation measurements, is quite determinate. It is well known that in the framework of the exchange model of ferro (ferri) magnetism, the dependence of the Curie temperature on the degree of short-range order α for the most important case where only the exchange integral for pairs of atoms that are magnetic-moment carriers ("magnetic atoms") is important is as follows [19]:

$$T_C(\alpha) = \frac{W}{k}\left[\ln\frac{(N-1)(c_F + \alpha c_D) + 1}{(N-1)(c_F + \alpha c_D) - 1}\right]^{-1}, \qquad (3)$$

where *W* is the energy of exchange interaction between two magnetic atoms, *k* is the Boltzmann constant, *N* is the coordination number,[2] c_F is the concentration of magnetic atoms, and c_D is the concentration of nonmagnetic atoms.

Although we cannot directly use Eq. (3) when considering a sufficiently complex picture of exchange interactions in a two-sublattice ferrite, qualitatively, it follows from this equation that an increase in the degree of atomic order α, i.e., in our case, a decrease in the number of neighboring magnetic ions Fe^{3+}, should lead to a decrease in T_C and that a decrease in α should result in an increase in T_C, which indeed is observed in magnetic and relaxation experiments.

3. CONCLUSIONS

Thus, based on the results of temperature measurements of the IF parameters in a zero magnetic field, i.e., of the logarithmic decrement Q^{-1} and resonance frequency of vibrations ν, as well as of the polytherms and isotherms of magnetization in ordered and disordered samples of lithium ferrite, we can arrive at some conclusions referring to the entire problem of the relation between the relaxation properties on the one hand and the structure and magnetism of ferrites on the other hand.

[2] It is obvious that only the values of α and *N* for the first coordination shell (α_1 and N_1) are important.

(1) At the Curie temperature T_C and at the $T_{1:3}$ temperature of the structural phase transition of the 1 : 3-type ordering in the octahedral sublattice, anomalies of low-frequency IF are observed in samples that differ in the initial degree of atomic ordering.

(2) The $T_{1:3}$ temperature of the 1 : 3 ordering phase transition is virtually independent of the direction of the temperature change and the degree of atomic order.

(3) A decrease in the degree of structural ordering in one of the sublattices of the ferrite increases T_C and changes the energy of the single-ion magnetocrystalline anisotropy.

(4) Below $T_{1:3}$, some features of IF connected with the vibration of structural (antiphase) domain walls in the field of elastic stresses were revealed.

(5) In disordered samples, a relaxation peak of IF caused by vibrations of ferrimagnetic domain walls in the field of elastic stresses is observed at $T < T_C$; in ordered samples, the presence of antiphase domains leads to suppression of this peak.

The results of this work are qualitative to a certain degree. Although we studied the internal friction and magnetic properties of a particular ferrimagnet, i.e., of lithium ferrite $Li_{0.5}Fe_{2.5}O_4$ with various degrees of atomic ordering, the state of the objects of the investigation could change substantially directly in the process of relaxation or magnetic measurements. This follows foremost from the appearance of weak superlattice reflections in the x-ray diffraction patterns of quenched samples after high-temperature measurements.

ACKNOWLEDGMENTS

This work was supported in part by the Scientific and Technical Center of Ukraine (project STSU no. 2266).

REFERENCES

1. E. W. Gorter and J. A. Schulkes, Phys. Rev. **90**, 487 (1953).
2. N. N. Efimova and Yu. A. Mamaluĭ, Ukr. Fiz. Zh. (Russ. Ed.) **20** (7), 1199 (1975).
3. Sh. Sh. Bashkirov, R. A. Iskhakov, A. B. Liberman, *et al.*, Ukr. Fiz. Zh. (Russ. Ed.) **21** (4), 543 (1976); Fiz. Tverd. Tela (Leningrad) **18** (9), 2565 (1976) [Sov. Phys. Solid State **18**, 1498 (1976)].
4. D. I. Volkov and V. I. Chechernikov, Nauchn. Dokl. Vyssh. Shk., Fiz.-Mat. Nauki, No. 2, 210 (1958).
5. P. B. Braun, Nature **170**, 1123 (1952).
6. E. M. Lifshitz, Zh. Éksp. Teor. Fiz. **11**, 255 (1941).
7. A. G. Khachaturyan, *The Theory of Phase Transformations and the Structure of Solid Solutions* (Nauka, Moscow, 1974).
8. L. D. Landau and I. M. Khalatnikov, Dokl. Akad. Nauk SSSR **96**, 469 (1954).
9. K. P. Belov, *Magnetostriction Effects and Their Technical Applications* (Nauka, Moscow, 1987); K. P. Belov, *Magnetic Transitions* (Fizmatgiz, Moscow, 1959; Consultants Bureau, New York, 1961).
10. V. M. Arzhavitin, V. N. Golovin, G. F. Tikhinskiĭ, *et al.*, Sverkhprovodimost: Fiz., Khim., Tekh. **2**, 153 (1989).
11. C. K. Burdett, Philos. Mag. **18**, 745 (1968).
12. I. K. Kamilov and Kh. K. Aliev, Usp. Fiz. Nauk **140** (4), 639 (1983) [Sov. Phys. Usp. **26**, 696 (1983)].
13. V. A. Finkel', *Structure of Rare-Earth Metals* (Metallurgiya, Moscow, 1978).
14. Ya. S. Umanskiĭ and Yu. A. Skakov, *Physics of Metals. Atomic Structure of Metals and Alloys* (Atomizdat, Moscow, 1978).
15. G. I. Kataev, A. F. Popkov, V. G. Shavrov, and V. V. Shubin, Zh. Éksp. Teor. Fiz. **89**, 1416 (1985) [Sov. Phys. JETP **62**, 820 (1985)].
16. H. G. van Bueren, *Imperfections in Crystals* (North-Holland, Amsterdam, 1961; Inostrannaya Literatura, Moscow, 1962).
17. M. I. Darby and D. E. Isaak, IEEE Trans. Magn. **MAG-10**, 259 (1974).
18. S. V. Vonsovskiĭ, *Magnetism* (Nauka, Moscow, 1971; Wiley, New York, 1974).
19. H. Sato, A. Arrott, and R. Kikuchi, J. Phys. Chem. Solids **10**, 19 (1959).

Translated by S. Gorin

Physics of the Solid State, Vol. 43, No. 11, 2001, pp. 2126–2129. Translated from Fizika Tverdogo Tela, Vol. 43, No. 11, 2001, pp. 2040–2042.
Original Russian Text Copyright © 2001 by Zavorotnev, Medvedeva.

MAGNETISM AND FERROELECTRICITY

"Latent" Paramagnetism and Incommensurate Structures in Three-Sublattice Magnets

Yu. D. Zavorotnev and L. I. Medvedeva

Donetsk Physicotechnical Institute, National Academy of Sciences of Ukraine, Donetsk, 83114 Ukraine

e-mail: zavorot@host.dipt.donetsk.ua

Received January 16, 2001; in final form, April 16, 2001

Abstract—The formation of superstructures due to the interaction of one-component and two-component order parameters in three-sublattice magnets is considered. It is shown that, in the general case, the propagation vector is located in the *XOY* plane and the irreducible vectors can rotate either within one plane or in two mutually perpendicular planes. Under the conditions of "latent" paramagnetism, no superstructure is formed. © *2001 MAIK "Nauka/Interperiodica".*

1. INTRODUCTION

The modern theory describing the formation of long-period structures has been elaborated sufficiently well. Earlier [1–3], it was shown that the formation of these structures can stem from competition between the interactions represented by invariants (quadratic in the first-order spatial derivatives) of the moments of spin density and the second- or fourth-degree invariants of these derivatives in terms of the density of the nonequilibrium thermodynamic potential. Another condition of the existence of the long-period structure is the smallness of the invariant that is linear in the first-order spatial derivatives, which can be provided by distinct space anisotropy of the exchange (or exchange–relativistic) interaction [4]. Dzyaloshinski [4] also considered the symmetry conditions of the existence of these invariants. More recently, Stefanovskiĭ [5] demonstrated that, unlike the situation considered in [4], the formation of a superstructure can occur with the participation of two order parameters which are transformed through different irreducible representations of the space group of symmetry of the paramagnetic phase. Moreover, Bar'yakhtar *et al.* [6] analyzed the formation conditions of superstructures in Cr_2BeO_4 and proved that the density of the nonequilibrium thermodynamic potential can be described by Dzyaloshinski-type invariants of an exchange nature. This situation becomes possible in the case when the expansion of the direct product of the three irreducible representations, according to which two order parameters (the magnetic vectors) are transformed, by the coordinate (in which the first-order derivative is calculated) involves a completely symmetric representation. In this case, the group with respect to which the order parameters are calculated is the permutation group of the magnetic ions in the unit cell. The exchange invariants deduced in [6] are composed of two one-component order parameters. Bar'yakhtar *et al.* [6] also determined the regularities of the formation and existence conditions of incommensurate structures. It was found that, for the one-component order parameters, the propagation vector is invariably aligned with one of the coordinate axes. It should be expected that, in the case of the two-component order parameter, the propagation vector can be arbitrarily directed along one of the coordinate planes. This situation can be realized in three-sublattice magnets. In these compounds, the number of order parameters is no greater than three. Specifically, iron phosphide (Fe_2P), which, as is known, exhibits an incommensurate structure [7], possesses two order parameters [8]: the one-component order parameter (the ferromagnetic vector **F**) and the two-component order parameter consisting of two antiferromagnetic vectors $\mathbf{L}_1$ and $\mathbf{L}_2$, which are transformed with respect to different rows of the same two-dimensional irreducible representation of the permutation group. Yablonski and Medvedeva [8] presented only the explicit form of the nonequilibrium thermodynamic potential and noted the possibility of forming a superstructure in principle, but appropriate calculations supporting this were not performed.

2. FORMALISM

As was noted above, crystals with a triangular structure of the Fe_2P type [8] exhibit two order parameters: the ferromagnetic vector $\mathbf{F} = \mathbf{S}_1 + \mathbf{S}_2 + \mathbf{S}_3$ (the one-component order parameter) and the six-dimensional vector **L** with two component antiferromagnetic vectors $\mathbf{L}_1 = 2^{-1/2}(\mathbf{S}_2 - \mathbf{S}_3)$ and $\mathbf{L}_2 = 6^{-1/2}(2\mathbf{S}_1 - \mathbf{S}_2 - \mathbf{S}_3)$, where $\mathbf{S}_i$ (i = 1, 2, 3) is the spin of the ith magnetic ion. The $\mathbf{L}_1$ and $\mathbf{L}_2$ vectors are transformed with respect to the different rows of the same two-dimensional irreducible representation E', as well as the Y and X components of the polar vector, and the **F** vector is transformed according to the completely symmetric irreduc-

ible representation of the permutation group D_{3h}. As was shown in [8], the density of the nonequilibrium thermodynamic potential in the absence of a magnetic field can be represented in the following form:

$$\Phi = \delta_1\mathbf{F}^2 + \delta_2(\mathbf{L}_1^2 + \mathbf{L}_2^2) + \Delta\left(\mathbf{F}\frac{\partial\mathbf{L}_1}{\partial y} - \mathbf{L}_1\frac{\partial\mathbf{F}}{\partial y} + \mathbf{F}\frac{\partial\mathbf{L}_2}{\partial x} - \mathbf{L}_2\frac{\partial\mathbf{F}_1}{\partial x}\right) + \alpha_1\left(\frac{\partial\mathbf{F}}{\partial x}\right)^2 + \alpha_2\left(\frac{\partial\mathbf{F}}{\partial y}\right)^2 + \alpha_3\left(\frac{\partial\mathbf{L}_1}{\partial y}\right)^2 + \alpha_4\left(\frac{\partial\mathbf{L}_2}{\partial x}\right)^2. \quad (1)$$

The appropriate system of Ostrogradski equations for the determination of the extrema has the form

$$\begin{cases} \alpha_1 F''_{i(xx)} + \alpha_2 F''_{i(yy)} - \Delta(L'_{i1(y)} + L'_{i2(x)}) - \delta_1 F_i = 0 \\ \alpha_3 L''_{i1(yy)} + \Delta F'_{i(y)} - \delta_2 L_{i1} = 0 \\ \alpha_4 L''_{i2(xx)} + \Delta F'_{i(x)} + \delta_2 L_{i2} = 0, \end{cases} \quad (2)$$

where $i = x, y, z$ denote the projections of the vectors and the parenthetic subscripts indicate the variables with respect to which the derivatives are calculated (the Z axis coincides with the threefold crystallographic axis).

Now, we change over to the spherical coordinates in the system of equations (2) in accordance with the relationships

$$F_z = |\mathbf{F}|\cos\theta_3, \quad L_{1z} = |\mathbf{L}_1|\cos\theta_1, \quad L_{2z} = |\mathbf{L}_2|\cos\theta_2,$$
$$F_x = |\mathbf{F}|\sin\theta_3\cos\varphi_3, \quad L_{1x} = |\mathbf{L}_1|\sin\theta_1\cos\varphi_1,$$
$$L_{2x} = |\mathbf{L}_2|\sin\theta_2\sin\varphi_2,$$
$$F_y = |\mathbf{F}|\sin\theta_3\sin\varphi_3, \quad L_{1y} = |\mathbf{L}_1|\sin\theta_1\sin\varphi_1,$$
$$L_{2y} = |\mathbf{L}_2|\sin\theta_2\sin\varphi_2,$$

where θ_1 and φ_1 ($i = 1, 2, 3$) are the polar and azimuthal angles, respectively.

It follows from the transformed system of equations that there exist the mutually independent solutions for the azimuthal angles:

$$\varphi_i = \pm\frac{\pi}{4}. \quad (3)$$

According to relationship (3), rotation of the irreducible vectors can occur in the following ways.

(1) All three vectors rotate in one plane if the azimuthal angles φ_i ($i = 1, 2, 3$) are of the same sign.

(2) Two of the three vectors rotate in one plane if their azimuthal angles φ are of the same sign and the third vector, with opposite sign of φ, rotates in the perpendicular plane.

Making allowance for relationships (3), we seek a solution to the system of Ostrogradski equations in the form

$$\theta_3 = k_x x + k_y y, \quad \theta_1 = \theta_3 + \rho_1, \quad \theta_2 = \theta_3 + \rho_2, \quad (4)$$

where ρ_i ($i = 1, 2$) are constants specifying the phase shift and k_x and k_y are the projections of the propagation vector onto the OX and OY axes, respectively. It follows from the minimum condition of the potential that the relationships $\rho_j = -\pi/2(\rho_j = \pi/2)$ ($j = 1, 2$) are satisfied at $\Delta > 0$ ($\Delta < 0$). It is evident that the phases of the polar angles of the antiferromagnetic vectors coincide with each other and are shifted through an angle of $\pi/2$ with respect to the ferromagnetic vector.

By substituting relationships (4) into the system of equations (2) rewritten in the spherical coordinates, we obtain a system of three homogeneous equations for determining the magnitudes of three irreducible vectors $\mathbf{F}$, $\mathbf{L}_1$, and $\mathbf{L}_2$. Then, we set the determinant of the system equal to zero and obtain the equation

$$-(\alpha_3 k_x^2 + \delta_2)(\alpha_4 k_y^2 + \delta_2)(\alpha_1 k_x^2 + \alpha_2 k_y^2 + \delta_1) + \Delta^2 k_x^2(\alpha_4 k_y^2 + \delta_2) + \Delta^2 k_y^2(\alpha_3 k_x^2 + \delta_2) = 0. \quad (5)$$

As can be seen from Eq. (5), the propagation vector of the superstructure is located in the XOY plane and has an arbitrary direction. Equation (5) specifies the relation between the k_x and k_y components. In order to obtain their actual values, it is necessary to determine the derivative of the density of the nonequilibrium thermodynamic potential with respect to k_x or k_y. Since the temperature T appears in the equations used for determining the k_x and k_y values, its variation affects both the magnitude $|\mathbf{k}|$ and the direction of the propagation vector. As was shown above, the azimuthal angles φ are temperature independent and constant. Therefore, the propagation vector $\mathbf{k}$ cannot be aligned with any of the possible planes of rotation of the irreducible vectors. In this case, the structures thus formed are either skew spiral structures, when all the order parameters rotate in the same plane, or mixed structures, provided the rotation occurs in different planes.

It should be noted that, in the framework of the theory accounting for one-dimensional order parameters, the propagation vector $\mathbf{k}$ of the superstructure is aligned only with one of the crystallographic axes and the temperature variation affects solely the magnitude and not the direction of the propagation vector [3].

3. RESULTS AND DISCUSSION

Let us now analyze Eq. (5). For simplicity, we assume that $\alpha_1 = \alpha_2$ and $\alpha_3 = \alpha_4$. Then, at $\delta_1 = 0$, we have

$$\alpha_4^2\alpha_1 k_x^2 k_y^2 k^2 + \alpha_4\delta_2\alpha_1 k^4 - 2\Delta^2\alpha_4 k_x^2 k_y^2 + k^2(\alpha_1\delta_2^2 - \Delta^2\delta_2) = 0, \quad (6)$$

where $k^2 = k_x^2 + k_y^2$. Similarly, at $\delta_2 = 0$, we obtain the expression

$$\alpha_1\alpha_4 k^2 = 2\Delta^2 - \alpha_4(T_N - T_C), \quad (7)$$

where T_N and T_C are the Néel and Curie temperatures, respectively.

We consider the following cases.

(i) $T_N > T_C$.

(a) $\delta_2 = 0$. In this case, the solution to Eq. (7) exists only when $\alpha_4(T_N - T_C) < 2\Delta^2$; i.e., the temperatures T_N and T_C should not significantly diverge one from the other. In the opposite situation, the formation of a superstructure becomes impossible.

(b) $\delta_1 = 0$ and $\delta_2 < 0$. Equation (6) involves two changes of sign in the sequence of coefficients, which results in two different positive solutions for k_x^2. Consequently, if the conditions of stability are met, two superstructures with different propagation vectors should occur near the T_C temperature.

(ii) $T_C > T_N$.

(a) $\delta_1 = 0$ and $\delta_2 > 0$. If $\alpha_1(T_C - T_N) > \Delta^2$, Eq. (6) has two changes of sign in the sequence of coefficients and, correspondingly, two positive solutions; otherwise, it has only one solution. In this case, the difference between the Curie and Néel temperatures should be sufficiently large. A similar requirement should be fulfilled in the case of the formation of superstructures due to the interaction of two one-component order parameters [9].

(b) $\delta_2 = 0$ and $\delta_1 < 0$. Equation (7) has solutions at any parameters; i.e., the superstructure can be formed at any difference between the Curie and Néel temperatures.

It is evident that, at $T_N > T_C$ and $T_C > T_N$, the formation conditions of superstructures differ radically. In the first case, the long-period structure exists only when the difference between the Curie and Néel temperatures is sufficiently small, whereas in the second case, this difference should be sufficiently large.

The above consideration of superstructures was performed without taking the specific configuration responsible for the particular superstructure into account. In the case of a two-component order parameter, the inclusion of the specific configuration in the analysis can substantially affect the results. For example, three-sublattice magnets can occur in the antiferromagnetic–ferromagnetic state in which $\mathbf{L}_1 = 0$ [8]. In this case, we have $\mathbf{S}_2 = \mathbf{S}_3$ and $\mathbf{S}_1 = -2\mathbf{S}_3 + \mathbf{S}_4$, where the term $\mathbf{S}_4$, as was shown in [8], appears as the result of the occurrence of fourth-degree invariants containing the product $\mathbf{F}\mathbf{L}_2^3$ in the nonequilibrium thermodynamic potential. It is easy to see that only the spatial derivatives with respect to x will appear in the density of the nonequilibrium thermodynamic potential (1); i.e., the propagation vector will be directed along the OX axis. The superstructure thus formed can be either a spiral-type structure or a cycloidal-type structure. Furthermore, a configuration with latent paramagnetism becomes possible [8, 10]. For this magnetic configuration in the system of crystallographically equivalent paramagnetic ions, the effective exchange field in one of the three sublattices turns is completely compensated and the first-order spin moment of this sublattice vanishes. Actually, for this configuration, we have $\mathbf{F} = \mathbf{L}_2 = 0$. Hence, it follows that $\mathbf{S}_1 = 0$ and $\mathbf{S}_2 = -\mathbf{S}_3$; i.e., the ions of the first sublattice have a paramagnetic nature, whereas the ions of the other sublattices form an antiferromagnetic structure. Since $\mathbf{F} = \mathbf{L}_2 = 0$ and invariants of a different nature are absent in the density of the nonequilibrium thermodynamic potential (1), the superstructure cannot be formed in the configuration with latent paramagnetism.

4. CONCLUSIONS

Thus, we can state that three-sublattice magnets are characterized by the following features.

(1) Three-sublattice magnets can form four types of superstructures, namely, cycloidal, spiral, mixed, and skew spiral structures. In the first two structures, the $\mathbf{L}_2$ vector becomes zero (the antiferromagnetic–ferrimagnetic state) and the $\mathbf{F}$ and $\mathbf{L}_1$ vectors rotate in the same plane. In structures of the third and fourth types, all the order parameters are nonzero and the $\mathbf{F}$, $\mathbf{L}_1$, and $\mathbf{L}_2$ vectors can rotate either in different, mutually perpendicular planes or in the same plane.

(2) The propagation vector $\mathbf{k}$ is located in the XOY plane and has an arbitrary direction. The magnitude of this vector and its direction can vary with temperature. In the antiferromagnetic–ferrimagnetic state, this vector has the only component k_x.

(3) A long-period structure cannot be formed in the configuration with latent paramagnetism.

(4) In the structures considered in this work, the propagation vector for all nonzero order parameters is generally located neither in the plane of rotation of the irreducible vectors nor in the perpendicular direction. This suggests that these superstructures are not spiral or cycloidal structures in a universally accepted sense.

ACKNOWLEDGMENTS

We would like to thank E.P. Stefanovskiĭ for his participation in discussions of the results.

REFERENCES

1. T. A. Kaplan, Phys. Rev. **116**, 888 (1959).
2. A. Yoshimori, J. Phys. Soc. Jpn. **14**, 807 (1959).
3. Yu. A. Izyumov, Usp. Fiz. Nauk **144**, 439 (1984) [Sov. Phys. Usp. **27**, 845 (1984)].
4. I. E. Dzyaloshinski, Zh. Éksp. Teor. Fiz. **47**, 992 (1964) [Sov. Phys. JETP **20**, 665 (1964)].
5. E. P. Stefanovskiĭ, Fiz. Tverd. Tela (Leningrad) **28** (11), 3452 (1986) [Sov. Phys. Solid State **28**, 1941 (1986)].
6. V. G. Bar'yakhtar, E. P. Stefanovskiĭ, and D. A. Yablonski, Pis'ma Zh. Éksp. Teor. Fiz. **42** (6), 258 (1985) [JETP Lett. **42**, 317 (1985)].
7. H. Fujii, T. Hokabe, K. Eguchi, *et al.*, J. Phys. Soc. Jpn. **51**, 414 (1982).
8. D. A. Yablonski and L. I. Medvedeva, Physica B (Amsterdam) **167**, 125 (1990).
9. V. G. Bar'yakhtar and E. P. Stefanovskiĭ, Fiz. Nizk. Temp. **22**, 904 (1996) [Low Temp. Phys. **22**, 693 (1996)].
10. Yu. M. Gufman, E. I. Kut'in, V. L. Lorman, and A. M. Prokhorov, Pis'ma Zh. Éksp. Teor. Fiz. **46**, 228 (1987) [JETP Lett. **46**, 287 (1987)].

Translated by O. Moskalev

Physics of the Solid State, Vol. 43, No. 11, 2001, pp. 2130–2135. Translated from Fizika Tverdogo Tela, Vol. 43, No. 11, 2001, pp. 2043–2047.
Original Russian Text Copyright © 2001 by Bespyatykh, Bugaev, Dikshteĭn.

MAGNETISM AND FERROELECTRICITY

Surface Polaritons in Composite Media with Time Dispersion of Permittivity and Permeability

Yu. I. Bespyatykh, A. S. Bugaev, and I. E. Dikshteĭn

Institute of Radio Engineering and Electronics (Fryazino Branch), Russian Academy of Sciences, pl. Vvedenskogo 1, Fryazino, Moscow oblast, 141120 Russia

Received March 1, 2001

Abstract—The propagation of electromagnetic waves in a composite medium based on an array of conducting wires in a ferromagnetic nonconducting matrix is discussed. It is demonstrated that, in certain ranges of frequencies and wavelengths, the composite under investigation can possess properties inherent in a "left-handed" medium. The regions of the existence of bulk and surface localized electromagnetic waves are explored. Consideration is given to the dispersion of surface electromagnetic waves in thick layers of the composite. © *2001 MAIK "Nauka/Interperiodica".*

1. INTRODUCTION

The design of new composites is of considerable physical and applied interest, because composite media can possess specific properties that are not observed in ordinary materials. In recent years, important theoretical and experimental results have been obtained for composite materials based on different conducting elements arranged in a dielectric nonmagnetic matrix. Under electromagnetic radiation, a periodic array composed of conducting elements is equivalent to an effective medium with a time dispersion of the permittivity and permeability when the radiation wavelength is much longer than both the element dimension and the lattice spacing.

Pendry *et al.* [1] proved that, in the long-wavelength limit, a three-dimensional array composed of very thin conducting straight wires behaves as an electron plasma in a metal. For a plane wave with frequency ω and wave vector $\mathbf{k}$, the permittivity ε of the electron plasma with frequency ω_p is represented by the relationship

$$\varepsilon(\omega) = 1 - \frac{\omega_p^2}{\omega(\omega - i\gamma)} \qquad (1)$$

and does not depend on the wave vector over a wide range of wavelengths. It is of importance that the permittivity $\varepsilon(\omega)$ is negative at $\omega < \omega_p$ and $\gamma = 0$. Although the damping parameter γ is substantially less than the plasma frequency ($\gamma \ll \omega_p$), the plasma waves in metals are observed only in the ultraviolet and visible frequency ranges. This is explained by the fact that metals exhibit rather high values of the electron concentration n, the plasma frequency $\omega_p = (ne^2/4\pi m)^{1/2}$, and the damping parameter γ. For example, these parameters for aluminum are as follows: $\omega_p = 15$ eV and $\gamma = 0.1$ eV. In [1], it was demonstrated that, in artificial materials made up of thin conducting wires, the mean concentration of charge carriers and the effective plasma frequency can be decreased by six orders of magnitude and the effective mass of charge carriers can be increased by one order of magnitude as compared to the effective electron mass in the bulk metal. In this case, the ratio γ/ω_p remains sufficiently small ($\gamma/\omega_p \propto 0.01$ for aluminum). The plasma resonance in these materials, unlike the bulk metal, occurs in the microwave range.

Periodic systems composed of different-type ring conducting elements (wire rings, split rings, helices, layers in the form of split rings, etc.) with a considerable effective permeability have been proposed and examined in recent works [2–6]. These systems are characterized by the resonant frequency of electromagnetic wave absorption. The dispersion of their effective permeability $\mu(\omega)$ in the long-wavelength range is described by the formula

$$\mu(\omega) = 1 - \frac{F\omega^2}{\omega^2 - \omega_0^2 + i\omega\Gamma}, \qquad (2)$$

where ω_0 is the resonant frequency, Γ is the dissipation factor, and F is a constant. It is worth noting that all these quantities depend on the internal structure and concentration of the conducting elements. As is the case with the transverse diagonal component of the permeability of a homogeneous magnetized isotropic ferromagnet, the effective permeability (2) in the vicinity of the resonance is negative in the high-frequency range. Smith *et al.* [6] noted that, by combining thin conducting straight wires and the aforementioned ring elements with a large inductance and capacitance, it is possible to construct composites whose effective permittivity and permeability are negative in a certain range of frequencies. This would allow experimental observations of the unusual effects, which were theoretically predicted by Pafomov [7] and Veselago [8–10] in the 1950s–1960s.

Earlier works [7–10] dealt primarily with the propagation of uniform plane electromagnetic waves in right-handed and left-handed media and with wave reflection from the interface between these media. However, it is important to know the specific features of the spectrum of excitations occurring in materials with a time dispersion of the general form, for example, the features of the spectrum of bulk and surface long waves in plane-parallel layers of a composite.

In the present work, we examined the spectrum of surface polaritons in a layer of a composite material based on a periodic lattice of conducting wires [1] in a ferromagnetic nonconducting matrix.

2. THEORETICAL ANALYSIS

Let us analyze the dispersion of surface electromagnetic waves in a sufficiently thick layer of a composite material. This layer covers the region $-L/2 \le y \le L/2$ in space and is composed of a ferrodielectric matrix involving a simple cubic lattice of thin conducting or superconducting wires (similar to the structure comprising a regular array of conducting wires in a dielectric nonmagnetic matrix [1]). In the case when the lattice spacing is very small compared to the layer thickness, the electromagnetic radiation wavelength, and the penetration depth of the electromagnetic wave, the high-frequency properties of the composite can be described within the continuous approximation. The volume percentage of the conducting material is small, and the permittivity tensor $\hat{\varepsilon}$ coincides with that calculated in [1], that is,

$$\hat{\varepsilon} = \varepsilon\delta_{ik}, \tag{3}$$

where the quantity ε is defined by formula (1). The effective plasma frequency ω_p and the parameter γ of damping at the expense of resistance losses in the conductors are expressed through the parameters of the conducting wires as follows:

$$\omega_p^2 = 2\pi c^2/a^2\ln(a/r), \quad \gamma = 4a^2\omega_p^2/r^2\sigma, \tag{4}$$

where σ is the conductivity, r is the wire radius, a is the lattice spacing, and c is the velocity of light in free space. Note that the γ/ω_p ratio is inversely proportional to the bulk concentration of the conducting material; hence, its value cannot be inappropriately low. Generally speaking, it is preferable to use superconductors for preparing composites with a high Q-factor in the microwave range. Hereafter, we assume that the damping effect in a metal and a ferromagnet is small and can be ignored. According to Pendry *et al.* [5], who calculated the permeability of the lattice of conducting rods arranged in a dielectric matrix, the permeability of this composite is proportional to the bulk concentration of the metal. Since the bulk concentration is assumed to be rather low, the effective permeability of the lattice of conducting elements in the ferromagnetic matrix is approximately equal to the permeability of the matrix. Therefore, for the layer in a tangential external magnetic field $\mathbf{H}_0 \| \mathbf{n}_z$, when the excitation amplitude varies with time t as $\exp(i\omega t)$, the permittivity is represented in the form

$$\varepsilon = \frac{\Omega^2 - \Omega_p^2}{\Omega^2}, \tag{5}$$

and the permeability tensor is given by

$$\hat{\mu} = \begin{pmatrix} \mu & i\nu & 0 \\ -i\nu & \mu & 0 \\ 0 & 0 & 1 \end{pmatrix}. \tag{6}$$

Here, $\Omega = \omega/\omega_M$, $\Omega_p = \omega_p/\omega_M$, $\omega_M = 4\pi g M_0$, $g > 0$ is the gyromagnetic ratio, M_0 is the saturation magnetization of the magnetic matrix,

$$\mu = 1 + \frac{\Omega_0}{\Omega_0^2 - \Omega^2}, \quad \nu = \frac{\Omega}{\Omega^2 - \Omega_0^2}, \qquad \Omega_0 = H_0/(4\pi M_0). \tag{7}$$

The electromagnetic field inside and outside the composite satisfies the Maxwell equations:

$$[\nabla \times \mathbf{e}] = -ik_0\mathbf{b}, \quad \nabla \cdot \mathbf{d} = 0, \qquad [\nabla \times \mathbf{h}] = -ik_0\mathbf{d}, \quad \nabla \cdot \mathbf{b} = 0, \tag{8}$$

where $k_0 = \omega/c$. The continuity conditions of the tangential components of the electric $\mathbf{e}$ and magnetic $\mathbf{h}$ fields and the normal components of the electric $\mathbf{d} = \hat{\varepsilon}\mathbf{e}$ and magnetic $\mathbf{b} = \hat{\mu}\mathbf{h}$ inductions are met at the layer boundary. We will restrict our consideration to the case of a transverse electric wave whose field is specified as $\{h_x, h_y, e_z\}$ and propagates along the $\mathbf{n}_x$ axis.

The solution to the system of Maxwell equations (8) with the boundary conditions at the interface will be sought under the assumption that the dependence of the electric field component e_z on the x and y coordinates is described by the expression

$$e_z = \begin{cases} a_1\exp(-ikx - q_0 y), & y > L/2 \\ [a_2\exp(q_1 y) + a_3 & \\ \times \exp(-q_1 y)]\exp(-ikx), & -L/2 \le y \le L/2 \\ a_4\exp(-ikx + q_0 y), & y < -L/2, \end{cases} \tag{9}$$

where

$$q_0 = \sqrt{k^2 - k_0^2}, \quad q_1 = \sqrt{k^2 - k_0^2\varepsilon\mu_\perp}, \qquad \mu_\perp = (\mu^2 - \nu^2)/\mu.$$

The expression for the magnetic induction $\mathbf{b}$ follows immediately from the first equation of system (8), and

the constants a_1, a_2, a_3, and a_4 are determined from the boundary conditions. We omit simple calculations and write the dispersion relationship for electromagnetic waves localized in the vicinity of the layer:

$$[q_1^2 + \mu_\perp^2 q_0^2 - (\nu/\mu)^2 k^2]\sinh(q_1 L) + 2\mu_\perp q_0 q_1 \cosh(q_1 L) = 0, \quad (10)$$

where $\mu^2 - \nu^2 \neq 0$.

In the limiting case of short wavelengths, we have $q_0 \cong q_1 \cong |k|$ and relationship (10) describes the dispersion of a Damon–Eshbach wave. The inequality

$$k^2 > k_0^2 \quad (11)$$

is the necessary and sufficient condition for the electromagnetic emission to be absent.

Equation (10) is transcendental, and, hence, its solutions in the general form can be found only by numerical methods.

From the standpoint of spin-wave electronics, the principal interest is in analyzing surface electromagnetic modes whose field amplitude exponentially decreases deep in the layer. In addition to inequality (11), the region of the existence of surface electromagnetic waves in the plane $k\Omega$ is limited by the inequality

$$k^2 > k_0^2 \varepsilon \mu_\perp. \quad (12)$$

If this inequality is not satisfied, the electromagnetic wave is a bulk wave.

For short wavelengths or thick layers, we have $q_1 L \gg 1$ and the dispersion relationship (10) takes the simple form

$$(q_1 + \mu_\perp q_0)^2 - (\nu/\mu)^2 k^2 = 0. \quad (13)$$

Since the left-hand side of Eq. (13) is an even function of the frequency Ω and the wave number k, the dispersion curves in the half-plane $k\Omega$ are symmetric with respect to the ordinate axis. After the appropriate rearrangement of the terms and squaring of the right-hand and left-hand sides of Eq. (13), we obtain the biquadratic equation for determining the dependence $k(\Omega)$, that is,

$$A_2 k^4 - A_1 k^2 - A_0 = 0, \quad (14)$$

where

$$A_2 = \mu_\perp^2[4 - (\mu_\perp + 1/\mu)^2],$$

$$A_1 = 2k_0^2\mu_\perp[2\mu_\perp(1 + \varepsilon\mu_\perp) - (\varepsilon + \mu_\perp)(\mu_\perp + 1/\mu)],$$

$$A_0 = k_0^4 \mu_\perp^2 (\varepsilon - \mu_\perp)^2.$$

One of the solutions to Eq. (14) is physically meaningless and results from the squaring of Eq. (13).

At $k^2 \gg k_0^2$, we have $|\varepsilon\mu_\perp| \gg 1$ and

$$k^2 \cong k_M^2 \cong \frac{(\Omega^2 - \Omega_p^2)(\Omega^2 - \Omega_0^2)}{2(\Omega_0 + 1/2) \pm \Omega \operatorname{sgn} k}, \quad k_M^2 = (\omega_M/c)^2, \quad \Omega_1 = \sqrt{\Omega_0(\Omega_0 + 1)}. \quad (15)$$

The signs $\pm$ in relationship (15) correspond to the propagation of the surface electromagnetic wave along the lower and upper boundaries of the layer. The dispersion of short surface waves depends on the normalized effective plasma frequency Ω_p. The surface waves are forward waves when $\Omega_p < \Omega_0 + 1/2$ and backward waves when $\Omega_p > \Omega_0 + 1/2$. This implies that the change in sign of the permittivity ε leads to a change in sign of the group velocity of the surface wave. The regions of existence of the bulk and surface localized wave solutions and the dispersion curves of the surface electromagnetic mode in the layer at different ratios of the quantities Ω_p, Ω_0, $\Omega_1 = \sqrt{\Omega_0(\Omega_0 + 1)}$, and $\Omega_2 = \Omega_0 + 1$ are qualitatively shown in Figs. 1–4.

In Figs. 1–4, straight lines *1* ($q_0 = 0$), which are described by the expression

$$|k| = \kappa_0(\Omega) = k_M \Omega, \quad (16)$$

separate the localized and nonlocalized wave solutions. Curves *2* and *3*, which are represented by the relationship

$$|k| = \kappa_1(\Omega) = k_M \sqrt{(\Omega^2 - \Omega_p^2)(\Omega_2^2 - \Omega^2)/(\Omega_1^2 - \Omega^2)} \quad (17)$$

and whose points correspond to $q_1 = 0$, are the boundaries between the regions of existence of bulk and surface waves. The curve described by formula (17) is doubly connected, because the inverse function $\Omega(\kappa_1)$ is determined from the biquadratic equation and has two positive branches. As a consequence, the region of the existence of bulk waves is singly connected, whereas the region of the existence of surface waves is doubly connected. The upper branch of the curve corresponding to relationship (17) is of no interest, because it completely lies in the region of nonlocalized solutions.

For $\Omega_p < \Omega_1$ (Fig. 1), the region of the existence of bulk waves (region *I*) is bounded by straight line *1* from the left, the lower $\kappa_1(\Omega)$ branch [curve *2*, relationship (17)] from below, and the straight line $\Omega = \Omega_1$ from above. The low-frequency region of the existence of surface waves (region *II*) is located to the right of straight line *1* and below the $\kappa_1(\Omega)$ branch (curve *2*). The high-frequency region of the existence of surface waves (region *III*) lies to the right of straight line *1* and above the straight line $\Omega = \Omega_1$. In region *II*, the dispersion curve of the surface electromagnetic wave (curve

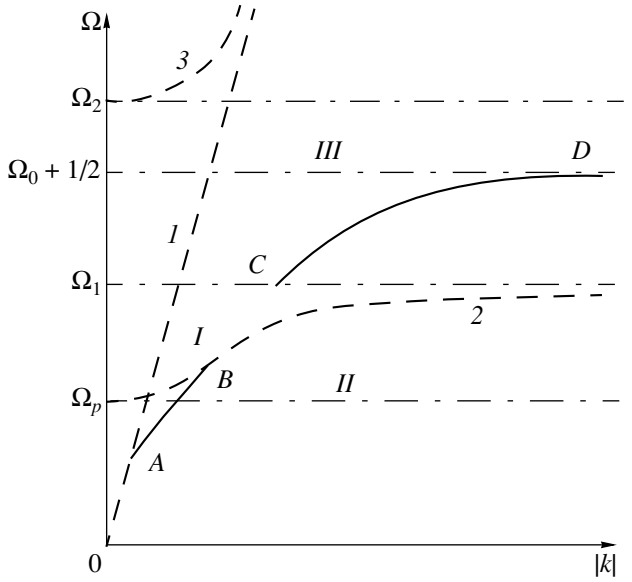

Fig. 1. Regions of the existence of (*I*) bulk and (*II*, *III*) surface localized waves and the dispersion curves of surface electromagnetic waves (curves *AB* and *CD*) at $\Omega_p < \Omega_1$.

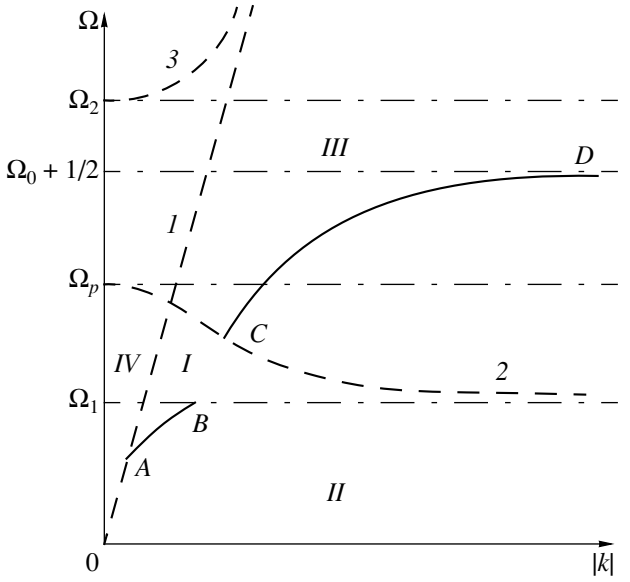

Fig. 2. Regions of the existence of (*I*) bulk and (*II*, *III*) surface localized waves and (*IV*) nonlocalized backward waves and the dispersion curves of surface electromagnetic waves (curves *AB* and *CD*) at $\Omega_1 < \Omega_p < \Omega_0 + 1/2$.

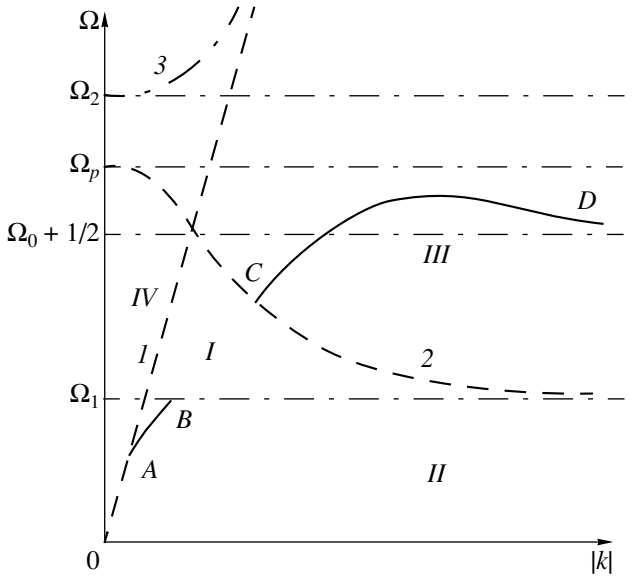

Fig. 3. Regions of the existence of (*I*) bulk and (*II*, *III*) surface localized waves and (*IV*) nonlocalized backward waves and the dispersion curves of surface electromagnetic waves (curves *AB* and *CD*) at $\Omega_0 + 1/2 < \Omega_p < \Omega_2$.

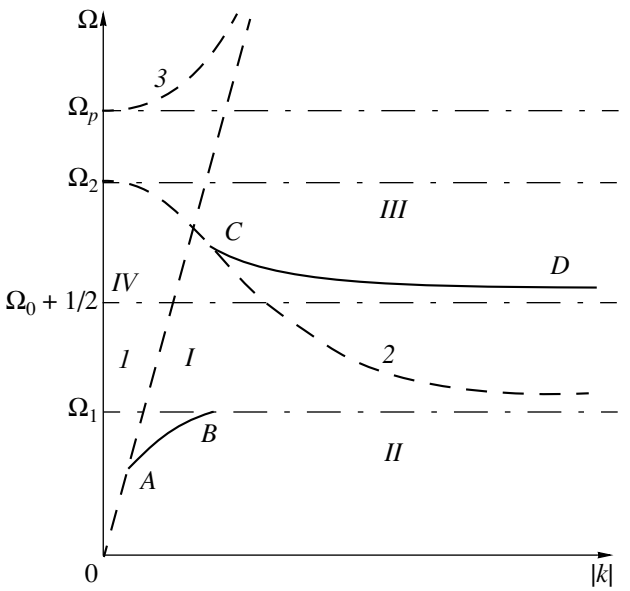

Fig. 4. Regions of the existence of (*I*) bulk and (*II*, *III*) surface localized waves and (*IV*) nonlocalized backward waves and the dispersion curves of surface electromagnetic waves (curves *AB* and *CD*) at $\Omega_p > \Omega_2$.

AB) terminates in the straight line $|k| = \kappa_0(\Omega) = k_M\Omega$ at point *A* with the coordinates

$$k = k_A = k_M\Omega_A,$$
$$\Omega = \Omega_A = \Omega_1\Omega_p(\Omega_0 + \Omega_p^2)^{-1/2} \tag{18}$$

and continuously goes into the branch of bulk waves in the lower branch of the curve $|k| = \kappa_1(\Omega)$ (curve *2*) at point *B* with the coordinates

$$k = k_B = \kappa_1(\Omega_B), \quad \Omega = \Omega_B. \tag{19}$$

In this case, the frequency Ω_B satisfies the equation

$$B_2\Omega_B^4 - B_1\Omega_B^2 + B_0 = 0, \quad B_2 = 1 + \Omega_2 + \Omega_p^2,$$
$$B_1 = \Omega_2^3 + (1 + 2\Omega_2^2)\Omega_p^2, \quad B_0 = \Omega_2^4\Omega_p^2.$$

In region *III*, the branch of surface waves (curve *CD*) terminates in the straight line $\Omega = \Omega_1$ at point *C* with the coordinates

$$|k| = k_C = k_M\Omega_1\Omega_2^{1/2}, \quad \Omega = \Omega_C = \Omega_1. \qquad (20)$$

The quantity $\mu_\perp$ has a feature at $\Omega = \Omega_1$. Consequently, at $\Omega \longrightarrow \Omega_1$, the depth q_1^{-1} of penetration of the surface wave into the composite tends to zero and the long-wave approximation in the vicinity of the line $\Omega = \Omega_1$ turns out to be inapplicable at any parameter Ω_p. It follows from relationship (15) that, at $|k| \longrightarrow \infty$, the wave frequency Ω tends to a value of $\Omega = \Omega_0 + 1/2$, which coincides with the upper boundary of the spectrum of surface waves in a ferromagnetic layer free from conducting elements. However, at $|k| \propto 2\pi/a$, it is necessary to take into account the periodicity of the system. In regions *II* and *III*, the surface waves are forward waves at any *k* value.

In the case where $\Omega_1 < \Omega_p < \Omega_2$ (Figs. 2, 3), the region of bulk localized electromagnetic waves in the plane $k\Omega$ is bounded by the straight lines $|k| = \kappa_0(\Omega) - k_M\Omega$ (line *1*) and $\Omega = \Omega_1$ from the left and below and by the lower branch *2* of the curve $|k| = \kappa_1(\Omega)$ from above. The remaining doubly connected part of the $k\Omega$ plane with the $|k|$ values lying to the right of straight line *1* (regions *II*, *III*) is the region in which the surface electromagnetic waves can exist. The dispersion of surface waves in region *II* (curve *AB*) is positive. The terminal point *A* of this curve is specified by coordinates (18), and the terminal point *B*, at which the surface wave changes over to the bulk wave, is defined by coordinates (20). In region *III*, the dispersion branch of surface waves terminates at point *C* with coordinates (19) and asymptotically approaches the straight line $\Omega = \Omega_0 + 1/2$ with an increase in $|k|$. At $\Omega_p < \Omega_0 + 1/2$, the surface waves are forward waves (Fig. 2). When $\Omega_p > \Omega_0 + 1/2$ (Fig. 3), the dispersion of surface waves can become negative with an increase in $|k|$.

For $\Omega_p > \Omega_2$ (Fig. 4), the regions of the existence of bulk and surface localized wave solutions are virtually identical to those described in the preceding case. The surface waves also occur in the lower region (curve *AB*) and are forward waves. The terminal points of the dispersion curve of surface waves (curve *AB*) are specified by the same coordinates as in the case where $\Omega_1 < \Omega_p < \Omega_2$. However, as the effective plasma frequency Ω_p increases, the dispersion curve *AB* approaches line *1* represented by the expression $|k| = \kappa(\Omega)$ and contracts to the intersection point of straight lines *1* ($q_0 = 0$) and $\Omega = \Omega_1$ with the coordinates

$$|k| = k_M\Omega_1, \quad \Omega = \Omega_1. \qquad (21)$$

It should be emphasized that, in the vicinity of this point, the long-wave approximation becomes incorrect. In the upper region *III*, the surface waves are backward waves; the dispersion branch of surface waves continuously goes into the branch of bulk waves at the point with the coordinates given by the formula (19).

Kaganov and Shalaeva [11] described the high-frequency branch of surface polaritons. In the system under investigation, this branch is absent, because we disregard the electric polarizability of the ferromagnetic matrix. This branch appears when the permittivity of the ferromagnet $\varepsilon_0 > 1$ is taken into account. For this purpose, it is necessary to calculate preliminarily the effective permittivity of the composite.

It is very important that the given composite is characterized by the region of nonlocalized bulk solutions in the $k\Omega$ plane (Figs. 2–4, region *IV*), in which the inequalities $\varepsilon < 0$, $\mu_\perp < 0$, $k^2 < k_0^2$, and $k^2 < k_0^2\varepsilon\mu_\perp$ are met simultaneously. It is easy to demonstrate that the sufficient condition for existence of this region is the fulfillment of the inequality

$$\Omega_p > \Omega_1. \qquad (22)$$

In this range of frequencies and wave numbers, the composite behaves as a left-handed medium and the phase velocity of the bulk electromagnetic wave is oppositely directed to the group velocity.

3. CONCLUSION

Thus, the interaction of magnetization oscillations with plasma oscillations leads to the appearance of an additional branch of surface electromagnetic waves in the long-wavelength excitation spectrum of the composite layer. In the composite layer, unlike a purely ferromagnetic layer, the surface electromagnetic waves can be forward, backward, and mixed waves depending on the plasma frequency (and its related sign of the effective permittivity).

It is worth noting that, in a certain frequency range, the studied composite with nonrigid requirements imposed on the parameters of conducting elements can possess properties inherent in a left-handed medium. The main advantage of this composite over the composite material proposed by Smith *et al.* [6] is that it can be produced using planar technology. For example, multilayer structures composed of yttrium iron garnet films alternating with two-dimensional conducting arrays that are prepared by photolithography are suitable for observing the violation of Snell's law. In this case, the main difficulties are most likely associated with the choice of the optimum parameters for conducting elements to provide appropriate attenuation of electromagnetic waves and with the necessity of preparing a sufficiently large bulk system.

The results obtained in this work on the propagation of electromagnetic waves in a composite material based on a three-dimensional cubic lattice composed of conducting elements are also valid for composite media with a two-dimensional array of conducting wires aligned parallel to the *z* axis.

ACKNOWLEDGMENTS

This work was supported by the Russian Foundation for Basic Research (project nos. 99-02-39009, 99-02-17404, and 01-02-16596), the Committee of Scientific Research of Poland, and the International Center of Science and Technology (project no. 1522).

REFERENCES

1. J. B. Pendry, A. J. Holden, W. J. Stewart, and I. Youngs, Phys. Rev. Lett. **76**, 4773 (1996).
2. M. V. Kostin and V. V. Shevchenko, Radiotekh. Élektron. (Moscow) **33**, 1526 (1988).
3. M. V. Kostin, Radiotekh. Élektron. (Moscow) **35**, 424 (1990).
4. M. V. Kostin and V. V. Shevchenko, Radiotekh. Élektron. (Moscow) **37**, 1992 (1992).
5. J. B. Pendry, A. J. Holden, D. J. Robbins, and W. J. Stewart, IEEE Trans. Microwave Theory Tech. **47**, 2075 (1999).
6. D. R. Smith, Willie J. Padilla, D. C. Vier, *et al.*, Phys. Rev. Lett. **84**, 4184 (2000).
7. V. E. Pafomov, Zh. Éksp. Teor. Fiz. **36**, 1853 (1959) [Sov. Phys. JETP **9**, 1321 (1959)].
8. V. G. Veselago, Fiz. Tverd. Tela (Leningrad) **8**, 3571 (1966) [Sov. Phys. Solid State **8**, 2854 (1966)].
9. V. G. Veselago, P. V. Glushkov, and A. M. Prokhorov, Radiotekh. Élektron. (Moscow) **12**, 1220 (1967).
10. V. G. Veselago, Usp. Fiz. Nauk **92**, 517 (1967) [Sov. Phys. Usp. **10**, 509 (1968)].
11. M. I. Kaganov and T. I. Shalaeva, Zh. Éksp. Teor. Fiz. **96**, 2185 (1989) [Sov. Phys. JETP **69**, 1237 (1989)].

Translated by O. Borovik-Romanova

Physics of the Solid State, Vol. 43, No. 11, 2001, pp. 2136–2139. Translated from Fizika Tverdogo Tela, Vol. 43, No. 11, 2001, pp. 2048–2051.
Original Russian Text Copyright © 2001 by Sheleg, Yachkovski, Kurilovich.

MAGNETISM AND FERROELECTRICITY

Ultrasonic Studies of $(CH_3)_2NH_2Al(SO_4)_2 \cdot 6H_2O$ Crystals Irradiated by γ Quanta and Electrons

A. U. Sheleg, A. Ya. Yachkovski, and N. F. Kurilovich

Institute of Solid State and Semiconductor Physics, National Academy of Sciences of Belarus, ul. Brovki 17, Minsk, 220072 Belarus

e-mail: sheleg@ifttp.bas-net.by

Received March 27, 2001

Abstract—The temperature dependence of the longitudinal-ultrasound velocities in $(CH_3)_2NH_2Al(SO_4)_2 \cdot 6H_2O$ crystals was studied using the echo-pulse technique in the 90–300 K range. The measurements were carried out along mutually perpendicular crystallographic directions *X, Y, Z* on samples both unirradiated and irradiated to various doses by γ quanta and an electron beam. The ultrasound velocity *V* in this crystal was shown to be anisotropic, with $V_{YY} > V_{XX} > V_{ZZ}$. The $V_{XX} = f(T)$, $V_{YY} = f(T)$, and $V_{ZZ} = f(T)$ curves exhibit anomalies in the form of breaks at the ferroelectric phase transition (PT) at $T_{c1} = 152$ K, as well as in the region of $T_{c2} = 218$ K. It was established that as the irradiation dose increases, the PT temperature T_{c1} decreases and the anomalies in the temperature dependences of the ultrasound velocities are smeared. © *2001 MAIK "Nauka/Interperiodica".*

1. INTRODUCTION

Dimethyl ammonium aluminum sulfate hexahydrate (DMAAS) $(CH_3)_2NH_2Al(SO_4)_2 \cdot 6H_2O$ belongs to the family of ferroelectrics–ferroelastics. This family has recently been a subject of intense investigation using various methods and is of considerable interest due to the number of phase transformations it undergoes. This crystal is a ferroelastic in the paraelectric phase. As the temperature decreases, a phase transition from the ferroelastic to a ferroelectric phase takes place at $T_{c1} = 152$ K [1]. Studies [2, 3] of the temperature dependences of the birefringence and plastic properties of DMAAS crystals revealed anomalies at $T \sim 110$ and 390 K, which suggest possible phase transformations at these temperatures. As shown in [4] and as later confirmed in [5] in an investigation of dielectric properties, DMAAS undergoes a low-temperature phase transition at $T \approx 75$ K whose nature remains unclear. In addition, the dielectric permittivity ε and $\tan\delta$ were found to behave anomalously within the 30–50 K range [5], which may also be connected with some transformations.

We report on a study of the temperature dependences of longitudinal-ultrasound velocities V_{XX}, V_{YY}, and V_{ZZ} measured along mutually perpendicular crystallographic axes *X, Y,* Z in crystalline DMAAS in the 90–300 K range and of their response to irradiation by γ quanta and an electron beam.

2. EXPERIMENTAL TECHNIQUE AND THE RESULTS OF THE STUDY

The longitudinal ultrasound velocities were measured using the echo pulse method with an IS-3 ultrasound velocity meter; the time between the reflected signals was determined by means of calibration marks. The longitudinal ultrasound waves were excited by an *X*-cut piezoelectric quartz plate. The hydrophobic liquid 136-157 provided a good acoustic contact between the sample and the measurement circuit throughout the temperature interval covered. The measurements were carried out at temperatures from 90 to 300 K and at a frequency of 10 kHz. The temperature variation rate was ~0.4 K/min. The samples chosen for the study were parallelepiped-shaped and measured $\sim 4.5 \times 4.5 \times 5$ mm. Because DMAAS crystals form a monoclinic structure with the unit cell parameters $a = 6.403$ Å, $b = 10.747$ Å, $c = 11.128$ Å, and $\beta = 100.47°$ [6], the sample faces were oriented in the following way: the crystallographic axis *X* was aligned with *a*, the *Y* axis was aligned parallel to the twofold symmetry axis (along the *b* crystallographic axis), and the *Z* axis was aligned perpendicular to both *X* and *Y*. The temperature was measured with a chromel–coppel thermocouple, which was attached directly to a sample connected to the measuring circuit. The temperature dependence of the ultrasound velocity was studied under quasi-static heating of samples cooled in liquid-nitrogen vapors. The heating was effected by means of a heater mounted on a thermostatting screen surrounding the measuring circuit. The absolute temperature was measured to within

1063-7834/01/4311-2136$21.00 © 2001 MAIK "Nauka/Interperiodica"

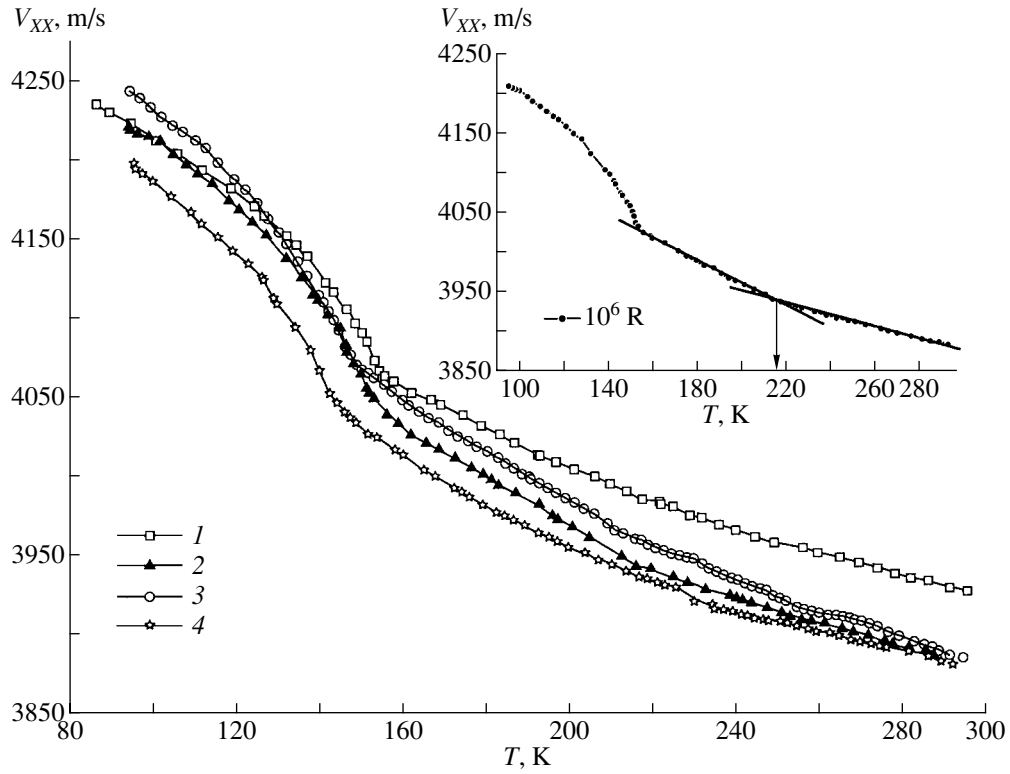

Fig. 1. Temperature dependences of the longitudinal-ultrasound velocity V_{XX} along the X crystallographic axis in the $(CH_3)_2NH_2Al(SO_4)_2 \cdot 6H_2O$ crystal measured on (*1*) an unirradiated sample and a sample irradiated by γ quanta to doses of 10^6 (inset), (*2*) 10^7, and (*3*) 10^8 R and (*4*) by an electron beam to a fluence of 10^{16} electrons/cm^2.

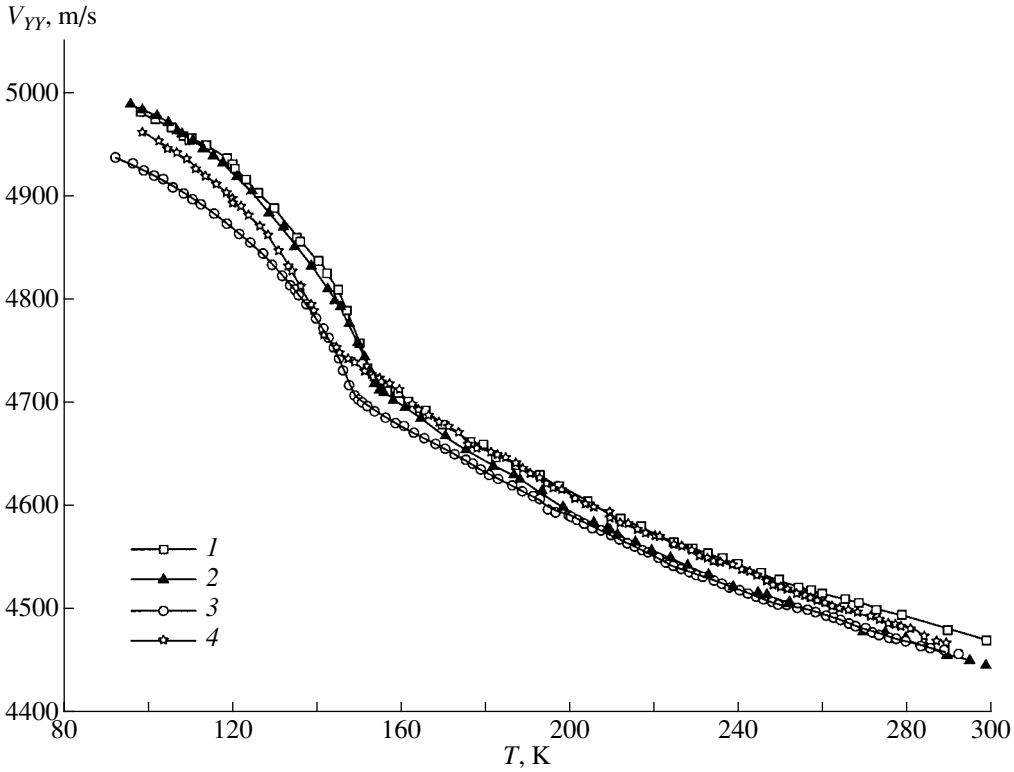

Fig. 2. Temperature dependences of the longitudinal ultrasound velocity V_{YY} along the Y crystallographic axis in the $(CH_3)_2NH_2Al(SO_4)_2 \cdot 6H_2O$ crystal measured on (*1*) an unirradiated sample and a sample irradiated by γ quanta to doses of (*2*) 10^7 and (*3*) 10^8 R and (*4*) by an electron beam to a fluence of 10^{16} electrons/cm^2.

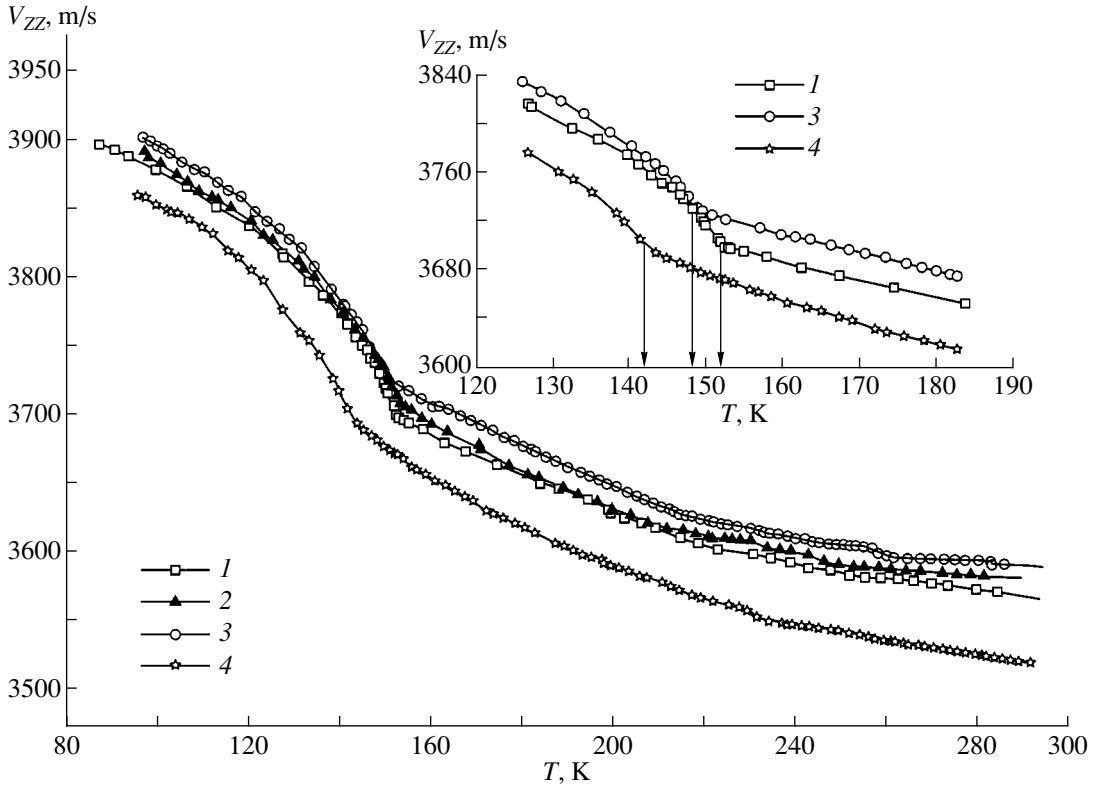

Fig. 3. Temperature dependences of the longitudinal ultrasound velocity V_{ZZ} along the Z crystallographic axis in the $(CH_3)_2NH_2Al(SO_4)_2 \cdot 6H_2O$ crystal measured on (*1*) an unirradiated sample and a sample irradiated by γ quanta to doses of (*2*) 10^7 and (*3*) 10^8 R and (*4*) by an electron beam to a fluence of 10^{16} electrons/cm^2. In the inset, arrows indicate the PT temperatures T_{c1} for (*1*) the unirradiated sample (152 K), the sample irradiated (*3*) by γ quanta to a dose of 10^8 R (148 K), and (*4*) by electrons (142 K).

0.8 K, and the precision of relative temperature measurements was no worse than 0.2 K. The samples were irradiated by Co^{60} γ quanta with the source strength of ≈120 R/s. The irradiation dose was accumulated through successive exposure of the same sample to 10^6, 10^7, and 10^8 R. The irradiation by electrons to a fluence of 10^{16} electrons/cm^2 was performed on a 6 MeV accelerator on samples which had been preirradiated by γ quanta to a dose of 10^8 R. The accuracy of measuring the changes in the longitudinal ultrasound velocity was $\sim 5 \times 10^{-5}$. The absolute velocities were measured to no worse than 3×10^{-2}.

The results of the measurements of the longitudinal ultrasound velocities in the *X*, *Y*, and *Z* crystallographic directions are plotted in Figs. 1–3, which reveal an anisotropy in the ultrasound velocities, with $V_{YY} > V_{XX} > V_{ZZ}$ throughout the temperature interval studied. Also shown are the same dependences obtained for samples irradiated to various doses by γ quanta and by electrons to a fluence of 1×10^{16} electrons/cm^2. As the sample temperature decreases, the velocity is seen to increase, until, at the phase transition (PT) point $T_{c1} = 152$ K, one observes an anomaly in the form of a distinct break, accompanied by a change in the pattern of the $V_{XX} = f(T)$, $V_{YY} = f(T)$, and $V_{ZZ} = f(T)$ curves below T_{c1}. Note that below the PT temperature, i.e., in the ferroelectric phase, the temperature dependence of the longitudinal ultrasound velocities is nonlinear in all crystallographic directions, whereas above T_{c1}, i.e., in the ferroelastic phase, this dependence can be considered as consisting of two linear parts within the regions of 152–218 and 218–300 K (inset to Fig. 1). Thus, below 218 K, one also observes a break. It should be noted, though, that the break-shaped anomalies in the $V_{XX} = f(T)$, $V_{YY} = f(T)$, and $V_{ZZ} = f(T)$ curves obtained on electron-irradiated samples in this temperature interval wash out. The $V_{YY} = f(T)$ curve obtained in [7] in studying the longitudinal ultrasound velocities made in DMAAS along the *b* axis only exhibits the same anomalies at temperatures of 152 and 218 K. While the nature of the anomaly at $T_{c2} = 218$ K remains unclear, it may be mentioned that a study [8] of the thermal expansion of a DMAAS crystal along the main crystallographic axes *a*, *b*, and *c* revealed small diffuse minima in the thermal expansion coefficients at $T \sim 220$ K. The sample irradiated by γ quanta to 10^8 R was subsequently bombarded by electrons. The irradiation-induced variation of the temperature dependence of ultrasound velocity is seen to follow the same pattern in all crystallographic directions, *X*, *Y*, and *Z*. γ irradiation shifts T_{c1} toward lower temperatures; indeed, at a dose of 10^8 R, $T_{c1} = 148$ K, and after electron irradiation, the PT temperature T_{c1} decreases by 10 K in comparison with the unirradiated sample (inset

to Fig. 3). Note that measurements were also performed on samples irradiated to 10^6 R, but because these results did not differ from those obtained for unirradiated samples, only the $V_{XX} = f(T)$ curve is presented for this dose (inset to Fig. 1).

As seen from Figs. 1–3, irradiation not only shifts the PT temperature but also smears the anomaly at T_{c1}; i.e., the breaks in the $V_{XX} = f(T)$, $V_{YY} = f(T)$, and $V_{ZZ} = f(T)$ curves become smoother. The displacement of the PT point T_{c1} toward lower temperatures implies that the region of existence of the ferroelectric phase in the DMAAS crystal narrows under irradiation. As shown in [9], this may be due to the decrease in excess PT energy associated with the decrease in the concentration of ferroelectrically active dipoles, which is caused in DMAAS by the formation of defects and structural distortions under irradiation.

REFERENCES

1. L. F. Kirpichnikova, E. F. Andreev, I. R. Ivanov, *et al.*, Kristallografiya **33** (6), 1437 (1988) [Sov. Phys. Crystallogr. **33**, 855 (1988)].
2. O. G. Vlokh, V. B. Kapustyanyk, I. I. Polovinko, *et al.*, Izv. Akad. Nauk SSSR, Ser. Fiz. **54** (6), 1143 (1990).
3. L. F. Kirpichnikova, A. A. Urusovskaya, V. I. Mozgovoĭ, *et al.*, Kristallografiya **36** (6), 1516 (1991) [Sov. Phys. Crystallogr. **36**, 859 (1991)].
4. A. Pietraszko, L. F. Kirpichnikova, and L. A. Shuvalov, Kristallografiya **40** (3), 569 (1995) [Crystallogr. Rep. **40**, 523 (1995)].
5. L. F. Kirpichnikova, W. Bednarsky, S. Waplak, *et al.*, Kristallografiya **44** (1), 111 (1999) [Crystallogr. Rep. **44**, 106 (1999)].
6. A. Pietraszko, K. Łukaszewicz, and L. F. Kirpichnicova, Pol. J. Chem. **67**, 1877 (1993).
7. S. Wöpke, G. Sorge, V. Müller, *et al.*, in *Proceedings of the 19th Spring Conference on Ferroelectricity, Martin-Luther-University, Halle-Wittenberg, 1991*, p. 121.
8. A. U. Sheleg, E. M. Zub, and K. N. Semenov, Fiz. Tverd. Tela (St. Petersburg) **42** (9), 1682 (2000) [Phys. Solid State **42**, 1731 (2000)].
9. S. A. Taraskin, B. A. Strukov, V. A. Fedorikhin, *et al.*, Fiz. Tverd. Tela (Leningrad) **19** (10), 2936 (1977) [Sov. Phys. Solid State **19**, 1721 (1977)].

Translated by G. Skrebtsov

Physics of the Solid State, Vol. 43, No. 11, 2001, pp. 2140–2145. Translated from Fizika Tverdogo Tela, Vol. 43, No. 11, 2001, pp. 2052–2057.
Original Russian Text Copyright © 2001 by Gladkiĭ, Kirikov, Pronina, Volk, Pankrath, Wölecke.

MAGNETISM AND FERROELECTRICITY

Anomalies in the Slow Polarization Kinetics of a Ferroelectric Relaxor in the Temperature Region of a Diffuse Phase Transition

V. V. Gladkiĭ*, V. A. Kirikov*, E. V. Pronina*, T. R. Volk*, R. Pankrath, and M. Wölecke****

**Shubnikov Institute of Crystallography, Russian Academy of Sciences, Leninskiĭ pr. 59, Moscow, 117333 Russia*

e-mail: glad@ns.crys.ras.ru

***Fachbereich Physik, Universität Osnabrück, Barbarastrasse 7, Osnabrück, D 49076 Germany*

Received April 3, 2001

Abstract—It is shown experimentally in the specific example of Cr-doped barium–strontium niobate that the anomalies in the infralow-frequency dielectric properties characteristic of a ferroelectric relaxor persist over the whole temperature region of the diffuse phase transition and decrease gradually with increasing temperature. Experimental data are presented on the anomalous quasi-static dielectric hysteresis loops, the slow polarization kinetics, and the anomalously broad energy-distribution spectra of potential barriers. The anomalies are a signature and a quantitative measure of the structural disorder typical of a relaxor. *© 2001 MAIK "Nauka/Interperiodica".*

1. INTRODUCTION

Relaxor ferroelectrics (relaxors) include a large group of oxide solid solutions, which are essentially inhomogeneous systems with a disordered structure [1, 2]. Relaxors are characterized by a random spatial distribution of the concentrations of some ions, strains, and an internal electric field; this entails breakdown of the local symmetry and distortion of the polarization dependence of the local free energy, with the latter acquiring the shape of an asymmetric double-minimum function [3]. Unlike a conventional homogeneous ferroelectric, the phase transition to the polar state and the anomalies in the physical properties of a relaxor are diffuse within a broad temperature region (the Curie region). In particular, the dielectric permittivity ε has a weakly pronounced broad maximum at a temperature T_m and a characteristic dispersion near T_m within the low-frequency range from 1 to 5000 kHz [1–3]. In the infralow-frequency range, down to 10^{-5} Hz, a large dispersion in ε persists even at temperatures $T \ll T_m$, the dielectric hysteresis loop of the electric-field dependence of polarization takes on an anomalous shape [4], and the energy distribution of potential barriers for the relaxation centers is anomalously broad and includes giant barriers. The anomalous loop and the energy spectrum of barriers give one an idea of the long-lived metastable states involved and are an indication and a measure of the structural disorder in a relaxor [5].

We have earlier observed and studied specific features in the polarization kinetics in the barium–strontium niobate ferroelectric relaxor $Sr_xBa_{1-x}Nb_2O_6$ (SBN) [4, 5]. However, the electrometric method employed by us and intended to detect slow polarization processes permits one to perform measurements only on samples with an electrical resistivity of no less than 10^{12} Ω cm. This restricted the accessible temperature range to $T < T_m$ in the compositions studied, thus precluding investigation of the polarization kinetics within the whole Curie region.

The present work was aimed at investigating the polarization kinetics of a relaxor within the Curie temperature region with inclusion of the T_m point. Obviously enough, relaxors with an as low as possible T_m temperature, near which one can expect the resistivity to be sufficiently high, are best suited to this type of investigation. It is known that T_m in the SBN can be lowered by increasing the strontium concentration [2] or by doping it with various impurities [6, 7].

2. THE CRYSTALS AND THE EXPERIMENTAL TECHNIQUE

We studied Cr-doped $Sr_xBa_{1-x}Nb_2O_6$ single crystals with $x = 0.61$ (SBN : Cr) grown by the Czochralski method at the Osnabrück University, Department of Physics (Germany). Doping the SBN with Cr results in a considerable lowering of T_m and a broadening of the maximum in ε [7]. The Cr concentration in the melt used to grow the crystal was $(2.02 \pm 0.015) \times 10^4$ ppm. This composition has the lowest T_m temperature of all the SBN compositions known to date. The sample was a polished polar *z*-cut plate measuring $2.5 \times 3 \times 0.7$ mm. Silver paste contacts were painted on the large plate sides. The sample temperature in the cryostat was maintained to within 0.03 K.

The permittivity was measured in the standard way at 1 kHz. The polarization was measured electrometrically using an equal-arm bridge with a maximum sensitivity of 20 μV in voltage and 2×10^{-9} μC in charge. The compensation of the voltage across the bridge was

controlled by a computer. The compensating voltage was measured in real time, and the data collected were used to calculate the crystal polarization. A detailed description of the automated setup, its operation, and data processing can be found in [8].

The polarization was measured in slowly varying (quasi-static) electric fields (dielectric hysteresis loops), as well as after turning on and turning off a dc field (relaxation processes) at various constant temperatures.

After a long time had passed and the polarization relaxation had practically come to a halt, the electrical resistivity of the sample was derived from the variation of the charge in the bridge circuit with time.

3. RESULTS AND DISCUSSION

3.1. Permittivity and Dielectric Hysteresis Loops

Figure 1 presents the temperature dependence of the permittivity ε of the SBN-0.61 : Cr crystal under study, which features a broad diffuse maximum typical of relaxors; the temperature of the maximum T_m = 244 K is substantially lower than the temperature T_m = 354 K for the undoped SBN-0.61 crystal [2]. Also shown are the experimental data on the dielectric loss tangent $\tan\delta$, which increases with decreasing temperature. Because of the relatively low T_m, the electrical resistivity ρ in the region of T_m is sufficiently large ($\rho \geq 10^{13}\ \Omega$ cm). Therefore, there was practically no need to introduce corrections to the constant electrical conductivity; this can distort slow-polarization measurements. The vertical arrows in Fig. 1 specify the temperatures at which the hysteresis loops were measured.

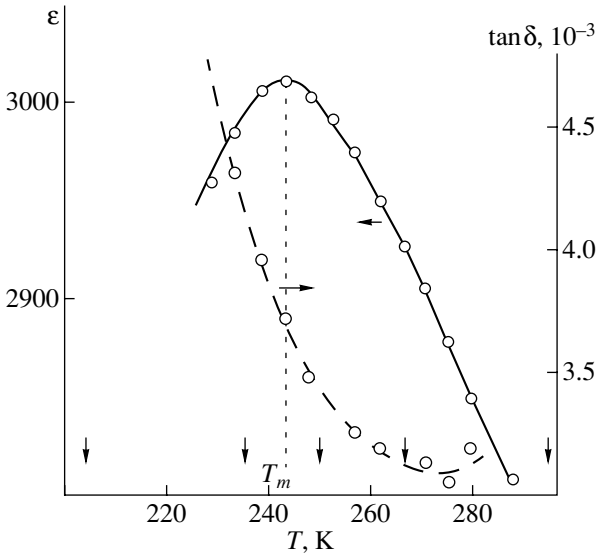

Fig. 1. Temperature dependences of the permittivity ε and of the dielectric loss tangent $\tan\delta$ of the SBN : Cr ferroelectric relaxor obtained at a frequency of 1 kHz. The vertical arrows specify the temperature of hysteresis loop measurement.

Figure 2 displays quasi-static dielectric hysteresis loops obtained at several temperatures in the T_m region. The figures adjoining the loop trajectories identify the sequence of the polarization variations. The filled circles relate to the beginning and end of the polarization switching process. The loops exhibit the characteristic features of the SBN relaxor [4, 5]: the first loop cycles are open nonreproducing curves, with the loop amplitude decreasing gradually; however, a few cycles later, it reaches saturation, with the trajectories of all subsequent cycles practically coinciding, i.e., becoming reproducible. These features may be caused by strong local internal electric fields E_i coming from structural inhomogeneities [4, 5]. The fields E_i bring about a strong asymmetry in the local double-minimum free energy F as a function of polarization P [3]. The field E_i and the parameters of the F function are random quantities. If the external field $E = 0$, one part of the crystal resides in a stable state and the other resides in a long-lived metastable state, which correspond to the deep and shallow minima in F, respectively. When a field E with a slowly varying amplitude is applied, the barriers separating the minima decrease in height and the thermally activated transition to the stable states grows more quickly. The reverse process is practically impossible; thus, part of the crystal no longer participates in the polarization switching by the external field with the same amplitude E and the amplitude of P decreases. Complete reversible polarization switching is possible only in a field E larger than the maximum E_i in the sample, which is apparently high [4, 5].

When the crystal is heated in the T_m region, the quasi-static hysteresis loop narrows and becomes smaller in amplitude, the noncoinciding trajectories of the first loops come closer together and merge, and the nonlinearity of the P dependence on E on the initial polarization curve of the cycles becomes less pronounced (Fig. 2). In other words, the quasi-static loop shows signs of degradation for $T > T_m$ similar to those recorded at higher measuring-field frequencies [9]. It is essential, however, that the quasi-static hysteresis loop retain the shape characteristic of a relaxor even at temperatures considerably in excess of T_m, i.e., apparently, throughout the region where the phase transition is diffuse (Fig. 2).

3.2. Polarization Relaxation

Investigation of polarization and depolarization kinetics in dc electric fields permits one to obtain additional information on the quasi-static hysteresis loops and structure of the SBN : Cr relaxor. Figure 3 presents, as an illustration, an evolution of polarization P with time t for the turning on (polarization process) and turning off (depolarization) of a weak field E = 0.43 kV/cm that is less than the half-width of the hysteresis loop and is effected at the same temperatures in the T_m region at

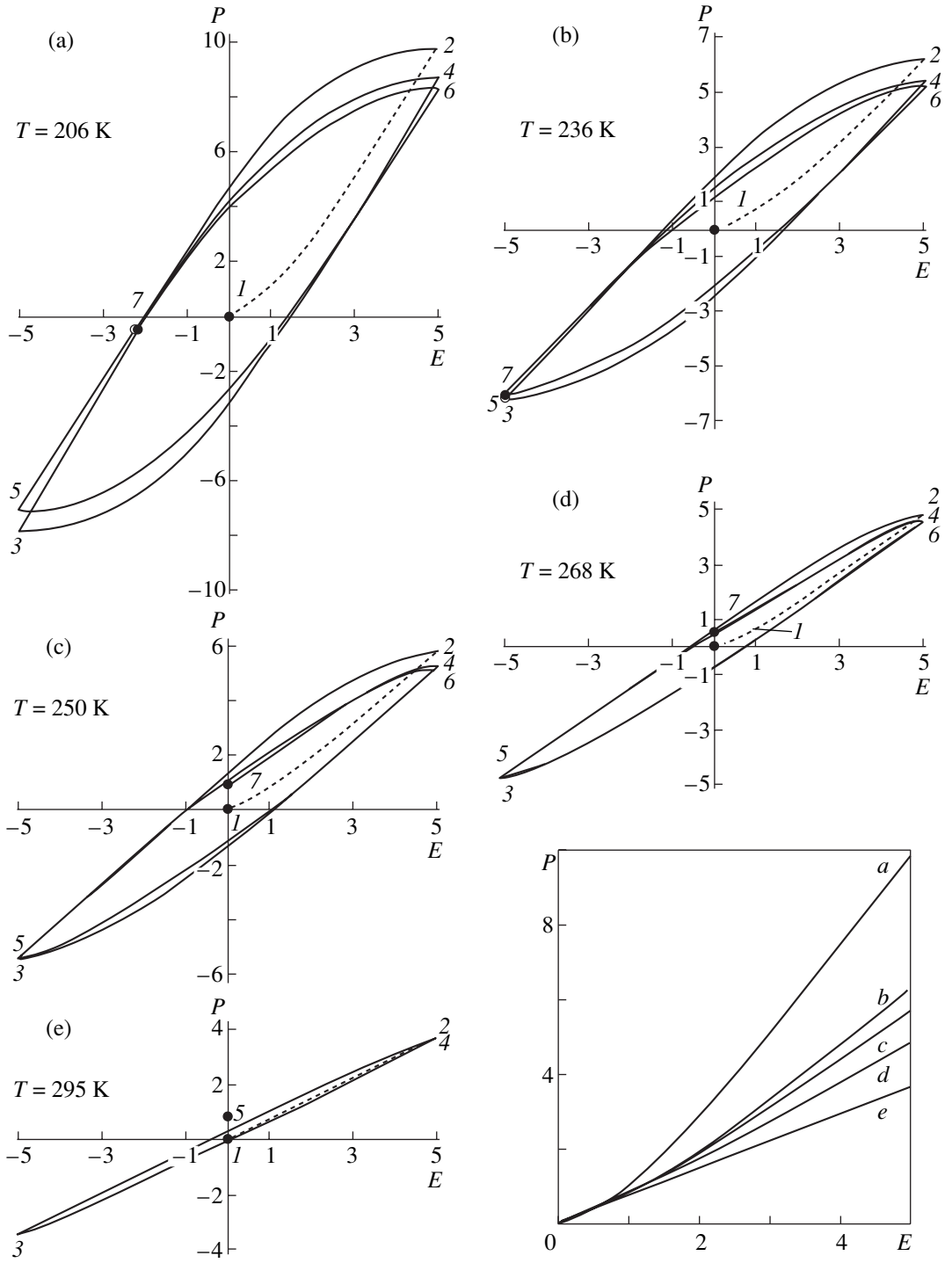

Fig. 2. Quasi-static dielectric hysteresis loops of the dependence of P ($\mu C/cm^2$) on E (kV/cm) for SBN : Cr obtained at temperatures of (K) (a) 206, (b) 236, (c) 250, (d) 268, and (e) 295. The E variation period is 1 h. The inset shows nonlinear P vs. E plots drawn for the first polarization switching cycle quarter.

which the hysteresis loops in Fig. 2 were obtained. Both processes start with the jump in ΔP characteristic of the SBN, to which contribute the avalanche over-barrier and fast processes through low barriers. After the jump, the pattern of the relaxation changes sharply: a slow thermally activated process begins, during which some crystal regions transfer from the long-lived metastable to stable states (see Fig. 3 and the insets to it). The jump ΔP is observed to occur at any field E within the range employed in the work, which is both smaller and larger

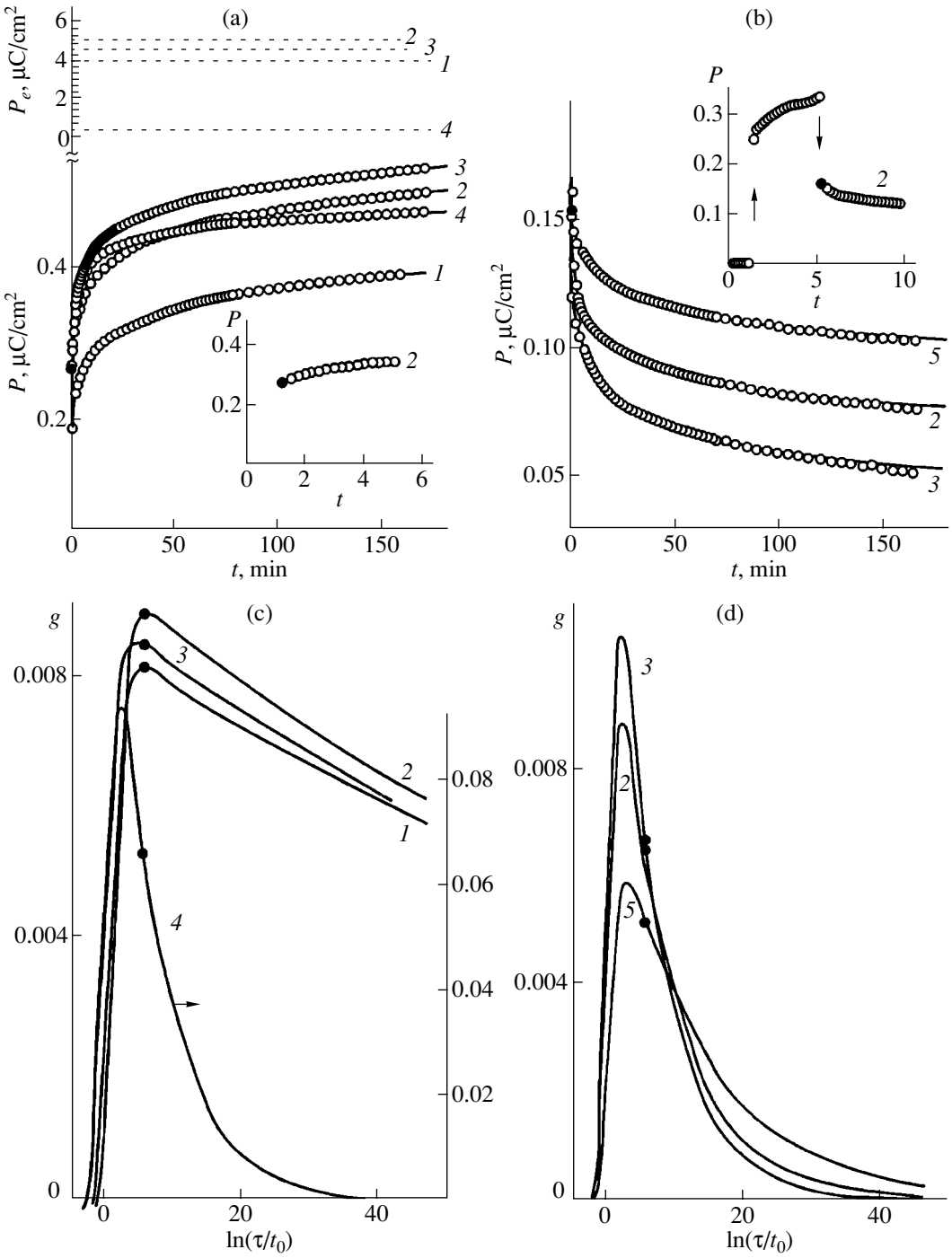

Fig. 3. (a, b) Relaxation of the polarization P and (c, d) $g(\ln\tau)$ spectra for the SBN : Cr at different temperatures T (K): (*1*) 205, (*2*) 236, (*3*) 249, (*4*) 268, and (*5*) 221; t_0 = 1 min. The insets show the beginning of the polarization and depolarization processes; the arrows identify the jumps ΔP occurring when the field E = 0.43 kV/cm is turned on and off.

than the half-width of the hysteresis loop; this indicates the absence of a common coercive field E_c. Unlike a conventional homogeneous ferroelectric [8], the relaxor is characterized by a broad distribution of E_c over the crystal volume.

The slow thermally activated stage of the $P(t)$ relaxation in the polarization and depolarization processes follows the universal power law

$$p(t) = [P_e - P(t)]/(P_e - P_0) = 1/(1 + t/a)^n, \quad (1)$$

Parameters of the P relaxation and of the energy spectrum of barriers g for an SBN : Cr crystal

Process	E, kV/cm	T, K	a, min	n	P_e, μC/cm^2	τ_m, min
Polarization	5	205.97	0.516 ± 0.05	0.054 ± 0.001	18.59 ± 0.04	9.55 ± 1.1
		236.16	0.643 ± 0.06	0.050 ± 0.001	16.72 ± 0.04	12.86 ± 1.5
		250.32	0.535 ± 0.06	0.054 ± 0.001	10.78 ± 0.02	9.91 ± 1.1
		281.68	0.185 ± 0.02	0.036 ± 0.0008	7.25 ± 0.02	5.15 ± 0.7
		295.02	0.29 ± 0.03	0.023 ± 0.0005	6.65 ± 0.01	12.61 ± 1.6
	0.43	205.00	0.881 ± 0.05	0.010 ± 0.0002	4.03 ± 0.1	88.1 ± 6.8
		236.00	1.658 ± 0.09	0.009 ± 0.0002	5.34 ± 0.01	184.2 ± 14.1
		249.24	0.373 ± 0.04	0.0089 ± 0.0002	4.82 ± 0.01	41.91 ± 5.4
		267.7	0.538 ± 0.05	0.1318 ± 0.001	0.63 ± 0.001	4.08 ± 0.4
Depolarization	0	221.3	0.807 ± 0.05	0.0739 ± 0.002	–0.01	10.92 ± 1.0
		236.08	0.642 ± 0.04	0.123 ± 0.001	0	5.22 ± 0.4
		249.2	0.518 ± 0.05	0.1509 ± 0.002	0	3.43 ± 0.4

where P_0 is the initial polarization at $t = 0$, P_e is the equilibrium polarization, and a and n are the fitting parameters [5]. If a crystal was not prepolarized before measurement, $P_0 = \Delta P$ for the polarization process. The $P(t)$ measurement data were fitted to Eq. (1) by the least squares method using a standard code. In Fig. 3, the $P(t)$ power-law relations are drawn by solid lines and the circles indicate experimental data. The latter deviate from the calculated lines by no more than 0.5%. The filled circles on curves *2* specify values of P_0. The error in determination of the parameters P_e, a, and n decreases with increasing $P(t)$ measurement time [10].

Assuming the relaxation centers to be independent, the dimensionless polarization $p(t)$ in Eq. (1) should obey the relation

$$p(t) = \int_0^\infty f(\tau)\exp(-t/\tau)d\tau, \qquad (2)$$

where $f(\tau)$ is the distribution function of the relaxation time τ. It appears more reasonable to use, in place of $f(\tau)$, a dimensionless function $g(\ln\tau) = \tau f(\tau)$, which describes the $\ln\tau$ distribution in the crystal or the distribution of potential barriers in energy U, because $U = kT\ln(\tau/\tau_0)$, where τ_0 is a kinetic coefficient. Accepting a power-law dependence of Eq. (1) for $p(t)$, we obtain

$$g = (1/\Gamma(n))(a/\tau)^n\exp(-a/\tau) \qquad (3)$$

with a maximum $g_{\max}$ at $\tau_m = a/n$ [10]. The parameters of the $P(t)$ relaxation and of the energy spectrum of barriers g are given in the table.

Note some features in the spectra g obtained at different temperatures (Fig. 3). For the polarization processes, $g(\ln\tau)$ are asymmetric relations involving giant relaxation times or giant potential barriers. For $T > T_m$, the $g(\ln\tau)$ spectrum becomes more symmetrical, narrows, and shifts toward shorter τ. For the depolarization processes, the $g(\ln\tau)$ relations are more symmetrical, and, in crystals heated above T_m, they behave like polarization spectra. The filled circles in the spectra presented in Fig. 3 correspond to the maximum polarization measurement times $t_m \simeq 170$ min. Therefore, some of the spectra corresponding to $\tau > \tau_m$ result from experimental data being extrapolated to long times. The $f(\tau)$ and $g(\ln\tau)$ distributions are normalized functions; i.e.,

$$\int_{-\infty}^{\infty} g(\ln\tau)d(\ln\tau) = \int_0^\infty f(\tau)d\tau = 1.$$

One can readily verify that the areas bounded by the $g(\ln\tau)$ curves in Fig. 3 are indeed close to unity. The width of the spectrum is $\Delta U = kT\ln(\tau_2/\tau_1)$, where τ_2 and τ_1 are the maximum and minimum values of τ, respectively, at which $g(\ln\tau) = 0$. Estimates yield $\Delta U \simeq 3.3$ eV for the polarization processes for $T \le T_m$ (curves *1–3* in Fig. 3c) and $\Delta U \simeq 0.4$ eV for depolarization for $T > T_m$ (curve *4* in Fig. 3c) and depolarization for $T = T_m$ (curves *2*, *3*, *5* in Fig. 3d).

The values of the P relaxation and $g(\ln\tau)$ spectrum parameters depend substantially on the polarizing field E, as was the case with the SBN compositions studied earlier [5]. For instance, for depolarization processes starting after crystal polarization in a weak field of 0.43 kV/cm, the equilibrium value $P_e \simeq 0$ (Fig. 3), while in stronger fields, $P_e \neq 0$ and grows with increasing E.

Figure 4 presents temperature dependences of some parameters of P relaxation and of the $g(\ln\tau)$ spectrum near the T_m point of the SBN : Cr relaxor obtained for polarization processes in dc fields of $E_1 = 0.43$ and $E_2 = 5$ kV/cm, the first of which is less than the half-width of the hysteresis loops within the temperature interval studied, while the second far exceeds this value (Fig. 2). One can see the temperature dependences of the jump $\Delta P = P_0$, of the equilibrium polarization P_e, and of the characteristic time τ_m. Note that the values of

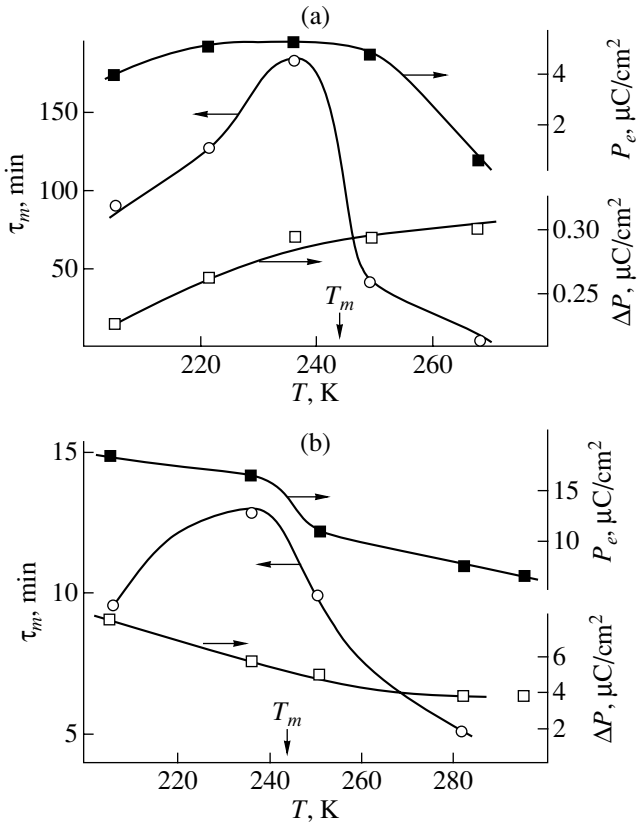

Fig. 4. Temperature dependences of the parameters ΔP, P_e, and τ_m of the P relaxation and of the $g(\ln\tau)$ spectra near the T_m point obtained for an electric field E equal to (a) 0.43 and (b) 5 kV/cm.

τ_m are substantially smaller and those of ΔP and P_e are larger in the E_2 field than those obtained in the E_1 field. One readily sees that P_e and τ_m exhibit weak anomalies around T_m = 244 K and decrease slowly in magnitude under heating above T_m, similar to the local P^2 obtained from thermal expansion measurements for a relaxor [3]. In the strong field E_2, these anomalies appear more diffuse. The ΔP jump increases slowly for E_1 and decreases for E_2 when the crystal is heated. The behavior of the temperature dependence $\Delta P(T)$ is governed by the competition of two processes, more specifically, a decrease in the height of potential barriers with a corresponding increase in the polarized part of the crystal volume on the one hand and a decrease in the polarization under heating on the other. For the weak field E_1, the first process is dominant, and for the E_2 field, which polarizes most of the crystal volume, the second process dominates. It is these factors that account qualitatively for the difference in the behavior of the $\Delta P(T)$ curves in Fig. 4.

4. CONCLUSIONS

Thus, near the diffuse phase transition, the polarization of the low-temperature ferroelectric relaxor Cr-doped barium–strontium niobate (SBN : Cr) reveals dielectric anomalies typical of such materials, namely, open and noncoinciding trajectories of the first few hysteresis cycles, the absence of a common coercive field and a common equilibrium polarization, and a broad distribution of the relaxation times or of the potential barrier energy over the crystal volume. The anomalies are detected only in the infralow-frequency range and persist within a broad temperature region, including the characteristic point T_m of the maximum low-frequency permittivity. The anomalies are a signature and a measure of structural disorder in relaxors and permit one to obtain quantitative information on the development of a diffuse phase transition from the nonpolar to polar state occurring under temperature variation.

ACKNOWLEDGMENTS

Sincere thanks are due to S.V. Nekhlyudov for preparation of the equipment for the study.

This study was supported by the Russian Foundation for Basic Research, project nos. 99-02-17303 and 00-02-16624.

REFERENCES

1. G. A. Smolenskiĭ, V. A. Isupov, and A. I. Agranovskaya, Fiz. Tverd. Tela (Leningrad) **1** (1), 167 (1959) [Sov. Phys. Solid State **1**, 147 (1959)].
2. M. E. Lines and A. M. Glass, *Principles and Applications of Ferroelectrics and Related Materials* (Oxford Univ. Press, Oxford, 1977; Mir, Moscow, 1981).
3. L. E. Cross, Ferroelectrics **76**, 241 (1987).
4. V. V. Gladkiĭ, V. A. Kirikov, S. V. Nekhlyudov, *et al.*, Pis'ma Zh. Éksp. Teor. Fiz. **71** (1), 38 (2000) [JETP Lett. **71**, 24 (2000)].
5. V. V. Gladkiĭ, V. A. Kirikov, S. V. Nekhlyudov, *et al.*, Fiz. Tverd. Tela (St. Petersburg) **42** (7), 1296 (2000) [Phys. Solid State **42**, 1334 (2000)].
6. T. R. Volk, V. Yu. Salabutin, L. I. Ivleva, *et al.*, Fiz. Tverd. Tela (St. Petersburg) **42** (11), 2006 (2000) [Phys. Solid State **42**, 2129 (2000)].
7. J. Seglins, S. Mendrics, R. Pankrath, *et al.*, Verhand. DPG **1** (33), 601 (1998).
8. V. V. Gladkiĭ, V. A. Kirikov, S. V. Nekhlyudov, and E. S. Ivanova, Fiz. Tverd. Tela (St. Petersburg) **39** (11), 2046 (1997) [Phys. Solid State **39**, 1829 (1997)].
9. W. J. Huang, D. Viehland, and R. R. Neurgaonkar, J. Appl. Phys. **76** (1), 490 (1994).
10. V. V. Gladkiĭ, V. A. Kirikov, E. S. Ivanova, and S. V. Nekhlyudov, Fiz. Tverd. Tela (St. Petersburg) **41** (3), 499 (1999) [Phys. Solid State **41**, 447 (1999)].

Translated by G. Skrebtsov

Physics of the Solid State, Vol. 43, No. 11, 2001, pp. 2146–2153. Translated from Fizika Tverdogo Tela, Vol. 43, No. 11, 2001, pp. 2058–2065.
Original Russian Text Copyright © 2001 by Guzhva, Lemanov, Markovin.

MAGNETISM AND FERROELECTRICITY

Dielectric Studies of Phase Transitions in the Ferroelectric $CdTiO_3$ and the $Sr_{1-x}Cd_xTiO_3$ Solid Solution

M. E. Guzhva, V. V. Lemanov, and P. A. Markovin

Ioffe Physicotechnical Institute, Russian Academy of Sciences, ul. Politekhnicheskaya 26, St. Petersburg, 194021 Russia
e-mail: p.markovin@pop.ioffe.rssi.ru

Received February 5, 2001; in final form, April 10, 2001

Abstract—Temperature dependences of the permittivity and of the dielectric hysteresis loops in ceramic samples of nominally pure $CdTiO_3$ and a $Sr_{1-x}Cd_xTiO_3$ solid solution were studied. At 76.5 ± 0.5 K, $CdTiO_3$ was established to undergo a ferroelectric phase transition close to the tricritical point. The temperature dependence of spontaneous polarization of $CdTiO_3$ is described within the Landau theory of phase transitions with the critical order parameter exponent ≈0.25. The phase diagram of the $Sr_{1-x}Cd_xTiO_3$ solid solution was drawn in (T, x) coordinates, and the critical concentration x_c = 0.002, above which an induced polar state sets in the solid solution, was determined. *© 2001 MAIK "Nauka/Interperiodica".*

1. INTRODUCTION

The ferroelectric phase transition in $CdTiO_3$ was first discovered in ceramic samples at 50 K by Smolenskiĭ in 1950 [1]. However, the low-temperature properties of nominally pure cadmium titanate have remained very poorly studied until recently. While optical [2] and dielectric [3] measurements of single-crystal and ceramic $CdTiO_3$ samples have been carried out, the conclusions drawn therein on the temperature and character of the ferroelectric transition are controversial. This makes a comprehensive investigation of the ferroelectric properties of $CdTiO_3$ a topical issue.

The $Sr_{1-x}Cd_xTiO_3$ solid solution used for the study of impurity-induced phase transitions in incipient ferroelectrics (quantum paraelectrics), the class to which pure $SrTiO_3$ belongs, is also of considerable interest. To date, systematic studies have been performed on such $SrTiO_3$-based compounds as $Sr_{1-x}Ca_xTiO_3$ [4] (incipient ferroelectric–incipient ferroelectric [5]) and $Sr_{1-x}Ba_xTiO_3$ [6, 7], $Sr_{1-x}Pb_xTiO_3$ [8] (incipient ferroelectric–ferroelectric solid solutions). $Sr_{1-x}Cd_xTiO_3$ is a new solid solution in the incipient ferroelectric–ferroelectric solid-solution system, in which the ferroelectric component ($CdTiO_3$) has the lowest Curie temperature among the systems studied thus far.

We earlier reported on a study of the dielectric properties of $CdTiO_3$ and $Sr_{1-x}Cd_xTiO_3$ [9]. This communication presents the results of a comprehensive investigation into the temperature dependences of permittivity ε and of spontaneous polarization P_s measured from dielectric hysteresis loops in ceramic samples of $CdTiO_3$ and $Sr_{1-x}Cd_xTiO_3$. These studies were used to determine the temperature and character of the ferroelectric phase transition in $CdTiO_3$, to construct the phase diagram, and to determine the character of the induced polar states in $Sr_{1-x}Cd_xTiO_3$.

2. EXPERIMENTAL

The temperature dependences of the permittivity and of the dielectric losses were obtained at frequencies of 1 kHz and 1 MHz with automatic digital bridges E7-8 (1 kHz) and E7-12 (1 MHz), which served to measure the total sample impedance. The relative error in the permittivity measurements was no greater than 0.2%. The measuring field amplitude for the E7-8 bridge (1 kHz) was ≈30 V/cm; for the E7-12 (1 MHz), ≈2.5 V/cm.

A fully automated setup representing a modified Sawyer–Tower circuit was developed to measure the dielectric hysteresis loops and the temperature dependences of spontaneous polarization. The setup permitted measurement of objects with small spontaneous and residual polarizations within the frequency range from 50 Hz to 1 kHz.

The temperature of samples mounted in a helium cryostat was monitored independently using copper–constantan and iron-doped copper–copper thermocouples and a KTG-type semiconductor pickup. During the experiment, the measurement procedure was controlled on a computer and, depending on the actual measurement regime, either a fixed sample temperature or rate of its variation was maintained. The absolute error of temperature measurement did not exceed 0.5 K, and the sensitivity was 0.1 K throughout the temperature range covered, 5–300 K.

$CdTiO_3$ and $Sr_{1-x}Cd_xTiO_3$ samples (x = 0.0025, 0.005, 0.01, 0.03, 0.05, 0.075, 0.1, 0.2, 0.5, 0.65, 0.75, and 0.85) were prepared using standard ceramic technology [10, 11]. $SrCO_3$ of ChDA grade and $CdCO_3$ and TiO_2 of OSCh grade were used as starting materials. The preliminary calcination was carried out at 1000–1100°C over 2 h. The batch was finally calcined for 1 h in platinum crucibles at temperatures ranging from 1125 to 1400°C (depending on the actual cadmium

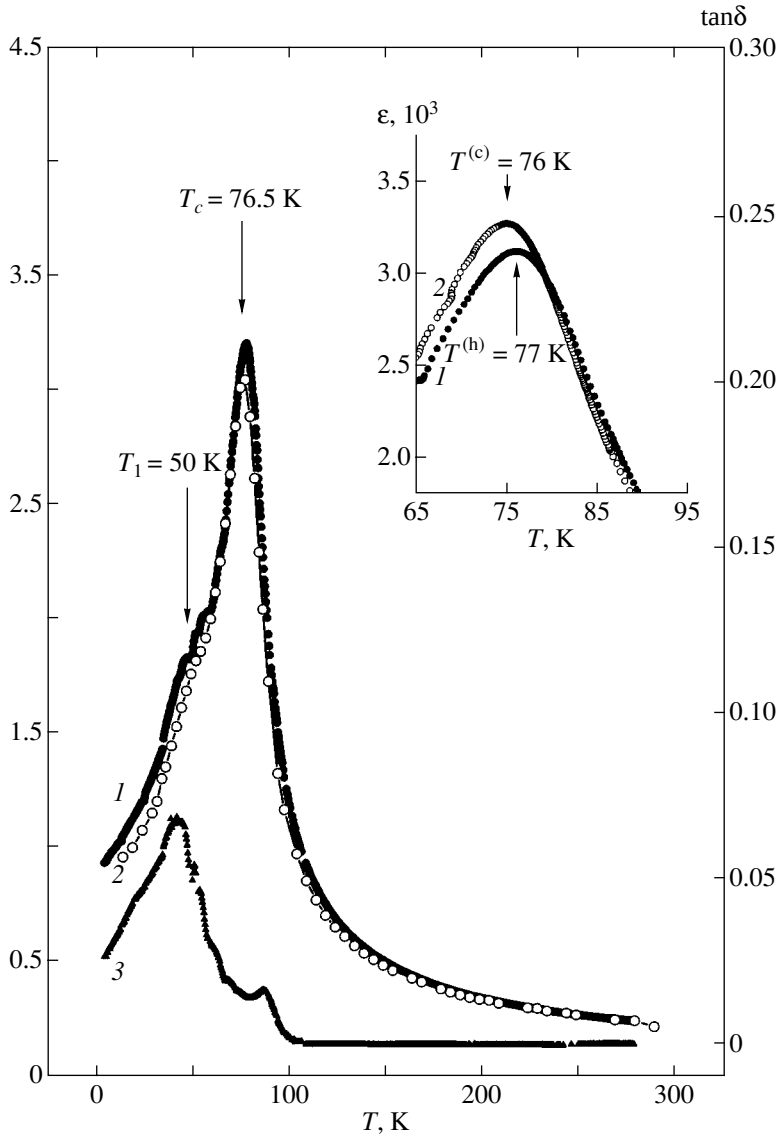

Fig. 1. (*1*, *2*) ε(*T*) and (*3*) $\tan\delta$ (*T*) dependences measured for $CdTiO_3$ at (*1*, *3*) 1 kHz and (*2*) 1 MHz. Inset: (*1*) ε(*T*), heating run, and (*2*) ε(*T*), cooling run (1 kHz).

concentration). The density of the samples chosen for the measurements was not less than 0.9–0.96 of the value given by the x-ray diffraction method. The cut samples were plates measuring ≈4 × 4 × 1 mm. The electrodes were made of silver paste fired on at 500°C. X-ray diffraction analysis showed the ceramic samples with $x = 1$ (pure $CdTiO_3$) to have rhombic symmetry at room temperature and the samples of the $Sr_{1-x}Cd_xTiO_3$ solid solution for $x \le 0.1$ to be single phase and to have the perovskite structure with cubic symmetry. $Sr_{1-x}Cd_xTiO_3$ samples with $x \ge 0.2$ were found to be double-phase. The x-ray diffraction measurements suggest that under the conditions chosen for the preparation of the ceramic samples, the $Sr_{1-x}Cd_xTiO_3$ solid solution is formed only at low $CdTiO_3$ concentrations ($x < 0.2$).

3. DIELECTRIC STUDIES OF $CdTiO_3$

Figure 1 presents the temperature dependences of the permittivity ε(*T*) and of the loss tangent $\tan\delta(T)$ obtained in $CdTiO_3$ at frequencies of 1 kHz and 1 MHz. The ε(*T*) relation passes through a maximum at T_c = 76.5 K, which indicates a ferroelectric phase transition. The values of T_c measured at 1 kHz and 1 MHz coincided to within 0.1 K. At the same time, the ε(*T*) relation exhibited a hysteresis near T_c (inset to Fig. 1). The difference between the temperatures at which ε reached a maximum under heating [$T^{(h)}$] and under cooling [$T^{(c)}$] of a sample $\Delta T = T^{(h)} - T^{(c)}$ was no greater than 1 K at a temperature variation rate of ≈1 K/min. The weak hysteresis indicates the phase transition to be of the first order and close to the second order. Approximation of

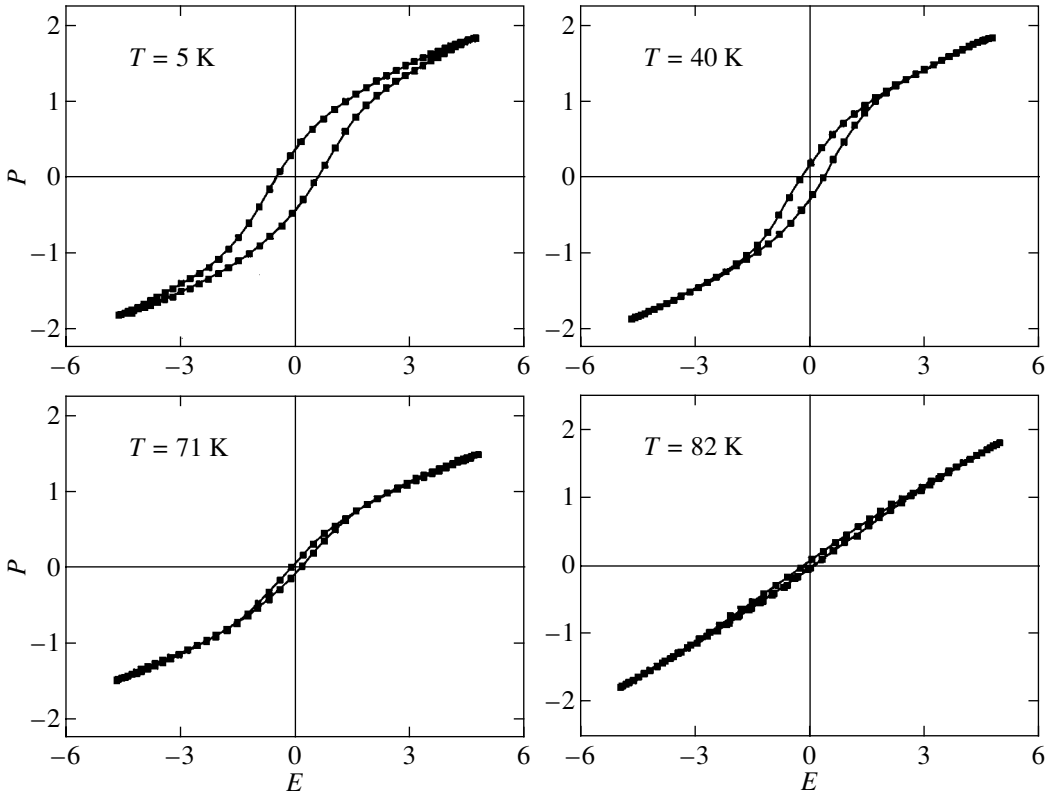

Fig. 2. Hysteresis loops in $CdTiO_3$. P axis in units of 10^{-6} C/cm^2 and E axis in units of kV/cm.

the inverse permittivity $\varepsilon^{-1}(T)$ using the Curie–Weiss law

$$\varepsilon^{-1} = (T - T_0)/C \quad (1)$$

yielded $T_0 = 73$ K and $C = 3.5 \times 10^4$ K for the Curie–Weiss constant, which is characteristic of displacive transitions [12].

As seen from Fig. 1, the $\varepsilon(T)$ relation has a weak anomaly at $T_1 \approx 50$ K, which is actually a shoulder on the experimental curve. This anomaly occurs at the maximum of dielectric losses, which was observed at 42 K. The nature of this anomaly is possibly related to another phase transition, as is the case, for instance, with the $BaTiO_3$ and $KNbO_3$ ferroelectric perovskites. Our studies do not, however, provide an unambiguous answer to the origin of the anomaly observed at T_1.

The measurements of hysteresis loops carried out in the 5–100 K range permitted determination of the temperature dependence of the spontaneous polarization P_s. Figure 2 displays $P(E)$ relations measured at a frequency of 50 Hz and temperatures of 5, 40, 71, and 82 K. The amplitude of the measuring electric field was ≈5.5 kV/cm. The temperature dependence of the spontaneous polarization P_s in $CdTiO_3$ is plotted in Fig. 3. The magnitude of the spontaneous polarization upon saturation was found to be $P_s = 9 \times 10^{-7}$ C/cm^2, which is an order of magnitude smaller than P_s in $BaTiO_3$. The residual polarization observed to exist at temperatures above T_c is due to the effect of the measuring field and is characteristic of measurements in strong electric fields [12].

A first-order ferroelectric phase transition is characterized by a jump in the order parameter (the spontaneous polarization P_s) at the transition point. However, unambiguous discrimination and determination of the magnitude of a small jump directly from $P_s(T)$ measurements (Fig. 3) presents difficulties, because the hysteresis loops are studied under a fairly strong electric field ($E \approx 5.5$ kV/cm). An electric field shifts the phase transition point and reduces the jump in P_s down to its complete disappearance at the electric critical point. In such measurements, the derivative dP_s/dT should pass through an extremum at the phase transition or go to infinity (at the electric critical point) [12–14]. Figure 4 shows the temperature dependence of the derivative dP_s/dT in $CdTiO_3$. One clearly sees a sharp minimum in this relation at a temperature $T = 77$ K, which coincides, within the temperature hysteresis of ε, with $T_c = 76.5$ K.

The weak temperature hysteresis of the permittivity and the absence of an experimentally observed jump in P_s suggest that the phase transition in $CdTiO_3$ occurs in the vicinity of the tricritical point. According to the Landau theory of phase transitions, the temperature dependence of the order parameter (in our case, the

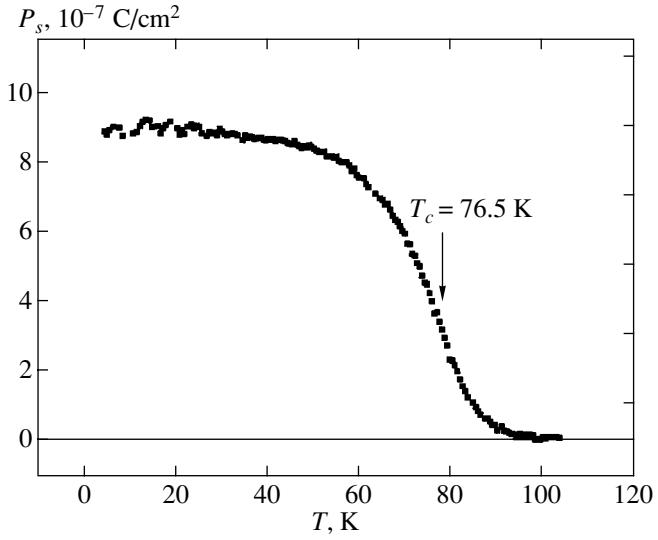

Fig. 3. $P_s(T)$ relation in $CdTiO_3$.

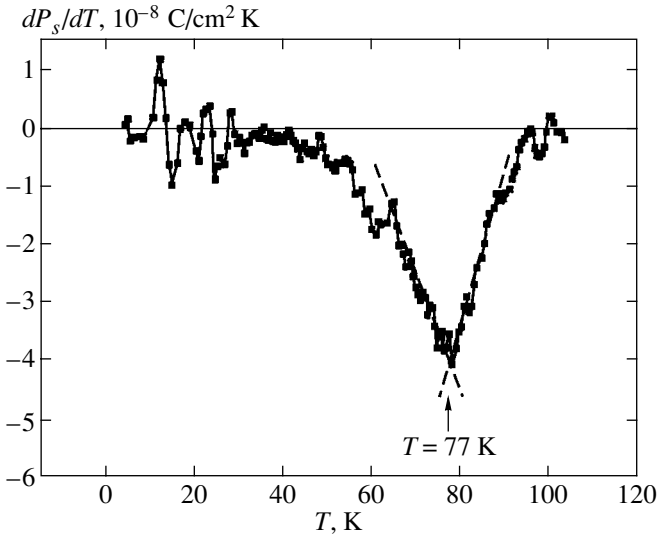

Fig. 4. Temperature dependence of the dP_s/dT derivative in $CdTiO_3$.

spontaneous polarization P_s) near T_c should follow the relation

$$P_s \sim (T_c - T)^{\beta},$$

where the critical order parameter exponent β at the tricritical point is $\beta = 0.25$ [13]. Figure 5 plots the temperature dependence of P_s^4. Within the temperature interval 60–75 K, $P_s^4(T)$ is a linear function of temperature, which yields $\beta = 0.25$ for the critical exponent. The magnitude of the critical order parameter exponent shows unambiguously that the ferroelectric transition in $CdTiO_3$ occurs practically at the tricritical point.

4. DIELECTRIC STUDIES OF THE $Sr_{1-x}Cd_xTiO_3$ SOLID SOLUTION

We turn now to studying the dielectric properties of $Sr_{1-x}Cd_xTiO_3$ in the concentration region $x \le 0.1$.

Figure 6 presents temperature dependences of the permittivity ε in $Sr_{1-x}Cd_xTiO_3$ obtained at $x = 0$, 0.0025, and 0.005. Also shown is the temperature dependence of the dielectric loss tangent $\tan\delta$ for the sample with $x = 0.0025$. At room temperature, the permittivity is approximately the same in all samples, $\varepsilon \approx 290$, which is close to the value $\varepsilon \approx 350$ found for pure $SrTiO_3$ [4, 12, 15]. The maximum in the $\varepsilon(T)$ relation observed in the samples studied can be related to a transition to the polar state, which is induced by Cd^{2+} impurity ions. For comparison, Fig. 6 shows the $\varepsilon(T)$ dependence for pure $SrTiO_3$ prepared using the same technology.

The $Sr_{1-x}Cd_xTiO_3$ sample with $x = 0.0025$ (curve *2* in Fig. 6) does not exhibit a maximum in ε at temperatures above 5 K. In the $x = 0.005$ sample, a maximum in $\varepsilon(T)$ was observed at a temperature $T_c = 11$ K (curves *3*, *4* in Fig. 6) at 1 kHz, but it is absent at 1 MHz. This result does not, however, permit an unambiguous conclusion regarding the existence of a frequency dispersion of ε, because the amplitude of the measuring field was about 3 V/cm at 1 MHz and an order of magnitude larger, 30 V/cm, at a frequency of 1 kHz. After the sample with $x = 0.005$ was maintained at $T = 5$ K in a measuring field at 1 kHz (with an amplitude ≈30 V/cm) for 30 min, its permittivity decreased by approximately 7%. After subsequent heating, the temperature T_c of the maximum in ε did not change, but the difference in the magnitude of ε persisted up to 30 K (curves *3*, *4* in

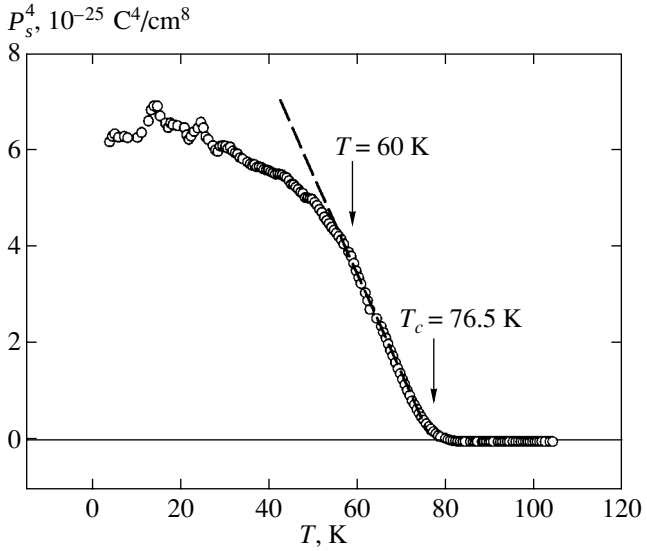

Fig. 5. $P_s^4(T)$ relation in $CdTiO_3$.

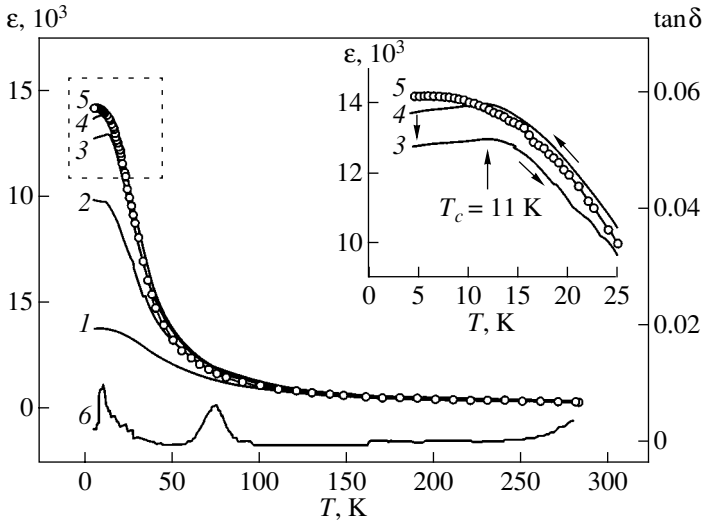

Fig. 6. (*1–5*) ε(*T*) and (*6*) tanδ (*T*) dependences for the $Sr_{1-x}Cd_xTiO_3$ system measured for $x < 0.01$. x = (*1*) 0 (1 kHz), (*2*) 0.0025 (1 kHz), (*3*) 0.005 (1 kHz, heating from 4.2 K), (*4*) 0.005 (1 kHz, cooling from 280 K), (*5*) 0.005 (1 MHz), and (*6*) 0.0025 (1 kHz). The inset shows the initial portions of curves *3*–*5*.

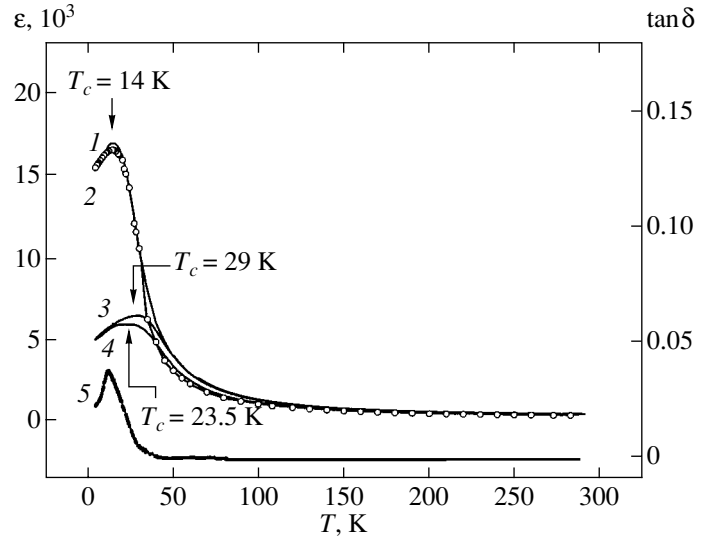

Fig. 7. (*1–4*) ε(*T*) and (*5*) tanδ (*T*) dependences for $Sr_{1-x}Cd_xTiO_3$ measured for x = 0.01, 0.03, and 0.05. (*1*) Solid line, 1 kHz, x = 0.01; (*2*) open circles, 1 MHz, x = 0.01; (*3*) 1 kHz, x = 0.05; (*4*) 1 kHz, x = 0.03; (*5*) 1 kHz, x = 0.01.

Fig. 6). A similar deviation of ε from ergodicity is characteristic of a glassy polar state [16]. As shown by dielectric hysteresis measurements made on samples with x = 0.0025 and 0.005 at temperatures from 5 to 50 K, the $Sr_{1-x}Cd_xTiO_3$ solid solution does not exhibit ferroelectric hysteresis at these concentrations. Below 30 K, the $P(E)$ dependence was nonlinear and had an S shape similar to that for pure strontium titanate. Thus, our studies show that the $Sr_{1-x}Cd_xTiO_3$ system does not undergo a transition to the ferroelectric state with long-range order at concentrations $x \le 0.005$. As for the x = 0.005 composition, the maximum in the permittivity and the nonergodicity in the ε(*T*) relation do not exclude the possibility of a polar glassy state for $T < 11$ K.

In $Sr_{1-x}Cd_xTiO_3$ samples with x = 0.01, 0.03, and 0.05, permittivity maxima were observed to exist at 1 kHz and 1 MHz at practically the same temperature (Fig. 7). The sample with x = 0.01 exhibits a distinct maximum in ε(*T*) (with the largest value of the permittivity for the $Sr_{1-x}Cd_xTiO_3$ system, $\varepsilon = 17 \times 10^3$) at T_c = 14 K, which is accompanied by a maximum in tanδ (*T*) at 12 K. As the $CdTiO_3$ concentration increases, the temperature of the maximum T_c increases, the maximum itself spreads out, and the

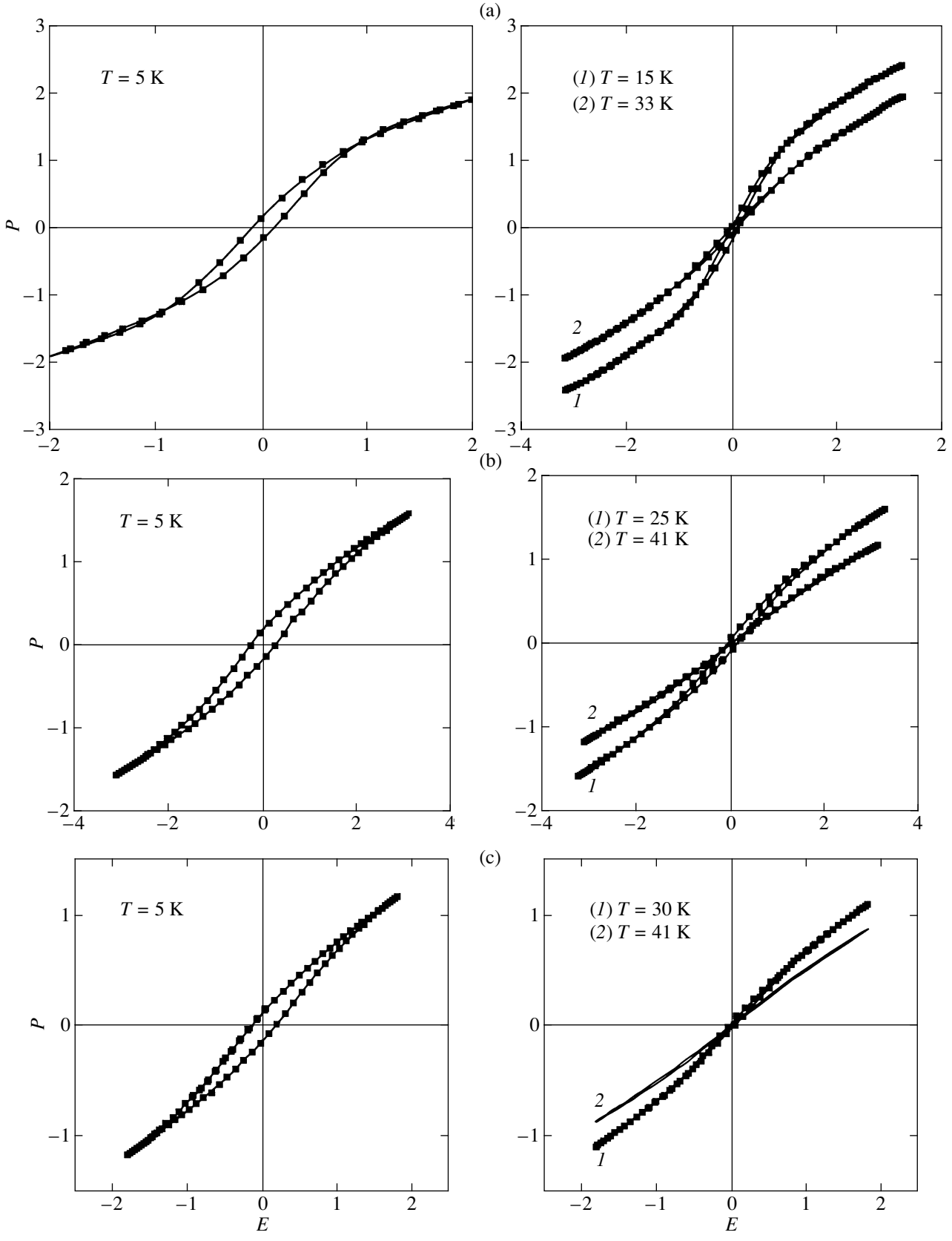

Fig. 8. Hysteresis loops in $Sr_{1-x}Cd_xTiO_3$ plotted for x = (a) 0.01, (b) 0.03, and (c) 0.05. P scale: 10^{-6} C/cm^2; E scale: kV/cm.

Temperatures T_c and the values of the permittivity measured at 1 kHz at these temperatures in the $Sr_{1-x}Cd_xTiO_3$ solid solution for concentrations $x \le 0.1$

x	T_c, K	$\varepsilon(T_c)$
0	–	3817
0.0025	–	9900
0.005	11	14003
0.01	14	17046
0.03	23.5	5940
0.05	29	6513
0.075	25	3592
0.1	22	2456

magnitude of ε at the maximum decreases. A similar behavior of $\varepsilon(T)$ at low impurity concentrations was observed earlier in other $SrTiO_3$-based solid solutions [4, 6, 8, 17]; note that the amplitude of $\varepsilon(T)$ in the $Sr_{1-x}Ca_xTiO_3$ system is the largest [4, 17] at the same impurity concentration as in $Sr_{1-x}Cd_xTiO_3$ ($x \approx 0.01$).

Figure 8 plots hysteresis loops measured on samples with $x = 0.01$, 0.03, and 0.05 at a frequency of 50 Hz. Below T_c, the $P(E)$ dependence has the shape of a narrow ferroelectric loop. This implies that at $0.01 \le x \le 0.05$, the $Sr_{1-x}Cd_xTiO_3$ solid solution undergoes a transition to a polar state with a nonzero switching spontaneous polarization P_s. Narrow hysteresis loops were also observed above T_c; this is due to electric-field-induced polarization. Unlike the $SrTiO_3$-based systems

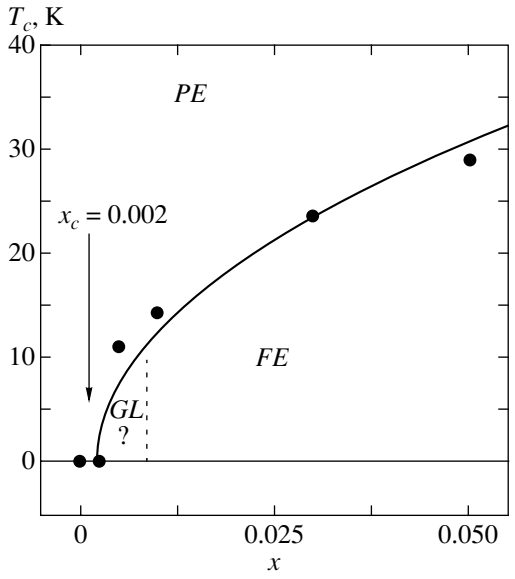

Fig. 9. T_c plotted vs. x for $Sr_{1-x}Cd_xTiO_3$. Points are the experimental data and the solid curve is fitting of the experimental data to the $T_c = 139(x - x_c)^{1/2}$ relation. *PE* is the paraelectric phase, *FE* is the ferroelectric phase, and *GL* is the glassy polar phase.

with the second ferroelectric component that were studied earlier ($Sr_{1-x}Ba_xTiO_3$ [6, 7], $Sr_{1-x}Pb_xTiO_3$ [8]), the magnitude of P_s in $Sr_{1-x}Cd_xTiO_3$ at low temperatures (at saturation) decreases with increasing Cd^{2+} concentration, namely, at $T = 5$ K, $P_s = 1 \times 10^{-6}$ C/cm^2 ($x = 0.01$), 0.5×10^{-6} C/cm^2 ($x = 0.03$), and 0.3×10^{-6} C/cm^2 ($x = 0.05$).

Fitting the experimental data on $\varepsilon(T)$ to the Curie–Weiss law in Eq. (1) within the 60–150 K temperature interval yielded similar values of T_0 for $0.01 \le x \le 0.05$, namely, $T_0 = 36$ K for $x = 0.01$ and 33 K for $x = 0.03$ and 0.05. Note that the difference $T_0 - T_c$ decreases with increasing x and, thus, $\varepsilon(T)$ measured in the $Sr_{1-x}Cd_xTiO_3$ solid solution at concentrations from 0.01 to 0.05 approaches, with increasing x, the relation characteristic of a ferroelectric undergoing a second-order phase transition.

As the concentration of the second component increases still more ($x = 0.075$, 0.1), the temperature of the maxima in $\varepsilon(T)$, in contrast to the systems $Sr_{1-x}Ca_xTiO_3$ [4], $Sr_{1-x}Ba_xTiO_3$ [6, 7], and $Sr_{1-x}Pb_xTiO_3$ [8], begins to decrease rapidly (table). This is accompanied by the onset of a weak frequency dispersion, which increases with increasing x, namely, $\Delta T = T_c(1\text{ MHz}) - T_c(1\text{ kHz}) = 1$ K for $x = 0.075$ and $\Delta T = 3$ K for $x = 0.1$. No dielectric hysteresis loops were observed in samples with $x = 0.075$ and 0.1, and the $P(E)$ relation was linear within the temperature range of 5 to 300 K and in electric fields of up to 4 kV/cm. Thus, the long-range ferroelectric order induced in $Sr_{1-x}Cd_xTiO_3$ at a cadmium concentration $x = 0.01$ breaks down already at $x = 0.075$.

Impurity-induced phase transitions in incipient ferroelectrics are characterized by the following dependence of the temperature corresponding to the maximum permittivity on the impurity concentration x [4]:

$$T_c = A(x - x_c)^{1/2}, \qquad (2)$$

where x_c is the critical concentration, which is usually determined by fitting the experimental data on $T_c(x)$ to relation (2). Figure 9 plots T_c vs. x for the $Sr_{1-x}Cd_xTiO_3$ solid solution obtained for $x \le 0.05$. Approximating the experimental relation through expression (2) yields $A = 139$ K and $x_c = 0.002$. The magnitude of the critical concentration in $Sr_{1-x}Cd_xTiO_3$ is close to that measured in other $SrTiO_3$-based solid-solution systems [4, 6–8, 18].

Summing up the dielectric properties of the $Sr_{1-x}Cd_xTiO_3$ solid solution, it should be noted that long-range ferroelectric order sets in for $Sr_{1-x}Cd_xTiO_3$ at concentrations $x > 0.005$ (its formation was observed at $x = 0.01$), i.e., at values different from the critical concentration x_c derived from Eq. (2). A glassy polar phase can exist within the concentration interval $0.01 > x > 0.002$. A similar transformation of polar states was observed to occur in the $Sr_{1-x}Ba_xTiO_3$ solid solution [6, 7], in which a glassy polar phase sets in for $x \ge 0.0027$ and long-range ferroelectric order occurs for $x \ge 0.035$. However, in order to confirm the existence of a glassy

polar state in $Sr_{1-x}Cd_xTiO_3$ at small x, additional studies are needed, in particular, on single crystals. The induced ferroelectric properties of $Sr_{1-x}Cd_xTiO_3$ vary with increasing impurity concentration differently than in other incipient ferroelectric–ferroelectric systems, such as $Sr_{1-x}Ba_xTiO_3$ [6, 7] and $Sr_{1-x}Pb_xTiO_3$ [8]. In $Sr_{1-x}Ba_xTiO_3$ and $Sr_{1-x}Pb_xTiO_3$, the spontaneous polarization and $T_c(x)$ grow monotonically with increasing concentration of the ferroelectric component. In $Sr_{1-x}Cd_xTiO_3$, as x increases in the $0.01 \le x < 0.075$ interval, the magnitude of P_s falls off monotonically, until at $x = 0.075$, the long-range order breaks down altogether. The disappearance of long-range order is accompanied by a change in the concentration dependence of the temperature position of the maxima in ε; more specifically, the temperature of the maxima in $\varepsilon(T)$ begins to decrease rapidly with increasing x for $x \ge 0.075$. As already mentioned, x-ray diffraction analysis shows that the $Sr_{1-x}Cd_xTiO_3$ solid solution does not form for $x \ge 0.2$. The weakening of the impurity-induced ferroelectric properties with increasing x in $Sr_{1-x}Cd_xTiO_3$ may be associated with approaching the solubility limit.

5. CONCLUSIONS

The results of this work can be summed up as follows. Our studies of the temperature dependence of the permittivity and of the dielectric hysteresis loops revealed that a ferroelectric phase transition close to the tricritical point occurs in $CdTiO_3$ at 76.5 ± 0.5 K. The temperature dependence of the spontaneous polarization in $CdTiO_3$ can be described within the Landau theory of phase transitions with a critical order parameter exponent equal to ≈ 0.25.

The temperature dependences of the permittivity and of the spontaneous polarization were studied in $Sr_{1-x}Cd_xTiO_3$. The phase diagram of this solid solution was constructed in (T, x) coordinates, and the critical concentration $x_c = 0.002$ was determined. It was shown that the dependence of the transition temperature to the polar state in $Sr_{1-x}Cd_xTiO_3$ on concentration x scales as $T_c = 139(x - x_c)^{1/2}$ for $x_c \le x \le 0.05$. In the concentration interval $0.01 \le x \le 0.05$, the induced polar state has a ferroelectric long-range order which breaks down as x increases to 0.075; this may be associated with approaching the solubility limit of $CdTiO_3$ in $Sr_{1-x}Cd_xTiO_3$.

ACKNOWLEDGMENTS

The authors express their gratitude to V.V. Krasovskaya for preparation of the $Sr_{1-x}Cd_xTiO_3$ ceramic samples.

This study was supported by the Russian Foundation for Basic Research, project nos. 00-02-16875 and 98-02-18161, and by NWO.

REFERENCES

1. G. A. Smolenskiĭ, V. A. Bokov, V. A. Isupov, N. N. Kraĭik, R. E. Pasynkov, A. I. Sokolov, and N. K. Yushin, *The Physics of Ferroelectric Phenomena* (Nauka, Leningrad, 1985).
2. H. El-Mallah, B. E. Watts, and B. Wanklyn, Phase Transit. **9**, 235 (1987).
3. T. Sugai and M. Wada, Jpn. J. Appl. Phys. **18** (9), 1709 (1979).
4. J. G. Bednorz and K. A. Müller, Phys. Rev. Lett. **52** (25), 2289 (1984).
5. V. V. Lemanov, A. V. Sotnikov, E. P. Smirnova, *et al.*, Solid State Commun. **110**, 611 (1999).
6. V. V. Lemanov, E. P. Smirnova, P. P. Syrnikov, and E. A. Tarakanov, Phys. Rev. B **54** (10), 3151 (1996).
7. M. E. Guzhva, W. Kleemann, V. V. Lemanov, and P. A. Markovin, Fiz. Tverd. Tela (St. Petersburg) **39** (4), 704 (1997) [Phys. Solid State **39**, 618 (1997)].
8. V. V. Lemanov, E. P. Smirnova, and E. A. Tarakanov, Fiz. Tverd. Tela (St. Petersburg) **39** (4), 714 (1997) [Phys. Solid State **39**, 628 (1997)].
9. M. E. Guzhva, V. V. Lemanov, P. A. Markovin, and T. A. Shaplygina, Ferroelectrics **218**, 93 (1998).
10. F. Jona and G. Shirane, *Ferroelectric Crystals* (Pergamon, Oxford, 1962; Mir, Moscow, 1965).
11. B. Jaffe, W. R. Cook, and H. Jaffe, *Piezoelectric Ceramics* (Academic, New York, 1971; Nauka, Moscow, 1974).
12. M. E. Lines and A. M. Glass, *Principles and Applications of Ferroelectrics and Related Materials* (Oxford Univ. Press, Oxford, 1977; Mir, Moscow, 1981).
13. B. A. Strukov and A. P. Levanyuk, *Physical Principles of Ferroelectric Phenomena in Crystals* (Nauka, Moscow, 1995).
14. J. C. Burfoot, *Ferroelectrics: An Introduction to the Physical Principles* (Van Nostrand, New York, 1967; Mir, Moscow, 1970).
15. T. Mitsui and W. B. Westphal, Phys. Rev. **124** (5), 1354 (1961).
16. S. L. Ginzburg, *Irreversible Processes in Spin Glasses* (Nauka, Moscow, 1989).
17. J. Dec, W. Kleemann, U. Bianchi, and J. G. Bednorz, Europhys. Lett. **29** (1), 31 (1995).
18. V. V. Lemanov, Fiz. Tverd. Tela (St. Petersburg) **39** (9), 1645 (1997) [Phys. Solid State **39**, 1468 (1997)].

Translated by G. Skrebtsov

Physics of the Solid State, Vol. 43, No. 11, 2001, pp. 2154–2157. Translated from Fizika Tverdogo Tela, Vol. 43, No. 11, 2001, pp. 2066–2069.
Original Russian Text Copyright © 2001 by Vtyurin, Bulou, Krylov, Voronov.

LATTICE DYNAMICS AND PHASE TRANSITIONS

Soft-Mode Condensation in Raman Spectra of the Rb_2KScF_6 Elpasolite

A. N. Vtyurin*, A. Bulou, A. S. Krylov*, and V. N. Voronov***

**Kirenskiĭ Institute of Physics, Siberian Division, Russian Academy of Sciences, Akademgorodok, Krasnoyarsk, 660036 Russia*

e-mail: vtyurin@iph.krasn.ru

***Université du Maine, Le Mans, Cedex 9, 72085 France*

Received April 5, 2001

Abstract—This paper reports on the first observation of soft-mode condensation in the Raman spectra of the Rb_2KScF_6 elpasolite crystal below the transition points from the cubic to tetragonal and, subsequently, monoclinic phase. © *2001 MAIK "Nauka/Interperiodica".*

1. INTRODUCTION

The A_2BCX_6 elpasolites (high-symmetry phase G_0, space group $Fm3m$, $Z = 4$), a family of perovskite-like crystals, are subjects of considerable interest because of their application potential and as model media to study phase-transition mechanisms [1]. Phase transitions (PT) in these structures are usually associated with the lattice becoming unstable to rotation of the CX_6 octahedral ions, which is caused by phonon-mode condensation. Soft mode condensation has been successfully observed before only in bromine-, chlorine-, and oxygen-containing elpasolites [2–5]. Studies of transitions in the fluorine compounds of this family performed, in particular, using vibrational spectroscopy are usually rendered difficult by their comparatively high temperatures. The Rb_2KScF_6 crystal appears a promising system from this standpoint. Indeed, its phase transition temperatures are relatively low: $T_1 = 252$ K (to the G_1 phase, space group $I114/m$, $Z = 2$) and $T_2 = 223$ K (to the G_2 phase, space group $P112_1/n$, $Z = 2$) [6]. This suggests that one could obtain spectra with narrow lines and a low background. A recent first-principles calculation of the stability and dynamics of the Rb_2KScF_6 lattice [7] showed that the phase transitions observed to occur in this crystal can also be due to soft phonon-mode condensation. Earlier studies of Raman scattering (RS) spectra did not, however, provide experimental support of this conjecture [8], just as in the case of other fluorine-containing elpasolites isomorphic with respect to Rb_2KScF_6 [9]. This stimulated the present study of the low-frequency Raman spectrum of the Rb_2KScF_6 crystal as a search for soft phonon modes.

2. CRYSTAL STRUCTURE AND NORMAL-MODE SYMMETRY

Figure 1 presents schematically the unit cell of the high-symmetry phase G_0. The vibrational representation can be reduced into irreducible representations (IR) at the Brillouin zone center as

$$\Gamma_{\text{vib}} = A_{1g}(xx, yy, zz) + E_g(xx, yy, zz) + 2F_{2g}(xz, yz, xy) + F_{1g} + 5F_{1u} + F_{2u},$$

where the parentheses contain the RS tensor components to which the corresponding vibrations contribute. The table identifies the atoms involved in these vibrations. The position symmetry of the ScF_6 group in the structure coincides with that of the free group, and the symmetries, types, and frequencies of its Raman-active normal vibrations taken from [10] are given in Fig. 2. Figure 3 displays the correlation diagram of the vibrations active in the RS spectra of the cubic and tetragonal phases. As follows from this diagram, only one lattice vibration mode (hard) is active in the spectrum of the cubic phase (the others being internal vibrations of the ScF_6 groups), but the soft mode hardening (which splits below the transition in two) can be seen in RS below the transition point.

Vibrational representation of the group symmetry of the Rb_2KScF_6 cubic phase

IR	A_{1g} (xx, yy, zz)	E_g (xx, yy, zz)	F_{1g}	F_{2g} (xz, yz, xy)	F_{1u}	F_{2u}
2Rb	–	–	–	1	1	–
K	–	–	–	–	1	–
Sc	–	–	–	–	1	–
6F	1	1	1	1	2	1
Γ_{vib}	1	1	1	2	5	1

Note: F_{1g} is the representation corresponding to the cubic-phase soft-mode symmetry.

1063-7834/01/4311-2154$21.00 © 2001 MAIK "Nauka/Interperiodica"

The transition to the G_2 phase occurs according to the X_5^+ representation of the G_0 phase (which corresponds to the Z_5^+ representation of the G_1 phase; we use here the notation of [9]) and is accompanied by primitive-cell doubling. The modes corresponding to the $X(Z)$ point in the Brillouin zone are Raman inactive; however, as can be seen from the correlation diagram in Fig. 4, they may also be observed below the second transition point.

3. EXPERIMENT

The samples for the experiment, measuring $2 \times 2 \times 4$ mm, were chosen from the same crystallization as in [6] and were cut such that, in the G_0 phase, their edges were aligned with the crystallographic axes (note that, after the phase transitions, a well-developed domain structure precluding measurement of polarized spectra in the low-temperature phases is formed). The crystals were optically transparent and did not contain colored defects or inclusions visible under a microscope. The spectra were obtained on a Jobin-Yvon T-64000 Raman spectrometer with CCD-array detection. To suppress the elastic scattering wing as much as possible, a triple-monochromator mode was used with subtraction of dispersion and with a low-frequency cutoff at 8 cm^{-1}. The spectral width of the slits was 1 cm^{-1}, the spectral size of the array cell was 650/1024 cm^{-1}, and the signal accumulation time was 600 s. The excitation was accomplished with 514.5 nm polarized radiation from a 500 mW Ar^+ laser. The sample temperature during spectral measurement was stabilized to no worse than 0.2 K.

4. RESULTS AND DISCUSSION

The number and polarization of the spectral lines detected in the high-temperature cubic phase far from the transition point agree well with calculations and earlier observations [8, 9]. The frequency of the only Raman-active lattice vibration mode at room temperature is 89 cm^{-1}, and it increases slightly under cooling; thus, it does not interfere with the observation of anomalies in the low-frequency part of the spectrum.

As the temperature is lowered, one observes the central scattering peak to grow in intensity and broaden a few degrees before the transition point. Below T_1, a broad wing appears near the central peak, which can be interpreted as an enhancement of a low-intensity broad band (Fig. 5); at lower temperatures, one can discriminate two maxima in it, at 26 and 39 cm^{-1}. Figure 6 shows the temperature dependence of the squared frequencies of the line maxima (the parameters of the overlapping profiles were derived with the SigmaPlot 5.0 program with a dispersive function used for line contours). No noticeable frequency shifts of these lines are observed to occur in the tetragonal phase (because of the background level being comparable to the line intensity, the line position could not be determined with a sufficiently high accuracy); one can only notice a certain redistribution of the intensity to higher frequencies within this band with decreasing temperature and a lowering of the central peak intensity, which is possibly caused by rearrangement of the domain structure.

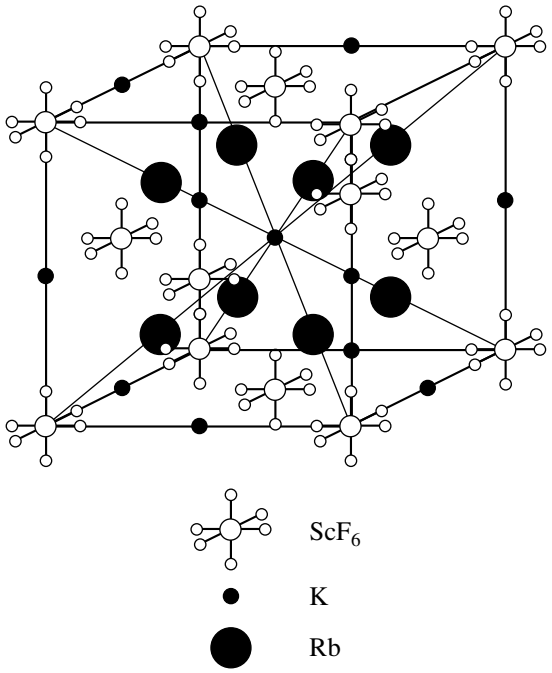

Fig. 1. Structure of the original phase G_0 of the Rb_2KScF_6 crystal.

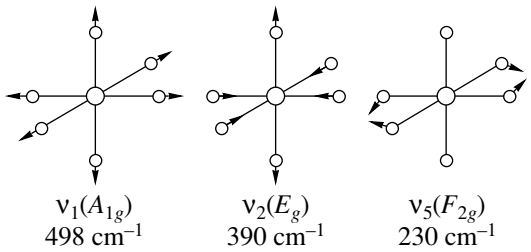

Fig. 2. Types of Raman-active normal modes of the ScF_6 group.

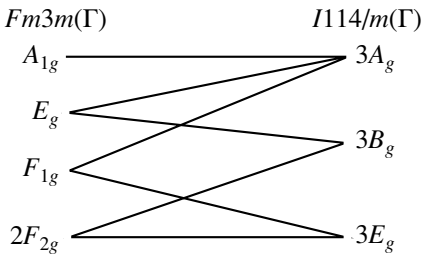

Fig. 3. Correlation diagram of the Raman-active modes of the cubic and tetragonal phases.

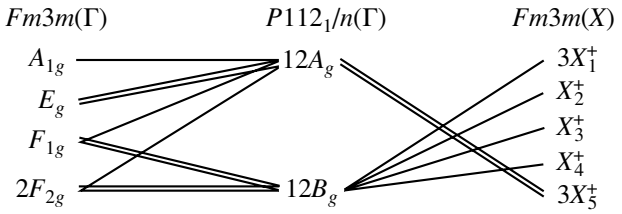

Fig. 4. Correlation diagram of the Raman-active modes of the cubic and monoclinic phases.

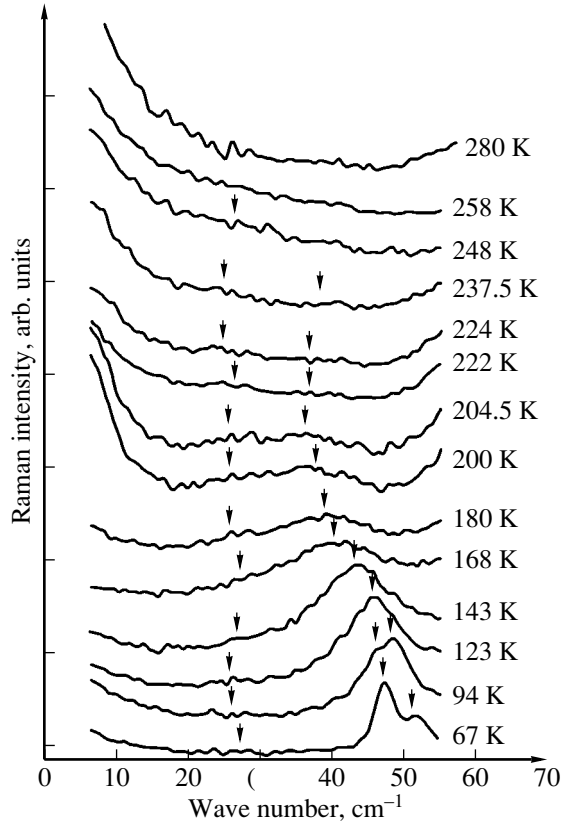

Fig. 5. Temperature-induced changes in the low-frequency part of the Rb_2KScF_6 spectrum.

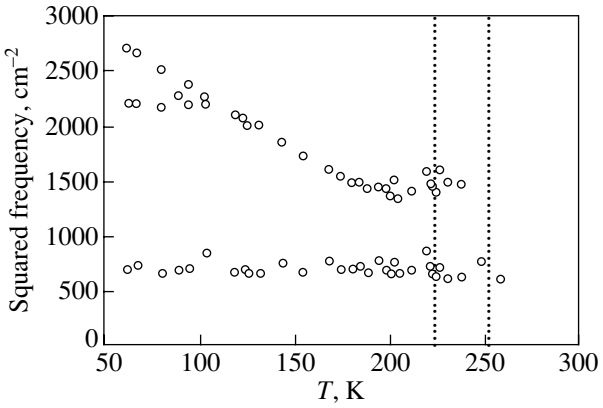

Fig. 6. Temperature dependence of the squared frequencies of the observed low-frequency lines.

As the second transition point is reached, the elastic scattering intensity increases in a jump and the band undergoes an intensity redistribution, with its high-frequency part growing noticeably. The frequency of this maximum increases monotonically under cooling. The temperature dependence of the squared frequency is close to being a linear dependence; this is a feature characteristic of soft modes associated with displacive phase transitions, either of the second order or of the first close to the second order. Below 100 K, where the line widths become smaller because of the decrease in anharmonicity, the corresponding band splits in two components. As the temperature is lowered still more, the high-frequency component of the doublet thus formed continues to move up, while the low-frequency one remains unchanged (47–48 cm^{-1}).

The lowest frequency maximum also remains practically in the same position (26–27 cm^{-1}). Its intensity falls off slowly, until it becomes practically indistinguishable against the background noise below 100 K.

Thus, one may conclude that the phase transformations in Rb_2KScF_6 studied here are accompanied by soft phonon-mode condensation; hence, they should be assigned to displacive transitions. As shown in using group-theoretical analysis, the first phase transition is associated with a rotation of the ScF_6^+ octahedral molecular ions (table), whereas the second one may be induced by a more complex deformation involving both rotation of these ions and cation displacement [8, 9]. At the same time, the first transition is accompanied by considerable pretransition effects and the lines forming below the transition point exhibit extremely low intensities and large widths, which may be caused by either strong order-parameter fluctuations over a broad enough temperature interval or by the onset of structural disorder in the pretransition region [11].

Because all critical vibrations in the low-temperature phase belong to one totally symmetric representation, their closeness in position and the strong temperature dependence of their frequencies must inevitably give rise to strong coupling and, hence, mixing of various types of vibrations. Thus, even if these strong fluctuation effects are originally related to the cubic-to-tetragonal phase transition, the interaction between the critical vibrations should also cause intense fluctuations of the order parameter governing the second transition. Only a substantial decrease in temperature weakens this coupling and permits reliable observation of the recovery of the corresponding modes.

ACKNOWLEDGMENTS

Sincere thanks are due to K.S. Aleksandrov, V.I. Zinenko, and I.N. Flerov for the samples and fruitful discussions of the results obtained.

This study was supported by the INTAS Foundation, grant no. 97-10177, and the Russian Foundation for Basic Research, project nos. 00-02-17792 and 00-15-96790.

REFERENCES

1. K. S. Aleksandrov and B. V. Beznosikov, *Perovskite-like Crystals* (Sib. Otd. Ross. Akad. Nauk, Novosibirsk, 1999).
2. W. Buhrer and H. U. Gudel, J. Phys. C **20** (8), 3809 (1987).
3. G. P. Knudsen, Solid State Commun. **49** (7), 1045 (1984).
4. F. Prokert and K. S. Aleksandrov, Phys. Status Solidi B **124** (2), 503 (1984).
5. G. Baldinozzi, Ph. Sciau, and A. Bulou, J. Phys.: Condens. Matter **7** (10), 8109 (1995).
6. I. N. Flerov, M. V. Gorev, S. V. Mel'nikova, *et al.*, Fiz. Tverd. Tela (St. Petersburg) **34** (7), 2185 (1992) [Sov. Phys. Solid State **34**, 1168 (1992)].
7. V. I. Zinenko and N. G. Zamkova, Zh. Éksp. Teor. Fiz. **118** (2), 359 (2000) [JETP **91**, 314 (2000)].
8. I. N. Flerov, M. V. Gorev, K. S. Aleksandrov, *et al.*, Mater. Sci. Eng., R **24** (3), 79 (1998).
9. M. Cousi, S. Khairoun, and A. Tressaud, Phys. Status Solidi A **98** (1), 423 (1986).
10. K. Nakamoto, *Infrared and Raman Spectra of Inorganic and Coordination Compounds* (Wiley, New York, 1986; Mir, Moscow, 1991).
11. A. Bulou, M. Rousseau, and J. Nouet, Ferroelectrics **104** (1), 373 (1990).

Translated by G. Skrebtsov

Physics of the Solid State, Vol. 43, No. 11, 2001, pp. 2158–2164. Translated from Fizika Tverdogo Tela, Vol. 43, No. 11, 2001, pp. 2070–2075.
Original Russian Text Copyright © 2001 by Belyaev, Volkov, Konopleva, Nazarkin, Razov, Soloveĭ, Chekanov.

LATTICE DYNAMICS AND PHASE TRANSITIONS

Kinetics of Radiation Damage and Martensitic Transformations in TiNi Alloys Irradiated with Neutrons

S. P. Belyaev*, A. E. Volkov*, R. F. Konopleva, I. V. Nazarkin**, A. I. Razov*, V. L. Soloveĭ**, and V. A. Chekanov****

** Smirnov Research Institute of Mathematics and Mechanics, St. Petersburg State University, St. Petersburg, 198904 Russia*
e-mail: spb@smel.math.spbu.ru

*** St. Petersburg Institute of Nuclear Physics, Russian Academy of Sciences, Gatchina, Leningrad oblast, 188300 Russia*

Received April 9, 2001

Abstract—The variation of the temperatures of martensitic transformations and the rate of radiation damage in TiNi alloys were studied upon irradiation with reactor neutrons. The irradiation was performed at temperatures of 120 and 335 K. In the process of irradiation, electrical resistance of the alloys was measured continuously and thermal cycling through the temperature range of martensitic transformations was carried out. The transformation temperatures were shown to decrease at different rates with increasing irradiation fluence. The electrical resistance increases linearly with increasing neutron fluence to 6.7×10^{18} cm^{-2} irrespective of the irradiation temperature. Deviation from a linear dependence is only observed when the irradiation leads to a change in the phase state of the alloy. The rate of the resistance increase only slightly depends on the irradiation temperature. In martensite, it is greater by a factor of 2–4 than that in austenite. Mechanisms of irradiation-induced modification of the structure of TiNi alloys that explain the experimental data obtained are discussed. © *2001 MAIK "Nauka/Interperiodica".*

INTRODUCTION

As the temperature changes, the TiNi alloy of equiatomic composition undergoes two martensitic transformations. In the process of cooling, the ordered high-temperature cubic phase *B*2 (CsCl type) sequentially transforms into a rhombohedral *R* phase and then into a monoclinic (monoclinically distorted orthorhombic) crystal structure *B*19'. Heating from the low-temperature state causes transitions in the inverse sequence: *B*19' $\longrightarrow$ *R* $\longrightarrow$ *B*2. Frequently, the transformation occurs directly from the *B*19' into the *B*2 phase without the intermediate *R* state.

The sequence of martensitic transformations in the TiNi alloy and the characteristic temperatures of the transitions are determined by many factors, such as the chemical composition of the base and the concentrations of alloying impurities, mechanical stresses, conditions of processing, thermomechanical treatment, etc. [1]. Among them, neutron irradiation is noteworthy, whose effect on the properties and structure of titanium nickelide has been intensely studied in recent years [2–12]. The interest of researchers in this problem is primarily connected with the need to predict the properties of this alloy, which exhibits a shape-memory effect and is a promising material for solving a number of problems that arise when constructing, exploiting, and repairing atomic and thermonuclear plants [13–15]. Of great importance is also the possibility of controlling martensitic transitions and the functional and mechanical properties of the TiNi alloy using irradiation with high-energy particles—a process that can easily be controlled and dosed.

It has been established to date that the temperatures of martensitic transitions are shifted toward lower temperatures range as a result of neutron irradiation [2–8]. Thus, according to [2–5], the temperature M_s of the onset of the *R* $\longrightarrow$ *B*19' transition decreases by more than 200 K after irradiation with fast neutrons ($E > 1$ MeV) to a fluence $\Phi = 8 \times 10^{19}$ cm^{-2} at a temperature $T_{irr} = 323$ K. The temperature T_R of the onset of the *B*2 $\longrightarrow$ *R* transformation decreases only slightly (by 1–20 K). These findings contradict the results of [7], where the shift of both T_R and M_s in the process of annealing of irradiated (to a fluence $\Phi = 8 \times 10^{19}$ cm^{-2} at $T_{irr} = 340$ K) samples of titanium nickelide was found to be the same. As was shown in [2–5], no shift in M_s and T_R occurs up to a dose of 1.1×10^{21} cm^{-2} if the irradiation is performed at enhanced temperatures (520 K). This fact indicates a sharp activation of the processes of radiation-defect annealing in the TiNi alloy near 500 K. In fact, as is emphasized in [3–5], the kinetics of martensitic transitions stops, depending on the neutron dose, at very small homologous irradiation temperatures, such as $T_{irr}/T_m = 0.33$, where T_m is the melting temperature.

Measurements performed directly in the process of irradiation at $T_{irr} = 170$ K showed that in the range of small fluences (to $\Phi = 6.7 \times 10^{18}$ cm^{-2}), the decrease in the temperatures of martensitic transformations in the TiNi alloy is described by the dependence

$$\Delta T_{irr} = d[\exp(-\Phi/\Phi_0) - 1], \quad (1)$$

where ΔT_{irr} is the increment in the temperature of the phase transition, Φ is the neutron fluence, and d and Φ_0

Table 1. Heat-treatment regimes and martensitic-transformation temperatures of the samples

No.	Heat-treatment regime	T_R, K	M_s, K	M_f, K	A_s, K
1	770 K, 2 h	315	250	195	295
2	770 K, 2 h	335	305	295	–
3	As-supplied	310	–	–	–
4	Same	320	250	205	–

are constants [6]. The different transformation temperatures are shifted with increasing dose at different rates. The temperatures of the start and finish of the $R \longrightarrow B19'$ transition (M_s and M_f, respectively) decrease by 80 K at a fluence of 6.7×10^{18} cm^{-2}, whereas T_R and A_f (A_f is the temperature of the finish of the reverse $B19' \longrightarrow B2$ transformation) change by 18 and 30 K, respectively.

On the whole, the available data suggest that neutron irradiation at temperatures below 500 K leads to a significant change in the temperatures of martensitic transformations in titanium nickelide. In its effect on the transformation temperatures, the irradiation can be comparable only to the variation of the chemical composition or alloying with a third component [16].

Most researchers ascribe the observed changes to the radiation-induced disordering of the crystal structure of the alloys [5–9]. In [7, 9–11], a decrease in the intensity of superlattice reflections in $Ti_{49}Ni_{51}$ was directly observed using neutron diffraction. The relative change in the intensity of superlattice maxima significantly exceeded that of fundamental reflections, which permitted the authors of the above papers to arrive at the conclusion that irradiation decreased the degree of long-range order of the alloy. In experiments on the annealing of irradiated samples, an empirical relation was established between the temperatures of martensitic transformations and the degree of long-range order in TiNi [7]. However, the radiation modification of the structure of the TiNi alloy is not restricted to only a decrease in the degree of long-range order. In [9–11], an amorphization of titanium nickelide upon irradiation with fast neutrons was revealed. In polycrystals, e.g., according to [1], the fraction of the amorphous phase is about 90% after neutron irradiation to a fluence of 6×10^{19} cm^{-2} at 340 K. The authors of [12] interpret the results of structural analysis of an irradiated TiNi alloy from the viewpoint of the processes of radiation-stimulated aging, which generates local inhomogeneities of chemical composition in the alloy. The aging is supposed to be stimulated by the high-intensity γ radiation, which always accompanies the irradiation in a reactor. In addition, it is stated that in the regions of atomic-collision cascades, elastic distortions arise in the lattice, which favor the continuous development of martensitic transformations in a wide temperature range from 300 to 4.2 K.

In this paper, we studied martensitic transformations and kinetic features of radiation-stimulated modification of the properties of TiNi alloys irradiated with reactor neutrons at various temperatures. In contrast to most papers, where investigations were performed on preliminarily irradiated samples, our measurements were carried out directly in the process of irradiation in a specially equipped reactor channel. We used the method of measuring electrical resistance. This characteristic, as is well known, is structure-sensitive with respect to both radiation defects and martensitic transformations.

1. EXPERIMENTAL

For experiments, we used samples of equiatomic titanium nickelide from various suppliers. The as-supplied samples were wires 0.5 mm in diameter and 30 mm in length deformed during the last processing step (drawing) to a reduction of area by 20–25%. Part of the samples were irradiated without any additional heat treatment; the others were annealed at 770 K for 2 h in an argon atmosphere. Before measurements, the samples were repeatedly cycled through the temperature range of martensitic transformations to stabilize their properties. Directly before placing the samples in the reactor channel, we measured the temperature dependence of resistance to determine the martensitic-transformation temperatures. The data for four test samples are given in Table 1 and in Fig. 1. In the figure, the vertical arrows indicate temperatures corresponding to various transformations in the titanium nickelide. The temperature T_R of the onset of the $B2 \longrightarrow R$ transition upon cooling is defined as the temperature of the onset of the anomalous rise of the electrical resistance; the temperature M_s of the onset of the $R(B2) \longrightarrow B19'$ transition is associated with a maximum in the $\rho(T)$ dependence; and the temperature M_f of the finish of the transformation into the $B19'$ martensite corresponds to the passage to a linear dependence of the resistance on temperature.

As can be seen from Fig. 1, the temperature dependences of the resistance differ substantially for heat-treated and untreated samples. In samples 1 and 2, the $B2 \longrightarrow R \longrightarrow B19'$ transformation sequence is observed upon cooling, whereas upon heating, the $B19'$ martensite appears to transform directly into the $B2$ austenite.

In the deformed samples 3 and 4, the stage of the rise of resistance upon cooling is strongly extended in

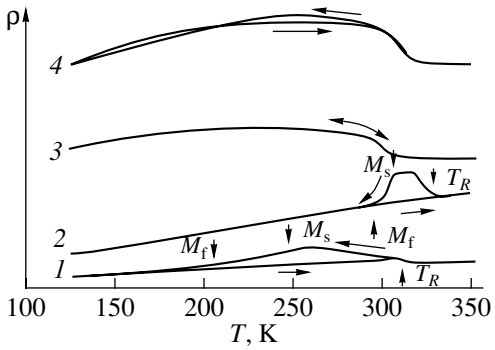

Fig. 1. Temperature dependences of resistance of the alloys in the unirradiated state. Figures near the curves denote the order numbers of the samples (see Table 1).

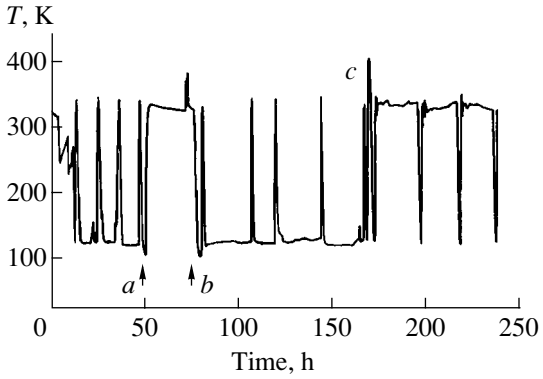

Fig. 2. Variation of the temperature in the reactor channel.

temperature and the temperature hysteresis is weak (the resistance changes upon cooing and heating in a similar manner). It may be assumed that in the samples that were not subjected to a heat treatment in the temperature range under study, the $B2 \longleftrightarrow R$ transition that is characterized by a small temperature hysteresis (2–5 K) is mainly realized, while the $R \longrightarrow B19'$ transition is suppressed to a significant extent.

The irradiation was performed in a low-temperature helium loop placed in one of the vertical channels of the VVR-M research reactor of the St. Petersburg Institute of Nuclear Physics, Russian Academy of Sciences. Helium cooled in a cryogenic system was circulated in the channel along a closed contour to remove heat released in samples due to radiation heating. The temperature in the loop was kept constant or changed according to a specified schedule by changing the rate of helium circulation and the degree of its cooling. The thermal insulation of the walls of the helium loop from the heat carrier of the reactor was ensured with a vacuum jacket. At a reactor power of 15 MW, the density of the fast-neutron flux with an energy of more than 1 MeV was 1×10^{13} cm^{-2} s^{-1}.

The electrical resistance was measured using a four-probe technique; the temperature was measured with a copper–constantan thermocouple. All the measurements were carried out continuously during the entire experiment. Each value of the resistance was determined as an average of four measurements performed using different polarities of the current and voltage signals. This permitted us to eliminate the effect of the thermopowers that arise at contacts between unlike conductors.

The irradiation with fast neutrons to a fluence of 5.5×10^{18} cm^{-2} was performed at a temperature $T_{irr} = 120 \pm 7$ K (in the martensitic state of the alloys), after which the temperature was increased and further irradiation was carried out at 335 ± 10 K (in the austenitic state). During the entire experiment, we measured the temperature dependences of the resistance in the course of intermediate thermal cycling through the interval of martensitic transformations without interrupting the irradiation. The rate of the temperature variation in the thermocycles was 2–3 K/min. The graph of the temperature variation in the course of the whole experiment is displayed in Fig. 2. The time interval *a*–*b* in this figure corresponds to a reactor suspension, when the helium circulation in the channel was stopped and the temperature established at a level of 330 K with a short-time rise to 380 K when the irradiation was restarted. Before the irradiation at a temperature $T_{irr} =$ 335 K, the temperature of the samples was increased to 400 K for 20 min (temperature peak *c* in Fig. 2).

2. RESULTS AND DISCUSSION

The temperature dependences of resistance obtained in the course of thermocycling allow us to analyze both the changes in the temperatures of martensitic transformations and the kinetics of the processes of radiation-stimulated changes in the structure of the materials. Several such dependences are shown in Fig. 3 for sample 2. It is seen that, with increasing neutron fluence, there occur substantial changes in the shape and position of the curves in the diagram field. First of all, note that the temperatures of martensitic transformations decrease in the course of irradiation. The process begins in the first hours of the irradiation of the material and is developed in accordance with Eq. (1) at different rates for different martensitic temperatures. The M_s and M_f temperatures decrease at greater rates than the T_R temperature. Thus, at the maximum fluence used in the experiments (6.7×10^{18} cm^{-2}), T_R decreases by 15–20 K, whereas M_s is diminished by 70–80 K. As a result, the temperature field of existence of the *R* phase expands and the martensitic transitions after irradiation occur in a much wider temperature range as compared to the initial unirradiated state. After irradiation, the $R \longrightarrow B19'$ transformation upon cooling may not be realized at all down to 120 K, and in the temperature range of thermocycling, only a resistance increase connected with the $B2 \longrightarrow R$ transition is observed. As an example of such a behavior, alloy 1 can be considered (Fig. 4), which after irradiation to a dose of 3.5×10^{18} cm^{-2}

exhibits an anhysteretic $\rho(T)$ dependence virtually without the stage of resistance decrease corresponding to the $R \longrightarrow B19'$ transition upon cooling.

Simultaneously with a change in the shape of the temperature dependences of resistance in the course of irradiation, their shift upward along the ρ axis occurs. According to the Matthiessen's rule, the $\rho(T)$ dependence should be shifted parallel to itself with increasing concentration of radiation defects. However, measurements show that the shift occurs inhomogeneously in the thermocycling range (Figs. 3, 4). The high-temperature branch of the $\rho(T)$ dependence is shifted at a smaller rate as compared to the low-temperature branch. This circumstance could be referred to a partial annealing of radiation defects with increasing temperature during thermocycling. However, the data given in Figs. 3 and 4 show that the nonclosure of the heating–cooling curves in a thermocycle is only small if it exists at all. This means that the recovery of electrical resistance due to an increase in temperature is small. In addition, the nonuniform shift of the $\rho(T)$ dependences is observed at $T_{irr} = 335$ K as well (Figs. 3, 4), when the temperature decreases rather than increases during thermocycling with respect to the irradiation temperature. In general, it is important to emphasize that the character of changes in the kinetics of martensitic transformations and electrical resistance are almost independent of the irradiation temperature and, consequently, of the structural state (martensitic or austenitic) in which the irradiation was performed.

With the above data, we can quantitatively estimate the observed behavior of the martensitic temperature using the following procedure. If in Figs. 3 and 4 we draw straight lines parallel to the ρ axis, the points of intersections of such isotherms with the $\rho(T)$ dependences will give us a picture of changes of the resistance at certain constant temperatures. Such constructions were performed for the isotherms corresponding to 130 and 335 K. These temperatures were chosen to eliminate, if possible, the factor of changes in the phase state of TiNi alloys related to neutron irradiation upon the analysis of the rate of accumulation of radiation damage. Indeed, the temperature of 335 K for all samples during the whole period of irradiation corresponded to a single-phase austenitic state and the temperature of 130 K corresponded to a martensitic state with a monoclinic structure $B19'$ for sample 2 and rhombohedral R structure for samples 3 and 4. Alloy 1 at 130 K had a $B19'$ structure at the beginning of irradiation and mainly a rhombohedral structure after a dose of 3.5×10^{18} cm^{-2} had been accumulated, as suggested by Fig. 4.

Figure 5 illustrates the dose dependences of radiation damage for samples 1 and 2. The points in the graphs include all intersections of the $\rho(T)$ dependences with the corresponding isotherms both upon heating and cooling both during thermal cycles and upon isothermal irradiation. The lines shown in the fig-

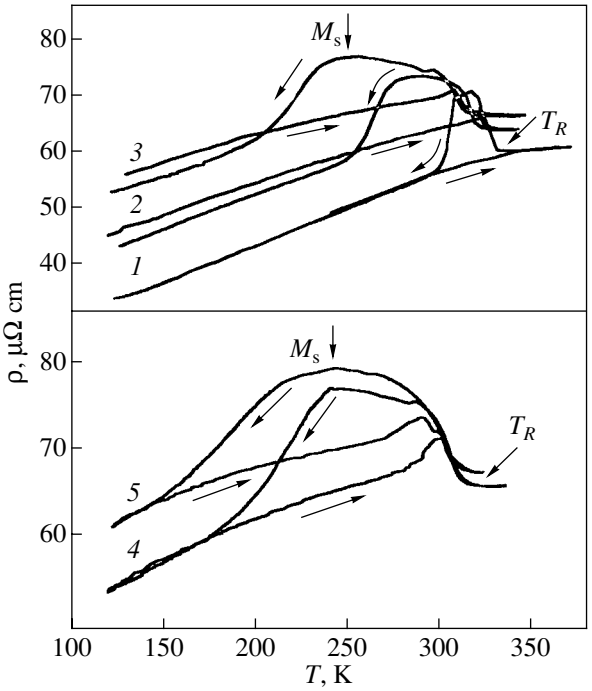

Fig. 3. Temperature dependences of the resistance of sample 2 in the (*1*) unirradiated state and after irradiation at a temperature of (*2*, *3*) 120 and (*4*, *5*) 335 K to a fluence of (*2*) 1.3×10^{18}, (*3*) 3.6×10^{18}, (*4*) 5.4×10^{18}, and (*5*) 6.7×10^{18} cm^{-2}.

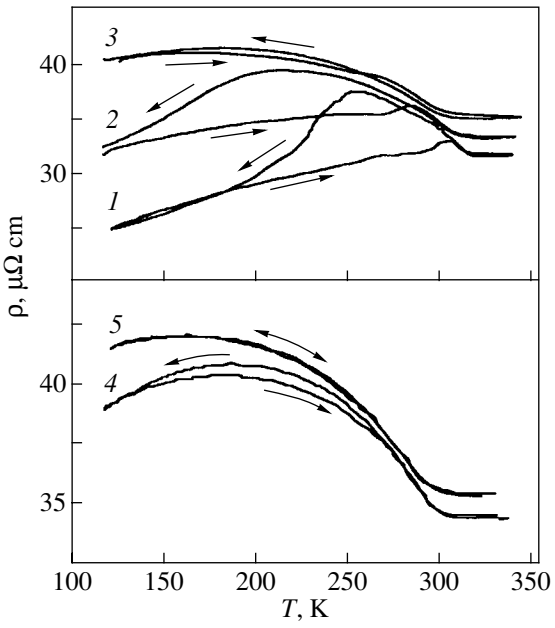

Fig. 4. Temperature dependences of the resistance of sample 1 in the (*1*) unirradiated state and after irradiation at a temperature of (*2*, *3*) 120 and (*4*, *5*) 335 K to a fluence of (*2*) 1.3×10^{18}, (*3*) 3.6×10^{18}, (*4*) 5.4×10^{18}, and (*5*) 6.7×10^{18} cm^{-2}.

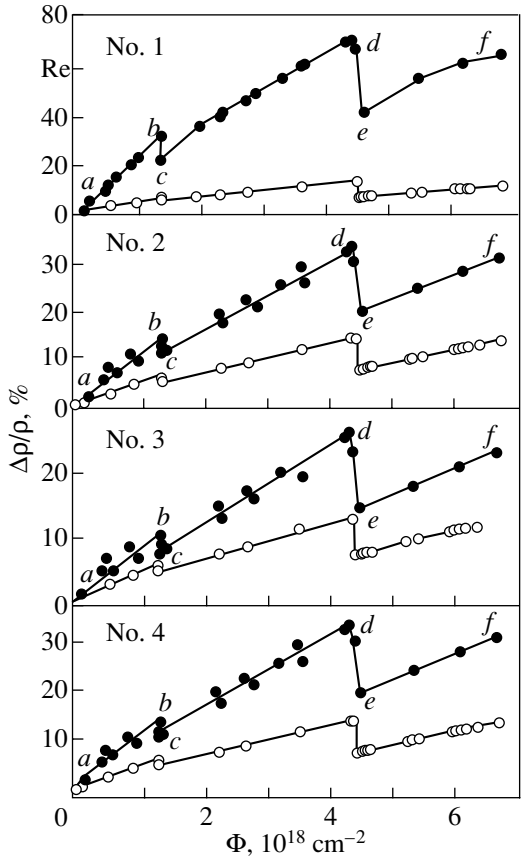

Fig. 5. Variation of the relative resistance at a temperature of (●) 130 and (○) 335 K as a function of the neutron fluence for samples 1–4 (Table 2) of the TiNi alloy.

ure can be divided into several segments. Segment *ab* corresponds to the initial irradiation at T_{irr} = 120 K; segment *bc*, to a partial recovery of resistance due to the stopping of the reactor (Fig. 2); *cd*, to the continued irradiation at 120 K; *de*, to the recovery of resistance related to a short-time heating of the sample upon the passage to irradiation at 335 K (temperature peak *c* in Fig. 2); and *ef*, to irradiation at 335 K. Changes in the resistance depending on the dose in all segments are satisfactorily approximated with straight lines whose slopes characterize the rates of radiation-stimulated changes in the structure of the TiNi alloys. One exception is sample 1 at 130 K. The results of the measurements of $d\rho/d\Phi$ are summarized in Table 2.

When analyzing these results, it was unexpectedly revealed that an increase in the irradiation temperature by 215 K only insignificantly affected $d\rho/d\Phi$. On average, the rate of an increase in the resistance decreased only by a factor of 1.2. At the same time, the magnitude of $d\rho/d\Phi$ strongly depended on the temperature at which it was measured. As is seen from Table 2, the rate of the change in the resistance estimated at 130 K is greater by a factor of 2–4 than that estimated at 335 K. In other words, the reaction of the martensitic phase of the TiNi alloys to neutron irradiation is sharper as compared to that of the austenitic phase irrespective of the irradiation temperature. Undoubtedly, this is due to the specific features of the crystal structure of the alloys being in various structural states.

Let us consider the physical factors that cause the phenomena observed. In pure metals, the rate of growth of electrical resistance upon neutron irradiation is proportional to the rate of growth of the point-defect concentration: $d\rho/d\Phi = \rho_p dC/d\Phi$, where C is the concentration of defects and ρ_p is the resistance increment per unit concentration. In the case of the TiNi alloy, it is also necessary to take into account the contributions to the resistance caused by solid-solution disordering [7–11] and amorphization of the crystal [9–11]. All these mechanisms of radiation-induced modification of the alloy structure are realized in both the martensitic and austenitic phases. However, a distinctive feature of martensitic phases in materials with thermoelastic martensitic transformations is their domain structure. Therefore, it is logical to suppose that in the martensitic state one more factor is operative, namely, that connected with the scattering of charge carriers from twin boundaries and boundaries separating structural domains with different crystallographic orientations. This assumption is based on the following considerations. Upon low-temperature irradiation, in the region of the localization of a thermal peak, a martensitic transformation may occur according to the scheme martensite ⟶ austenite ⟶ martensite of another ori-

Table 2. Rate of resistance changes at various stages of irradiation of TiNi samples

No.	Rate of resistance change $d\rho/d\Phi$, 10^{-18} μΩ cm^2					
	T = 130 K			T = 335 K		
	T_{irr} = 120 K		T_{irr} = 335 K	T_{irr} = 120 K		T_{irr} = 335 K
	ab	*cd*	*ef*	*ab*	*cd*	*ef*
1	6.1	4.1	2.5	1.4	0.9	0.8
2	8.8	6.0	5.6	3.1	1.6	1.3
3	5.7	4.6	3.2	3.3	2.3	2.0
4	12	8.6	6.0	5.2	3.7	3.3

entation. As a result, there arise new structural domains whose dimensions are comparable with the dimensions of the thermal spike. In addition, elastic lattice distortions that arise near the displacement spikes can lead to a heterogeneous nucleation of martensite crystals. Since the number of displacement peaks increases with increasing fluence, the number of centers of nucleation of the new phase also increases upon austenite ⟶ martensite transitions. It is understandable that the above processes are accompanied by an increase in the density of domain boundaries upon irradiation and lead to an additional contribution to resistance.

Therefore, on the assumption of the additivity of contribution caused by different types of defects [17], we may write

$$\frac{d\rho}{d\Phi} = \rho_p \frac{dC}{d\Phi} + \rho_a \frac{dV_a}{d\Phi} + \rho_d \frac{dS}{d\Phi} + \rho_b \frac{dD}{d\Phi}, \qquad (2)$$

where V_a is the volume fraction of the amorphous phase, S is the degree of long-range order, D is the density of domain and twin boundaries, ρ_b is the resistance increment per unit density of boundaries, and ρ_a and ρ_d are the coefficients that characterize the resistance change upon amorphization and disordering, respectively.

The data obtained in this paper permit us to compare the contribution of amorphization to the total magnitude of resistance. The degree of amorphization was estimated from the measurements of the magnitudes of the features in the temperature dependences of the resistance connected with the martensitic transitions (an increase in the resistance upon the $B2 \longrightarrow R$ transformation and a decrease in the resistance upon the $R \longrightarrow B19'$ transformation). We assumed that the amorphization should cause a decrease in the magnitudes of these features, since martensitic transitions occur only in crystalline regions of a material and the amorphous component is excluded from the transformation process. Figure 6 demonstrates that $\Delta\rho_{B2 \to R}$ and $\Delta\rho_{R \to B19'}$ virtually do not change upon irradiation of sample 2. Similar dependences were also obtained for other samples. Therefore, we can state that no amorphization occurs under the chosen conditions up to a fluence of 7×10^{18} cm^{-2}.

Thus, the second term in Eq. (2) can be discarded. Note also that the last term is nonzero only in the two-phase or martensitic state of the alloy and gives no contribution to the resistance of the austenite. This explains the differences in the rates of growth of ρ corresponding to martensite and austenite upon irradiation. On the whole, the picture of the radiation-induced modification of the structure of titanium nickelide is very complex and is associated with changes in several structural parameters.

In conclusion, we pay special attention to the difference in the functional relations between the temperatures of martensitic transformations in TiNi and the electrical resistance on the one hand and the neutron fluence on the other hand. The exponential decrease in the temperatures of phase transitions and the linear growth of resistance require a coordinated explanation based on an analysis of the structural mechanisms of the modification of the properties of irradiated alloys, which is the task of our further investigations.

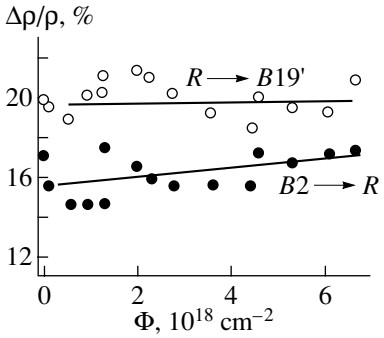

Fig. 6. Resistance increment upon the $B2 \longrightarrow R$ and $R \longrightarrow B19'$ transformations depending on the fluence for sample 2.

ACKNOWLEDGMENTS

This work was supported in part by the State Program "Neutron Studies of Condensed Matter" (project no. 107) and the Program for the Support of Leading Scientific Schools by the Russian Foundation for Basic Research (project nos. 00-15-96027 and 00-15-96023). We are also grateful to G.V. Kolobanov for his assistance in the experiments and to the group of technicians who ensured the operation of the cryogenic plant at the St. Petersburg Institute of Nuclear Physics.

REFERENCES

1. *Materials with Shape Memory Effect: Reference Edition*, Ed. by V. A. Likhachev (Nauchno-Issled. Inst. Khim. Sankt-Peterb. Gos. Univ., St. Petersburg, 1997).
2. T. Hoshiya, F. Takada, and Y. Ichihashi, Mater. Sci. Eng., A **130** (2), 185 (1990).
3. T. Hoshiya, F. Takada, and Y. Ichihashi, Mater. Sci. Forum **56–58**, 577 (1990).
4. T. Hoshiya, S. Shimakawa, Y. Ichihashi, *et al.*, J. Nucl. Mater. 1119 (1991).
5. T. Hoshiya, S. Den, H. Ito, *et al.*, J. Jpn. Inst. Met. **55** (10), 1054 (1991).
6. S. P. Belyaev, A. E. Volkov, R. F. Konopleva, *et al.*, Fiz. Tverd. Tela (St. Petersburg) **40** (9), 1705 (1998) [Phys. Solid State **40**, 1550 (1998)].
7. S. F. Dubinin, S. G. Teploukhov, and V. D. Parkhomenko, Fiz. Met. Metalloved. **78** (2), 84 (1994) [Phys. Met. Metallogr. **78** (2), 182 (1994)].
8. A. Kimura, S. Miyazaki, H. Horikawa, and K. Yamauchi, in *Proceedings of the International Conference on Martensitic Transformations, ICOMAT'92, Monterey, CA, 1992*, p. 935.

9. S. F. Dubinin, S. G. Teploukhov, and V. D. Parkhomenko, Fiz. Met. Metalloved. **82** (3), 136 (1996) [Phys. Met. Metallogr. **82** (3), 297 (1996)].
10. S. F. Dubinin, V. D. Parkhomenko, and S. G. Teploukhov, Fiz. Met. Metalloved. **85** (3), 119 (1998) [Phys. Met. Metallogr. **85** (3), 332 (1998)].
11. S. F. Dubinin, V. D. Parkhomenko, and S. G. Teploukhov, Fiz. Met. Metalloved. **88** (2), 111 (1999) [Phys. Met. Metallogr. **88** (2), 208 (1999)].
12. S. F. Dubinin, S. G. Teploukhov, and V. D. Parkhomenko, Fiz. Met. Metalloved. **87** (1), 75 (1999) [Phys. Met. Metallogr. **87** (1), 66 (1999)].
13. M. Nishikawa, S. Toda, E. Tachibana, *et al.*, Fusion Eng. Des. **10**, 509 (1989).
14. M. Nishikawa, E. Tachibana, K. Watanabe, *et al.*, Fusion Eng. Des. **5**, 401 (1988).
15. R. R. Ionaĭtis and M. A. Tuktorov, At. Tekh. Rubezhom **2**, 3 (1997).
16. V. N. Khachin, V. G. Pushchin, and V. V. Kondrat'ev, *Titanium Nickelide: Structure and Properties* (Nauka, Moscow, 1992).
17. M. W. Thompson, *Defects and Radiation Damage in Metals* (Cambridge Univ. Press, Cambridge, 1969; Mir, Moscow, 1971).

Translated by S. Gorin

Physics of the Solid State, Vol. 43, No. 11, 2001, pp. 2165–2170. Translated from Fizika Tverdogo Tela, Vol. 43, No. 11, 2001, pp. 2076–2080.
Original Russian Text Copyright © 2001 by Voronin, Shchennikov, Berger, Glazkov, Kozlenko, Savenko, Tikhomirov.

LATTICE DYNAMICS AND PHASE TRANSITIONS

Neutron Diffraction Investigation of the Structural Transition in $HgSe_{1-x}S_x$ Ternary Mercury Chalcogenide Systems at High Pressures

V. I. Voronin, V. V. Shchennikov**, I. F. Berger***, V. P. Glazkov****, D. P. Kozlenko*, B. N. Savenko*, and S. V. Tikhomirov***

** Joint Institute for Nuclear Research, Dubna, Moscow oblast, 141980 Russia*

*** Institute of Metal Physics, Ural Division, Russian Academy of Sciences, ul. S. Kovalevskoĭ 18, Yekaterinburg, 620219 Russia*

**** Institute of Solid-State Chemistry, Ural Division, Russian Academy of Sciences, Pervomaĭskaya ul. 91, Yekaterinburg, 620219 Russia*

***** Russian Research Centre Kurchatov Institute, pl. Kurchatova 1, Moscow, 123182 Russia*

e-mail: phisica@ifm.e-burg.su

Received April 12, 2001

Abstract—The structure of $HgSe_{1-x}S_x$ ternary mercury chalcogenides at high pressures up to 35 kbar is investigated by neutron diffraction. It is found under pressure, that the $HgSe_{1-x}S_x$ compounds undergo, a phase transition from the cubic sphalerite-type to the hexagonal cinnabar-type structure, which is accompanied by a jumpwise change in the unit cell volume and interatomic distances. The unit cell parameters and the positional parameters of Hg and Se (S) atoms in the high-pressure hexagonal phase are determined. A two-phase state is revealed in the phase transition region. © *2001 MAIK "Nauka/Interperiodica".*

1. INTRODUCTION

The investigation of mercury chalcogenides Hg*X* (where *X* = S, Se, and Te) under pressure is of particular interest, because these compounds undergo structural [1–9] and electron phase transitions [10]. In recent years, the effect of pressure on the structure of compounds in binary mercury chalcogenide systems has been intensively studied by x-ray diffraction [5–9].

At pressure $P \sim 8$–14 kbar and room temperature, the HgSe and HgTe compounds undergo a structural phase transition from the cubic sphalerite phase (space group $F\bar{4}3m$) to the hexagonal cinnabar phase (space group $P3_121$) [7], which is attended by a semimetal–semiconductor electron transition [10]. Bridgman [1] was the first to propose the structure of the high-pressure phase in HgSe and HgTe, which was subsequently confirmed in [2–5]. Another representative of this class of compounds, namely, HgS (cinnabar), has a similar hexagonal structure even under normal conditions [5]. High-pressure phases with a cinnabar-type structure are also observed in ZnTe and CdTe [6, 7]. As the pressure increases, chalcogenides of mercury, cadmium, and zinc undergo a phase transition from the hexagonal cinnabar-type to the cubic NaCl-type structure [6, 7]. The pressure of this transition increases with a decrease in the radius of the chalcogenide ion and is approximately equal to 80 kbar for HgTe and 160 kbar for HgSe and exceeds 200 kbar for HgS [5].

The cinnabar structure (Fig. 1) is intermediate between the cubic sphalerite structure with a coordination number of four and the NaCl structure with a coordination number of six and can be treated as a distorted NaCl lattice [7]. This structure is characterized by two positional parameters: Hg atoms occupy the 3a positions (u, 0, 1/3) and Se (S) atoms are located at the 3b positions (v, 0, 5/6) in the unit cell. The cinnabar structure in different compounds can differ substantially

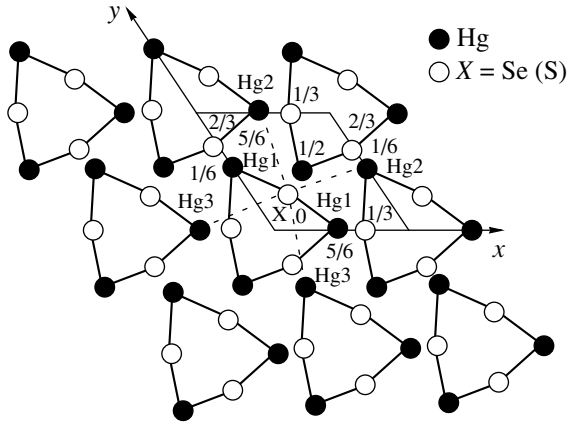

Fig. 1. Projection of the hexagonal cinnabar structure onto the *xy* plane. The *z* coordinates of the chalcogen *X* (*X* = Se and S) and mercury atoms and the shortest distances Hg1–*X*, Hg2–*X*, and Hg3–*X* are shown.

1063-7834/01/4311-2165$21.00 © 2001 MAIK "Nauka/Interperiodica"

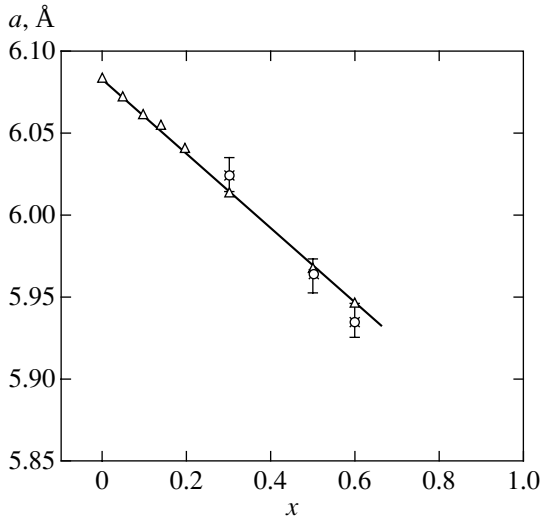

Fig. 2. Dependence of the lattice parameter of a cubic sphalerite structure on the sulfur content x in the $HgSe_{1-x}S_x$ crystals under normal pressure according to the x-ray diffraction data (triangles), neutron diffraction results obtained on a D7a diffractometer (crosses), and diffraction data obtained using a DN-12 spectrometer (circles). The solid line is the linear interpolation of the experimental data.

depending on the positional parameters u and v. For example, the coordination number in the cinnabar structure is equal to 2 + 4 in HgS and 4 + 2 in HgTe and CdTe [6, 9].

The effect of pressure on the structure of compounds in the $HgSe_{1-x}S_x$ and $HgTe_{1-x}S_x$ ternary mercury chalcogenide systems has not been adequately investigated. It is known that under pressure, these compounds undergo electron phase transitions of the semimetal–semiconductor type which noticeably affect the thermoelectric and galvanomagnetic properties [11–14]. It should be noted that the resistivity jumps observed in HgTe and HgSe binary compounds correspond to the phase transition from the cubic sphalerite-type to the hexagonal cinnabar-type structure [1–7]. It was assumed that a transition of the sphalerite–cinnabar type also occurs in ternary compounds [11]. However, direct structural investigations of high-pressure phases in these compounds were not performed.

Since the amplitude of x-ray scattering by Hg atoms is considerably larger than that for chalcogenide atoms (X = Se and S), the accuracy in determining the location of X atoms in the structure by using x-ray diffraction analysis can be insufficiently high. It is more preferable to investigate the structure of mercury chalcogenides by neutron diffraction, because the amplitudes of neutron scattering by Hg and X atoms are comparable in magnitude.

In the present work, the structure of $HgSe_{1-x}S_x$ ternary mercury chalcogenide compounds at pressures up to 35 kbar was studied by neutron powder diffraction.

2. EXPERIMENTAL TECHNIQUE

We studied the $HgSe_{1-x}S_x$ compounds with sulfur content $x \approx 0.302$, 0.508, and 0.601, which were used in compression measurements of the electrical resistivity in our earlier works [11–14]. The synthesis of the samples was described in [11, 12]. The samples were characterized by x-ray and neutron diffraction analyses. The sample composition was determined by x-ray microanalysis on a Superprobe-JCXA-733 spectrometer [12].

The neutron diffraction investigations at pressures up to 10 kbar were performed on an IVV-2M stationary reactor (Institute of Metal Physics, Ural Division, Russian Academy of Sciences, Yekaterinburg) using a D7a diffractometer under normal conditions and a D3b diffractometer at high pressures. The wavelength λ of monochromatic neutrons was equal to 1.66 Å. The resolutions $\Delta d/d$ of the diffractometers were 0.023 and 0.03, respectively. The time taken for one neutron diffraction pattern to be measured was approximately 12 h. Hydrostatic pressure was produced in a high-pressure piston–cylinder-type chamber fabricated from a TiZr alloy with an operating volume $V \sim 1$ cm^3 [15]. Liquid Freon-11 with a boiling temperature of 25°C served as the pressure-transferring medium. The usability of Freon-11 was limited by its crystallization at a pressure of 9.5 kbar.s

The experiments at higher pressures (up to 35 kbar) were carried out in high-pressure chambers with sapphire anvils [16] with the use of a DN-12 spectrometer [17] and an IBR-2 pulsed high-flux reactor (Frank Laboratory of Neutron Physics, Joint Institute for Nuclear Research, Dubna). In this case, the volume V of the studied samples was ~2 mm^3. The diffraction spectra were recorded at the scattering angle $2\theta = 90°$. The diffractometer resolution $\Delta d/d$ for this scattering angle at wavelength $\lambda = 2$ Å was 0.02. The characteristic time of measuring one spectrum was 20 h. The pressure in the chamber was measured from the shift of the ruby luminescence line with an accuracy of 0.5 kbar. All the measurements were performed at room temperature.

3. RESULTS AND DISCUSSION

Analysis of the x-ray and neutron diffraction patterns revealed that, under normal conditions, the $HgSe_{1-x}S_x$ ($0.03 \le x \le 0.6$) crystals have a cubic sphalerite structure and the unit cell parameter almost linearly decreases with an increase in the sulfur content x (Fig. 2).

Figure 3 displays fragments of the neutron diffraction patterns of the $HgSe_{0.5}S_{0.5}$ compound at different pressures, which were recorded using the D3b diffractometer. The neutron diffraction patterns at normal pressure and $P \approx 3$ kbar are virtually identical. At $P = 6$ kbar, the diffraction patterns exhibit new peaks whose intensities increase with a further increase in pressure, whereas the intensities of the reflections associated with the initial

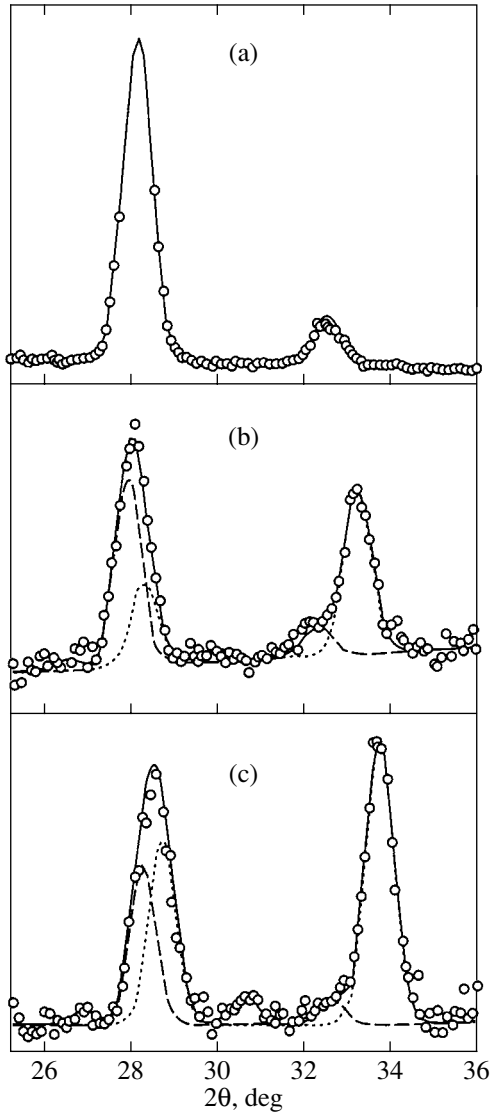

Fig. 3. Fragments of the neutron diffraction patterns of the $HgSe_{0.5}S_{0.5}$ compound at pressures of (a) 3, (b) 6, and (c) 8 kbar. Points are the experimental data, and solid lines represent the profiles calculated by the Rietveld method. The dashed and dotted lines show the contributions to the total profile from the cubic sphalerite and hexagonal cinnabar phases, respectively. Measurements are carried out using an IVV-2M stationary reactor, D3b diffractometer, and a high-pressure titanium–zirconium chamber of the piston–cylinder type.

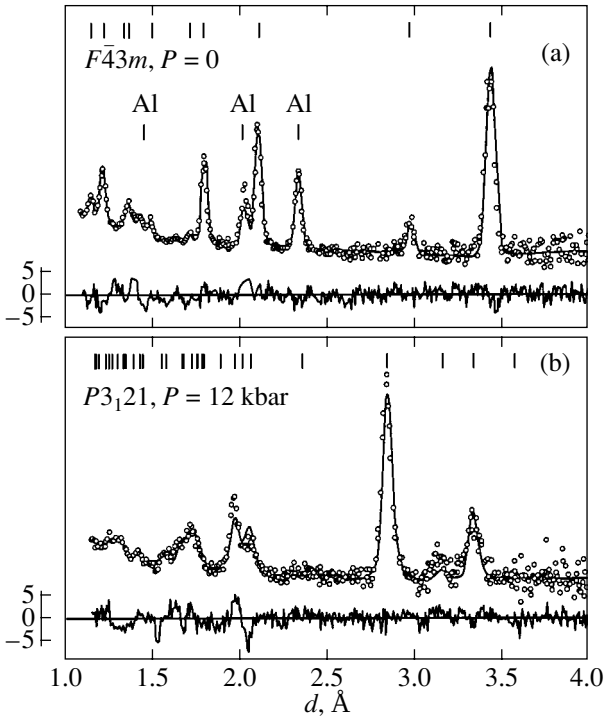

Fig. 4. Fragments of the diffraction spectra of the $HgSe_{0.4}S_{0.6}$ compound at (a) normal pressure and (b) $P = 12$ kbar. Points are the experimental data, and solid lines represent the profiles calculated by the Rietveld method. The difference curves are normalized to the root-mean-square deviation at the point. The spectrum measured under normal conditions is processed with due regard for the contribution of the aluminum foil used as a container. Measurements are performed by the time-of-flight technique using a DN-12 spectrometer, IBR-2 pulsed reactor, and a high-pressure chamber with sapphire anvils. The scattering angle 2θ is 90°.

cubic sphalerite phase decrease. The Rietveld profile analysis of the diffraction data demonstrated that the new peaks are attributed to the hexagonal cinnabar structure. At pressures above 8 kbar, the diffraction patterns correspond to the single-phase state with a cinnabar structure. The phase with a cristobalite structure, which was observed in the HgSe and HgTe compounds near the structural transition [7], was not found in the studied compound.

Therefore, in the pressure range from 6 to 8 kbar, the $HgSe_{0.5}S_{0.5}$ compound is in a two-phase state (Fig. 3), in which the concentration of the cinnabar phase increases and the concentration of the initial sphalerite phase decreases with an increase in the pressure. Recent investigations into the electrical properties of the $HgSe_{1-x}S_x$ compounds [11–14] revealed that metastable states with a high resistivity but with a positive temperature coefficient of resistance and a high electron mobility are observed at pressures of 6–8 kbar. This phenomenon was explained by the existence of two phases in the system, namely, the semimetal phase with a sphalerite-type structure and the semiconductor phase with a cinnabar-type structure, which is in agreement with our results. McMahon and Nelmes [7] observed inclusions of the initial sphalerite phase in the binary HgSe and HgTe compounds at pressures as high as 20 kbar.

For the $HgSe_{0.7}S_{0.3}$ and $HgSe_{0.4}S_{0.6}$ compounds, an increase in pressure also leads to the structural transition to the cinnabar phase. Figure 4 shows fragments of the diffraction spectra of the $HgSe_{0.4}S_{0.6}$ compound at

Structure parameters of sphalerite (the unit cell parameter a_c and the interatomic distance Hg–*X*) and cinnabar (the unit cell parameters *a* and *c* and the shortest interatomic distances Hg1–*X*, Hg2–*X*, and Hg3–*X*) phases of the $HgSe_{1-x}S_x$ compounds at normal and high pressures

	$HgSe_{0.7}S_{0.3}$	$HgSe_{0.5}S_{0.5}$			$HgSe_{0.4}S_{0.6}$	
Cubic phase (sphalerite structure type)						
P, kbar	0	0	6	8	0	
a_c, Å	6.012(5)	5.963(5)	5.945(5)	5.943(5)	5.947(5)	
Hg–*X*, Å	2.603(5)	2.582(5)	2.574(5)	2.573(5)	2.576(5)	
Hexagonal phase (cinnabar structure type)						
P, kbar	17	6	8	17	12	32
a, Å	4.164(5)	4.174(5)	4.158(5)	4.142(5)	4.118(5)	4.069(5)
c, Å	9.513(5)	9.571(5)	9.534(5)	9.470(5)	9.465(5)	9.353(5)
c/*a*	2.285	2.29	2.29	2.286	2.298	2.299
u	0.642(8)	–	–	0.652(8)	0.663(8)	0.663(8)
v	0.523(8)	–	–	0.512(8)	0.514(8)	0.506(8)
Hg1–*X*, Å	2.52(2)	–	–	2.45(2)	2.44(2)	2.39(2)
Hg2–*X*, Å	2.82(2)	–	–	2.90(2)	2.91(2)	2.89(2)
Hg3–*X*, Å	3.44(2)	–	–	3.40(2)	3.35(2)	3.33(2)

Note: In the cinnabar phase, the Hg and *X* (*X* = Se and S) atoms occupy positions of the (*u*, 0, 1/3) and (*v*, 0, 5/6) types, respectively.

pressures $P = 0$ and 12 kbar, which were recorded on the DN-12 spectrometer.

The diffraction data were processed by the Rietveld method according to the MRIA [18] (the spectra were obtained on the DN-12 spectrometer) and Fullprof [19] (the patterns measured with D3b and D7a diffractometers) programs by using the known structure models [7]: the space group $F\bar{4}3m$ for the initial cubic sphalerite phase and the space group $P3_121$ for the high-pressure phase with a hexagonal cinnabar structure. Reasoning from the results obtained earlier for HgSe, HgTe, and HgS binary mercury chalcogenide systems [6–9], it was assumed that, in the cinnabar structure, the Hg atoms occupy the 3a positions (*u*, 0, 1/3) and the Se (S) atoms are located at the 3b positions (*v*, 0, 5/6). The positional parameters *u* and *v* for hexagonal cinnabar modifications of HgSe and HgS are close in magnitude: $u \sim 0.7$ and $v \sim 0.5$ [7].

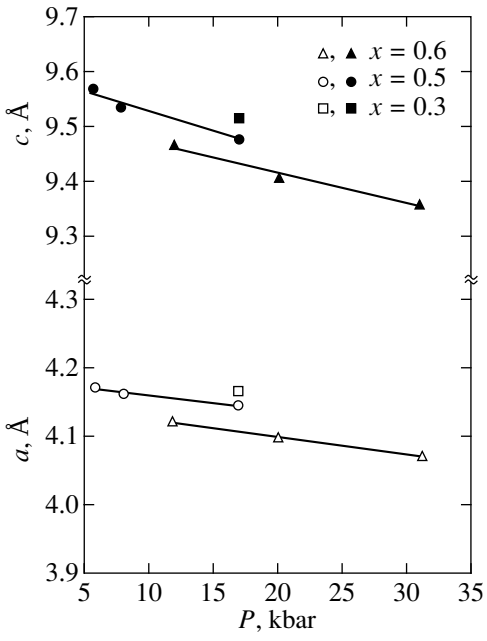

Fig. 5. Pressure dependences of the lattice parameters *a* (open symbols) and *c* (closed symbols) of the hexagonal cinnabar phase in $HgSe_{1-x}S_x$ compounds. Solid lines are the linear interpolation of the experimental data.

The structure parameters for the $HgSe_{1-x}S_x$ compounds ($x = 0.3$, 0.5, and 0.6) at different pressures were obtained from the diffraction data processed by the Rietveld method. The results obtained are listed in the table. The characteristic *R* factors for the diffraction spectrum of the $HgSe_{0.4}S_{0.6}$ compound at $P = 12$ kbar (Fig. 4) in the cinnabar phase are as follows: $R_p = 9.37\%$ and $R_{wp} = 7.24\%$.

The compressibility of the $HgSe_{1-x}S_x$ compounds has an anisotropic nature. As the pressure increases, the unit cell parameter *c* decreases more rapidly compared to the parameter *a* (Fig. 5). Note that the *c*/*a* ratio varies only slightly with a change in pressure (see table).

As in the binary HgSe and HgTe compounds [1–7, 20], the transition from the cubic to the hexagonal phase is accompanied by a jump in the unit cell volume $\Delta V/V \approx 8\%$ (Fig. 6). The pressure of the onset of the

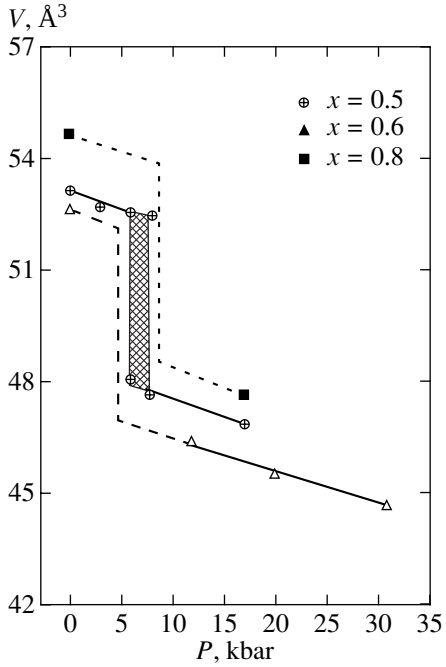

Fig. 6. Pressure dependences of the unit cell volume per molecular unit in the $HgSe_{1-x}S_x$ compounds. Solid lines are the linear interpolation of the experimental data. The hatched region corresponds to a two-phase state in the $HgSe_{0.5}S_{0.5}$ compound. The dashed and dotted lines represent the hypothetical dependences $V(P)$ near the sphalerite–cinnabar phase transition in $HgSe_{0.4}S_{0.6}$ and $HgSe_{0.7}S_{0.3}$ compounds, respectively. The phase-transition pressures are taken from [12].

phase transition in $HgSe_{0.5}S_{0.5}$ agrees well with the pressure $P \approx 5$ kbar determined earlier from electrical resistivity measurements [12]. The linear interpolation of the experimental dependence $V(P)$ (Fig. 6) results in the following estimates of the bulk modulus $B_0 = V/dP/dV|_{V=V_0}$ in the hexagonal cinnabar phase: B_0 = 480 kbar for $HgSe_{0.5}S_{0.5}$ and B_0 = 590 kbar for $HgSe_{0.4}S_{0.6}$. The calculations were performed using unit cell volumes per molecular unit (extrapolated to $P = 0$): $V_0 = 48.58$ Å^3 for $HgSe_{0.5}S_{0.5}$ and $V_0 = 47.18$ Å^3 for $HgSe_{0.4}S_{0.6}$. These values of B_0 are comparable (in order of magnitude) to the bulk moduli for the phases with a cinnabar structure in other mercury chalcogenides: B_0 is equal to 410 kbar for HgTe and 320 kbar for CdTe [21].

It is seen from the table that, in the hexagonal cinnabar phase of the $HgSe_{1-x}S_x$ compounds, an increase in the concentration of sulfur atoms from x = 0.3 to 0.6 leads to an increase in the positional parameter u for Hg atoms from 0.642(8) to 0.663(8) and to a decrease in the positional parameter v for Se (S) atoms from 0.523(8) to 0.509(8). Binary compounds exhibit a similar behavior of the positional parameters depending on the size of the chalcogen ions. Specifically, u = 0.72 and v = 0.48 for HgS at P = 0 [9] and u = 0.666 and v = 0.540 for HgSe at P = 23 kbar [22]. According to Wright *et al.* [9], the cinnabar phases in the HgS and HgTe compounds have coordination numbers equal to 2 + 4 and 4 + 2, respectively. However, the coordination of the $HgSe_{1-x}S_x$ compounds has a different character (see table), which is similar to the coordination (2 + 2 + 2) of the HgSe compound [22].

4. CONCLUSION

Thus, the results obtained in the present work demonstrated that, as the pressure increases, the ternary mercury chalcogenide compounds $HgSe_{1-x}S_x$ ($0.3 \le x \le 0.6$), like the binary HgSe and HgTe compounds, undergo a phase transition from the cubic sphalerite-type to the hexagonal cinnabar-type structure. The hexagonal cinnabar phase is characterized by a coordination number of 2 + 2 + 2, as is the case with the cinnabar phase of the HgSe compound [22] (the coordination number in the cinnabar structure of HgS is 2 + 4). The metastable two-phase state was revealed in the phase transition region, which is in agreement with the results of investigations into the electrical properties of the $HgSe_{1-x}S_x$ compounds [12]. The two-phase state in the sphalerite–cinnabar transition region was observed earlier in HgTe and HgSe binary mercury chalcogenide compounds. The inference was made that this state is formed as the result of a slowing down of the phase transition under investigation [22].

ACKNOWLEDGMENTS

We are grateful to V.M. Frasunyak and N.P. Gavaleshko for supplying the samples.

This work was supported by the Russian Foundation for Basic Research (project nos. 00-02-17199, 00-02-17077, and 01-02-17203), the State Program of Support for Leading Scientific Schools of the Russian Federation (project nos. 00-15-96778 and 00-15-96581), the State Scientific and Technical Program "Topical Directions in the Physics of Condensed Matter: Neutron Investigations of Condensed Matter" (State Contract no. 107-19(00)-P-DO1), and the State Scientific and Technical Program "Physics of Quantum and Wave Processes: Statistical Physics" (project no. VIII-6).

REFERENCES

1. P. W. Bridgman, Proc. Am. Acad. Arts Sci. **74** (3), 21 (1940).
2. J. A. Kafalas, H. G. Gatos, M. C. Lavine, and M. D. Banus, J. Phys. Chem. Solids **23** (11), 1541 (1962).
3. A. N. Mariano and E. P. Warekois, Science **142**, 672 (1963).
4. S. Narita, M. Egawa, K. Suizu, *et al.*, Appl. Phys. **2** (3), 151 (1973).
5. A. Werner, H. D. Hochheimer, K. Strössner, and A. Jayaraman, Phys. Rev. B **28** (6), 3330 (1983).

6. A. San Miguel, A. Polian, and J. P. Itié, J. Phys. Chem. Solids **56** (3/4), 555 (1995).
7. M. I. McMahon and R. J. Nelmes, Phys. Status Solidi B **198** (1), 389 (1996).
8. T. L. Huang and A. L. Ruoff, Phys. Rev. B **31**, 5976 (1985).
9. N. G. Wright, M. I. McMahon, R. J. Nelmes, and A. San Miguel, Phys. Rev. B **48**, 13111 (1993).
10. I. M. Tsidil'kovskiĭ, V. V. Shchennikov, and N. G. Gluzman, Fiz. Tverd. Tela (Leningrad) **24**, 2658 (1982) [Sov. Phys. Solid State **24**, 1507 (1982)].
11. V. V. Shchennikov, N. P. Gavaleshko, and V. M. Frasunyak, Fiz. Tverd. Tela (St. Petersburg) **35**, 389 (1993) [Phys. Solid State **35**, 199 (1993)].
12. V. V. Shchennikov, N. P. Gavaleshko, V. M. Frasunyak, and V. I. Osotov, Fiz. Tverd. Tela (St. Petersburg) **37** (8), 2398 (1995) [Phys. Solid State **37**, 1311 (1995)].
13. V. V. Shchennikov, Fiz. Tverd. Tela (St. Petersburg) **37** (4), 1015 (1995) [Phys. Solid State **37**, 551 (1995)].
14. V. V. Shchennikov, in *Process, Equipment, and Materials Control in Integrated Circuit Manufacturing IV,* Ed. by A. J. Toprac and Kim Dang; Proc. SPIE **3507**, 254 (1998).
15. A. N. Ivanov, D. F. Litvin, B. N. Savenko, *et al.*, High Press. Res. **14**, 209 (1995).
16. V. P. Glazkov and I. N. Goncharenko, Fiz. Tekh. Vys. Davleniĭ **1**, 56 (1991).
17. V. L. Aksenov, A. M. Balagurov, V. P. Glazkov, *et al.*, Physica B (Amsterdam) **265**, 258 (1999).
18. V. B. Zlokazov and V. V. Chernyshev, J. Appl. Crystallogr. **25**, 447 (1992).
19. J. Rodríguez-Carvajal, Physica B (Amsterdam) **192**, 55 (1993).
20. P. J. Ford, A. J. Miller, G. A. Saunders, *et al.*, J. Phys. C **15**, 657 (1982).
21. A. San Miguel, N. G. Wright, M. I. McMahon, and R. J. Nelmes, Phys. Rev. B **51** (14), 8731 (1995).
22. M. I. McMahon, R. J. Nelmes, H. Liu, and S. A. Belmonte, Phys. Rev. Lett. **77**, 1781 (1996).

Translated by O. Borovik-Romanova

Physics of the Solid State, Vol. 43, No. 11, 2001, pp. 2171–2181. Translated from Fizika Tverdogo Tela, Vol. 43, No. 11, 2001, pp. 2081–2090.
Original Russian Text Copyright © 2001 by Gorbach, Kovalev, Usatenko.

LOW-DIMENSIONAL SYSTEMS AND SURFACE PHYSICS

Solitons in a Diatomic Chain with Competing Nonlinearities

A. V. Gorbach[1], A. S. Kovalev[2], and O. V. Usatenko[1, 3]

[1]*Kharkov State University, Kharkov, 61077 Ukraine*
e-mail: univ@kharkov.ua

[2]*Verkin Institute of Low-Temperature Physics and Engineering, National Academy of Sciences of Ukraine, Kharkov, 61164 Ukraine*

[3]*Institute of Radiophysics and Electronics, National Academy of Sciences of Ukraine, Kharkov, 61085 Ukraine*

Received February 22, 2001

Abstract—A one-dimensional diatomic chain whose energy contains cubic and quartic terms in the atomic displacements is considered. A modified asymptotic method is proposed for finding soliton solutions to equations describing systems with nonlinearities of various symmetry. It is shown that the dynamics of the model in question can be described in terms of equations that are similar to the dynamic equations for a diatomic chain with an even potential function. Soliton solutions of a new, unusual type are found in the specific case of a free diatomic chain with a purely cubic anharmonic potential. © *2001 MAIK "Nauka/Interperiodica".*

1. INTRODUCTION

Elastic mono- and polyatomic chains are particularly attractive for their use in studying nonlinear dynamics. Although these models are simple, studying them provides some insight into the physical nature of intricate nonlinear excitations occurring in real crystals.

Recently, diatomic and polyatomic chains have been widely considered in investigation of the properties of so-called gap and near-gap solitons, whose energy parameters lie within or near the gap in the linear-wave spectrum of a system [1–8]. The majority of relevant papers deal with systems with an anharmonic potential as a symmetric function of atomic displacements. However, a more general case, where the interaction potential contains terms that are asymmetric with respect to atomic displacements, is also of considerable interest. The simplest model of a monatomic chain with such a potential was considered in [9].

In this paper, we consider a diatomic chain with a nonlinear interparticle interaction placed in an anharmonic external potential in the case where both the interparticle and external potentials contain symmetric and asymmetric terms with respect to atomic displacements. A modified asymptotic method is developed for finding static solutions of the system. In contrast to the method proposed in [8], our method is applicable to a chain with an asymmetric potential. A method for finding traveling-wave solutions for such systems is also developed. Possible static and traveling-wave solutions are analyzed qualitatively in the phase plane in the specific case of a potential in which the anharmonic terms are purely asymmetric. Analytical expressions for soliton solutions of a special type are derived for the case of a free chain (in a zero external potential) with cubic anharmonic interparticle interaction.

2. STATEMENT OF THE PROBLEM AND ANALYSIS OF THE LINEAR SYSTEM

We consider a one-dimensional diatomic chain of alternate atoms of masses M and m ($M > m$) characterized by an anharmonic interparticle interaction potential

$$U(\xi_n) = \frac{K_2}{2}(\xi_n - \xi_{n-1})^2 + \frac{K_3}{3}(\xi_n - \xi_{n-1})^3 + \frac{K_4}{4}(\xi_n - \xi_{n-1})^4. \quad (1)$$

The chain is placed in an anharmonic external potential

$$V(\xi_n) = \frac{\gamma_2}{2}\xi_n^2 + \frac{\gamma_3}{3}\xi_n^3 + \frac{\gamma_4}{4}\xi_n^4, \quad (2)$$

where ξ_n is the displacement of the nth atom and K_2 and γ_2 are positive constants. In what follows, the difference between the atomic masses is assumed to be small, $(M - m) \ll M, m$; therefore, the gap in the frequency spectrum of the linear waves is narrow.

The equation of motion of the nth atom is

$$\mu[1 + \epsilon^2\cos(\pi n)]\frac{d^2\xi_n}{dt^2} + K_2(2\xi_n - \xi_{n+1} - \xi_{n-1}) + \gamma_2\xi_n + K_3[(\xi_n - \xi_{n+1})^2 + (\xi_n - \xi_{n-1})^2] + \gamma_3\xi_n^2 + K_4[(\xi_n - \xi_{n+1})^3 + (\xi_n - \xi_{n-1})^3] + \gamma_4\xi_n^3 = 0, \quad (3)$$

where $\mu = (M + m)/2$ and $\epsilon^2 = (M - m)/(M + m) \ll 1$.

In order to analyze the properties of linear waves in the system under study, the general solution to the lin-

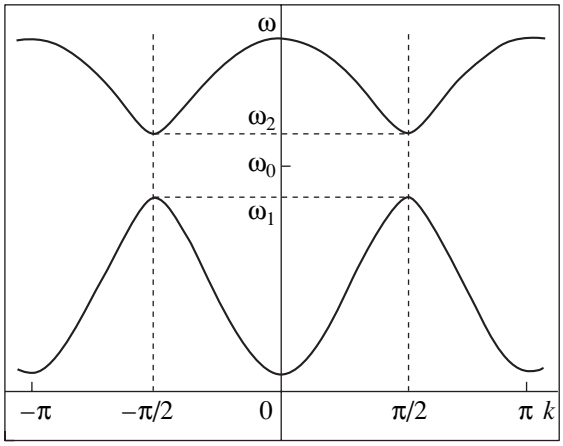

Fig. 1. Dispersion relation of linear waves described by Eq. (5).

earized equations (3) is written as a sum of two fields, which describe oscillations of light and heavy particles:

$$\begin{aligned}\xi_n &= G\exp(i\omega t - ikn) + \text{c.c.}, \quad n = \pm 1, \pm 3, \ldots \\ &= F\exp(i\omega t - ikn) + \text{c.c.}, \quad n = 0, \pm 2, \pm 4, \ldots .\end{aligned} \tag{4}$$

Particles of each type are conveniently enumerated separately; thereby, enumeration of the unit cells is also accomplished [1–5].

The dispersion relation of linear waves described by Eq. (4) is plotted in Fig. 1 and has the form

$$\omega^4 - (\omega_1^2 + \omega_2^2)\omega^2 + \omega_1^2\omega_2^2 - \tilde{\omega}_1^2\tilde{\omega}_2^2\cos^2(ka) = 0, \tag{5}$$

where $\omega_1^2 = (2K_2 + \gamma_2)/M$, $\omega_2^2 = (2K_2 + \gamma_2)/m$, $\tilde{\omega}_1^2 = 2K_2/M$, $\tilde{\omega}_2^2 = 2K_2/m$, and a is the lattice parameter (which is taken to be unity in what follows). At $k = \pm k_0 = \pm\pi/2$, the linear-wave spectrum has a gap, which is limited by the frequencies ω_1 and ω_2. The gap width is proportional to the mass difference, $(\omega_2^2 - \omega_1^2) = (2K_2 + \gamma_2)(M - m)/Mm$; therefore, it is a small parameter.

The ratio between the amplitudes of oscillations of heavy and light particles is determined by the frequency of the linear waves [10]:

$$\frac{F}{G} = \mp\sqrt{\left(1 - \frac{\omega^2}{\omega_2^2}\right)\left(1 - \frac{\omega^2}{\omega_1^2}\right)^{-1}}. \tag{6}$$

Here, the upper and lower signs correspond to excitations with frequencies lying in the ranges over which the frequency increases and decreases, respectively, with increasing wave number.

For the lower branch of the vibrational spectrum, i.e., at $\omega \le \omega_1$, the amplitude of an oscillation of heavy atoms F is larger than that of light atoms G. At $\omega = \omega_1$, the amplitude of light atoms vanishes and the heavy atoms oscillate in counterphase. For the upper branch of the spectrum, at $\omega \ge \omega_2$, the amplitude of an oscillation of light atoms is larger than that of heavy atoms. At $\omega = \omega_2$, the latter amplitude vanishes and the light atoms oscillate in counterphase. Therefore, the lower oscillation branch can be referred to as that of heavy particles; the upper branch, as that of light particles.

In Eq. (4), the wave number k lies in the range $(-\pi/2, \pi/2)$ (between the two dashed lines in Fig. 1), i.e., in the first Brillouin zone (see, e.g., [11]).

There is another approach, in which the general solution to the linearized equations (3) is written in the same form for heavy and light particles [7, 10]:

$$\xi_n = A\exp i(\omega t - kn) + B\exp i(\omega t - (k - \pi)n). \tag{7}$$

In this case, the general solution consists of two waves which have the same frequency and group velocity but differ in amplitude and phase velocity (this method is sometimes referred to as two-wave approximation [7, 10]). The amplitudes A and B of the partial waves are not independent; their ratio is determined by the frequency of the waves [7, 10]:

$$\frac{B}{A} = \frac{\sqrt{\left|1 - \omega^2/\omega_2^2\right|} \pm \sqrt{\left|1 - \omega^2/\omega_1^2\right|}}{\sqrt{\left|1 - \omega^2/\omega_2^2\right|} \mp \sqrt{\left|1 - \omega^2/\omega_1^2\right|}}, \tag{8}$$

where the upper and lower signs correspond to the respective signs in Eq. (6).

The wave numbers of the two waves in solution (7) lie within the so-called extended Brillouin zone, i.e., in the $(-\pi, \pi)$ range. The first Brillouin zone is inadequate in this case, because all atoms of the chain are numbered sequentially without regard of the fact that there are two types of particles. The decrease in the unit-cell size leads to an extended Brillouin zone, which coincides with the Brillouin zone of a monatomic chain.

From Eqs. (4) and (7), one can easily find the following relations between amplitudes F, G and A, B:

$$\begin{aligned}G &= A + B, \\ F &= A - B.\end{aligned} \tag{9}$$

Thus, both approaches are equivalent and appropriate for describing linear and nonlinear waves.

3. STATIC SOLITONS

In studying nonlinear waves, the vicinity of the point $k_0 = \pi/2$ (i.e., the values of $k = k_0 + \kappa$ with $\kappa \ll k_0$) is of most interest; in this region, both branches of the linear-wave spectrum described by Eq. (5) are approximately parabolic.

As a preliminary, we consider static solutions to Eq. (3) that correspond to the wave number $k \equiv k_0$. We employ an asymptotic method to seek the solution and successively consider (i) the case of an anharmonic external potential (external nonlinearity) and a linear interparticle interaction in the system (Subsection 3.1), (ii) the case of nonlinear interparticle interaction (inter-

nal nonlinearity) and a zero external potential (Subsection 3.2), and (iii) the general case of both types of nonlinearity present in the system (Subsection 3.3).

3.1. The Case of an Anharmonic External Potential

We assume that the interaction between particles is bilinear [$K_3 = K_4 = 0$ in Eq. (1)] but the external potential is anharmonic. The dynamics of a monatomic chain with interaction of this type was analyzed in [9]. In this case, the equations of motion (3) take the form

$$\begin{aligned} &M\frac{d^2v_n}{dt^2} + K_2(2v_n - w_{n+1} - w_{n-1}) \\ &+ \gamma_2 v_n + \gamma_3 v_n^2 + \gamma_4 v_n^3 = 0, \quad n = 2j, \\ &m\frac{d^2w_n}{dt^2} + K_2(2w_n - v_{n+1} - v_{n-1}) \\ &+ \gamma_2 w_n + \gamma_3 w_n^2 + \gamma_4 w_n^3 = 0, \quad n = 2j+1, \end{aligned} \tag{10}$$

where v_n and w_n are the displacements of heavy and light particles, respectively.

In the linear approximation at $k = k_0$, as indicated above, neighboring atoms of the same type oscillate in counterphase (their displacements are opposite in sign). When nonlinearity is included, the displacements of neighboring atoms in each sublattice remain opposite in sign but their magnitudes become different because the anharmonic potential is asymmetric along the direction of atomic displacements [9]. The general solution to the nonlinear equations in (3) can be expanded in terms of harmonics with frequencies that are multiples of ω. The displacements of neighboring atoms of the same type are opposite in sign in the odd harmonics (with frequencies ω, 3ω, 5ω, …) but are of the same sign in the even harmonics (with frequencies 0, 2ω, 4ω, …). This feature of the general solution to the nonlinear equations (3) was ignored in [12], which led, in our opinion, to incorrect final results.

Thus, the general solution to Eq. (3) can be written as

$$\begin{aligned} v_n \equiv v_{2j} &= \epsilon^2 f_n^{(0)} + \epsilon(-1)^j f_n^{(1)}\cos(\omega t) \\ &+ \epsilon^2 f_n^{(2)}\cos(2\omega t) + \epsilon^3(-1)^j f_n^{(3)}\cos(3\omega t) + \dots, \\ w_n \equiv w_{2j+1} &= \epsilon^2 g_n^{(0)} + \epsilon(-1)^j g_n^{(1)}\cos(\omega t) \\ &+ \epsilon^2 g_n^{(2)}\cos(2\omega t) + \epsilon^3(-1)^j g_n^{(3)}\cos(3\omega t) + \dots, \end{aligned} \tag{11}$$

where $f^{(i)}$ and $g^{(i)}$ are smooth functions of index n in the long-wavelength limit and $\epsilon^2 = (M - m)/(M + m)$ is the small parameter in which the expansion is made.

We go to the continuum limit by replacing the discrete index n with a continuous coordinate x and expand the functions $f^{(i)}$ and $g^{(i)}$ in a Taylor series to within terms of the order ϵ^2:

$$\begin{aligned} f^{(i)}(x \pm 1) &= f^{(i)}(x) \pm \frac{df^{(i)}}{dx} + \mathbb{O}(\epsilon^3), \\ g^{(i)}(x \pm 1) &= g^{(i)}(x) \pm \frac{dg^{(i)}}{dx} + \mathbb{O}(\epsilon^3), \end{aligned} \tag{12}$$

where $i = 1, 2, 3, \dots$. As will be shown below, $df^{(i)}/dx$ and $dg^{(i)}/dx$ are of the order of ϵ^2.

Substituting expansions (11) and (12) into Eq. (10) and equating the coefficients of the same harmonics gives a closed set of equations for $f^{(0)}$, $g^{(0)}$, $f^{(1)}$, $g^{(1)}$, $f^{(2)}$, and $g^{(2)}$:

$$\begin{aligned} &(2K_2 + \gamma_2) f^{(0)} - 2K_2 g^{(0)} + \frac{\gamma_3}{2}F^2 = 0, \\ &(2K_2 + \gamma_2) g^{(0)} - 2K_2 f^{(0)} + \frac{\gamma_3}{2}G^2 = 0, \\ &(-4M\omega^2 + 2K_2 + \gamma_2) f^{(2)} - 2K_2 g^{(2)} + \frac{\gamma_3}{2}F^2 = 0, \\ &(-4m\omega^2 + 2K_2 + \gamma_2) g^{(2)} - 2K_2 f^{(2)} + \frac{\gamma_3}{2}G^2 = 0, \\ &\delta_1 F - \frac{2K_2}{\epsilon^2}\frac{dG}{dx} + \gamma_3 F(2f^{(0)} + f^{(2)}) + \frac{3\gamma_4}{4}F^3 = 0, \\ &\delta_2 G + \frac{2K_2}{\epsilon^2}\frac{dF}{dx} + \gamma_3 G(2g^{(0)} + g^{(2)}) + \frac{3\gamma_4}{4}G^3 = 0, \end{aligned} \tag{13}$$

where $F \equiv f^{(1)}$, $G \equiv g^{(1)}$, and δ_i are parameters characterizing the deviations of ω from the upper and lower edges of the gap:

$$\begin{aligned} \delta_1 &= \frac{M(\omega_1^2 - \omega^2)}{\epsilon^2}, \\ \delta_2 &= \frac{m(\omega_2^2 - \omega^2)}{\epsilon^2}. \end{aligned} \tag{14}$$

Since the gap width and the deviations of the frequencies in question from the gap edges are of the order ϵ^2, we have $\delta_i \sim 1$.

One can express $f^{(0)}$, $g^{(0)}$, $f^{(2)}$, and $g^{(2)}$ in terms of G and F by using the first four algebraic equations of set (13) and derive a set of differential equations for these two functions. By scaling the coordinate, $(\epsilon^2/2K_2)x \longrightarrow x$, the set of first-order differential equations for F and G can be written as

$$\begin{aligned} \frac{dG}{dx} &= \delta_1 F - \beta F(F^2 + pG^2), \\ -\frac{dF}{dx} &= \delta_2 G - \beta G(G^2 + pF^2), \end{aligned} \tag{15}$$

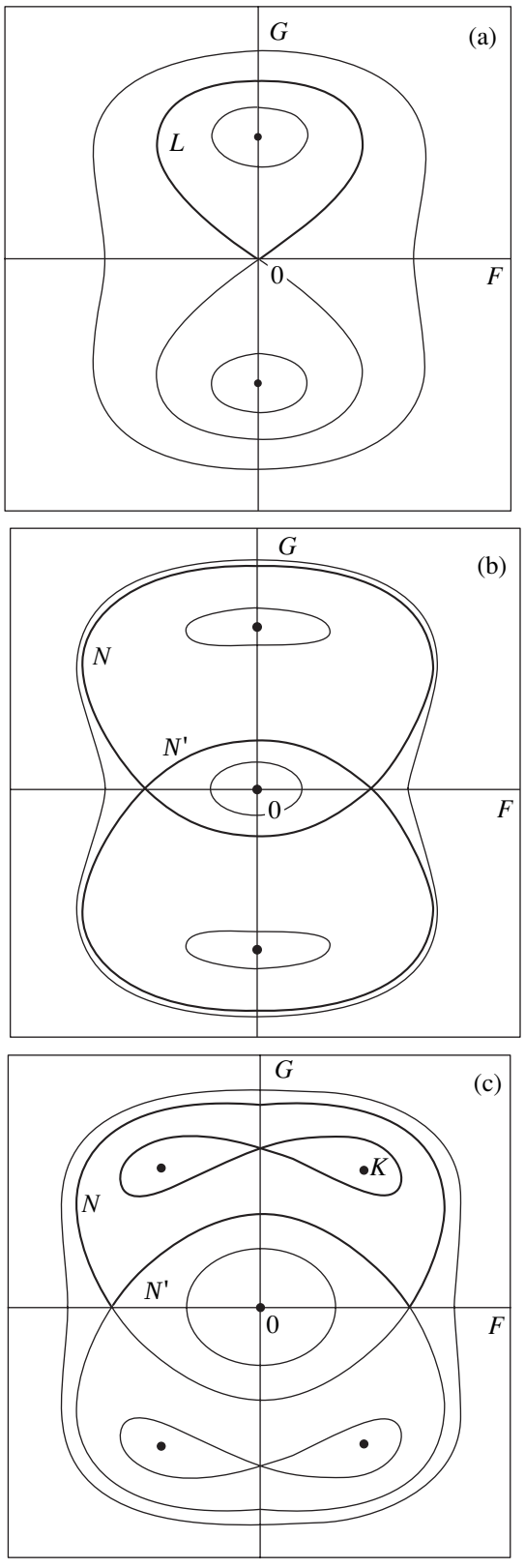

Fig. 2. Phase portraits for the set of equations (15) in the case of purely cubic external nonlinearity for the frequency of the nonlinear excitation lying in the ranges (a) $\omega_1 < \omega < \omega_2$, (b) $\omega_* < \omega < \omega_1$, and (c) $\omega < \omega_*$.

where β and p are expressed through the parameters of the model in question as

$$\beta = \gamma_3^2(2K_2 + \gamma_2) \times \frac{16(2K_2 + \gamma_2)^2 - \gamma_2(4K_2 + \gamma_2)}{2\gamma_2(4K_2 + \gamma_2)[8(2K_2 + \gamma_2)^2 + \gamma_2(4K_2 + \gamma_2)]} - \frac{3}{4}\gamma_4,$$
$$p = \frac{1}{\beta}\gamma_3^2 K_2 \frac{16(2K_2 + \gamma_2)^2 + 3\gamma_2(4K_2 + \gamma_2)}{\gamma_2(4K_2 + \gamma_2)[8(2K_2 + \gamma_2)^2 + \gamma_2(4K_2 + \gamma_2)]}. \quad (16)$$

(In principle, the parameter β can be eliminated from the set of equations (15) through appropriate renormalization of the field amplitudes F and G.)

Equations (15) have the form of Hamilton equations for canonically conjugate variables (coordinate G and momentum F) with the Hamiltonian

$$H = \frac{\delta_1}{2}F^2 + \frac{\delta_2}{2}G^2 - \frac{\beta}{4}(F^4 + G^4) - p\frac{\beta}{2}F^2G^2. \quad (17)$$

The coordinate x plays the role of effective time.

Equations (15) are similar to the dynamic equations that describe a nonlinear diatomic chain with an even anharmonic-potential function; these equations were considered in detail in [5, 6]. In this paper, we restrict our consideration to the specific case of an external potential with cubic nonlinearity ($\gamma_4 = 0$). In this case, the coefficients p and β are subject to the conditions $\beta > 0$ and $0 < p < 1$.

It is convenient to examine possible solutions to the set of equations (15) in the (F, G) phase plane. The phase portrait of the system under study is determined by the parameters δ_1 and δ_2, that is, by the frequency of a nonlinear excitation.

At $\omega > \omega_2$ ($\delta_1 < 0$, $\delta_2 < 0$), i.e., above the upper branch of the linear-wave spectrum, there is a single fixed point in the (F, G) plane, which is of the center type and has coordinates $F = 0$ and $G = 0$. In this frequency range, set (15) has only solutions that are periodic in space in the form of cnoidal waves.

At the upper edge of the gap ($\omega = \omega_2$, $\delta_2 = 0$), a bifurcation occurs and the center at $F = 0$, $G = 0$ is replaced by three fixed points in the (F, G) phase plane, so that, in the $\omega_1 < \omega < \omega_2$ frequency range, there is a fixed point of the saddle type at $F = 0$, $G = 0$ and two fixed points of the center type at $F = 0$, $G = \pm\sqrt{\delta_2/\beta}$ (Fig. 2a). Thus, closed separatrices of the L type arise in the gap of the spectrum; they go out of the saddle point, pass around one of the centers, and return to the saddle. These separatrices correspond to soliton solutions, that is, to gap solitons. In an L-type soliton, both fields F and G tend to zero at infinity. The amplitude of oscillation of light atoms G is larger than that of heavy atoms F. Such a soliton can be thought of as a local oscillation of light particles accompanied by small-amplitude oscillations of heavy particles.

At the lower edge of the gap ($\omega = \omega_1$, $\delta_1 = 0$), another bifurcation occurs: the saddle at $F = 0$, $G = 0$ is transformed into a center at the same point and two new saddles with coordinates $F = \pm\sqrt{\delta_1/\beta}$, $G = 0$ (Fig. 2b). In the frequency range $(\omega_1 - p\omega_2)/(1-p) = \omega_* < \omega < \omega_1$, there are separatrices of two types, *N* and *N'*, which correspond to so-called near-gap solitons. An *N*-type soliton, as well as an *L*-type soliton, is a soliton of the light-particle field: the amplitude *G* is larger than the amplitude *F* in such a soliton. However, in contrast to a gap soliton, the amplitude *F* in a near-gap *N* soliton tends to a nonzero value at infinity. The *N'* soliton is similar to the *N* soliton, but it is a soliton of the heavy-particle field, because the amplitude *F* in it is larger than *G*.

Finally, at the frequency $\omega = \omega_*$ ($\delta_1 = p\delta_2$), the last bifurcation occurs: the centers at $F = 0$, $G = \pm\sqrt{\delta_2/\beta}$ are replaced by saddles with the same coordinates and centers with coordinates $F = \pm\sqrt{\delta_1 - p\delta_2/(1-p^2)}$, $G = \pm\sqrt{\delta_2 - p\delta_1/(1-p^2)}$ (Fig. 2c). Therefore, in the frequency range $\omega < \omega_* < \omega_1$, new separatrices, of the *K* type arise in addition to the separatrices of the *N* and *N'* types. The *K*-type separatrices correspond to near-gap solitons in which coupled oscillation of the heavy-particle field is accompanied by light-particle oscillation that does not decay at infinity. The *K* soliton is a combination of a bright soliton of the *F* field and a dark soliton of the *G* field; that is, excitations of the heavy-particle field are localized within a well produced by condensed excitations of light particles.

Using the integral of motion (17), one can integrate set (15) and derive analytical expressions for all types of soliton solutions described above [1, 6].

3.2. The Case of Nonlinear Interparticle Interaction

Let us consider a diatomic chain in the absence of an external potential [$\gamma_2 = \gamma_3 = \gamma_4 = 0$ in Eq. (2)] but with nonlinear interparticle interaction described by Eq. (1). In this case, the equations of motion (3) become

$$\begin{aligned} &M\frac{d^2v_n}{dt^2} + K_2(2v_n - w_{n+1} - w_{n-1}) \\ &+ K_3[(v_n - w_{n-1})^2 - (v_n - w_{n+1})^2] \\ &+ K_4[(v_n - w_{n-1})^3 + (v_n - w_{n+1})^3] = 0, \quad n = 2j, \\ &m\frac{d^2w_n}{dt^2} + K_2(2w_n - v_{n+1} - v_{n-1}) \\ &+ K_3[(w_n - v_{n-1})^2 - (w_n - n_{n+1})^2] \\ &+ K_4[(w_n - v_{n-1})^3 - (w_n - v_{n+1})^3] = 0, \quad n = 2j+1. \end{aligned} \tag{18}$$

As in the case of external nonlinearity, we seek a solution to the set of equations (18) in the form of Eq. (11). Passing to the continuum limit and substituting Eq. (11) into Eq. (18), we arrive at a set of equations for $f^{(i)}$ and $g^{(i)}$:

$$\begin{aligned} &2K_2(f^{(0)} - g^{(0)}) + K_3FG = 0, \\ &(-4M\omega^2 + 2K_2)f^{(2)} - 2K_2g^{(2)} + K_3FG = 0, \\ &(-4m\omega^2 + 2K_2)g^{(2)} - 2K_2f^{(2)} - K_3FG = 0, \\ &\delta_1 F - \frac{dG}{dx} + 2K_3G[2(f^{(0)} - g^{(0)}) + f^{(2)} - g^{(2)}] \\ &+ \frac{3}{2}K_4(F^3 + FG^2) = 0, \\ &\delta_2 G + \frac{dF}{dx} + 2K_3F[2(f^{(0)} - g^{(0)}) + f^{(2)} - g^{(2)}] \\ &+ \frac{3}{2}K_4(G^3 + GF^2) = 0. \end{aligned} \tag{19}$$

Here, as before, δ_i are the deviations of the frequency ω from the lower and upper edges of the gap [see Eq. (14)], $F \equiv f^{(1)}$, $G \equiv g^{(1)}$, and the coordinate is scaled: $(\epsilon^2/2K_2)x \longrightarrow x$.

Eliminating the functions $f^{(0)}$, $g^{(0)}$, $f^{(2)}$, and $g^{(2)}$, we obtain Hamiltonian equations for the functions *F* and *G*, which have the form of Eq. (15) with the parameters β and *p* equal to

$$\begin{aligned} \beta &= -\frac{3}{2}K_4, \\ p &= 1 - \frac{2}{3}\frac{K_3^2}{K_2K_4}. \end{aligned} \tag{20}$$

It should be noted that in [12], the form of the solution assumed for an analogous set of equations was incorrect, with the consequence that the equations derived were not of the Hamiltonian form.

Of special interest is the case where $K_4 = 0$ and, hence, the anharmonic part of the interparticle interaction potential in Eq. (1) contains only the asymmetric term in atomic displacements. In this case, set (15) for the variables *F* and *G* takes the form

$$\begin{aligned} \frac{dG}{dx} &= \delta_1 F - \frac{K_3^2}{K_2}FG^2, \\ -\frac{dF}{dx} &= \delta_2 G - \frac{K_3^2}{K_2}GF^2. \end{aligned} \tag{21}$$

These equations have no static-soliton solutions but admit traveling solitons, as will be shown below. At frequencies $\omega > \omega_2$ ($\delta_1, \delta_2 < 0$), i.e., above the gap in the linear-wave spectrum, there is a single fixed point in the (*F*, *G*) phase plane with coordinates $F = 0$ and $G = 0$. In this frequency range, set (21) has only solutions that are periodic in space. At the edge of the gap ($\omega = \omega_2$), the

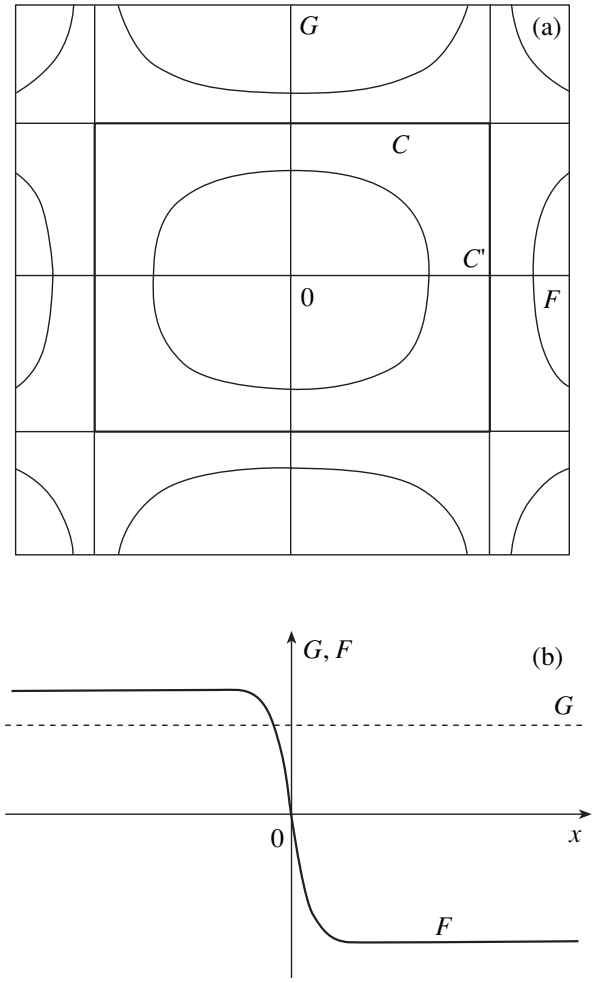

Fig. 3. (a) Phase portrait of Eq. (21) and (b) the soliton solution corresponding to separatrix *C*.

center is transformed into a fixed line $F = 0$, which, in turn, is replaced by a fixed point of the saddle type at $F = G = 0$ within the gap $\omega_1 < \omega < \omega_2$. In this frequency range, set (21) has only unphysical singular solutions. At the lower edge of the gap ($\omega = \omega_1$), the saddle is replaced by five fixed points: a center at $F = G = 0$ and four saddle points with coordinates $F = \pm\sqrt{\delta_2 2K_2/K_3^2}$ and $G = \pm\sqrt{\delta_1 2K_2/K_3^2}$ (Fig. 3a). Separatrices *C* and *C*' separate solutions of two types: those in which the *F* and *G* fields vary periodically with the space coordinate (as in the solutions above the gap) and (unphysical) those in which one of the fields increases infinitely with the space coordinate. The separatrices themselves correspond to a special type of solution in which one of the fields has the form of a kink, while the other is a constant over the entire chain (Fig. 3b). The solutions corresponding to the *C* separatrices have the form

$$G = \pm\sqrt{\frac{\delta_1 2K_2}{K_3^2}},$$
$$F = \mp\sqrt{\frac{\delta_2 2K_2}{K_3^2}}\tanh[\sqrt{\delta_1\delta_2}\delta_2 x], \tag{22}$$

and the solutions corresponding to the *C*' separatrices are

$$F = \pm\sqrt{\frac{\delta_2 2K_2}{K_3^2}},$$
$$G = \mp\sqrt{\frac{\delta_1 2K_2}{K_3^2}}\tanh[\sqrt{\delta_1\delta_2}\delta_1 x]. \tag{23}$$

3.3. The Case of Nonlinear Internal Interaction and an Anharmonic External Potential

It is easy to verify that a combination of the two types of nonlinearity does not lead to physically new results. As before, the closed set of equations for the variables *F* and *G* has the form of set (15), in which the parameters β and *p* are expressed through the constants K_2, K_3, K_4, γ_2, γ_3, and γ_4; the corresponding formulas are similar to Eq. (16) and have the form

$$\beta = \gamma_3^2(2K_2 + \gamma_2)$$
$$\times\frac{16(2K_2+\gamma_2)^2 - \gamma_2(4K_2+\gamma_2)}{2\gamma_2(4K_2+\gamma_2)[8(2K_2+\gamma_2)^2 + \gamma_2(4K_2+\gamma_2)]}$$
$$-\frac{3}{4}(2K_4+\gamma_4), \tag{24}$$

$$p = \frac{1}{\beta}\left\{\gamma_3^2 K_2\frac{16(2K_2+\gamma_2)^2 + 3\gamma_2(4K_2+\gamma_2)}{\gamma_2(4K_2+\gamma_2)[8(2K_2+\gamma_2)^2 + \gamma_2(4K_2+\gamma_2)]}\right.$$
$$\left.+\frac{3}{2}K_4 + -\frac{K_3^2}{K_2}\right\}.$$

Therefore, the set of equations (15) describes static solutions to set (3) in the general case of external and internal nonlinearities that are cubic and quartic in the atomic displacements. Equations (15) are similar to those derived in [5, 6] describing the nonlinear dynamics of a diatomic chain with external and internal quartic nonlinearities (the case of an even potential function). All possible solutions to set (15) are qualitatively analyzed and described in [5]. A method for solving this set of equations analytically is described in detail in [1, 6].

4. TRAVELING SOLITONS

Now, we examine moving solutions to the set of equations (3). For the sake of simplicity, only potentials with cubic nonlinearity are considered, putting the parameters K_4 and γ_4 equal to zero in Eqs. (1) and (2). As shown above, the inclusion of terms that are quartic in the atomic displacements in the potential does not significantly affect the solutions to the nonlinear equations.

It is convenient to analyze solutions by using the two-wave approximation. Near the linear-wave spectrum gap ($\epsilon \ll 1$), we seek a solution to Eq. (3) to within terms of the order ϵ^2 in the form of Eq. (7):

$$\begin{aligned}\xi_n &= \epsilon\left[A_1\exp\left(-i\frac{\pi n}{2}\right) + A_2\exp\left(i\frac{\pi n}{2}\right)\right]\exp(i\omega t)\\ &+ \epsilon^2\{[B_1\exp(-i\pi n) + B_2]\exp(i2\omega t)\\ &+ \frac{1}{2}[C_1\exp(-i\pi n) + C_2]\} + \text{c.c.},\end{aligned} \tag{25}$$

where A_i, B_i, and C_i are functions of the atomic index n and time t.

In this section, as in Section 3, we consider the cases of external nonlinearity alone (Subsection 4.1), of internal nonlinearity alone (Subsection 4.2), and of both types of nonlinearity (Subsection 4.3).

4.1. The Case of an Anharmonic External Potential

We assume the interparticle interaction to be linear and put $K_3 = K_4 = 0$ in Eqs. (1) and (3).

Substituting Eq. (25) into Eq. (3) and equating the sums of the coefficients of identical exponentials to zero, we arrive at a set of algebraic equations for the variables A_i, B_i, and C_i in the long-wavelength limit,

$$\begin{aligned}\gamma_2(C_2 + C_2^*) + 2\gamma_3[|A_1|^2 + |A_2|^2] &= 0,\\ (4K_2 + \gamma_2)(C_1 + C_1^*) + 2\gamma_3[A_1A_2^* + A_2A_1^*] &= 0,\\ (-4\omega^2\mu + \gamma_2)B_2 + 2\gamma_3A_1A_2 &= 0,\\ (-4\omega^2\mu + 4K_2 + \gamma_2)B_1 + \gamma_3(A_1^2 + A_2^2) &= 0\end{aligned} \tag{26}$$

and, in addition, at a set of two differential equations for A_1 and A_2,

$$\begin{aligned}&i2\omega\mu\frac{\partial A_1}{\partial t} + i2K_2\frac{\partial A_1}{\partial x} + (-\omega^2\mu + 2K_2 + \gamma_2)A_1\\ &- \omega^2\mu\epsilon^2A_2 + \gamma_3\epsilon^2[2(B_1A_1^* + B_2A_2^*)\\ &+ (C_1 + C_1^*)A_2 + (C_2 + C_2^*)A_1] = 0,\\ &i2\omega\mu\frac{\partial A_2}{\partial t} - i2K_2\frac{\partial A_2}{\partial x} + (-\omega^2\mu + 2K_2 + \gamma_2)A_2\\ &- \omega^2\mu\epsilon^2A_1 + \gamma_3\epsilon^2[2(B_1A_2^* + B_2A_1^*)\\ &+ (C_1 + C_1^*)A_1 + (C_2 + C_2^*)A_2] = 0.\end{aligned} \tag{27}$$

We represent the frequency in the form $\omega = \omega_0 + \delta$, where δ is of the order of ϵ^2 and $\omega_0^2 = (2K_2 + \gamma_2)/\mu$ corresponds to the midgap of the linear-wave spectrum; hence, δ is the deviation of the frequency from the midgap.

After scaling the time, space coordinate, and amplitudes,

$$\frac{\omega_0\epsilon^2}{2}t \longrightarrow t, \quad \frac{2K_2 + \gamma_2}{2K_2}\epsilon^2x \longrightarrow x,$$

$$2\gamma_3\sqrt{\frac{8K_2 + 5\gamma_2}{\gamma_2(4K_2 + 3\gamma_2)(2K_2 + \gamma_2)}}A_i = F_i,$$

we obtain a set of two differential equations for F_i in dimensionless variables:

$$\begin{aligned}-\frac{\partial F_1}{\partial t} - \frac{\partial F_1}{\partial x} &= i\Omega F_1 + iF_2\\ &+ \frac{i}{2}[F_1(|F_1|^2 + p_1|F_2|^2) + p_2F_2^2F_1^*],\\ -\frac{\partial F_2}{\partial t} + \frac{\partial F_2}{\partial x} &= i\Omega F_2 + iF_1\\ &+ \frac{i}{2}[F_2(|F_2|^2 + p_1|F_1|^2) + p_2F_1^2F_2^*],\end{aligned} \tag{28}$$

where $\Omega = 2\delta/\omega_2\epsilon^2$ is the dimensionless deviation of the frequency from the midgap and the parameters p_1 and p_2 are expressed through the ratio of the constants K_2 and γ_2 ($\chi = K_2/\gamma_2$) as

$$\begin{aligned}p_1 &= 2\frac{32\chi^2 + 24\chi + 5}{(8\chi + 3)(8\chi + 5)} > 0,\\ p_2 &= \frac{(4\chi + 5)}{(8\chi + 5)(4\chi + 1)} > 0\end{aligned} \tag{29}$$

(it will be recalled that K_2 and γ_2 are positive).

Equations (28) are similar to equations that describe the nonlinear dynamics of a diatomic chain in an external even potential [8] and of a monatomic chain in an external double-barrier potential [13].

By introducing new real variables u_1, u_2, s, and q,

$$\begin{aligned}F_1 &= u_1\exp(iq + is),\\ F_2 &= u_2\exp(iq - is),\end{aligned} \tag{30}$$

one can obtain the equations

$$\frac{du_1}{dz} = -u_1\sin(2s) - \beta u_1^3\sin(4s), \tag{31}$$

$$\frac{ds}{dz} = -\nu - \cos(2s) - \alpha u_1^2 - \beta u_1^2\cos(4s), \tag{32}$$

$$\frac{dq}{dz} = -\nu V - \frac{V}{\sqrt{1 - V^2}(1 + V)}u_1^2, \tag{33}$$

$$u_2 = \sqrt{\frac{1 - V}{1 + V}}u_1, \tag{34}$$

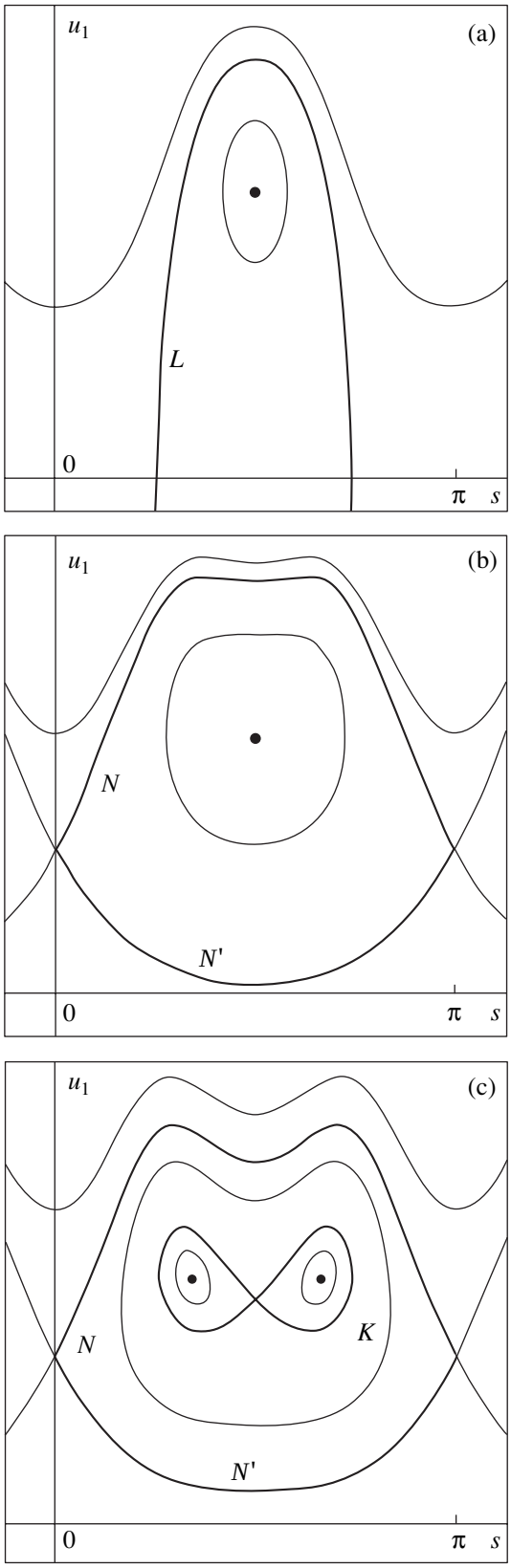

Fig. 4. Phase portraits of the set of equations (31) and (32) with parameters α and β given by Eq. (35) (the case of cubic external nonlinearity) for values of parameter ν lying in the ranges (a) $-1 < \nu < 1$, (b) $\nu_* < \nu < -1$, and (c) $\nu < \nu_*$.

where $z = (x - Vt)/\sqrt{1 - V^2}$ and $\nu(\Omega, V)$, $\alpha(V, p_1, p_2)$ and $\beta(V, p_1, p_2)$ are given by

$$\nu = \frac{\Omega}{\sqrt{1 - V^2}},$$
$$\alpha = \frac{1 + V^2 + p_1(1 - V^2)}{2(1 + V)\sqrt{1 - V^2}}, \quad (35)$$
$$\beta = \frac{p_2(1 - V^2)}{2(1 + V)\sqrt{1 - V^2}}.$$

The relation between the amplitudes u_1 and u_2 given by Eq. (34) corresponds to two-parametric solutions to the set of equations (28); as the parameters, one can conveniently take the frequency Ω and the velocity V. We note that, in addition to two-parametric solutions, Eqs. (28) also admit a wider class of three-parametric solutions [8, 14], which are not considered in this paper. Three-parametric solutions were investigated comprehensively in [14].

Equations (31) and (32) form a closed set of Hamilton equations with the effective Hamiltonian

$$H = (\nu + \cos(2s))u_1^2 + \frac{\alpha}{2}u_1^4 + \frac{\beta}{2}u_1^4\cos(4s), \quad (36)$$

where u_1^2 and $2s$ can be considered to be canonically conjugate variables (coordinate and momentum); the coordinate z, effective time.

It is convenient to investigate possible solutions to Eqs. (31) and (32) in the (u_1, s) phase plane. The character of the phase portrait of the system under study depends on the parameter ν, which is a function of the frequency and velocity of the nonlinear excitation [see Eq. (35)]. In the general case, the phase portrait is symmetric relative to the $u_1 = 0$ axis and periodic in the variable s with a period of π. Therefore, we can consider it only in the region $u_1 > 0$ and $0 < s < \pi$ (Fig. 4).

At $\nu > 1$, the frequency of the nonlinear excitation lies above the upper branch of the linear-wave spectrum ($\Omega > \sqrt{1 - V^2}$) and there are no fixed points in the (u_1, s) phase plane; therefore, soliton solutions are absent in this frequency range. At $\Omega = \sqrt{1 - V^2}$ ($\nu = 1$), a fixed point arises with coordinates $u_1 = 0$ and $s = \pi/2$. In the region of parameters V and Ω over which $-1 < \nu < 1$, this fixed point is replaced by two saddle points with coordinates $u_1 = 0$, $s = \pi \pm \arccos(-\nu)/2$ and a center at $u_1 = \sqrt{(1 - \nu)(\alpha + \beta)}$, $s = \pi/2$ (Fig. 4a). The saddle points are connected by separatrices L, which correspond to traveling gap solitons. In these solitons, the amplitudes u_1 and u_2 tend to nonzero values as $z \longrightarrow \pm\infty$ and the phase s is changed by $\Delta_s = \arccos(-\nu)$ as the coordinate z increases from $-\infty$ to $+\infty$.

At $\nu = -1$ (the lower branch of the linear-wave spectrum, $\Omega = -\sqrt{1 - V^2}$), another bifurcation occurs, with the result that, in the range of ν values $-(\alpha - \beta)/2\beta = \nu_* < \nu < -1$, two saddle points with coordinates $u_1 = \sqrt{(-\nu - 1)(\alpha + \beta)}$ and $s = 0, \pi$ and a center with coordinates $u_1 = \sqrt{(-\nu + 1)(\alpha + \beta)}$ and $s = \pi/2$ arise in the (u_1, s) phase plane (Fig. 4b). The saddles are connected by separatrices of the *N* and *N*' types, which correspond to traveling near-gap solitons. In contrast to gap solitons of the *L* type, the amplitudes u_1 and u_2 in *N*- and *N*'-type solitons tend to nonzero values as $z \longrightarrow \pm\infty$ and the phase s is changed by $\Delta_s = \pi$ as the coordinate z increases from $-\infty$ to $+\infty$.

Finally, at $\nu = \nu_* = -(\alpha - \beta)/2\beta$, the final bifurcation occurs: the center at $u_1 = \sqrt{(-\nu + 1)(\alpha + \beta)}$ and $s = \pi/2$ is replaced by a saddle point with the same coordinates and two new centers with coordinates $u_1 = \sqrt{-\nu/(\alpha - \beta)}$ and $s = \pi \pm \arccos(\nu_*/\nu)/2$ (Fig. 4c); in addition to the *N* and *N*' types, a new type of separatrix (*K* type) appears in this case. In the range $\nu < \nu_*$, there are three types (*N*, *N*', *K*) of traveling near-gap solitons. The characteristic feature of solitons of the *K* type is that the overall change in phase s in them is zero as the coordinate z increases from $-\infty$ to $+\infty$.

Traveling *L* solitons and near-gap solitons of the *N*, *N*', and *K* types were investigated comprehensively in [8, 13].

4.2. The Case of Nonlinear Interparticle Interaction

In this case, the coefficients γ_2, γ_3, and γ_4 are zero in Eq. (3) (there is no external potential).

As before, we seek a solution to Eq. (3) in the form of Eq. (25). By substituting Eq. (25) into Eq. (3) and going over to dimensionless variables,

$$\frac{\omega_0\epsilon^2}{2}t \longrightarrow t, \quad \epsilon^2 x \longrightarrow x, \quad \sqrt{\frac{8K_3^2}{K_2}}A_i = F_i,$$

we obtain a set of two differential equations for F_i,

$$\begin{aligned} -\frac{\partial F_1}{\partial t} - \frac{\partial F_1}{\partial x} &= i\Omega F_1 + iF_2 \\ &+ \frac{i}{2}[F_1(|F_1|^2 + 2|F_2|^2) - 3F_2^2F_1^*], \\ -\frac{\partial F_2}{\partial t} + \frac{\partial F_2}{\partial x} &= i\Omega F_2 + iF_1 \\ &+ \frac{i}{2}[F_2(|F_2|^2 + 2|F_1|^2) - 3F_1^2F_2^*], \end{aligned} \tag{37}$$

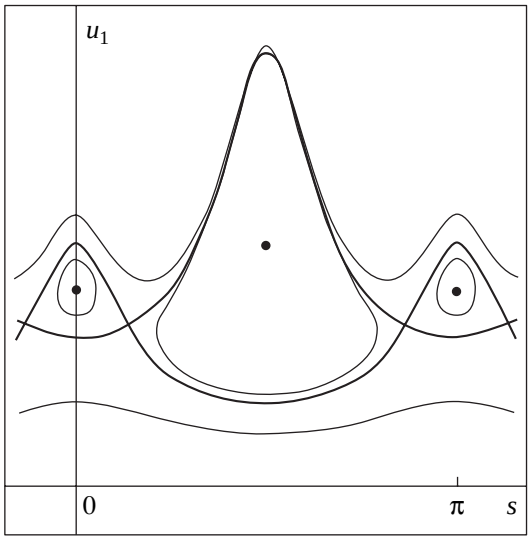

Fig. 5. Phase portrait of the set of equations (31) and (32) with parameters α and β given by Eq. (38) (the case of cubic internal nonlinearity) for values of parameter ν lying in the range $\nu < \nu_*$.

where $\omega_0 = \sqrt{2K_2/\epsilon^2}$ is the frequency that corresponds to the midgap and $\Omega = 2\delta/\omega_0\epsilon^2$ is the dimensionless deviation of the frequency from the midgap.

Introducing real variables u_1, u_2, s, and q in accordance with Eq. (30), we arrive at Eqs. (31)–(34) for them, in which the coefficients α and β are

$$\begin{aligned} \alpha &= \frac{3 - V^2}{2(1 + V)\sqrt{1 - V^2}}, \\ \beta &= -\frac{3(1 - V^2)}{2(1 + V)\sqrt{1 - V^2}}. \end{aligned} \tag{38}$$

The evolution of the phase portrait of the set of equations (31) and (32) in the case in question is similar to that in the case of external nonlinearity alone described in Subsection 4.1. As before, as the parameter ν is varied, three bifurcations occur successively. The bifurcations at $\nu = 1$ and $\nu = -1$ (the upper and lower branches of the linear-wave spectrum, respectively) are qualitatively similar to the respective bifurcations described above. Therefore, the phase portraits of the set of equations (31) and (32) in the ranges $-1 < \nu < 1$ and $-(\alpha + \beta)/2\beta = \nu_* < \nu < -1$ in the case under study are similar to the respective phase portraits in the case of external nonlinearity alone (Figs. 4a, 4b). However, the bifurcation at $\nu = \nu_*$ is different: each of the saddles at $u_1 = \sqrt{(-\nu - 1)(\alpha + \beta)}$ and $s = 0, \pi$ is transformed into a center with the same coordinates and two new saddles with coordinates $u_1 = \sqrt{-\nu/(\alpha - \beta)}$ and $s = \pm\arccos(\nu_*/\nu)/2$ (Fig. 5). Therefore, at $\nu \le \nu_*$, the phase portrait of the set of

equations (31) and (32) has separatrices of four types: N, N', $\tilde{N}$, and $\tilde{N}'$; they correspond to traveling near-gap solitons which are analogous in character to the near-gap solitons of the N and N' types that exist in the range $\nu_* < \nu < -1$, but the asymptotic behavior of the phase s at infinity (as $z \longrightarrow \pm\infty$) is different in them.

Thus, in the case of internal cubic nonlinearity, traveling gap solitons (of the L type) and traveling near-gap solitons (of the N, N', $\tilde{N}$, and $\tilde{N}'$ types) can exist in the system. At the same time, as shown in Subsection 3.2, there are no static soliton solutions in this case. In this connection, it is of interest to analyze the transition from traveling solitons to static ones. It can be shown that the amplitudes of L, N, and $\tilde{N}$ solitons near $z = 0$ (i.e., in the vicinity of the center of a soliton) increase indefinitely as $V \longrightarrow 0$. (It should be noted, however, that the small-amplitude approximation we employ here becomes inapplicable in this case.) Soliton solutions of the N' and $\tilde{N}'$ types are transformed into the localized solutions described by Eqs. (22) and (23) as $V \longrightarrow 0$; these solutions correspond to separatrices C and C' in Fig. 3a.

As an example, we write out expressions for the traveling gap soliton of the L type:

$$s = \frac{\pi}{2} = \arctan[X],$$

$$u_1 = \left\{(1+V)\sqrt{1-V^2}\frac{2(1+\nu)(1+X^2)}{V^2(1+X^4)+4(6-5V^2)X^2} \times \frac{1}{\cosh^2(2-\sqrt{1-\nu^2}z)}\right\}^{1/2}, \quad (39)$$

$$q = \nu V z + \frac{V}{\sqrt{2-V^2}}\arctan\left[2\sqrt{2-V^2}\frac{X}{1-X^2}\right],$$

where

$$X = \sqrt{\frac{1+\nu}{1-\nu}}\tan(2-\sqrt{1-\nu^2}z).$$

It is seen from these expressions that at a low velocity ($|V| \ll 1$), the amplitude u_1 increases indefinitely in the vicinity of $z = 0$. Therefore, the asymptotic method employed here is inadequate for the investigation of solitons moving at a low velocity in the case of a system with cubic internal nonlinearity. Within the small-amplitude approximation, there are no static solitons nor solitons moving at a low velocity in the system under study.

4.3. The General Case of a Cubic Anharmonic Potential

As in the case of static solutions, a combination of the two types of nonlinearity does not lead to physically new results. In the general case of external and internal cubic nonlinearity present in the system, we substitute Eq. (25) into Eq. (3) and, going over to dimensionless variables,

$$\frac{\omega_0\epsilon^2}{2}t \longrightarrow t, \quad \frac{2K_2+\gamma_2}{2K_2}\epsilon^2 x \longrightarrow x, \quad \eta A_i = F_i,$$

$$\eta = 2\gamma_3^2\frac{8K_2+5\gamma_2}{\gamma_2(4K_2+3\gamma_2)(2K_2+\gamma_2)} + \frac{4K_3^2}{K_2},$$

obtain for F_i a set of two differential equations of the form of Eq. (28) with the parameters p_1 and p_2 given by

$$p_1 = \frac{1}{\eta} \times\left[4\gamma_3^2\frac{32K_2^2+24K_2\gamma_2+5\gamma_2^2}{\gamma_2(8K_2+3\gamma^2)(4K_2+3\gamma_2)(2K_2+\gamma_2)} + \frac{8K_3^2}{K_2}\right],$$

$$p_2 = \frac{1}{\eta}\left[2\gamma_3^2\frac{4K_2+5\gamma_2}{(4K_2+\gamma_2)(2K_2+\gamma_2)} - \frac{12K_3^2}{K_2}\right].$$

The structure of solutions to these nonlinear equations depends on the relationship between the coefficients γ_3 and K_3, characterizing the external and internal nonlinearity, respectively. Equations of the form of Eq. (28) were analyzed comprehensively in [8] for various values of the parameters involved.

5. CONCLUSIONS

In this paper, we considered the general case of a nonlinear diatomic chain in which the interparticle interaction potential and the external anharmonic potential contain both even and odd terms in atomic displacements. By using a modified asymptotic method, which takes into account the asymmetry of the anharmonic potential in the atomic displacements, static solutions to the system were found to satisfy dynamic equations that are different from those derived in [12]. We also developed an asymptotic method which allows one to find solutions corresponding to traveling solitons. It was shown that the dynamics of nonmoving and moving solitons can be described by differential equations which are identical to those that describe the nonlinear dynamics of a diatomic chain with an even potential function. A qualitative analysis of possible static and traveling solitons was performed in the phase plane for particular cases of external and internal nonlinearities. In the latter case, the system has no static small-amplitude soliton solutions; there are only solutions that are periodic in space in the form of so-called cnoidal waves and special solutions in which the envelope of oscillations of particles of one type has

the form of a kink. However, traveling small-amplitude solitons exist in the case where the interparticle interaction potential has cubic nonlinearity.

ACKNOWLEDGMENTS

This study was supported in part by the INTAS-99, grant no. 167, and the MNOP program, grant USU no. 082087.

REFERENCES

1. O. Chubykalo, A. Kovalev, and O. Usatenko, Phys. Rev. B **47** (6), 3153 (1993).
2. O. Chubykalo and Yu. Kivshar, Phys. Rev. E **48** (5), 4128 (1993).
3. A. S. Kovalev, K. V. Kladko, and O. V. Usatenko, J. Phys. Soc. Jpn. **64** (7), 2464 (1995).
4. O. V. Usatenko, A. S. Kovalev, and A. A. Vialov, in *Fluctuation Phenomena: Disorder and Nonlinearity*, Ed. by A. R. Bishop, S. Jiménez, and L. Vázquez (World Scientific, Singapore, 1994), p. 286; O. V. Ustatenko, A. S. Kovalev, and A. A. Vyalov, Fiz. Tverd. Tela (St. Petersburg) **37** (8), 2487 (1995) [Phys. Solid State **37**, 1362 (1995)].
5. A. S. Kovalev, O. V. Usatenko, and A. V. Gorbach, Phys. Rev. E **60** (2), 2309 (1999).
6. A. S. Kovalev, O. V. Usatenko, and A. V. Gorbach, Élektromag. Yavleniya **1** (3), 324 (1998).
7. A. S. Gorshkov, O. N. Ermakova, and V. F. Marchenko, Nonlinearity **10** (4), 1007 (1997).
8. A. S. Kovalev, O. V. Usatenko, and A. V. Gorbach, Fiz. Tverd. Tela (St. Petersburg) **43** (9), 1600 (2001) [Phys. Solid State **43**, 1665 (2001)].
9. A. M. Kosevich and A. S. Kovalev, Zh. Éksp. Teor. Fiz. **67** (5), 1793 (1974) [Sov. Phys. JETP **40**, 891 (1975)].
10. P. S. Landa and V. F. Marchenko, Usp. Fiz. Nauk **161** (9), 201 (1991) [Sov. Phys. Usp. **34**, 830 (1991)].
11. A. M. Kosevich, *Theory of Crystal Lattice* (Khar'kovsk. Gos. Univ., Khar'kov, 1988).
12. Yu. S. Kivshar, O. A. Chubykalo, O. V. Usatenko, and D. M. Grinyoff, Int. J. Mod. Phys. B **9** (22), 2963 (1995).
13. A. S. Kovalev, O. V. Usatenko, and A. V. Gorbach, Fiz. Nizk. Temp. (in press).
14. J. Feng and F. K. Kneubuhl, IEEE J. Quantum Electron. **29** (2), 590 (1993).

Translated by Yu. Epifanov

Physics of the Solid State, Vol. 43, No. 11, 2001, pp. 2182–2191. Translated from Fizika Tverdogo Tela, Vol. 43, No. 11, 2001, pp. 2091–2099.
Original Russian Text Copyright © 2001 by Korovin, Lang, Contreras-Solorio, Pavlov.

LOW-DIMENSIONAL SYSTEMS AND SURFACE PHYSICS

The Role of Spatial Dispersion of an Electromagnetic Wave in Its Penetration through a Quantum Well

L. I. Korovin[1], I. G. Lang[1], D. A. Contreras-Solorio[2], and S. T. Pavlov[2, 3]

[1]*Ioffe Physicotechnical Institute, Russian Academy of Sciences, Politekhnicheskaya ul. 26, St. Petersburg, 194021 Russia*

[2]*Escuela de Física de la UAZ, Apartado Postal c-580, Zacatecas, 98060 México*

[3]*Lebedev Institute of Physics, Russian Academy of Sciences, Leninskiĭ pr. 53, Moscow, 117924 Russia*

e-mail: ilang@dor.ioffe.rssi.ru

e-mail: pavlov@ahobon.reduaz.mx

Received April 3, 2001

Abstract—The theory of light penetration through a quantum well in a strong magnetic field perpendicular to the well plane is developed under the conditions where interband transitions occur in the well. The light wavelength is assumed to be comparable to the well width. The relationships for the reflection, absorption, and transmission are derived with due regard for the spatial dispersion of a monochromatic light wave and the difference between the refractive indices of the quantum well and the barrier. The normal incidence of light with respect to the well plane is considered, and one excited level is taken into account. It is demonstrated that the above two factors most strongly affect the reflection, because the reflection from the well boundaries appears in addition to the reflection caused by interband transitions in the quantum well. The most radical changes in the reflection are observed in the case when the reciprocal radiative lifetime of the excited state in the quantum well is short compared to the reciprocal nonradiative lifetime. In the range of large well widths, the applicability of the theory is limited by the existence condition of quantum well levels. © *2001 MAIK "Nauka/Interperiodica".*

1. INTRODUCTION

When light passes through a quantum well, the reflected and transmitted waves exhibit characteristic features which allow one to judge the electronic processes proceeding in this well [1–4]. The most interesting results are obtained in the case when the energy levels of an electronic system are discrete. This situation arises in a strong magnetic field directed perpendicularly to the well plane or when exciton states in a zero magnetic field are taken into account. Modern semiconductor technology provides a means for producing high-quality quantum wells for which the radiative broadening of the absorption peak can be comparable to the contributions from nonradiative relaxation mechanisms and can even exceed them. In this case, consideration cannot be reduced to an approximation linear in the interaction of electrons with the electromagnetic field and all the higher-order terms in this interaction should be taken into account [5–18].

A number of works have been devoted to the investigation of the reflection, absorption, and transmission of an electromagnetic wave that interacts with discrete levels of an electronic system of a quantum well at frequencies corresponding to interband transitions [12–18]. In these works, both light pulses [12–17] and monochromatic radiation [18] were treated as exciting waves. Allowance was made for one [16], two [17, 18], and a larger number of excited levels [15]. The results obtained in these studies are valid for relatively narrow quantum wells when the following inequality is satisfied:

$$\kappa d \ll 1, \tag{1}$$

where d is the quantum well width and κ is the magnitude of the light wave vector $\mathbf{k}$. In actual fact, the parameter κd in the aforementioned works was taken equal to zero and the calculated reflection, absorption, and transmission were independent of the well width d.

The value of κ can be numerically estimated from the lasing wavelength of a gallium arsenide heterolaser. This wavelength is equal to 0.8μ, and the corresponding energy $\hbar\omega_l$ is 1.6 eV. If the refractive index ν of the quantum well material is equal to 3.5, then $\kappa = \nu\omega_l/c = 2.8 \times 10^5$ cm^{-1} (where c is the velocity of light in free space). At the well width $d = 500$ Å, the κd parameter is equal to 1.4. Therefore, in the case of sufficiently wide wells, the allowance made for the spatial dispersion of an exciting wave can turn out to be significant.

For wide quantum wells, the inequality $d \gg a_0$ (where a_0 is the lattice constant) is very strong and the penetration of a light wave through a quantum well can be described by the Maxwell equations for a continuous medium. In the strict sense, this approach requires inclusion of the difference between the refractive indices of the barrier and the well. Hence, there should appear an additional reflection from the quantum well boundaries. This reflection decreases with a decrease in the κd parameter but, in the range $\kappa d \simeq 1$, in certain

cases, can be equal or exceed the reflection due to interband transitions in the quantum well itself. A change in the reflection of a light wave is accompanied by a change in its transmission. Therefore, the difference between the refractive indices of the barrier and the quantum well should be allowed for in addition to the spatial dispersion of the electromagnetic wave.

The aim of the present work was to analyze the effect of these two factors on the reflection, absorption, and transmission of electromagnetic waves that penetrate through quantum wells and induce interband transitions in them.

2. THE MODEL AND BASIC RELATIONS

We consider a system that consists of a deep semiconductor quantum well located in the range $0 \le z \le d$ and two semi-infinite barriers. A strong constant magnetic field is directed perpendicularly to the well plane (along the z axis). It is assumed that an external electromagnetic wave propagates along the z axis from negative values of z, the barriers are transparent to the wave, and the wave is absorbed in the quantum well and induces resonant interband transitions. Analysis is carried out at zero temperature for the situation when, in the ground state, the valence band is completely filled and the conduction band is empty. Only the states that are formed after the transfer of an electron from the valence band to the conduction band with the formation of a hole in the valence band are considered to be excited. This is valid within the approximation linear in the wave amplitude. We will consider the light frequencies close to the band gap of the quantum well when a small fraction of valence electrons participates in the absorption. These electrons are located near the extremum of the band and can be described by the effective mass method. In this case, for deep quantum wells, the electron tunneling into the barrier can be ignored and the barrier–quantum well boundary can be regarded as a sharp boundary, which implies that the current in the barrier is absent. Moreover, the levels close to the well bottom can be treated within the approximation of an infinitely deep well, even though this restriction is not rigid and the theory can be generalized to the case of wells with a finite depth. The system under consideration is inhomogeneous. Since the size of the inhomogeneity (quantum well) is less or of the order of the light wavelength, the optical characteristics of this system should be determined from solutions of the Maxwell equations, in which the current and charge densities should be represented by relationships obtained in the framework of the microscopic approach [19, 20].

The final results will be obtained for one discrete level of the electronic system in the quantum well. The influence of other levels on the reflection and absorption of light can be neglected when the frequency ω_l of exciting light is close to the frequency ω_0 of the interband transition. The exciton levels in a zero magnetic field or the levels in a strong magnetic field perpendicular to the well plane are discrete in the quantum well at $\hbar\mathbf{K}_\perp = 0$, where $\hbar\mathbf{K}_\perp$ is the vector of the total quasimomentum of an electron–hole pair in the well plane. As a convenient example, we will analyze the level of an electron–hole pair in a strong magnetic field without regard for the Coulomb interaction between an electron and a hole. This interaction is considered a weak perturbation for sufficiently strong fields and not very wide wells [21]. However, the exciton effect does not lead to radical changes in the results obtained in the work and only affects the radiative broadening γ_r of the electronic excitation introduced below. The same is true for the exciton levels in a zero magnetic field.

Let us calculate the high-frequency current density induced by exciting light in the quantum well. For any spatially inhomogeneous electronic system, it is possible to introduce the electrical conductivity tensor $\sigma_{\alpha\beta}(\mathbf{k}, \omega|\mathbf{r})$ that relates the mean current density $\mathbf{J}(\mathbf{r}, t)$ and the electric field by the expression

$$J_\alpha(\mathbf{r}, t) = (2\pi)^{-4}\int d\mathbf{k}\int_0^\infty d\omega\sigma_{\alpha\beta}(\mathbf{k}, \omega|\mathbf{r}) \times E_\beta(\mathbf{k}, \omega)\exp[i(\mathbf{kr} - \omega t)] + \text{c.c.}, \quad (2)$$

$$E_\beta(\mathbf{k}, \omega) = \int d\mathbf{r}\int_{-\infty}^\infty dt E_\beta(\mathbf{r}, t)\exp[-i(\mathbf{kr} - \omega t)]. \quad (3)$$

Since the temperature is assumed to be zero, the current density is averaged over the ground state of the electronic system, that is,

$$\mathbf{J}(\mathbf{r}, t) = \langle 0|\hat{\mathbf{J}}(\mathbf{r}, t)|0\rangle, \quad (4)$$

where $\hat{\mathbf{J}}(\mathbf{r}, t)$ is the current density operator within the approximation linear in the external field. The electrical conductivity tensor is defined by the formula[1]

$$\sigma_{\alpha\beta}(\mathbf{k}, \omega|\mathbf{r}) = (i/\hbar)\int d\mathbf{r}'\int_{-\infty}^\infty dt'\Theta(t') \times\langle|[j_\alpha(\mathbf{r}, t), \tilde{d}_\beta(\mathbf{r} - \mathbf{r}', t - t')]|0\rangle. \quad (5)$$

Here, $\Theta(t)$ is the Heaviside function and $j_\alpha(\mathbf{r}, t)$ is the Cartesian projection of the current density operator in the absence of an external electromagnetic field but with due regard for the strong constant magnetic field

$$\mathbf{H} = \text{rot}\mathbf{A}^{(0)}(\mathbf{r}), \quad (6)$$

[1] The terms containing the multipliers of the order of $\kappa v/\omega$ (where v is the electron velocity) are omitted in formula (5).

where $\mathbf{A}^{(0)}(\mathbf{r})$ is its vector potential. The $j_\alpha(\mathbf{r}, t)$ operator has the form

$$j_\alpha(\mathbf{r}, t) = \exp(i\mathcal{H}t/\hbar) j_\alpha(\mathbf{r}) \exp(-i\mathcal{H}t/\hbar), \quad (7)$$

$$j_\alpha(\mathbf{r}) = (e/2)\sum_i [v_{i\alpha}\delta(\mathbf{r}-\mathbf{r}_i) + \delta(\mathbf{r}-\mathbf{r}_i)v_{i\alpha}], \quad (8)$$

$$v_{i\alpha} = -i(\hbar/m_0)\partial/\partial r_{i\alpha} - (e/m_0 c)A_\alpha^{(0)}(\mathbf{r}_i), \quad (9)$$

where $\mathcal{H}$ is the Hamiltonian of the electronic system that accounts for the strong magnetic field and disregards the external electromagnetic field,

$$\tilde{d}_\alpha(\mathbf{r}, t) = \exp(i\mathcal{H}t/\hbar)\tilde{d}_\alpha(\mathbf{r})\exp(-i\mathcal{H}t/\hbar), \quad (10)$$

$$\tilde{d}_\alpha(\mathbf{r}) = e\sum_i (r_{i\alpha} - \langle 0|r_{i\alpha}|0\rangle)\delta(\mathbf{r}-\mathbf{r}_i). \quad (11)$$

By using the effective mass method for electrons and holes near extrema of the valence and conduction bands and making allowance for the system homogeneity in the quantum well plane, from relationships (2) and (5), we obtain

$$\bar{J}_\alpha(z, t) = \frac{i}{4\pi^2}\frac{(e/m_0)^2}{\hbar\omega_g a_H^2}\int_{-\infty}^{\infty} d\omega e^{-i\omega t} \times \sum_\chi \Phi_\chi(z)\left[\frac{p_{cv\alpha}^{j*}p_{cv\beta}^{j}}{\omega-\omega_\chi+i\gamma_\chi/2} + \frac{p_{cv\alpha}^{j}p_{cv\beta}^{j*}}{\omega+\omega_\chi+i\gamma_\chi/2}\right] \times \int_{-\infty}^{\infty} dz'\Phi_\chi(z')E_\beta(z', \omega), \quad (12)$$

where $\bar{J}(z, t)$ is the electric field induced–current density averaged over the ground state of the electronic system. The bar indicates additional averaging of the current density over a unit cell, which is possible at $d \gg a_0$. The following designations are used in formula (12): m_0 is the bare electron mass; $\hbar\omega_g$ is the band gap; $a_H = (c\hbar/|e|H)^{1/2}$ is the magnetic length; χ is the set of indices

$$\chi = (j, \lambda), \quad \lambda = (n = n_c = n_v, m_c, m_v); \quad (13)$$

j is the number of the valence band (because the valence band is degenerate in cubic crystals, which will be considered in the work); $n_c(n_v)$ are the Landau quantum numbers of electrons (holes); $m_c(m_v)$ are the quantum numbers of the size quantization of electrons (holes) along the z axis;

$$\Phi_\lambda(z) = (2/d)\sin(\pi m_c z/d)\sin(\pi m_v z/d) \quad (14)$$

is the product of the electron and hole wave functions dependent on z;

$$E_\beta(z, \omega) = \int_{-\infty}^{\infty} dt \exp(i\omega t)E_\beta(z, t); \quad (15)$$

$\mathbf{p}_{cv}^j$ is the quasi-momentum interband matrix element corresponding to the transition from a maximum of the valence band to the conduction band bottom;

$$\hbar\omega_\lambda = \hbar\omega_g + \varepsilon(m_c) + \varepsilon(m_v) + \hbar\Omega_\mu(n + 1/2) \quad (16)$$

is the energy of the electronic excitation with the λ indices; $\varepsilon(m_c)$ [$\varepsilon(m_v)$] is the energy of an electron (a hole) in the size quantization levels; $\Omega_\mu = |e|H/\mu c$ is the cyclotron frequency; $\mu = m_e m_h/(m_e + m_h)$; $m_e(m_h)$ is the effective electron (hole) mass; and γ_λ is the reciprocal nonradiative lifetime of the excited state with the quantum numbers λ. In deducing relationship (12), we used the expression

$$\mathbf{r}_{cv} = -(i/m_0\omega_g)\mathbf{p}_{cv}, \quad (17)$$

where $\mathbf{r}_{cv}$ is the interband matrix element of the radius vector $\mathbf{r}$. Relationship (12) is applicable not only in the case of a monochromatic exciting wave but also in the case of pulse excitation.

Then, we apply the model (see [15–18]) in which the $\mathbf{p}_{cv}^j$ vectors for two degenerate bands have the form

$$\mathbf{p}_{cv}^{\mathrm{I}} = p_{cv}(\mathbf{e}_x - i\mathbf{e}_y)/\sqrt{2}, \quad \mathbf{p}_{cv}^{\mathrm{II}} = p_{cv}(\mathbf{e}_x + i\mathbf{e}_y)/\sqrt{2}, \quad (18)$$

where $\mathbf{e}_x$ and $\mathbf{e}_y$ are the unit vectors along the x and y axes and p_{cv} is the real constant. This model corresponds to heavy holes in crystals with a zinc blende structure when the z axis is aligned along a fourfold symmetry axis [22, 23]. For the circular polarization vectors of exciting light

$$\mathbf{e}_l = (\mathbf{e}_x \pm i\mathbf{e}_y)/\sqrt{2}, \quad (19)$$

the following condition of polarization vector conservation is satisfied:

$$\sum_{j=\mathrm{I,II}}\left[\frac{\mathbf{p}_{cv}^{j*}(\mathbf{e}_l\mathbf{p}_{cv}^{j})}{\omega-\omega_\lambda+i\gamma_\lambda/2} + \frac{\mathbf{p}_{cv}^{j}(\mathbf{e}_l\mathbf{p}_{cv}^{j*})}{\omega+\omega_\lambda+i\gamma_\lambda/2}\right] = \mathbf{e}_l p_{cv}^2\left[\frac{1}{\omega-\omega_\lambda+i\gamma_\lambda/2} + \frac{1}{\omega+\omega_\lambda+i\gamma_\lambda/2}\right], \quad (20)$$

where $\mathbf{e}_l$ is either of vectors (19). As a result, the use of these vectors renders subsequent calculations less cumbersome. Since the projection p_{cvz} is equal to 0 for the model defined by expressions (18), the $\bar{\mathbf{J}}(z, t)$ current density is transverse and the induced charge density

$\rho(z, t)$ is equal to 0. Then, the gauge can be chosen as follows: $\varphi(z, t) = 0$ [where $\varphi(z, t)$ is the scalar potential] and

$$\mathbf{E}(z, t) = -(1/c)\partial\mathbf{A}(z, t)/\partial t, \quad \mathbf{H}(z, t) = \mathrm{rot}\mathbf{A}(z, t),$$

where $\mathbf{A}(z, t)$ is the vector potential of the electromagnetic wave. With the use of the expression

$$E_\alpha(z, \omega) = (i\omega/c)A_\alpha(z, \omega), \tag{21}$$

we change over to the vector potential in formula (12). The result is conveniently expressed as

$$\bar{J}_\alpha(z, t) = -\frac{e_{l\alpha}\gamma_r\nu}{8\pi^2}\sum_\lambda \Phi_\lambda(z) \times \int_{-\infty}^{\infty} \omega d\omega e^{-i\omega t}\left[\frac{1}{\omega - \omega_\lambda + i\gamma_\lambda/2} + \frac{1}{\omega + \omega_\lambda + i\gamma_\lambda/2}\right] \times \int_0^d dz' A(z', \omega)\Phi_\lambda(z') + \text{c.c.}, \tag{22}$$

where

$$\gamma_r = (2e^2/\hbar c\nu)(p_{cv}^2/m_0\hbar\omega_g)(|e|H/m_0c) \tag{23}$$

is the reciprocal radiative lifetime of an electron–hole pair in the magnetic field at $\kappa d = 0$ [13, 18] and the scalar $A(z, \omega)$ is given by the formula

$$\mathbf{A}(z, \omega) = \mathbf{e}_l A(z, \omega) + \mathbf{e}_l^* A^*(z, -\omega). \tag{24}$$

3. THE ELECTRIC FIELD OF AN ELECTROMAGNETIC WAVE

Further calculations will be performed under two assumptions. First, we assume that the plane wave is monochromatic with the frequency ω_l; i.e., in formula (24),

$$A(z, \omega) = 2\pi\delta(\omega - \omega_l)A(z), \tag{25}$$

and the $\mathbf{A}(z, t)$ vector takes the form

$$\mathbf{A}(z, t) = \mathbf{e}_l \exp(-i\omega_l t)A(z) + \text{c.c.} \tag{26}$$

Second, we will include only one excited level in the quantum well. The other levels are assumed to be sufficiently far from the chosen level, and their effect is ignored. The scalar amplitude $A(z)$ of the vector potential in the barrier region is defined by the equation

$$d^2A/dz^2 + \kappa_1^2 A = 0, \quad \kappa_1 = \nu_1\omega_l/c, \quad z \le 0, \quad z \ge d, \tag{27}$$

where ν_1 is the refractive index of the barrier. In the quantum well region $0 \le z \le d$, we have the equation

$$d^2A/dz^2 + \kappa^2 A = -(4\pi/c)\bar{J}(z). \tag{28}$$

Here, according to formulas (22) and (25), the scalar amplitude $\bar{J}(z)$ of the current density with due regard for one excited level is written as

$$\bar{J}(z) = -(\gamma_r\nu\omega_l/4\pi)\Phi(z)\int_0^d dz' A(z')\Phi(z') \times [(\omega_l - \omega_0 + i\gamma/2)^{-1} + (\omega_l + \omega_0 + i\gamma/2)^{-1}] + \text{c.c.}, \tag{29}$$

where, for simplicity, we used the designations

$$\Phi_\lambda(z) = \Phi(z), \quad \omega_\lambda = \omega_0, \quad \gamma_\lambda = \gamma. \tag{30}$$

Near the resonance $\omega_l = \omega_0$, the term proportional to $(\omega_l + \omega_0 + i\gamma/2)^{-1}$ in Eq. (29) is disregarded. Equation (29) is integro-differential. If the solution of Eq. (29) is formally represented as the sum of the general solution of a homogeneous equation and the particular solution of a nonhomogeneous equation, Eq. (29) transforms into the Fredholm integral equation of the second kind[2]

$$A(z) = C_1 e^{i\kappa z} + C_2 e^{-i\kappa z} - \frac{i(\gamma_r/2)F(z)}{\omega_l - \omega_0 + i\gamma/2}\int_0^d dz' A(z')\Phi(z'). \tag{31}$$

Here, C_1 and C_2 are arbitrary constants, which are determined from the boundary conditions in the planes $z = 0$ and d, and the function $F(z)$ is given by

$$F(z) = \exp(i\kappa z)\int_0^z dz' \exp(-i\kappa z')\Phi(z') + \exp(-i\kappa z)\int_z^d dz' \exp(i\kappa z')\Phi(z'). \tag{32}$$

At $\gamma_r \ll \gamma$, the integral term in Eq. (31) is a small perturbation. Hence, it is sufficient to allow for the first approximation with respect to this term. In the case of $\gamma_r \ge \gamma$, the complete iteration series should be taken into account. By representing the sought function $A(z)$ as the series

$$A(z) = A_0(z) + A_1(z) + A_2(z) + \ldots, \quad A_0(z) = C_1\exp(i\kappa z) + C_2\exp(-i\kappa z) \tag{33}$$

and substituting it into Eq. (31), we obtain the recurrent relation

$$A_j(z) = sF(z)\int_0^d dz'\Phi(z')A_{j-1}(z'), \quad j = 1, 2, 3\ldots.$$

[2] A similar equation for an inversion layer was considered in [24].

The use of this relation enables us to reduce series (33) to the geometric progression

$$\begin{aligned} A(z) &= A_0(z) - hsF(z)(1 - s\varepsilon + s^2\varepsilon^2 - \ldots) \\ &= A_0(z) - hsF(z)/(1 + s\varepsilon), \end{aligned} \tag{34}$$

where, for simplicity, we introduced the designations

$$\int_0^d dz\Phi(z)A_0 = h, \quad i(\gamma_r/2)/(\omega_l - \omega_0 + i\gamma_r/2) = s$$

and the complex function

$$\varepsilon = \varepsilon' + i\varepsilon'' = \int_0^d dz'\Phi(z')F(z'). \tag{35}$$

Substitution of h, s, and ε into relationship (34) gives the following solution:

$$\begin{aligned} A(z) &= C_1 e^{i\kappa z} + C_2 e^{-i\kappa z} - \frac{i(\gamma_r/2)F(z)}{\omega_l - \omega_0 + i(\gamma + \gamma_r\varepsilon)/2} \\ &\times \int_0^d dz'(C_1 e^{i\kappa z'} + C_2 e^{-i\kappa z'})\Phi(z'). \end{aligned} \tag{36}$$

The complex quantity ε determines changes in the broadening and shifts of the level due to spatial dispersion of the wave. As follows from definition (35), in the limiting case $\kappa d = 0$, $\varepsilon = \delta_{m_c m_v}$ and the integral on the right-hand side of solution (36) is equal to $(C_1 + C_2)\delta_{m_c m_v}$; i.e., in this limiting case, only the allowed transitions with $m_c = m_v$ contribute to the current. For $\kappa d \neq 0$, the forbidden transition at $m_c \neq m_v$ also contributes to the interband current and leads to the appearance of the ε quantity in the denominator of solution (36). However, $\varepsilon \longrightarrow 0$ at $\kappa d \longrightarrow 0$. Note also that the function $F(z)$ [formula (32)] is equal to $\delta_{m_c m_v}$ at $\kappa d \longrightarrow 0$. Hereafter, we will treat only the case of the allowed transitions.

The solution of Eq. (27) is written as

$$\begin{aligned} A^l(z) &= A_0\exp(i\kappa_1 z) + C_R\exp(-i\kappa_1 z), \quad z \le 0, \\ A^r(z) &= C_T\exp(i\kappa_1 z), \quad z \ge d, \end{aligned} \tag{37}$$

where C_R and C_T determine the amplitudes of the wave reflected from the well and the wave transmitted through the well. At the boundaries $z = 0$ and d, the continuity of the wave magnetic field provides continuity of dA/dz and the continuity of the tangential projections of the electric field ensures the continuity of $A(z)$. As a result, the coefficients C_1, C_2, C_R, and C_T are defined by the expressions

$$\begin{aligned} C_i &= A_0\mathcal{C}_i \quad (i = 1, 2), \quad C_{R(T)} = A_0\mathcal{C}_{R(T)}, \\ \mathcal{C}_1 &= (2/\Delta)\exp(-i\kappa d)[1 + \zeta + (1 - \zeta)\mathcal{N}], \\ \mathcal{C}_2 &= -(2/\Delta)(1 - \zeta)[\exp(i\kappa d) + \mathcal{N}], \quad \mathcal{C}_R = \rho/\Delta, \\ \mathcal{C}_T &= 4\zeta\exp(-i\kappa_1 d)[1 + \exp(-i\kappa d)\mathcal{N}]/\Delta, \end{aligned} \tag{38}$$

$$\begin{aligned} \Delta &= (\zeta + 1)^2\exp(-i\kappa d) - (\zeta - 1)^2\exp(i\kappa d) \\ &- 2(\zeta - 1)\mathcal{N}[(\zeta + 1)\exp(-i\kappa d) + \zeta - 1], \\ \rho &= 2i(\zeta^2 - 1)\sin\kappa d \\ &+ 2[(\zeta^2 + 1)\exp(-i\kappa d) + \zeta^2 - 1]\mathcal{N}, \end{aligned} \tag{39}$$

where

$$\zeta = \kappa/\kappa_1 = \nu/\nu_1, \tag{40}$$

$$\begin{aligned} \mathcal{N} &= -sF^2(0) \\ &= -i(\gamma_r/2)F^2(0)/[\omega_l - \omega_0 + i(\gamma + \gamma_r\varepsilon)/2]. \end{aligned} \tag{41}$$

By returning to the time representation and changing over from $A(z)$ to the electric fields on the left $[E^l(z, t)]$ and right $[E^r(z, t)]$ of the quantum well in relationship (37), we obtain

$$\mathbf{E}^l(z, t) = \mathbf{e}_l E_0 e^{-i\omega_l t}[e^{i\kappa_1 z} + \mathcal{C}_R e^{-i\kappa_1 z}] + \text{c.c.}, \tag{42}$$

$$\mathbf{E}^r(z, t) = \mathbf{e}_l E_0 \mathcal{C}_T e^{-i(\omega_l t - \kappa_1 z)} + \text{c.c.} \tag{43}$$

The electric field inside the well is given by formula (36) after replacing $A(z)$ by $E(z)$ and changing over to the time representation. The relationships for the fields include ε and $F(0)$. The expression for the field inside the well, in addition, involves the $F(z)$ function, which contributes to the coordinate dependence of the field. At $m_c = m_v = m$, the $F(z)$ and ε quantities are described by the formulas

$$\begin{aligned} F(z) &= iB\{2 - \exp(i\kappa z) - \exp[i\kappa(d - z)] \\ &- (\kappa d/\pi m)^2\sin^2(\pi m z/d)\}, \\ F(0) &= F(d) = iB[1 - \exp(i\kappa d)], \end{aligned} \tag{44}$$

$$B = \frac{4\pi^2 m^2}{\kappa d[4\pi^2 m^2 - (\kappa d)^2]}, \tag{45}$$

$$\begin{aligned} \varepsilon' &= F^2(0)\exp(-i\kappa d) = 4B^2\sin^2(\kappa d/2), \\ \varepsilon'' &= 2B[1 - B\sin\kappa d - 3(\kappa d)^2/8\pi^2 m^2]. \end{aligned} \tag{46}$$

The dependences of ε' and ε'' on the κd parameter are displayed in Fig. 1.

In the limiting case of a homogeneous medium ($\kappa_1 = \kappa$), we have

$$\mathbf{E}^l(z, t) = \mathbf{e}_l E_0 e^{-i\omega_l t}\left[e^{i\kappa z} - \frac{i(\tilde{\gamma}_r/2)}{\Omega + i\Gamma/2}e^{i\kappa(d - z)}\right] + \text{c.c.}, \tag{47}$$

$$\mathbf{E}^r(z, t) = \mathbf{e}_l E_0 e^{-i(\omega_l t - \kappa z)}\left[1 - \frac{i(\tilde{\gamma}_r/2)}{\Omega + i\Gamma/2}\right] + \text{c.c.}, \tag{48}$$

where we introduced the following new designations:

$$\Omega = \omega_l - \omega_0 - \varepsilon''\gamma_r/2, \quad \Gamma = \gamma + \tilde{\gamma}_r,$$
$$\tilde{\gamma}_r = \gamma_r \left| \int_0^d dz \exp(i\kappa z)\Phi(z) \right|^2 = \gamma_r \varepsilon'. \tag{49}$$

The field inside the well has the form

$$\mathbf{E}(z, t) = \mathbf{e}_l E_0 e^{-i\omega_l t}\left[e^{i\kappa z} - \frac{i(\gamma_r/2)F(0)F(z)}{\Omega + i\Gamma/2} \right] + \text{c.c.} \tag{50}$$

The quantity $\tilde{\gamma}_r$ coincides with the reciprocal radiative lifetime calculated in [13] and [18] for an electron–hole pair in a strong magnetic field at $\mathbf{K}_\perp = 0$ for an arbitrary value of κd. A comparison of expressions (47) and (48) with the corresponding relationships obtained in [18] for the fields on the left and right of the well shows that, at $\kappa d \neq 0$, γ_r is replaced by $\tilde{\gamma}_r$, the level is shifted by $\gamma_r\varepsilon''$, and the additional multiplier $\exp(i\kappa d)$ appears in the formula for the wave induced on the left of the well. It can be demonstrated that, upon replacement of $d - z$ by z, the field induced on the left of the well coincides with that induced on the right of the well. It is seen from formula (46) and Fig. 1 that $\tilde{\gamma}_r$ decreases with an increase in κd. At $\kappa d \gg 1$, $\tilde{\gamma}_r \longrightarrow 0$, which corresponds to a change-over from the quantum well to a bulk crystal. In this case, the contribution from one level to the induced fields and, hence, to the absorption and reflection tends to zero.

In the limiting case $\gamma_r = 0$, formulas (42) and (43) lead to the standard solution for a monochromatic wave propagating in a medium containing a transparent layer of another material [26].

4. REFLECTION, ABSORPTION, AND TRANSMISSION OF AN ELECTROMAGNETIC WAVE

Therefore, according to expression (42), the electric field vector $\Delta\mathbf{E}^l(z, t)$ of the reflected wave with a circular polarization is written as

$$\Delta\mathbf{E}^l(z, t) = \mathbf{e}_l E_0 \mathscr{C}_R e^{-i(\omega_l t + \kappa_1 z)} + \text{c.c.} \tag{51}$$

According to expression (43), the field vector of the transmitted wave is represented as

$$\mathbf{E}^r(z, t) = \mathbf{e}_l E_0 \mathscr{C}_T e^{-i(\omega_l t - \kappa_1 z)} + \text{c.c.} \tag{52}$$

By analogy with [18], we introduce the fraction of the reflected energy $\mathscr{R}$, which is defined as the ratio between the magnitudes of the incident and reflected energy fluxes, i.e.,

$$\mathscr{R} = |\mathscr{C}_R|^2. \tag{53}$$

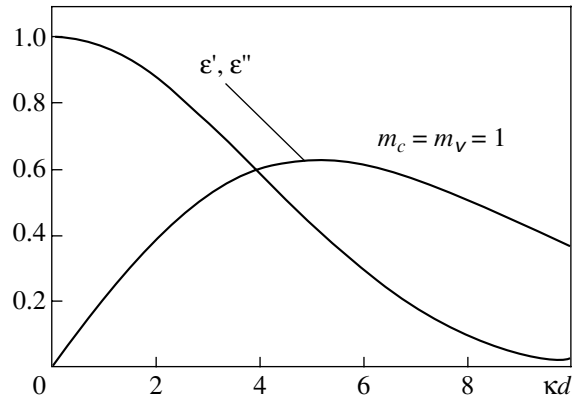

Fig. 1. Functions ε' and ε'' determining the change in width and the shift in reflection, transmission, and absorption peaks with inclusion of the spatial dispersion in the case of a homogeneous medium. $m_c(m_v)$ are the quantum numbers of the size quantization of electrons (holes).

The fraction of the transmitted energy $\mathscr{T}$ is given by

$$\mathscr{T} = |\mathscr{C}_T|^2, \tag{54}$$

and the fraction of the absorbed energy $\mathscr{A}$ is determined as

$$\mathscr{A} = 1 - \mathscr{R} - \mathscr{T}. \tag{55}$$

First, we examine how the spatial dispersion affects the frequency dependence of the reflection when the medium is homogeneous. In this case, from formulas (38), (39), and (53)–(55), we find

$$\mathscr{R} = \frac{(\tilde{\gamma}_r/2)^2}{\Omega^2 + \Gamma^2/4}, \quad \mathscr{A} = \frac{\gamma\tilde{\gamma}_r/2}{\Omega^2 + \Gamma^2/4},$$
$$\mathscr{T} = \frac{\Omega^2 + \gamma^2/4}{\Omega^2 + \Gamma^2/4}. \tag{56}$$

These expressions coincide in form with those obtained in the absence of dispersion. The difference consists in replacing the constant γ_r by the function $\tilde{\gamma}_r$ ($\tilde{\gamma}_r \longrightarrow \gamma_r$ at $\kappa d \longrightarrow 0$) and the appearance of the function ε'', which determines the shift of the extremum in the corresponding curve and vanishes in the limit $\kappa d = 0$.

In the case of reflection, the spatial dispersion has the strongest effect at $\gamma \gg \gamma_r$. Actually, at $\gamma \ll \gamma_r$, the maximum reflection $\mathscr{R}_{\max} \cong 1$ in the reflection curve defined by relationships (56) is approximately equal to 1 and almost does not depend on κd. On the other hand, at $\gamma \gg \gamma_r$, $\tilde{\gamma}_r$ in the denominator of formulas (56) makes a small contribution to the dependence on κd and this dependence is governed by the $\tilde{\gamma}_r$ function in the numerator. However, in this case, $\mathscr{R}_{\max} = (\tilde{\gamma}_r/\gamma)^2 \ll 1$. The opposite situation is observed for transmission. At $\gamma \ll \gamma_r$, the minimum transmission $\mathscr{T}_{\min}$ in the transmission curve is equal to $(\gamma/\tilde{\gamma})^2 \ll 1$, noticeably depends on

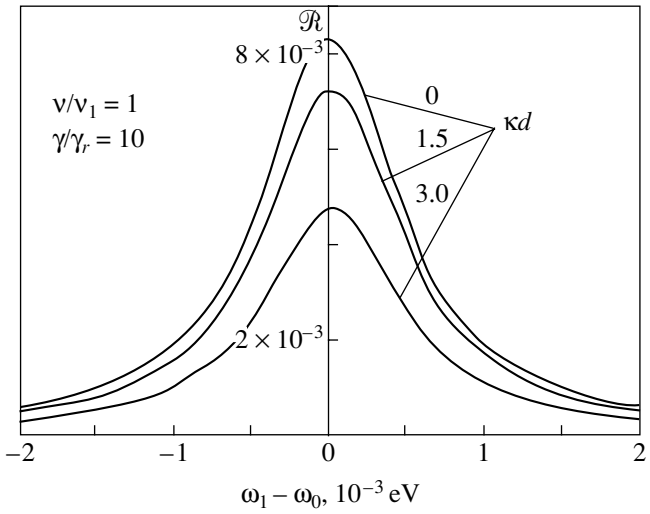

Fig. 2. Effect of spatial dispersion on the frequency dependence of the reflection $\mathcal{R}$ for a homogeneous medium. $\zeta = 1$, $\gamma/\gamma_r = 10$, $\gamma_r = 10^{-4}$ eV, and $m_c = m_\nu = 1$.

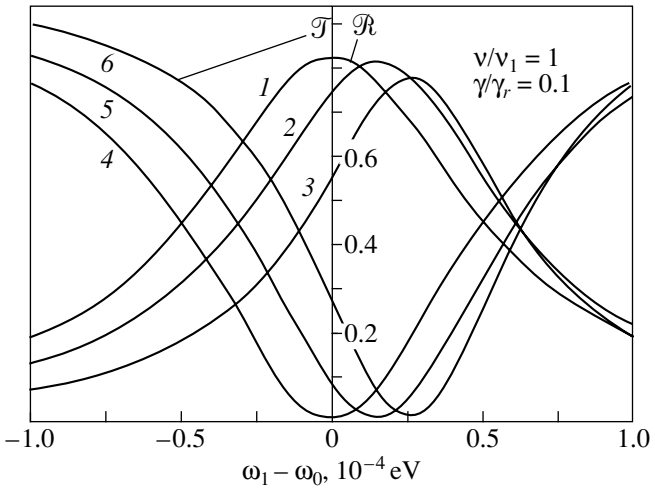

Fig. 3. Effect of spatial dispersion on the frequency dependences of (*1–3*) the reflection $\mathcal{R}$ and (*4–6*) the transmission $\mathcal{T}$ for a homogeneous medium at κd = (*1*, *4*) 0, (*2*, *5*) 1.5, and (*3*, *6*) 3. $\zeta = 1$, $\gamma/\gamma_r = 0.1$, $\gamma_r = 10^{-4}$ eV, and $m_c = m_\nu = 1$.

κd, and increases with an increase in κd. At the same time, for $\gamma \gg \gamma_r$, $\mathcal{T} \cong 1$ and only slightly depends on κd. The absorption $\mathcal{A}_{\max}$ at the maximum in these limiting cases is equal to $2\gamma/\tilde{\gamma}_r$ at $\gamma \ll \gamma_r$ and $2\tilde{\gamma}_r/\gamma$ at $\gamma \gg \gamma_r$. In both cases, $\mathcal{A}_{\max} \ll 1$ but $\mathcal{A}_{\max} \gg \mathcal{R}_{\max}$ at $\gamma \gg \gamma_r$ and $\mathcal{A}_{\max} \gg \mathcal{T}_{\min}$ at $\gamma \ll \gamma_r$. The frequency dependences of $\mathcal{R}$, $\mathcal{A}$, and $\mathcal{T}$ for the limiting cases $\gamma \gg \gamma_r$ and $\gamma \ll \gamma_r$ are plotted in Figs. 2–4.

Figure 2 demonstrates how the spatial dispersion affects the height and width of the reflection peak. These parameters increase with an increase in κd. At the same time, the frequency shift of the peak is virtually absent, since $\varepsilon''\gamma_r \ll \gamma$. By contrast, the dispersion leads to a shift of the reflection peak in Fig. 3 without changing its shape. The dependence of the transmission $\mathcal{T}$ at $\gamma \ll \gamma_r$ is also depicted in Fig. 3. In this case, an increase in κd results in a shift of $\mathcal{T}_{\min}$ and its increase, which is poorly seen because of the chosen scale along the ordinate axis. The dependences of the absorption $\mathcal{A}$ for the two limiting cases are displayed in Fig. 4. A series of narrow peaks (Fig. 4b, $\gamma \ll \gamma_r$) clearly illustrates both an increase in the absorption $\mathcal{A}_{\max}$ and its shift. This shift (as for $\mathcal{T}$ in Fig. 2) is associated with the fact that $\mathcal{A}_{\max} \sim \tilde{\gamma}_r^{-1}$ and $\varepsilon''\gamma_r \cong \tilde{\gamma}_r$. As follows from the curves depicted in Fig. 4a, at $\gamma \gg \gamma_r$, the shift is small and $\mathcal{A}_{\max}$ decreases with an increase in κd.

If the medium inhomogeneity is taken into consideration, i.e., in the case when $\zeta \neq 1$ ($\nu \neq \nu_1$) and the spa-

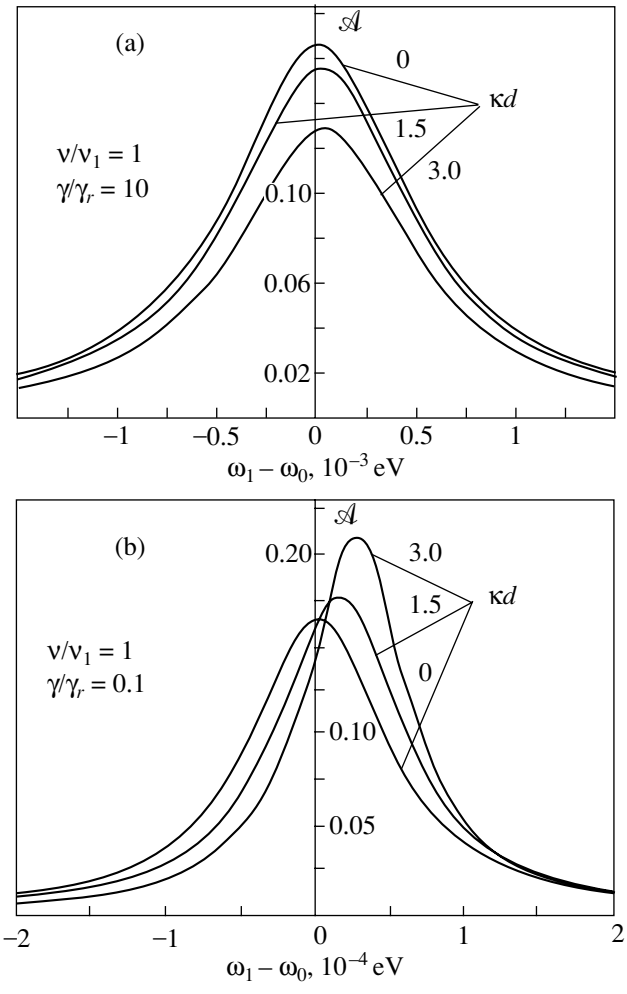

Fig. 4. Effect of spatial dispersion on the frequency dependence of the absorption $\mathcal{A}$ for a homogeneous medium at (a) $\gamma \gg \gamma_r$ and (b) $\gamma \ll \gamma_r$. $\zeta = 1$, $\gamma_r = 10^{-4}$ eV, and $m_c = m_\nu = 1$.

tial dispersion is ignored, instead of formulas (56), we have the expressions

$$\mathcal{R} = \frac{\zeta^2(\gamma_r/2)^2}{\Omega^2 + (\gamma + \zeta\gamma_r)^2/4}, \quad \mathcal{A} = \frac{\zeta\gamma\gamma_r/2}{\Omega^2 + (\gamma + \zeta\gamma_r)^2/4},$$
$$\mathcal{T} = \frac{\Omega^2 + \gamma^2/4}{\Omega^2 + (\gamma + \zeta\gamma_r)^2/4}. \tag{57}$$

As is seen from expressions (57), in this limiting case, γ_r is replaced by the quantity $\zeta\gamma_r$ defined by relationship (23), in which the refractive index ν_1 refers to the barrier material. This result coincides with the expressions obtained in our earlier work [18].

5. THE GENERAL CASE

In this section, we analyze the general case when the medium is inhomogeneous and the spatial dispersion is substantial. By using formulas (38), (39), and (41), the reflection can be represented in the form

$$\mathcal{R} = \left\{\frac{(\tilde{\gamma}_r/2)^2 X_1}{\Omega^2 + \Gamma^2/4} + \nu_1 - \frac{(\tilde{\gamma}_r/2)(Y_1\Omega + Z_1\Gamma/2)}{\Omega^2 + \Gamma^2/4}\right\}/|\Delta|^2, \tag{58}$$

$$|\Delta|^2 = \nu + \frac{(\tilde{\gamma}_r/2)^2 X - (\tilde{\gamma}_r/2)(Y\Omega + Z\Gamma/2)}{\Omega^2 + \Gamma^2/4}, \tag{59}$$

where

$$\nu = 4\zeta^2\cos^2\kappa d + (\zeta^2+1)^2\sin^2\kappa d,$$
$$\nu_1 = (\zeta^2-1)^2\sin^2\kappa d, \tag{60}$$

$$X = 2(\zeta-1)^2[\zeta^2 + 1 + (\zeta^2-1)\cos\kappa d],$$
$$X_1 = 2[\zeta^4 + 1 + (\zeta^4-1)\cos\kappa d], \tag{61}$$

$$Y = 2(\zeta-1)^2(\zeta+1)[(\zeta+1)\cos\kappa d + \zeta - 1]\sin\kappa d,$$
$$Y_1 = 2\zeta^2(\zeta^2-1)\sin\kappa d, \tag{62}$$

$$Z = 2(\zeta-1)\{(\zeta-1)(\zeta+1)^2\sin^2\kappa d - 2\zeta[(\zeta+1)\cos\kappa d + \zeta - 1]\}, \tag{63}$$
$$Z_1 = 2(\zeta-1)^3(\zeta+1)\sin\kappa d.$$

The main contribution to the denominator [defined by formula (59)] of the $\mathcal{R}$ function is made by the function ν ($\nu \gg 1$). The other terms are small and can be disregarded. The exception is the term proportional to Γ, which makes a substantial contribution at $\gamma \ll \tilde{\gamma}_r$. In the numerator of $\mathcal{R}$, the function ν_1 describes the reflection from the quantum well boundaries. This reflection in the frequency range corresponding to the peak width does not depend on the light frequency and vanishes in the limiting cases $\kappa d \longrightarrow 0$ and $\zeta \longrightarrow 0$ [see relationship (60)]. At $\gamma \ll \tilde{\gamma}_r$, the first term in the numerator of expression (58) predominantly contributes to the reflection and $\mathcal{R}$, in this case, is approximately equal to 1. For $\gamma \gg \tilde{\gamma}_r$, the first term becomes small and the ν_1 function and the term proportional to Ω (which is responsible for reflection peak asymmetry) play a considerable role. The frequency dependence of the reflection is shown in Fig. 5. It can be seen that the peaks are strongly asymmetric and the dependence of $\mathcal{R}_{max}$ on κd is nonmonotonic. The nonmonotonic behavior is determined by the magnitude and sign of the Y_1 function

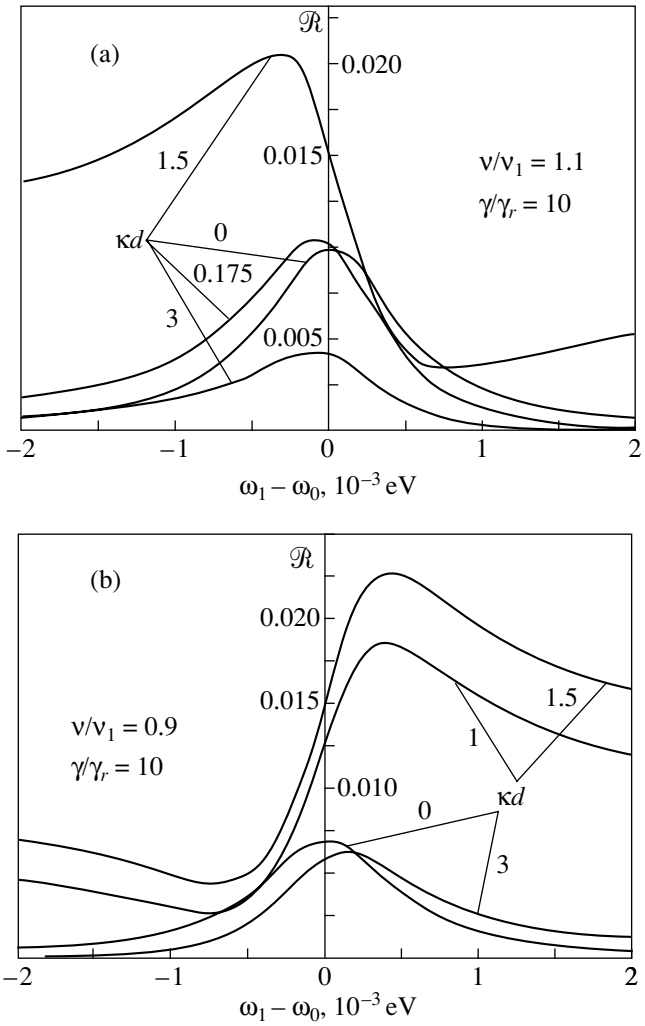

Fig. 5. Frequency dependences of the reflection $\mathcal{R}$ with inclusion of the spatial dispersion of the light and the inhomogeneity of the medium at ζ: (a) >1 (the curve at $\kappa d = 0.175$ corresponds to GaAs) and (b) <1. $\gamma \gg \gamma_r$, $\gamma_r = 10^{-4}$ eV, and $m_c = m_v = 1$.

given by expression (62). In particular, Y_1 varies from 0.507 (Fig. 5a, curve at $\kappa d = 1.5$) to 0.072 (Fig. 5a, curve at $\kappa d = 3$). In the latter case, $Y_1\Omega$ weakly affects the peak shape and the asymmetry is insignificant, because the main contribution is made by the first term in expression (58). The same situation is observed in Fig. 5b. However, in this case, $Y_1 < 0$ and the peak maximum occurs at $\Omega > 0$. At $\gamma_r \longrightarrow 0$,

$$\mathcal{R} = \frac{v_1}{v} = \frac{(\zeta^2 - 1)^2 \sin^2 \kappa d}{4\zeta^2 \cos^2 \kappa d + (\zeta^2 + 1)^2 \sin^2 \kappa d}. \quad (64)$$

This corresponds to a reflection from a plane transparent layer in a medium with a different refractive index. A comparison of Figs. 2 and 5 permits us to draw the inference that the medium inhomogeneity results in a stronger dependence of the reflection on the κd parameter.

The absorption $\mathcal{A}$ and the transmission $\mathcal{T}$ are defined by the relationships

$$\mathcal{A} = \frac{4\zeta[\zeta^2 + 1 + (\zeta^2 - 1)\cos \kappa d]\gamma\tilde{\gamma}_r}{|\Delta|^2(\Omega^2 + \Gamma^2/4)}, \quad (65)$$

$$\mathcal{T} = \frac{4\zeta^2(\Omega^2 + \gamma^2/4)}{|\Delta|^2(\Omega^2 + \Gamma^2/4)}, \quad (66)$$

which, in the limiting cases $\zeta = 1$ and $\kappa d = 0$, change over into expressions (56) and (57), respectively. As was noted above, the v_1 function associated with the reflection from the well boundaries and the term proportional to Ω in the numerator appreciably contribute to the reflection curve. It is these terms that determine strong shifts of the peak maximum and the appearance of a minimum. On the other hand, expressions (65) for the absorption $\mathcal{A}$ and relationship (66) for the transmission $\mathcal{T}$ coincide in form with those obtained for a homogeneous medium. The difference resides in the appearance of multipliers that are virtually independent of Ω and weakly depend on κd. Therefore, the effect of the medium inhomogeneity on the absorption and transmission is considerably weaker than that on the reflection.

6. CONCLUSIONS

The above analysis allows us to make the general conclusion that inclusion of the spatial dispersion of the electromagnetic wave and the medium inhomogeneity most strongly affects the reflection and leads to a radical change in the shape of the reflection peak. The changes are most pronounced in the limiting case $\gamma \gg \tilde{\gamma}_r$ when $\mathcal{R}_{\max} \simeq (\tilde{\gamma}_r/\gamma)^2$. This is explained by the fact that the v_1 function described by expression (60) and the term linear in Ω in relationship (58) are small and can affect the first term only if it is also small. In the other limiting case $\gamma \ll \tilde{\gamma}_r$, $\mathcal{R}_{\max} \simeq 1$ and the influence of the above terms is almost negligible. When either the spatial dispersion or the medium inhomogeneity is taken into account, the reflection changes rather weakly, because, in these limiting cases, $v_1 = Y = Y_1 = 0$. At $\gamma \gg \tilde{\gamma}_r$, the medium inhomogeneity and the spatial dispersion have a weaker effect on the $\mathcal{A}$ and $\mathcal{T}$ quantities. Indeed, it follows from expression (66) that, in this case, $\mathcal{T} \simeq 1$ and a substantial change in the small quantity $\mathcal{R}_{\max}$ weakly affects $\mathcal{T}_{\min}$. The same is true for $\mathcal{A}_{\max} \gg \mathcal{R}_{\max}$.

The dependences of the $\mathcal{R}$, $\mathcal{A}$, and $\mathcal{T}$ functions on the κd parameter, which characterizes the spatial dispersion of the wave in the quantum well, were obtained for square quantum wells and infinitely high barriers. In real semiconductor heterostructures, impurity electrons of the barrier transfer to the quantum well and distort its square shape in the vicinity of boundaries. Therefore, the theory developed above is valid for pure materials and wide wells when the size of distorted boundary regions is small compared to the well width. Moreover, the theory is true for deep wells in which the location of the first levels and the corresponding wave functions only slightly differ from those in an infinitely deep well. The one-level approximation used above assumes that energy spacing between the adjacent levels in the quantum well is larger than the width of the level under consideration. This imposes the restriction on the well width from above. For example, at $d = 500$ Å and $m_c = 0.06m_0$, the difference between the energies of the two lowest-lying levels of size quantization is equal to approximately 10^{-3} eV.

The results obtained above are valid in the case when the Coulomb interaction weakly affects the spectrum of electron–hole pairs generated by light. The corresponding corrections are small if the following inequalities are satisfied [21, 26]:

$$a_{\text{exc}}^2 \gg a_H^2, \quad a_{\text{exc}} \gg d, \quad (67)$$

where a_H is the magnetic length and $a_{\text{exc}} = \hbar^2\varepsilon_0/\mu e^2$ is the radius of a Wannier–Mott exciton in a zero magnetic field. It can be seen that the first inequality (67) can be met in sufficiently strong magnetic fields. As regards the second inequality, the larger the permittivity ε_0 of the material of the quantum well and the smaller the reduced effective mass μ of the electron and hole, the better the fulfillment of this inequality. Note that the second condition (67) for heterostructures based on gallium arsenide is satisfied at $d \le 150$ Å, when the spatial dispersion and the medium inhomogeneity have a comparatively weak effect on the quantities studied. This is evident from Fig. 5a, in which the curve at $\kappa d = 0.175$ corresponds to a gallium arsenide quantum well of width $d \simeq 62$ Å. In this case, the second inequality is approximately met, but the shift and asymmetry of the reflection peak are small. When the second inequality (67) is not fulfilled, the dependence of the wave function on the z coordinate cannot be represented by formula (14). However, the exciton effect does not bring about radical changes in the results obtained and only affects the aforementioned radiative broadening γ_r of

the electronic excitation. The same holds true for the exciton levels in a zero magnetic field.

ACKNOWLEDGMENTS

This work was supported by the Russian Foundation for Basic Research (project no. 00-02-16904) and the International Scientific and Technical Program "Physics of Solid-State Nanostructures" (project no. 97-1099). S.T. Pavlov acknowledges the support and hospitality of Zacatecas University and the Mexican CONACyT. D.A. Contreras-Solorio acknowledges the support of the CONACyT (27736-E).

REFERENCES

1. H. Stolz, *Time-Resolved Light Scattering from Excitons* (Springer-Verlag, Berlin, 1994), Springer Tracts Mod. Phys. **130**.
2. J. Shah, *Ultrafast Spectroscopy of Semiconductors and Semiconductor Nanostructures* (Springer-Verlag, Berlin, 1996).
3. H. Hang and S. W. Koch, *Quantum Theory of the Optical and Electronic Properties of Semiconductors* (World Scientific, Singapore, 1993).
4. S. Mucamel, *Principles of Nonlinear Optical Spectroscopy* (Oxford Univ. Press, Oxford, 1995).
5. L. C. Andreani, F. Tassone, and F. Bassani, Solid State Commun. **77** (11), 641 (1991).
6. L. C. Andreani, in *Confined Electrons and Photons*, Ed. by E. Burstein and C. Weisbuch (Plenum, New York, 1995), p. 57.
7. E. L. Ivchenko, Fiz. Tverd. Tela (Leningrad) **33** (8), 2388 (1991) [Sov. Phys. Solid State **33**, 1344 (1991)].
8. F. Tassone, F. Bassani, and L. C. Andreani, Phys. Rev. B **45** (11), 6023 (1992).
9. T. Stroucken, A. Knorr, C. Anthony, *et al.*, Phys. Rev. Lett. **74** (9), 2391 (1995).
10. T. Stroucken, A. Knorr, P. Thomas, and S. W. Koch, Phys. Rev. B **53** (4), 2026 (1996).
11. M. Hübner, T. Kuhl, S. Haas, *et al.*, Solid State Commun. **105** (2), 105 (1998).
12. I. G. Lang, V. I. Belitsky, and M. Cardona, Phys. Status Solidi A **164** (1), 307 (1997).
13. I. G. Lang and V. I. Belitsky, Phys. Lett. A **245** (3–4), 329 (1998).
14. I. G. Lang and V. I. Belitsky, Solid State Commun. **107** (10), 577 (1998).
15. I. G. Lang, L. I. Korovin, D. A. Contreras-Solorio, and S. T. Pavlov, Fiz. Tverd. Tela (St. Petersburg) **43** (6), 1117 (2001) [Phys. Solid State **43**, 1159 (2001)]; cond-mat/0004178.
16. L. I. Korovin, I. G. Lang, D. A. Contreras-Solorio, and S. T. Pavlov, Fiz. Tverd. Tela (St. Petersburg) **42** (12), 2230 (2000) [Phys. Solid State **42**, 2300 (2000)]; cond-mat/0006364.
17. D. A. Contreras-Solorio, S. T. Pavlov, L. I. Korovin, and I. G. Lang, Phys. Rev. B **62** (23), 16815 (2000); cond-mat/0002229.
18. I. G. Lang, L. I. Korovin, D. A. Contreras-Solorio, and S. T. Pavlov, cond-mat/0001248.
19. C. V. Duke, Phys. Rev. **168**, 816 (1968).
20. A. Ya. Shik, Fiz. Tverd. Tela (Leningrad) **12** (1), 67 (1970) [Sov. Phys. Solid State **12**, 53 (1970)].
21. I. V. Lerner and Yu. E. Lozovik, Zh. Éksp. Teor. Fiz. **78** (3), 1167 (1980) [Sov. Phys. JETP **51**, 588 (1980)].
22. J. M. Luttinger and W. Kohn, Phys. Rev. **97**, 869 (1955).
23. I. M. Tsidil'kovskiĭ, *Band Structure of Semiconductors* (Nauka, Moscow, 1978).
24. L. I. Korovin and B. É. Éshpulatov, Fiz. Tverd. Tela (Leningrad) **21** (12), 3703 (1979) [Sov. Phys. Solid State **21**, 2137 (1979)].
25. L. I. Korovin, I. G. Lang, and S. T. Pavlov, Zh. Éksp. Teor. Fiz. **118** (2), 388 (2000) [JETP **91**, 338 (2000)]; cond-mat/0004373.
26. L. D. Landau and E. M. Lifshitz, *Course of Theoretical Physics*, Vol. 8: *Electrodynamics of Continuous Media* (Nauka, Moscow, 1982; Pergamon, New York, 1984).

Translated by O. Borovik-Romanova

Physics of the Solid State, Vol. 43, No. 11, 2001, pp. 2192–2198. Translated from Fizika Tverdogo Tela, Vol. 43, No. 11, 2001, pp. 2100–2106.
Original Russian Text Copyright © 2001 by Stepanov, Popok, Hole, Bukharaev.

LOW-DIMENSIONAL SYSTEMS AND SURFACE PHYSICS

Interaction of High-Power Laser Pulses with Glasses Containing Implanted Metallic Nanoparticles

A. L. Stepanov[1, 2], V. N. Popok[3, 4], D. E. Hole[5], and A. A. Bukharaev[2]

[1]*I Physikalisches Institut, Aachen Technical University RWTH, Aachen, D-52056 Germany*

[2]*Kazan Physicotechnical Institute, Russian Academy of Sciences, Sibirskiĭ trakt 10/7, Kazan, 420029 Tatarstan, Russia*

[3]*Belarussian State University, pr. F. Skoriny 4, Minsk, 220050 Belarus*

[4]*Göteborg University and Chalmers University of Technology, Göteborg, S-41296 Sweden*

[5]*University of Sussex, Brighton BN1 9QH, United Kingdom*

e-mail: stepanov@physik.rwth-aachen.de

Received March 1, 2001

Abstract—Sodium calcium silicate glasses with Ag^+ implanted ions are studied. The ion implantation conditions are as follows: the energy is 60 keV, the dose is 7×10^{16} cm^{-2}, and the ion current density is 10 μA/cm^2. Ion implantation provides the formation of a composite layer that incorporates silver nanoparticles in the surface region of glass. The size distribution of nanoparticles over the depth in the composite layer is strongly nonuniform. The effect of a high-power pulsed excimer laser on the composite layer is investigated. It is found that, under laser irradiation, the size of silver nanoparticles in the implanted layer decreases but the size distribution of nanoparticles over the depth remains nonuniform, even though it becomes slightly narrower compared to that observed prior to irradiation. The experimental results are interpreted in terms of the effects of the melting of glass and metallic particles on a nanosecond scale. © *2001 MAIK "Nauka/Interperiodica".*

1. INTRODUCTION

Investigation into the action of high-power laser pulses on dielectrics containing metallic nanoparticles (DMNs) for the purpose of producing materials with new optical properties is an urgent problem [1, 2]. The considerable attention focused on this problem in recent years has been motivated by rapid progress in modern microelectronics based on nanostructured materials and the necessity of elaborating basic concepts regarding the effect of high-power light beams on the properties of inhomogeneous composite media [3]. In particular, numerous works in this field have been aimed at analyzing controllable changes in size, geometric shape, size distribution, and in phase structure of metallic nanoparticles. For example, a number of experimental works dealt with the pulsed laser (Nd : YAG) processing of aqueous silver colloidal solutions prepared by chemical deposition [4] and metal–polymer nanostructures [5]; photochromic aluminosilicate glasses containing metallic nanoparticles [6]; and optical waveguides based on sodium calcium silicate glasses with silver clusters synthesized through the ion-exchange technique followed by ion or electron irradiation [7, 8]. Of special interest are the studies concerned with laser processing of various DMNs synthesized by ion implantation [9, 10]. Note that ion implantation is a very promising method for the production of nanoparticles [9, 11]. This method makes it possible to attain the highest filling factors upon incorporation of metal atoms into the solid matrix beyond the equilibrium solubility limit. Materials synthesized through ion implantation can be successfully modified by varying parameters such as the lasing wavelength, pulse energy, and pulse duration. Battaglin *et al.* [12] showed that spherical titanium silicide nanoparticles produced by ion implantation in quartz can be transformed into ellipsoidal particles under exposure to Nd : YAG laser radiation in the visible and near-IR spectral ranges. Bukharaev *et al.* [13] demonstrated that the crystal structure of iron particles implanted into silicon dioxide can be modified under exposure to ruby laser radiation (λ = 690 nm).

In all the aforementioned works, laser processing was performed at wavelengths corresponding to the spectral range of optical transparency of the dielectric matrices used in the experiments and, hence, high-power laser pulses were absorbed by metallic nanoparticles. Recently, Wood *et al.* [14] proposed a new approach to the laser annealing of implanted DMNs. According to this approach, sodium calcium silicate glasses with silver nanoparticles are exposed to high-power pulses of an ArF excimer laser at a wavelength of 193 nm, which corresponds to the absorption range of these glasses. It was found that the reflectivity of DMNs decreases under laser irradiation due to structural modification of the glasses or implanted metallic particles. This technique has opened up fresh opportunities for controlling changes in nanoparticle size in DMNs with the use of laser technology. In our recent works [1, 2], we used a combined technique of KrF

excimer laser (λ = 248 nm) processing and thermal annealing in order to decrease the scatter in the size of silver nanoparticles implanted into sodium calcium silicate glasses.

Although practical advances have been made in this area, a number of problems concerning the mechanisms responsible for the modification of DMNs subjected to high-power laser pulses, specifically under irradiation of materials at wavelengths corresponding to the absorption of dielectrics, remain unresolved. The aim of the present work was to investigate experimentally the effect of high-power laser pulses on DMNs formed through implantation and to elucidate the regularities in the transformations of metallic nanoparticles.

2. EXPERIMENTAL TECHNIQUE

Sodium calcium silicate glass (Societa Italiana Vetro) with a homogeneous composition of chemical components (70% SiO_2, 20% Na_2O, 10% CaO) and an optical transparency of ~90% in the spectral range 350–900 nm was used as a substrate for a composite material. Samples were prepared in the form of 0.15-mm-thick plates 2×2 cm in size. The implantation was performed on a Whickham implanter with $^{107}Ag^+$ ions at an energy of 60 keV with a dose of 7×10^{16} ion/cm^2 and an ion current density of 10 μA/cm^2 under vacuum (the residual pressure was 10^{-5} Torr). The substrate temperature during the implantation did not exceed 45°C. The laser processing of implanted glasses was carried out using five pulses of a krypton excimer laser (ALTEX 210) at a frequency of 1 Hz. The pulse duration was equal to 25 ns. The wavelength was 248 nm, which corresponded to the spectral absorption range of the glass. The total released energy was equal to 0.2 J/cm^2. The change in energy from pulse to pulse was checked against a DGX FL150A-EX-RP (OPHIR) laser energy meter and did not exceed 2%. The reproducibility of the results of the laser processing of DMNs was checked using five samples implanted and irradiated under identical conditions. Since the differences in the quantities measured did not exceed 8%, we considered the results obtained for only one of these sample.

The distribution of silver atoms over the depth in the glass bulk was determined using the Rutherford backscattering technique with $^4He^+$ ions (1.89 MeV) at the backscattering angle $\theta = 150°$. The $^4He^+$ ions were generated by a van de Graaf electrostatic accelerator. The energy resolution was better than 21 keV, and the ion current density did not exceed 10 nA. The experimental Rutherford backscattering spectra were transformed to the depth profiles of implanted silver ions according to the Data Furnace software package [15]. The uniformity of the size distribution of nanoparticles in the samples was checked using reflection and transmission optical spectroscopy. The optical spectra were measured at room temperature with a Monolight single-beam waveguide instrument in the wavelength range 300–800 nm at normal light incidence to the sample surface. The microtopograms of the surface of the implanted samples and the samples exposed to laser radiation were obtained using a Solver-P4 scanning probe microscope operating in the atomic-force microscope (AFM) mode. The measurements were performed in the vibrational mode. The vibration amplitude of the microprobe near its resonance frequency varied from 10 to 100 nm. The vertical displacement of a sensitive probe in the microscope in the course of line-by-line scanning of the sample surface was recorded with the use of a low-intensity laser beam reflected from an analyzing tip. The surface profile was formed upon short-term touch of the surface by a tip (tapping mode). All the scanned area was 2×2 μm. The measurements were carried out in air.

3. ION SYNTHESIS OF DMN

It is known that low-energy (<100 keV) ion implantation leads to a statistically nonuniform distribution of implanted metal ions over the glass depth [16]. This implies that the depth distribution differs from the typical symmetrical Gaussian profile predicted in accordance with traditional statistical theories [17]. In the experimental (obtained using Rutherford backscattering) distributions of silver ions in sodium calcium silicate glass under the ion implantation conditions used in the present work, the concentration of the impurity metal is maximum near the irradiated glass surface and monotonically decreases when going deeper into the sample down to 60 nm. The features of these distributions were previously explained in [18, 19] by the effects of surface sputtering and dynamic changes in the phase composition of glass during ion implantation; close examination of these features is beyond the scope of the present work.

An excess of silver concentration in glass above the solubility limit in the course of ion implantation leads to nucleation of the metallic nanoparticles. By assuming that the nucleation and growth of nanoparticles result from the sequential addition of silver atoms (neutralized implanted Ag^+ ions), the inference can be made that these processes depend on both the diffusion coefficient and the local concentration of silver atoms. At a relatively low mobility of silver atoms in the glass matrix at temperatures close to room temperature, nanoparticles predominantly grow at the expense of newly implanted metal ions (the so-called particle growth under conditions of limited diffusion [11, 20]). Since the absolute concentration of metal ions in the implanted layer increases according to the distribution of impurities over the depth, the sizes of metallic particles formed at different depths appear to be proportional to the metal filling factor of the glass at the same depth; i.e., they are determined by the concentration profile of implanted ions. Therefore, in the studied samples with a maximum silver concentration near the surface, the largest nanoparticles are also formed near the surface and a decrease in the impurity concentration

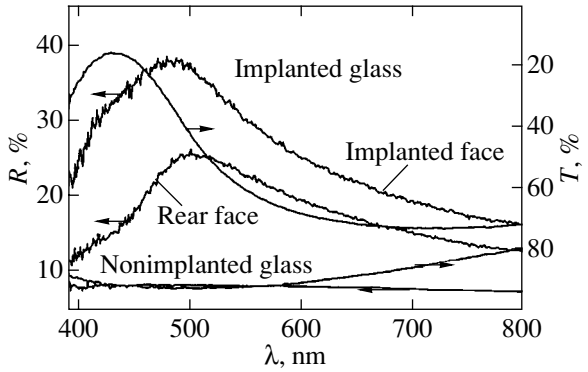

Fig. 1. Transmittance (*T*) and reflectance (*R*) optical spectra of sodium calcium silicate glass implanted with silver ions. The reflectance is measured for the implanted and rear faces of the sample.

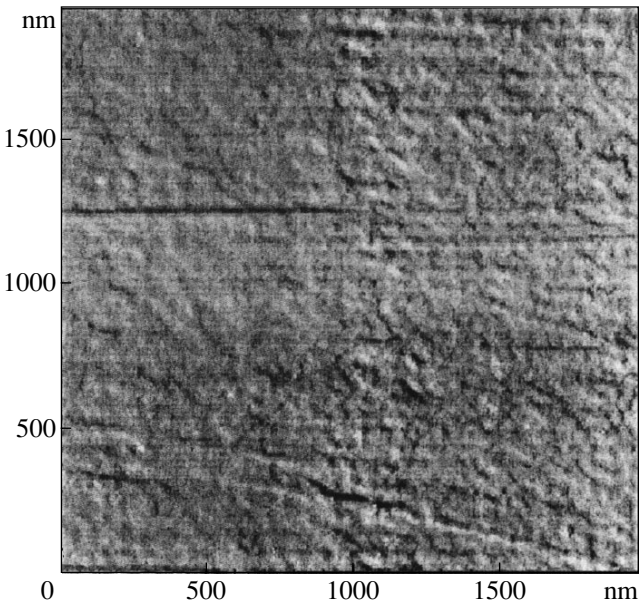

Fig. 2. AFM image of the surface of sodium calcium silicate glass prior to ion implantation.

deep into the sample is attended by a decrease in the particle size. This nonuniform size distribution of nanoparticles in the bulk has been confirmed by electron microscopic observations of cross sections of implanted glasses [21].

Figure 1 shows the experimental reflectance and transmittance optical spectra of sodium calcium silicate glass implanted with silver ions. The broad selective spectral bands observed in the visible range due to the formation of silver nanoparticles in the glass are associated with the plasma polariton resonance [22, 23]. The transmittance spectra (typical of the chosen implantation conditions [21–24]) measured for the implanted and rear faces of sodium calcium silicate glass turn out to be identical and exhibit a deep, almost symmetrical minimum near 430 nm. The reflectance spectra have a more complex shape and differ for the implanted and rear sample faces. The reflectance spectrum of the implanted surface consists of overlapping bands with a clear-cut shoulder in the short-wavelength range and a maximum at 490 nm. The reflectance spectrum of the rear sample face exhibits a pronounced maximum in a longer-wavelength range at approximately 505 nm. Consequently, reflection optical spectroscopy can be applied to evaluate qualitatively the degree of nonuniformity of the size distribution of nanoparticles over the sample depth. It should be noted that this technique is less laborious and expensive than electron microscopy [22].

The AFM images of the surface of sodium calcium silicate glass prior to and after the ion implantation are displayed in Figs. 2 and 3, respectively. As can be seen, the surface of the nonimplanted glass is virtually smooth, whereas the implanted sample surface is characterized by hemispherical bumps and hollows with a mean size of ~100–150 nm. The formation of this structure (Fig. 3) is associated with the sputtering of the glass surface that occurs during ion implantation, which results in the uncovering of metallic nanoparticles nucleated in the surface layer [25, 26]. Approximate calculations demonstrate that the thickness of the sputtered sodium calcium silicate glass layer at the used energy and dose of the ion implantation is equal to several tens of nanometers [19].

4. IRRADIATION OF DMN WITH HIGH-POWER LASER PULSES

4.1. Size distribution of nanoparticles over the depth. The Rutherford backscattering spectra of silver-implanted sodium calcium silicate glasses prior to and after laser irradiation are depicted in Fig. 4. As follows from these spectra, the exposure of the glass to high-power laser pulses brings about a decrease in the silver concentration by approximately 30%. A similar pattern was observed earlier upon exposure of inorganic glasses containing silver [14] and bismuth [27] clusters to excimer laser radiation and was explained by the heating of DMNs followed by the evaporation of metal atoms from the glass surface. At the same time, it can be seen from Fig. 4 that the laser irradiation leads not to a shift in the silver concentration maximum but to a certain broadening of the silver distribution toward deeper regions. It is evident that the observed diffusion outflow of silver atoms from the sodium calcium silicate glass surface is also determined by the heating of DMN material during its interaction with a laser pulse. It is believed that the thermal diffusion and evaporation of silver from the surface of sodium calcium silicate glass should necessarily be preceded by the decomposition of nanoparticles into individual atoms.

The transmittance and reflectance optical spectra of the implanted samples after pulsed laser processing are shown in Fig. 5. It is seen from the transmittance spec-

tra (Fig. 5a) that the intensity of the band corresponding to the absorption associated with silver nanoparticles in the initial implanted sample is considerably less (16% at a minimum) than that (23%) for the sample subjected to laser processing. Moreover, the minimum of the transmission band of the composite glass after laser processing is insignificantly shifted (by 3–5 nm) toward the short-wavelength range. The laser processing more noticeably affects the reflectance spectra of different sample faces (Figs. 5b, 5c). The reflection band in the spectrum of the implanted surface subjected to laser irradiation is narrower than that of the initial implanted sample. The reflection band maximum is shifted toward the short-wavelength range (from 490 to 450 nm), and its intensity decreases from 38 to 27%. A similar (though not so pronounced) shift in the reflection band (by ~5 nm) is observed in the spectrum of the rear nonimplanted face. In this case, the maximum of the spectral band is located at 500 nm and its intensity decreases to 13%. However, despite the symbate shift in the reflection bands toward the UV spectral range after laser irradiation, they differ noticeably. This indicates that the size distribution of silver particles over the depth in sodium calcium silicate glass remains nonuniform; however, the nonuniformity becomes less pronounced than that in the implanted samples prior to laser annealing. A decrease in the intensity of the reflection bands is caused by a decrease in the concentration of silver nanoparticles after laser irradiation.

According to the Mie theory as applied to the optical properties of small-sized metallic particles [23], the shift observed in the location of the reflection band maxima toward the short-wavelength range suggests that the pulsed laser processing of implanted sodium calcium silicate glasses results in a decrease in the mean size of metallic nanoparticles. On the other hand, in the framework of the effective medium theory [22, 23], the observed short-wavelength shift in the spectra of silver-implanted glasses should be interpreted as a decrease in the factor of filling of the surface glass layer by metallic particles, i.e., as a decrease in the fraction of silver that occurs as nanoparticles rather than as individual atoms in a dielectric. Since the size distribution of particles over the depth for implanted materials coincides with the concentration profile of an impurity and corresponds to the metal filling factor of the dielectric and, furthermore, the reflectance spectra of the implanted and rear faces remain different after laser irradiation, we can draw the inference that the largest silver nanoparticles are located near the glass surface and their mean size is reduced after laser processing.

The AFM observations confirm the inference that the size of silver nanoparticles in sodium calcium silicate glass decreases under laser irradiation. A comparison of the surface images prior to (Fig. 3) and after laser irradiation (Fig. 6) shows that the size of nanoparticles corresponding to bumps on the surface decreases by approximately one order of magnitude [28].

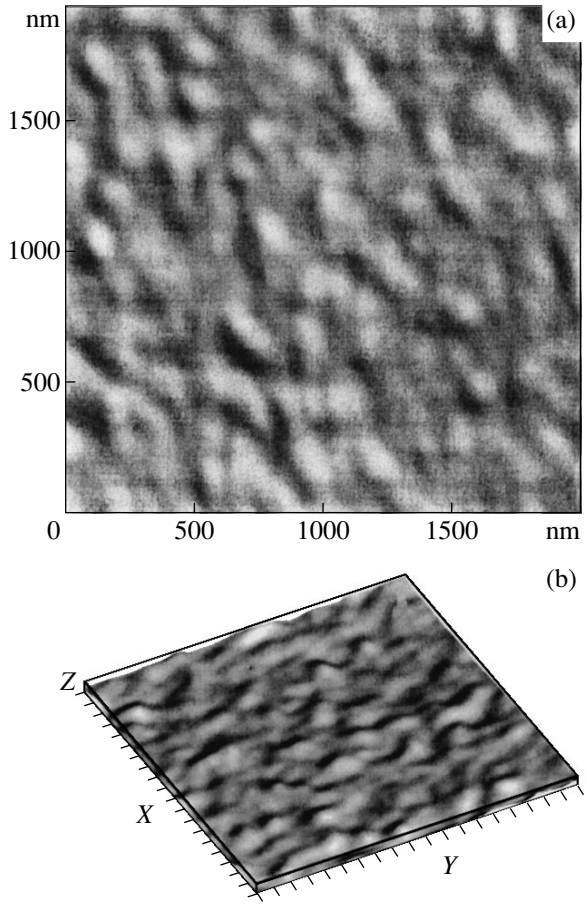

Fig. 3. AFM images of the surface of sodium calcium silicate glass implanted with silver ions: (a) top view and (b) top view under lateral illumination. The step along the *X* and *Y* axes is 100 nm, and the step along the *Z* axis is 3 nm.

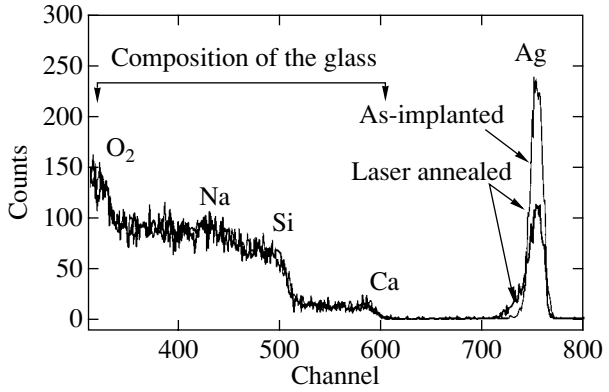

Fig. 4. Rutherford backscattering spectra of sodium calcium silicate glass with implanted silver ions prior to and after laser irradiation.

4.2. Heating and melting of a DMN surface layer under laser irradiation. The interaction between high-power laser radiation and a material depends on the parameters of the beam laser and the physicochem-

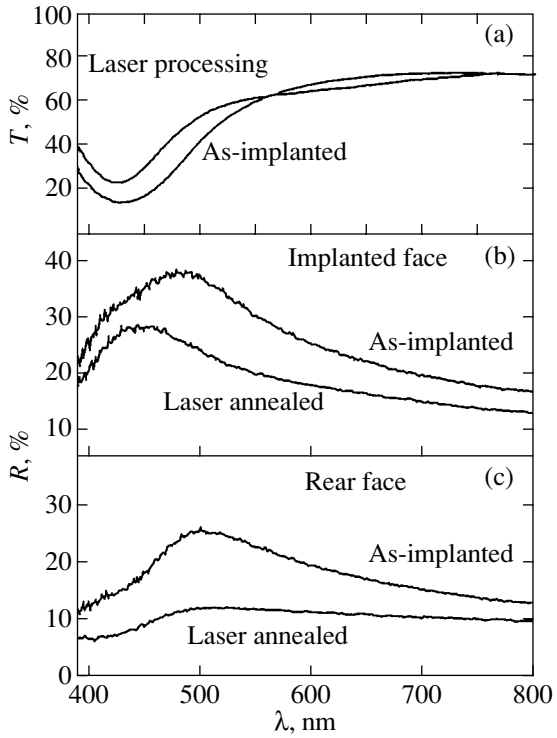

Fig. 5. (a) Transmittance and (b, c) reflectance optical spectra of sodium calcium silicate glass prior to and after pulsed laser irradiation. The reflectance is measured for (b) implanted and (c) rear faces of the sample.

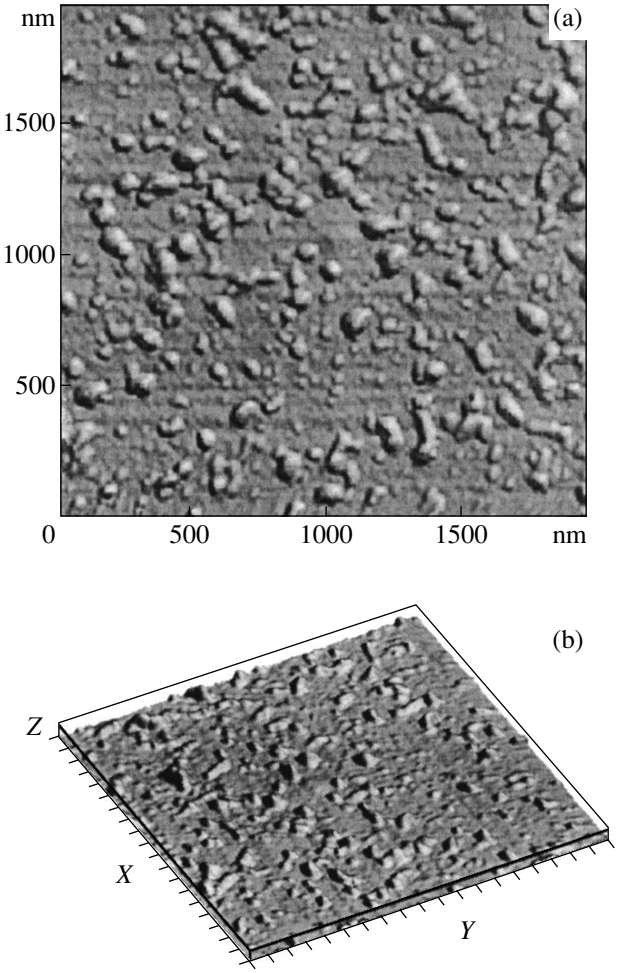

Fig. 6. AFM images of the surface of sodium calcium silicate glass with implanted silver ions after irradiation with an excimer laser: (a) top view and (b) top view under lateral illumination. The step along the *X* and *Y* axes is 100 nm, and the step along the *Z* axis is 40 nm.

ical properties of the DMN composite used. At the initial instant, this interaction is not thermal (does not result in heating) and leads only to electronic and vibrational photoexcitations. Further development of the situation through thermal (photothermal) or nonthermal (photochemical) processes is predominantly governed by the photoexcitation relaxation times. For the DMN materials under consideration, the corresponding excitation and relaxation processes can be divided into those associated with the glass matrix and those with the metallic inclusions. Excimer laser radiation with a wavelength of 248 nm (5 eV) corresponds to the spectral absorption range of sodium calcium silicate glass. Since the band gap of this glass is equal to ~3.5 eV, the laser radiation generates electron–hole pairs via the direct excitation of electrons from the valence band to the conduction band. In metallic silver nanoparticles, laser radiation at the same wavelength brings about the excitation of electrons from both the valence and conduction bands. Consequently, the energy of absorbed photons in the metal immediately transforms into the thermal energy, whereas the absorption of radiation in the glass at the initial stage leads only to an increase in the number of interband electron transitions, i.e., to an increase in the concentration of electron–hole pairs [3]. In metals, the time of electron–electron collisions is of the order of 10^{-14}–10^{-13} s and the times of electron–phonon relaxations are usually one or two orders of magnitude longer [29]. In nonmetallic materials, the times of interband electron transitions lie in the range 10^{-12}–10^{-6} s [3]. Therefore, for the most part, the above times are substantially shorter than the duration of the laser pulse used (25 ns). Thus, the transformation of laser radiation in DMNs can be treated as a relaxation of imparted energy that directly results in heating of the composite material (glass and metal simultaneously), i.e., as such sequential processes as the heating of the surface layer, its melting, and (or) evaporation (ablation) in the time range from nanoseconds to microseconds. For the sodium calcium silicate glasses used, the total energy released during the laser pulse was appreciably lower than the ablation threshold (5 J/cm^2 for the excimer laser at 248 nm [30]), and, hence, surface sputtering was assumed to be absent.

Since the wavelength (248 nm) of the excimer laser is much more than the typical size of nanoparticles synthesized through implantation [9, 21], the optical prop-

erties of the DMN formed can be considered in terms of the effective medium theory [23]. This approach allows us to treat a composite material as homogeneous, to apply the laws of geometrical optics for the directed propagation of light, and to evaluate the optical length α^{-1} of laser pulse penetration into the composite material (where α is the linear absorption coefficient). We consider the case when the laser radiation is absorbed and transforms into thermal energy in the sodium calcium silicate glass layer of thickness α^{-1}. According to the estimates made in [31], this thickness is equal to several microns, which is considerably larger than the thickness of the implanted region. The implanted surface layer, in which the radiation energy is absorbed, can be considered an internal heat source in the sample. The development of the thermal process is governed by the heat source, diffusion redistribution of heat, and its reemission and convection losses. At nanosecond laser pulses, the thickness of the layer absorbing the radiation exceeds the heat diffusion length $L(\tau) = (D\tau)^{1/2}$, where D is the thermal diffusivity of the material and τ is the laser pulse duration. Since the energy of high-power radiation transforms within a relatively thin absorbing layer, the surface region of the sample rapidly heats up and melts [3]. At the pulse duration $\tau = 25$ ns, the heat diffusion length in sodium calcium silicate glass is approximately equal to 115 nm [32]. Although the heat diffusion length L is somewhat less than α^{-1}, it is larger than the thickness of the implanted layer in sodium calcium silicate glass. The estimates performed in our earlier work [32] show that, upon exposure of sodium calcium silicate glass to KrF excimer laser radiation, the temperature at the glass surface reaches 700°C, which exceeds the melting point of this glass. This temperature also appears to be sufficient for the melting of the synthesized silver nanoparticles to take place, because it is known that the melting temperature of metals appreciably decreases when the particle sizes decrease to nanometers [33]. For example, according to Castro *et al.* [34], the melting temperature of silver decreases from 960°C for a bulk material to ~500°C for nanoparticles less than 50 nm in size. Consequently, an increase in the temperature of the glass matrix to a certain temperature exceeding the melting point of metallic nanoparticles brings about their melting, which results in a decrease in particle size up to their complete disappearance. Direct absorption of laser radiation by the metal can also lead to heating of the silver nanoparticles. However, in the heated dielectric matrix containing nanoparticles, their melting should apparently occur at a higher rate. The melting of nanoparticles in the composite layer, as a whole, is a nontrivial process, and its correct description requires consideration of several processes, such as the migration of surface atoms (surface "remelting"), structural fluctuations (quasi-melting), and the formation of mixed liquid–solid phases [33]. The destruction of nanoparticles proceeds in stages. The above effects depend on the nanoparticle size; i.e., small-sized particles decrease more rapidly as compared to large-sized particles. As a result, the size distribution of nanoparticles formed in sodium calcium silicate glass upon ion implantation remains nonuniform after laser processing.

5. CONCLUSION

Thus, we investigated the formation of silver nanoparticles in sodium calcium silicate glass through ion implantation and their modification under exposure to high-power pulses of an excimer laser. It was demonstrated that the size distribution of nanoparticles over the depth is not uniform. The largest-sized silver clusters are formed near the surface, and the decrease in impurity concentration deep into the sample is attended by a decrease in the particle size. Exposure to high-power pulses of the excimer laser leads to heating of the surface layer of sodium calcium silicate glass with silver nanoparticles. This brings about a decrease in the particle size due to melting; however, the scatter in the size of nanoparticles over the depth remains unchanged. It was shown that silver atoms formed upon melting of nanoparticles can both evaporate and be involved in limited diffusion deep into the sample. Consideration was given to the physical principles of the melting of metallic nanoparticles in dielectrics under laser irradiation.

ACKNOWLEDGMENTS

We would like to thank Prof. P. Townsend (University of Sussex, UK) for many pieces of helpful advice regarding the performance of the experiments and discussions of the results.

This work was supported by the Russian Foundation for Basic Research, project nos. 99-02-17767 and 00-15-96615. A.L. Stepanov acknowledges the support of Alexander von Humboldt-Stiftung (Germany). V.N. Popok acknowledges the support of the Swedish Natural Science Research Council (SNFR), which made his visit to the Göteborg University and the Chalmers University of Technology possible.

REFERENCES

1. A. L. Stepanov and V. N. Popok, Zh. Prikl. Spektrosk. **68**, 120 (2001).
2. A. L. Stepanov, I. B. Khaĭbullin, P. D. Townsend, D. E. Hole, and A. A. Bukharaev, RF Patent No. 2156490 (2000).
3. D. Bauerle, *Laser Processing and Chemistry* (Springer-Verlag, Berlin, 1996).
4. A. Takami, H. Yamada, K. Nakano, and S. Koda, Jpn. J. Appl. Phys. **35**, L781 (1996).
5. J. Werner, A. Heilmann, and O. Stenzel, Int. J. Electron. **77**, 945 (1994).
6. A. Alella, T. Honda, A. Liu, and L. Hesselink, Opt. Lett. **22**, 967 (1997).

7. F. Gonella, G. Mattei, P. Mazzoldi, *et al.*, Appl. Phys. Lett. **69**, 3101 (1996).
8. D. H. Osborne, R. H. Haglund, Jr., F. Gonella, and F. Garrido, Appl. Phys. B **B66**, 517 (1998).
9. P. D. Townsend, P. J. Chandler, and L. Zhang, *Optical Effects of Ion Implantation* (Univ. of Cambridge Press, Cambridge, 1994).
10. R. F. Haglund, Jr., Mater. Sci. Eng. A **253**, 275 (1998).
11. A. Miotello, G. De Marchi, G. Mattei, *et al.*, Phys. Rev. B **63**, 75409 (2001).
12. G. Battaglin, E. Borsella, E. Cattaruzza, *et al.*, Nucl. Instrum. Methods Phys. Res. B **141**, 274 (1998).
13. A. A. Bukharaev, A. V. Kazakov, R. V. Manapov, and I. B. Khaĭbullin, Fiz. Tverd. Tela (Leningrad) **33**, 1018 (1991) [Sov. Phys. Solid State **33**, 578 (1991)].
14. R. A. Wood, P. D. Townsend, N. D. Skelland, *et al.*, J. Appl. Phys. **74**, 5754 (1993).
15. N. P. Barradas, C. Jeynes, and R. P. Webb, Appl. Phys. Lett. **71**, 291 (1997).
16. P. D. Townsend, J. C. Kelly, and N. E. W. Hartley, *Ion Implantation, Sputtering, and Their Application* (Pergamon, London, 1976).
17. J. F. Ziegler, J. P. Biersak, and U. Littmark, *The Stopping and Range of Ions in Solids* (Pergamon, New York, 1996).
18. A. L. Stepanov, V. A. Zhikharev, D. E. Hole, *et al.*, Nucl. Instrum. Methods Phys. Res. B **166**, 26 (2000).
19. A. L. Stepanov, V. A. Zhikharev, and I. B. Khaĭbullin, Fiz. Tverd. Tela (St. Petersburg) **43**, 733 (2001) [Phys. Solid State **43**, 766 (2001)].
20. A. C. Zettlemoyer, *Nucleation* (Pergamon, New York, 1969).
21. L. C. Nistor, J. van Landuyt, J. D. Barton, *et al.*, J. Non-Cryst. Solids **162**, 217 (1993).
22. A. L. Stepanov, Opt. Spektrosk. **89**, 444 (2000) [Opt. Spectrosc. **89**, 408 (2000)].
23. U. Kreibig and M. Vollmer, *Optical Properties of Metal Clusters* (Springer-Verlag, Berlin, 1995).
24. A. L. Stepanov, D. E. Hole, and P. D. Townsend, J. Non-Cryst. Solids **260**, 65 (1999).
25. A. A. Bukharaev, V. M. Janduganov, E. A. Samarsky, and N. V. Berdunov, Appl. Surf. Sci. **103**, 49 (1996).
26. M. T. Pham, W. Matz, and H. Seifarth, Anal. Chim. Acta **350**, 209 (1997).
27. S. Y. Park, T. Isobe, M. Senna, *et al.*, Appl. Phys. Lett. **73**, 2687 (1998).
28. A. A. Bukharaev, D. V. Ovchinnikov, N. I. Nurgazizov, *et al.*, Fiz. Tverd. Tela (St. Petersburg) **40**, 1277 (1998) [Phys. Solid State **40**, 1163 (1998)].
29. J. Y. Bigot, J. C. Merle, O. Cregut, and A. Daunois, Phys. Rev. Lett. **75**, 4702 (1995).
30. C. Buerhop, B. Blumenthal, R. Weissmann, *et al.*, Appl. Phys. Lett. **46**, 430 (1990).
31. P. D. Townsend and J. Olivares, Appl. Surf. Sci. **109**, 275 (1997).
32. A. L. Stepanov, D. E. Hole, and P. D. Townsend, Nucl. Instrum. Methods Phys. Res. B **149**, 89 (1999).
33. L. D. Marks, Rep. Prog. Phys. **57**, 603 (1994).
34. T. Castro, R. Reifenberg, E. Choi, and R. P. Andres, Phys. Rev. B **42**, 8548 (1990).

Translated by O. Borovik-Romanova

Physics of the Solid State, Vol. 43, No. 11, 2001, pp. 2199–2203. Translated from Fizika Tverdogo Tela, Vol. 43, No. 11, 2001, pp. 2107–2111.
Original Russian Text Copyright © 2001 by Kilian, Vettegren, Svetlov.

LOW-DIMENSIONAL SYSTEMS AND SURFACE PHYSICS

Hierarchy of Defect Ensembles on the Surface of Loaded Copper

H. G. Kilian*, V. I. Vettegren, and V. N. Svetlov****

** Abteilung of Experimentelle Physik, Universität Ulm, Ulm, D-89069 Germany*

*** Ioffe Physicotechnical Institute, Russian Academy of Sciences, Politekhnicheskaya ul. 26, St. Petersburg, 194021 Russia*

e-mail: Victor.Vettegren@pop.ioffe.rssi.ru

Received March 22, 2001

Abstract—The evolution of the distribution of nanodefects formed on the surface of polished copper foils under tensile stresses is investigated. It is found that nanodefects form four ensembles. The energies of formation and the mean sizes of nanodefects in two consecutive ensembles differ, respectively, by a factor of three. When the concentration of nanodefects in a particular ensemble reaches a thermodynamically optimum value (≈5%), some of these nanodefects annihilate and the other nanodefects transform to nanodefects of the following ensemble. The load applied to the sample continuously generates nanodefects comprising the first ensemble, which leads to periodic oscillations of the nanodefect concentration in all four ensembles. © *2001 MAIK "Nauka/Interperiodica".*

1. INTRODUCTION

Recent investigations [1–8] of the surface of metals (Cu, Au, Mo, and Pd) with the use of scanning tunneling microscopy have demonstrated that defects of nanometer size are formed on the polished metal surface under tensile stresses (Fig. 1). These defects are generated and annihilate through the motion of material strips in the directions parallel to the dislocation glide planes. In our previous work [8], the nanodefect formation was considered within the model of reversible aggregation of atomic steps formed at sites of the emergence of dislocations on the metal surface. It was found that the distribution $n(y)$ (where y is the size of a nanodefect, i.e., the length of its walls) is determined by the maximum entropy and can be described by the canonical distribution of the thermodynamic probability. As is known [9], this distribution can be represented in the form of the Γ-function density:

$$n(y) = n_0 y^2 \exp(-\beta y \Delta U_0). \quad (1)$$

Here, ΔU_0 is the energy of aggregation of atomic steps, $\beta \equiv 1/k_B T$, k_B is the Boltzmann constant, T is the temperature, and n_0 is the normalization constant.

The mean size of nanodefects $\langle y \rangle$ and the energy of their formation ΔU_0 are related by the expression [8]

$$\langle y \rangle = \frac{\beta \Delta U_0}{3}. \quad (2)$$

The aim of the present work was to investigate the accumulation kinetics of nanodefects on the surface of loaded copper and to elucidate the hierarchy of the distribution of their ensembles.

2. EXPERIMENTAL TECHNIQUE

We studied the surface profiles of high-purity copper (99.96%) foils approximately 60 μm thick. The samples were cut out parallel to the axis of foil rolling by using special knives, polished with a GOI paste, and washed in alcohol and acetone. A spring device designed at the laboratory was used for loading the samples.

The topograms of the copper surface under a load of 380 MPa were recorded at different instants of time after loading. The scanned area was 10 × 10 μm, and the distance between two sequential scans was equal to 100 nm. By this means, only the nanodefects whose lengths were greater than 50 nm could be recorded.

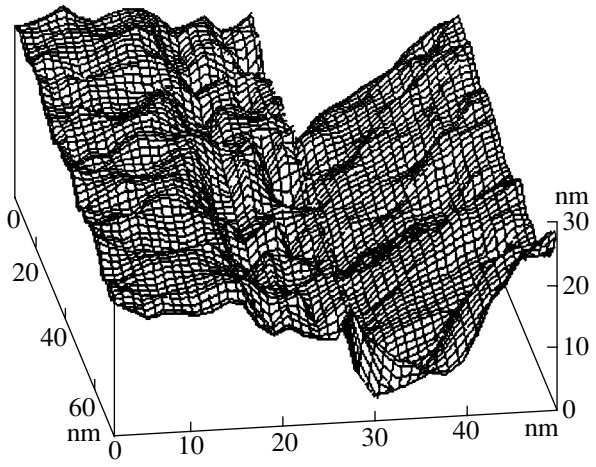

Fig. 1. A nanodefect formed on the copper surface under load.

1063-7834/01/4311-2199$21.00 © 2001 MAIK "Nauka/Interperiodica"

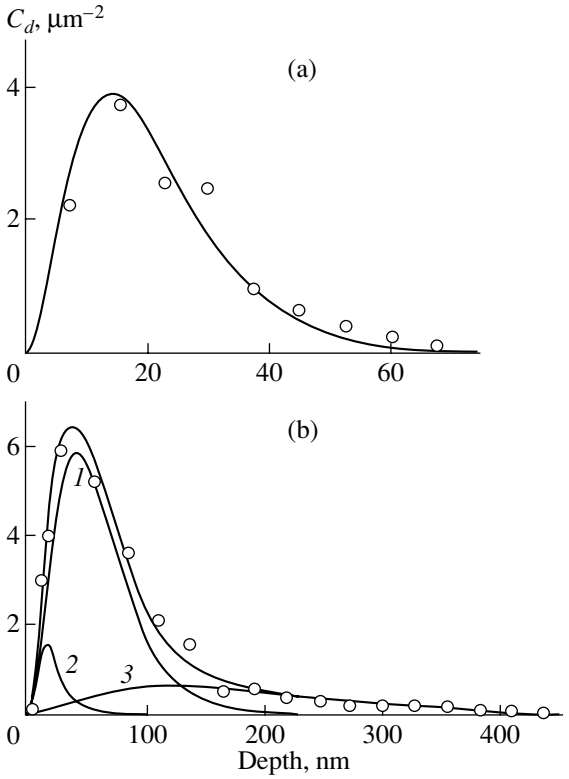

Fig. 2. Depth distributions of nanodefects on the surface of copper within (a) 21 and (b) 144 h after loading. Solid lines correspond to calculations according to (a) relationship (1) and (b) relationship (3). (*1–3*) Distributions of nanodefects for the first, second, and third ensembles.

The shape of a nanodefect on the copper surface (see Fig. 1) does not depend on its size. As can be seen from Fig. 1, one of the nanodefect walls is nearly perpendicular to the surface and the second wall makes an angle of ≈30° with the surface. In order to determine the length y of the walls of a nanodefect, it was sufficient to measure its depth d (i.e., the length of the wall perpendicular to the surface) and to calculate y ($y \approx 3.92d$). The nanodefect depth was measured for each scan. Large-sized nanodefects (with a length of more than 200–300 nm) were intersected by scans several times; however, their depths differed from one another in two sequential scans. These findings were explained under the assumption that, in our samples, the length of dislocations emerging on the surface was less than 100 nm. Hence, the different cross sections of a large-sized nanodefect were considered independent.

The magnification of the image in the direction perpendicular to the surface plane was equal to 6.7×10^4. This made it possible to examine nanodefects more than ≈4 nm in depth. The number of nanodefects in the topograms ranged from 1500 to 5500 depending on the time elapsed after loading of the sample, which ensured sufficiently reliable statistical size distribution of the nanodefects.

3. SIZE DISTRIBUTIONS OF DEFECTS

A detailed analysis of the topograms demonstrated that the empirical size distribution of nanodefects is described by relationship (1) only at short times elapsed after loading: $t \le 0.1\tau_f$, where τ_f is the time prior to fracture of the sample (sample endurance) (Fig. 2a). At $t > 0.1\tau_f$, the size distribution of nanodefects should be described using at least four expressions of type (1) with different energies ΔU_{0i} (Fig. 2b):

$$n_e(y) = \sum_{i=1}^{4} n_{0i} y_i^2 \exp(-\beta y_i \Delta U_{0i}). \qquad (3)$$

Consequently, all nanodefects can be divided into four ensembles. The energies of formation of nanodefects comprising these four ensembles are as follows: $\Delta U_{01} \approx 0.058 k_B T$ for the first ensemble, $\Delta U_{02} \approx 0.019 k_B T$ for the second ensemble, $\Delta U_{03} \approx 0.0063 k_B T$ for the third ensemble, and $\Delta U_{04} \approx 0.0021 k_B T$ for the fourth ensemble. The mean depths of nanodefects in these ensembles are as follows: $\langle d_1 \rangle = 20$ nm for the first ensemble, $\langle d_2 \rangle = 60$ nm for the second ensemble, $\langle d_3 \rangle = 180$ nm for the third ensemble, and $\langle d_4 \rangle = 550$ nm for the fourth ensemble.

Therefore, the energies of formation and the mean depths of nanodefects in two consecutive ensembles differ, respectively, by a factor of three:

$$\frac{\Delta U_{01}}{\Delta U_{02}} = \frac{\Delta U_{02}}{\Delta U_{03}} = \frac{\Delta U_{03}}{\Delta U_{04}} = \frac{\langle d_2 \rangle}{\langle d_1 \rangle} = \frac{\langle d_3 \rangle}{\langle d_2 \rangle} = \frac{\langle d_4 \rangle}{\langle d_3 \rangle} = 3. \qquad (4)$$

In addition to the distribution of nanodefects on the surface of loaded metal (Cu, Mo, Au, and Pd) foils, relationship (1) adequately describes the size distributions of carbon black aggregates in filled rubbers [10], supramolecular formations on the surface of vitreous poly(methyl methacrylate) [11], *E-coli* bacteria [12], and yeast fungi [12], as well as the angular distribution of dislocation boundaries in deformed Al samples [13]. Therefore, the stationary Γ-distribution over sizes in the studied systems is attained in a state that is far from equilibrium even though the concentration of structural units continuously varies with time.

4. ACCUMULATION KINETICS OF DEFECTS

In order to elucidate the factors responsible for the formation of nanodefect ensembles, we investigated the accumulation kinetics of nanodefects at different times elapsed after loading. As an example, Fig. 3 displays four fragments of the topograms of the copper surface, which were recorded within 16, 165, 238, and 356 h after loading of the sample. It can be seen that the defect concentration in the topograms obtained within 16 and 238 h after loading is higher than that in the two other cases (within 165 and 356 h after loading).

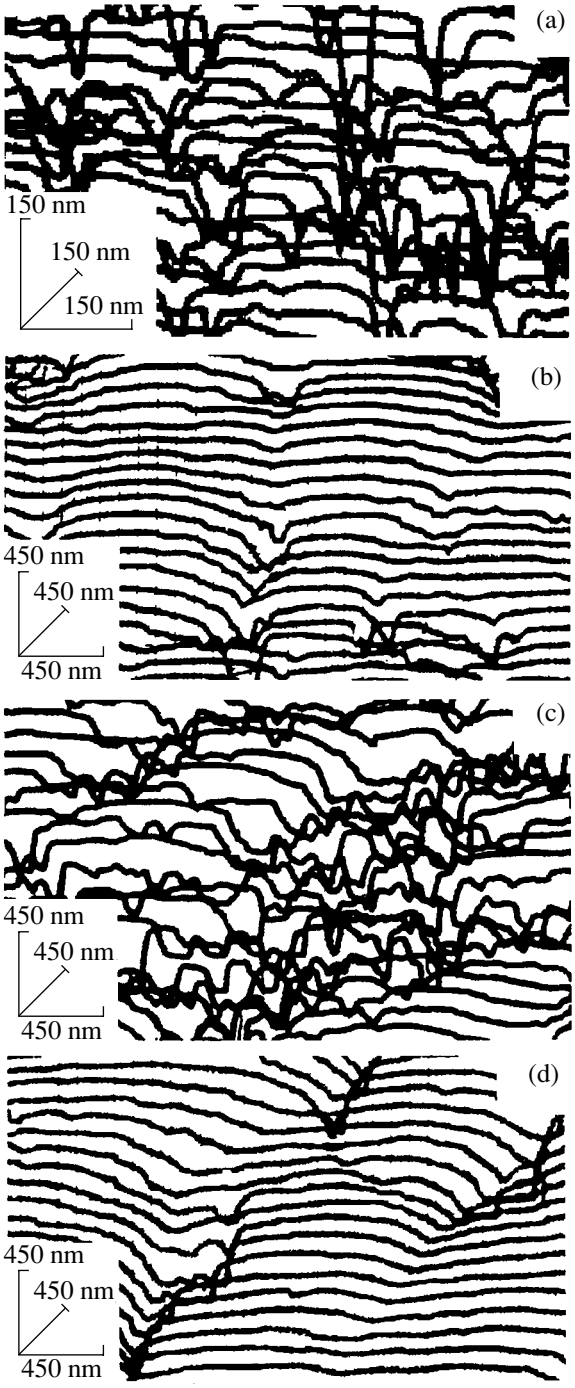

Fig. 3. Fragments of the topograms of the copper surface at different instants of time after loading: (a) 16, (b) 165, (c) 238, and (d) 356 h.

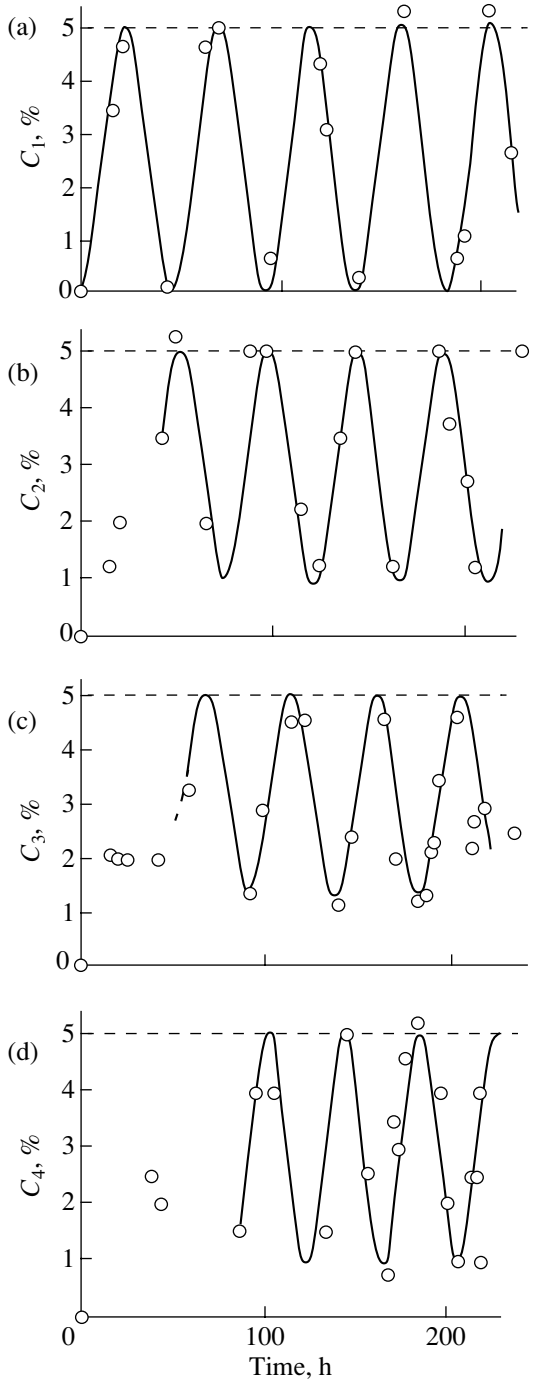

Fig. 4. Time dependences of the concentration of nanodefects forming four ensembles on the copper surface. Mean nanodefect depth in each ensemble: (a) 20, (b) 60, (c) 180, and (d) 540 nm.

A close examination of the topograms revealed that both the total concentration of nanodefects and their concentrations in each of the four ensembles oscillate with time. The oscillation period is approximately equal to 45 h (Fig. 4). The nanodefect concentrations in consecutive ensembles oscillate in antiphase: an increase in the concentration of large-sized nanodefects is always attended by a decrease in the concentration of small-sized nanodefects. Therefore, the kinetics of defect formation has a hierarchic character; i.e., nano-

defects of the $(i + 1)$th rank are formed only from nanodefects of the ith rank. This is clearly seen from Fig. 4: the deeper the nanodefects forming a particular ensemble, the longer the time it takes for the nanodefect concentration to begin to vary periodically with time.

Tomilin *et al.* [14, 15] revealed that the initiation of cracks formed in Westerly and Harcourt granites under compressive stresses is hierarchic in character and that the cracks also form four ensembles. It seems likely that the defect formation in loaded materials exhibits a hierarchic character not only in metals but in other solids as well.

The maximum concentration of nanodefects in each ensemble is found to be $X_c = 5 \pm 1\%$. Earlier [8], we proved that this value corresponds to the thermodynamically optimum concentration of nanodefects in the surface layer of metals. At this concentration, the mean distance $\langle L \rangle$ between two neighboring defects is e times larger (where e is the base of natural logarithm) than their mean size $\langle y \rangle$ [8]:

$$\frac{\langle L \rangle}{\langle y \rangle} = \frac{1}{\sqrt[3]{X_c}} \approx 2.7. \quad (5)$$

Numerous investigations of crack accumulation in various solids (polymers, metals, ionic crystals, glasses, and rocks) under load [15–18] have demonstrated that cracks begin to coalesce when their concentration in the bulk of a solid reaches the value at which criterion (5) is satisfied. The above results indicate that the criterion for coalescence (5) is valid for both cracks and nanodefects on the surface of loaded metals.

The observed oscillations of the nanodefect concentration can be explained in terms of this criterion as follows. The stresses bring about the emergence of dislocations on the surface, which, in turn, leads to the formation of first-rank nanodefects. The concentration of nanodefects increases to a thermodynamically optimum value $X_c \approx 0.05$, at which the entropy of mixing nanodefects with atoms of the crystal lattice becomes maximum [8]. Thereafter, some of these nanodefects annihilate, while the other nanodefects increase in depth by a factor of three and form an ensemble of second-rank nanodefects. The concentration of second-rank nanodefects increases and reaches 5%, after which a portion of these nanodefects annihilate and the other nanodefects transform into third-rank nanodefects, etc. This process is thermodynamically favorable, because the energy of formation of new large-sized nanodefects is less than that of small-sized nanodefects by a factor of three. The load applied to the sample continuously generates new portions of first-rank nanodefects. As a result, after the transformation of some of these nanodefects into second-rank nanodefects, the first-rank nanodefects begin to accumulate again and the process occurs over and over.

According to the theory of consecutive reactions [19], the oscillation frequency ν and the rate constant k_1 for the formation of first-rank defects are related by the expression

$$k_1 \approx 12\nu. \quad (6)$$

Under the experimental conditions (room temperature and a load of 380 MPa), we have $\nu \approx 6.2 \times 10^{-6}$ s^{-1} and $k_1 \approx 7.4 \times 10^{-5}$ s^{-1}. At the same time, the rate of steady-state creep $\dot{\varepsilon}$ is two orders of magnitude smaller: $\dot{\varepsilon} \approx 6 \times 10^{-7}$ s^{-1}.

In the case when the formation of nanodefects occurs as the result of thermal fluctuations, the activation energy of formation is $U_1 = k_B T \ln \frac{k_0}{k_1} = k_B T \ln \frac{10^{13}}{k_1} \approx 43$ kJ/mol and the activation energy of steady-state creep is $U_0 = k_B T \ln \frac{10^{13}}{\dot{\varepsilon}} \approx 52$ kJ/mol.

5. THE MECHANISM OF NANODEFECT COALESCENCE

In many studies concerned with the accumulation of cracks in loaded materials, the crack coalescence subject to condition (5) is interpreted under the assumption that cracks are randomly arranged in a loaded solid. In this case, the possibility exists of forming clusters in which several small-sized cracks appear very close to one another and coalesce to form a large-sized crack.

This concept is in good agreement with the results obtained in the study of nanodefects. The nanodefect walls consist of steps 5–50 nm wide (Fig. 1), which are formed upon the emergence of dislocations generated by a cluster of nearby sources [1, 2, 5, 6].

As follows from the results described above, the clusters of dislocation sources are delocalized in the surface layer of loaded metals. Analysis of the distribution of nanodefects shows that the clusters of dislocation sources also form four ensembles in which the distributions are represented by expression (1) for the Γ-function density.

The length of the nanodefect walls in the first-rank ensemble is approximately equal to 80 nm. These walls are formed upon the emergence of ≈300 dislocations generated by clusters of first-rank sources. The second ensemble involves clusters of second-rank dislocation sources that generate ≈900 dislocations. The third and fourth ensembles consist of clusters generating ≈2700 and ≈8000 dislocations, respectively.

The load applied to the sample generates dislocation sources at a rate equal to the creep rate. The rate of formation of first-rank clusters from these sources is two orders of magnitude higher. Then, there arise clusters of second-rank dislocation sources, etc.

6. CONCLUSION

Thus, it was demonstrated that nanodefects form four ensembles on the surface of loaded copper. The energy of formation of nanodefects in each of the following ensembles is three times smaller and the size of these nanodefects is three times larger than those in the preceding ensemble. When the concentration of nanodefects in a particular ensemble reaches a thermodynamically optimum value (≈5%), some of these nanodefects annihilate and others transform into nanodefects of the following ensemble. The load applied to the sample continuously generates nanodefects that form the first ensemble, which brings about periodic oscillations of the nanodefect concentration in all four ensembles.

ACKNOWLEDGMENTS

This work was supported by the Ministry of Education of the Russian Federation, project no. E00-4.0-21.

REFERENCES

1. V. I. Vettegren, S. Sh. Rakhimov, and V. N. Svetlov, Fiz. Tverd. Tela (St. Petersburg) **38** (2), 590 (1996) [Phys. Solid State **38**, 323 (1996)]; Fiz. Tverd. Tela (St. Petersburg) **38** (4), 1142 (1996) [Phys. Solid State **38**, 632 (1996)]; Fiz. Tverd. Tela (St. Petersburg) **39** (9), 1560 (1997) [Phys. Solid State **39**, 1389 (1997)]; Fiz. Tverd. Tela (St. Petersburg) **40** (12), 2180 (1998) [Phys. Solid State **40**, 1977 (1998)].
2. V. I. Vettegren, S. Sh. Rakhimov, and V. N. Svetlov, Proc. SPIE **3345**, 226 (1998).
3. G. Welzel, J. Plessing, and H. Neuhauser, Phys. Status Solidi A **166**, 791 (1997).
4. J. Plessing, Ch. Achmus, H. Neuhauser, *et al.*, Z. Metallkd. **88** (8), 630 (1997).
5. V. I. Vettegren, V. L. Gilyarov, S. Sh. Rakhimov, and V. N. Svetlov, Fiz. Tverd. Tela (St. Petersburg) **40** (4), 668 (1998) [Phys. Solid State **40**, 614 (1998)].
6. V. I. Vettegren, S. Sh. Rakhimov, and V. N. Svetlov, Neorg. Mater. **35** (6), 756 (1999).
7. M. Kugler, A. Hampel, and H. Neuhauser, Phys. Status Solidi A **175**, 513 (1999).
8. H. G. Kilian, V. I. Vettegren, and V. N. Svetlov, Fiz. Tverd. Tela (St. Petersburg) **42** (11), 2024 (2000) [Phys. Solid State **42**, 2083 (2000)].
9. B. L. Lavenda, *Statistical Physics: A Probabilistic Approach* (Wiley, New York, 1997).
10. H. G. Kilian, to be published in Rubber Chem. Technol. (2001).
11. H. G. Kilian, R. Metzler, and B. Zink, J. Chem. Phys. **107** (12), 8697 (1997).
12. H. G. Kilian, M. Koepf, and V. I. Vettegren, to be published in Prog. Colloid Polym. Sci. (2001).
13. D. A. Hughes, Q. Liu, D. C. Crzan, and N. Hansen, Acta Mater. **45** (1), 105 (1997).
14. N. G. Tomilin, E. E. Damaskinskaya, and V. S. Kuksenko, Fiz. Tverd. Tela (St. Petersburg) **36** (10), 3101 (1994) [Phys. Solid State **36**, 1649 (1994)].
15. V. Kuksenko, N. Tomilin, E. Damaskinskaja, and D. Lockner, Pure Appl. Geophys. **146** (2), 253 (1996).
16. V. S. Kuksenko, V. S. Ryskin, V. I. Betechtin, and A. I. Slutsker, Int. J. Fract. Mech. **11** (4), 829 (1975).
17. V. S. Kuksenko and V. P. Tamuzs, *Fracture Micromechanics of Polymer Materials* (Zinatne, Riga, 1978; Nijhoff, Boston, 1981).
18. V. A. Petrov, A. Ya. Bashkarev, and V. I. Vettegren, *Physical Principles for Prediction of the Fracture in Structural Materials* (Politekhnika, St. Petersburg, 1993).
19. N. M. Emanuel' and D. G. Knorre, *Chemical Kinetics: Homogeneous Reactions* (Vysshaya Shkola, Moscow, 1969; Wiley, New York, 1973).

Translated by O. Borovik-Romanova